Analysis of uncertainty propagation in nuclear fuel cycle scenarios

Guillaume Krivtchik

▶ **To cite this version:**

Guillaume Krivtchik. Analysis of uncertainty propagation in nuclear fuel cycle scenarios. Chemical and Process Engineering. Université de Grenoble, 2014. English. NNT : 2014GRENI050 . tel-01131207

HAL Id: tel-01131207
https://theses.hal.science/tel-01131207

Submitted on 13 Mar 2015

HAL is a multi-disciplinary open access archive for the deposit and dissemination of scientific research documents, whether they are published or not. The documents may come from teaching and research institutions in France or abroad, or from public or private research centers.

L'archive ouverte pluridisciplinaire **HAL**, est destinée au dépôt et à la diffusion de documents scientifiques de niveau recherche, publiés ou non, émanant des établissements d'enseignement et de recherche français ou étrangers, des laboratoires publics ou privés.

UNIVERSITÉ DE GRENOBLE

THÈSE

Pour obtenir le grade de

DOCTEUR DE L'UNIVERSITÉ DE GRENOBLE

Spécialité : **Mécanique des fluides, Énergétique, Procédés**

Arrêté ministériel : 7 août 2006

Présentée par

Guillaume KRIVTCHIK

Thèse dirigée par **Dr. Patrick BLAISE**
et encadrée par **Mme Christine COQUELET-PASCAL, M. Joël LE MER, M. Claude GARZENNE**

préparée au sein du **Laboratoire d'Études du Cycle** et de **l'école doctorale I-MEP2 : Ingéniérie - Matériaux, Mécanique, Environnement, Énergétique, Procédés, Production**

Analysis of uncertainty propagation in nuclear fuel cycle scenarios

Thèse soutenue publiquement le **10 octobre 2014**, devant le jury composé de :

Madame Elsa MERLE-LUCOTTE
CNRS, Présidente
Monsieur Bertrand IOOSS
EDF R&D, Université Paul Sabatier, Rapporteur
Monsieur Sylvain DAVID
CNRS, Rapporteur
Monsieur Patrick BLAISE
CEA, Directeur de thèse
Monsieur Bernard BONIN
CEA, Examinateur
Monsieur Cheikh DIOP
CEA, Examinateur
Madame Christine COQUELET-PASCAL
CEA, Invitée
Monsieur Joël LE MER
EDF R&D, Invité
Monsieur Adrien BIDAUD
CNRS, Invité

Remerciements

Ces travaux de thèse ont été effectués au Laboratoire d'Etudes du Cycle dont je souhaite remercier le chef, Romain Eschbach. De même, je remercie MM. Jean-Paul Grouiller et Frédéric Varaine, ancien et actuel chefs du Service de Physique des Réacteurs et du Cycle du CEA Cadarache.

Je remercie Mme Elsa Merle-Lucotte d'avoir présidé mon jury de thèse, ainsi que MM. Bertrand Iooss et Sylvain David d'avoir relu si attentivement mon manuscrit. Je remercie également les membres de mon jury, MM. Bernard Bonin, Cheikh Diop et Adrien Bidaud, pour leurs questions ô combien nombreuses et pertinentes.

Je souhaite remercier très vivement mon directeur de thèse Patrick Blaise pour ses précieux conseils, son inébranlable jovialité et ses blagounettes tout au long de cette aventure. Je remercie également très chaleureusement mon encadrante CEA Christine Coquelet-Pascal pour son aide et sa disponibilité, sa gentillesse, son dynamisme et ses leçons de vie. Je remercie aussi mes encadrants EDF Joël Le Mer et Claude Garzenne de m'avoir aidé tout en me laissant une grande liberté d'action.

Travailler au sein de l'équipe des scénarios fut un plaisir. Je remercie Maryan pour ses leçons de sagesse et les mille réponses à mes mille questions de première année de thèse, et Marion pour sa gentillesse et sa disponibilité.

Je remercie Cécile de m'avoir encadré durant mon projet de fin d'études, ce qui m'a permis de découvrir le LECy. Merci à David, mon premier stagiaire, pour sa bonne humeur perpétuelle et sa résistance à l'épreuve des métamodèles. Je remercie toute l'équipe du LECy, passée et présente, avec qui j'ai pu discuter, échanger, réfléchir, ou bien à qui j'ai demandé de l'aide. Je souhaite aussi remercier les gens d'autres laboratoires qui ont accepté de m'aider durant ma thèse, en particulier Laurent Buiron pour les scripts et les explications ERANOS, Gilles Noguere pour les matrices de covariance, Amandine Marrel et Michel Marquès pour la propagation de l'incertitude.

Je remercie très chaleureusement Amalia pour son accortise, ses blagues douteuses et pour les pauses thé/café/maté/biscuit/mandarine/banane/abricot (il y a toujours un prétexte) qui ont égayé ce périple, ainsi que Coralie pour sa bonne humeur, sa gentillesse et ses intarissables sujets de conversation. Je remercie le Moison pour son travail quasi-remarquable et son efficacité à presque toute épreuve. Merci aussi à Tatane, à Spennat' et au Docteur pour leur jovialité.

Merci de tout cœur à 瑤子, à mes parents et à mes grand-parents qui ont pris soin de moi pendant ces trois années.

Je remercie sans les citer tous ceux qui m'ont soutenu mais n'auront jamais vraiment envie de lire ce manuscrit. Je ne vous obligerai pas, c'est promis.

雲をりをり
人をやすめる
月見かな

Bashô

Contents

Glossary **25**

1 Introduction **27**
1.1 Context . . . 28
1.2 Analysis of the problem . . . 28
1.3 Physical models for uncertainty propagation . . . 30
1.3.1 Nuclides of interest . . . 30
1.3.2 Cooling computation . . . 30
1.3.3 Irradiation computation . . . 31
1.3.3.1 Surrogate models . . . 31
1.3.3.2 Parameters taken into account . . . 31
1.3.3.3 Construction of surrogate models . . . 31
1.3.3.4 Implementation . . . 32
1.3.4 Equivalence models . . . 33
1.4 Uncertainty data . . . 33
1.4.1 Classification . . . 33
1.4.2 Nuclear data . . . 33
1.4.3 Scenario parameters and hypotheses . . . 34
1.5 Uncertainty propagation studies . . . 34
1.5.1 Method . . . 34
1.5.2 Applications . . . 35

2 Numerical tools **37**
2.1 Evolution: CESAR . . . 38
2.1.1 Introduction . . . 38
2.1.2 Nuclear data . . . 38
2.1.3 Evolution calculation . . . 40
2.1.3.1 Introduction . . . 40
2.1.3.2 Irradiation calculation . . . 40
2.1.3.3 Cooling calculation . . . 42
2.2 Scenario: COSI . . . 42
2.2.1 Introduction . . . 42
2.2.2 Energy, needs and mass flows . . . 43
2.2.2.1 Mass flows . . . 43
2.2.2.2 Energy demand and production . . . 44
2.2.3 Facilities and physical models . . . 44

2.2.3.1 Introduction . . . 44
2.2.3.2 Front-end path . . . 45
2.2.3.3 Reactors and fuel . . . 46
2.2.3.4 Reprocessing plants . . . 47
2.2.3.5 Back-end path . . . 48
2.2.3.6 Waste storage and waste disposal . . . 48
2.2.3.7 Finished warehouses . . . 49
2.2.3.8 Transportation . . . 49
2.2.3.9 Various delays . . . 49
2.3 Neutron transport calculation . . . 49
2.3.1 APOLLO2 . . . 50
2.3.2 ERANOS . . . 50
2.4 Statistical analysis: URANIE . . . 50

3 Evolution models 53
3.1 Irradiation models for actinides . . . 54
3.1.1 Specifications . . . 54
3.1.1.1 Identification of actinides to be estimated . . . 54
3.1.1.2 Accuracy of the estimators . . . 55
3.1.1.3 Remark concerning the short-lived radioactive nuclides . . . 56
3.1.2 Sampling . . . 56
3.1.2.1 Parameters . . . 56
3.1.2.2 Design of experiment . . . 79
3.1.3 Regression . . . 82
3.1.3.1 Polynomial regressions . . . 82
3.1.3.2 Artificial Neural Networks . . . 101
3.2 Irradiation models for fission products . . . 111
3.2.1 Specifications . . . 111
3.2.1.1 Fission products and decay heat . . . 111
3.2.1.2 Fission products involved in decay heat uncertainty . . . 112
3.2.1.3 Accuracy of the estimators . . . 113
3.2.1.4 Fission products to estimate . . . 113
3.2.2 Sampling . . . 115
3.2.2.1 Parameters . . . 115
3.2.2.2 Design of experiment . . . 124
3.2.3 Regression . . . 125
3.2.3.1 Qualitative analysis of the model . . . 125
3.2.3.2 Artificial Neural Networks . . . 126
3.2.4 Calculation of decay heat . . . 131
3.2.4.1 Introduction . . . 131
3.2.4.2 Cooling calculation . . . 133
3.2.4.3 Calculation schema . . . 134
3.2.4.4 Validation of decay heat computation . . . 134
3.3 Blankets . . . 143
3.3.1 Introduction . . . 143
3.3.2 Fertile blanket . . . 143

3.3.2.1 Description . . . 143
3.3.2.2 Methods . . . 144
3.4 Conclusions and perspectives . . . 148
3.4.1 Conclusions . . . 148
3.4.2 Perspectives . . . 148

4 Equivalence models 151
4.1 Introduction . . . 152
4.2 State of the art . . . 152
4.2.1 Presentation . . . 152
4.2.2 Perturbative SFR MOX model . . . 152
4.2.2.1 Equivalent plutonium content . . . 152
4.2.2.2 Uncertainty propagation . . . 154
4.2.2.3 Advantages and drawbacks . . . 154
4.2.3 Transport calculation for SFR MOX . . . 155
4.2.3.1 Overview . . . 155
4.2.3.2 Advantages and drawbacks . . . 155
4.2.4 Tabulated PWR MOX model . . . 156
4.2.4.1 Presentation . . . 156
4.2.4.2 Advantages and drawbacks . . . 156
4.2.5 Conclusions . . . 156
4.3 Data-driven equivalence models . . . 157
4.3.1 Introduction . . . 157
4.3.2 SFR MOX equivalence models . . . 157
4.3.2.1 Introduction . . . 157
4.3.2.2 Method A: estimator based on iterative transport computations . . . 157
4.3.2.3 Method B: straightforward estimation . . . 162
4.3.2.4 Equivalence models for uncertainty propagation studies . . . 166
4.3.3 PWR MOX equivalence model . . . 169
4.3.3.1 Description of the method . . . 169
4.3.3.2 Application . . . 171
4.3.3.3 Analysis of the model . . . 173
4.3.4 Implementation in COSI . . . 174
4.4 Conclusions and perspectives . . . 175

5 Uncertainty data 179
5.1 Introduction . . . 180
5.2 Nuclear data . . . 180
5.2.1 Condensation of covariance matrix . . . 180
5.2.1.1 Introduction . . . 180
5.2.1.2 Condensation of intra-reaction covariance matrices . . . 180
5.2.1.3 Condensation of inter-reaction covariance matrices . . . 182
5.2.1.4 Cross-sections correlation between different spectra . . . 186
5.2.1.5 Results . . . 188
5.2.2 Fission yields . . . 196
5.2.2.1 Introduction . . . 196
5.2.2.2 Fission yields uncertainty . . . 196

5.3 Scenario parameters and hypotheses . . . 196
5.3.1 Introduction . . . 196
5.3.2 Scenario hypotheses . . . 196
5.3.3 Scenario parameters . . . 197
5.3.3.1 Introduction . . . 197
5.3.3.2 Natural uranium isotopic composition . . . 197
5.3.3.3 Durations . . . 197
5.3.3.4 Enrichment plant . . . 198
5.3.3.5 Fabrication plant . . . 198
5.3.3.6 Reprocessing plant . . . 198
5.3.3.7 Reactor . . . 199
5.3.3.8 Burnup . . . 200
5.3.4 Conclusions and perspectives . . . 208

6 Uncertainty propagation studies 211
6.1 Irradiation computation . . . 212
6.1.1 Uncertainty propagation in irradiation computation . . . 212
6.1.1.1 Introduction . . . 212
6.1.1.2 PWR UOX fuel . . . 212
6.1.1.3 PWR MOX fuel . . . 215
6.1.1.4 SFR MOX fuel . . . 217
6.1.2 Irradiation surrogate models in scenario computations . . . 219
6.1.2.1 Implementation . . . 219
6.1.2.2 Remarks concerning uncertainty propagation . . . 220
6.2 Uncertainty propagation in scenario studies . . . 223
6.2.1 Scenario A: Historical French PWR fleet . . . 223
6.2.1.1 Introduction . . . 223
6.2.1.2 Objectives . . . 223
6.2.1.3 Description of the scenario . . . 223
6.2.1.4 Comparison of COSI-CESAR and COSI-MeSAR . . . 225
6.2.1.5 Uncertainty propagation . . . 226
6.2.2 Scenario B: French PWR fleet transition scenario, industrial application . . . 230
6.2.2.1 Introduction . . . 230
6.2.2.2 Objectives . . . 230
6.2.2.3 Description of the scenario . . . 230
6.2.2.4 Burnup uncertainty propagation . . . 231
6.2.3 Scenario C: French PWR fleet transition scenario, no minor actinides recycling 243
6.2.3.1 Introduction . . . 243
6.2.3.2 Objectives . . . 243
6.2.3.3 Description of the scenario . . . 243
6.2.3.4 Uncertainty propagation . . . 245
6.2.3.5 Equivalence model analysis . . . 247
6.2.4 Scenario D: French PWR fleet transition scenario, americium recycling . . . 254
6.2.4.1 Introduction . . . 254
6.2.4.2 Objectives . . . 254
6.2.4.3 Description of the scenario . . . 255

6.2.4.4 Comparison of burnup and ND uncertainty . . . 260
6.2.4.5 Impact of natural uranium isotopy . . . 266
6.2.4.6 Feasibility study . . . 266
6.2.4.7 Conclusions . . . 274

7 Conclusions 277
7.1 Introduction . . . 277
7.2 Physical models for uncertainty propagation . . . 277
7.2.1 Introduction . . . 277
7.2.2 Nuclides of interest . . . 277
7.2.3 Cooling model . . . 278
7.2.4 Depletion models . . . 278
7.2.5 Equivalence models . . . 279
7.2.6 Conclusions for physical models . . . 280
7.3 Data . . . 280
7.3.1 Introduction . . . 280
7.3.2 Physical parameters . . . 281
7.3.3 Scenario parameters . . . 281
7.4 Application . . . 282

Appendix A Design of experiments for irradiation surrogate models 283
A.1 DOE for polynomial regressions . . . 284
A.1.1 PWR UOX fuel, low burnup . . . 284
A.1.2 PWR UOX fuel, nominal burnup . . . 285
A.1.3 PWR repU fuel . . . 286
A.1.4 PWR MOX fuel, low burnup . . . 287
A.1.5 PWR MOX fuel, nominal burnup . . . 288
A.1.6 SFR MOX fuel, low burnup . . . 289
A.1.7 SFR MOX fuel, nominal burnup . . . 290
A.2 DOE for ANN . . . 292
A.2.1 PWR UOX fuel, low burnup . . . 292
A.2.2 PWR UOX fuel, nominal burnup . . . 293
A.2.3 PWR MOX fuel, low burnup . . . 294
A.2.4 PWR MOX fuel, nominal burnup . . . 295
A.2.5 PWR repU fuel . . . 296
A.2.6 SFR MOX fuel, low burnup . . . 297
A.2.7 SFR MOX fuel, nominal burnup . . . 298
A.2.8 SFR internal blanket . . . 299
A.2.9 SFR inferior blanket . . . 300
A.2.10 SFR americium bearing blanket . . . 301

Appendix B Surrogate models: quality indices 303
B.1 Polynomial regressions quality indices . . . 304
B.1.1 PWR UOX fuel, low burnup, ^{240}Pu estimator . . . 304
B.1.2 PWR UOX fuel, nominal burnup, ^{239}Pu estimator . . . 305
B.1.3 PWR repU fuel, ^{239}Pu estimator . . . 306
B.1.4 PWR MOX fuel, low burnup, ^{241}Am estimator . . . 307

B.1.5 PWR MOX fuel, nominal burnup, ^{241}Am estimator . . . 308
B.1.6 SFR MOX fuel, low burnup, ^{239}Pu estimator . . . 309
B.2 ANN quality indices . . . 310
B.2.1 PWR UOX fuel, low burnup, ^{244}Cm estimator . . . 310
B.2.2 PWR MOX fuel, nominal burnup, ^{241}Am estimator . . . 311

Appendix C Résumé en Français 313
C.1 Contexte . . . 314
C.2 Codes de calcul . . . 315
C.2.1 CESAR . . . 315
C.2.2 COSI . . . 316
C.3 Analyse du problème . . . 316
C.4 Modèles physiques adaptés à la propagation des incertitudes . . . 319
C.4.1 Noyaux d'intérêt . . . 319
C.4.2 Calcul de refroidissement . . . 319
C.4.3 Calcul d'irradiation . . . 320
C.4.3.1 Métamodèles . . . 320
C.4.3.2 Paramètres pris en compte . . . 320
C.4.3.3 Construction de métamodèles . . . 321
C.4.3.4 Implementation . . . 323
C.4.4 Modèles d'équivalence . . . 325
C.5 Paramètres associés à une incertitude . . . 328
C.5.1 Classification . . . 328
C.5.2 Données nucléaires . . . 328
C.5.3 Paramètres et hypothèses des scénarios . . . 330
C.6 Études de propagation d'incertitude . . . 331
C.6.1 Méthode . . . 331
C.6.2 Applications . . . 331
C.6.2.1 Propagation d'incertitudes dans les calculs d'irradiation . . . 331
C.6.2.2 Scénario A : Parc REP historique français . . . 333
C.6.2.3 Scénario B : scénario industriel de transition . . . 337
C.6.2.4 Scénario C : Scénario académique de transition sans recyclage des actinides mineurs . . . 340
C.6.2.5 Scénario D : Scénario académique de transition avec recyclage des actinides mineurs . . . 344
C.7 Conclusions . . . 348

List of Figures

2.1 Nuclear data generation for CESAR5.3 . . . 40
2.2 COSI flow scheme . . . 43
2.3 Operating diagram of COSI data set . . . 45
2.4 View of a spent fuel interim storage . . . 48
2.5 View of a waste storage . . . 49

3.1 Comparison of two power sampling methods . . . 58
3.2 Typical burnup cumulative distribution in a scenario calculation . . . 61
3.3 Burnup sampling in the case of a polynomial (degree 2) irradiation function . . . 65
3.4 Burnup sampling in the case of an exponential irradiation function . . . 66
3.5 Construction of the exponential estimator of the irradiation function . . . 67
3.6 Image of uniform distribution through g . . . 67
3.7 Image of estimated exponential distribution through g . . . 68
3.8 Correlation matrix of $\sigma_s\left(^1\mathrm{H}\right)$ . . . 70
3.9 Standard deviation of $\sigma_s\left(^1\mathrm{H}\right)$ . . . 70
3.10 Correlation matrix of $\sigma_s\left(^{16}\mathrm{O}\right)$ . . . 71
3.11 Standard deviation of $\sigma_s\left(^{16}\mathrm{O}\right)$ . . . 71
3.12 Partial sampling matrix of PWR UOX fuel irradiated at sub-nominal burnup . . . 81
3.13 Partial DOE matrix of PWR UOX fuel irradiated at sub-nominal burnup . . . 82
3.14 Plutonium concentrations after irradiation in function of the uranium enrichment for PWR UOX fuel . . . 84
3.15 Curium concentrations after irradiation in function of the uranium enrichment in PWR UOX fuel . . . 84
3.16 Evolution of several final plutonium concentrations in function of the ^{239}Pu mass fraction for PWR MOX fuel . . . 86
3.17 Evolution of several final curium concentrations in function of the ^{239}Pu mass fraction for PWR MOX fuel . . . 86
3.18 Evolution of the final Pu concentration in function of the burnup for PWR UOX fuel 87
3.19 Evolution of the final Cm concentration in function of the burnup for PWR UOX fuel 87
3.20 Construction of a polynomial regression . . . 89
3.21 Identity card of the ^{239}Pu estimator in PWR UOX fuel, BU<41GWd/tHM . . . 93
3.22 Identity card of the ^{244}Cm estimator in PWR UOX fuel, BU<41GWd/tHM . . . 94
3.23 Prediction coefficient q^2 in function of hidden neurons and sample size . . . 102
3.24 Equivalent prediction q_e in function of hidden neurons and sample size . . . 102
3.25 Identity card of the ^{239}Pu estimator in PWR UOX fuel, BU>38GWd/tHM . . . 110
3.26 Decay heat uncertainty for an elementary ^{235}U fission . . . 111

3.27 Decomposition of variance for an elementary ^{235}U fission 112
3.28 QQ plot of renormalized normal laws with a sum constraint 122
3.29 Identity card of the ^{134}Cs estimator in PWR UOX fuel, BU<43GWd/tHM 132
3.30 Decay paths of fission products 133
3.31 Calculation of decay heat via artificial neural networks and deterministic Bateman equation solution 135
3.32 Comparison of decay heat calculated via ANN+deterministic Bateman and CE-SAR5.3 for PWR UOX fuel 136
3.33 Comparison of decay heat calculated via ANN+deterministic Bateman and CE-SAR5.3 for PWR UOX fuel 137
3.34 Comparison of decay heat calculated via ANN+deterministic Bateman and CE-SAR5.3 for PWR repU fuel 138
3.35 Comparison of decay heat calculated via ANN+deterministic Bateman and CE-SAR5.3 for PWR MOX fuel, nominal burnup, isotopy A 139
3.36 Comparison of decay heat calculated via ANN+deterministic Bateman and CE-SAR5.3 for PWR MOX fuel, nominal burnup, isotopy B 139
3.37 Comparison of decay heat calculated via ANN+deterministic Bateman and CE-SAR5.3 for PWR MOX fuel low burnup 140
3.38 Comparison of decay heat calculated via ANN+deterministic Bateman and CE-SAR5.3 for SFR CFV fuel 141
3.39 Different steps for validation of decay heat uncertainty propagation using MeSAR 142
3.40 Identity card of the ^{239}Pu estimator in PWR UOX fuel, BU>38GWd/tHM 147

4.1 Plutonium content such that $\rho(\overline{\mathrm{BU}}_{end\ of\ cycle}) = 0$ in function of ^{239}Pu isotopy for SFR CFV equivalence model 159
4.2 Global quality indicators of the plutonium content ANN estimators for SFR CFV equivalence model, method A 159
4.3 Comparison of the plutonium content (%) computed with ERANOS and its ANN estimator (3 neurons in hidden layer) 160
4.4 Absolute error of the Pu content (%) estimator in function of the Pu content (%) . . 160
4.5 End of cycle reactivity in function of the plutonium content for SFR CFV core . . . 161
4.6 Relative difference with linear regression in function of the plutonium content for SFR CFV core 162
4.7 End of cycle reactivity in function of the plutonium content for SFR CFV core . . . 163
4.8 End of cycle reactivity in function of the ^{239}Pu isotopy for SFR CFV core 164
4.9 Global quality indicators of the plutonium content ANN estimators, method B . . 164
4.10 Comparison of the plutonium content computed iteratively with ERANOS and the ANN estimator made according to method B (5 neurons in hidden layer) 165
4.11 Global quality indicators of the plutonium content ANN estimators for SFR CFV equivalence model for cross-sections uncertainty propagation 167
4.12 Global quality indicators of the plutonium content ANN estimators for PWR MOX equivalence model dedicated to cross-sections uncertainty propagation 172

5.1 Fuel cycle back-end 197
5.2 Batch sequence in a core 200
5.3 Representation of a core at the end of an irradiation cycle 202

6.1 Actinides decay chains . . . 213
6.2 Scenario A: fuel cycle in 2010 . . . 224
6.3 Scenario A: balance and inventory of the plutonium stock in 2010 . . . 227
6.4 Scenario B: evolution of nuclear energy production . . . 231
6.5 Scenario B: evolution of the inventories of different elements of interest . . . 233
6.6 Scenario B: evolution of the inventories relative standard deviation for different elements of interest . . . 234
6.7 Scenario B: CDF of the inventories distributions in 2150 . . . 234
6.8 Scenario B: EPR^{TM}MOX fresh fuel isotopy . . . 235
6.9 Scenario B: EPR^{TM}MOX fresh fuel isotopy relative standard deviation . . . 236
6.10 Scenario B: histogram of EPR^{TM}MOX fresh fuel ^{239}Pu isotopy in 2069 and 2071 . . . 237
6.11 Scenario B: EPR^{TM}MOX fresh fuel isotopy relative standard deviation after 2090 . 238
6.12 Scenario B: decay heat of EPR^{TM}MOX fuel . . . 238
6.13 Scenario B: relative standard deviation of decay heat of EPR^{TM}MOX fuel . . . 239
6.14 Scenario B: uncertainty of EPR^{TM}MOX decay heat (methods α, β and γ) . . . 240
6.15 Scenario B: plutonium inventory relative standard deviation (methods α, β and γ) 241
6.16 Scenario B: americium inventory relative standard deviation (methods α, β and γ) 241
6.17 Scenario B: neptunium inventory relative standard deviation (methods α, β and γ) 241
6.18 Scenario B: curium inventory relative standard deviation (methods α, β and γ) . . 242
6.19 Scenario C: fuel cycle before 2038 . . . 243
6.20 Scenario C: fuel cycle between 2038 and 2100 . . . 244
6.21 Scenario C: fuel cycle after 2100 . . . 244
6.22 Scenario C: evolution of the inventories of different elements of interest . . . 246
6.23 Scenario C: evolution of the inventories relative standard deviation for different elements of interest . . . 246
6.24 Scenario C: CPY MOX fresh fuel plutonium content, calculated with different equivalence models . . . 247
6.25 Scenario C: CPY MOX fresh fuel plutonium content relative standard deviation . 248
6.26 Scenario C: CPY MOX fresh/spent fuel plutonium quality and downgrade . . . 249
6.27 Scenario C: CPY MOX fresh fuel plutonium quality relative standard deviation . . 249
6.28 Scenario C: CPY MOX plutonium downgrade relative standard deviation . . . 250
6.29 Scenario C: SFR MOX fresh fuel plutonium content, calculated with different equivalence models . . . 251
6.30 Scenario C: SFR MOX fresh fuel plutonium content relative standard deviation . . 252
6.31 Scenario C: SFR MOX fresh fuel plutonium quality relative standard deviation . . 252
6.32 Scenario D: fuel cycle after 2100 . . . 255
6.33 Scenario D: evolution of the inventories of different elements of interest . . . 257
6.34 Scenario D: evolution of the inventories relative standard deviation for different elements of interest . . . 257
6.35 Scenario D: histogram of AmBB cumulative fabrication needs in 2150 . . . 259
6.36 Scenario D: CDF of AmBB fabrication needs in 2150 and Gaussian fit . . . 260
6.37 Scenario D: histogram of spent fuel inventory in 2150 . . . 261
6.38 Scenario D: CDF of spent fuel inventory in 2150 and Gaussian fit . . . 261
6.39 Scenario D: comparison of uncertainty sources for plutonium inventory . . . 262
6.40 Scenario D: comparison of uncertainty sources for americium inventory . . . 262
6.41 Scenario D: comparison of uncertainty sources for curium inventory . . . 263

6.42 Scenario D: AmBB DH in function of cooling time 263
6.43 Scenario D: comparison of uncertainty sources for AmBB DH after 5 years of cooling264
6.44 Scenario D: comparison of uncertainty sources for EPR^{TM}MOX DH after 5 years of cooling 265
6.45 Scenario D: plutonium margin 267
6.46 Scenario D: plutonium deficit complementary cumulative distribution function . . 268
6.47 Scenario D: parallel plot of plutonium deficit and first year deficit 268
6.48 Scenario D: impact of reprocessing plant plutonium recovery rate on feasibility . . 269
6.49 Scenario D: impact of SFR fuel fabrication time on scenario feasibility 271
6.50 Scenario D: AmBB DH contributors in function of cooling time 272
6.51 Scenario D: AmBB DH uncertainty in function of cooling time 273
6.52 Scenario D: feasibility in function of max_{DH} 273

B.1 Identity card of the ^{240}Pu polynomial estimator in PWR UOX fuel, BU<41GWd/tHM304
B.2 Identity card of the ^{239}Pu polynomial estimator in PWR UOX fuel, BU$\geq$41GWd/tHM305
B.3 Identity card of the ^{239}Pu polynomial estimator in PWR repU fuel 306
B.4 Identity card of the ^{241}Am polynomial estimator in PWR MOX fuel, BU<45GWd/tHM307
B.5 Identity card of the ^{241}Am polynomial estimator in PWR MOX fuel, BU$\geq$45GWd/tHM308
B.6 Identity card of the ^{239}Pu estimator in SFR MOX fuel, BU<96GWd/tHM 309
B.7 Identity card of the ^{244}Cm ANN estimator in PWR UOX fuel, BU<43GWd/tHM . . 310
B.8 Identity card of the ^{241}Am ANN estimator in PWR MOX fuel, BU>38GWd/tHM . . 311

C.1 Génération de bibliothèques de sections efficaces pour CESAR5.3 315
C.2 Flux de masse dans le cycle du combustible simulés par COSI 316
C.3 Processus de fabrication de métamodèles d'irradiation 322
C.4 Fonctionnement d'un réseau de neurones 323
C.5 Calcul de la puissance résiduelle via réseaux de neurones et solutions analytiques de l'équation de Bateman 324
C.6 Comparaison de la puissance résiduelle calculée via (ANN et solutions analytique de Bateman) et CESAR5.3 pour du combustible REP MOX irradié à 46GWj/tML . 325
C.7 Comparaison des teneurs calculées avec le modèle d'équivalence statistique et ERANOS 326
C.8 Scenario A : cycle du combustible 2010 335
C.9 Scénario B : évolution des inventaires de différents éléments d'intérêt 338
C.10 Scenario B : évolution des écart-types relatifs des inventaires de différents éléments d'intérêt 338
C.11 Scenario B : incertitude de la puissance résiduelle du combustible EPR MOX refroidi 10 ans (méthodes α, β et γ) 339
C.12 Scenario B : incertitude de l'inventaire en américium (méthodes α, β et γ) 340
C.13 Scenario C : cycle du combustible avant 2038 340
C.14 Scenario C : cycle du combustible entre 2038 et 2100 341
C.15 Scenario C : cycle du combustible après 2100 341
C.16 Scenario C : évolution des inventaires en différents éléments d'intérêt 342
C.17 Scenario C : évolution des écarts-types relatifs des inventaires en différents éléments d'intérêt 342
C.18 Scenario C : teneur plutonium en CPY MOX, calculée avec différents modèles d'équivalence 343

C.19 Scénario C : écart-type relatif de la teneur plutonium en CPY MOX 344
C.20 Scenario C : écart-type relatif de la teneur plutonium en RNR 344
C.21 Scenario D : cycle du combustible après 2100 345
C.22 Scenario D : inventaires de différents éléments d'intérêt 346
C.23 Scenario D: evolution of the inventories relative standard deviation for different elements of interest 346
C.24 Scenario D : comparaison des sources d'incertidue pour l'inventaire en américium 347
C.25 Scenario D : comparaison des sources d'incertitude pour la puissance résiduelle des CCAm après 5 ans de refroidissement 347

List of Tables

3.1 Contribution of several actinides to heavy nuclides mass fraction in irradiated PWR UOX fuel . . . 54
3.2 Contribution of several actinides to heavy nuclides decay heat in irradiated PWR UOX fuel . . . 54
3.3 Impact of the variability of the load factor on the output balance of PWR UOX fuel 59
3.4 Impact of inter-cycle model on various nuclides after 5 years of cooling . . . 60
3.5 Division of a domain of variation into two different designs of experiments . . . 61
3.6 Quantification on the precision on $\mathcal{D}$, $\mathcal{D}_1$ and $\mathcal{D}_2$ . . . 62
3.7 Sensitivity of concentrations after irradiation up to 45GWd/tHM to scattering cross-section in PWR UOX fuel . . . 69
3.8 Uncertainty of concentrations after irradiation due to ^{1}H scattering cross-section in PWR UOX fuel . . . 71
3.10 Pu vector for ^{1}H scattering cross-section impact study in PWR MOX fuel . . . 73
3.9 Uncertainty of concentrations after irradiation due to ^{16}O scattering cross-section in PWR UOX fuel . . . 73
3.11 Uncertainty of concentrations after irradiation due to ^{1}H scattering cross-section in PWR MOX fuel . . . 74
3.12 Cross-section uncertainty in PWR UOX spectrum before and after irradiation . . . 75
3.13 Pu vector for cross-section uncertainty condensation in PWR MOX fuel . . . 75
3.14 Cross-section uncertainty in PWR MOX spectrum before and after irradiation . . 76
3.15 Q_{eff} values of several radioactive actinides . . . 78
3.16 Summary of the parameters taken into account for actinides surrogate models . . 79
3.17 Number of monomials in a d-degree polynomial of n variables . . . 83
3.18 Pu vector for study of the linearity of fresh fuel composition in PWR MOX fuel . . 84
3.19 Measure of the linearity of the impact of the uranium enrichment on final concentrations of different nuclides for PWR UOX fuel . . . 85
3.20 Measure of the linearity of the ^{239}Pu isotopy on final concentrations of different nuclides for PWR MOX fuel . . . 85
3.21 Linearity measure for the burnup impact on final concentrations for different nuclides in PWR UOX fuel . . . 86
3.22 Determination of the lower bound degree for polynomial estimation for PWR UOX fuel . . . 87
3.23 Evolution of r^2 and q^2 in function of the sample size for ^{239}Pu in PWR UOX fuel . . 90
3.24 Quality indexes of low burnup PWR UOX actinides polynomial surrogate model . 92
3.25 Quality indexes of high burnup PWR UOX actinides polynomial surrogate model . 95
3.26 Quality indexes of PWR repU actinides polynomial surrogate model . . . 96

3.27 Quality indexes of low burnup PWR MOX actinides polynomial surrogate model . 97
3.28 Quality indexes of high burnup PWR MOX actinides polynomial surrogate model . 98
3.29 Quality indexes of low burnup SFR MOX actinides polynomial surrogate model . . 99
3.30 Quality indexes of high burnup SFR MOX actinides polynomial surrogate model . 100
3.31 Quality indexes of low burnup PWR UOX actinides ANN surrogate model 106
3.32 Quality indexes of high burnup PWR UOX actinides ANN surrogate model 106
3.33 Quality indexes of low burnup PWR MOX actinides ANN surrogate model 107
3.34 Quality indexes of high burnup PWR MOX actinides ANN surrogate model 107
3.35 Quality indexes of PWR repU actinides ANN surrogate model 108
3.36 Quality indexes of low burnup SFR actinides ANN surrogate model 108
3.37 Quality indexes of high burnup SFR actinides ANN surrogate model 109
3.38 Percentage of decay heat calculated using `List_FP` and `List_Actinides` 113
3.39 Fission products taken into account and associated decay paths 114
3.40 Sensitivity of fission product concentration to its initial concentration 115
3.41 Importance of different fission yields for production of ^{85}Kr 117
3.42 Importance of different fission yields for production of ^{90}Sr 117
3.43 Importance of different fission yields for production of ^{95}Zr 117
3.44 Importance of different fission yields for production of ^{106}Ru 117
3.45 Importance of different fission yields for production of ^{134}Cs 118
3.46 Importance of different fission yields for production of ^{137}Cs 118
3.47 Importance of different fission yields for production of ^{144}Ce 118
3.48 Importance of different fission yields for production of ^{147}Pm 118
3.49 Importance of different fission yields for production of ^{154}Eu 119
3.50 Chain heads taken into account during the sampling process 119
3.51 Partial correlation matrix of $x \rightarrow {}^{90}$Sr fission yield perturbations 121
3.52 Partial correlation matrix of $^{235}\text{U} \rightarrow x$ fission yield perturbations 121
3.53 Fission products capture cross-section sensitivity in PWR UOX fuel 124
3.54 Fission products capture cross-section sensitivity in PWR MOX 125
3.55 Summary of the parameters taken into account for fission products surrogate models 126
3.56 Local sensitivity of $X \rightarrow {}^{106}$Ru fission yields 127
3.57 Quality indexes of low burnup PWR UOX fission products ANN surrogate model . 129
3.58 Quality indexes of high burnup PWR UOX fission products ANN surrogate model 129
3.59 Quality indexes of low burnup PWR MOX fission products ANN surrogate model . 129
3.60 Quality indexes of high burnup PWR MOX fission products ANN surrogate model 130
3.61 Quality indexes of high burnup PWR repU fission products ANN surrogate model 130
3.62 Quality indexes of low burnup SFR MOX fission products ANN surrogate model . 130
3.63 Quality indexes of high burnup SFR fission products ANN surrogate model 131
3.64 Fresh fuel composition for PWR repU decay heat benchmark 137
3.65 Plutonium vector for PWR MOX decay heat benchmark 138
3.66 Plutonium vector for PWR MOX low burnup, decay heat benchmark 140
3.67 Plutonium vector for SFR MOX decay heat benchmark 141
3.68 Parameters of the (core + blanket) system 143
3.69 Quality indexes of fertile blankets in SFR reactor 146

4.1 Intervals of variation for CFV equivalence model, method A 158
4.2 Bias of the Pu content estimators for SFR CFV equivalence model, method A . . . 159

4.3 Intervals of variation for CFV equivalence model, method B 163
4.4 Global quality indicators of the plutonium content ANN estimators, method B . . 165
4.5 Bias of SFR CFV Pu content estimators, calculated on the test sample, method B . 165
4.6 Summary of the parameters taken into account for SFR CFV equivalence models . 166
4.7 Bias of SFR CFV Pu content estimators for cross-sections uncertainty propagation, calculated on the test sample 168
4.8 Plutonium vector for SFR CFV equivalence model study 168
4.9 Cross-sections uncertainty ranking for SFR CFV equivalence model 170
4.10 Intervals of variation for PWR MOX equivalence model 171
4.11 Mean bias of the PWR MOX Pu content estimators for uncertainty propagation, calculated on the test sample 172
4.12 Plutonium vectors for PWR MOX equivalence model study 173
4.13 Cross-sections uncertainty ranking for PWR MOX equivalence model 175

5.1 33 groups condensation mesh 189
5.2 Plutonium vector in PWR MOX core 189
5.3 Plutonium vector in SFR CFV core 189
5.4 ^{234}U PWR UOX - PWR MOX - SFR MOX 1-group covariance matrix 189
5.5 ^{235}U PWR UOX - PWR MOX - SFR MOX 1-group covariance matrix 190
5.6 ^{236}U PWR UOX - PWR MOX - SFR MOX 1-group covariance matrix 190
5.7 ^{238}U PWR UOX - PWR MOX - SFR MOX 1-group covariance matrix 190
5.8 ^{237}Np PWR UOX - PWR MOX - SFR MOX 1-group covariance matrix 191
5.9 ^{239}Np PWR UOX - PWR MOX - SFR MOX 1-group covariance matrix 191
5.10 ^{238}Pu PWR UOX - PWR MOX - SFR MOX 1-group covariance matrix 191
5.11 ^{239}Pu PWR UOX - PWR MOX - SFR MOX 1-group covariance matrix 192
5.12 ^{240}Pu PWR UOX - PWR MOX - SFR MOX 1-group covariance matrix 192
5.13 ^{241}Pu PWR UOX - PWR MOX - SFR MOX 1-group covariance matrix 192
5.14 ^{242}Pu PWR UOX - PWR MOX - SFR MOX 1-group covariance matrix 193
5.15 ^{241}Am PWR UOX - PWR MOX - SFR MOX 1-group covariance matrix 193
5.16 ^{242M}Am PWR UOX - PWR MOX - SFR MOX 1-group covariance matrix 193
5.17 ^{243}Am PWR UOX - PWR MOX - SFR MOX 1-group covariance matrix 194
5.18 ^{242}Cm PWR UOX - PWR MOX - SFR MOX 1-group covariance matrix 194
5.19 ^{243}Cm PWR UOX - PWR MOX - SFR MOX 1-group covariance matrix 194
5.20 ^{244}Cm PWR UOX - PWR MOX - SFR MOX 1-group covariance matrix 195
5.21 ^{245}Cm PWR UOX - PWR MOX - SFR MOX 1-group covariance matrix 195
5.22 ^{246}Cm PWR UOX - PWR MOX - SFR MOX 1-group covariance matrix 195
5.23 Natural uranium isotopy range of variation 197
5.24 Recovery rates at reprocessing plant 199
5.25 Burnup correlation matrix of consecutive batches in a core, fractionation $N = 3$ . . 201
5.26 Impact of reloading date on discharge burnup uncertainty 203
5.27 Impact of irradiation power on discharge burnup uncertainty 204

6.1 Cross-sections uncertainty sources in PWR UOX irradiation calculation 214
6.2 Pu vector for cross-section uncertainty propagation in PWR MOX fuel 215
6.3 Cross-sections uncertainty sources in PWR MOX irradiation calculation 216
6.4 Pu vector for cross-section uncertainty propagation in PWR MOX fuel 217
6.5 Cross-sections uncertainty sources in SFR MOX irradiation calculation 218

6.6 Comparison of the quality of estimators on the whole domain of validity and for a fixed set of irradiation parameters, PWR UOX high burnup fuel 221
6.7 Comparison of the quality of estimators on the whole domain of validity and for a fixed composition and nuclear data set, PWR UOX high burnup fuel 221
6.8 COSI-CESAR and COSI-MeSAR burnup sensitivity-uncertainty comparison . . . 222
6.9 Scenario A: comparison of COSI-CESAR and COSI-MeSAR on several results (31/12/2010) 225
6.10 Scenario A: comparison of ANDRA and COSI-MeSAR on several results (31/12/2010) 226
6.11 Scenario A: plutonium inventory in function of the accounting date and associated uncertainty 228
6.12 Scenario B: mean, median and nominal value of the inventories in 2150 235
6.13 Infinite plutonium isotopy 256
6.14 Burnup and nuclear data correlation between different systems in a scenario calculation 265
6.15 Scenario D: impact of natural uranium isotopic composition 266

A.1 PWR UOX, low burnup sampling distributions for polynomial estimator 284
A.2 PWR UOX, nominal burnup sampling distributions for polynomial estimator . . . 285
A.3 PWR repU sampling distributions for polynomial estimator 286
A.4 PWR MOX, low burnup sampling distributions for polynomial estimator 287
A.5 PWR MOX, nominal burnup sampling distributions for polynomial estimator . . . 288
A.6 SFR MOX, BU<96GWd/tHM sampling distributions 289
A.7 SFR MOX, BU<96GWd/tHM sampling distributions 290
A.8 PWR UOX, low burnup sampling distributions for ANN estimator 292
A.9 PWR UOX, nominal burnup sampling distributions for ANN estimator 293
A.10 PWR MOX, low burnup sampling distributions for ANN estimator 294
A.11 PWR MOX, nominal burnup sampling distributions for ANN estimator 295
A.12 PWR repU sampling distributions for ANN estimator 296
A.13 SFR MOX, low burnup sampling distributions for ANN estimator 297
A.14 SFR MOX, nominal burnup sampling distributions for ANN estimator 298
A.15 SFR internal blanket sampling distributions for ANN estimator 299
A.16 SFR inferior blanket sampling distributions for ANN estimator 300
A.17 SFR americium bearing blanket sampling distributions for ANN estimator 301

C.1 Résumé des paramètres pris en compte pour la construction de métamodèles des concentrations du combustible irradié 321
C.2 Vecteur plutonium pour l'étude du modèle d'équivalence RNR 327
C.3 Analyse préliminaire de propagation d'incertitude pour le modèle d'équivalence RNR statistique 327
C.4 Matrice de covariance du ^{239}Pu dans les spectres REP UOX - REP MOX - RNR Na 329
C.5 Impact des incertitudes des sections efficaces sur l'irradiation d'un combustible REP UOX 332
C.6 Vecteur plutonium pour la propagation de l'incertitude des sections efficaces dans du combustible REP MOX 333
C.7 Impact des incertitudes des sections efficaces sur l'irradiation d'un combustible REP MOX 334

C.8 Scénario A : comparaison de COSI-CESAR et COSI-MeSAR pour différents résultats d'intérêt, au 31/12/2010 336
C.9 Scénario A : comparaison ANDRA, COSI-MeSAR et incertitude, au 31/12/2010 . . 336
C.10 Scénario A :inventaire en plutonium disponible calculé à différentes dates en fonction de la date de comptage, et incertitude associée 336

Glossary

AGR	Advanced Gas-cooled Reactor
AmBB	Americium Bearing Blanket
ANN	Artificial Neural Network
BBL	Bibliothèque (encrypted, parameterized energy-integrated cross-sections library)
BU	Burnup
CDF	Cumulative Distribution Function
CEA	Commissariat à l'Énergie atomique et aux Énergies Alternatives
CFV	Cœur à Faible Vidange
CY	Cumulative fission yield
DH	Decay Heat
DOE	Design Of Experiments
EFPD	Effective Full Power Days
EPR	European Pressurized Reactor
FB	Fertile Blanket
FP	Fission Product
HM	Heavy Metal
IY	Independent fission Yield
LMFBR	Liquid Metal Fast Breeder Reactor
LHS	Latin Hypercube Sampling
LWR	Light Water Reactor
MA	Minor Actinides
MABB	Minor Actindes Bearing Blanket
MOX	Mixed Oxydes
ND	Nuclear Data
OAT	One At a Time
PCC	Pearson product-moment Correlation Coefficient
PDF	Probability Density Function
PWR	Pressurized Water Reactor
RAM	Random Access Memory
repU	Reprocessed Uranium
RSD	Relative Standard Deviation
SD	Standard Deviation
SFR	Sodium Fast Reactor
UOX	Uranium Oxyde
Var	Variance
XS	Cross-Section

Chapter 1

Introduction

Contents

1.1 Context 28
1.2 Analysis of the problem 28
1.3 Physical models for uncertainty propagation 30
1.3.1 Nuclides of interest 30
1.3.2 Cooling computation 30
1.3.3 Irradiation computation 31
1.3.4 Equivalence models 33
1.4 Uncertainty data 33
1.4.1 Classification 33
1.4.2 Nuclear data 33
1.4.3 Scenario parameters and hypotheses 34
1.5 Uncertainty propagation studies 34
1.5.1 Method 34
1.5.2 Applications 35

1.1 Context

Scenario studies simulate the whole fuel cycle over a period of time, from extraction of natural resources to geological storage. Transition scenario studies compare different reactor fleet evolutions, such as introduction of SFR, and fuel management options, such as plutonim recycling or minor actinides partitioning and transmutation, for the future nuclear fuel cycle. Therefore, they constitute a decision-making support. Consequently uncertainty propagation studies, which are necessary to assess the robustness of the studies, are strategic. In the frame of the French act for waste management, these studies evaluate the sustainability of SFR deployment in terms of plutonium availability, as well as the impact on fuel cycle facilities of minor actinides transmutation.

Scenario codes, such as COSI, contain advanced physical models, validated with reference codes, for cooling, depletion, and equivalence. They model the mass flows (actinides, fission products, etc.) and their isotopic composition between the different fuel cycle facilities in dynamic scenarios.

However, several parameters generate uncertainty in scenario studies:

- nuclear data, such as cross-sections and fission yields;
- scenario parameters, for fuel reactors and facilities description, such as fuel burnup or reprocessing plant recovery rate.

The need to evaluate the uncertainty propagation on scenario results is all the more important that transplutonium elements may have a significant impact on facilities, and their cross-sections have a greater uncertainty than major actinides. Furthermore, recent scenarios have been produced through fuel cycle optimization, consequently their sustainability may be more impacted by these sources of uncertainty.

The aim of this work is to develop and use an uncertainty propagation method for of dynamic transition scenario studies, and to apply this method to reference scenarios.

This work is limited to the uranium-plutonium cycle.

1.2 Analysis of the problem

Computation codes used in this work are presented in chapter 2. Scenario computations are performed with COSI (see section 2.2), irradiation and cooling computations are performed with CESAR (see section 2.1).

A scenario computation is a complex object. Recent scenario computations model the behavior and the interaction of dozens of reactors, fuel cycle facilities, mass flows; and timescales are both continuous and discontinuous, with the presence of many threshold effects:

- continuous: irradiation and cooling models, recovery rates, mass losses, etc.;
- discontinuous: fuel management and reprocessing strategy (batches are not homogenized).

A first uncertainty propagation method would be based on perturbation of analytical fuel cycle equations. Recent studies [1.1] have shown that obtention of analytical formulae for the fuel cycle comes at the price of important simplifications and hypotheses on fluxes, spectra, core geometry,

equivalence models, cross-sections, etc. These hypotheses may have an important impact on both results and their associated uncertainty.

Stochastic uncertainty propagation methods seem well suited to such complex problems, such as scenario studies: sampling input parameters according to their distribution, with consideration of proper correlation between parameters, and analysis of the system output (variance, correlations, etc.) gives information concerning uncertainty propagation in the system. This method does not require hypotheses nor physical simplification of the model, and is well adapted for interaction analysis between the different variables.

One of the main drawbacks of this method is the computation time, and the number of evaluations required to compute variance, or other results of interest, with a satisfying precision. It is difficult to assess such number, but it increases with the number of parameters and the complexity of the system. In a scenario computation, many parameters are associated with an uncertainty. These parameters include (see chapter 5):

- nuclear data, used for depletion and equivalence models (see section 5.2):
  - cross-sections: covariance matrices of a high number of nuclides, including actinides and fission products;
  - fission yields: spectrum-dependent fission yields uncertainties;
- scenario parameters, for fuel, reactors and plants description (see section 5.3):
  - rates of the different fuel cycle plants;
  - fuel burnup and reactor power, yield, load factor, etc.;
  - reprocessing strategy (list of batches, fuel types, etc.);
  - composition of natural uranium, etc.

The total amount of parameters is generally around 200[1], which means that the number of runs required for uncertainty propagation is at least 200.

In the case of recent scenario studies, COSI execution time is between a few hours (mass balances) to more than 24 hours (inventories). Computation time heavily depends on the scenario complexity and details, the type of reactors, and scenario duration (generally more than 150 years). Taking into account the fact that a COSI simulation requires a high amount of RAM, and is not distributed in the general case (overlapping of simultaneous runs on the same workstation), we obtain unreasonable uncertainty propagation timescales. Therefore, it is necessary to find a method to accelerate such computation.

A solution to this problem would be to perform uncertainty propagation studies on simplified scenarios, and generalize the results to complex scenarios, possibly with a transposition factor taking into account the transposition of results. Such transposition factor could be built from representativity, using a methodology similar to [1.2], with a scalar product between sensitivity vectors in both versions of the scenario, weighted by the covariance matrix. However, scenario computations are very nonlinear, and many threshold effects appear and disappear during the *complexity increase* and *sophistication* process, therefore sensitivity measures would not be sufficient to build such factor. Consequently uncertainty obtained with simplified scenarios might not be representative of actual uncertainties.

Simplification cannot occur in the scenario itself. However, the physical models may be simplified, as every physical information in the system does not contribute to the results of interest,

[1] In the case of a reference burnup uncertainty propagation computation, the number of parameters is approximately 5000 (see section 6.2.2.4).

and many parameters may be negligible. Decomposition of the simulation time gives the following result:

- irradiation and cooling models: $\approx 99\%$ for most results;
- other physical models (equivalence, decay heat, fuel management, etc.): $<< 1\%$;
- various operations: $\approx 1\%$.

We observe that irradiation and cooling models are heavily dominant, while the impact of other models and operations on the computation time is negligible. We also observe that the more complex the scenario is, the more negligible other models are. Consequently, the computation time problem can be solved through simplification of these physical models, provided the simplified models compute results of interest accurately enough and the computation time gain is significant.

In section 1.3 we expose the methodology used in this work so as to accelerate such models.

1.3 Physical models for uncertainty propagation

1.3.1 Nuclides of interest

Most of the scenario results are directly linked with the isotopic composition of stocks or fuel batches. Consequently it is not possible to reduce the system to a scalar mass. Furthermore, previous studies[2] have shown that considering a system composed of only a few elements, such as uranium and plutonium, does not give satisfying results as soon as PWR MOX or SFR MOX are involved.

However, every nuclide does not contribute to scenario results of interest. For instance, stable fission products have no impact on decay heat, or actinides inventories. Consequently it is not necessary to calculate them in this work. Furthermore, reduction of the list of nuclides to be estimated reduces the amount of RAM required for the computation and accelerates the mass flows computation. The list of nuclides that have to be calculated in this work is presented in sections 3.1.1.1 and 3.2.1.2.

1.3.2 Cooling computation

First, in the case of cooling, the COSI reference scheme runs CESAR (depletion code coupled with COSI) to perform cooling computation for each fuel batch and stock. In COSI, each time information concerning isotopy of a given fuel batch or any stock is accessed, a cooling computation is performed. Isotopy is accessed very often because most of the intermediate operations and results (fresh fuel composition, update of stocks composition, decay heat tests, etc.) require this information. Consequently, several thousands of cooling computations are performed with CESAR during a scenario computation.

In this work, we replaced CESAR cooling computation with simple analytical cooling formulae. This operation is discussed in section 3.2.4.2. As a limited analytic cooling model was already implemented in COSI, we used the structure of this model, and simply added nuclides of interest in terms of scenario results, such as several fission products.

[2] CEA communication, 2012

1.3.3 Irradiation computation

1.3.3.1 Surrogate models

A surrogate model is a simple analytical model of a computation code. It is generally built when performing operations that require a high number of code runs, such as optimization or uncertainty propagation. A simple example of surrogate model is the linear regression, which is an accurate estimator of the system output in function of the input, where the system is locally linear.

There are many types of surrogate models:

- multiple linear regression;
- polynomial regression;
- artificial neural networks;
- kriging, etc.

The type of surrogate model is generally chosen in function of the nature of the problem: number of parameters, non-linearity and interactions, etc.

1.3.3.2 Parameters taken into account

Two types of parameters have to be taken into account for surrogate models. First, the surrogate model must correctly estimate the results of the code, therefore parameters with a non-zero sensitivity are included. Discussions and sensitivity studies determining the impact of these parameters (fresh fuel composition, irradiation parameters, etc.) are presented in section 3.1.2.1.

Surrogate models also have to model uncertainty propagation. However, several parameters subject to uncertainty, such as cross-sections, are not directly included in CESAR data set, consequently we had to add these parameters as well, and perform perturbed depletion computations so as to take these parameters into account. In the case of cross-sections for estimation of actinides concentration in spent fuel (see section 3.1.2.1.4), we study impact of scattering cross-sections and spectra, and take into account capture and fission cross-sections of approximately 20 actinides. Impacts of decay energies and effective fission energy are discussed as well.

In the case of fission products (FP) estimators, more parameters are taken into account (see section 3.2.2.1). The fission yields uncertainties and the capture cross-sections of several fission reactions are included as well. In section 3.2.2.1.4.2 we provide a sensitivity study concerning capture cross-sections impacting fission products of interest.

1.3.3.3 Construction of surrogate models

In this work, we constructed surrogate models of the irradiation code CESAR, which means we built estimators of CESAR output in function of its input. However, we have to model the concentration in spent fuel of several nuclides for every depletion computation. Consequently the surrogate models are not directly estimators of the output, but a set of estimators: at least one for each nuclide of interest.

Furthermore, the CESAR domain of validity is very wide. It covers most of the existing fuel types and associated irradiation: PWR UOX, PWR MOX, PWR reprocessed uranium, SFR MOX,

fertile blankets, MA bearing blankets, etc. Consequently, we divided this domain into different sub-domains, and built a set of estimator in each sub-domain.

First, we built polynomial regressions for actinides. This type of estimator was chosen because of the physical meaning of its internal parameters: linear terms are slopes, interaction is modeled with multiplication of parameters, etc. Section 3.1 describes the construction process of such estimators, according to the usual process:

1. sample parameters (section 3.1.2);
2. run the code on the design of experiments;
3. build and test estimators (section 3.1.3.1).

In the general case, polynomial regressions return satisfying results: the estimators are very close to the code results. However, several nuclides remain hard to estimate correctly, such as most of the curium isotopes. Rather than increasing the complexity (number of monomials, degree) of polynomial estimators, which has diminishing returns and introduces over-fitting, we decided to use a different type of estimators.

Artificial Neural Networks (ANN) seem to be adapted to the characteristics of irradiation computations. Indeed they are well adapted for *moderately* nonlinear functions of a *moderately high* number of parameters. Their construction follows the same scheme as polynomial estimators, and is described in section 3.1.3.2, which also features a few studies aiming at simplifying and formatting the sample.

ANN gave satisfying results, and the difficult cases for polynomial regressions were significantly improved using ANN. Consequently, ANN were also used for estimation of radioactive fission products, which contribute to decay heat. Some of these fission products are especially hard to estimate because they are radioactive, depend non-linearly on cross-sections of both actinides and fission products, and have to be parameterized with a high number of fission yields. Section 3.2 describes the process of fission products estimators construction. First, fission products contributing to decay heat (and their parents, through decay or neutron capture) are identified, then physical parameters generating uncertainty in these FP concentrations are discussed. Finally, ANN FP estimators are built.

An essential step during construction of ANN estimators is their validation:

- result accuracy;
- uncertainty propagation capabilities.

Every estimator needs to be tested on a test sample, in general different from the learning sample. Different quality indicators are tested.

1.3.3.4 Implementation

Both polynomial regression and ANN were implemented in COSI, and a new, fast computation scheme, named COSI-MeSAR, was established. The time gain is superior to 1000 for complex scenarios, and computation time is between a few seconds and a few minutes for any of the scenarios modeled in this work. Implementation was performed so as to be user friendly: it is very easy to import a pre-existing scenario and switch its scheme to COSI-MeSAR.

1.3.4 Equivalence models

A second type of physical model in scenario computation also generates uncertainty: the equivalence models. They are discussed in chapter 4. The equivalence models calculate the fresh fuel enrichment (for instance plutonium content in PWR MOX) so as to be representative of nominal fuel behavior. The equivalence condition is generally formulated in terms of end-of-cycle mean core reactivity. As this results from a physical computation, it is therefore associated with an uncertainty.

First, the state of the art of equivalence models is exposed and discussed. The conclusion is that the present equivalent models, as implemented in COSI, are not suited to uncertainty propagation computation, for the following reasons:

- existing analytical models neglect irradiation, which has a strong impact on the result and its uncertainty;
- current black-box models are not suited to cross-sections perturbations management;
- models based on transport and depletion codes are too time-consuming for stochastic uncertainty propagation.

Consequently, a new type of equivalence model is developed, and exposed in section 4.3. It is based on ANN, constructed with data calculated with neutron transport and depletion codes. The input of the model are the fresh fuel isotopy, the irradiation parameters (burnup, core fractionation, etc.), cross-sections perturbations and the equivalence criterion (for instance the core target reactivity in pcm at the end of the irradiation cycle). The output of the model is the fresh fuel content such that target reactivity is reached at the end of the irradiation cycle. Those models are built then tested on databases calculated with APOLLO2 (for thermal spectra) and ERANOS (for fast spectra) transport calculation. A short preliminary uncertainty propagation and ranking study is then performed for each equivalence models.

1.4 Uncertainty data

1.4.1 Classification

We classified different types of parameters generating uncertainty in scenario computations:

- nuclear data, linked to physical measure, such as cross-sections;
- scenario parameters, linked to the nuclear industry.

In chapter 5, we estimate and discuss the uncertainty value associated with these parameters.

1.4.2 Nuclear data

Several physical parameters generate uncertainty in scenario studies via evolution and equivalence models. First, we studied cross-sections (see section 5.2.1). Cross-section covariance matrices contain their energy-dependent uncertainty and correlation, for a given energy mesh. However, the physical models in COSI do not handle multi-group data, therefore it was necessary to produce 1-group uncertainties, adapted to each spectrum of interest, from covariance matrices. Furthermore, as transition scenario computation model different types of reactors in the same simulation, knowledge of correlation of cross-sections in different spectra was required.

Therefore we developed a method that calculates such uncertainty, as well as correlations between 1-group cross-sections of different reactions, in different spectrum. For instance, this method calculates the correlation between ^{238}U capture cross-section in PWR UOX and PWR MOX spectra, or the correlation between ^{239}Pu capture in PWR UOX spectrum and ^{239}Pu fission in SFR spectrum.

Given that ENDF B-VII contains uncertainty data for all cross-sections of interest, we based this work on this evaluation. First, we built covariance matrices in convenient energy meshes from the evaluation, then we produced the sensitivity vectors used in this condensation method, then we applied the method to produce relative standard deviation and correlation for the nuclides of interest. Results are exposed in section 5.2.1.5.

Fission yields also generate uncertainty. However, data in a convenient format is already available in nuclear data evaluations (see section 5.2.2). We also chose ENDF B-VII so as to be consistent with cross-sections uncertainty data.

We note that these results were also used during construction of depletion and equivalence models, so as to parameterize them accordingly.

1.4.3 Scenario parameters and hypotheses

Several parameters of the nuclear industry used in scenario simulations are associated with uncertainty, variability or indecision. They are discussed in section 5.3. First, we separated this set of parameters into two subsets:

- *scenario parameters*, which generate uncertainty;
- *scenario hypotheses*, which constitute the scenario backbone, and depend on decision-making hypotheses, not measurement or prediction uncertainties.

The list of scenario parameters (see section 5.3.3) generating uncertainty was established, and the uncertainty or at least the range of these parameters was estimated. This work is based on industrial feedback and experimental results. Scenario parameters include burnup, fuel fabrication time, reprocessing plant recovery rates, mass losses at different fuel plants, etc. Due to COSI data structure, burnup uncertainty can be difficult to model in pre-existing scenarios, and the uncertainty propagation method becomes difficult to apply, and requires a deep data set modification as well as introduction of thousands of parameters. Therefore, a study dedicated to burnup uncertainty is performed in section 5.3.3.8, and different sampling methods are discussed, so as to take burnup uncertainty and correlation into account in an appropriate way.

Scenario hypotheses (see section 5.3.2) are not associated with any uncertainty in these studies: we considered that changing a scenario hypothesis generates a different scenario. Those parameters include: fuel type, stretch-out, reactors starting date, reprocessing capacity, etc. However, sensitivity studies can be performed to assess the impact on the fuel cycle.

1.5 Uncertainty propagation studies

1.5.1 Method

Uncertainty propagation studies are performed in section 6.

The uncertainty propagation methodology is straightforward: we sample the parameters associated with an uncertainty according to their distribution and analyze the distribution of the results. Correlations between parameters are taken into account when available. In studies that consider different parameters, we sampled these parameters altogether. We also performed several other studies, such as decomposition of variance, which consists in impact magnitude analysis of the different parameters; or feasibility studies, which determine the probability that scenarios fail at a given moment, mostly because of a lack of fissile material.

1.5.2 Applications

First, in section 6.1 we calculate uncertainty and analyze the variance of spent fuel concentrations in the frame of irradiation computations for PWR UOX, PWR MOX and SFR fuel, so as to determine the uncertainty of spent fuel concentrations for nuclides of interest, as well as the contribution of the different physical parameters to the uncertainty. Even though input parameters of the depletion models vary in a scenario calculation, this study gives an idea of the impact magnitude of different physical parameters.

In section 6.2.1, we compare the COSI results with the results obtained with the new scheme COSI-MeSAR in the frame of the French historical PWR fleet (scenario A). Then, we compare these results with ANDRA data. The results are discussed in section 6.2.1.5.

In section 6.2.2 we work on an industrial transition scenario (scenario B), whose hypotheses are discussed between CEA and its industrial partners. First, we perform a brief uncertainty propagation, taking into account burnup uncertainty only. Then, we used this scenario so as to test the simplified burnup sampling methods defined in section 5.3.3.8 and their impact on several scenario results of interest.

In section 6.2.3, we work on an academic transition scenario (scenario C), which models SFR deployment without minor actinides transmutation. First, we calculate nuclear data and burnup uncertainties propagation on a few scenario results. Then, we analyze the behavior of data-driven equivalence models, whose construction is explained in section 4, in scenario computations. After that we discuss the impact of burnup and nuclear data uncertainties through equivalence models on scenario results.

Finally, in section 6.2.4, we study a transition scenario (scenario D, which is based on scenario C), which models SFR deployment with americium only transmutation in americium bearing blankets. First, we calculate nuclear data and burnup uncertainties propagation on several scenario results: global actinides inventories, natural uranium consumption, fuel fabrication needs and spent fuel inventory. Then, we analyze the contribution of nuclear data and burnup to total variance on different types of results. After that, we perform a feasibility study for scenario D, which consists in calculating the probability that fissile material lacks at a certain point. We also provide several sensitivity studies to parameters such as reprocessing plant recovery rate and front-end durations, and analyze the impact of decay heat uncertainty on the scenario feasibility.

These applications of the method allows us to conclude on uncertainty propagation in scenario studies with COSI.

Bibliography

[1.1] R. Craplet and J. Ahn. Mathematical modeling and its applications for mass flow in a nuclear fuel cycle. *Nuclear technology*, 177:pages 314–335, 2012.

[1.2] N. Dos Santos. *Optimisation de l'approche de représentativité et de transposition pour la conception neutronique de programmes expérimentaux dans les maquettes critiques*. PhD thesis, Ecole doctorale I-MEP2, 2013.

Chapter 2

Numerical tools

Contents

2.1 Evolution: CESAR 38
2.1.1 Introduction 38
2.1.2 Nuclear data 38
2.1.3 Evolution calculation 40
2.2 Scenario: COSI 42
2.2.1 Introduction 42
2.2.2 Energy, needs and mass flows 43
2.2.3 Facilities and physical models 44
2.3 Neutron transport calculation 49
2.3.1 APOLLO2 50
2.3.2 ERANOS 50
2.4 Statistical analysis: URANIE 50

2.1 Evolution: CESAR

2.1.1 Introduction

CESAR [2.1] (Code d'Évolution Simplifié Appliqué au Retraitement, *Simplified Evolution Code Applied to Reprocessing*) is a simplified depletion code. It computes nuclear fuel evolution in (irradiation) and out (cooling) of the reactor, as well as physical parameters of interest: mass balance, decay heat, radio-toxicity, etc.

CESAR has been developed by CEA and AREVA NC for 30 years, and provides characterizations for all types of nuclear fuel and waste, as well as structural materials.

In this work, the CESAR5.3 version was used. It is based on JEFF-3.1.1 [2.2] nuclear library, and is constantly checked against the CEA referenced and qualified depletion code DARWIN [2.3]. CESAR incorporates the CEA qualification based on dissolution analyses of fuel rod samples as well as La Hague reprocessing plant feedback experience.

CESAR is the reference code used at AREVA La Hague to compute evolution, in and out of pile, of spent fuel physical parameters including activity, decay heat, neutron and gamma sources and spectra, in the frame of technical and economic studies, fuel acceptance and fuel physics characterization, criticality studies, decay heat studies, etc.

CESAR5.3 qualification results are available in [2.1].

2.1.2 Nuclear data

In order to solve numerically Bateman irradiation equation (see section 2.1.3.2), CESAR requires nuclear data, including:

- atomic masses;
- cross-sections;
- fission yields;
- radioactive decay periods;
- energies (fission, capture, decay, etc.).

Masses and periods do not depend on the spectrum, therefore they are extracted one and for all from nuclear databases.

Fission and capture energies depend on the spectrum because they are a function of the incident neutron energy.

Fission yields also depend on the spectrum. CESAR5.3 uses two fission yields databases, one for thermal spectra and one for fast spectra. PWR MOX are considered as thermal. The energy-integrated fission yield η is approximated by an average of fission yields for fast and thermal neutrons weighted by fission rates τ in typical thermal and fast spectra.

$$\eta = \frac{\tau_{thermal}}{\tau_{thermal} + \tau_{fast}} \times \eta_{thermal} + \frac{\tau_{fast}}{\tau_{thermal} + \tau_{fast}} \times \eta_{fast} \tag{2.1}$$

This approximation is possible because fission yields are not very sensitive to the incident neutron energy.

The case is different for cross-sections. They are extremely energy-dependent, and are subject to complex and non-linear phenomena such as resonances. As a consequence, cross-sections are heavily dependent on the spectrum at any irradiation time, i.e. any burnup step. However, CESAR is not a neutron transport code, and cannot evaluate the spectrum at each burnup step. Furthermore, CESAR is an industrial code, which means it has heavy CPU time constraints: performing transport computation at each burnup step is therefore not possible. The adopted strategy was to build cross-sections estimators, so as to predict them at each moment of irradiation.

As explained, cross-sections are functions of the spectrum, which is itself a function of the fuel composition at a given time, and fuel composition at any burnup step solely depends on the fresh fuel composition and the burnup. Therefore, for a given geometry, fresh fuel composition and burnup are sufficient to build cross-sections estimators.

In the case of CESAR, cross-sections are estimated by Legendre polynomials. The design of experiments for construction of these polynomials is one step at a time (OAT). Parameters depend on the fuel type, and may include different parameters chosen in function of the fresh fuel composition:

- burnup;
- ^{235}U initial enrichment;
- ^{239}Pu initial content, etc.

Prior transport computations are required to calculate cross-sections. They are generally performed using APOLLO2 [2.4] in the case of thermal spectra and ERANOS [2.5] in the case of fast spectra. Transport calculations are based on reference calculation schemes. Creation of cross-sections estimators, in function of burnup and different transport computation parameters, is performed by APOGENE tool [2.1]. Finally, 1-group parameterized cross-sections are stored in ciphered data libraries called *BBL*. Each BBL has its own domain of validity in terms of fresh fuel composition, burnup and specific power.

Figure 2.1 illustrates the process of nuclear data generation for a CESAR5.3 computation, and then irradiation computation. The parameters are as follows:

- $\sigma(E)$: point-wise cross-sections;
- $\sigma(BU)$: burnup-dependent (and potentially fresh-fuel dependent) energy-integrated cross-sections;
- y_0 : fresh fuel mass fraction;
- BU : burnup;
- Δt_{irr} : irradiation time.
- N : concentrations after irradiation.

The steps in the blue frames concern nuclear data and are performed once and for all for each fuel type. They represent the construction of a BBL. Data in the green frame is the set of parameters fora CESAR computation. CESAR computation is in the red frame, and results in the orange frame.

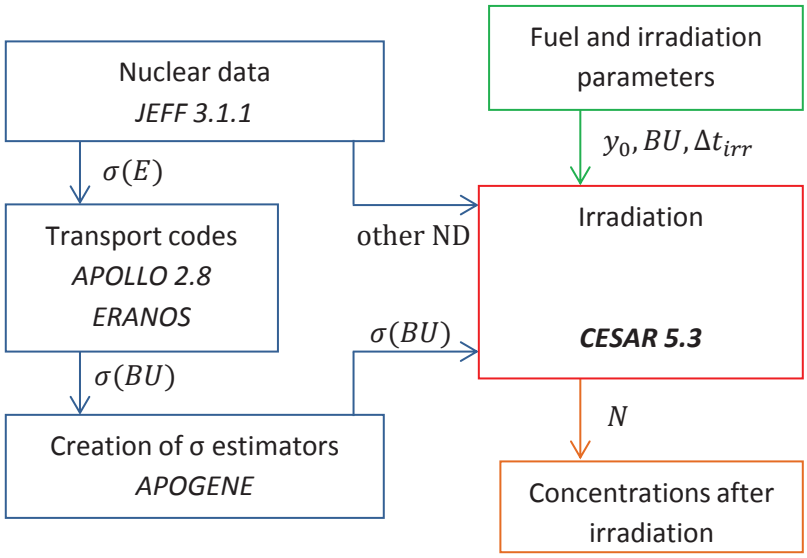

Figure 2.1: Nuclear data generation for CESAR5.3

2.1.3 Evolution calculation

2.1.3.1 Introduction

Evolution computation means resolution of a differential equations system: Bateman equations. We denote λ_α, λ_{β^+}, λ_{β^-}, λ_{IT}, λ_{SF} the α, β^+, β^-, isomeric transition and spontaneous fission decay constants respectively. We also denote R_x the branching ratio of decay mode x and T_x its half-life. We have:

$$\begin{cases} \lambda_{total} &= \sum\limits_{i \in \text{decay modes}} \lambda_i \\ T_{total} &= \dfrac{ln(2)}{\lambda_{total}} \\ \lambda_x &= R_x \lambda_{total} \\ 1 &= \sum\limits_{i \in \text{decay modes}} R_i \end{cases} \tag{2.2}$$

The Bateman equations in irradiation and cooling computation are discussed in the next paragraphs.

2.1.3.2 Irradiation calculation

2.1.3.2.1 Flux computation

The first step consists in computing the flux. The time variable is discretized. Flux is evaluated at each time step. We denote t the number of the considered time step. The flux at t is computed in function of the system state at time $(t-1)$. We have:

- for the system:
  - BU the burnup (in MWd/tHM *i.e.* MegaWatts days per ton of initial heavy metal);
  - ϕ the neutron flux (in n.m^{-2}.s^{-1} ie neutrons per square meter per second);
  - HN the heavy nuclides (actinides) (dimensionless);
  - FP the fission products (dimensionless);
  - AP the activation products (from impurities and structure materials) (dimensionless);
  - m_0 the initial heavy nuclides mass (tons)
- for isotope i:
  - $NF(i)$ the cumulative number of fissions (dimensionless);
  - $NC(i)$ the cumulative number of captures (dimensionless);
  - $\overline{E_f}(i)$the mean fission energy (MWd);
  - $\overline{E_c}(i)$ the mean capture energy (MWd);
  - σ_r energy-integrated cross-section of reaction r on isotope i (c=capture, f=fission, a=absorption≈f+c).

The burnup is calculated as follows:

$$BU = \frac{\sum\limits_{i \in HN} NF(i)\overline{E_f(i)} + \sum\limits_{i \in \{HN,FP,AP\}} NC(i)\overline{E_c(i)}}{m_0} \tag{2.3}$$

The cumulative number of fissions and captures are given by:

$$\begin{cases} \dfrac{dNF(i \in HN)}{dt} &= \sigma_f(i,t) \times N(i,t) \times \phi(t) \\ \dfrac{dNC(i \in HN,FP,AP)}{dt} &= \sigma_c(i,t) \times N(i,t) \times \phi(t) \end{cases} \tag{2.4}$$

We consider time intervals Δt small enough to integrate the previous equations. Let ΔNF denote the number of fissions between t and $t + \Delta t$, and ΔNC the captures. Then, we have:

$$\begin{cases} \Delta NF &= \sum\limits_{i \in HN} \sigma_f(i,t-1) \times N(i,t-1) \times \phi(t) \times \Delta t \\ \Delta NC &= \sum\limits_{i \in \{HN,FP,AP\}} \sigma_c(i,t-1) \times N(i,t-1) \times \phi(t) \times \Delta t \end{cases} \tag{2.5}$$

Finally the flux is calculated as:

$$\phi(t) = \frac{\Delta BU}{\Delta t} \times \frac{m_0}{\sum\limits_{i \in HN,FP,AP} N(i,t-1)\left(\sigma_f(i,t-1)\overline{E_f(i)} + \sigma_c(i,t-1)\overline{E_c(i)}\right)} \tag{2.6}$$

We note that the evolution chains are truncated; consequently the results are only consistent after 90 days of cooling.

2.1.3.2.2 Concentrations computation

Once the flux is computed, each nuclide evolution is then evaluated. For instance, in the case of heavy nuclide $\left[\begin{smallmatrix}\mathrm{A}\\ \mathrm{Z}\end{smallmatrix}\right]$, the balance expresses as follows:

$$\begin{aligned}\frac{dN(\left[\begin{smallmatrix}\mathrm{A}\\ \mathrm{Z}\end{smallmatrix}\right],t)}{dt} &= \sigma_c N(\left[\begin{smallmatrix}\mathrm{A\text{-}1}\\ \mathrm{Z}\end{smallmatrix}\right],t)\times\phi(t)\\ &+ \sum_{i\xrightarrow{mode}\left[\begin{smallmatrix}\mathrm{A}\\ \mathrm{Z}\end{smallmatrix}\right]}\lambda_{mode}(i)N(i,t)\\ &- \sigma_a N(\left[\begin{smallmatrix}\mathrm{A}\\ \mathrm{Z}\end{smallmatrix}\right],t)\times\phi(t)\\ &- \lambda_{total}(\left[\begin{smallmatrix}\mathrm{A}\\ \mathrm{Z}\end{smallmatrix}\right])N(\left[\begin{smallmatrix}\mathrm{A}\\ \mathrm{Z}\end{smallmatrix}\right],t)\end{aligned} \tag{2.7}$$

This equation is solved using a second order Runge-Kutta method.

2.1.3.3 Cooling calculation

The cooling calculation is expressed as equation 2.7 with a null flux:

$$\begin{aligned}\frac{dN(\left[\begin{smallmatrix}\mathrm{A}\\ \mathrm{Z}\end{smallmatrix}\right],t)}{dt} &= \sum_{i\xrightarrow{mode}\left[\begin{smallmatrix}\mathrm{A}\\ \mathrm{Z}\end{smallmatrix}\right]}\lambda_{mode}(i)N(i,t)\\ &- \lambda_{total}(\left[\begin{smallmatrix}\mathrm{A}\\ \mathrm{Z}\end{smallmatrix}\right])N(\left[\begin{smallmatrix}\mathrm{A}\\ \mathrm{Z}\end{smallmatrix}\right],t)\end{aligned} \tag{2.8}$$

This equation, much simpler than equation 2.7, does not require a Runge-Kutta solver, then a matricial resolution is implemented.

2.2 Scenario: COSI

2.2.1 Introduction

Nuclear systems, composed of reactors and various fuel and cycle facilities, are quite complex. In order to have a complete overview of nuclear systems, it is required to follow precisely material flows, detailed by nuclide, at each step of the front-end and back-end fuel cycle. COSI [2.6, 7] is a scenario code being developed at CEA Cadarache since 1985. It simulates a pool of nuclear electricity generating plants, and the associated fuel cycle facilities. COSI was designed to study various short, medium and long-term options for the introduction of various types of nuclear reactors. In the frame of the French Act for waste management, scenario studies are carried out with COSI. The code enables comparison of different options of evolution of the French reactor fleet, as well as the different options of partitioning and transmutation of minor actinides and plutonium [2.8].

Nuclear systems are composed of various facilities:

- mines;
- enrichment plants;

- fabrication plants;
- reactors;
- reprocessing plants;
- vitrification plants;
- material interim storage;
- disposal, etc.

Each facility corresponds to at least one physical model. For instance, reactors contain an irradiation model, and fabrication plants contain an equivalence model.

Those facilities are linked via material flows and needs. For instance, reactors need fuel from fabrication plants, and fabrication plants produce fuel for reactors.

Figure 2.2 illustrates the material flow and needs as implemented in COSI. Material flows can have additional binary steps causing delay (minimum waiting time, physical constraints on decay heat, etc.).

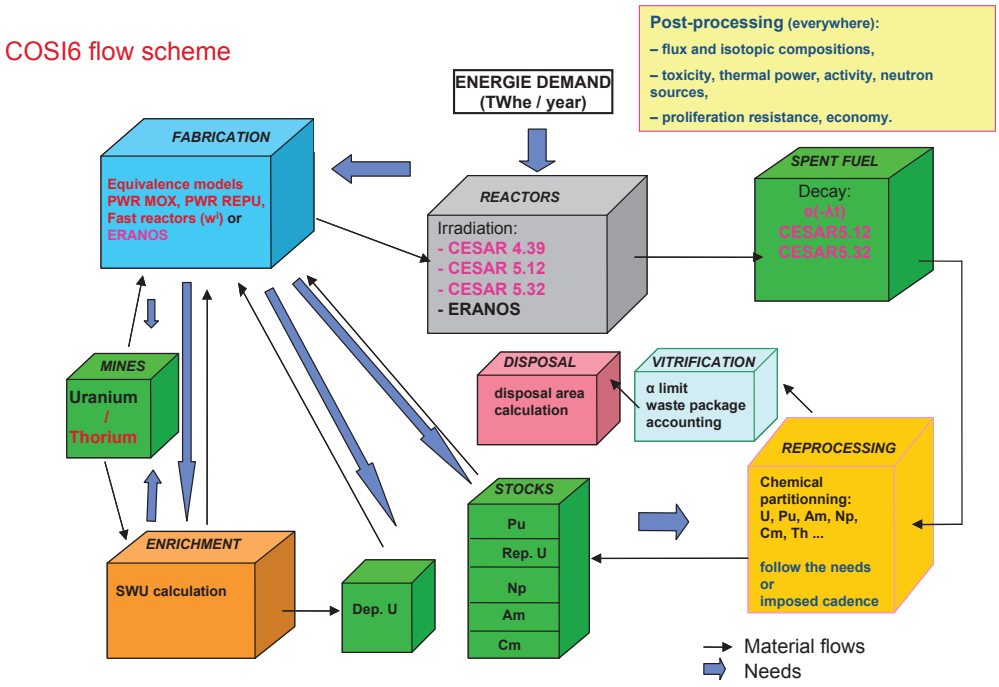

Figure 2.2: COSI flow scheme

2.2.2 Energy, needs and mass flows

2.2.2.1 Mass flows

A large number of nuclides, including heavy nuclides and fission products, are modeled in COSI. Mass flows are always detailed in terms of isotopic composition.

In COSI, mass flows are not continuous, but sequential, as in the actual fuel cycles. For instance, the input mass flow for a given reactor is not continuous in function of time, and consists in a discrete sequence of batches. However time is continuous, and evolution computation is performed for any time interval, when needed.

Approximately 100 heavy nuclides and 200 fission products are taken into account in COSI, including uranium, neptunium, americium, curium nuclides, and most of the fission products contributing to decay heat at the fuel cycle time scale ($\geq$1 year). The list of nuclides is consistent with CESAR5.3 list of nuclides.

2.2.2.2 Energy demand and production

2.2.2.2.1 Energy production

Annual energy production per reactor is expressed in TWhe/year (TeraWatt $\times$ hour of electric energy per year), and is calculated as:

$$E_i = 24 \times 10^{-6} \times \sum_{j \in batches} \text{BU}_j \times M_j \times D_{i,j} \times \eta \tag{2.9}$$

With:

- E_i: electrical energy production of a given reactor during year i;
- M_j: mass of fuel batch j (tons of heavy metal);
- BU_j: discharge burnup for fuel batch j in MWd/tHM (MegaWatts $\times$ days per ton of Heavy Metal);
- η: reactor yield (dimensionless, conversion of thermal energy into electric energy);
- $D_{i,j}$: proportion on year i of the irradiation time of fuel batch j;
- the numerical constant corresponds to the conversion of TWh into MWd.

The reactor fleet energy production is equal to the sum over reactors of energy production per reactor.

2.2.2.2.2 Energy demand

Annual energy demand is expressed in TWhe/year. The objective of the energy demand function in COSI is to equalize energy demand and energy production.

It is possible to reverse equation 2.9 and use energy demand to create a reactor fleet and determine the reactors' successions of loadings, i.e. to calculate the fuel mass in each reactor at any time of the scenario so as to produce exactly the energy demand.

2.2.3 Facilities and physical models

2.2.3.1 Introduction

Figure 2.3, taken from [2.7], is the operating diagram of a COSI data set. This section explains the function of the different steps. The green dotted arrows indicate associations between fuel / batches properties and front-end / back-end paths. The black arrows indicate inclusion relation. Large arrows indicate mass flows in the fuel cycle, and red arrows other mass flows.

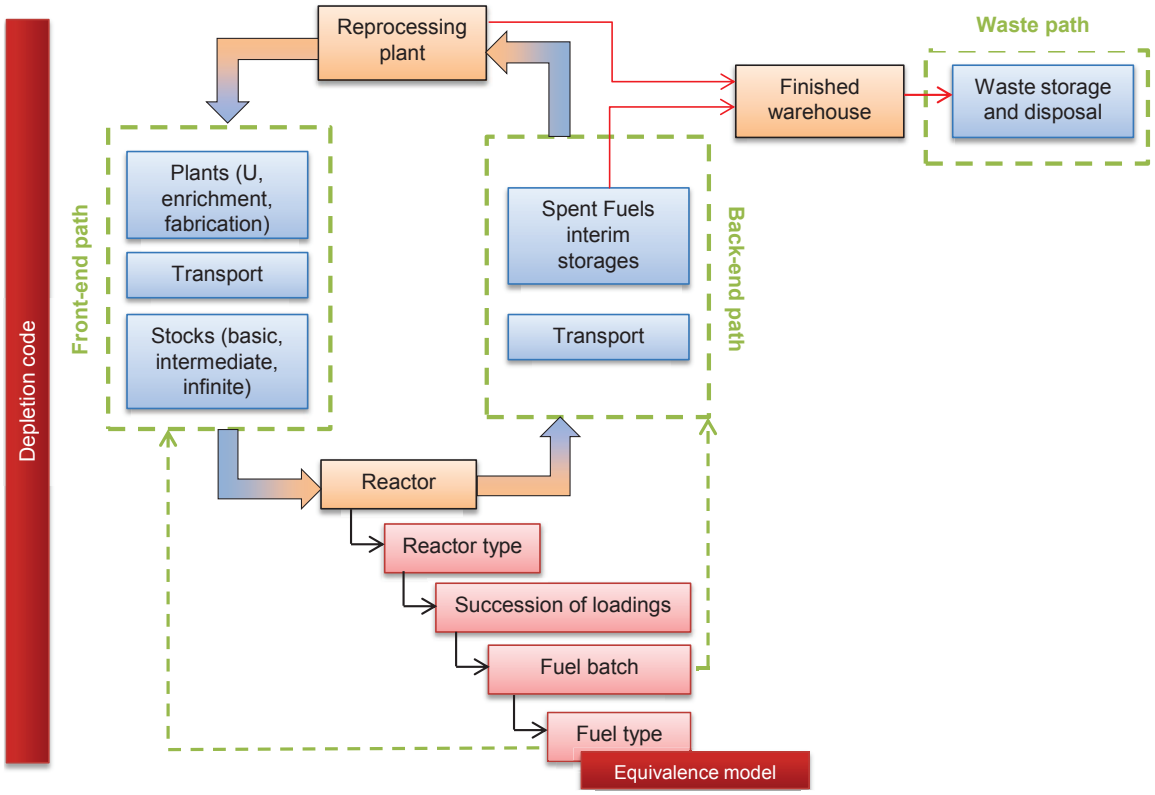

Figure 2.3: Operating diagram of COSI data set

2.2.3.2 Front-end path

2.2.3.2.1 Plants

2.2.3.2.1.1 Uranium plants

Uranium plants perform uranium extraction or conversion.

They are associated with an operation time (see section 2.2.3.9), losses and heavy metal capacity.

2.2.3.2.1.2 Enrichment plants

Enrichment plants perform uranium enrichment. Different enrichment processes are implemented, including:

- gaseous diffusion;
- ultra-centrifugation;
- new processes.

Enriched uranium isotopy is given by equation 2.10 using the following notations:

- $iso(j) = \dfrac{m(j \in U)}{\sum\limits_{i \in U} m(i)}$ the isotopy fo the nuclide j, m being the mass;
- U_e the enriched uranium;
- U_f the uranium feeding the enrichment plant (natural or reprocessed uranium);
- $K(j)$ the transfer coefficient of isotope j, which depends on the enrichment process.

$$\frac{iso(^{j}U_e)}{iso(^{j}U_f)} = 1 + K(j)\left(\frac{iso(^{235}U_e)}{iso(^{235}U_f)} - 1\right)\frac{1 - iso(^{j}U_f)}{1 - iso(^{235}U_f)} \tag{2.10}$$

Enrichment plant produces enriched uranium and depleted uranium. ^{235}U isotopy in depleted uranium is called enrichment tail. They are associated with an operation time (see section 2.2.3.9), annual uranium losses and annual separative work unit (SWU) capacity.

2.2.3.2.1.3 Fabrication plants

The fabrication plants perform fuel fabrication. They produce fresh fuel and determine its composition from constitutive materials. Equivalence models (see chapter 4) determine the enrichment or content for different fuel types, including:

- PWR MOX (plutonium content);
- PWR repU (uranium enrichment);
- SFR (plutonium content).

Different equivalence models can exist for the same fuel type so as to take specifics into account (different core geometries, presence of americium in fresh fuel, etc.).

PWR UOX enrichment is fixed (i.e. chosen by the user, not calculated with a physical model) given that natural uranium composition is not time-dependent.

Fuel fabrication plants are associated with an operation time (see section 2.2.3.9), losses and heavy metal capacity.

2.2.3.2.2 Transportation

The back-end transportation works the same as front-end transportation, and introduces a delay in the path (see section 2.2.3.9).

2.2.3.2.3 Stocks

The stocks are facilities which can contain material. They are not associated with any physical model besides cooling (see section 2.2.3.9). However, cooling duration is not defined in the stock itself, but depends on other plants. They are usually used to model stocks of depleted uranium, separated plutonium, reprocessed uranium or waste.

2.2.3.3 Reactors and fuel

2.2.3.3.1 Reactor

The reactors are associated with starting and shutdown dates, as well as a load factor. They belong to a reactor type.

2.2.3.3.2 Reactor type

A reactor type defines a net yield, as well as a succession of loadings (the sequence of batches that will be irradiated in each reactor of a given reactor type).

2.2.3.3.3 Succession of loadings

The succession of loadings defines a cycle length in EFPD (effective full power days), as well as the fuel batches, mass and number of irradiation cycles. A succession of loading may include different loadings, associated with different cycle lengths or number of cycles.

2.2.3.3.4 Fuel batch

The fuel batch indicates the batch nature (used to distinguish batches together at the back-end path), minimum cooling time and/or maximum decay heat before reprocessing and/or transportation, and a back-end path.

2.2.3.3.5 Fuel type

The fuel type determines the burnup, the equivalence model (see section 4), the front-end path and the irradiation model. The irradiation models include:

- CESAR [2.1] (different versions according to ND referential);
- ERANOS [2.5] (SFR only).

CESAR5.3 is the main calculation model, it computes the composition (with a detail by nuclide) of irradiated fuel in function of:

- fuel type (name of the BBL, see section 2.1.2);
- fresh fuel composition;
- irradiation parameters: end of irradiation burnup, irradiation time.

2.2.3.4 Reprocessing plants

Reprocessing plants perform fuel reprocessing. This consists in extracting elements of interest from irradiated fuel, in order to feed stocks that will produce fresh fuel, and reduce the amount of waste. The irradiated fuel storage plants feeding reprocessing plants are usually distinguished in terms of fuel type (PWR UOX, PWR MOX, SFR, blankets, etc.). Separated elements stocks are produced from mixtures of irradiated fuels, and the user defines the nature of the different spent fuel batches and the proportions of the mix each year. For instance, plutonium for SFR reactor can be produced using a mix of 60% PWR UOX and 40% PWR MOX irradiated fuel. The irradiated fuels nature and proportions can be adapted each year of the scenario. User defines himself the proportions of the spent fuel mix for producing fresh fuel (there is no automated optimization at the moment). Reprocessing plant can operate in function of the fuel demand (driven by reactors and their successions of loadings) or in function of a production objective (in tons of heavy metal per year).

Reprocessing plants are associated with an operation time (see section 2.2.3.9), recovery rates, order of requisition (first batch arrived is reprocessed first or last), annual heavy metal capacity, annual plutonium capacity and sampling rate[1].

[1] A reprocessing plant with a yearly capacity X and a sampling rate Y processes X/Y tons every $1/Y$ year.

2.2.3.5 Back-end path

2.2.3.5.1 Spent fuel interim storage

Downstream of a reactor, irradiated fuel is stored in spent fuel interim storage plants. The properties of irradiated batches include:

- batch nature (so as to be distinguished at the reprocessing plant);
- minimum cooling time before transportation or reprocessing;
- maximum decay heat for transportation or reprocessing.

Figure 2.4 shows a spent fuel interim storage.

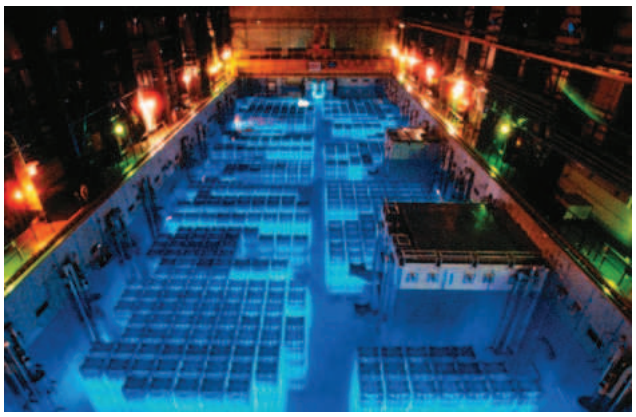

Figure 2.4: View of a spent fuel interim storage

2.2.3.5.2 Transportation

Back-end transportation works the same was as front-end transportation, and introduces a delay in the path (see section 2.2.3.9).

2.2.3.6 Waste storage and waste disposal

Waste storage and waste disposal host wastes for respectively finite and infinite time periods.

Figure 2.5 represents a waste storage.

Figure 2.5: View of a waste storage

2.2.3.7 Finished warehouses

Finished warehouses transform waste material into packages. The properties of finished warehouses include:

- operation time (see section 2.2.3.9);
- package mass and volume;
- maximum material mass;
- technological limits (function of the material isotopic composition).

The maximum α radioactivity is an example of technological limit for packages.

2.2.3.8 Transportation

Transportation involves transportation of the material (fresh fuel, spent fuel, etc.). They are associated with an operation time (see section 2.2.3.9).

2.2.3.9 Various delays

Various steps take time, including transportations linking fuel facilities together. Therefore they are associated with a cooling model. The cooling models in COSI are:

- CESAR: matricial resolution of Bateman cooling equation;
- intern iterative resolution of Bateman equation for heavy nuclides (Runge-Kutta);
- intern analytical resolution of Bateman cooling equation for heavy nuclides (sum of exponential functions).

The reference scheme uses CESAR5.3 for matricial resolution.

2.3 Neutron transport calculation

The fuel cycle is dependent on input data coming from transport calculation. In the context of this work, thermal and fast neutron transport deterministic lattice codes have been used. They are detailed hereafter.

2.3.1 APOLLO2

APOLLO2 [2.4] is a deterministic neutron calculation code system developed by CEA. It resolves 2D multicell transport equation, using different solvers: collision probability method (P_{ij}), discret ordinates (S_n) method, or the method of characteristics (MOC). It has been validated on a large experimental database for both UOX and MOX LWR applications.

2.3.2 ERANOS

ERANOS [2.5] is a deterministic neutron transport code system developed by CEA for fast reactor core calculation, as well as shielding and fuel cycle calculation. Core calculations are performed in two steps:

- 1D or 2D cell/lattice level, using the ECCO cell code for cross-sections calculation and collapsing;
- core level, using discrete ordinates (S_n) methods.

2.4 Statistical analysis: URANIE

URANIE [2.9] is a *sensitivity and uncertainty* platform developed by CEA. It regroups methods and algorithms for sensitivity and uncertainty analysis. URANIE is based on the object-oriented data analysis framework ROOT [2.10]. The main modules include:

- DataServer: data tables and data processing tools;
- Sampler: generation of design of experiments;
- Modeler: construction of surrogate models;
- Launcher: interface with other codes of functions;
- Sensitivity: sensitivity analysis tools;
- Optimizer: mono- and multi-objective optimization algorithms.

The ROOT C++ interpreter allows advanced customization of data treatment with URANIE.

Bibliography

[2.1] J.M. Vidal, R. Eschbach, A. Launay, C. Binet, and J.F. Thro. CESAR5.3: an industrial tool for nuclear fuel and waste characterization with associated qualification - 12067. In *WM2012 Conference*, 2012.

[2.2] A. Santamarina, D. Bernard, P. Blaise, et al. The JEFF-3.1.1 Nuclear Data Library, JEFF Report 22, Validation Results from JEF-2.2 to JEFF-3.1.1. Technical report, OECD, 2009.

[2.3] A. Tzilanizara, C. Diop, B. Nimal, M. Detoc, L. Luneville, M. Chiron, T.D. Huynh, I. Bresard, I. Eid, J.C. Klein, et al. DARWIN: an evolution code system for a large range of applications. In *Procs of ICRS-9*, 1999.

[2.4] A. Santamarina, D. Bernard, P. Blaise, L. Erradi, P. Leconte, R. Le Tellier, C. Vaglio, and J-F. Vidal. APOLLO2.8: a validated code package for PWR neutronics calculations. In *Advances in Nuclear Fuel Management IV (ANFM 2009), Hilton Island, South Carolina, USA*, 2009.

[2.5] G. Rimpault, D. Plisson, J. Tommasi, R. Jacqmin, J-M. Rieunier, D. Verrier, and D. Biron. The ERANOS Code and Data System for Fast Reactors Neutronic Analyses. In *Proc. of PHYSOR 2002*, 2002.

[2.6] R. Eschbach, M. Meyer, C. Coquelet-Pascal, M. Tiphine, G. Krivtchik, and C. Cany. New developments and prospects on COSI, the simulation software for fuel cycle analysis. In *Global 2013*, 2013.

[2.7] SPRC/LECy. *COSI6 users manual*. CEA, 2014.

[2.8] C. Coquelet-Pascal, M. Meyer, R. Eschbach, C. Chabert, C. Garzenne, P. Barbrault, L. Van Den Durpel, T. Duquesnoy, M. Caron-Charles, B. Carlier, and J.-C. Lefevre. Comparison of different scenarios for the deployment of fast reactors in france - results obtained with COSI. In *Proceedings of GLOBAL 2011*, 2011.

[2.9] F. Gaudier. URANIE: the CEA/DEN uncertainty and sensitivity platform. In *Procedia Social and Behavioral Sciences*, volume 2, pages 7660–7661, 2010.

[2.10] R. Brun and F. Rademakers. ROOT - an object oriented data analysis framework. In *AIHENP*, 1996.

Chapter 3

Evolution models

Contents

3.1 Irradiation models for actinides 54
3.1.1 Specifications 54
3.1.2 Sampling 56
3.1.3 Regression 82
3.2 Irradiation models for fission products 111
3.2.1 Specifications 111
3.2.2 Sampling 115
3.2.3 Regression 125
3.2.4 Calculation of decay heat 131
3.3 Blankets 143
3.3.1 Introduction 143
3.3.2 Fertile blanket 143
3.4 Conclusions and perspectives 148
3.4.1 Conclusions 148
3.4.2 Perspectives 148

3.1 Irradiation models for actinides

3.1.1 Specifications

3.1.1.1 Identification of actinides to be estimated

A lot of actinides are present in the fuel cycle. A few of those were present from the beginning, such as ^{235}U or ^{238}U. The presence of other actinides (isotopes of U, Np, Pu, Am, Cm, etc.) usually results from a succession of captures and/or decay on these nuclides.

Given that the main goal of this study is to calculate scenario results and their associated uncertainty, actinides irradiation models will have to calculate the concentration after irradiation of nuclides that contribute to those results.

Nuclides have several ways to contribute to typical scenario results. Those ways of contribution, which are correlated, are described below:

- nuclide representing a non-negligible part of a given mass balance or inventory;
- nuclides contributing to decay heat;
- nuclide contributing to radio-toxicity;
- nuclide having an impact on reactivity via Boltzmann equation.

Moreover, the nuclide contribution depends on their phase (solid/liquid/gas) in the different fuel cycle steps.

For instance, in the case of a PWR UOX fuel irradiated up to 45GWd/tHM with a specific power of 31W/gHM, then cooled for 1 year, the contributions of different actinides to several results can be calculated. Results are shown in tables 3.1 and 3.2.

Nuclide	contribution to mass	cumulative contribution
^{238}U	96.983%	96.983%
^{235}U	1.136%	98.119%
^{239}Pu	0.640%	98.758%
^{236}U	0.606%	99.364%
^{240}Pu	0.273%	99.638%
^{241}Pu	0.161%	99.799%
^{242}Pu	0.070%	99.869%
^{237}Np	0.065%	99.934%
^{238}Pu	0.030%	99.964%
^{243}Am	0.015%	99.979%
^{241}Am	0.014%	99.993%
^{244}Cm	0.005%	99.998%
^{234}U	0.001%	99.999%
^{242}Cm	0.000%	99.999%

Table 3.1: Contribution of several actinides to heavy nuclides mass fraction in irradiated PWR UOX fuel

Nuclide	contribution to decay heat	cumulative contribution
^{242}Cm	60.461%	60.461%
^{238}Pu	17.600%	78.061%
^{244}Cm	16.135%	94.197%
^{240}Pu	2.030%	96.226%
^{241}Am	1.692%	97.918%
^{239}Pu	1.296%	99.214%
^{241}Pu	0.556%	99.770%
^{243}Am	0.101%	99.870%
^{243}Cm	0.101%	99.971%
^{242}Pu	0.009%	99.980%
^{239}Np	0.008%	99.998%
^{236}Pu	0.003%	99.991%
^{245}Cm	0.002%	99.993%
^{242}Am	0.002%	99.994%

Table 3.2: Contribution of several actinides to heavy nuclides decay heat in irradiated PWR UOX fuel

The mass of several elements at a given time are part of scenario results. It is the case for the uranium, neptunium, americium and curium inventories (this work is limited to U-Pu cycle),

which are usually calculated each year of a scenario. Therefore, all of the isotopes of these nuclides with non-negligible half-lives have to be calculated.

A list of actinides representing a high contribution percentage to the different scenario results was established. It results from a study of contribution to the mass of different inventories of interest and a decay heat study contribution, presented in 3.2.1.2 page 112. This list is as follows:

$$\texttt{list_Actinides} = \left\{ \begin{array}{c} {}^{234}\mathrm{U}, {}^{235}\mathrm{U}, {}^{236}\mathrm{U}, {}^{238}\mathrm{U}, \\ {}^{237}\mathrm{Np}, {}^{239}\mathrm{Np}, \\ {}^{241}\mathrm{Am}, {}^{242M}\mathrm{Am}, {}^{243}\mathrm{Am}, \\ {}^{238}\mathrm{Pu}, {}^{239}\mathrm{Pu}, {}^{240}\mathrm{Pu}, {}^{241}\mathrm{Pu}, {}^{242}\mathrm{Pu}, \\ {}^{242}\mathrm{Cm}, {}^{243}\mathrm{Cm}, {}^{244}\mathrm{Cm}, {}^{245}\mathrm{Cm}, {}^{246}\mathrm{Cm} \end{array} \right.$$

This list is complete enough to be used for PWR UOX, PWR repU, PWR MOX, SFR MOX fuel as well as fertile blankets, i.e. the complete list of fuels for a reference transition scenario (thorium fuel cycle excepted). Further studies may include heavier nuclides such as Cf isotopes.

3.1.1.2 Accuracy of the estimators

The quantification of the estimators' accuracy is an extremely important part of the statistical modeling process. Frequently, when uncertainty propagation or global sensitivity studies are performed, surrogate models of the result itself are constructed. Then, indicators such as the prediction coefficient, which describe the percentage of the variance calculated during uncertainty propagation through the estimator are calculated.

However, due to reasons explained in part 6.1.2.2, the situation in this study is different. We do not build estimators of the scenario results themselves, but estimators of the concentrations of nuclides after irradiation, which are then reprocessed by COSI. Therefore the estimators do not only have to allow a high percentage of variance propagation (global accuracy), but they also have to be precise in terms of estimation of the results (local accuracy on every area of the domain of variation).

Furthermore, we need those estimators to be valid on a wide range. Indeed, in a scenario study, the irradiation parameters and fuel composition of a given core type can vary, and the surrogate model have to be valid for each of those sets of parameters. The surrogate models must also be valid for different scenarios, so as to be able to perform uncertainty propagation studies on various scenarios without having to build additional surrogate models.

A preliminary condition is given now: an estimator can be considered satisfactory if its mean error does not exceed 0.5%. Let y_i be the mass fraction after irradiation for a precise case i, $\hat{y}_i$ the estimator of the mass fraction in the case i, and $\bar{y}$ be the mean value of the y_i on a design of experiment representative of the actual distribution of parameters containing N points, then this relation expresses as follows by equation 3.1:

$$\frac{\sum\limits_{1 \leq i \leq N} |y_i - \hat{y}_i|}{\sum\limits_{1 \leq i \leq N} y_i} \leq 0.5\% \tag{3.1}$$

This indicator has the following advantages:

- it is more *stable* than a local indicator, such as a maximum;
- it does not depend on the width of the parameters' range.

However, satisfaction of this indicator is not always a possibility. Further details on the accuracy of the estimators are given in sections 3.1.3.1.5.1 for polynomial estimators and 3.1.3.2.4.1 for artificial neural network estimators.

3.1.1.3 Remark concerning the short-lived radioactive nuclides

Several short-live radioactive actinides (as well as other nuclides) are produced during irradiation. For instance small concentrations of ^{237}U are found in irradiated fuel. However this nuclide swiftly decays into ^{237}Np.

$$^{237}\mathrm{U} \xrightarrow{T_{1/2}=6.7d} {}^{237}\mathrm{Np}$$

We studied the impact of the estimation of (^{237}Np+^{237}U) instead of (^{237}Np) alone and did not estimate ^{237}U. ^{237}U concentration after irradiation is so low that its impact is negligible and therefore does not improve significantly the quality of the surrogate models. This result was obtained for the following short-lived nuclides:

$$\begin{aligned}
^{237}\mathrm{U} &\xrightarrow{T_{1/2}=6.7d} {}^{237}\mathrm{Np}\\
^{238}\mathrm{Np} &\xrightarrow{T_{1/2}=2.1d} {}^{238}\mathrm{Pu}\\
^{243}\mathrm{Pu} &\xrightarrow{T_{1/2}=5h} {}^{243}\mathrm{Am}\\
^{244}\mathrm{Am} &\xrightarrow{T_{1/2}=10h} {}^{244}\mathrm{Cm}
\end{aligned}$$

3.1.2 Sampling

3.1.2.1 Parameters

3.1.2.1.1 Introduction

The uncertainty value of parameters that are not taken into account during the sampling step cannot be propagated to scenario results. Therefore all parameters having a non-negligible contribution to the uncertainty of the mass fraction of the nuclides from `list_Actinides` have to be taken into account. There are different kinds of parameters, that are described in the next sections.

3.1.2.1.2 Description of the fuel assembly and spectrum

The mass fractions of the different nuclides present in the fuel before irradiation are taken into account. In order to be representative of every possible fuel composition, the mass fractions of all nuclides but ^{238}U are sampled uniformly in a zone covering more[1] than their usual domain of

[1]Sampling parameters only within the domain of variation may degrade the estimators' accuracy on the borders of the domain.

variation. The mass fraction of ^{238}U, significantly higher than the other mass fractions, is used to complete the fuel composition.

The geometry of the fuel assembly is considered subject to no uncertainty.

The spectrum is indirectly taken into account (see section 2.1). For each cross-section library used by CESAR, a series of neutron transport and depletion calculation is performed by APOLLO2 or ERANOS. The fuel composition determines the spectrum, and self-shielding calculation is performed according to this spectrum. The self-shielded cross-sections computed by the transport code are then stored in data files. These files are read by an appropriate tool that performs (Legendre) polynomial regressions to model the self-shielded cross-sections in function of the burnup and fuel composition, and stores the models in the so-called library. Therefore, even though the spectrum itself is not calculated by CESAR, it is taken into account during the estimation of self-shielded cross-sections in function of the burnup and fuel composition.

Sampling the spectrum is not necessary as it is an implicit function of fuel composition.

3.1.2.1.3 Description of the irradiation parameters

3.1.2.1.3.1 Determination of the main parameters

The three main irradiation parameters are the burnup (BU in GWd/tHM), the irradiation length (L in days) and the specific power ($\mathcal{P}$ in W/gHM). They are linked by the relation 3.2.

$$\mathcal{P} = \frac{\mathrm{BU}}{\mathrm{L}} \tag{3.2}$$

Therefore two among three parameters are enough to describe the irradiation. The burnup will be sampled uniformly given that its impact on the Bateman equation is strong, but the other parameter has to be chosen among L and $\mathcal{P}$.

The domain of variation of L (for instance compared to its mean value) is much larger than the domain of variation of $\mathcal{P}$. L can vary from 100 days to a few years, for instance in the case of starting batches or nominal batches, whereas for a given fuel, $\mathcal{P}$ only varies of a few percents. For instance, in the case of PWR UOX, $\mathcal{P}$ usually ranges from 28 to 32W/gHM. Furthermore, when L is sampled in its own domain of variation, the power obtained through equation 3.2 reaches extreme values that are never encountered, whereas when $\mathcal{P}$ is sampled in its own domain of variation, L varies more or less linearly according to BU, in reasonable intervals, which is much more adapted to a precise and concise description.

Figure 3.1 illustrates this phenomenon. In black, we sampled burnup and duration uniformly in their respective domaines, and calculated power as $\mathcal{P} = \frac{BU}{L}$, while in red, we sample burnup and power in their respective domains, and calculated duration as $L = \frac{BU}{\mathcal{P}}$. We observe that most of the first case return irradiation power outside of its actual boundaries.

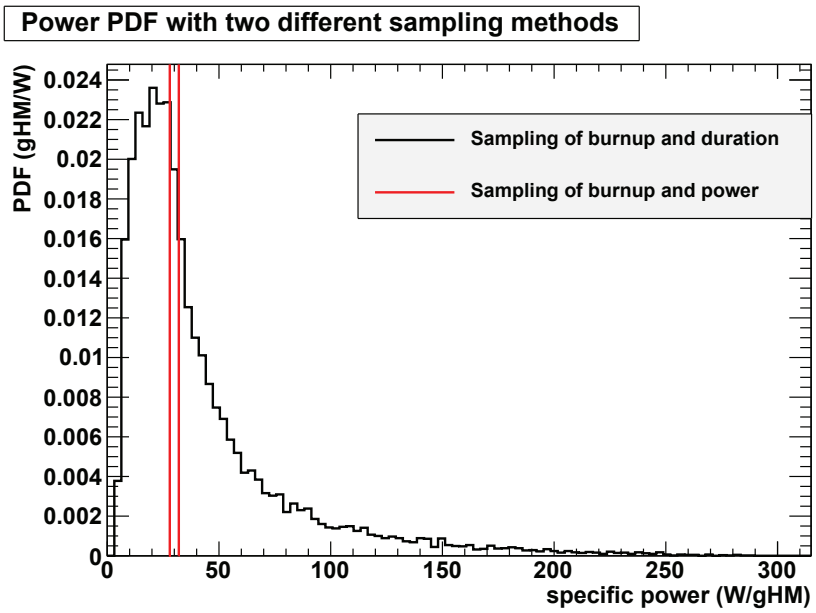

Figure 3.1: Comparison of two power sampling methods

The burnup and specific power are taken into account and sampled in their respective ranges, the irradiation length is calculated according to equation 3.2.

3.1.2.1.3.2 Impact study of a time-dependent load factor

The impact of the irradiation history can be evaluated. Usually, in scenario studies, fuel is considered to be irradiated at a constant specific power, $\bar{\mathcal{P}}$, which is calculated according to equation 3.3, $\bar{f}$ being the mean load factor.

$$\bar{\mathcal{P}} = \bar{f} \times \mathcal{P}_{\text{nominal}} \tag{3.3}$$

However, in practice, this factor is not constant, and varies with time. The impact of the time-dependence of a load factor can be studied, in order to answer the following question: *considering a distribution of time-dependent load factors, is the final concentration of every isotope after irradiation at mean load factor equal to the mean of the concentrations obtained at different load factors?*, i.e. *does a dispersion of load factors introduce a bias in results?* In order to answer this question, the following study was carried for a PWR UOX fuel assembly enriched at 4.5%. The total burnup was considered constant and equal to 45GWd/tHM. The irradiation was divided in three different steps, of equal length. For each step, the average burnup follows a normal distribution, its average is 15GWd/tHM and its standard deviation is 1GWd/tHM. Let f_i be the load factor for step i. We have:

$$\begin{cases} i & \in & \{1,2,3\} \\ f_i & = & \mathcal{N}(\mu = 1, \sigma = 6.67\%) \\ \bar{f}_i & = & 1 \end{cases} \tag{3.4}$$

f is the mean load factor, consequently we have:

$$\begin{cases} f &= 1/3 \times (f_1 + f_2 + f_3) \\ f &= \mathcal{N}(\mu = 1, \sigma = 3.85\%) \\ \bar{f} &= 1 \end{cases} \tag{3.5}$$

The output balance of nuclide X at mean load factor is noted $X(\bar{f})$, the mean output balance of a nuclide considering the dispersion of f is noted $\bar{X}$ and its relative standard deviation is noted $\sigma(X)$. We also note the relative bias $\delta(X)$:

$$\delta(X) = \frac{\bar{X}}{X(\bar{f})} - 1 \tag{3.6}$$

nuclide	$\delta(X)$ (%)	$\sigma(X)$ (%)	nuclide	$\delta(X)$ (%)	$\sigma(X)$ (%)
^{234}U	0.01	1.36	^{242}Pu	0.00	0.03
^{235}U	0.00	0.00	^{241}Am	0.05	1.79
^{236}U	0.00	0.00	^{242M}Am	0.09	3.97
^{238}U	0.00	0.00	^{243}Am	0.00	0.01
^{237}Np	0.00	0.01	^{242}Cm	-0.12	1.32
^{239}Np	0.00	0.01	^{243}Cm	-0.11	2.22
^{238}Pu	-0.02	0.40	^{244}Cm	0.00	0.13
^{239}Pu	0.00	0.04	^{245}Cm	0.00	0.11
^{240}Pu	0.00	0.02	^{246}Cm	0.00	0.09
^{241}Pu	0.00	0.13	^{241}Am + ^{241}Pu	0.00	0.02

Table 3.3: Impact of the variability of the load factor on the output balance of PWR UOX fuel

Results are summarized in table 3.3. The impact of the load factor time-dependence is small for most of the nuclides in `list_Actinides`. The impact on ^{241}Am is high, but we can expect this difference to diminish with time, given that it results from the delay in the creation of ^{241}Pu, which then decays to form ^{241}Am. The case is different for ^{242M}Am. The transmutation flow leading to ^{242M}Am is rather complex, and creation of ^{242M}Am is a highly power-dependent phenomenon given it depends on the presence of ^{241}Am during irradiation, as shown in equation 3.7.

$$^{240}\text{Pu} \xrightarrow{(n,\gamma)} {}^{241}\text{Pu} \xrightarrow{(\beta-)} {}^{241}\text{Am} \xrightarrow{(n,0)} {}^{242M}\text{Am} \tag{3.7}$$

It has to be noted that this study is conservative. Indeed, the load factor can vary on a daily basis, and therefore the irradiation calculation could have been cut into as many segments as there are days in a fuel irradiation. This effect, coupled with the quasi-linearity of the impact of small perturbation of the load factor, would have as a consequence to erase, through integration of the small fluctuations, the impact of the dispersion of a time-dependent load factor with short periods. Indeed the relative standard deviation of the mean f on N irradiation steps following the same distribution $\mathcal{N}(\mu = 1, \sigma = k\%)$ is: $\sigma(\bar{f}) = k/\sqrt{N}$.

Modeling a dispersion of load factors as a mean load factor introduces very few bias to the output balance of actinides.

3.1.2.1.3.3 Impact study of the fuel history

In COSI, irradiation history is approximated. Inter-cycle times are not taken into account directly. Instead, a constant mean irradiation power $\overline{\mathcal{P}}$ is considered, with: $\overline{\mathcal{P}} = \frac{1}{T}\int_0^T \mathcal{P}(t)dt$, with T the complete irradiation duration.

The impact of this approximation was assessed in the case of PWR UOX and PWR MOX fuel after 5 years of cooling. In both cases, we modeled:

- 5 irradiation cycles (9GWd/tHM, 252 days per cycle, 4 inter-cycles of 60 days each). $\overline{\mathcal{P}}$ = 30.0W/gHM;
- 1 irradiation cycle (45GWd/tHM, 1500 days). $\overline{\mathcal{P}}$ = 30.0W/gHM.

Table 3.4 summarizes the results for various nuclides of interest. $\delta(X)$ has the same definition as in the previous paragraph.

nuclide	$\delta(X)$ in UOX	$\delta(X)$ in MOX
^{234}U	0.41%	-0.05%
^{235}U	0.04%	0.00%
^{236}U	0.00%	-0.01%
^{238}U	0.00%	0.00%
^{237}Np	0.06%	0.03%
^{239}Np	-0.04%	-0.06%
^{238}Pu	-0.17%	-0.22%
^{239}Pu	-0.22%	-0.01%
^{240}Pu	-0.03%	0.00%
^{241}Pu	-0.23%	-0.08%

nuclide	$\delta(X)$ in UOX	$\delta(X)$ in MOX
^{242}Pu	0.00%	0.01%
^{241}Am	0.56%	0.17%
^{242M}Am	3.33%	-1.12%
^{243}Am	-0.04%	-0.06%
^{242}Cm	-5.47%	-4.21%
^{243}Cm	-4.31%	0.84%
^{244}Cm	-0.20%	-0.16%
^{245}Cm	-0.06%	0.05%
^{246}Cm	0.02%	0.05%

Table 3.4: Impact of inter-cycle model on various nuclides after 5 years of cooling

We observe that for most of the nuclides, the impact is very small.

Recent developments in COSI allowed to take full irradiation history into account, including inter-cycles. Therefore this bias will be eliminated in further scenario studies.

3.1.2.1.3.4 Sampling tweaks for the burnup

It will be shown in section 3.1.3.1.2.3, in the case of the estimation of actinide concentrations after irradiation, that burnup is by far the strongest contributor in terms of importance and non-linearity. The immediate consequence is that taking into account the burnup degrades the quality of estimators more than any other parameter. Two tweaks were used in order to moderate this effect.

a) Division of the design of experiment Figure 3.2 represents the cumulative distribution function of the burnup in a typical transition scenario calculation. The distribution of burnup is asymmetric, and we can roughly divide the domain of variation into two sub-domains: less than nominal burnup, which covers a wide range of under-represented burnup values, and nominal or higher burnup, which covers a narrow and high density region. For instance, in the case of PWR UOX fuel, this separation intuitively occurs around 41GWd/tHM. Indeed the domain under 41GWd/tHM represents 66% of the domain of variation, whereas $F_{UOX}(41GWd/tHM) \approx 0.32$.

Parameter	$\mathcal{D}$		$\mathcal{D}_1$		$\mathcal{D}_2$	
	min	max	min	max	min	max
BU	$\mathrm{BU}_{\min}$	$\mathrm{BU}_{\max}$	$\mathrm{BU}_{\min}$	BU_0	BU_0	$\mathrm{BU}_{\max}$
$\mathcal{P}$	$\mathcal{P}_{\min}$	$\mathcal{P}_{\max}$	$\mathcal{P}_{\min}$	$\mathcal{P}_{\max}$	$\mathcal{P}_{\min}$	$\mathcal{P}_{\max}$
y_i	$y_{i,\min}$	$y_{i,\max}$	$y_{i,\min}$	$y_{i,\max}$	$y_{i,\min}$	$y_{i,\max}$
$\Delta\sigma_i$	$\Delta\sigma_{i\min}$	$\Delta\sigma_{i\max}$	$\Delta\sigma_{i\min}$	$\Delta\sigma_{i\max}$	$\Delta\sigma_{i\min}$	$\Delta\sigma_{i\max}$

Table 3.5: Division of a domain of variation into two different designs of experiments

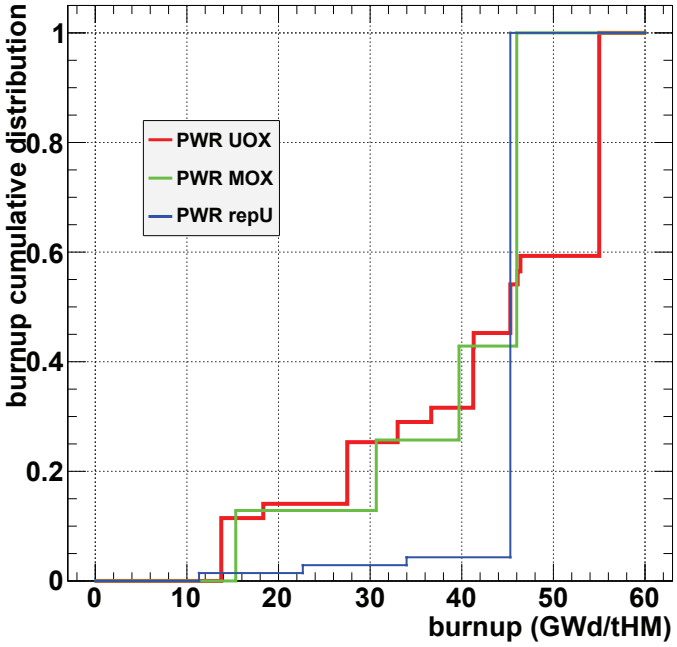

Figure 3.2: Typical burnup cumulative distribution in a scenario calculation

This observation can be transformed into a gain in precision for the surrogate model: is it possible to take this into account during the sampling process or the construction process of the surrogate model?

We consider a design of experiment $\mathcal{D}$ associated to a fresh fuel type, for instance PWR UOX fuel. $\mathcal{D}$ is parameterized in mass fraction, burnup, specific power, etc. We study the impact of the division of $\mathcal{D}$ into two sub-domains of itself, $\mathcal{D}_1$ and $\mathcal{D}_2$, in function of the burnup, all other things remaining equal, as shown on table 3.5.

The division of the domain of variation is usually done such as $\mathcal{D}_1$ includes sub-nominal irradiation calculation (starting and shutting-down batches, etc.) whereas $\mathcal{D}_2$ is representative of fuel irradiated at nominal burnup or higher (nominal conditions, stretch-out):

$$\begin{cases} \mathcal{D}_1 = [\mathrm{BU}_{min}, \mathrm{BU}_0] \\ \mathcal{D}_2 = [\mathrm{BU}_0, \mathrm{BU}_{max}] \end{cases} \tag{3.8}$$

Definition of BU_0 is shown in equation 3.9. ε is chosen such that sub-nominal batches are in $\mathcal{D}_1$

Estimator	$\mathcal{D}$		$\mathcal{D}_1$		$\mathcal{D}_2$	
	RMAE	q^2	RMAE	q^2	RMAE	q^2
^{239}Pu	$1.708 \cdot 10^{-3}$	0.9997	$9.013 \cdot 10^{-4}$	0.9999	$3.759 \cdot 10^{-4}$	0.9997
^{240}Pu	$5.169 \cdot 10^{-3}$	0.9995	$3.597 \cdot 10^{-3}$	0.9997	$1.013 \cdot 10^{-3}$	0.9996
^{241}Pu	$7.150 \cdot 10^{-3}$	0.9991	$3.111 \cdot 10^{-3}$	0.9999	$9.739 \cdot 10^{-4}$	0.9995
^{244}Cm	$2.658 \cdot 10^{-2}$	0.9985	$4.016 \cdot 10^{-2}$	0.9968	$1.188 \cdot 10^{-2}$	0.9982

Table 3.6: Quantification on the precision on $\mathcal{D}$, $\mathcal{D}_1$ and $\mathcal{D}_2$

and nominal batches in $\mathcal{D}_2$.

$$\text{BU}_0 = \text{nominal burnup} \times (1 - \varepsilon),\ \varepsilon \ll 1 \tag{3.9}$$

This division is highly asymmetric, the objective being to favor the accuracy of the estimator on the fuel batches which represent the most important part of the total mass, i.e. batches irradiated at nominal burnup.

Regressions are performed on $\mathcal{D}_1$, $\mathcal{D}_2$ and $\mathcal{D} = \mathcal{D}_1 \cup \mathcal{D}_2$. Test samples are $\mathcal{D}'_1$, $\mathcal{D}'_2$ and $\mathcal{D}' = \mathcal{D}'_1 \cup \mathcal{D}'_2$. $\mathcal{D}'_1$, $\mathcal{D}'_2$ are sampled using the same distributions and sample sizes as $\mathcal{D}_1$ and $\mathcal{D}_2$.

The construction of $\mathcal{D}$ imposes $card(\mathcal{D}) = card(\mathcal{D}_1) + card(\mathcal{D}_2)$, therefore a potential gain in accuracy will only result from the division of $\mathcal{D}$, not from an increase of the global sample size. In order to compare comparable things, we establish the following test for the accuracy of estimators built on $\mathcal{D}$, $\mathcal{D}_1$ and $\mathcal{D}_2$:

1. construction of polynomial regression $\mathbb{P}_1$ on $\mathcal{D}_1$, to reach a criterion q_1^2. $\mathbb{P}_1$ is a combination of the set of monomials $\mathcal{M}_1$.
2. construction of polynomial regression $\mathbb{P}_2$ on $\mathcal{D}_2$, to reach a criterion $q_2^2 = q_1^2$. $\mathbb{P}_2$ is a combination of the set of monomials $\mathcal{M}_2$.
3. construction of polynomial regression $\mathbb{P}_0$ on $\mathcal{D} = \mathcal{D}_1 \cup \mathcal{D}_2$. $\mathbb{P}_0$ is a combination of the set of monomials $\mathcal{M}_1 \cup \mathcal{M}_2$. A single simple least squares regression is performed.

Results concerning several important actinides are summarized in table 3.6. We define the relative mean absolute error (RMAE) of the estimator $\hat{\theta}$ of θ over the test sample such as (eq. 3.10):

$$\text{RMAE}(\hat{\theta}) = \frac{\mathbb{E}|\hat{\theta} - \theta|}{\mathbb{E}(\theta)} \tag{3.10}$$

We also remark that in the case of the ^{244}Cm estimator, RMAE coefficient is higher for $\mathcal{D}_1$ than for $\mathcal{D}_2$. Although counter-intuitive at first, we can assess that it mostly comes from the repartition of ^{244}Cm in function of the burnup: there is very few ^{244}Cm produced at low burnup, therefore normalization through $\mathbb{E}(^{244}\text{Cm})$ strongly increases the value of RMAE. A measure of the effective gain can be the comparison of the PRESS[2] coefficients of $\mathbb{P}_0$, $\mathbb{P}_1$ and $\mathbb{P}_2$ calculated over the test samples. PRESS is in (atoms/ton)^2 in the case of concentrations after irradiation.

$$\begin{cases} \text{PRESS}(\mathbb{P}_0, ^{244}\text{Cm}) &= 2.097 \cdot 10^{46} \\ \text{PRESS}(\mathbb{P}_1, ^{244}\text{Cm}) &= 1.391 \cdot 10^{45} \\ \text{PRESS}(\mathbb{P}_2, ^{244}\text{Cm}) &= 7.242 \cdot 10^{45} \end{cases} \tag{3.11}$$

[2]Predicted residual sum of squares: PRESS $= \sum_{i=1}^{n} (y_i - \hat{y}_i)^2$ on the test sample.

Consequently $\text{PRESS}(\mathbb{P}_0, {}^{244}\text{Cm}) \approx 2.43 \times (\text{PRESS}(\mathbb{P}_1, {}^{244}\text{Cm}) + \text{PRESS}(\mathbb{P}_2, {}^{244}\text{Cm}))$ and we have:

$$\begin{cases} card(\mathcal{D}') = card(\mathcal{D}'_1) + card(\mathcal{D}'_2) \\ \text{PRESS}(\mathbb{P}_1, {}^{244}\text{Cm}) + \text{PRESS}(\mathbb{P}_2, {}^{244}\text{Cm}) < \text{PRESS}(\mathbb{P}_0, {}^{244}\text{Cm}) \end{cases} \tag{3.12}$$

Finally:

Division of the DOE into two sub-domains in function of the burnup increases the accuracy of the estimator, especially in the nominal burnup sub-domain.

The gain increases with non-linearity of the isotope, the gain for isotopes relatively linear in function of the burnup is small. This gain in precision is free from the point of view of the size of the DOE and it even reduces the construction time of the regressions.

b) Non-uniform burnup sampling

Introduction

Until now we have only considered uniform sampling for every parameter, including the burnup, so as to cover equally every domain of the design of experiment, and obtain an estimator which precision is as homogeneous as possible over the DOE (even though the lack of fit of the estimators is not homogeneous).

It is even preferable to have a higher sampling density at high burnup because the most difficult nuclides to describe are usually formed only at high burnup.

However some concentrations after irradiation are highly increasing in function of the burnup, therefore certain zones of the output space are much less dense than others. This is especially detrimental in the case of very heavy nuclides. We look for a sampling distribution of the burnup that would homogenize the precision over the DOE without artificially biasing the least squares method.

We define:

- X the random variable representing the burnup, and its associated PDF $f_{X,I}$ defined on the interval $I = [a, b]$.
- g the function of irradiation, calculating the concentration after irradiation in function of the burnup.
- Y the random variable representing a concentration after irradiation, with $Y = g(X)$.

The burnup function g is monotonic therefore the probability density function f_Y of Y can be calculated as shown in equation 3.13 (change of variables in PDF + derivation of the inverse function):

$$f_Y(Y) = \left| \frac{1}{g'(g^{-1}(Y))} \right| f_X(g^{-1}(Y)) \tag{3.13}$$

A non-uniform PDF for Y will alter the process of construction of the estimator of the concentration after irradiation because it biases the value of the residual sum of squares during the application of the least squares method.

Monomial approximation

We propose to give a rough approximation of a function leading to an approximately uniform density of Y. First, we define our irradiation function: $g(X) = kX^{\alpha}$. This function is monotonic,

and representative of the production of a nuclide obtained after roughly α successive radiative captures from an isotope present in the initial composition. k is a scalar, its value is linked to the reaction rates in the system.

For instance, in the case of production of ^{244}Cm from ^{239}Pu (eq. 3.14) in MOX fuel we have $\alpha \approx 5$.

$$^{239}\text{Pu} \xrightarrow{4\ (n,\gamma)} {}^{243}\text{Pu} \xrightarrow{\beta-} {}^{243}\text{Am} \xrightarrow{(n,\gamma)} {}^{244}\text{Am} \xrightarrow{\beta-} {}^{244}\text{Cm} \tag{3.14}$$

We have:

$$\begin{cases} g(X) = kX^{\alpha} = Y \\ g'(X) = k\alpha X^{\alpha-1} \\ g^{-1}(Y) = k^{-1/\alpha}Y^{1/\alpha} = X \end{cases} \tag{3.15}$$

We inject the relations 3.15 in 3.13 and obtain:

$$f_X(X) = k^{1/\alpha}\alpha Y^{\frac{\alpha-1}{\alpha}} f_Y(Y) \tag{3.16}$$

Let $I_y = g(I)$, $l \in \mathbb{R}^{*+}$. We define the function $\mathbb{1}_{I_y}$ such that:

$$\begin{cases} \mathbb{1}_{I_y}(x) &= 1 \text{ if } x \in I_y \\ \mathbb{1}_{I_y}(x) &= 0 \text{ if } x \notin I_y \end{cases} \tag{3.17}$$

We want f_Y to be uniform over its domain of variation: $f_Y = l \times \mathbb{1}_{I_y}$ with $I_y = g(I)$. We obtain, for $X \in I$:

$$f_X(X) = k\alpha l X^{\alpha-1} \tag{3.18}$$

For a given irradiation function $g : X \mapsto X^{\alpha}$, the sampling distribution of the burnup $f_X : X \mapsto kX^{\alpha-1},\ k \in \mathbb{R}^{*+}$ such as integration of f_X over I is 1, leads to a uniform a posteriori distribution of the concentration.

Example: the case of $\alpha = 1$ is trivial: a uniform distribution of the burnup gives a uniform distribution of the concentration. In the case of $\alpha = 2$ we build a test-sample with a linear distribution and apply the irradiation law $g(X) = X^2$. The relation 3.18 implies that using a polynomial burnup distribution of degree $\alpha - 1 = 1$ (ie a linear distribution) will produce a uniform distribution for the concentration. Figure 3.3 illustrates this application for a test-case:

1. burnup is sampled using a linear distribution
2. concentration distribution is evaluated as the image of the burnup distribution through the irradiation function. Its distribution is indeed uniform over its domain of variation.

Exponential approximation

In the case of an exponential irradiation function the same calculation can be performed. For instance $g(X) = ke^{\lambda X},\ (k, \lambda) \in (\mathbb{R}^{*+})^2$ gives:

$$f_X(X) = Ke^{\lambda X},\ K \in \mathbb{R} \tag{3.19}$$

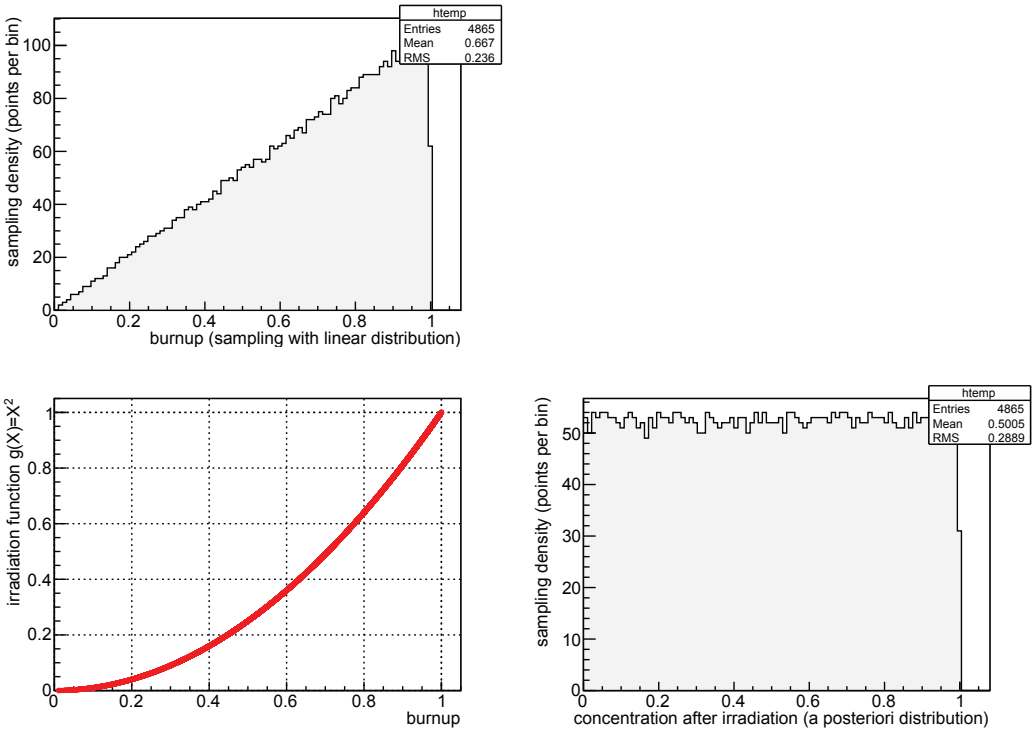

Figure 3.3: Burnup sampling in the case of a polynomial (degree 2) irradiation function

This result is interesting because if we approximate the burnup function over its domain of variation as an exponential function of parameter λ (and measure λ), then we can obtain a more or less uniform distribution of the concentration after irradiation using a burnup sampling of parameter λ.

Example: in the case $(\lambda = 2, k = 1/3000)$, we build a test-sample with exponential distribution and apply the irradiation law $g(X) = 1/3000 \times e^{2X}$. Relation 3.19 implies that using a exponential burnup distribution of parameter $\lambda = 2$ will produce a uniform distribution for the concentration. For instance, we choose: $f_X(X) = K\left(e^{2(X-1)}\right)$ on $I = [0, 1]$. Figure 3.4 illustrates this application for a test-case:

We obtain a uniform *a posteriori* distribution for the concentration after irradiation.

General case

In the general case, the irradiation function is neither a monomial nor an exponential function: it is more or less a polynomial with terms present at 2 or more degrees. We propose the following method in order to produce a *very approximately* homogeneous sample:

1. application of the irradiation function on a few points of the DOE
2. construction of an exponential estimator of the irradiation function (for instance using the least squares method). We obtain the estimator $\hat{\lambda}$ of the exponential parameter, even though the irradiation function is not really exponential.
3. construction of the sampling using $\hat{\lambda}$ as the exponential distribution parameter.

Example: let $g : X \mapsto X/5 + 6X^2 + 5X^4$ be the irradiation function. We note that g is not a Taylor development of an exponential function. We perform an exponential regression of g over

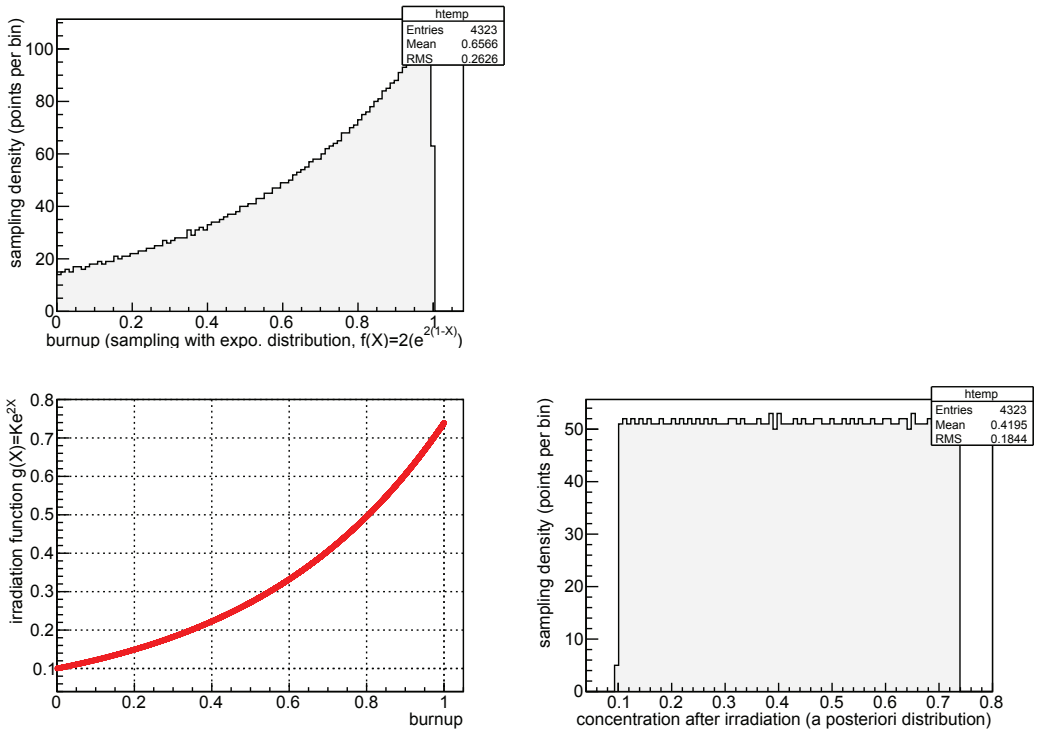

Figure 3.4: Burnup sampling in the case of an exponential irradiation function

its domain of variation $I = [0, 1]$ and obtain its estimator $\hat{g} : X \mapsto Ke^{\hat{\lambda}X},\ \hat{\lambda} \approx 3.61$.

Figure 3.5 illustrates the construction of the exponential estimator, and its flaws.

Then we build an exponential distribution of the burnup over I using an exponential distribution with $\lambda = 3.61$. Finally we compute the image of this distribution through g and obtain the *a posteriori* distribution of the concentration after irradiation.

Figure 3.6 represents the image of I when the burnup is distributed following a uniform distribution. We notice that near-zero cases are over-represented, and give few information during the construction of the concentration estimator (given that when a concentration is almost null, it is not important to predict it accurately). On the other side, figure 3.7 represents the image of I when the burnup is sampled according to an exponential distribution, where λ is estimated from an exponential estimator of the irradiation function. Even though the distribution is not uniform, but just an approximation of it, it is much more useful for the construction of the estimator of the concentration.

Consequently:

> *An exponential sampling of the burnup based on an estimation of the irradiation function is well adapted to the construction of convenient samples..*

On a side note, we can remark that the new sampling function can be interpreted as an importance function that could be applied to weight the least squares method. However, the specificity of our case is that changing the sampling method is less time-consuming than implementing a weight in the least squares method, therefore we chose to adapt the samples. Furthermore a high density sampling at high burnup is interesting because of the higher degree of interaction

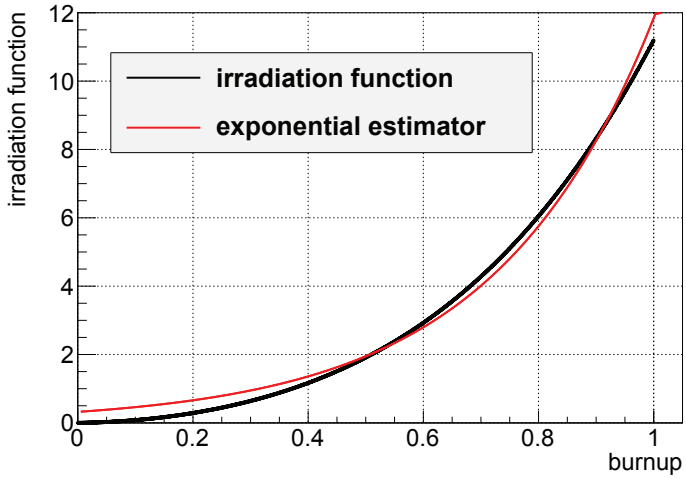

Figure 3.5: Construction of the exponential estimator of the irradiation function

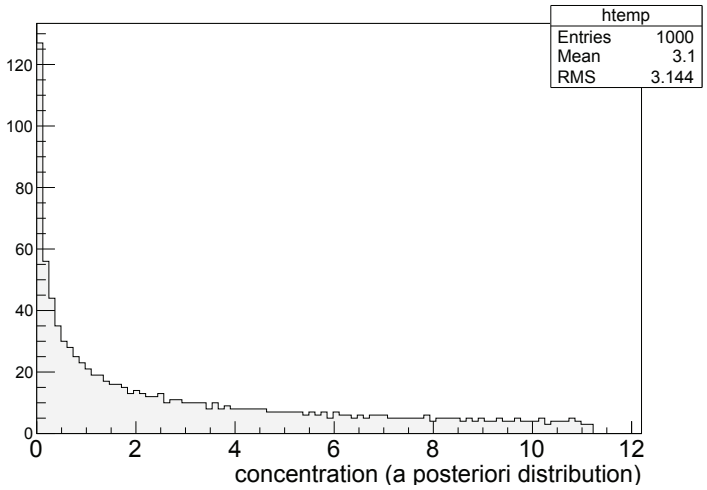

Figure 3.6: Image of uniform distribution through g

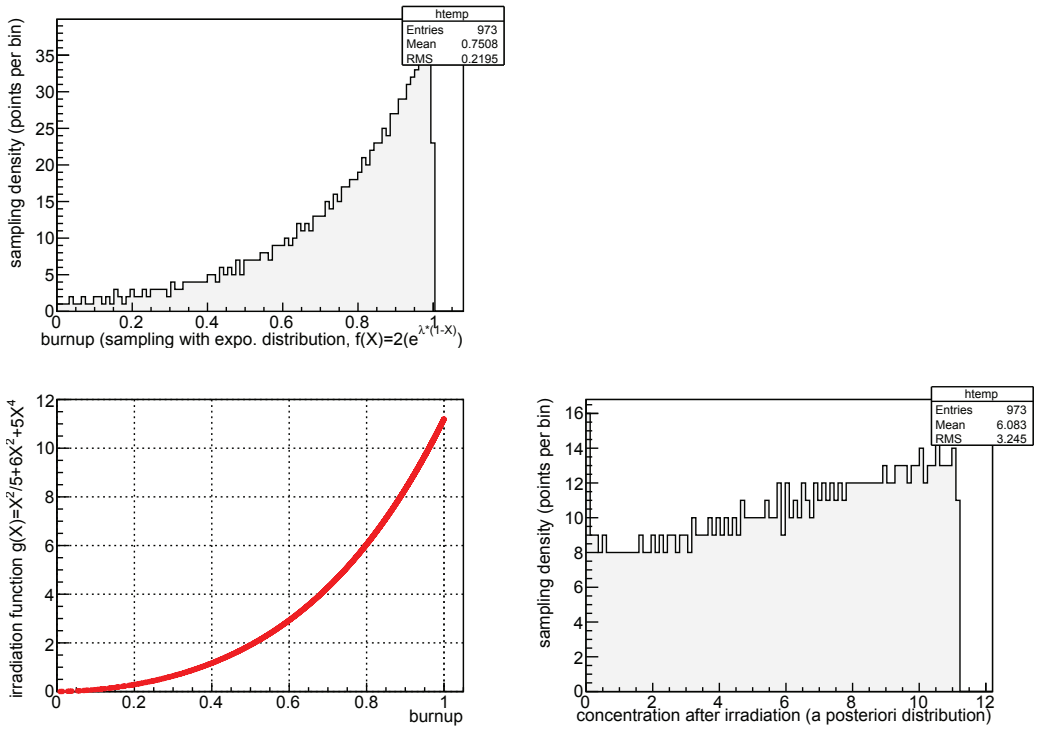

Figure 3.7: Image of estimated exponential distribution through g

between the parameters.

3.1.2.1.4 Cross-sections

3.1.2.1.4.1 Introduction

Several perturbation values are associated to cross-sections. The perturbation values are scalars, defined in one energetic group only. Therefore the value of the perturbation can depend on the spectrum. The calculation of one energy group uncertainties is described in part 5.2.1. Perturbations of the capture (σ_c) and fission (σ_f) cross-sections of the isotopes of `list_Actinides` are defined. The perturbation values are sampled using uniform distributions, covering domain defined according to standard deviation values, in order to be representative of the perturbations on all the domain: $I_i \approx \left[-\sqrt{3}SD(i)\ ,\ \sqrt{3}SD(i)\right]$. This interval ensures the possibility to create a model able to take into account a uniform sampling of the cross-section in order to perform uncertainty propagation. Analysis of the Gaussian repartition function on this interval shows that the confidence level is only 91.6%, which is not optimal, but this model is mostly designed as a first approach to uncertainty propagation.

Section 3.1.2.1.4.2 shows that the impact of scattering cross-section uncertainty on concentrations after irradiation is weak. Consequently scattering cross-section perturbations will not be considered as parameters for the irradiation surrogate models.

Section 3.1.2.1.4.3 shows that the impact of the spectrum change during irradiation is such as one-group cross-section uncertainty is almost the same before and after irradiation. Therefore only one value of cross-section perturbation per type of fuel will be taken into account for the

$S_{i,j} = \frac{\sigma_s(j)}{C_i}\frac{\partial C(i)}{\partial \sigma_s(j)}$		j					
		^{235}U	^{238}U	^{239}Pu	^{nat}Zr	^{1}H $\in$ H$_2$O	^{16}O
i	^{235}U	0.00	-0.02	0.00	-0.01	-0.51	0.02
	^{238}U	0.00	0.00	0.00	0.00	0.01	0.00
	^{237}Np	0.00	-0.01	0.00	-0.01	-0.57	-0.02
	^{238}Pu	0.00	0.00	0.00	-0.01	-0.93	-0.03
	^{239}Pu	0.00	0.00	0.00	0.00	-1.06	0.04
	^{240}Pu	0.00	0.01	0.00	0.01	-0.29	0.02
	^{241}Pu	0.00	0.01	0.00	0.01	-0.87	0.05
	^{242}Pu	0.01	0.04	0.00	0.01	-1.02	0.03
	^{243}Am	0.00	0.05	0.00	0.01	-0.58	0.02
	^{242}Cm	0.00	0.03	0.00	0.01	-0.58	0.03
	^{244}Cm	0.00	0.07	0.00	0.01	-1.16	0.01

Table 3.7: Sensitivity of concentrations after irradiation up to 45GWd/tHM to scattering cross-section in PWR UOX fuel

construction of irradiation surrogate models.

3.1.2.1.4.2 Impact of scattering cross-section on irradiation calculation

a) Overview

The impact of elastic scattering cross-section perturbation on different nuclides can be calculated with neutron transport codes. A first rough estimation of the impact can be obtained through 1-group perturbation of the scattering cross-section of nuclides. We calculate the sensitivity of several concentrations to elastic scattering perturbation according to equation 3.20.

$$S_{i,j} = \frac{\sigma_s(j)}{C_i}\frac{\partial C(i)}{\partial \sigma_s(j)} \tag{3.20}$$

Numerical application was performed in the case of a PWR UOX fuel assembly (EPR, 17×17) irradiated at 45GWd/tHM. Sensitivity was calculated using OAT method, and perturbation of cross-sections is performed via `CHABINT` module in APOLLO2: direct perturbation of cross-sections after self-shielding. Perturbations are not re-evaluated at each irradiation step. The perturbations are computed for 1% bias in cross-sections. The sensitivity values obtained are shown in table 3.7. We noted ^{nat}Zr the natural zirconium, and performed a totally correlated scattering cross-section perturbation of each isotope of zirconium, which is conservative.

It appears that the sensitivity of every isotope but ^{1}H $\in$ H$_2$O and ^{16}O is very low. Considering the uncertainty of these cross-sections being rather low (a few percents), we can neglect their impact on the final concentrations. The cases of ^{1}H and ^{16}O have to be studied specifically.

We accept the hypothesis of scattering cross-section uncertainty's weakness of the impact on concentrations after irradiation in PWR UOX fuel for the rest of the study, with the exception of ^{1}H and ^{16}O.

b) Study of ^{1}H in PWR UOX fuel

The case of $^1\mathrm{H} \in \mathrm{H_2O}$ is different: its sensitivity is much higher. The study must be refined to analyze the impact of the uncertainty on final concentrations. The first step is the acquisition of $\sigma_s\left(^1\mathrm{H} \in \mathrm{H_2O}\right)$ uncertainty data. The covariance data of this cross-section can be found for instance in the ENDF B-VII [3.1] evaluation or in COMAC [3.2]. The correlation matrix in a 175 energy groups scheme is shown on figure 3.8 and the energy-dependent relative standard deviation on figure 3.9.

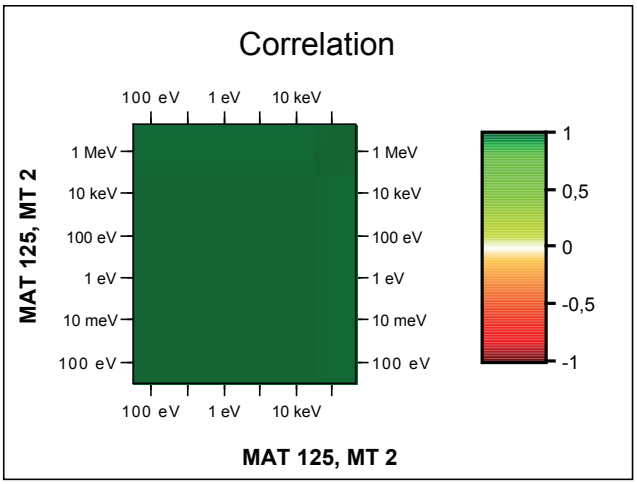

Figure 3.8: Correlation matrix of $\sigma_s\left(^1\mathrm{H}\right)$

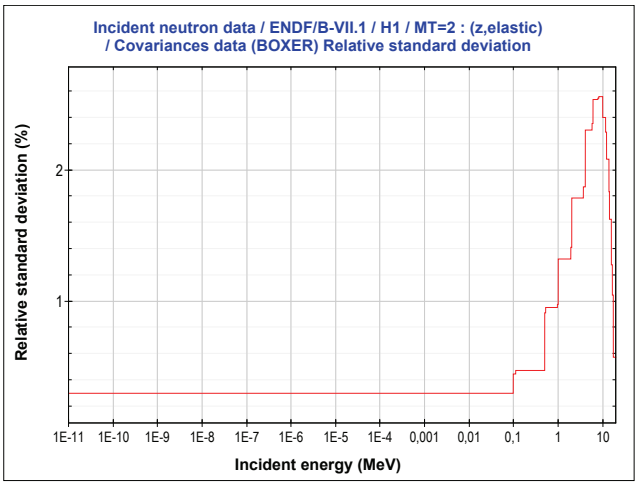

Figure 3.9: Standard deviation of $\sigma_s\left(^1\mathrm{H}\right)$

This correlation matrix is very special: all groups are almost fully correlated. This leads to a remarkable property: the covariance matrix can be modeled as an energy-dependent vector of uncertainty, whose shape is the same as shown on figure 3.9. Therefore this energy-dependent perturbation is considered for the evaluation of the uncertainty of several minor actinides due to the uncertainty of $\sigma_s\left(^1\mathrm{H}\right)$.

Considering the small amplitude of variation of this cross-section, we assume the linearity of the impact of its perturbation to the final concentrations, and the absence of significant interactions between scattering perturbation and other factors. Consequently:

$$\frac{\partial C_i(\sigma_s(^1\mathrm{H})}{\partial \sigma_s(^1\mathrm{H})} \approx \frac{C_i(\sigma_s(^1\mathrm{H}) + \sqrt{Var\left(\sigma_s(^1\mathrm{H})\right)}) - C_i(\sigma_s(^1\mathrm{H}))}{\sqrt{Var\left(\sigma_s(^1\mathrm{H})\right)}} \tag{3.21}$$

We use the first order of the Taylor expansion for the second moment (variance) of functions (concentration) of a random variable (cross-section) and obtain:

$$Var\left(C_i\right) \approx \left(\frac{C_i(\sigma_s(^1\mathrm{H}) + \sqrt{Var\left(\sigma_s(^1\mathrm{H})\right)}) - C_i(\sigma_s(^1\mathrm{H}))}{\sqrt{Var\left(\sigma_s(^1\mathrm{H})\right)}}\right)^2 \times Var\left(\sigma_s(^1\mathrm{H}))\right) \tag{3.22}$$

Therefore, we have:

$$\frac{\sqrt{Var\left(C_i\right)}}{C_i} \approx \left|\frac{C_i(\sigma_s\left(^1\mathrm{H}\right) + \sqrt{Var\left(\sigma_s\left(^1\mathrm{H}\right)\right)}) - C_i(\sigma_s\left(^1\mathrm{H}\right))}{C_i(\sigma_s\left(^1\mathrm{H}\right))}\right| = \delta C_i \tag{3.23}$$

Hence the values of δC_i can be calculated in only two direct runs. The values obtained for δC_i are shown on table 3.8. Although δC_i are always positive, we attributed the sign of the sensitivity value to them .

i	$\delta C_i \sim \frac{\sqrt{Var(C_i)}}{C_i}$ (%)
^{235}U	-0.24
^{238}U	0.00
^{237}Np	-0.24
^{238}Pu	-0.29
^{239}Pu	-0.35
^{240}Pu	-0.05
^{241}Pu	-0.23
^{242}Pu	0.13
^{241}Am	-0.31
^{243}Am	0.00
^{242}Cm	-0.07
^{244}Cm	-0.10

Table 3.8: Uncertainty of concentrations after irradiation due to ^{1}H scattering cross-section in PWR UOX fuel

The uncertainty resulting from the uncertainty of $\sigma_s\left(^{1}\mathrm{H}\right)$ is small (less than 0.5% in any case).

We accept the hypothesis of the weakness of the impact of ^{1}H scattering cross-section uncertainty on concentrations after irradiation in PWR UOX fuel for the rest of the study.

A further study may consider construction of irradiation surrogate models through transport+irradiation calculations in order to take into account this parameter natively.

c) Study of ^{16}O in PWR UOX fuel

The case of ^{16}O is more or less similar to ^{1}H, with a lower sensitivity. ENDF B-VII data concerning the covariance matrix of $\sigma_s(^{16}\mathrm{O})$ is shown on figure 3.10 and its energy-dependent relative standard deviation on figure 3.11.

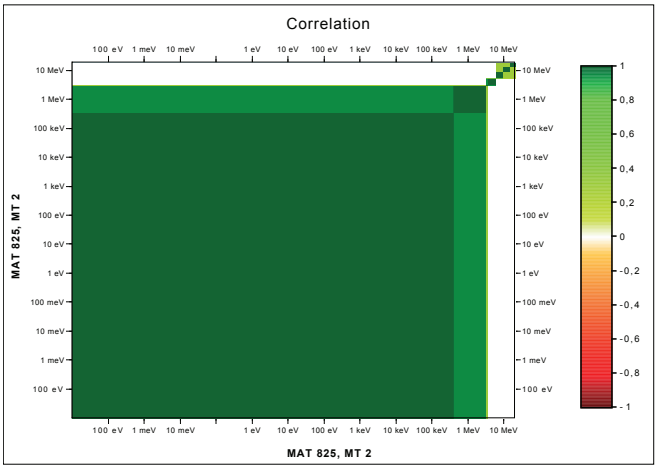

Figure 3.10: Correlation matrix of $\sigma_s\left(^{16}\mathrm{O}\right)$

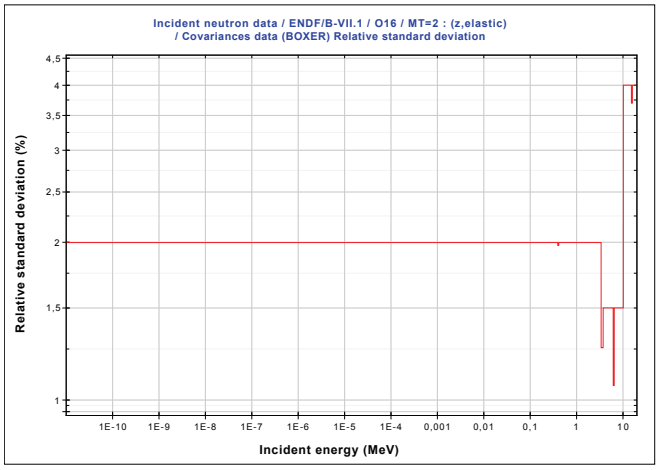

Figure 3.11: Standard deviation of $\sigma_s\left(^{16}\mathrm{O}\right)$

We divide the energy range in 3 energetic macro-groups a, b and c, corresponding to the 3 diagonal macro-groups on figure 3.10. These 3 groups are uncorrelated because the correlation is a block diagonal matrix. We make the following assumptions, which consists in associating in each macro-group a unique value of uncertainty, equal to the maximum value found in the macro-group:

$$\begin{cases} \frac{\sqrt{Var(\sigma_s(^{16}\mathrm{O}))}}{\sigma_s(^{16}\mathrm{O})} & = & 2.0\% \text{ for } E < 3.329\mathrm{MeV} & group\ a \\ \frac{\sqrt{Var(\sigma_s(^{16}\mathrm{O}))}}{\sigma_s(^{16}\mathrm{O})} & = & 1.5\% \text{ for } 3.329\mathrm{MeV} < E < 10.000\mathrm{MeV} & group\ b \\ \frac{\sqrt{Var(\sigma_s(^{16}\mathrm{O}))}}{\sigma_s(^{16}\mathrm{O})} & = & 4.0\% \text{ for } E > 10.000\mathrm{MeV} & group\ c \end{cases} \tag{3.24}$$

We assume, as usual, Gaussian uncertainty of nuclear data.

We perform one reference computation and three perturbed computations, one per macro-group. The value of the cross-section perturbation is its standard deviation. The values of the perturbations are low (less than 5%). Therefore we can assume the absence of significant interactions between these macro-groups. Given that these three macro-groups are uncorrelated, and the interactions are negligible, we have:

$$\begin{array}{rcl} \delta C_i & \sim & \frac{\sqrt{Var(C_i)}}{C_i} = \frac{\sqrt{Var(C_{i,a})+Var(C_{i,b})+Var(C_{i,c})}}{C_i} \\ i.e.\quad \delta C_i & \sim & \sqrt{\delta C_{i,a}^2 + \delta C_{i,b}^2 + \delta C_{i,c}^2} \end{array} \tag{3.25}$$

The same method can be used as in **a)** to evaluate the uncertainty propagation in each macro-group $\delta C_{i,j}$, computing only the reference case and the perturbed case.

Hence only four computations give us information to estimate the concentrations after irradiation's uncertainty associated due to ^{16}O scattering cross-section uncertainty.

The values for δC_i in each macro-group and on the whole energetic domain, in the case of ^{16}O perturbation cross-section are exposed in table 3.9. Each and every uncertainty value of concentration after irradiation is below 0.12%. We can conclude that impact of the uncertainty of $\sigma_s(^{16}\mathrm{O})$ on actinides concentrations after irradiation is minor and can be neglected for the rest of the study.

isotope	mass fraction (%)
^{238}Pu	3.06
^{239}Pu	52.53
^{240}Pu	25.86
^{241}Pu	8.32
^{242}Pu	8.55
^{241}Am	1.68

Table 3.10: Pu vector for ^{1}H scattering cross-section impact study in PWR MOX fuel

i	$\delta C_{i,a}$ (%)	$\delta C_{i,b}$ (%)	$\delta C_{i,c}$ (%)	δC_i (%)
^{235}U	0.04	0.00	0.00	0.04
^{238}U	0.00	0.00	0.00	0.00
^{237}Np	0.01	0.02	0.01	0.02
^{238}Pu	0.02	0.02	0.01	0.03
^{239}Pu	0.10	0.00	0.00	0.10
^{240}Pu	0.04	0.00	0.00	0.04
^{241}Pu	0.03	0.00	0.00	0.03
^{242}Pu	0.05	0.01	0.00	0.05
^{241}Am	0.12	0.00	0.00	0.12
^{243}Am	0.04	0.00	0.00	0.04
^{242}Cm	0.07	0.00	0.00	0.07
^{244}Cm	0.02	0.00	0.00	0.02

Table 3.9: Uncertainty of concentrations after irradiation due to ^{16}O scattering cross-section in PWR UOX fuel

We accept the hypothesis of the weakness of the impact of ^{16}O scattering cross-section uncertainty on concentrations after irradiation in PWR UOX fuel for the rest of the study.

d) Study of ^{1}H in PWR MOX fuel

^{1}H being the nuclide with highest scattering sensitivity value, its sensitivity was computed in the case of PWR MOX fuel. Fuel is MOX with UOX environment, MOX is divided in three zones, plutonium mean mass content is 10.1025% and Pu vector is shown in table 3.10. Impact is studied at 46GWd/tHM, the method is the same as described in **b)**.

The values obtained for δC_i are shown on table 3.11. Although δC_i are always positive, we attributed them the sign of the sensitivity value.

i	$\delta C_i \sim \frac{\sqrt{Var(C_i)}}{C_i}$ (%)
^{235}U	-0.04
^{238}U	0.01
^{237}Np	-0.76
^{238}Pu	-0.01
^{239}Pu	-0.21
^{240}Pu	0.02
^{241}Pu	-0.04
^{242}Pu	0.08
^{241}Am	-0.06
^{243}Am	0.01
^{242}Cm	0.05
^{244}Cm	-0.05

Table 3.11: Uncertainty of concentrations after irradiation due to ^{1}H scattering cross-section in PWR MOX fuel

The impact of ^{1}H scattering cross-section is low: less than 0.1% in any case with the exception of ^{237}Np at 0.76%. Considering ^{1}H is the most contributing nuclide to scattering, we choose to neglect the impact of scattering in PWR MOX fuel.

We accept the hypothesis of the weakness of the impact of scattering cross-section uncertainty on concentrations after irradiation in PWR MOX fuel for the rest of the study.

d) Study of ^{23}Na in SFR MOX fuel

The impact of this cross-section was not studied in this work, but should be investigated in further studies.

3.1.2.1.4.3 Impact of spectrum on scalar cross-section uncertainty

Cross-section uncertainty is energy-dependent, therefore spectrum has an impact on the scalar value of energy-integrated uncertainty.

For a given fuel type, the spectrum changes during irradiation, because of modification of mass fractions.

Section 5.2.1 shows a method of energy-dependent cross-section covariance matrix condensation, based on the principle of conservation of reaction rates uncertainty. Besides the scalar uncertainty values for cross-sections, an application of this method is the comparison of scalar values of cross-section considering two different spectra.

For instance, in the case of PWR UOX fuel enriched at 4.4%, scalar uncertainty condensed from covariance matrices before and after irradiation at 45GWd/tHM is shown in table 3.12. ENDF B-VII data was used. Computation of reaction rates and irradiation was performed by APOLLO2. Several nuclides such as Cm isotopes are not present before irradiation, and were introduced as traces (mass fraction = 10^{-15}) in fresh fuel. Relative values of uncertainty are presented here. We noted: $u(\sigma_f(\%)) = 100 \times \frac{\sqrt{Var(\sigma_f)}}{\sigma_f}$.

It appears that irradiation has little impact on scalar uncertainty for most nuclides. The only nuclide whose uncertainty changes appears to be ^{240}Pu, this effect may be a result from changes in self-shielding, which is important in the case of ^{240}Pu.

nuclide	before irradiation			after irradiation		
	$u(\sigma_c(\%))$	$u(\sigma_f(\%))$	$cor(\sigma_c,\sigma_f)(\%)$	$u(\sigma_c(\%))$	$u(\sigma_f(\%))$	$cor(\sigma_c,\sigma_f)(\%)$
^{234}U	2.98	20.03	0.00	2.91	19.82	0.00
^{235}U	1.37	0.33	-33.78	1.34	0.33	-35.16
^{236}U	3.80	22.70	0.00	3.71	21.81	0.00
^{238}U	1.42	0.52	0.01	1.43	0.52	0.02
^{237}Np	4.64	2.83	0.00	4.58	2.82	0.00
^{239}Np	32.65	147.89	0.00	32.49	147.11	0.00
^{238}Pu	9.81	0.24	0.00	9.83	0.22	0.00
^{239}Pu	1.15	0.77	-53.75	1.13	0.77	-51.11
^{240}Pu	1.66	3.06	0.00	1.61	1.99	0.00
^{241}Pu	2.13	1.47	0.00	2.15	1.47	0.00
^{242}Pu	11.49	1.87	0.00	11.42	1.87	0.00
^{241}Am	5.07	4.90	0.85	5.12	4.61	1.36
^{242m}Am	23.66	4.67	0.00	23.75	4.69	0.00
^{243}Am	3.61	8.08	0.00	3.59	8.05	0.00
^{242}Cm	13.43	4.62	44.10	13.74	4.68	47.34
^{243}Cm	28.37	6.65	12.18	28.36	6.50	11.53
^{244}Cm	8.25	4.03	-4.61	8.26	4.21	-4.68
^{245}Cm	18.58	8.37	11.14	18.88	8.54	11.15

Table 3.12: Cross-section uncertainty in PWR UOX spectrum before and after irradiation

The same computation was performed for PWR MOX fuel in PWR UOX environment. Pu mass content is 8.65%, Pu vector is shown in table 3.13. These fuel characteristics correspond to typical MOX fuel in the present French fleet (MOX parity, expected burnup=45GWd/tHM). Cross-section scalar uncertainty was computed for fresh fuel and for fuel irradiated at 45GWd/tHM. Results of cross-section scalar uncertainty in PWR MOX fuel are shown in table 3.14.

Impact of irradiation on cross-section uncertainty and correlation is small, and will be neglected for this study. However, each type of fuel (PWR UOX, PWR MOX, etc.) will be associated with a different set of covariance matrices.

In the general case, we will take into account the maximum value of the cross-section uncertainty

isotope	mass fraction (%)
^{238}Pu	2.5
^{239}Pu	54.5
^{240}Pu	25.2
^{241}Pu	8.6
^{242}Pu	7.9
^{241}Am	1.3

Table 3.13: Pu vector for cross-section uncertainty condensation in PWR MOX fuel

nuclide	before irradiation			after irradiation		
	$u(\sigma_c(\%))$	$u(\sigma_f(\%))$	$cor(\sigma_c,\sigma_f)(\%)$	$u(\sigma_c(\%))$	$u(\sigma_f(\%))$	$cor(\sigma_c,\sigma_f)(\%)$
^{234}U	3.15	19.92	0.00	3.58	20.01	0.00
^{235}U	3.92	0.36	-1.00	3.40	0.36	-1.30
^{236}U	3.19	21.25	0.00	2.71	21.17	0.00
^{238}U	1.50	13.58	-0.44	1.53	14.02	-0.42
^{237}Np	4.15	4.33	0.00	4.36	4.39	0.00
^{239}Np	30.91	237.17	0.00	31.70	238.45	0.00
^{238}Pu	9.69	0.43	0.00	9.73	0.42	0.00
^{239}Pu	4.92	0.41	0.49	4.21	0.41	0.40
^{240}Pu	8.57	5.48	0.00	6.88	5.93	0.00
^{241}Pu	4.64	0.76	0.00	4.02	0.76	0.00
^{242}Pu	5.81	4.36	0.00	5.27	4.54	0.00
^{241}Am	5.02	3.12	0.21	5.20	3.19	0.28
^{242M}Am	17.92	10.85	0.00	18.38	10.60	0.00
^{243}Am	2.38	6.11	0.00	2.39	6.07	0.00
^{242}Cm	8.73	4.56	4.39	8.69	4.50	5.15
^{243}Cm	27.11	2.60	2.66	27.21	2.60	4.03
^{244}Cm	9.14	3.00	2.59	8.50	3.05	3.77
^{245}Cm	16.44	2.44	1.64	16.47	2.44	2.19
^{246}Cm	18.67	8.89	-0.14	19.24	9.40	-0.11

Table 3.14: Cross-section uncertainty in PWR MOX spectrum before and after irradiation

and correlation before or after irradiation for the whole computation.

The case of SFR fuel was not studied in this work. However, as cross-sections are generally less spectrum-dependent in SFR spectra, we assumed that uncertainty was similar in fresh and irradiated fuel.

3.1.2.1.5 Fission yields

The contribution of fission yield perturbations on the final concentration of actinides is very small, and results from the spectrum modification by the fission products.

The weakness of fission yields impact is assessed using results of section 3.2: for every fuel type, several fission yields were sampled. The sensitivity of concentrations of actinides after irradiation was assessed, and the result was always a null sensitivity. These fission yields correspond to fission products involved in decay heat only, therefore several isotopes, for instance the stable isotopes involved in burnup credit, were neglected. However, we can reasonably assume that the impact of fission yield leading to those isotopes is negligible.

The influence of the uncertainty of fission yields is neglected for this study.

3.1.2.1.6 Energies

3.1.2.1.6.1 Effective fission energy

Fission produces energy. The amount of energy per fission transformed into heat is called effective fission energy, E_{eff}, defined as [3.3]:

$$E_{eff} = E_{total} - \langle E_\nu \rangle - \Delta E_{\beta\gamma} \tag{3.26}$$

with E_{total} the total energy emitted in the fission process (from absorption of the neutron to β decay of product fragments), $\langle E_\nu \rangle$ the mean energy taken by anti-neutrinos during β decay of fission fragments and $\Delta E_{\beta\gamma}$ the energy of β electron and photons from fission fragments that did not decay at a given moment. The standard deviation of E_{eff} is around or below 0.10% for ^{235}U, ^{239,241}Pu and about 0.22% for ^{238}U [3.3].

The impact of fission energy uncertainty on final concentrations is indirect. It modifies the amount of fissions necessary to reach the final burnup, which is imposed in our study.

PWR UOX fresh fuel contains only one major fissile nuclide, ^{235}U. Given that fission energy produces approximately $\alpha \approx 60\%$ of the total energy, the remaining energy coming from (n, γ) and $(n$,el), the number of fissions N necessary to reach a given burnup BU can be (very) roughly approximated as:

$$N = \frac{\alpha BU}{E_{eff}} \tag{3.27}$$

Intuitively, we can note that the ratio α is a monotonically increasing function of the effective fission energy, expressed as:

$$\alpha = \frac{\text{energy from fission}}{\text{energy from fission} + \text{other energy}} = \frac{E_{eff}}{E_{eff} + a} \ , \ a \in \mathbb{R}^{*+} \tag{3.28}$$

Indeed, for a given burnup to be reached, when the fission energy increases, the part of fission in total energy increases. For a bias of ^{235}U effective fission energy $dE_{eff} \ll E_{eff}$, we obtain:

$$\frac{dN}{dE_{eff}} = \frac{d\alpha}{dE_{eff}} \frac{N}{\alpha} - \frac{N}{E_{eff}} \Leftrightarrow \frac{dN}{N} = \frac{d\alpha}{\alpha} - \frac{dE_{eff}}{E_{eff}} \tag{3.29}$$

Given that α is monotonically increasing in function of the effective fission energy and:

$$\frac{d\alpha}{\alpha} = \frac{dE_{eff}}{E_{eff}} \frac{a}{E_{eff} + a} \text{ with } 0 < \frac{a}{E_{eff} + a} < 1 \tag{3.30}$$

we obtain:

$$\left| \frac{d\alpha}{\alpha} - \frac{dE_{eff}}{E_{eff}} \right| = \left| \frac{dE_{eff}}{E_{eff}} \times \left(\frac{a}{E_{eff} + a} - 1 \right) \right| < \left| \frac{dE_{eff}}{E_{eff}} \right| \tag{3.31}$$

We inject 3.31 in 3.29 and obtain:

$$\left| \frac{dN}{N} \right| < \left| \frac{dE_{eff}}{E_{eff}} \right| \tag{3.32}$$

actinide	$T_{1/2}$	$\sqrt{Var(Q_{eff})}/\mathbb{E}(Q_{eff})$
^{237}U	6.75d	0.2118%
^{239}U	23.47m	0.1980%
^{238}Np	2.12d	0.0851%
^{239}Np	2.36d	0.2633%
^{238}Pu	87.70y	0.0036%
^{241}Pu	14.33y	0.9558%
^{241}Am	432.80y	0.0021%
^{242}Am	16.04h	0.8906%
^{242M}Am	141.00y	0.9859%
^{242}Cm	162.85d	0.0013%
^{243}Cm	30.00y	0.0433%

Table 3.15: Q_{eff} values of several radioactive actinides

As the number of fission reactions is directly[3] linked to the final concentration of every nuclide in irradiated fuel, we can estimate that the magnitude of the impact of perturbation of effective fission energy is less than $\frac{\sigma(E_{eff})}{E_{eff}} \approx 0.1\%$, which can be neglected for our study.

In the case of competitive fission reactions, α is expressed as:

$$\alpha_i = \frac{\text{energy from fission } i}{\text{energy from fission } i + \text{other energy}} \tag{3.33}$$

and the impact is even lower if we consider that the effective fission energies of the different fissile nuclides are uncorrelated, because of the usual process of addition of uncorrelated distributions:

$$\left|\frac{\sigma(N)}{N}\right| < max\left|\frac{\sigma(E_{eff})}{E_{eff}}\right| \tag{3.34}$$

Impact of the uncertainty of the effective fission energy is negligible in our study.

3.1.2.1.6.2 Decay energy

The uncertainty of the decay energy of fission products is already taken into account in the effective fission energy uncertainty.

The decay energies of actinides are generally well-known. For instance, the Q_{eff} (mean global amount of energy released by the decay) of ^{241}Am has an associated standard deviation of 0.0021%.

Table 3.15 gives the Q_{eff} relative standard deviation of several radioactive actinides, taken from JEFF-3.1.1 database. Those nuclides are obtained through neutron capture or decay of common actinides in fuel.

We can observe that the Q_{eff} are generally well-known.

[3] although sometimes non-linearly, because of spectrum effects, competitive reactions and radioactive decays

Given the small contribution of actinides decay energy to the burnup and the accuracy of the Q_{eff}, we assume the hypothesis of weak impact of actinides decay energy uncertainty on the burnup.

However, it would be interesting to estimate the magnitude of this effect in a next study.

3.1.2.1.7 Parameters taken into account: summary

Table 3.16 summarizes which parameters are taken into account or neglected for actinides surrogate models. Neglected parameters are only taken into account as their mean value.

parameter	taken into account	neglected	number of parameters
burnup	×		1
irradiation length	×		1
specific power	×		(calculated, not sampled)
non-uniform load factor		×	
fresh fuel mass fractions	×		$2 \rightarrow 9$
actinides fission XS	×		19
actinides capture XS	×		19
FP capture XS		×	
actinides scattering XS		×	
FP scattering XS		×	
other nuclides scattering XS		×	
fission yields		×	
effective fission energy		×	
mass		×	
half-life		×	

Table 3.16: Summary of the parameters taken into account for actinides surrogate models

3.1.2.2 Design of experiment

3.1.2.2.1 Presentation

There are several approaches to generate the sample. Our design of experiments is characterized by the following assertions:

- there are approximately $40 < n < 50$ different parameters to be sampled at the same time;
- parameters are not correlated *a priori* even if we have information concerning correlations;
- the impact of each input parameter on the output is smooth (monotonic or has only one extremum over its domain of variation);
- there are few interactions between parameters, with the exception of burnup, which interacts with other parameters;
- statistical regression method will be applied on the sample;
- a run of CESAR is *reasonably* short, i.e. around 10 seconds, depending on the cross-section library and the burnup.

We can conclude that the CESAR calculation time for the construction of the design of experiments in the aim of building polynomial surrogate models is not really a limiting parameter in our study, hence the gain of adaptive low-discrepancy sequences is limited.

Given the convenience of its implementation in URANIE (see section 2.4) and its superiority over simple random sampling, we chose Latin Hypercube Sampling (LHS) as a sampling method for our designs of experiments.

3.1.2.2.2 Determination of the sample size

The sample size has to be chosen in function of the estimator. Sample size is determined in section 3.1.3.1.4 in the case of polynomial regressions and in section 3.1.3.2.1 in the case of artificial neural networks.

3.1.2.2.3 Application

All the parameters are sampled at the same time. LHS was chosen as the sampling method. The design of experiment for the fabrication sample contains 1000 points, those for the test sample also contain 1000 points. This almost ensures that the error of the estimators comes from a saturation (lack of fit) of the estimators, rather than a lack of knowledge.

Figure 3.12 shows a part of the multivariate sampling matrix in the case of PWR UOX fuel, irradiated at sub-nominal burnup. The color is representative of the density of irradiation computations per bin. Additional dimensions corresponding to fission and capture cross-section perturbations are not represented.

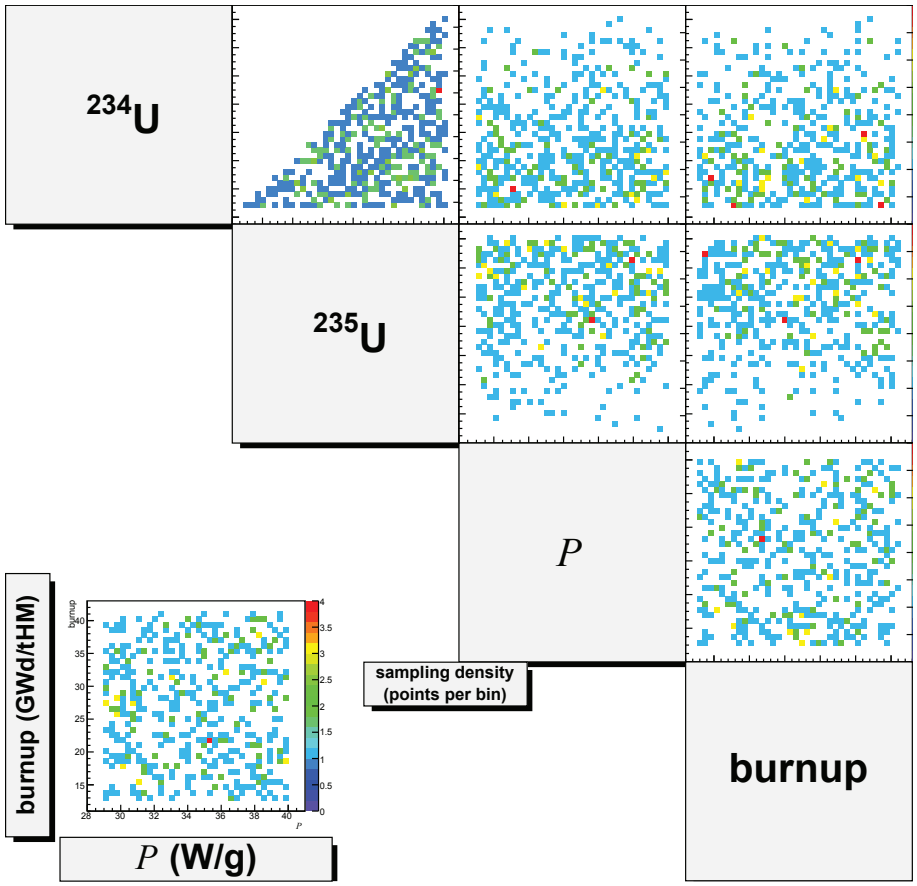

Figure 3.12: Partial sampling matrix of PWR UOX fuel irradiated at sub-nominal burnup

Although parameters are sampled without *a priori* correlations, *a posteriori* correlations sometimes appear due to limitations in the domain of validity of CESAR BBL (see section 2.1.2). This is for instance the case for PWR UOX fuel, where a boundary given by equation 3.35 appears. These limitations originate from the construction of one energy group cross-section libraries on a limited fuel composition domain.

$$y(^{234}\mathrm{U}) < \alpha \times y(^{235}\mathrm{U}), \quad \alpha \in \mathbb{R}^{*+} \tag{3.35}$$

The length of irradiation and the ^{238}U mass fraction are calculated in function of the parameters sampled. The partial design of experiment (DOE) matrix, which is the translation of the sampling matrix into CESAR input data, is shown on figure 3.13.

As expected, the length of irradiation is strongly correlated with the burnup, and the ^{238}U mass fraction with ^{235}U.

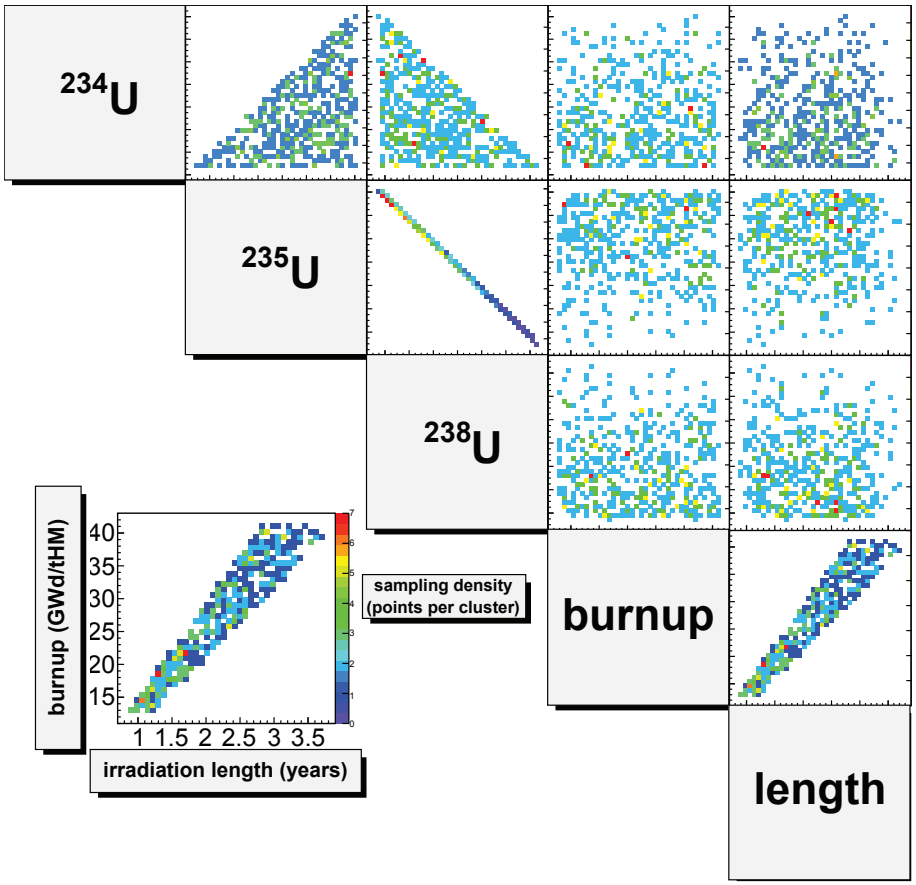

Figure 3.13: Partial DOE matrix of PWR UOX fuel irradiated at sub-nominal burnup

3.1.3 Regression

3.1.3.1 Polynomial regressions

3.1.3.1.1 Presentation

The polynomial regressions were chosen for a first approach given their simplicity and their physical interpretation. Indeed, the first order coefficients are the sensitivities of the different parameters in the model, given that the design of experiments is uncorrelated, and the higher order terms give information about the non-linearity (sign of the second order term, etc.) interaction (synergy between parameters) of parameters. The numerical value of monomials is highly informative, and is sometimes used for short local or even global sensitivity studies. Therefore polynomial models are not black-box models, although the numerical value and sign of high-order monomials are sometimes difficult to interpret.

The polynomial regressions also have several downsides. First, high-degree polynomials can lead to non-physical oscillations or collapses, especially near the boundaries of the design of experiment. Therefore it is generally advised to stay under a reasonable degree (usually between 2 and 5). However, this constraint introduces a lack of fit, inherent to the model, that any design of experiment cannot overcome. Another constraint, common to most of the estimators, is the exponential scaling of the models complexity with the non-linearity of the model output and the

number of parameters.

The evolution of the number of monomials N in a d-degree polynomial as a function of p parameters is given in equation 3.36. Numeric application for a few cases is shown in table 3.17.

$$N = \sum_{i=0}^{d} \binom{p+i-1}{i} \tag{3.36}$$

N		degree of the polynomial				
		0	**1**	**2**	**3**	**4**
parameters	**1**	1	2	3	4	5
	2	1	3	6	10	15
	5	1	6	21	56	126
	10	1	11	66	286	1001
	20	1	21	231	1771	10626
	50	1	51	1326	23426	316251

Table 3.17: Number of monomials in a d-degree polynomial of n variables

However, in practice, not every term in the polynomial is computed, since the contribution of most of the monomials is negligible, and an iterative method allows computing only the N_0 first terms to reach a given coefficient of determination. In the case of actinides, the model complexity remains reasonable due to the weakness of interactions between parameters (usually polynomials of 40 monomials or less are adequate, as shown in part 3.1.3.1.5), and therefore polynomial models can be accepted.

Artificial neural networks are presented as an alternative to polynomials in section 3.1.3.2.

3.1.3.1.2 Determination of the model's parameters

3.1.3.1.2.1 Overview

The parameters of polynomial regressions have to be chosen among the DOE parameters (presented in part 3.1.2.1), or directly accessible through them. The parameters to be taken into account are as follows:

- Burnup and specific power are uncorrelated in our sampling and therefore used to describe fully the irradiation parameters;
- All the initial mass fractions except $y\left(^{238}\mathrm{U}\right)$ are taken into account. The parameter $y\left(^{238}\mathrm{U}\right)$ is not considered as it results from the other parameters and its account being taken would add an unnecessary degree of freedom to the system;
- Every cross-section perturbation is taken into account. Several perturbations may have an almost null effect, however they are still considered, in order to obtain at least linear tendencies.
- Fission yield perturbations are not taken into account.

The maximum degree is a supplementary parameter intervening in the construction of polynomial regressions. A short study is carried out to determine the best degree to use.

isotope	isotopy (^{i}Pu/Pu, %)
^{238}Pu	2.5
^{239}Pu	54.5
^{240}Pu	25.2
^{241}Pu	8.6
^{242}Pu	7.9
^{241}Am	1.3

Table 3.18: Pu vector for study of the linearity of fresh fuel composition in PWR MOX fuel

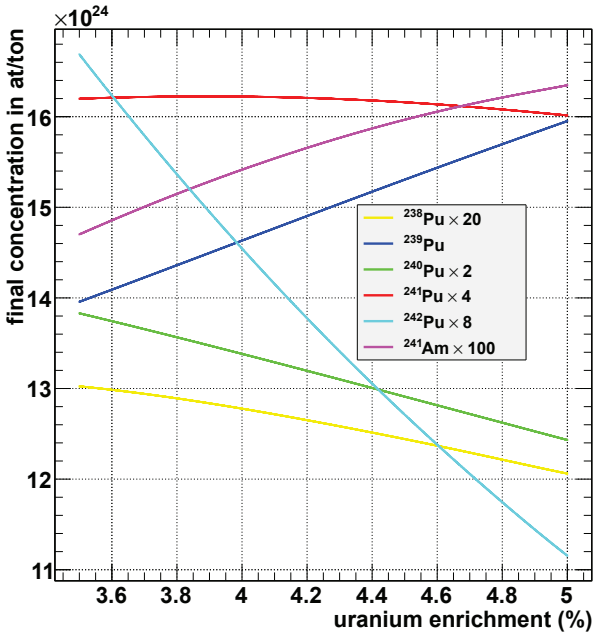

Figure 3.14: Plutonium concentrations after irradiation in function of the uranium enrichment for PWR UOX fuel

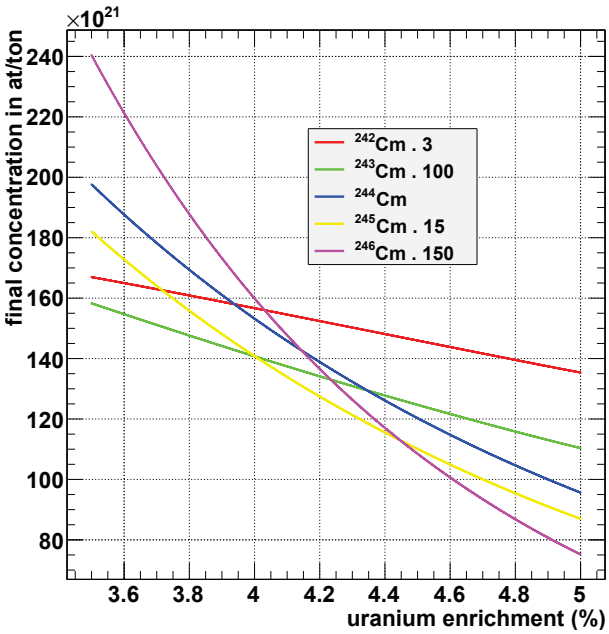

Figure 3.15: Curium concentrations after irradiation in function of the uranium enrichment in PWR UOX fuel

3.1.3.1.2.2 Fresh fuel composition impact linearity

Figure 3.14 represents the plutonium concentration after irradiation of PWR UOX fuel irradiated at 45 GWd/tHM in function of the initial uranium enrichment, and figure 3.15 the curium concentrations. Concentrations are calculated with CESAR5.3.

We can observe that these isotopes depend roughly linearly (with the exception of some curium isotopes) on the initial enrichment on the whole domain of sampling.

The linearity of the impact of the enrichment can be quantified with the coefficient of determination of a simple linear regression using linear least squares. Indeed, the Pearson product-moment correlation coefficient (PCC) is a quantitative measure of the linear correlation between two variables, and in the case of simple linear least squares regressions, the determination coefficient r^2 is equal to PCC: $r^2 = \text{PCC}$. r^2 quantifies the ratio of linearity of the impact of the enrichment on the concentrations after irradiation. For instance, $r^2 = 0.90$ can be interpreted as 90% of the variance of the output is explained by a linear dependence with the input parameter. Since we consider only one parameter, the remaining 10% correspond to a non-linear impact. The

nuclide	PCC	nuclide	PCC
^{234}U	0.998	^{242}Pu	0.996
^{235}U	0.998	^{241}Am	0.986
^{236}U	0.999	^{242M}Am	0.996
^{238}U	0.999	^{243}Am	0.994
^{237}Np	0.991	^{242}Cm	1.000
^{238}Pu	0.994	^{243}Cm	0.998
^{239}Pu	1.000	^{244}Cm	0.987
^{240}Pu	1.000	^{245}Cm	0.988
^{241}Pu	0.779	^{246}Cm	0.972

Table 3.19: Measure of the linearity of the impact of the uranium enrichment on final concentrations of different nuclides for PWR UOX fuel

nuclide	PCC	nuclide	PCC
^{234}U	0.997	^{242}Pu	0.998
^{235}U	0.999	^{241}Am	0.999
^{236}U	0.999	^{242M}Am	0.999
^{238}U	1.000	^{243}Am	1.000
^{237}Np	0.999	^{242}Cm	0.994
^{238}Pu	0.982	^{243}Cm	1.000
^{239}Pu	0.999	^{244}Cm	0.999
^{240}Pu	0.999	^{245}Cm	0.999
^{241}Pu	0.995	^{246}Cm	0.996

Table 3.20: Measure of the linearity of the ^{239}Pu isotopy on final concentrations of different nuclides for PWR MOX fuel

values of $r^2 =$ PCC for several significant nuclides are shown in table 3.19 for PWR UOX fuel.

The PCC for most of the final concentrations (except ^{241}Pu) in function of the fuel enrichment is almost equal to 1, which is characteristic of an almost linear impact . PCC degrades in the case of heaviest nuclides such as curium isotopes. The PCC value for ^{241}Pu is much lower, therefore a linear regression is not sufficient to describe its evolution. However, given the very small amplitude of variation of ^{241}Pu in function of the enrichment, we can assume that a low-order polynomial regression can model it more or less accurately.

Figure 3.16 represents the plutonium concentration after irradiation of PWR MOX fuel irradiated at 45GWd/tHM in function of the initial ^{239}Pu mass fraction, and figure 3.17 the curium concentrations. Reference Pu vector of PWR MOX fuel for this study is shown in table 3.18. The PCC results are shown in table 3.17.

The results are similar: the impact of the fresh fuel ^{239}Pu is more or less linear. We assume that this result extends to the other nuclides in fresh fuel, and to other types of fuel.

3.1.3.1.2.3 Burnup impact linearity

Figure 3.18 (respectively 3.19) represents the evolution of the plutonium (resp. curium) vector composition for irradiated PWR UOX fuel enriched at 4.5% in function of the burnup. We can

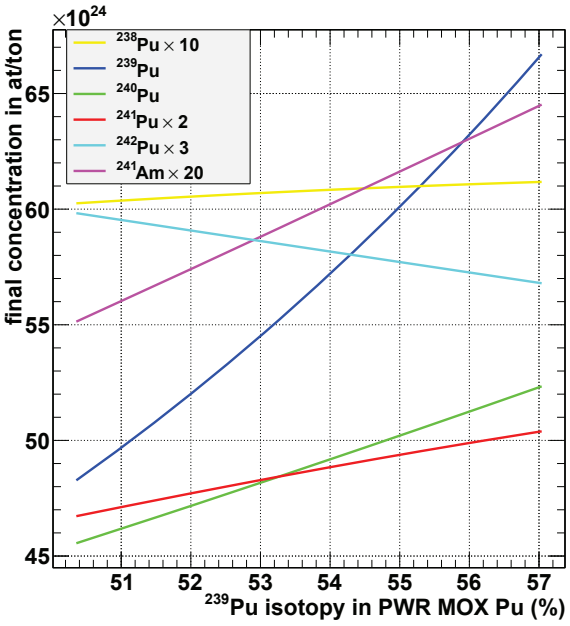

Figure 3.16: Evolution of several final plutonium concentrations in function of the ^{239}Pu mass fraction for PWR MOX fuel

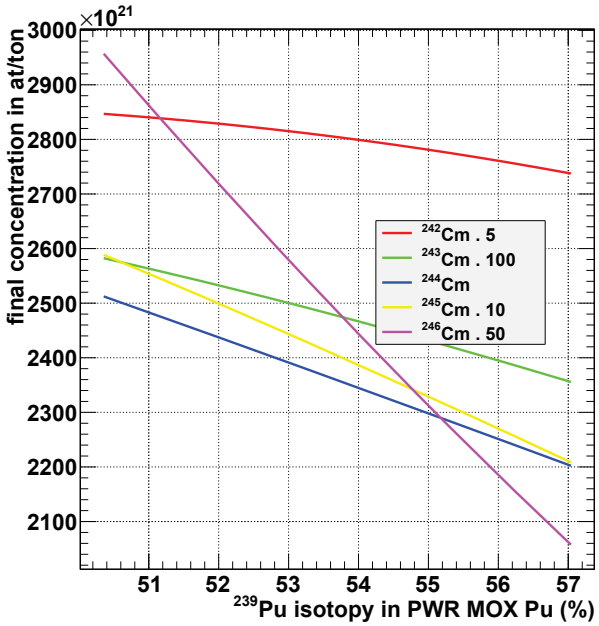

Figure 3.17: Evolution of several final curium concentrations in function of the ^{239}Pu mass fraction for PWR MOX fuel

observe that the burnup impact on final concentrations is not linear.

Even though in this case graphs are sufficient to point out the non-linearity of the impact of the burnup, PCC coefficients are calculated, as a comparison for part 3.1.3.1.2.2.

nuclide	PCC
^{234}U	0.996
^{235}U	0.977
^{236}U	0.943
^{238}U	0.998
^{237}Np	0.999
^{238}Pu	0.955
^{239}Pu	0.668
^{240}Pu	0.987
^{241}Pu	0.972

nuclide	PCC
^{242}Pu	0.967
^{241}Am	0.990
^{242M}Am	0.988
^{243}Am	0.910
^{242}Cm	0.977
^{243}Cm	0.914
^{244}Cm	0.813
^{245}Cm	0.768
^{246}Cm	0.662

Table 3.21: Linearity measure for the burnup impact on final concentrations for different nuclides in PWR UOX fuel

Intuitively, the degree of the polynomial estimation of the final concentration of a given actinide depends on the number of successive radiative captures necessary to obtain it from an initial nuclide present in the fresh fuel. This estimation is not flawless since it does not take into account the kinetic of transmutation of the successive *fathers* of the actinide.

We evaluate the lower bound degree of the polynomial judged *satisfying* for the description of a final concentration in function of the burnup. The criteria of satisfaction is arbitrarily chosen as $r^2 > 0.999$. The algorithms are shown in section 3.1.3.1.3. The *lower bound degree* corresponds

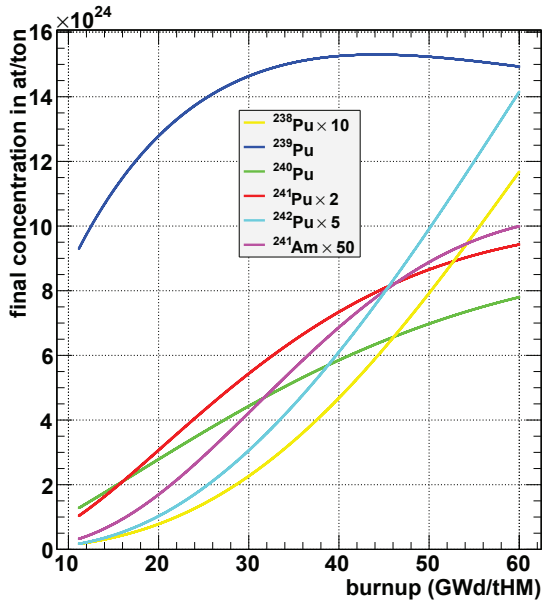

Figure 3.18: Evolution of the final Pu concentration in function of the burnup for PWR UOX fuel

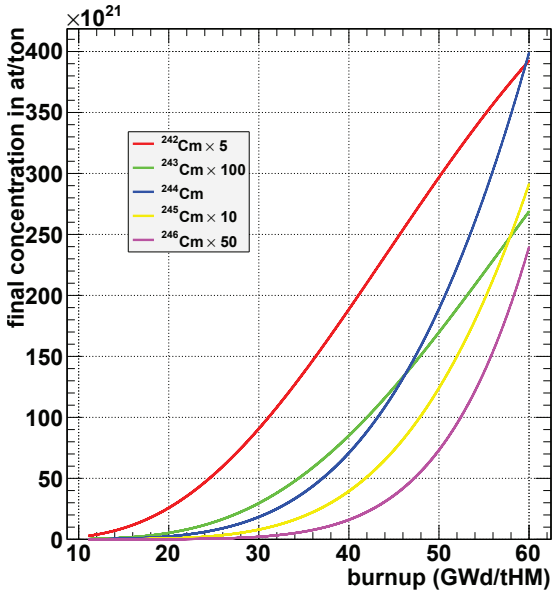

Figure 3.19: Evolution of the final Cm concentration in function of the burnup for PWR UOX fuel

to the minimum degree of a polynomial modeling this output such as $r^2 > 0.999$.

Results are shown in table 3.22.

nuclide	lower bound degree	nuclide	lower bound degree
^{234}U	2	^{242}Pu	2
^{235}U	2	^{241}Am	3
^{236}U	2	^{242M}Am	3
^{238}U	2	^{243}Am	2
^{237}Np	1	^{242}Cm	3
^{238}Pu	2	^{243}Cm	2
^{239}Pu	3	^{244}Cm	3
^{240}Pu	2	^{245}Cm	3
^{241}Pu	2	^{246}Cm	4

Table 3.22: Determination of the lower bound degree for polynomial estimation for PWR UOX fuel

It appears that polynomials of degree 4 or less are sufficient to model the evolution of final concentrations in function of the burnup for the given design of experiments.

On a side note the degree for ^{239}Pu models is relatively high because of the complex transmutation kinetic of ^{239}Pu in PWR UOX reactor (reaction rates of creation and disappearance are more or less similar).

3.1.3.1.2.4 Generic equation

The general shape of the polynomial regression for the concentration C after irradiation is shown in equation 3.37.

$$C = \sum_{i=1}^{n} \alpha_i \times \prod_{j \in fuel} y_j^{d_{ji}} \times \prod_{r \in reactions} \left(1 + \frac{\Delta\sigma_r}{\sigma_r}\right)^{d_{ri}} \times \mathrm{BU}^{d_{\mathrm{BU}i}} \times \mathcal{P}^{d_{\mathcal{P}i}} \tag{3.37}$$

The impact of fuel composition $\{y_j\}$ was proven to be relatively linear. In the same way, we assess that the impact of cross-sections perturbations is approximately linear. The impact of the specific power $\mathcal{P}$ is small, and relatively linear. The impact of the burnup was shown in part 3.1.3.1.2.3 to be more or less polynomial, with a degree up to 4. A nonlinear effect interacting with another effect can lead to higher degree monomials. However it is generally advised not to exceed degree 4 in order to keep good generalization properties, because of the collapses it can cause in the quality of estimators in some areas of the design of experiment.

Therefore the degree of the polynomial is chosen less or equal to 4, as expressed in equation 3.38. This implies the following restrictive rules:

- each monomial will depend on few parameters at the same time, especially if their power is high,
- the maximal power of any term is less or equal to 4

$$\forall i \; 0 \leq \sum_j d_{ij} + \sum_r d_{ri} + d_{\mathrm{BU}i} + d_{\mathcal{P}i} \leq 4 \tag{3.38}$$

3.1.3.1.3 Algorithmic

URANIE is able to build polynomial regressions given the following elements:

- an initial set S_0 of parameters $\{p_i\}$
- a function to model y
- a design of experiment Γ containing the values of $\{p_i\}$ and y
- a low bound b of the value of a global indicator Q of quality to reach: determination or prediction

The URANIE `TPolynomialRegression` algorithm for the construction of polynomial regressions is as follows:

1.
   - $S \leftarrow S_0$
   - Construction of a linear regression $\tilde{y} : S \rightarrow \mathbb{R}$ by the least squares method
   - If $Q \geq b$ then end of the algorithm. Else, go to step 2
2.
   - $\forall (i,j) \; / \; \{p_i p_j\} \notin S \wedge \{p_i, p_j\} \in S_0 \times S_0$ construction of the function $\tilde{y} : S + \{p_i p_j\} \rightarrow \mathbb{R}$ by the least squares method
   - Computation of Q_{ij} (red dots on figure 3.20)
   - Selection of the best set of parameters according to $Q_{i,j}$: $S + p_\alpha p_\beta$ (blue dots)
   - $Q \leftarrow \max_{i,j}(Q_{ij})$
   - Replacement of the set by the new best set: $S \leftarrow S + \{p_\alpha p_\beta\}$
   - If $Q \geq b$ then end of the algorithm. Else, go to step 2.

The algorithm is primarily implemented to produce degree 2 polynomial regressions, but it is possible to tweak it to produce degree 4 polynomials. The process of linear regression is performed using the least squares method.

Figure 3.20 represents the process of construction of the polynomial estimator. The expected value of r^2 over the construction sample is $r^2 \geq 0.999$ (green line). First a linear regression is performed (red dot on the bottom left). The associated determination coefficient is $r^2 \approx 0.988 < 0.999$. Then a linear regression is performed with all of the parameters plus a degree 2 monomial combining two parameters (red dots for 1 added monomial). The best combination (blue dot) has an associated determination coefficient still inferior to 0.999, therefore another monomial has to be added. This operation is realized until $r^2 \geq 0.999$. The last blue dot is above the green line: 4 supplementary monomials are enough to provide a polynomial regression with the expected global accuracy.

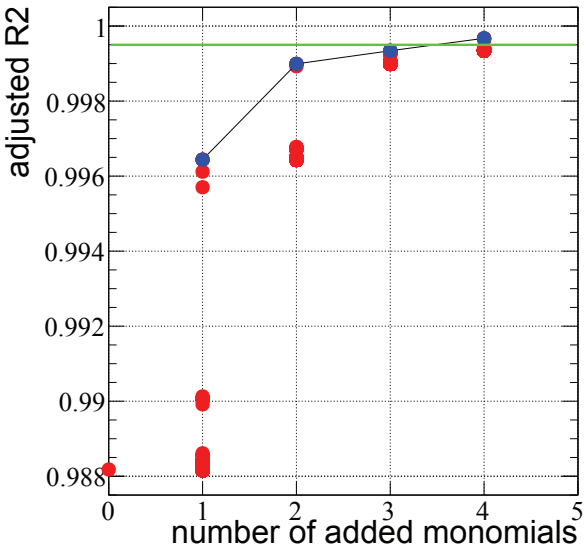

Figure 3.20: Construction of a polynomial regression

3.1.3.1.4 Determination of the sample size for polynomial regressions

The sample size is the result of the study of evolution of the prediction coefficient in function of the construction sample size. We carry the following study: for a few different construction samples of different size, we build a polynomial regression of an output (for instance the concentration of ^{239}Pu after irradiation in PWR UOX fuel) in function of the input parameters. The criteria for the construction of polynomial estimators was chosen as: $r^2_{construction\ sample} \geq 0.9999$. This value is arbitrary, but is more or less representative of the precision we expect from surrogate models.

Then we export this function and apply it on test sample, different from the construction sample. The test sample is always the same. Finally, the prediction coefficient q^2 of the estimator is calculated from the test sample. Values are shown on table 3.23, the prediction coefficient obtained through *jackknife* (simple resampling method) on the construction sample and the number of monomials which degree is at least two (non-linearity and interactions) are shown as well.

We can observe that:

- estimation of q^2 through *jackknife* does not give satisfying results for small construction samples, however for bigger samples the q^2 obtained with *jackknife* tends toward the q^2 computed on a test sample.

sample size	nb $d \geq 2$ mono.	r^2 (construction)	q^2 (jackknife)	q^2 (test sample)
50	3	0.999942	0.999352	0.996548
100	4	0.999903	0.999686	0.998977
200	7	0.999913	0.999830	0.999807
500	8	0.999906	0.999874	0.999745
1000	10	0.999918	0.999905	0.999913
1500	10	0.999914	0.999904	0.999911

Table 3.23: Evolution of r^2 and q^2 in function of the sample size for ^{239}Pu in PWR UOX fuel

- global quality (q^2) is good even for relatively small construction samples because most of parameters have a smooth impact on the output.
- a sample of size 1000 is sufficient in the case of estimation of actinides' concentrations after irradiation.

We conclude that a sample of size 1000 is sufficient in the case of estimation of actinides.

More that 1000 points do not give supplementary information for the construction of an estimator which $r^2 \geq 0.9999$, and the number of monomials necessary to improve the precision increases exponentially above that limit.

As a side result, we observe that q^2 computed with the jackknife method gives satisfying results (slight overestimation) for large samples and will be used to quantify quickly the global accuracy of the estimators.

Polynomial regressions are not adapted to the construction of more accurate estimators, in that case artificial neural networks were preferred (part 3.1.3.2). The main reason is that it is not always possible to obtain a satisfactory low-degree Taylor approximation of the functions of concentrations after irradiation, even in the case of continuous monotonic functions.

3.1.3.1.5 Application

3.1.3.1.5.1 Overview

The sampling distributions of the different DOE parameters are presented in appendix A.1 for each surrogate model associated to a fuel type.

In this section, we compare the quality indicators for the polynomial regressions.

It has to be noted that given that the distributions of the input parameters are different for each fuel cycle scenario, whereas we usually build only one irradiation model per type of fuel, which has to be valid for every scenario. Therefore the quality indicators are computed on a test-base which parameters' distributions do not follow a scenario in particular, but rather a plausible distribution including the distributions of every scenario[4]. Consequently this indicator will not truly represent the percentage of variance propagated by the model during uncertainty computation in scenario calculations, but rather a general quality of the model on its whole domain of application.

[4]for instance, fresh PWR MOX fuel isotopy results from PWR UOX reactors fleet, irradiation parameters and fuel reprocessing strategy, which are not similar in different scenarios.

For each estimated concentration after irradiation of each fuel type, an identity card of the estimator is stored. This card contains information assessing the general quality of the estimator on its domain of validity, and can be used to determine whether it is accurate enough for the considered application.

The typical scenario calculation requires an amount of 7 ($\sim$one per fuel type $\times$ burnup domain[5]) surrogate models $\times$ 19 estimators (one per concentration after irradiation) = 133 actinides estimators, without consideration of fission products. The list of fuel types is shown on equation 3.39 (without consideration of minor actinides transmutation[6]).

$$\texttt{list_fuel_types=}\begin{cases}\text{PWR UOX, less than nominal burnup}\\ \text{PWR UOX, nominal burnup}\\ \text{PWR repU, all burnup}\\ \text{PWR MOX, less than nominal burnup}\\ \text{PWR MOX, nominal burnup}\\ \text{SFR MOX, less than nominal burnup}\\ \text{SFR MOX, nominal burnup}\end{cases} \tag{3.39}$$

Sections 3.1.3.1.5.2 to 3.1.3.1.5.8 show the properties of the fabrication and test samples for these surrogate models, as well as several quality indicators. Values over 1000% are noted $+++$. These results provide good information to determine whether estimators are suited to perform uncertainty propagation, however it is wiser to also use graphs representing the estimators and the residuals. Construction of these graphs is automated, and is done at the same time as construction of the estimators. A few examples of these graphs (identify cards) are presented in the next sections.

Other examples concerning polynomial regression identity cards are available in appendix B.1.

The precision of each estimator was tested on a test base, different from the fabrication sample. We denote y the concentration after irradiation of an actinide, $\bar{y}$ the mean of y on the test sample and $\hat{y}$ the estimator of y calculated on the test sample. The following quality indexes are calculated on a test sample (with the exception of r^2, calculated on construction sample):

$$\begin{cases} r^2, q^2 & \text{variance propagation indicators}\\ max\,|\hat{y}/y-1| & \text{maximum value of the relative error}\\ mean\,|\hat{y}/y-1| & \text{mean value of the relative error}\\ max\,|(\hat{y}-y)/\bar{y}| & \text{maximum value of the absolute error compared to the mean}\\ mean\,|(\hat{y}-y)/\bar{y}| & \text{mean value of the absolute error compared to the mean}\end{cases} \tag{3.40}$$

3.1.3.1.5.2 PWR UOX fuel, less than nominal burnup

This surrogate model is adapted to the description of a wide range of PWR UOX fuel, irradiated at a less than nominal burnup of usual current PWR UOX fuel (<41GWd/tHM). It can be used to describe starting and shutdown batches, as well as historical PWR UOX fuel management at 33GWd/tHM. Parameters are sampled without correlation except the irradiation length and ^{238}U mass fraction which are calculated a posteriori. The sample size is 500, and LHS is used as the sampling method.

[5] see section 3.1.2.1.3.4 for more details on the burnup

[6] Irradiation surrogate models for actinides transmutation only use ANN estimators, described in section 3.1.3.2.

Polynomial regressions are performed for each concentration after irradiation of interest according to the method described in 3.1.3.1.3. The optimal values of r^2 as the quality criterion are obtained by iteration (precision vs. size of the polynomials). Every parameter sampled is used for the construction of the polynomial estimators. The values of quality indicators calculated for each estimator on the construction sample and a mirror test sample are given in table 3.24.

actinide	r^2	q^2	$max\|\hat{y}/y-1\|$	$mean\|\hat{y}/y-1\|$	$max\|(\hat{y}-y)/\bar{y}\|$	$mean\|(\hat{y}-y)/\bar{y}\|$
^{234}U	0.9996	0.9995	1.30 %	0.27 %	1.15 %	0.26 %
^{235}U	1.0000	1.0000	0.72 %	0.11 %	0.31 %	0.09 %
^{236}U	0.9998	0.9998	0.96 %	0.22 %	0.88 %	0.22 %
^{238}U	1.0000	1.0000	0.01 %	0.00 %	0.01 %	0.00 %
^{237}Np	1.0000	1.0000	2.20 %	0.24 %	0.85 %	0.21 %
^{239}Np	0.9965	0.9959	2.33 %	0.66 %	2.34 %	0.65 %
^{238}Pu	0.9995	0.9994	14.68 %	2.05 %	6.17 %	1.31 %
^{239}Pu	0.9999	0.9998	0.50 %	0.10 %	0.38 %	0.10 %
^{240}Pu	0.9998	0.9998	2.14 %	0.39 %	1.60 %	0.36 %
^{241}Pu	0.9999	0.9999	3.23 %	0.46 %	1.27 %	0.37 %
^{242}Pu	0.9997	0.9997	14.57 %	1.75 %	4.16 %	0.90 %
^{241}Am	0.9996	0.9994	13.94 %	1.47 %	7.03 %	0.98 %
^{242M}Am	0.9996	0.9994	20.19 %	1.64 %	6.38 %	1.01 %
^{243}Am	0.9992	0.9992	115.84 %	6.72 %	9.57 %	2.15 %
^{242}Cm	0.9997	0.9995	40.66 %	3.22 %	6.96 %	1.33 %
^{243}Cm	0.9990	0.9987	258.36 %	10.95 %	15.96 %	2.67 %
^{244}Cm	0.9975	0.9967	459.06 %	27.61 %	35.87 %	4.82 %
^{245}Cm	0.9956	0.9906	$+++$ %	91.07 %	101.17 %	8.37 %
^{246}Cm	0.9859	0.9840	$+++$ %	607.47 %	110.39 %	14.27 %

Table 3.24: Quality indexes of low burnup PWR UOX actinides polynomial surrogate model

For each concentration after irradiation estimated by a polynomial, a table summarizing several quality tests of the estimator is created. Figure 3.21 is a representation of this table in the case of the concentration of ^{239}Pu after irradiation, figure B.1 describes the case of ^{240}Pu and figure 3.22 the case of ^{244}Cm. The same analysis was performed for every estimator contained in the surrogate model.

Identification cards contain the following information:

- in the grey box:
  - general information concerning the fuel type and the ANN properties;
  - local and global quality indicators;
- top-right: representation of the output of interest in function of an important parameter (depending on the case, burnup is often the most sensitive parameter);
- middle-left: representation of the estimator in function of the output of interest;
- middle-right and bottom-left: representation of the bias in function of the output of interest;
- bottom-right: histogram of the bias.

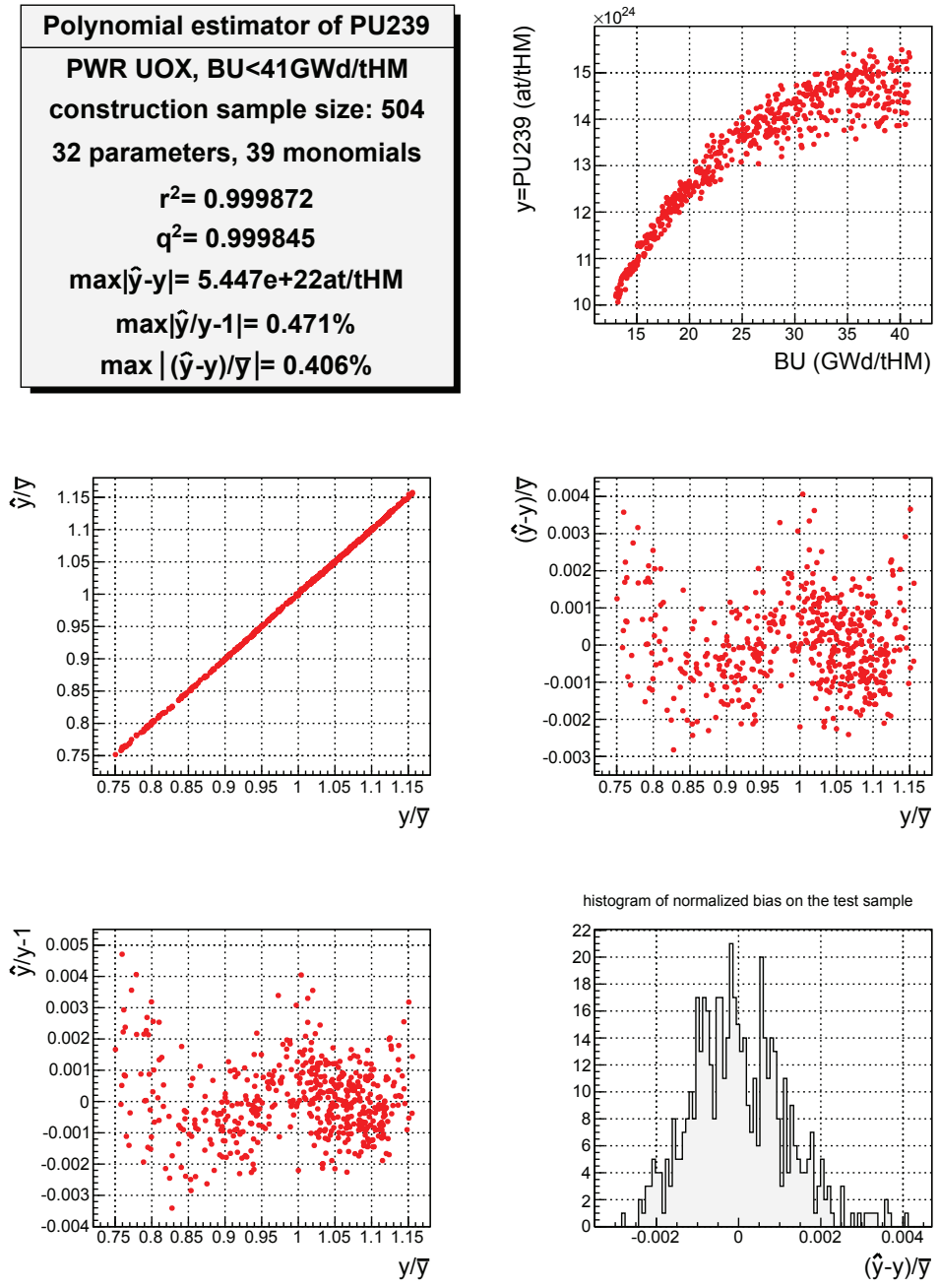

Figure 3.21: Identity card of the ^{239}Pu estimator in PWR UOX fuel, BU<41GWd/tHM

Overall the quality of this ^{239}Pu estimator (figure 3.21) is satisfying. The maximum of the relative error is low (0.47%). The bias is usually inferior to 0.2% of the mean value. This estimator is suited to uncertainty propagation.

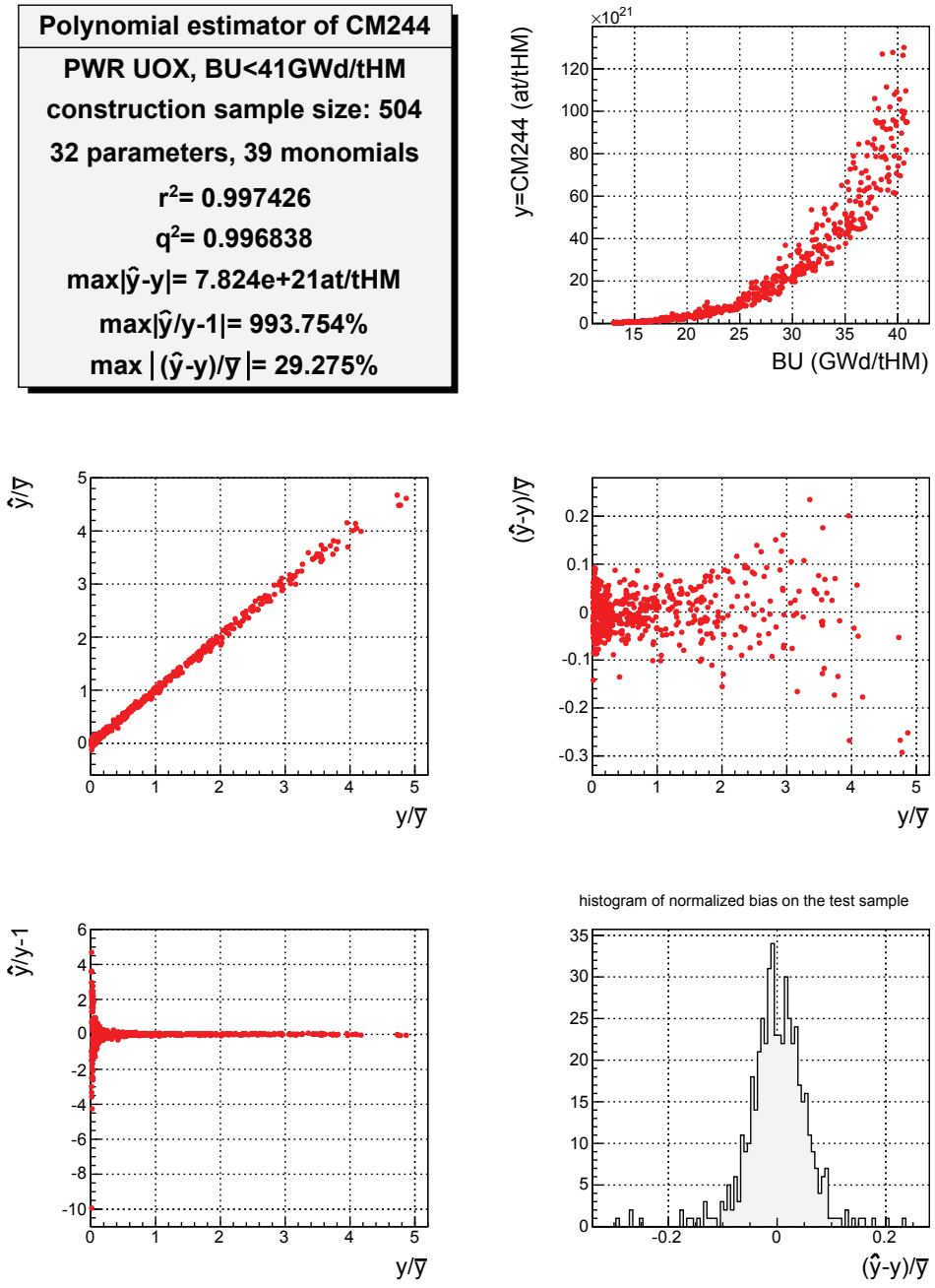

Figure 3.22: Identity card of the ^{244}Cm estimator in PWR UOX fuel, BU<41GWd/tHM

The quality of this model (figure 3.22) is not satisfying: the absolute error $(\hat{y} - y)/\bar{y}$ is much too high. Several points even return negative values of the concentration. The nail-shaped diagram on the bottom-left is a sign of a very wide and not accurately estimated dispersion of the concentration. This estimator is not well adapted for estimation of ^{244}Cm or uncertainty propagation, and construction of a more precise model is considered, as shown in section 3.1.3.2. The identity card of the ^{244}Cm ANN estimator in the same spectrum is shown in appendix B.2.1.

3.1.3.1.5.3 PWR UOX fuel, nominal burnup

This surrogate model is aimed at the description of PWR UOX fuel irradiated at nominal burnup or more. While its domain of validity is smaller than the model described on section 3.1.3.1.5.2, it is more frequently used as the nominal PWR UOX irradiation model, therefore its precision is expected to be higher.

The parameters sampling is described in appendix A.1.2 page 285.

Table 3.25 summarizes the global quality of the estimators. Figure B.2 represents the identity card of an estimator (^{239}Pu) among the others.

actinide	r^2	q^2	$max\|\hat{y}/y-1\|$	$mean\|\hat{y}/y-1\|$	$max\|(\hat{y}-y)/\bar{y}\|$	$mean\|(\hat{y}-y)/\bar{y}\|$
^{234}U	0.9998	0.9998	0.68 %	0.15 %	0.60 %	0.15 %
^{235}U	0.9999	0.9999	1.25 %	0.19 %	0.74 %	0.16 %
^{236}U	0.9995	0.9994	0.56 %	0.14 %	0.59 %	0.14 %
^{238}U	1.0000	1.0000	0.00 %	0.00 %	0.00 %	0.00 %
^{237}Np	0.9996	0.9995	0.55 %	0.18 %	0.64 %	0.18 %
^{239}Np	0.9997	0.9997	0.67 %	0.13 %	0.53 %	0.13 %
^{238}Pu	0.9996	0.9994	2.38 %	0.31 %	2.41 %	0.32 %
^{239}Pu	0.9998	0.9997	0.19 %	0.04 %	0.17 %	0.04 %
^{240}Pu	0.9996	0.9996	0.44 %	0.10 %	0.38 %	0.10 %
^{241}Pu	0.9996	0.9996	0.32 %	0.09 %	0.34 %	0.09 %
^{242}Pu	0.9996	0.9994	1.47 %	0.35 %	1.58 %	0.36 %
^{241}Am	0.9994	0.9992	1.03 %	0.26 %	0.94 %	0.26 %
^{242M}Am	0.9994	0.9989	1.13 %	0.30 %	0.99 %	0.30 %
^{243}Am	0.9996	0.9994	2.01 %	0.51 %	2.65 %	0.51 %
^{242}Cm	0.9998	0.9996	1.22 %	0.21 %	0.98 %	0.21 %
^{243}Cm	0.9992	0.9988	4.72 %	0.65 %	2.40 %	0.65 %
^{244}Cm	0.9986	0.9975	7.52 %	1.43 %	9.17 %	1.36 %
^{245}Cm	0.9974	0.9968	13.24 %	2.28 %	9.08 %	1.96 %
^{246}Cm	0.9919	0.9868	82.16 %	7.71 %	35.99 %	5.71 %

Table 3.25: Quality indexes of high burnup PWR UOX actinides polynomial surrogate model

3.1.3.1.5.4 PWR repU fuel, all burnup

This surrogate model is aimed at the description of PWR repU irradiated fuel. Its domain of validity covers the whole burnup range. This result comes from the narrow range of the initial mass fractions: the composition of most repU batches is the same, therefore the model is easier to produce as it contains very few interaction terms.

The parameters sampling is described in appendix A.1.3 page 286. The sample size is 500, LHS is used as the sampling method. Table 3.26 summarizes the global quality of the estimators. Figure B.3 page B.3 represents the identity card of an estimator (^{239}Pu) among the others.

actinide	r^2	q^2	$max\|\hat{y}/y-1\|$	$mean\|\hat{y}/y-1\|$	$max\|(\hat{y}-y)/\bar{y}\|$	$mean\|(\hat{y}-y)/\bar{y}\|$
^{234}U	1.0000	1.0000	0.23 %	0.04 %	0.19 %	0.04 %
^{235}U	1.0000	1.0000	0.24 %	0.06 %	0.23 %	0.06 %
^{236}U	1.0000	1.0000	0.05 %	0.01 %	0.05 %	0.01 %
^{238}U	1.0000	1.0000	0.00 %	0.00 %	0.00 %	0.00 %
^{237}Np	1.0000	1.0000	0.33 %	0.07 %	0.19 %	0.06 %
^{239}Np	0.9997	0.9997	0.40 %	0.10 %	0.36 %	0.10 %
^{238}Pu	1.0000	0.9999	6.54 %	0.53 %	1.68 %	0.32 %
^{239}Pu	0.9999	0.9999	0.75 %	0.10 %	0.53 %	0.09 %
^{240}Pu	1.0000	1.0000	0.82 %	0.12 %	0.30 %	0.09 %
^{241}Pu	0.9999	0.9999	3.52 %	0.46 %	1.24 %	0.29 %
^{242}Pu	0.9999	0.9999	23.32 %	1.61 %	2.59 %	0.49 %
^{241}Am	0.9999	0.9999	7.24 %	0.84 %	1.55 %	0.38 %
^{242M}Am	0.9999	0.9999	13.64 %	1.34 %	1.91 %	0.43 %
^{243}Am	0.9998	0.9997	150.46 %	8.10 %	5.66 %	1.11 %
^{242}Cm	0.9999	0.9999	67.60 %	2.92 %	2.52 %	0.55 %
^{243}Cm	0.9996	0.9992	645.24 %	27.47 %	8.54 %	1.91 %
^{244}Cm	0.9994	0.9993	+++	59.93 %	7.25 %	2.15 %
^{245}Cm	0.9975	0.9957	+++	409.20 %	25.40 %	5.36 %
^{246}Cm	0.9924	0.9897	+++	+++	40.98 %	9.71 %

Table 3.26: Quality indexes of PWR repU actinides polynomial surrogate model

3.1.3.1.5.5 PWR MOX fuel, less than nominal burnup

This surrogate model is adapted to the description of a wide range of PWR MOX fuel, irradiated at a less than nominal burnup of usual modern PWR MOX fuel. It is mostly used to describe starting and shutdown batches. The parameters sampling is described in appendix A.1.4 page A.1.4. Parameters are sampled without correlations except the irradiation length and ^{238}U mass fraction which are calculated a posteriori. The sample size is 1000, LHS is used as the sampling method. Table 3.27 summarizes the global quality of the estimators. Figure B.4 page 307 represents the identity card of an estimator (^{241}Am) among the others.

actinide	r^2	q^2	$max\|\hat{y}/y-1\|$	$mean\|\hat{y}/y-1\|$	$max\|(\hat{y}-y)/\bar{y}\|$	$mean\|(\hat{y}-y)/\bar{y}\|$
^{234}U	0.9996	0.9995	1.60 %	0.36 %	1.81 %	0.34 %
^{235}U	1.0000	0.9999	4.49 %	0.42 %	1.10 %	0.30 %
^{236}U	0.9998	0.9998	6.30 %	0.72 %	2.42 %	0.54 %
^{238}U	1.0000	1.0000	0.01 %	0.00 %	0.01 %	0.00 %
^{237}Np	0.9994	0.9994	6.04 %	0.78 %	3.38 %	0.72 %
^{239}Np	0.9960	0.9910	3.92 %	0.73 %	4.55 %	0.74 %
^{238}Pu	0.9991	0.9989	1.69 %	0.41 %	1.85 %	0.41 %
^{239}Pu	0.9999	0.9999	0.81 %	0.17 %	0.75 %	0.16 %
^{240}Pu	0.9968	0.9965	0.88 %	0.31 %	0.85 %	0.31 %
^{241}Pu	0.9952	0.9917	2.33 %	0.51 %	1.93 %	0.50 %
^{242}Pu	0.9991	0.9987	1.43 %	0.36 %	1.57 %	0.36 %
^{241}Am	0.9971	0.9967	3.22 %	0.64 %	3.33 %	0.65 %
^{242M}Am	0.9930	0.9925	5.77 %	1.05 %	3.75 %	0.99 %
^{243}Am	0.9990	0.9990	3.24 %	0.75 %	2.22 %	0.67 %
^{242}Cm	0.9949	0.9922	3.85 %	0.95 %	5.40 %	0.94 %
^{243}Cm	0.9963	0.9958	13.08 %	1.94 %	5.76 %	1.63 %
^{244}Cm	0.9988	0.9986	8.76 %	1.87 %	5.62 %	1.50 %
^{245}Cm	0.9977	0.9962	48.53 %	5.23 %	14.38 %	3.22 %
^{246}Cm	0.9872	0.9869	512.13 %	27.75 %	37.41 %	8.49 %

Table 3.27: Quality indexes of low burnup PWR MOX actinides polynomial surrogate model

3.1.3.1.5.6 PWR MOX fuel, nominal burnup

This surrogate model is aimed at the description of PWR MOX fuel irradiated at nominal burnup or higher. While its validity domain is smaller than the model described on section 3.1.3.1.5.5, it is more frequently used as the nominal PWR MOX irradiation model, therefore its precision is expected to be higher.

The validity domain of this surrogate model is the same as described in appendix A.1.5 page 288. The sample size is 500, LHS is used as the sampling method.

Table 3.28 summarizes the global quality of the estimators. Figure B.5 page 308 represents the identity card of an estimator (^{241}Am) among the others.

actinide	r^2	q^2	$max\|\hat{y}/y-1\|$	$mean\|\hat{y}/y-1\|$	$max\|(\hat{y}-y)/\bar{y}\|$	$mean\|(\hat{y}-y)/\bar{y}\|$
^{234}U	0.9992	0.9990	1.83 %	0.40 %	1.86 %	0.40 %
^{235}U	1.0000	1.0000	2.64 %	0.39 %	0.76 %	0.23 %
^{236}U	1.0000	1.0000	3.60 %	0.40 %	1.04 %	0.23 %
^{238}U	0.9999	0.9999	0.01 %	0.00 %	0.01 %	0.00 %
^{237}Np	0.9996	0.9995	2.02 %	0.36 %	1.39 %	0.32 %
^{239}Np	0.9996	0.9994	0.61 %	0.17 %	0.66 %	0.17 %
^{238}Pu	0.9993	0.9994	0.90 %	0.26 %	1.00 %	0.27 %
^{239}Pu	0.9997	0.9995	1.14 %	0.19 %	0.92 %	0.18 %
^{240}Pu	0.9976	0.9973	0.82 %	0.25 %	0.83 %	0.25 %
^{241}Pu	0.9982	0.9974	0.68 %	0.17 %	0.70 %	0.17 %
^{242}Pu	0.9995	0.9992	1.03 %	0.27 %	0.90 %	0.26 %
^{241}Am	0.9978	0.9968	1.66 %	0.53 %	1.88 %	0.52 %
^{242M}Am	0.9981	0.9977	1.99 %	0.49 %	1.77 %	0.48 %
^{243}Am	0.9986	0.9984	1.12 %	0.34 %	1.22 %	0.34 %
^{242}Cm	0.9988	0.9982	1.07 %	0.27 %	1.19 %	0.28 %
^{243}Cm	0.9976	0.9966	3.20 %	0.68 %	3.22 %	0.67 %
^{244}Cm	0.9967	0.9943	5.32 %	0.80 %	3.89 %	0.79 %
^{245}Cm	0.9936	0.9899	5.51 %	1.30 %	5.54 %	1.29 %
^{246}Cm	0.9844	0.9813	11.28 %	3.08 %	14.00 %	2.96 %

Table 3.28: Quality indexes of high burnup PWR MOX actinides polynomial surrogate model

3.1.3.1.5.7 SFR MOX fuel, less than nominal burnup

This surrogate model is adapted to the description of a wide range of SFR MOX fuel, irradiated at a less than nominal burnup. It is used to describe starting and shutdown batches. The parameters sampling is described in appendix A.1.6. Parameters are sampled without correlations except the irradiation length and ^{238}U mass fraction which are calculated a posteriori. The sample size is 1000, LHS is used as the sampling method. Table 3.29 summarizes the global quality of the estimators. Figure B.6 page 309 represents the identity card of an estimator (^{239}Pu) among the others.

actinide	r^2	q^2	$max\|\hat{y}/y-1\|$	$mean\|\hat{y}/y-1\|$	$max\|(\hat{y}-y)/\bar{y}\|$	$mean\|(\hat{y}-y)/\bar{y}\|$
^{234}U	0.9995	0.9993	1.70 %	0.36 %	2.50 %	0.34 %
^{235}U	0.9999	0.9998	0.76 %	0.19 %	0.82 %	0.18 %
^{236}U	0.9999	0.9999	0.41 %	0.06 %	0.47 %	0.06 %
^{238}U	0.9999	0.9998	0.14 %	0.03 %	0.13 %	0.03 %
^{237}Np	0.9998	0.9998	2.55 %	0.43 %	1.34 %	0.37 %
^{239}Np	0.9976	0.9968	0.99 %	0.24 %	1.03 %	0.24 %
^{238}Pu	0.9998	0.9996	6.07 %	0.82 %	3.22 %	0.57 %
^{239}Pu	0.9997	0.9997	0.30 %	0.08 %	0.29 %	0.08 %
^{240}Pu	1.0000	0.9999	0.45 %	0.06 %	0.39 %	0.06 %
^{241}Pu	0.9997	0.9996	1.22 %	0.27 %	0.94 %	0.27 %
^{242}Pu	1.0000	1.0000	0.97 %	0.20 %	0.72 %	0.18 %
^{241}Am	0.9995	0.9990	2.49 %	0.49 %	2.70 %	0.49 %
^{242M}Am	0.9996	0.9995	2.73 %	0.75 %	2.52 %	0.67 %
^{243}Am	0.9996	0.9995	5.52 %	1.06 %	3.23 %	0.89 %
^{242}Cm	0.9992	0.9983	3.42 %	0.76 %	3.17 %	0.76 %
^{243}Cm	0.9977	0.9968	28.44 %	2.66 %	8.51 %	2.04 %
^{244}Cm	0.9988	0.9975	19.43 %	3.27 %	14.24 %	2.56 %
^{245}Cm	0.9960	0.9919	260.89 %	16.53 %	35.67 %	6.74 %
^{246}Cm	0.9880	0.9837	878.47 %	55.86 %	67.24 %	11.63 %

Table 3.29: Quality indexes of low burnup SFR MOX actinides polynomial surrogate model

3.1.3.1.5.8 SFR MOX fuel, nominal burnup

This surrogate model is adapted to the description of SFR MOX fuel, irradiated at nominal burnup. The parameters sampling is described in appendix A.1.7 page 290. Parameters are sampled without correlations except the irradiation length and ^{238}U mass fraction which are calculated a posteriori. The sample size is 1000, LHS is used as the sampling method. Table 3.30 summarizes the global quality of the estimators.

It has to be noted that due to fabrication constraints (burnup is fixed for this estimator), this estimator is not suited to burnup uncertainty propagation.

actinide	r^2	q^2	$max\|\hat{y}/y-1\|$	$mean\|\hat{y}/y-1\|$	$max\|(\hat{y}-y)/\bar{y}\|$	$mean\|(\hat{y}-y)/\bar{y}\|$
^{234}U	1.0000	1.0000	0.31 %	0.06 %	0.26 %	0.06 %
^{235}U	1.0000	1.0000	0.16 %	0.04 %	0.15 %	0.04 %
^{236}U	1.0000	1.0000	0.07 %	0.02 %	0.06 %	0.02 %
^{238}U	1.0000	1.0000	0.02 %	0.00 %	0.02 %	0.00 %
^{237}Np	0.9997	0.9994	0.71 %	0.12 %	0.71 %	0.12 %
^{239}Np	0.9996	0.9994	0.67 %	0.12 %	0.56 %	0.12 %
^{238}Pu	1.0000	1.0000	1.47 %	0.13 %	0.34 %	0.07 %
^{239}Pu	1.0000	1.0000	0.10 %	0.02 %	0.11 %	0.02 %
^{240}Pu	1.0000	1.0000	0.09 %	0.02 %	0.08 %	0.02 %
^{241}Pu	1.0000	1.0000	0.84 %	0.14 %	0.49 %	0.13 %
^{242}Pu	1.0000	1.0000	0.63 %	0.07 %	0.27 %	0.05 %
^{241}Am	1.0000	1.0000	0.39 %	0.09 %	0.29 %	0.08 %
^{242M}Am	0.9995	0.9992	4.11 %	0.51 %	2.59 %	0.47 %
^{243}Am	0.9999	0.9998	3.92 %	0.54 %	1.65 %	0.39 %
^{242}Cm	0.9998	0.9996	2.89 %	0.34 %	1.80 %	0.33 %
^{243}Cm	0.9977	0.9972	6.85 %	1.07 %	4.82 %	1.01 %
^{244}Cm	0.9989	0.9986	6.85 %	1.36 %	4.09 %	1.11 %
^{245}Cm	0.9962	0.9952	15.72 %	2.43 %	11.86 %	2.09 %
^{246}Cm	0.9872	0.9869	29.92 %	4.84 %	14.99 %	3.87 %

Table 3.30: Quality indexes of high burnup SFR MOX actinides polynomial surrogate model

3.1.3.1.5.9 Summary and conclusions

Seven irradiation surrogate models for actinides, composed of 137 polynomial regressions were built using polynomial regressions. A lot of actinides are predicted with a satisfying accuracy around nominal burnup. Precision tends to decrease for lower burnup values, usually corresponding to starting, shutdown or transition batches.

Several actinides are difficult to predict. These actinides are produced through several radiative capture reactions and decays. Their behavior is highly non-linear in function of the burnup. Furthermore interaction effects usually occur, and are difficult to model with polynomials.

Polynomial regressions can be used in a first approach to perform sensitivity studies on scenario results, but they limit the field of the study. They are not suited to estimate accurately the uncertainty on curium inventories and to a lesser extent americium inventories, despite the importance of these results.

In the light of these results, we chose to develop another library of irradiation surrogate models more adapted to dealing with non-linearity, though still compatible with a relatively high number of parameters: estimators based on artificial neural networks.

Section 3.1.3.2 is dedicated to construction of irradiation surrogate models using artificial neural network estimators.

3.1.3.2 Artificial Neural Networks

3.1.3.2.1 Determination of the number of hidden neurons and the sample size

The following properties of neural networks justify their relevance in the case of the estimation of concentrations after irradiation. First, concerning the domain of definition of the neural networks [3.4]:

> Let $\phi(.)$ be a non constant, bounded and monotonically increasing continuous function. Let I_m denote the m-dimensional unit hypercube $[0,1]^m$. The space of continuous functions on I_m is denoted by $C(I_m)$. Then, given any function $f \in C(I_m)$ and $\varepsilon > 0$, there exist an integer N and real constants α_i, $b_i \in \mathbb{R}$, $w_i \in \mathbb{R}^m$, where $i = 1...N$ such that we may define:
>
> $$F(x) = \sum_{i=1}^{N} \alpha_i \phi\left(w_i^T x + b_i\right)$$
>
> as an approximate realization of the function f where f is independent of ϕ; that is,
>
> $$|F(x) - f(x)| < \varepsilon$$
>
> for all $x \in I_m$. It is equivalent to say that functions of the form $F(x)$ are dense in $C(I_m)$.

This property shows that it is possible to approximate any continuous function with *one-layer* neural networks, with no condition on the activation function (the case of sigmoid functions, used in this work, was previously demonstrated in [3.5]).

Then, concerning the structure of neural networks [3.6]:

> The error in the approximation of functions by artificial neural networks is bounded. For an artificial neural network with one layer of n sigmoidal nodes [*hidden neurons*], the integrated squared error of approximation, integrating on a bounded subset of d variables, is bounded by c'_f/n, where c'_f depends on a norm of the Fourier transform of the function being approximated. This rate of approximation is achieved under growth constraints on the magnitudes of the parameters of the network. (...). Because of the economy of number of parameters, order nd instead of n^d, these approximation rates permit satisfactory estimators of functions using artificial neural networks even in moderately high-dimensional problems.

This property is fundamental for neural networks, and is called principle of parsimony [3.7]. For a low number of parameters ANN are equivalent to linear estimators. However, in our case ($d > 40$) they clearly show their superiority to linear estimators (including polynomials, etc.).

Considering these two properties, we will build one-layer neural networks to estimate concentrations after irradiation.

There is no theorem nor general law that predicts accurately the optimal number of hidden neurons [3.7]. A lack of hidden neurons leads to a model unable to follow the tendency of a function, whereas an excess of hidden neurons over-fits the sample, and learns the points of the sample rather than the tendency. This problem is know under the denomination *bias-variance dilemma* or *bias-variance tradeoff*. Its optimal solution is to be found case by case through experimentation, although some rules are persistent, for instance:

- the number of points has to be much higher than the number of parameters;

- all other things remaining equal, the neural network with less hidden neurons will have better generalization properties.

The optimal size of the fabrication sample of a neural network is not simple to predict either, but the problem is different.

The prediction q^2 is well adapted to estimators, however it is not very convenient to compare different high-quality estimators.

Therefore we define another indicator of quality, equivalent prediction q_e, in equation 3.41. An estimator which $q_e = 1$ ($q^2 = 0.999$) is considered satisfying, an estimator which $q_e = 2$ ($q^2 = 0.9995$) is twice better, and only half as good if $q_e = 0.5$ ($q^2 = 0.998$).

$$q_e = \frac{1 - 0.999}{1 - q^2} \tag{3.41}$$

For a given nuclide, the precision of the estimator was evaluated for different combinations of fabrication sample size and number of hidden neurons. The precision in function of the sample size and the number of neurons are represented on two different scales on figures 3.23 and 3.24. The following tendencies are noted:

- for a given number of hidden neurons, the precision increases with size, however a saturation occurs systematically. Most of the information is learned, and it is not possible to bend the network anymore. The saturation occurs later for higher number of hidden neurons.
- for a small sample size (for instance less than 1000 points, to be compared to ∼40 parameters), a high number of hidden neurons give a worse result. Their construction does not respect the principle of parsimony. The prediction worsens faster for a high number of hidden neurons.
- for a large sample size, a higher number of neurons (within reasonable bounds) give better results.

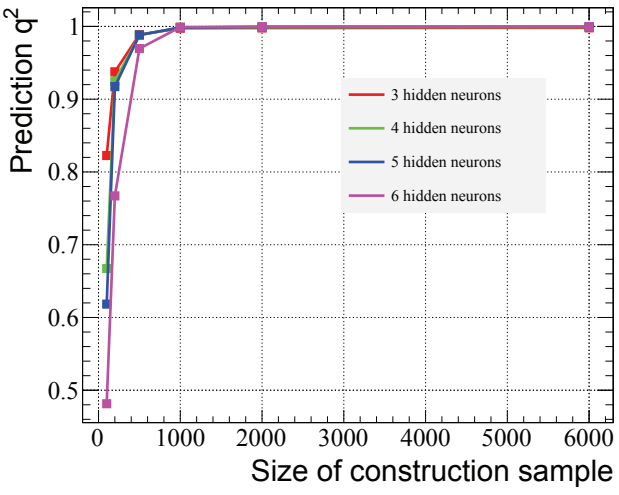

Figure 3.23: Prediction coefficient q^2 in function of hidden neurons and sample size

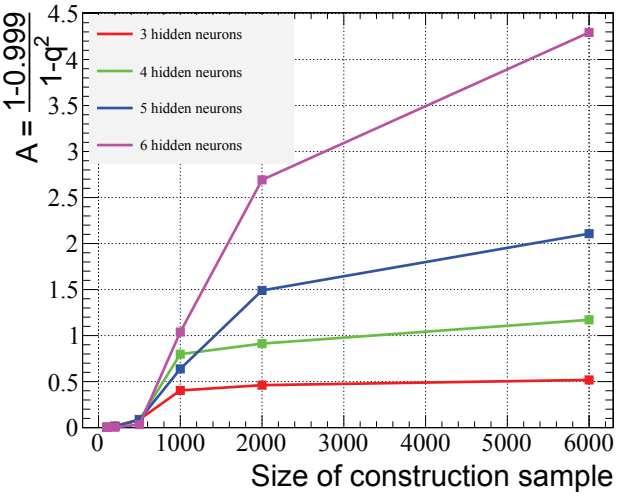

Figure 3.24: Equivalent prediction q_e in function of hidden neurons and sample size

3.1.3.2.2 Reduction of the parameters space

3.1.3.2.2.1 Introduction

In an one-layer ANN, each parameter is bound to n weights, n being the number of hidden neurons. So as to reduce the complexity of the ANN, it is necessary to reduce the number of parameters, eliminating:

- the parameters which have no influence on the output;
- the parameters linked to other parameters.

Furthermore, parameters without significant impact degrade the quality of the neural network adding degrees of freedom to the model, thus degrading the performance of ANN construction algorithms and the quality of ANN itself.

3.1.3.2.2.2 Correlated input parameters

In our case, the parameters of the neural networks are all physical parameters, which can be associated to a physical meaning. Therefore we will not proceed to methods dedicated to the analysis of input spaces such as PCA (Principle Components Analysis, conversion of possibly correlated values to a set of linearly uncorrelated variables, called principal components [3.8]), but rather to a physical analysis, *by hand*, of our input space.

a) Mass fractions
The construction of our design experiment, considering the mass fraction rather than the mass itself, adds a relation between our parameters:

$$\sum_{i=1}^{N} \frac{m_i}{m_{tot}} = 1 \tag{3.42}$$

Therefore one reduces the parameters space of the ANN by removing a parameter, for instance the initial mass fraction of ^{238}U, which is directly calculated from the mass fractions of the other parameters, and adds no information to the system.

b) Irradiation parameters
The irradiation length is strongly correlated with the burnup. Even though it was convenient to consider the irradiation length instead of the specific power as an input parameter in the case of the construction of multiple polynomial regressions, the use of this input could be detrimental to the quality of the neural network. Therefore specific power, which is not correlated with burnup in our sampling method, was used instead of irradiation length.

c) Other parameters
Cross-sections are sampled without taking correlations into account.

3.1.3.2.2.3 Parameters which have no influence

For a given nuclide which concentration after irradiation has to be predicted, several initial mass fractions do not contribute to the concentration. It is possible to estimate the influence of each initial mass fraction with sensitivity studies. However, the result of these studies is often trivial.

For instance, in the case of the prediction of ^{239}Pu in SFR MOX fuel, the impact of initial ^{234}U mass fraction is negligible. Therefore this mass fraction was not taken into account in this case.

This brief analysis was performed for every type of fuel and several initial mass fractions were removed accordingly from the set of parameters.

3.1.3.2.2.4 Final parameters space

According to considerations of 3.1.3.2.2.2 and 3.1.3.2.2.3, the subset of uncorrelated parameters taken into account for the estimation of actinides concentrations using neural networks is as follows, i the actinides present in substantial concentration before irradiation, and j the actinides which cross-section perturbation is taken into account:

$$parameters = \left\{ \frac{m_i}{m}, \text{BU}, \mathcal{P}_{irrad}, \frac{\Delta\sigma_j}{\sigma_j} \right\} \tag{3.43}$$

3.1.3.2.3 Algorithmic

URANIE is able to build artificial neural networks based regressions given the following elements:

- an initial set S_0 of parameters $\{p_i\}$
- a function to model y
- a design of experiment Γ containing the values of $\{p_i\}$ and y
- the number of neurons in the hidden layer
- an activation function (the logistic function is often used)
- the number of iterations N_{ite} and initializations N_{ini} per iteration
- and an hyper-parameter, the function tolerance, used in Newton optimization algorithm trust region

The URANIE `TANNModeler` algorithm for the construction of one-layered artificial neural network is as follows:

- for($i = 0,\ i < N_{ite},\ i++$)
  - for($j = 0,\ j < N_{ini},\ j++$)
    - randomized generation of weights w_i
    - optimization of the cost function (error sum of squares + weight decay)
  - selection of the best network (among N_{ini}) on the construction sample
- selection of the best network (among N_{ite}) on a the test sample

We encapsulated this algorithm into a function optimizing the number of neurons in the hidden layer.

3.1.3.2.4 Application

3.1.3.2.4.1 Overview

The actinides estimators based on artificial neural networks were constructed according to the previous studies. For each fuel type and burnup range, a surrogate model was constructed as an array of ANN estimators.

The boundaries of the design of experiments have been extended comparatively to section 3.1.3.1.5. Indeed, given that the artificial neural networks tolerate interactions better than polynomial regressions, we chose to enlarge the following intervals of variation:

- cross-section perturbations: given that the distribution of a cross-section uncertainty is assumed Gaussian, we chose intervals such as the use of a Gaussian distribution was possible while performing uncertainty propagation with surrogate models. We chose to sample uniformly on rounded up intervals $I_i \approx [-3SD(\sigma_i), +3SD(\sigma_i)]$ for each cross-section σ_i, $SD(\sigma_i)$ being the relative uncertainty of the cross-section. Analysis of the Gaussian repartition function shows that the confidence level is 99.8% on this interval, which is satisfying. Therefore each cross-sections sampling interval is $\sqrt{3}$ times larger than the intervals for construction of polynomial regressions. This significantly complicates the construction of the regression, as shown on section 3.1.3.2.4.3.
- mass fractions: we chose to slightly extend several mass fractions intervals, so as to produce more generic surrogate models, which may be adapted to a wider range of scenario computations
- burnup: we slightly extended the intervals such as two surrogate of a same fuel type now overlap on a small domain. This was done in order to be more predictive in this domain.

The precision of each estimator was tested on a test base, different from the fabrication sample. We denote y the concentration after irradiation of a fission product, $\bar{y}$ the mean of y on the test sample and $\hat{y}$ the estimator of y calculated on the test sample. The following quality indexes are calculated on a test sample (with the exception of r^2, calculated on construction sample):

$$\begin{cases} r^2, q^2 & \text{variance propagation indicators} \\ max\,|\hat{y}/y - 1| & \text{maximum value of the relative error} \\ mean\,|\hat{y}/y - 1| & \text{mean value of the relative error} \\ max\,|(\hat{y} - y)/\bar{y}| & \text{maximum value of the absolute error compared to the mean} \\ mean\,|(\hat{y} - y)/\bar{y}| & \text{mean value of the absolute error compared to the mean} \end{cases} \tag{3.44}$$

3.1.3.2.4.2 Analysis of the quality of the estimators

Tables 3.31 to 3.37 shows the quality indexes for ANN-based surrogate models of actinides for every studied fuel type. The values exceeding 1000% are noted $+++$. These results provide good information to determine whether estimators are suited to perform uncertainty propagation, however it is wiser to also use graphs representing the estimators and the residuals. A few examples of these graphs are presented in section 3.1.3.2.4.3 and in appendix B.2.

Artificial neural networks return better results than polynomial regression. While their domain of validity is wider, their quality indexes, in particular $mean\,|(\hat{y} - y)/\bar{y}|$, are better.

3.1.3.2.4.3 Examples

Quality indexes, such as maximum relative error, mean error, etc. are useful to determine whether an estimator is satisfying, but not sufficient. It is generally advised to analyze the shape of the estimator and the residuals. This analysis was performed for every estimator. This step was automated, and *identity cards*, summarizing the most important and decisive information concerning the estimators were created at the same time as the estimators.

actinide	r^2	q^2	$max\|\hat{y}/y-1\|$	$mean\|\hat{y}/y-1\|$	$max\|(\hat{y}-y)/\bar{y}\|$	$mean\|(\hat{y}-y)/\bar{y}\|$
^{234}U	1.0000	1.0000	3.38 %	0.20 %	2.08 %	0.17 %
^{235}U	1.0000	1.0000	6.54 %	0.31 %	4.99 %	0.23 %
^{236}U	1.0000	1.0000	3.43 %	0.10 %	1.38 %	0.09 %
^{238}U	1.0000	1.0000	0.02 %	0.00 %	0.02 %	0.00 %
^{237}Np	1.0000	1.0000	6.83 %	0.17 %	1.34 %	0.13 %
^{239}Np	0.9999	0.9999	1.48 %	0.12 %	1.17 %	0.12 %
^{238}Pu	0.9998	0.9998	63.50 %	0.87 %	4.11 %	0.48 %
^{239}Pu	1.0000	0.9999	1.77 %	0.09 %	1.18 %	0.09 %
^{240}Pu	0.9999	0.9999	8.31 %	0.18 %	2.77 %	0.14 %
^{241}Pu	0.9999	0.9999	6.88 %	0.22 %	1.37 %	0.19 %
^{242}Pu	0.9998	0.9998	720.62 %	1.58 %	8.70 %	0.49 %
^{241}Am	0.9998	0.9998	28.79 %	0.54 %	3.28 %	0.36 %
^{242M}Am	0.9997	0.9997	$+++$ %	8.30 %	10.73 %	0.86 %
^{243}Am	0.9996	0.9995	5.52 %	1.06 %	3.23 %	0.89 %
^{242}Cm	0.9998	0.9998	$+++$ %	4.00 %	4.49 %	0.41 %
^{243}Cm	0.9997	0.9996	$+++$ %	6.89 %	24.30 %	0.93 %
^{244}Cm	0.9997	0.9995	$+++$ %	10.06 %	27.32 %	1.32 %
^{245}Cm	0.9985	0.9980	$+++$ %	31.18 %	42.89 %	3.00 %
^{246}Cm	0.9880	0.9837	$+++$ %	34.58 %	118.62 %	4.64 %

Table 3.31: Quality indexes of low burnup PWR UOX actinides ANN surrogate model

actinide	r^2	q^2	$max\|\hat{y}/y-1\|$	$mean\|\hat{y}/y-1\|$	$max\|(\hat{y}-y)/\bar{y}\|$	$mean\|(\hat{y}-y)/\bar{y}\|$
^{234}U	1.0000	1.0000	2.09%	0.20%	1.24%	0.16%
^{235}U	1.0000	1.0000	8.18%	0.20%	0.85%	0.13%
^{236}U	1.0000	1.0000	0.94%	0.06%	0.38%	0.05%
^{238}U	1.0000	1.0000	0.02%	0.00%	0.02%	0.00%
^{237}Np	0.9999	0.9999	1.28%	0.10%	1.37%	0.10%
^{239}Np	0.9999	0.9990	0.81%	0.10%	0.86%	0.10%
^{238}Pu	0.9999	0.9999	2.02%	0.25%	2.88%	0.24%
^{239}Pu	0.9999	0.9999	0.04%	0.06%	0.36%	0.06%
^{240}Pu	1.0000	0.9999	0.42%	0.07%	0.58%	0.07%
^{241}Pu	0.9998	0.9998	0.74%	0.12%	0.74%	0.12%
^{242}Pu	0.9999	0.9999	0.30%	0.34%	3.77%	0.33%
^{241}Am	0.9999	0.9999	1.64%	0.18%	2.29%	0.18%
^{242M}Am	0.9998	0.9998	2.93%	0.26%	2.02%	0.25%
^{243}Am	0.9998	0.9997	7.52%	0.66%	6.09%	0.58%
^{242}Cm	0.9999	0.9999	1.06%	0.18%	1.26%	0.18%
^{243}Cm	0.9999	0.9998	10.17%	0.50%	5.21%	0.44%
^{244}Cm	0.9997	0.9996	29.14%	1.19%	17.10%	0.94%
^{245}Cm	0.9993	0.9989	78.48%	2.32%	32.53%	1.57%
^{246}Cm	0.9987	0.9978	+++%	14.26%	71.84%	3.37%

Table 3.32: Quality indexes of high burnup PWR UOX actinides ANN surrogate model

actinide	r^2	q^2	$max\|\hat{y}/y-1\|$	$mean\|\hat{y}/y-1\|$	$max\|(\hat{y}-y)/\bar{y}\|$	$mean\|(\hat{y}-y)/\bar{y}\|$
^{234}U	0.9998	0.9998	2.59 %	0.22 %	1.79 %	0.22 %
^{235}U	1.0000	1.0000	7.40 %	0.26 %	3.73 %	0.18 %
^{236}U	0.9999	0.9999	12.66 %	0.48 %	5.65 %	0.35 %
^{238}U	1.0000	1.0000	0.04 %	0.00 %	0.04 %	0.00 %
^{237}Np	0.9985	0.9984	14.10 %	1.11 %	4.18 %	0.97 %
^{239}Np	0.9997	0.9997	1.24 %	0.16 %	1.17 %	0.16 %
^{238}Pu	0.9998	0.9997	3.60 %	0.21 %	2.36 %	0.21 %
^{239}Pu	0.9999	0.9999	0.76 %	0.13 %	1.24 %	0.13 %
^{240}Pu	0.9971	0.9968	1.05 %	0.11 %	1.03 %	0.11 %
^{241}Pu	0.9994	0.9993	1.50 %	0.16 %	1.30 %	0.16 %
^{242}Pu	0.9997	0.9997	3.32 %	0.21 %	3.39 %	0.20 %
^{241}Am	0.9946	0.9937	2.95 %	0.31 %	3.54 %	0.30 %
^{242M}Am	0.9994	0.9993	4.89 %	0.95 %	3.75 %	0.29 %
^{243}Am	0.9997	0.9996	10.82 %	0.46 %	6.09 %	0.42 %
^{242}Cm	0.9992	0.9989	7.92 %	0.30 %	4.37 %	0.30 %
^{243}Cm	0.9996	0.9995	40.40 %	0.77 %	7.09 %	0.65 %
^{244}Cm	0.9994	0.9993	357.94 %	1.32 %	9.30 %	0.85 %
^{245}Cm	0.9991	0.9990	$+++$ %	3.21 %	17.24 %	1.31 %
^{246}Cm	0.9983	0.9978	$+++$ %	12.82 %	34.91 %	2.93 %

Table 3.33: Quality indexes of low burnup PWR MOX actinides ANN surrogate model

actinide	r^2	q^2	$max\|\hat{y}/y-1\|$	$mean\|\hat{y}/y-1\|$	$max\|(\hat{y}-y)/\bar{y}\|$	$mean\|(\hat{y}-y)/\bar{y}\|$
^{234}U	0.9999	0.9999	1.19 %	0.16 %	1.04 %	0.16 %
^{235}U	1.0000	1.0000	3.72 %	0.21 %	1.29 %	0.15 %
^{236}U	1.0000	1.0000	4.50 %	0.33 %	1.64 %	0.25 %
^{238}U	0.9999	0.9999	0.02 %	0.01 %	0.02 %	0.01 %
^{237}Np	0.9987	0.9986	3.58 %	0.65 %	2.38 %	0.63 %
^{239}Np	0.9998	0.9998	0.84 %	0.14 %	0.83 %	0.14 %
^{238}Pu	0.9999	0.9999	1.14 %	0.15 %	0.88 %	0.15 %
^{239}Pu	0.9999	0.9999	0.54 %	0.08 %	0.47 %	0.08 %
^{240}Pu	0.9999	0.9999	0.55 %	0.08 %	0.54 %	0.08 %
^{241}Pu	0.9998	0.9997	0.60 %	0.09 %	0.57 %	0.09 %
^{242}Pu	0.9999	0.9999	1.00 %	0.15 %	0.94 %	0.15 %
^{241}Am	0.9997	0.9997	1.45 %	0.23 %	1.44 %	0.22 %
^{242M}Am	0.9997	0.9996	1.23 %	0.20 %	1.18 %	0.20 %
^{243}Am	0.9998	0.9997	2.14 %	0.30 %	2.29 %	0.29 %
^{242}Cm	0.9997	0.9996	1.01 %	0.14 %	1.18 %	0.14 %
^{243}Cm	0.9998	0.9998	5.27 %	0.39 %	3.60 %	0.37 %
^{244}Cm	0.9996	0.9995	4.09 %	0.48 %	3.57 %	0.47 %
^{245}Cm	0.9994	0.9992	9.87 %	0.81 %	5.92 %	0.76 %
^{246}Cm	0.9990	0.9988	116.75 %	2.11 %	13.70 %	1.56 %

Table 3.34: Quality indexes of high burnup PWR MOX actinides ANN surrogate model

actinide	r^2	q^2	$max\|\hat{y}/y-1\|$	$mean\|\hat{y}/y-1\|$	$max\|(\hat{y}-y)/\bar{y}\|$	$mean\|(\hat{y}-y)/\bar{y}\|$
^{234}U	1.0000	1.0000	54.43 %	0.53 %	2.13 %	0.15 %
^{235}U	1.0000	1.0000	0.68 %	0.10 %	1.43 %	0.09 %
^{236}U	1.0000	1.0000	0.79 %	0.04 %	0.57 %	0.04 %
^{238}U	1.0000	1.0000	0.02 %	0.00 %	0.02 %	0.00 %
^{237}Np	1.0000	0.9999	4.67 %	0.12 %	1.68 %	0.11 %
^{239}Np	0.9999	0.9999	0.95 %	0.10 %	0.84 %	0.10 %
^{238}Pu	0.9999	0.9999	47.49 %	0.34 %	2.45 %	0.24 %
^{239}Pu	0.9998	0.9997	1.40 %	0.11 %	0.96 %	0.10 %
^{240}Pu	0.9999	0.9999	7.26 %	0.16 %	2.11 %	0.14 %
^{241}Pu	0.9999	0.9999	15.41 %	0.20 %	3.44 %	0.16 %
^{242}Pu	0.9999	0.9999	814.11 %	1.01 %	2.78 %	0.31 %
^{241}Am	0.9999	0.9999	69.62 %	0.47 %	4.28 %	0.28 %
^{242M}Am	0.9999	0.9999	152.24 %	0.55 %	2.48 %	0.28 %
^{243}Am	0.9999	0.9999	$+++$ %	4.28 %	3.71 %	0.50 %
^{242}Cm	0.9999	0.9999	$+++$ %	4.00 %	4.97 %	0.35 %
^{243}Cm	0.9999	0.9998	$+++$ %	3.93 %	6.03 %	0.53 %
^{244}Cm	0.9996	0.9995	$+++$ %	9.77 %	13.19 %	1.11 %
^{245}Cm	0.9988	0.9986	$+++$ %	18.62 %	17.34 %	2.15 %
^{246}Cm	0.9980	0.9976	$+++$ %	23.39 %	42.97 %	3.55 %

Table 3.35: Quality indexes of PWR repU actinides ANN surrogate model

actinide	r^2	q^2	$max\|\hat{y}/y-1\|$	$mean\|\hat{y}/y-1\|$	$max\|(\hat{y}-y)/\bar{y}\|$	$mean\|(\hat{y}-y)/\bar{y}\|$
^{234}U	0.9998	0.9998	2.59 %	0.22 %	1.79 %	0.22 %
^{235}U	0.9999	0.9999	5.38 %	0.43 %	3.95 %	0.37 %
^{236}U	0.9999	0.9999	13.64 %	0.34 %	4.97 %	0.27 %
^{238}U	0.9999	0.9999	0.13 %	0.02 %	0.14 %	0.02 %
^{237}Np	0.9998	0.9997	17.57 %	0.31 %	3.76 %	0.26 %
^{239}Np	0.9996	0.9996	1.99 %	0.15 %	2.07 %	0.15 %
^{238}Pu	0.9999	0.9998	10.39 %	0.38 %	6.32 %	0.33 %
^{239}Pu	0.9999	0.9999	1.11 %	0.06 %	1.08 %	0.06 %
^{240}Pu	1.0000	0.9999	1.21 %	0.06 %	1.49 %	0.06 %
^{241}Pu	0.9998	0.9998	5.85 %	0.19 %	6.88 %	0.18 %
^{242}Pu	0.9999	0.9999	10.80 %	0.38 %	4.45 %	0.29 %
^{241}Am	0.9998	0.9997	25.77 %	0.34 %	8.31 %	0.31 %
^{242M}Am	0.9998	0.9997	$+++$ %	1.03 %	10.69 %	0.43 %
^{243}Am	0.9999	0.9998	649.50 %	0.84 %	5.60 %	0.48 %
^{242}Cm	0.9997	0.9993	95.12 %	0.51 %	17.53 %	0.40 %
^{243}Cm	0.9994	0.9992	569.96 %	2.14 %	18.65 %	1.01 %
^{244}Cm	0.9995	0.9994	$+++$ %	15.44 %	11.41 %	1.14 %
^{245}Cm	0.9984	0.9983	$+++$ %	18.42 %	26.24 %	2.31 %
^{246}Cm	0.9982	0.9975	$+++$ %	28.15 %	53.98 %	3.63 %

Table 3.36: Quality indexes of low burnup SFR actinides ANN surrogate model

actinide	r^2	q^2	$max\|\hat{y}/y-1\|$	$mean\|\hat{y}/y-1\|$	$max\|(\hat{y}-y)/\bar{y}\|$	$mean\|(\hat{y}-y)/\bar{y}\|$
^{234}U	0.9999	0.9999	1.66 %	0.20 %	1.06 %	0.19 %
^{235}U	0.9997	0.9996	3.31 %	0.67 %	1.93 %	0.58 %
^{236}U	0.9999	0.9999	1.71 %	0.28 %	1.33 %	0.25 %
^{238}U	0.9998	0.9997	0.13 %	0.02 %	0.13 %	0.02 %
^{237}Np	0.9996	0.9995	0.57 %	0.12 %	0.60 %	0.12 %
^{239}Np	0.9997	0.9997	0.79 %	0.12 %	0.79 %	0.12 %
^{238}Pu	0.9999	0.9998	4.18 %	0.40 %	2.15 %	0.35 %
^{239}Pu	0.9999	0.9999	0.29 %	0.05 %	0.30 %	0.05 %
^{240}Pu	0.9999	0.9999	0.48 %	0.08 %	0.43 %	0.07 %
^{241}Pu	1.0000	0.9999	0.65 %	0.09 %	0.70 %	0.08 %
^{242}Pu	1.0000	1.0000	1.97 %	0.22 %	1.52 %	0.19 %
^{241}Am	0.9999	0.9999	1.36 %	0.20 %	1.13 %	0.20 %
^{242M}Am	0.9999	0.9999	1.95 %	0.23 %	1.53 %	0.21 %
^{243}Am	0.9999	0.9998	4.67 %	0.54 %	2.46 %	0.44 %
^{242}Cm	0.9998	0.9998	2.33 %	0.28 %	1.71 %	0.27 %
^{243}Cm	0.9996	0.9994	7.15 %	0.86 %	5.81 %	0.78 %
^{244}Cm	0.9998	0.9997	22.78 %	0.87 %	6.96 %	0.68 %
^{245}Cm	0.9995	0.9994	18.51 %	1.49 %	7.52 %	1.13 %
^{246}Cm	0.9980	0.9976	$+++$ %	11.48 %	22.27 %	2.94 %

Table 3.37: Quality indexes of high burnup SFR actinides ANN surrogate model

Hundreds of identity cards were created and analyzed, in order to check and iteratively improve the quality of estimators. This section provides a few examples.

Other examples concerning ANN quality indexes are available in appendix B.2.

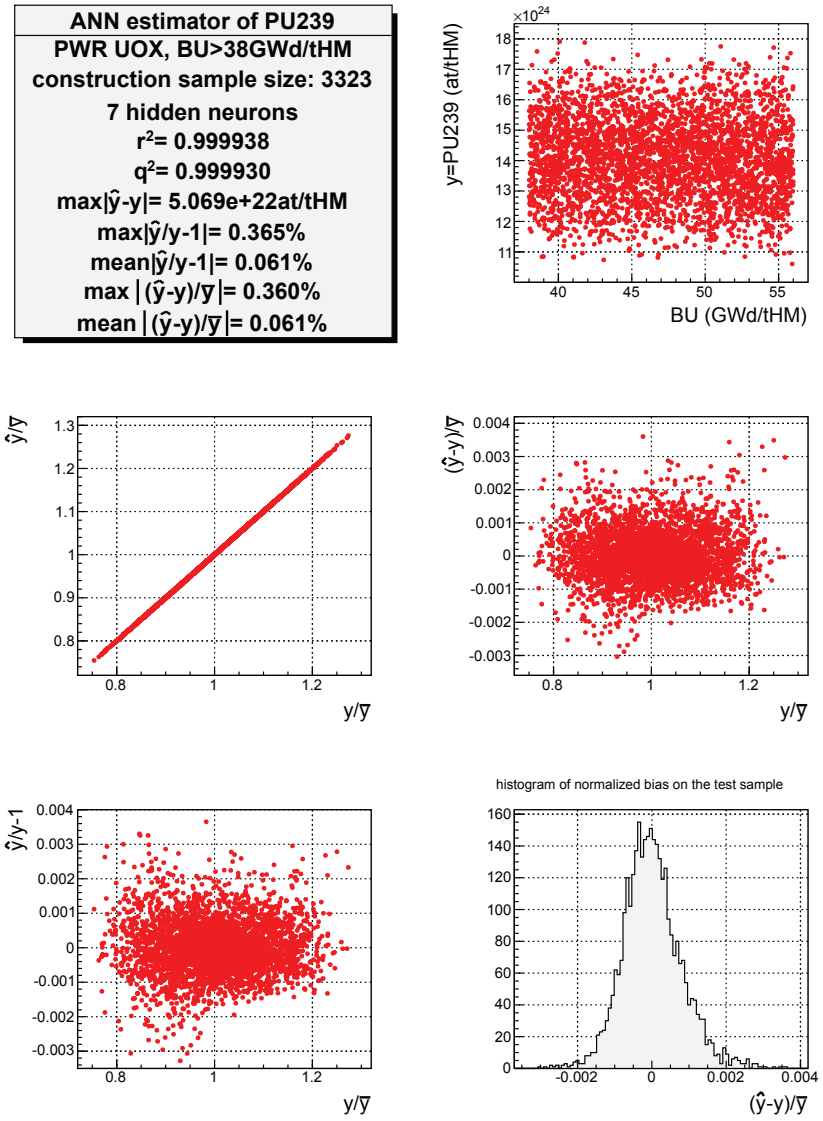

Figure 3.25: Identity card of the ^{239}Pu estimator in PWR UOX fuel, BU>38GWd/tHM

Figure 3.25 represents the identity card of ^{239}Pu in the case of PWR UOX fuel at nominal burnup or more. First of all, we can compare the evolution of ^{239}Pu in function of the burnup (top-right graph) on figures B.2 (page 305) and 3.25: dispersion of ^{239}Pu is much more important in this design of experiment than in the previous one, mainly because the change in cross-section perturbations sampling interval. The overall quality of the estimator is very satisfying: the relative and absolute error remain very low, and the prediction coefficient is high. The wideness of the domain of validity of this estimator is such as it can be used in order to propagate almost any uncertainty value of its parameters. In comparison, a polynomial estimator (39 monomials) constructed on this design of experiment has a prediction coefficient $q^2 = 0.918$ and a mean error $mean\left(\frac{\hat{y}-y}{\bar{y}}\right) = 17.37\%$.

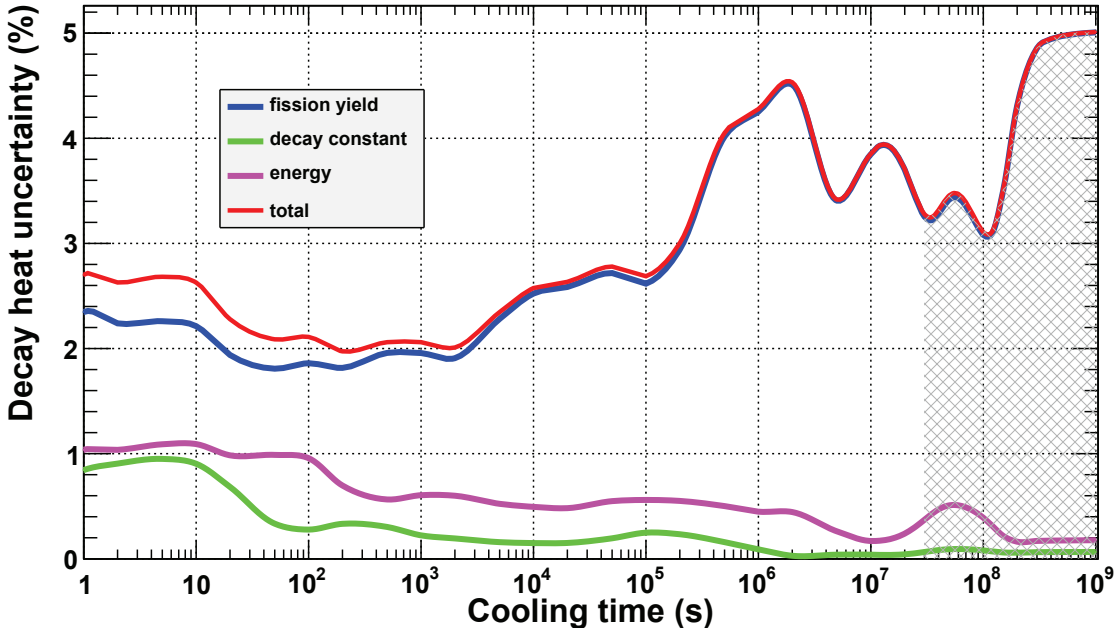

Figure 3.26: Decay heat uncertainty for an elementary ^{235}U fission

3.2 Irradiation models for fission products

3.2.1 Specifications

3.2.1.1 Fission products and decay heat

Fission products contribute to several scenario results in general, and decay heat in particular. This work is not aimed at describing the decay heat at short or relatively short times ($t << 1$ year) but rather calculating the decay heat in the context of fuel transportation and treatment ($t \geq 1$ year) and its associated uncertainty.

The contribution of the different uncertainty sources for an elementary fission of ^{235}U was studied in [3.9]. The data is represented on figure 3.26, correlation effects are not taken into account. The shaded zone ($t \geq 1$ year) represents the zone this work focuses on. It appears that fission yields are the main contributors to the total uncertainty.

A post-treatment of these data is shown on figure 3.27: for ($t \geq 1$ year), the fission yields uncertainty is responsible for more than 97.8% of the variance of the decay heat resulting from an elementary fission of ^{235}U.

The results are similar for the elementary fission of ^{239}Pu, and we assume the generalization of this result to most of fissile nuclides. Therefore, uncertainties on energy and decay constants will not be taken into account, and only fission yield uncertainty propagation will be calculated.

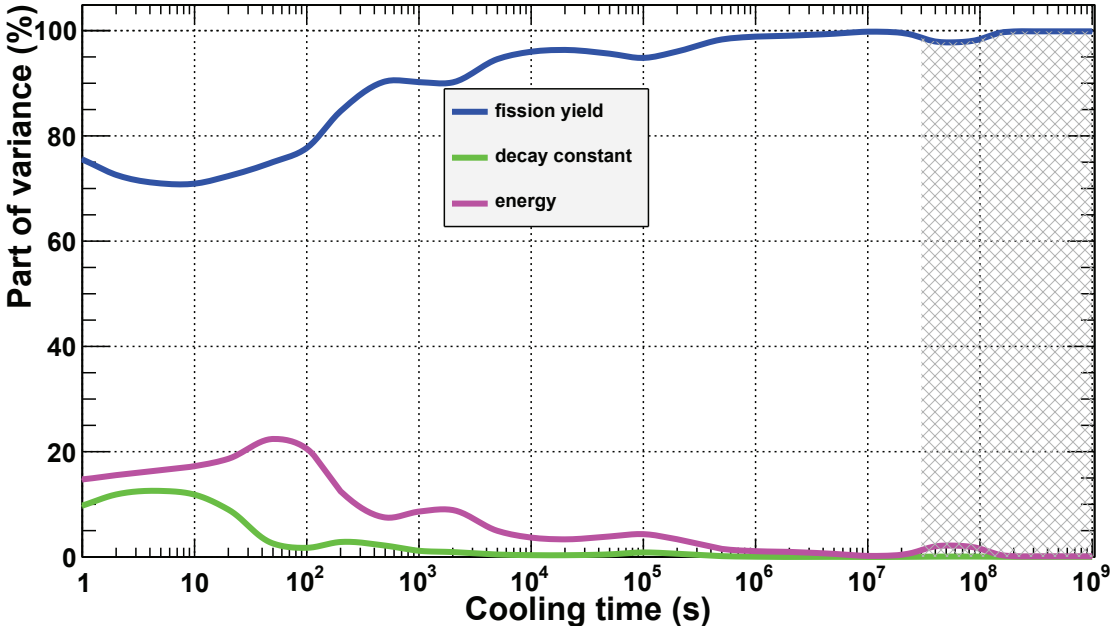

Figure 3.27: Decomposition of variance for an elementary ^{235}U fission

3.2.1.2 Fission products involved in decay heat uncertainty

The decay heat (DH) is calculated according to equation 3.45, as a sum of the system's compositions weighted by associated decay constants and energies.

$$DH(t) = \sum_{i \in \text{nuclides}} N_i(t) \times \lambda_i \times E_i \tag{3.45}$$

Therefore, so as to be able to estimate the decay heat of a system, it is necessary to know its composition, and especially the concentration of the most radioactive nuclides at a given time. [3.10] provides information concerning this problem:

- actinides contribute to less than 30% of decay heat up to $\sim 10^8$s for a wide range of fuel, including AGR, ^{233}U-^{232}Th LWR, PWR and LMFBR fuel [3.10];
- activation products have an extremely minor contribution to decay heat in the case of thermal reactors, but according to [3.10] ^{60}Co, formed through activation of nickel in steel structures, contributes up to 10% of the decay heat at 5 years cooling in SFR. Further work may study ^{60}Co concentration, for instance using DARWIN [3.11].
- the rest of decay heat comes from fission products.

The actinides and fission products contributing to decay heat have to be identified. A decay heat decomposition performed at CEA with DARWIN [3.12**?**] showed that taking into account a dozen of fission products allows a rather precise description of decay heat between 1 and 50 years in the case of PWR fuel. The following lists of nuclides are defined:

$$\texttt{List_FP} = \left\{^{85}\text{Kr}, ^{90}\text{Sr}, ^{90}\text{Y}, ^{95}\text{Zr}, ^{95}\text{Nb}, ^{106}\text{Rh}, ^{134}\text{Cs}, ^{137}\text{Cs}, ^{137M}\text{Ba}, ^{144}\text{Ce}, ^{144}\text{Pr}, ^{147}\text{Pm}, ^{154}\text{Eu}\right\}$$

$$\texttt{List_Actinides} = \left\{^{238}\text{Pu}, ^{239}\text{Pu}, ^{240}\text{Pu}, ^{241}\text{Pu}, ^{241}\text{Am}, ^{242}\text{Cm}, ^{243}\text{Cm}, ^{244}\text{Cm}\right\}$$

The proportion of decay heat due to the nuclides of `List_FP` and `List_Actinides` in the case of PWR UOX and PWR MOX fuel is shown in table 3.38, calculated in [3.12**?**].

cooling time	0.5y	1y	5y	10y	20y	30y	50y
% DH in PWR UOX	96.37	98.64	99.34	99.62	99.8	99.8	99.71
% DH in PWR MOX	96.52	98.62	99.11	99.47	99.65	99.62	99.53

Table 3.38: Percentage of decay heat calculated using `List_FP` and `List_Actinides`

Considering the nuclides contained in `List_FP` and `List_Actinides` allows calculating more than 98.6% of the decay heat after 1 year. Considering the minimum time of fuel cooling before treatment in a fuel cycle being generally between superior to 3 years and inferior to 10 years, this list permits being representative of most of the decay heat at times of interest. The combination of this result and those of figure 3.26 shows that at times of interest, approximately 99% of more than 99% of the uncertainty can be calculated using this shortened list.

In the case of SFR fuel, we do not have an equivalent list of the main contributors to decay heat. Hence we make an assumption: we assume that the contributors of decay heat in SFR fuel are approximately the same as in PWR UOX and MOX fuel. The fission/capture ratios are much higher in SFR fuel, therefore the proportion of actinides and fission products will be different. However, the list of fission products to be estimated is already quite large, plus the fission yields are not fundamentally different between a PWR and a SFR spectrum for most of the fission products of interest. Therefore we do not validate the hypothesis in this section, but the *a posteriori* analysis of the performance of the estimator of decay heat in part 3.2.4.4.7 determines that the results are valid.

3.2.1.3 Accuracy of the estimators

In scenario studies, the individual precision of fission products is usually not important as a direct result, therefore there is no point in giving a precision criterion for each fission product. However decay heat is a direct result: it impacts many domains of the fuel cycle, and fuel reprocessing in particular. Therefore the precision goal can be given in terms of decay heat estimation.

Decay heat is difficult to estimate fully using surrogate models. Indeed contribution to decay heat comes from many different sources. Calculating each of the decay heat sources accurately would significantly increase calculation time, whereas giving rough estimators may provide very large bias.

A compromise is to determine a given list of fission products which contribute to *most* of the decay heat, and estimate it as accurately as possible, within reasonable boundaries.

3.2.1.4 Fission products to estimate

The fission products of `list_FP` are involved in the decay chains presented in table 3.39.

Nuclide	Decay path taken into account
^{85}Kr	$^{85}\text{Kr} \xrightarrow[\beta-]{10.75y} {}^{85}\text{Rb}$ (stable)
^{90}Sr	$^{90}\text{Sr} \xrightarrow[\beta-]{18.74y} {}^{90}\text{Y} \xrightarrow[\beta-]{2.67d} {}^{90}\text{Zr}$ (stable)
^{95}Zr	$^{95}\text{Zr} \xrightarrow[\beta-]{64.03d} {}^{95}\text{Nb} \xrightarrow[IT]{34.99d} {}^{95}\text{Mo}$ (stable)
^{106}Ru	$^{106}\text{Ru} \xrightarrow[\beta-]{1.02y} {}^{106}\text{Rh} \xrightarrow[\beta-]{30.0s} {}^{106}\text{Pd}$ (stable)
^{134}Cs	$^{134}\text{Cs} \xrightarrow[\beta-]{2.06y} {}^{134}\text{Ba}$ (stable)
^{137}Cs	$^{137}\text{Cs} \xrightarrow[\beta-]{30.04y} {}^{137M}\text{Ba} \xrightarrow[IT]{2.55min} {}^{137}\text{Ba}$ (stable)
^{144}Ce	$^{144}\text{Ce} \xrightarrow[\beta-]{285.0d} {}^{144}\text{Pr} \xrightarrow[\beta-]{17.28min} {}^{144}\text{Nd}$ ($\sim$ stable)
^{147}Pm	$^{147}\text{Pm} \xrightarrow[\beta-]{2.62y} {}^{147}\text{Sm}$ (stable)
^{154}Eu	$^{154}\text{Eu} \xrightarrow[\beta-]{8.59y} {}^{154}\text{Gd}$ (stable)

Table 3.39: Fission products taken into account and associated decay paths

Some of the fission products listed above, which are involved in decay heat uncertainty, have very short half-lives. This is for instance the case of ^{90}Y, which is responsible for a substantial part of decay heat ($\sim$17% at 5 years in PWR UOX fuel). Given that:

- $T_{1/2}\left(^{90}\text{Y}\right) = 2.67d$
- $T_{1/2}\left(^{90}\text{Sr} \rightarrow {}^{90}\text{Y}\right) = 18.74y$
- at the end of irradiation, $C\left(^{90}\text{Y}\right) \ll C\left(^{90}\text{Sr}\right)$

It appears that most of the ^{90}Y mass fraction in the fuel after a few years of cooling comes from the progressive decay of ^{90}Sr, not from the initial mass of ^{90}Y.

So as to generalize this result, and determine which fission product concentration at a time t is dependent on its concentration before cooling, it is possible to calculate the sensitivity of a fission product concentration to its own concentration immediately after irradiation. The following development is based on the decay chain of equation 3.46.

$$A \xrightarrow{\lambda_A} B \xrightarrow{\lambda_B} C \tag{3.46}$$

For initial concentrations after irradiation A_0 and B_0, the solution of Bateman equation for $B(t)$ is as follows (in our case, $\lambda_A \neq \lambda_B$):

$$B(t) = B_0 e^{-\lambda_B t} + A_0 \frac{\lambda_A}{\lambda_B - \lambda_A}\left(e^{-\lambda_A t} - e^{-\lambda_B t}\right) \tag{3.47}$$

Therefore the sensitivity of $B(t)$ to its initial concentration is expressed as follows:

$$\frac{B_0}{B(t)}\frac{\partial B(t)}{\partial B_0} = \frac{1}{1 - \frac{A_0}{B_0}\frac{\lambda_A}{\lambda_B - \lambda_A}\left[1 - e^{(\lambda_B - \lambda_A)t}\right]} \tag{3.48}$$

The numerical application of 3.48 performed for average initial concentrations A_0 and B_0 after

irradiation, for a PWR UOX fuel irradiated at 46GWd/tHM for given cooling time values, is shown on table 3.40.

cooling time	0.1y	0.5y	1y	2y	3y	5y	10y	t $\gg$ 10y
^{90}Y	9.49%	1.70%	0.66%	0.19%	0.07%	0.01%	0.00%	0.00%
^{95}Nb	53.95%	9.88%	1.75%	0.07%	0.00%	0.00%	0.00%	0.00%
^{106}Rh	0.00%	0.00%	0.00%	0.00%	0.00%	0.00%	0.00%	0.00%
^{137M}Ba	0.00%	0.00%	0.00%	0.00%	0.00%	0.00%	0.00%	0.00%
^{144}Pr	0.00%	0.00%	0.00%	0.00%	0.00%	0.00%	0.00%	0.00%

Table 3.40: Sensitivity of fission product concentration to its initial concentration

We can conclude that for the characteristic times of fuel reprocessing ($t \geq 1y$) it is not necessary to take into account the initial concentrations of ^{90}Y, ^{95}Nb, ^{137M}Ba, ^{106}Rh and ^{144}Pr.

We assume that this result extends to PWR MOX and SFR MOX fuel. We do not perform numerical application for these types of fuel, however results shown in section 3.2.4.4 validate the predictiveness of the model.

Finally, the definitive list of isotopes which concentration has to be estimated at the end of irradiation is as follows:

$$\texttt{list_FP_estimators} = \left\{^{85}\text{Kr}, ^{90}\text{Sr}, ^{95}\text{Zr}, ^{106}\text{Ru}, ^{134}\text{Cs}, ^{137}\text{Cs}, ^{144}\text{Ce}, ^{147}\text{Pm}, ^{154}\text{Eu}\right\}$$

The knowledge of the concentration of isotopes in `list_FP_estimators` immediately after irradiation (t_0) is sufficient to determine accurately the concentration of every isotope of `list_FP` at $t_0 + \Delta t$ with $\Delta t \geq 1y$, and therefore the decay heat at that time. Consequently estimators of `list_FP_estimators` are sufficient to describe the decay heat at $t_0 + \Delta t$, and other isotopes will not be estimated.

3.2.2 Sampling

3.2.2.1 Parameters

3.2.2.1.1 Introduction

The sampling process for prediction of decay heat is based on the same principles as the sampling of actinides concentration estimators using ANN surrogate models (section 3.1.3.2). Results for sampling of burnup, load factor, mass fractions, etc. are still valid. The aim of this section is to produce a sample which we will use to build ANN surrogate models for fission products of interest.

3.2.2.1.2 Description of fuel assembly and irradiation parameters

Description of the fuel assembly is the same as described in part 3.1.2.1.2. The irradiation parameters are the same as described in part 3.1.2.1.3. Burnup sampling tweaks (division of the DOE and exponential sampling) are applied given the high dependence of artificial networks towards the design of experiments.

3.2.2.1.3 Fission yields

3.2.2.1.3.1 Introduction

A fission yield is called *independent* when it takes into account the number of atoms formed directly in fission, and *cumulative* when it takes into account the atoms that accumulate from fission, decay of precursors and delayed-neutron emission (but not from neutron reactions on fission products) [3.10].

For the rest of this work, we will denote *CY* the cumulative yields and *IY* the independent yields.

In some cases, the number of atoms of a fission product depends both on independent and cumulative fission products. For instance, in the case of ^{154}Eu, the number of atoms depends on the cumulative fission yields of its indirect precursors, ^{152}Sm and ^{153}Sm, the independent fission yield of its direct precursor ^{153}Eu, as well as its own independent fission yields. Let X be the sum of the fissile nuclides in the system, then we have:

$$\begin{aligned} N(^{154}\mathrm{Eu}) &= N(X \xrightarrow{cumulative} {}^{151}\mathrm{Pm} \xrightarrow{\beta-} {}^{151}\mathrm{Sm} \xrightarrow{(n,\gamma)} {}^{152}\mathrm{Sm} \xrightarrow{(n,\gamma)} {}^{153}\mathrm{Sm} \xrightarrow{\beta-} {}^{153}\mathrm{Eu} \xrightarrow{(n,\gamma)} {}^{154}\mathrm{Eu}) \quad (a) \\ &+ N(X \xrightarrow{cumulative} {}^{152}\mathrm{Sm} \xrightarrow{(n,\gamma)} {}^{153}\mathrm{Sm} \xrightarrow{\beta-} {}^{153}\mathrm{Eu} \xrightarrow{(n,\gamma)} {}^{154}\mathrm{Eu}) \quad (b) \\ &+ N(X \xrightarrow{cumulative} {}^{153}\mathrm{Sm} \xrightarrow{\beta-} {}^{153}\mathrm{Eu} \xrightarrow{(n,\gamma)} {}^{154}\mathrm{Eu}) \quad (c) \\ &+ N(X \xrightarrow{independent} {}^{153}\mathrm{Eu} \xrightarrow{(n,\gamma)} {}^{154}\mathrm{Eu}) \quad (d) \\ &+ N(X \xrightarrow{independent} {}^{154}\mathrm{Eu}) \quad (e) \end{aligned} \tag{3.49}$$

The different pathways are not equal contributors to the concentration after irradiation of a given fission product. For instance, in the case of SFR MOX fuel, an analysis made with CESAR showed that the path (a) produces 3.8% of the total concentration, the path (b) 10%, the path (c) more than 86%, whereas paths (d) and (e) produce very small amounts of ^{154}Eu. Determination of a complete list of fission yields to take into account in order to be representative of the total amount of each fission product of `list_FP_estimators` is shown on section 3.2.2.1.3.2.

3.2.2.1.3.2 Fission yields taken into account

Only the yields resulting from the fission of ^{235}U, ^{238}U, ^{238}Pu, ^{239}Pu, ^{240}Pu, ^{241}Pu and ^{242}Pu are taken into account, given that they represent a large percentage of all fission reactions in PWR UOX, PWR repU, PWR MOX and SFR MOX fuel. Analysis with CESAR on several fission products shows that this usually represents more than 99% of the production of those isotopes. Other actinides (mostly ^{241}Am and ^{242M}Am) are not neglected (their fission yields are taken into account), but the uncertainty associated to their fission yields will not be propagated in this work.

As shown in equation 3.49, taking into account the impact of the fission products contributing to decay heat is not enough: a study of the pathways leading to those nuclides has to be made, in order to answer the question: *which fission yields have an important sensitivity on a given fission product?* This study was performed in the case of SFR MOX fuel irradiated at 116GWd/tHM using CESAR5.3 (using JEFF-3.1.1 data) and computing the one-at-a-time sensitivity effect of many fission yields, in order to be representative of most of the fission product mass.

Results for isotopes of `list_FP_estimators` are shown in table 3.41 to 3.49, we call *importance* the percentage of a given fission product produced from a given chain head. The sensitivity of the fission products concentrations to the other fission yields is weak, and we will assume, during this study, that the associated uncertainty scarcely propagates toward concentrations after irradiation and therefore decay heat. Further work may contradict this statement.

Each table is associated to an equation summarizing the formation of the fission product studied.

$$\begin{aligned} N(^{85}\mathrm{Kr}) &= N(Y \xrightarrow{cumulative} {}^{84}\mathrm{Kr} \xrightarrow{(n,\gamma)} {}^{85}\mathrm{Kr}) \\ &+ N(Z \xrightarrow{cumulative} {}^{85}\mathrm{Kr}) \end{aligned}$$

chain head	importance
^{84}Kr (CY)	6.40%
^{85}Kr (CY)	93.47%
sum	99.87%

Table 3.41: Importance of different fission yields for production of ^{85}Kr

$$N(^{90}\mathrm{Sr}) = N(Z \xrightarrow{cumulative} {}^{90}\mathrm{Sr})$$

chain head	importance
^{90}Sr (CY)	99.98%
sum	99.98 %

Table 3.42: Importance of different fission yields for production of ^{90}Sr

$$N(^{95}\mathrm{Zr}) = N(Z \xrightarrow{cumulative} {}^{95}\mathrm{Zr})$$

chain head	importance
^{95}Zr (CY)	99.02%
sum	99.02%

Table 3.43: Importance of different fission yields for production of ^{95}Zr

$$N(^{106}\mathrm{Ru}) = N(Z \xrightarrow{cumulative} {}^{106}\mathrm{Ru})$$

chain head	importance
^{106}Ru (CY)	100.00%
sum	100.00%

Table 3.44: Importance of different fission yields for production of ^{106}Ru

$$\begin{aligned} N(^{134}\mathrm{Cs}) &= N(X \xrightarrow{cumulative} {}^{133}\mathrm{I} \xrightarrow{\beta-} {}^{133}\mathrm{Xe} \xrightarrow{\beta-} {}^{133}\mathrm{Cs} \xrightarrow{(n,\gamma)} {}^{134}\mathrm{Cs}) \\ &+ N(X \xrightarrow{cumulative} {}^{134}\mathrm{Cs}) \end{aligned}$$

chain head	importance
^{133}I (CY)	98.70%
^{134}Cs (IY)	0.10%
sum	98.80%

Table 3.45: Importance of different fission yields for production of ^{134}Cs

$$N(^{137}\mathrm{Cs}) = N(Z \xrightarrow{cumulative} {}^{137}\mathrm{Cs})$$

chain head	importance
^{137}Cs (CY)	100.00%
sum	100.00%

Table 3.46: Importance of different fission yields for production of ^{137}Cs

$$N(^{144}\mathrm{Ce}) = N(Z \xrightarrow{cumulative} {}^{144}\mathrm{Ce})$$

chain head	importance
^{144}Ce (CY)	100.00%
sum	100.00%

Table 3.47: Importance of different fission yields for production of ^{144}Ce

$$\begin{aligned} N(^{147}\mathrm{Pm}) &= N(Z \xrightarrow{cumulative} {}^{146}\mathrm{Nd} \xrightarrow{(n,\gamma)} {}^{147}\mathrm{Nd} \xrightarrow{\beta-} {}^{147}\mathrm{Pm}) \\ &+ N(Z \xrightarrow{cumulative} {}^{147}\mathrm{Nd} \xrightarrow{\beta-} {}^{147}\mathrm{Pm}) \end{aligned}$$

chain head	importance
^{146}Nd (CY)	4.85%
^{147}Nd (CY)	94.61%
sum	99.46%

Table 3.48: Importance of different fission yields for production of ^{147}Pm

$$
\begin{aligned}
N(^{154}\mathrm{Eu}) &= N(X \xrightarrow{cumulative} {}^{151}\mathrm{Pm} \xrightarrow{\beta-} {}^{151}\mathrm{Sm} \xrightarrow{(n,\gamma)} {}^{152}\mathrm{Sm} \xrightarrow{(n,\gamma)} {}^{153}\mathrm{Sm} \xrightarrow{\beta-} {}^{153}\mathrm{Eu} \xrightarrow{(n,\gamma)} {}^{154}\mathrm{Eu}) \\
&+ N(X \xrightarrow{cumulative} {}^{152}\mathrm{Sm} \xrightarrow{(n,\gamma)} {}^{153}\mathrm{Sm} \xrightarrow{\beta-} {}^{153}\mathrm{Eu} \xrightarrow{(n,\gamma)} {}^{154}\mathrm{Eu}) \\
&+ N(X \xrightarrow{cumulative} {}^{153}\mathrm{Sm} \xrightarrow{\beta-} {}^{153}\mathrm{Eu} \xrightarrow{(n,\gamma)} {}^{154}\mathrm{Eu}) \\
&+ N(X \xrightarrow{independent} {}^{153}\mathrm{Eu} \xrightarrow{(n,\gamma)} {}^{154}\mathrm{Eu}) \\
&+ N(X \xrightarrow{independent} {}^{154}\mathrm{Eu})
\end{aligned}
$$

chain head	importance
^{151}Pm (CY)	3.80%
^{152}Sm (CY)	10.01%
^{153}Sm (CY)	86.01%
sum	99.82 %

Table 3.49: Importance of different fission yields for production of ^{154}Eu

Consequently we can determine the list of fission yields to be taken into account in order to perform uncertainty propagation of fission yield uncertainty. The list is shown in table 3.50, with:

$$x = \{^{235}\mathrm{U}, ^{238}\mathrm{U}, ^{238}\mathrm{Pu}, ^{239}\mathrm{Pu}, ^{240}\mathrm{Pu}, ^{241}\mathrm{Pu}, ^{242}\mathrm{Pu}\} \tag{3.50}$$

Fission yield	Type
$x \rightarrow {}^{84}$Kr	cumulative
$x \rightarrow {}^{85}$Kr	cumulative
$x \rightarrow {}^{90}$Sr	cumulative
$x \rightarrow {}^{95}$Zr	cumulative
$x \rightarrow {}^{106}$Ru	cumulative
$x \rightarrow {}^{133}$I	cumulative
$x \rightarrow {}^{132}$Te	cumulative
$x \rightarrow {}^{137}$Cs	cumulative
$x \rightarrow {}^{144}$Ce	cumulative
$x \rightarrow {}^{146}$Nd	cumulative
$x \rightarrow {}^{147}$Nd	cumulative
$x \rightarrow {}^{151}$Pm	cumulative
$x \rightarrow {}^{152}$Sm	cumulative
$x \rightarrow {}^{153}$Sm	cumulative

Table 3.50: Chain heads taken into account during the sampling process

Numeric values of fission yields at the thermal point and 400keV are available online for several nuclear data evaluations (http://www.oecd-nea.org/janis/), including JEFF-3.1.1. Given that fission yields are very similar at the thermal point and at 400keV (the relative difference is usually inferior to a few percents), we consider these results still valid for PWR spectra.

Consequently the dimension of the parameters space of the sampled fission yields is equal to:

$$\begin{aligned} dim(\text{FY param. space}) &= card(\{\text{fissile actinides}\}) \times card(\{\text{chain heads}\}) \\ &= 7 \times 14 \\ &= 94 \end{aligned} \tag{3.51}$$

3.2.2.1.3.3 Sampling process

The sampling process of the fission yields is debatable. The system does not have as many degrees of freedom as there are fission yields, because of conservation laws. For the fission of a given amount of nuclides, ${}^{A_i}_{Z_i}X_i \xrightarrow{y_{i,j}} {}^{A_{i,j}}_{Z_{i,j}}Y_{i,j}$, the conservation laws are as follows:

1. conservation of the number of fission products: $\forall i \sum_j y_{i,j} = 2$ (neglecting ternary fission);
2. conservation of the mass: $\sum_{i,j} A_{i,j} = \sum_i A_i$;
3. conservation of the nuclear charge: $\sum_{i,j} Z_{i,j} = \sum_i Z_i$;
4. complementarity: for an individual fission of i, $\sum_j Z_{i,j} = Z_i$.

Sampling the fission yields according to these constraints is a difficult task, and was not performed for this work. Two sampling methods were tested and compared. Method A considers conservation law number 1; method B considers no conservation law.

The fission yields are sampled according to the following way:

1. *Methods A, B*: fission yields perturbation f_i are sampled uniformly in $[-3\text{SD}; +3\text{SD}]$ intervals, SD being the standard deviation of the fission yield[7]. These intervals correspond to the 99.% confidence interval for normal distributions. The average value is obtained by an average of fission yields for thermal and fast neutrons weighted by the fission rates of a thermal spectrum or a fast spectrum, according to the fuel type: $\eta_i^0 = \frac{\tau_{th}}{\tau_{th}+\tau_{fast}} \times \eta_i^{th} + \frac{\tau_{fast}}{\tau_{th}+\tau_{fast}} \times \eta_i^{fast}$. This work utilizes JEFF-3.1.1 fission yield data, available at http://www.oecd-nea.org/janis/. Large intervals are considered because during the calculation of uncertainty propagation, normal or log-normal distributions will be used.
2. *Methods A, B*: perturbed fission yields are calculated by $\eta_i = \eta_i^0 \times f_i$
3. *Method A only*: fission yields are re-normalized according to: $\forall i \sum_j y_{i,j} = 2$. They are calculated as follows: $\tilde{\eta}_i = \eta_i \times \frac{\sum_{j \in fissile\ nuclide} \eta_j^0}{\sum_{j \in fissile\ nuclide} \eta_j}$, and re-normalized perturbation are calculated by: $\tilde{f}_i = \frac{\eta_j}{\eta_j^0} \times \frac{\sum_{j \in fissile\ nuclide} \eta_j^0}{\sum_{j \in fissile\ nuclide} \eta_j}$

It is possible to analyze the impact of the method on the sample by representing the correlation matrices of several input factors. For instance, table 3.51 represents the *a posteriori* correlation between the perturbation of different fission yields leading to the same fission product, ^{90}Sr.

It appears that the perturbations of fission yields coming from different nuclides are merely correlated. The correlations between the different terms are very low and are not stable from a sampling generation to another. This result comes from the dissociation of the four different renormalization conditions (one per main fissile).

Table 3.52 represents the *a posteriori* correlation between $\tilde{f}$ perturbation factors for ^{235}U obtained after application of the sampling method in a PWR spectrum. For instance, it shows that

[7] In the case of $\sigma > 33\%$, we sampled on the uniform intervals $[-100\%; +100\%]$

x	^{235}U	^{238}U	^{238}Pu	^{239}Pu	^{240}Pu	^{241}Pu	^{242}Pu
^{235}U	1.000	0.000	-0.001	0.003	-0.002	-0.002	0.000
^{238}U	0.000	1.000	-0.003	-0.002	-0.001	-0.001	0.005
^{238}Pu	-0.001	-0.003	1.000	0.003	0.004	-0.004	-0.002
^{239}Pu	0.003	-0.002	0.003	1.000	-0.001	-0.002	0.001
^{240}Pu	-0.002	-0.001	0.004	-0.001	1.000	0.001	0.003
^{241}Pu	-0.002	-0.001	-0.004	-0.002	0.001	1.000	0.001
^{242}Pu	0.000	0.005	-0.002	0.001	0.003	0.001	1.000

Table 3.51: Partial correlation matrix of $x \rightarrow {}^{90}$Sr fission yield perturbations

$Cor\left(\tilde{f}\left(^{235}\mathrm{U}, ^{84}\mathrm{Kr}\right), \tilde{f}\left(^{235}\mathrm{U}, ^{85}\mathrm{Kr}\right)\right) = -0.07$. It appears that the method leads to many negative correlation factors between the $\tilde{f}$ ratios, resulting from the renormalization (increasing a perturbation leads to reducing other factors). Several successive sampling generations showed that this result is stable and scarcely varies with the sample size.

x	^{84}Kr	^{85}Kr	^{90}Sr	^{95}Zr	^{106}Ru	^{133}I	^{132}Te	^{137}Cs	^{144}Ce	^{146}Nd	^{147}Nd	^{151}Pm	^{152}Sm	^{153}Sm
^{84}Kr	1.00	-0.07	-0.07	-0.08	-0.08	-0.08	-0.08	-0.08	-0.08	-0.07	-0.08	-0.08	-0.07	-0.07
^{85}Kr	-0.07	1.00	-0.08	-0.07	-0.08	-0.07	-0.08	-0.08	-0.09	-0.08	-0.07	-0.08	-0.08	-0.08
^{90}Sr	-0.07	-0.08	1.00	-0.08	-0.08	-0.07	-0.08	-0.08	-0.08	-0.08	-0.07	-0.08	-0.08	-0.08
^{95}Zr	-0.08	-0.07	-0.08	1.00	-0.08	-0.07	-0.08	-0.08	-0.08	-0.07	-0.08	-0.07	-0.08	-0.08
^{106}Ru	-0.08	-0.08	-0.08	-0.08	1.00	-0.08	-0.07	-0.08	-0.07	-0.07	-0.08	-0.08	-0.07	-0.08
^{133}I	-0.08	-0.07	-0.07	-0.07	-0.08	1.00	-0.07	-0.08	-0.08	-0.08	-0.08	-0.08	-0.08	-0.07
^{132}Te	-0.08	-0.08	-0.08	-0.08	-0.07	-0.07	1.00	-0.07	-0.08	-0.08	-0.08	-0.08	-0.08	-0.08
^{137}Cs	-0.08	-0.08	-0.08	-0.08	-0.08	-0.08	-0.07	1.00	-0.07	-0.07	-0.08	-0.08	-0.08	-0.08
^{144}Ce	-0.08	-0.09	-0.08	-0.08	-0.07	-0.08	-0.08	-0.07	1.00	-0.08	-0.08	-0.07	-0.08	-0.08
^{146}Nd	-0.07	-0.08	-0.08	-0.07	-0.07	-0.08	-0.08	-0.07	-0.08	1.00	-0.07	-0.08	-0.08	-0.08
^{147}Nd	-0.08	-0.07	-0.07	-0.08	-0.08	-0.08	-0.08	-0.08	-0.08	-0.07	1.00	-0.07	-0.08	-0.08
^{151}Pm	-0.08	-0.08	-0.08	-0.07	-0.08	-0.08	-0.08	-0.08	-0.07	-0.08	-0.07	1.00	-0.07	-0.08
^{152}Sm	-0.07	-0.08	-0.08	-0.08	-0.07	-0.08	-0.08	-0.08	-0.08	-0.08	-0.08	-0.07	1.00	-0.08
^{153}Sm	-0.07	-0.08	-0.08	-0.08	-0.08	-0.07	-0.08	-0.08	-0.08	-0.08	-0.08	-0.08	-0.08	1.00

Table 3.52: Partial correlation matrix of $^{235}\mathrm{U} \rightarrow x$ fission yield perturbations

The correlation value between these fission yields is high (absolute value around 7%). This raises the issue of the application of the conservation law in our example. The influence of a conservation law on correlation between linked parameters decreases with the number of parameters subsequently linked. In our case, the law links the values of a large amount of fission yields. However, this study considers fewer perturbations of fission yields that physically exist, given that several fission products do not contribute to decay heat. Therefore, if we apply the conservation law to a restricted number of fission yields, its correlation power is artificially increased, and the correlations between yields are given too negative values.

Furthermore, such a renormalization alters the shape of the distributions and even their standard deviation. The example of a sum constraint on a few normal distributions is shown on figure 3.28. The distributions are all normal laws $\mathcal{N}(1, 0.1)$, and the sum constraint is performed on 2, 3 and 10 distributions. It appears that the quantiles of the normalized distributions are biased, and even the standard deviation is modified.

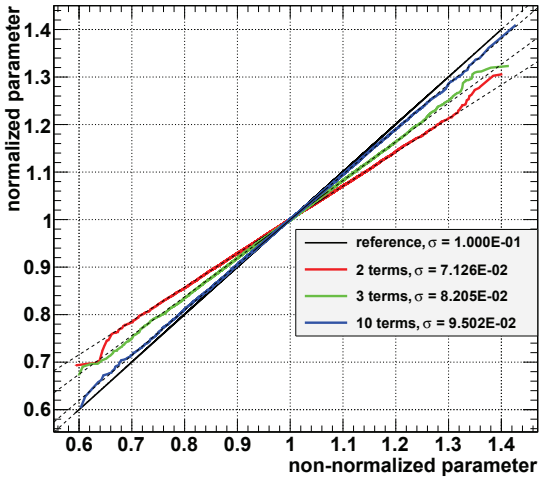

Figure 3.28: QQ plot of renormalized normal laws with a sum constraint

Our conclusion is that the conservation law must not be applied without considering the variation of every fission yield, at least during the sampling process. This leads us to use a non-correlated design of experiment, and the subsequent distributions will not respect certain physical criteria. However, despite describing non-physical situations, these points are still located inside the domain of validity of the models, therefore the physical models will remain accurate with regards to the input data, and the observed trends can still be used to construct surrogate models. These surrogate models will be used to estimate physical situation, which are in a subset of the domain of validity of the models.

3.2.2.1.4 Cross-sections

3.2.2.1.4.1 Actinides cross-sections

The same cross-section perturbations are considered for the construction of fission products estimators as for the actinides estimators. Perturbations on the fission and capture cross-sections of the following nuclides are considered:
^{235}U, ^{238}U, ^{238}Pu, ^{239}Pu, ^{240}Pu, ^{241}Pu, ^{242}Pu, ^{241}Am, ^{243}Am, ^{237}Np, ^{242}Cm, ^{243}Cm, ^{244}Cm, ^{245}Cm.

Cross-section perturbations are sampled uncorrelated, following uniform distributions in wide intervals (length $\gg$ uncertainty), so as to stay valid at extreme values while sampling uncertainty using Gaussian distributions.

Further work may consider cross-sections of other nuclides as well, including ^{234}U, ^{236}U, etc. In order to keep a limited number of parameters, the first step of the study would be a sensitivity study assessing the impact of cross-sections on concentrations of interest, so as to determine negligible parameters.

3.2.2.1.4.2 Fission products cross-sections

Fission products have a null fission cross-section and therefore are not subject to fission cross-section uncertainty.

In order to determine which fission product radiative capture (n,γ) cross-section have an impact on fission products concentrations after irradiation, we can perform a sensitivity study, and compute the one-at-a-time sensitivity $S_{i,j} = \frac{\sigma_c(j)}{C(i)}\frac{\partial C(i)}{\partial \sigma_c(j)}$. However, in order to reduce the studied domain, we can make the following assumption: the indirect effect of the i sensitivity (changes in concentration due to changes in spectrum only) is null. We translate this assumption into equation 3.52.

$$If\ (j \neq i) \wedge (j\ \textit{does not belong to the chain leading to formation of}\ i)\ \text{then} \frac{\sigma_c(j)}{C(i)}\frac{\partial C(i)}{\partial \sigma_c(j)} = 0 \quad (3.52)$$

Therefore we limit the domain of our study to the chains leading to formation of fission products of interest. We performed the study in the case of PWR MOX and PWR UOX fuel, both irradiated at 45GWd/tHM. In the case of SFR fuel we assume that sensitivity is very low because the fast spectrum makes capture reaction rates very low.

The selection of nuclides whose capture cross-section sensitivity is studied comes from the study of section 3.2.2.1.3.2: any fission product present in a chain is studied.

In the case of cumulative fission yields, sensitivity of the precursors' cross-sections is not calculated, as their capture cross-section uncertainty is a part of the cumulative yield uncertainty.

Sensitivity values are calculated on a $[+0\%,\ +100\%]$ variation interval of $\sigma_c(j)$. Results of the study are summarized in table 3.53 in the case of PWR UOX fuel and in table 3.54 in the case of PWR MOX fuel. The 1-group cross-section uncertainty σ_j value computed through method presented in section 5.2.1 and the resulting product $S_{i,j} \times \sigma_j$ are shown as well, in order to determine whether the uncertainty associated to a given cross-section contributes to the concentration after irradiation of any fission product. We used this latter indicator to determine whether it is required to take a cross-section uncertainty into account for the construction of surrogate models.

Uncertainty data is produced using ENDF-BVII evaluation files when available, and TENDL-2013 (available at http://www.talys.eu/tendl-2013/) otherwise. Uncertainty data concerning ^{133}Xe, ^{133}I and ^{137}Cs was unavailable in both evaluated nuclear data files, however their null sensitivity allows not taking these nuclides into account.

Most of the values of $sensitivity\ \times uncertainty$ are low, and therefore we will assume that the contribution to global uncertainty on decay heat is minor.

> *The nuclides which* (n,γ) *cross-section contributes to decay heat uncertainty in a* non-negligible *way are summarized in* `list_XS_FP`. Non-negligible *is arbitrarily defined here as* uncertainty of the fission product concentration due to a given cross-section is 1% or more of the nominal value of the fission product.
> `list_XS_FP` $= \{^{133}\text{Cs},\ ^{134}\text{Cs},\ ^{147}\text{Pm},\ ^{152}\text{Sm},\ ^{153}\text{Eu},\ ^{154}\text{Eu}\}$

3.2.2.1.5 Parameters taken into account: summary

Table 3.55 summarizes which parameters are taken into account or neglected. Neglected parameters are only taken into account as their mean value.

i (concentration)	j ((n,γ)XS)	sensitivity $S_{i,j}$	$\sigma_c(j)$ (uncertainty)	$S_{i,j} \times \sigma_c(j)$
^{85}Kr	^{84}Kr	+0.011	86.32% (TENDL-2013)	0.95%
^{85}Kr	^{85}Kr	-0.002	91.15% (TENDL-2013)	0.18%
^{90}Sr	^{90}Sr	-0.001	>100% (TENDL-2013)	∼0.11%
^{95}Zr	^{95}Zr	-0.001	>100% (TENDL-2013)	∼0.12%
^{106}Ru	^{106}Ru	-0.001	501.59% (TENDL-2013)	0.50%
^{134}Cs	^{133}I	+0.000	×	×
^{134}Cs	^{133}Xe	-0.003	×	×
^{134}Cs	^{133}Cs	+0.771	12.26% (ENDF B-VII)	9.45%
^{134}Cs	^{134}Cs	-0.080	24.20% (TENDL-2013)	1.94%
^{137}Cs	^{137}Cs	-0.001	×	×
^{144}Ce	^{144}Ce	-0.001	>100% (TENDL-2013)	∼0.12%
^{147}Pm	^{146}Nd	+0.005	14.02% (ENDF B-VII)	0.07%
^{147}Pm	^{147}Nd	-0.014	20.04% (TENDL-2013)	0.29%
^{147}Pm	^{147}Pm	-0.345	9.07% (ENDF B-VII)	3.13%
^{154}Eu	^{151}Pm	-0.001	>100% (TENDL-2013)	∼0.10%
^{154}Eu	^{151}Sm	+0.021	5.71% (ENDF B-VII)	0.12%
^{154}Eu	^{152}Sm	+0.204	7.11% (ENDF B-VII)	1.45%
^{154}Eu	^{153}Sm	-0.005	61.35% (TENDL-2013)	0.31%
^{154}Eu	^{153}Eu	+0.350	5.66% (ENDF B-VII)	1.98%
^{154}Eu	^{154}Eu	-0.441	35.19% (TENDL-2013)	15.52%

Table 3.53: Fission products capture cross-section sensitivity in PWR UOX fuel

3.2.2.2 Design of experiment

The design of experiment results naturally from the study of the parameters. The sampling method chosen was Latin Hypercube Sampling (LHS), especially justified in this case considering the high dimension of the input space (up to ~ 145 independent variables in the case of MOX fuel).

The problem of the fission products estimation in function of fission yields and other parameters is different from the problem of the actinides estimation, because it contains several highly sensitive variables (approximately 5) per estimator (the burnup and the fission yields) instead of only 1 (the burnup).

The impact of these variables, if taken one at a time, is more linear, mostly fission products are formed more or less linearly in function of the burnup. However strong interactions take place between burnup, cross-sections and fission yields. Consequently a large sample is required to build accurate estimators.

The DOE for construction of ANN estimators are shown in appendix A.2.

The design of experiment of the fabrication samples contains approximately 5000 points, those for the test sample also contain 5000 points. This almost ensures that the error of the estimators come from a saturation (lack of fit) of the estimators, rather than a lack of knowledge.

i (concentration)	j ((n,γ)XS)	sensitivity $S_{i,j}$	$\sigma_c(j)$ (uncertainty)	$S_{i,j} \times \sigma_c(j)$
^{85}Kr	^{84}Kr	+0.011	>100% (TENDL-2013)	∼1.10%
^{85}Kr	^{85}Kr	-0.013	77.69% (TENDL-2013)	1.01%
^{90}Sr	^{90}Sr	-0.001	>100% (TENDL-2013)	∼0.10%
^{95}Zr	^{95}Zr	-0.000	>100% (TENDL-2013)	<0.01%
^{106}Ru	^{106}Ru	-0.001	501.59% (TENDL-2013)	0.50%
^{134}Cs	^{133}I	+0.000	×	×
^{134}Cs	^{133}Xe	-0.002	×	×
^{134}Cs	^{133}Cs	+0.811	15.46% (ENDF B-VII)	12.37%
^{134}Cs	^{134}Cs	-0.041	25.22% (TENDL-2013)	1.03%
^{137}Cs	^{137}Cs	-0.000	×	×
^{144}Ce	^{144}Ce	-0.001	>100% (TENDL-2013)	∼0.10%
^{147}Pm	^{146}Nd	+0.004	15.46% (ENDF B-VII)	0.06%
^{147}Pm	^{147}Nd	-0.009	35.56% (TENDL-2013)	0.32%
^{147}Pm	^{147}Pm	-0.316	9.47% (ENDF B-VII)	2.99%
^{154}Eu	^{151}Pm	+0.001	98.31% (TENDL-2013)	0.10%
^{154}Eu	^{151}Sm	+0.069	6.24% (ENDF B-VII)	0.43%
^{154}Eu	^{152}Sm	+0.299	7.85% (ENDF B-VII)	2.34%
^{154}Eu	^{153}Sm	-0.004	46.70% (TENDL-2013)	0.19%
^{154}Eu	^{153}Eu	+0.492	6.19% (ENDF B-VII)	3.04%
^{154}Eu	^{154}Eu	-0.353	42.48% (TENDL-2013)	15.00%

Table 3.54: Fission products capture cross-section sensitivity in PWR MOX

3.2.3 Regression

3.2.3.1 Qualitative analysis of the model

The major difference between actinides and fission products concentrations after irradiation is the impact of fission yields and fission products cross-sections, which considerably increases the dimension of input parameters space. We give here the example of ^{154}Eu, which is the most difficult case. Concentration after irradiation varies in function of the composition of the fresh fuel, burnup, power, actinides fission and capture cross-sections, fission yields from (^{235,238}U, ^{239,240,241,242}Pu) to (^{151}Pm, ^{152,153}Sm), and radiative capture cross-sections of ^{152}Sm and ^{153,154}Sm. Furthermore, we can intuitively think that several of these parameters interact multiplicatively: impact of capture cross-section of ^{153}Sm increases with its concentration, which increases with its formation rate, which increases with both fission yields leading to it and actinides fission cross-sections. Hence, although not so non-linear in function of the burnup, fission products concentrations after irradiation remain relatively hard to estimate, and are subject to a high amount of strong interactions between parameters.

This remark invalidates more or less the use of polynomial regressions for construction of fission products surrogate models. Furthermore, the limits of polynomial regressions for estimation of concentrations after irradiation were already exposed in section 3.1.3.1.5.9. However, artificial neural networks seem particularly adapted to model such physical quantities.

parameter	taken into account	neglected	number of parameters
burnup	×		1
irradiation length	×		1
specific power	×		(calculated, not sampled)
non-uniform load factor		×	
fresh fuel mass fractions	×		$2 \rightarrow 9$
actinides fission XS	×		19
actinides capture XS	×		19
FP capture XS	×		6
actinides scattering XS		×	
FP scattering XS		×	
other nuclides scattering XS		×	
fission yields	×		94
effective fission energy		×	
mass		×	
half-life		×	

Table 3.55: Summary of the parameters taken into account for fission products surrogate models

3.2.3.2 Artificial Neural Networks

3.2.3.2.1 Reduction of the parameters space

3.2.3.2.1.1 Introduction

The considerations taken into account in section 3.1.3.2.2 apply here too. The main difference is the presence of fission yields as parameters. These yields are studied in section 3.2.3.2.1.2.

3.2.3.2.1.2 Correlated input parameters

As explained in 3.2.2.1.3, the fission yields were sampled without correlations nor constraints.

The irradiation length is strongly correlated with the burnup. Even though it was convenient to consider the irradiation length instead of the specific power as an input parameter in the case of the construction of multiple polynomial regressions, the use of this input could be detrimental to the quality of the neural network. Therefore the specific power, which is not correlated with the burnup in our sampling method (see section 3.1.2.1.3), was used in this case, instead of the irradiation length.

Cross-sections perturbations were sampled without taking into account correlations even though inter-reaction covariance matrices are available[8].

Initial mass fractions are sampled without correlations due to any renormalization. Indeed physical nature of nuclear fuel on uranium matrix allows us to use the initial mass fraction of ^{238}U as a buffer for other mass fractions. The mass fraction of ^{238}U, as a combination of other mass fractions, will not be taken into account as a parameter during the construction of artificial neural networks.

[8]However inter-reaction covariance data is taken into account during the uncertainty propagation step.

$\frac{1}{\overline{C(^{106}\mathrm{Ru})}}\frac{\partial C(^{106}\mathrm{Ru})}{\partial \tilde{f}(X\to Y)}$		X						
		^{235}U	^{238}U	^{238}Pu	^{239}Pu	^{240}Pu	^{241}Pu	^{22}Pu
Y	^{84}Kr	0.00	0.00	0.00	0.00	0.00	0.00	0.00
	^{85}Kr	0.00	0.00	0.00	0.00	0.00	0.00	0.00
	^{90}Sr	0.00	0.00	0.00	0.00	0.00	0.00	0.00
	^{95}Zr	0.00	0.00	0.00	0.00	0.00	0.00	0.00
	^{132}Te	0.00	0.00	0.00	0.00	0.00	0.00	0.00
	^{106}Ru	**0.50**	**0.08**	0.00	**0.35**	0.00	**0.07**	0.00
	^{133}I	0.00	0.00	0.00	0.00	0.00	0.00	0.00
	^{137}Cs	0.00	0.00	0.00	0.00	0.00	0.00	0.00
	^{144}Ce	0.00	0.00	0.00	0.00	0.00	0.00	0.00
	^{146}Nd	0.00	0.00	0.00	0.00	0.00	0.00	0.00
	^{147}Nd	0.00	0.00	0.00	0.00	0.00	0.00	0.00
	^{151}Pm	0.00	0.00	0.00	0.00	0.00	0.00	0.00
	^{152}Sm	0.00	0.00	0.00	0.00	0.00	0.00	0.00
	^{153}Sm	0.00	0.00	0.00	0.00	0.00	0.00	0.00

Table 3.56: Local sensitivity of $X \to ^{106}$Ru fission yields

3.2.3.2.1.3 Parameters with no influence

The same considerations concerning mass fractions are taken into account as in section 3.1.3.2.2.3: mass fractions which have no impact on the concentrations after irradiation will not be considered as parameters of the associated artificial neural network.

Several cross-sections have an extremely small impact on fission products concentrations after irradiation. It is the case for several Np and Cm cross-sections, which impact, calculated as local sensitivity measures on the construction samples, is undetectable, even with a low statistic error.

A brief sensitivity study on a non-correlated sample shows that the fission yield $X \to Y$ has almost no influence on the formation of the fission product Z when Z does not belong to the decay chain of Y. The case of the concentration of ^{106}Ru in irradiated PWR UOX fuel is shown on table 3.56, with $\overline{C\,(^{106}\mathrm{Ru})}$ the mean concentration of ^{106}Ru after irradiation. The local sensitivity index of ^{106}Ru to every fission yield taken into account during the sampling process is calculated.

Hence, during the construction of the fission product Y estimator, only the fission yields $X \to Z$ will be taken into account, with $Z = Y$ or Z being a chain head leading to Y, and the influence of the other fission yields will be neglected.

3.2.3.2.1.4 Final parameters space

According to considerations of 3.2.3.2.1.2 and 3.2.3.2.1.3, the subset of sensitive and uncorrelated parameters taken into account for the estimation of fission product Y using neural networks is as follows, with $Z = Y$ or Z being a chain head leading to Y, i the actinides present in substantial concentration before irradiation, j the actinides which fission and capture cross-section perturbation is taken into account, and k the fission products which capture cross-section is taken into account:

$$parameters = \left\{ \frac{m_i}{m}, \text{BU}, \mathcal{P}_{irrad}, \frac{\Delta\sigma_c(j)}{\sigma_c(j)}, \frac{\Delta\sigma_f(j)}{\sigma_f(j)}, \frac{\Delta\sigma_c(k)}{\sigma_c(k)}, \tilde{f}\left({}^{235,238}\text{U}, {}^{238,239,240,241,242}\text{Pu} \rightarrow Z\right) \right\} \tag{3.53}$$

3.2.3.2.2 Determination of hidden neurons and sample size

The same considerations were taken into account as in section 3.1.3.2.1. The sample size is usually around 5000 for both construction and test samples, and the number of neurons in the hidden layer is case-dependent, usually between 6 and 10.

3.2.3.2.3 Application

3.2.3.2.3.1 Overview

Fission products ANN are constructed, on the whole, the same way as actinides ANN.

The precision of each estimator was tested on a test base, different from the fabrication sample. We denote y the concentration after irradiation of a fission product, $\bar{y}$ the mean of y on the test sample and $\hat{y}$ the estimator of y calculated on the test sample. The following quality indexes are calculated on a test sample (with the exception of r^2, calculated on construction sample):

$$\begin{cases} r^2, q^2 & \text{variance propagation indicators} \\ max\,|\hat{y}-y| & \text{maximum value of the absolute error} \\ max\,|\hat{y}/y-1| & \text{maximum value of the relative error} \\ mean\,|\hat{y}/y-1| & \text{mean value of the relative error} \\ max\,|(\hat{y}-y)/\bar{y}| & \text{maximum value of the absolute error compared to the mean} \\ mean\,|(\hat{y}-y)/\bar{y}| & \text{mean value of the absolute error compared to the mean} \end{cases} \tag{3.54}$$

A satisfying result (typically $< 1\%$) for the maximum value of the relative error is usually the most difficult criterion to reach. In the case of several concentrations after irradiation, it was not possible to reach satisfying values for this criterion, and the maximum value of the absolute error compared to the mean had to be used.

For each actinides surrogate model corresponding to a fuel type, the complementary fission products surrogate model was built.

3.2.3.2.3.2 Estimators quality analysis

Tables 3.57 to 3.63 summarize the quality indexes of each fission product estimator in every fuel type. Values above 1000% are noted $+++$.

actinide	r^2	q^2	$max\|\hat{y}/y-1\|$	$mean\|\hat{y}/y-1\|$	$max\|(\hat{y}-y)/\bar{y}\|$	$mean\|(\hat{y}-y)/\bar{y}\|$
^{85}Kr	0.9998	0.9998	7.78%	0.34%	3.05%	0.30%
^{90}Sr	0.9999	0.9999	5.34%	0.28%	3.23%	0.24%
^{95}Zr	0.9997	0.9996	4.83%	0.31%	4.16%	0.30%
^{106}Ru	0.9997	0.9996	14.15%	0.56%	4.36%	0.46%
^{134}Cs	0.9996	0.9994	137.32%	1.32%	10.68%	0.70%
^{137}Cs	0.9998	0.9998	7.50%	0.30%	2.73%	0.26%
^{144}Ce	0.9997	0.9996	5.50%	0.34%	3.24%	0.32%
^{147}Pm	0.9993	0.9991	8.58%	0.53%	6.97%	0.49%
^{154}Eu	0.9991	0.9983	$+++$	7.71%	30.76%	1.82%

Table 3.57: Quality indexes of low burnup PWR UOX fission products ANN surrogate model

actinide	r^2	q^2	$max\|\hat{y}/y-1\|$	$mean\|\hat{y}/y-1\|$	$max\|(\hat{y}-y)/\bar{y}\|$	$mean\|(\hat{y}-y)/\bar{y}\|$
^{85}Kr	0.9998	0.9997	3.26%	0.31%	2.64%	0.30%
^{90}Sr	0.9998	0.9998	3.64%	0.28%	2.41%	0.26%
^{95}Zr	0.9998	0.9997	4.12%	0.27%	2.18%	0.26%
^{106}Ru	0.9997	0.9996	2.95%	0.36%	3.59%	0.36%
^{134}Cs	0.9995	0.9993	7.32%	0.62%	5.30%	0.59%
^{137}Cs	0.9999	0.9998	1.96%	0.22%	1.85%	0.21%
^{144}Ce	0.9997	0.9996	4.37%	0.32%	3.27%	0.30%
^{147}Pm	0.9996	0.9995	2.93%	0.36%	2.55%	0.35%
^{154}Eu	0.9989	0.9983	31.11%	2.20%	30.73%	1.92%

Table 3.58: Quality indexes of high burnup PWR UOX fission products ANN surrogate model

actinide	r^2	q^2	$max\|\hat{y}/y-1\|$	$mean\|\hat{y}/y-1\|$	$max\|(\hat{y}-y)/\bar{y}\|$	$mean\|(\hat{y}-y)/\bar{y}\|$
^{85}Kr	0.9998	0.9997	12.75%	0.41%	2.98%	0.35%
^{90}Sr	0.9998	0.9997	12.47%	0.40%	2.76%	0.34%
^{95}Zr	0.9998	0.9997	3.39%	0.26%	3.48%	0.25%
^{106}Ru	0.9998	0.9998	7.37%	0.27%	5.37%	0.24%
^{134}Cs	0.9995	0.9994	442.43%	1.29%	7.65%	0.78%
^{137}Cs	0.9998	0.9998	8.51%	0.36%	2.67%	0.31%
^{144}Ce	0.9998	0.9997	5.46%	0.29%	3.67%	0.27%
^{147}Pm	0.9996	0.9995	5.99%	0.40%	3.46%	0.38%
^{154}Eu	0.9996	0.9995	82.16%	1.07%	9.34%	0.78%

Table 3.59: Quality indexes of low burnup PWR MOX fission products ANN surrogate model

actinide	r^2	q^2	$max\|\hat{y}/y-1\|$	$mean\|\hat{y}/y-1\|$	$max\|(\hat{y}-y)/\bar{y}\|$	$mean\|(\hat{y}-y)/\bar{y}\|$
^{85}Kr	0.9999	0.9998	1.37%	0.19%	1.20%	0.18%
^{90}Sr	0.9998	0.9998	2.37%	0.20%	1.65%	0.19%
^{95}Zr	0.9999	0.9999	1.20%	0.15%	1.61%	0.15%
^{106}Ru	0.9999	0.9999	1.72%	0.18%	1.93%	0.17%
^{134}Cs	0.9997	0.9997	2.56%	0.38%	2.76%	0.37%
^{137}Cs	0.9999	0.9999	1.66%	0.14%	1.10%	0.13%
^{144}Ce	0.9999	0.9998	1.44%	0.20%	1.46%	0.19%
^{147}Pm	0.9997	0.9997	1.79%	0.27%	1.60%	0.27%
^{154}Eu	0.9997	0.9996	3.80%	0.51%	4.62%	0.50%

Table 3.60: Quality indexes of high burnup PWR MOX fission products ANN surrogate model

actinide	r^2	q^2	$max\|\hat{y}/y-1\|$	$mean\|\hat{y}/y-1\|$	$max\|(\hat{y}-y)/\bar{y}\|$	$mean\|(\hat{y}-y)/\bar{y}\|$
^{85}Kr	0.9999	0.9999	5.00%	0.24%	2.35%	0.23%
^{90}Sr	0.9999	0.9999	9.23%	0.29%	2.69%	0.26%
^{95}Zr	0.9996	0.9995	6.41%	0.33%	6.41%	0.33%
^{106}Ru	0.9997	0.9996	0.49%	2.70%	0.45%	0.45%
^{134}Cs	0.9997	0.9997	29.70%	0.66%	3.87%	0.54%
^{137}Cs	0.9998	0.9998	6.99%	0.33%	2.24%	0.28%
^{144}Ce	0.9998	0.9997	4.94%	0.26%	4.82%	0.25%
^{147}Pm	0.9993	0.9992	6.23%	0.46%	5.08%	0.43%
^{154}Eu	0.9997	0.9996	336.79%	1.74%	14.67%	0.99%

Table 3.61: Quality indexes of high burnup PWR repU fission products ANN surrogate model

actinide	r^2	q^2	$max\|\hat{y}/y-1\|$	$mean\|\hat{y}/y-1\|$	$max\|(\hat{y}-y)/\bar{y}\|$	$mean\|(\hat{y}-y)/\bar{y}\|$
^{85}Kr	0.9997	0.9996	18.89%	0.53%	3.47%	0.45%
^{90}Sr	0.9983	0.9976	18.15%	1.02%	9.67%	0.92%
^{95}Zr	0.9992	0.9991	10.28%	0.46%	9.22%	0.44%
^{106}Ru	0.9995	0.9994	0.43%	3.76%	0.40%	0.40%
^{134}Cs	0.9994	0.9993	$+++$	4.64%	9.98%	0.85%
^{137}Cs	0.9998	0.9997	15.16%	0.43%	2.85%	0.37%
^{144}Ce	0.9992	0.9989	7.80%	0.55%	4.66%	0.51%
^{147}Pm	0.9994	0.9992	13.06%	0.56%	5.09%	0.51%
^{154}Eu	0.9994	0.9991	$+++$	1.64%	6.99%	0.90%

Table 3.62: Quality indexes of low burnup SFR MOX fission products ANN surrogate model

actinide	r^2	q^2	$max\|\hat{y}/y-1\|$	$mean\|\hat{y}/y-1\|$	$max\|(\hat{y}-y)/\bar{y}\|$	$mean\|(\hat{y}-y)/\bar{y}\|$
^{85}Kr	0.9993	0.9988	3.15%	0.52%	3.09%	0.50%
^{90}Sr	0.9953	0.9922	8.62%	1.26%	8.24%	1.23%
^{95}Zr	0.9996	0.9994	3.74%	0.39%	2.51%	0.38%
^{106}Ru	0.9997	0.9996	3.62%	0.33%	2.37%	0.31%
^{134}Cs	0.9991	0.9986	5.13%	0.81%	4.72%	0.78%
^{137}Cs	0.9997	0.9995	2.55%	0.36%	2.05%	0.35%
^{144}Ce	0.9996	0.9993	2.40%	0.40%	2.17%	0.39%
^{147}Pm	0.9988	0.9977	4.97%	0.72%	4.62%	0.69%
^{154}Eu	0.9988	0.9977	5.15%	0.99%	5.24%	0.95%

Table 3.63: Quality indexes of high burnup SFR fission products ANN surrogate model

3.2.3.2.3.3 Examples

Figure 3.29 represents the identity card of ^{134}Cs estimator in PWR UOX fuel irradiated at less than nominal burnup. The absolute error remains relatively low, although the quality of the estimator degrades for very low burnup values. 10 hidden neurons were necessary to model accurately the behavior of ^{134}Cs in function of the multiple parameters of the estimator. Overall this estimator is accurate enough for uncertainty propagation studies.

3.2.3.2.3.4 Remark concerning ^{154}Eu

Globally the accuracy of the estimators is satisfying. However, precision of ^{154}Eu estimators remains quite low, for any surrogate model. Analysis of the residuals showed that this lack of fit is mostly due to ^{154}Eu radiative capture cross-section uncertainty.

The uncertainty of ^{154}Eu radiative capture cross-section used in this work is obtained from TENDL-2013 database. Comparison of this value with other values of uncertainty, for instance uncertainty of energy-integrated cross-section at thermal point, pointed a large difference between uncertainty values (largely above the difference between CESAR computation and ANN estimation).

Refinement of ^{154}Eu cross-section data may be an opportunity to reduce decay heat uncertainty.

3.2.4 Calculation of decay heat

3.2.4.1 Introduction

As previously shown in section 3.2.1.2, decay heat of irradiated fuel is calculated at a given time t in function of the fuel composition:

$$DH(t) = \sum_{i \in \text{nuclides}} N_i(t) \times \lambda_i \times E_i \tag{3.55}$$

It is a function of the concentrations at a given time. Fission products and actinides surrogate models provide the concentrations N_i just after irradiation. Therefore, so as to be able to compute

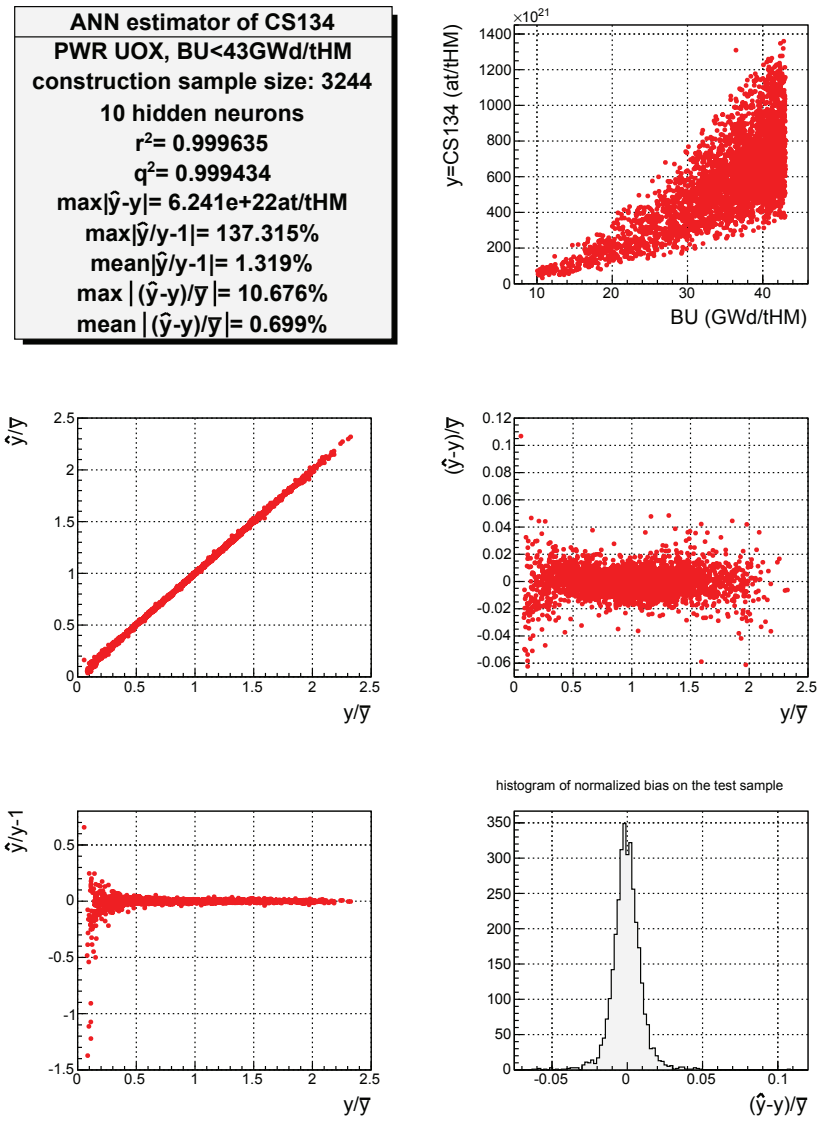

Figure 3.29: Identity card of the ^{134}Cs estimator in PWR UOX fuel, BU<43GWd/tHM

decay heat at a given time after irradiation, it is necessary to perform cooling calculation on these nuclides.

Before modeling cooling calculation with any kind of surrogate model, it is wise to perform a qualitative analysis of the problem. We can make the following comments:

- the number of parameters is very high: there are as many parameters as there are nuclides in irradiated fuel ($n \gg 100$);
- each parameter varies in almost its full range;
- concentrations are highly dependent on concentrations (including its own) at zero time and on the time, interactions are strong;
- time-dependence is non-linear (sum of exponential decays).

Therefore the construction of such a surrogate model would be time-consuming, there is a high chance that precision would not be satisfying.

However analytic resolution of the Bateman equation out of irradiation makes few hypotheses, is quite straightforward, and analytic solutions were already implemented in COSI for several actinides. On the calculation time point of view, solutions are calculated directly, without iterations, leading to a very time-effective computation.

Hence we chose to update the COSI package devoted to analytic resolution of Bateman equation and extend its domain of definition of the models to fission products, instead of using specific surrogate models.

3.2.4.2 Cooling calculation

3.2.4.2.1 Analytic solutions of Bateman equation

The analytic solution of the Bateman equation for a given nuclide depends on the number of successive father it has. These equations were already implemented in COSI for the actinides.

A very singular situation is encountered in the case of the fission products of interest: decay chains are short. Each of the decay chains of interest can be modeled by one of the situations shown in figure 3.30.

Case 1 $\xrightarrow{fission} A \xrightarrow{\lambda_A} B$ (stable)
Case 2 $\xrightarrow{fission} A \xrightarrow{\lambda_A} B \xrightarrow{\lambda_B} C$ (stable)

Figure 3.30: Decay paths of fission products

The concentrations after irradiation of A and B are noted A_0 and B_0, the cooling time is noted t. The instant $t = 0$ corresponds to the end of irradiation.

The analytic solution in case 1 is:

$$A(t \geq 0) = A_0 e^{-\lambda_A t} \tag{3.56}$$

The analytic solution in case 2 is:

$$\begin{cases} A(t \geq 0) = A_0 e^{-\lambda_A t} \\ B(t \geq 0) = \frac{\lambda_A}{\lambda_B - \lambda_A} A_0 e^{-\lambda_A t} + (B_0 - \frac{\lambda_A}{\lambda_B - \lambda_A} A_0) e^{-\lambda_B t} \end{cases} \tag{3.57}$$

Given that the last nuclide in the chains is stable, it does not contribute to decay heat, hence it is not necessary to calculate its concentration.

3.2.4.2.2 Application

Analytic solutions presented in paragraph 3.2.4.2.1 were implemented for the decay chains of equation 3.58. A virtual concentration, modeling the end of chains, was introduced in order to respect mass conservation.

$$\begin{cases} {}^{85}Kr \xrightarrow[\beta-]{10.75y} {}^{85}Rb(stable) \\ {}^{90}Sr \xrightarrow[\beta-]{18.74y} {}^{90}Y \xrightarrow[\beta-]{2.67d} {}^{90}Zr(stable) \\ {}^{95}Zr \xrightarrow[\beta-]{64.03d} {}^{95}Nb \xrightarrow[\beta-]{34.99d} {}^{95}Mo(stable) \\ {}^{106}Ru \xrightarrow[\beta-]{1.02y} {}^{106}Rh \xrightarrow[\beta-]{30.0s} {}^{106}Pd(stable) \\ {}^{134}Cs \xrightarrow[\beta-]{2.06y} {}^{134}Ba(stable) \\ {}^{137}Cs \xrightarrow[\beta-]{30.04y} {}^{137M}Ba \xrightarrow[IT]{2.55min} {}^{137}Ba(stable) \\ {}^{144}Ce \xrightarrow[\beta-]{285.0d} {}^{144}Pr \xrightarrow[\beta-]{17.28min} {}^{144}Nd(\sim stable) \\ {}^{147}Pm \xrightarrow[\beta-]{2.62y} {}^{147}Sm(stable) \\ {}^{154}Eu \xrightarrow[\beta-]{8.59y} {}^{154}Gd(stable) \end{cases} \tag{3.58}$$

3.2.4.3 Calculation schema

Figure 3.31 page 135 illustrates the decay heat calculation route via artificial networks as we implemented it in COSI. It consists in an analytic post-treatment (cooling + calculation of decay heat) of a concatenation of several surrogate model results (concentrations after irradiation).

3.2.4.4 Validation of decay heat computation

3.2.4.4.1 Overview

It is necessary to assess the quality of the estimation of the decay heat, which is not a direct result of the surrogate models. In the next parts, the decay heat will be calculated by COSI-CESAR5.3 on one side and COSI-Surrogate Models with analytic Bateman cooling on the other side, for a few benchmarks. The decay heat will be calculated for irradiated fuel between 1 and 20 years of cooling, which corresponds to the key dates from the point of view of the fuel treatment. The bias caused by the use of surrogate models and analytic Bateman equation solution will be calculated as shown on equation 3.59:

$$\text{bias}(\%) = \left(\frac{\text{decay heat(COSI-Surrogate Models-Analytic Bateman)}}{\text{decay heat(COSI-CESAR5.3)}} - 1 \right) \times 100 \tag{3.59}$$

Paragraphs 3.2.4.4.2 to 3.2.4.4.7 provide a visual validation of the estimator of decay heat for different fuel types.

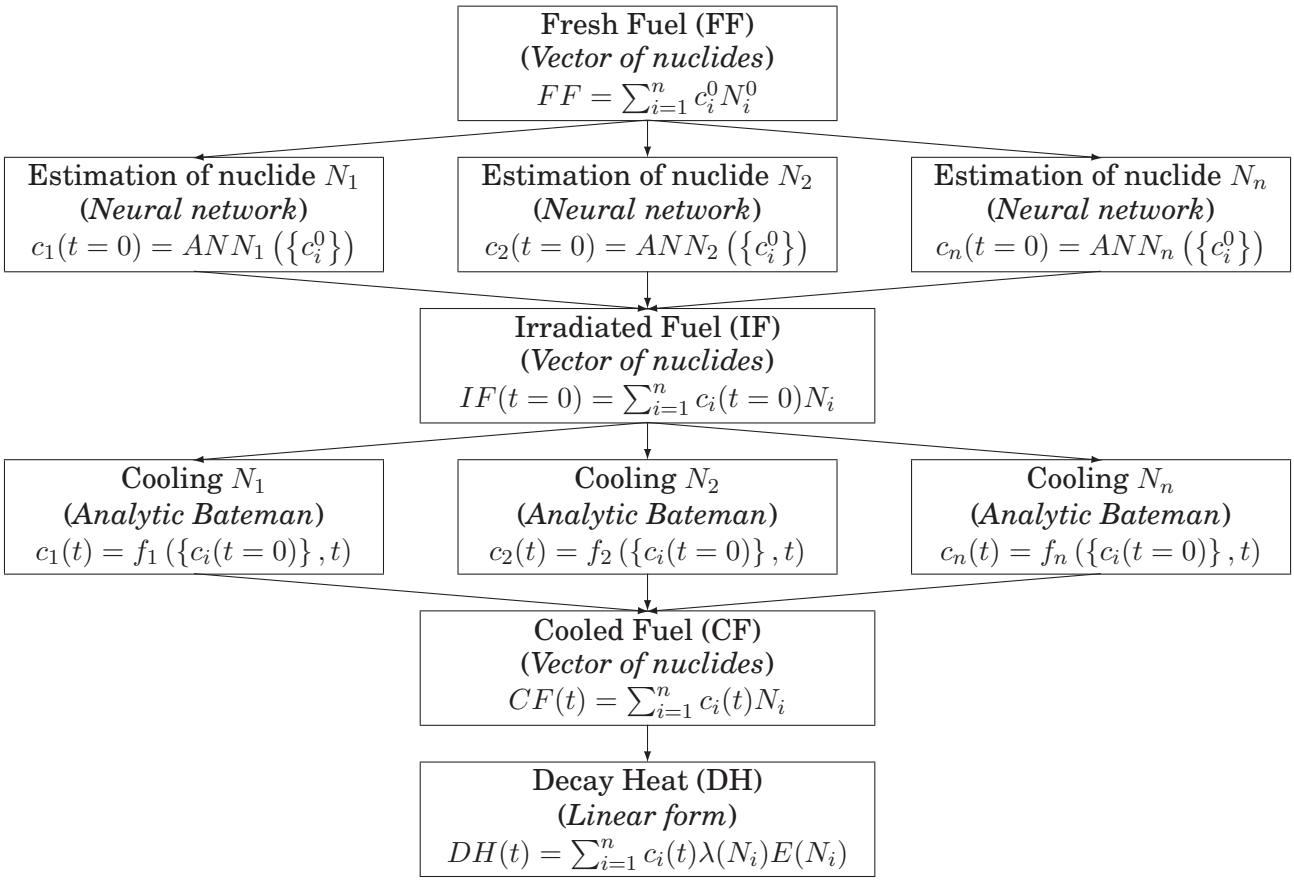

Figure 3.31: Calculation of decay heat via artificial neural networks and deterministic Bateman equation solution

3.2.4.4.2 PWR UOX fuel, nominal burnup

This benchmark is for PWR UOX fuel irradiated around nominal burnup. The fuel composition is enriched uranium (mass enrichment = 4.5%). The fuel is irradiated up to 45GWd/tHM in 1468 days. Figure 3.32 represents the decay heat calculated via COSI-CESAR5.3 and COSI-Surrogate Models-Analytic Bateman.

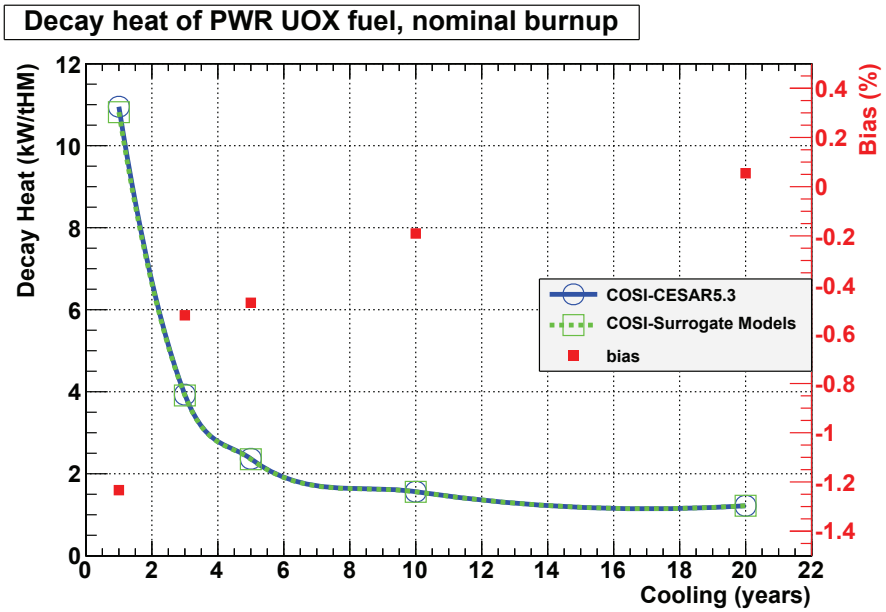

Figure 3.32: Comparison of decay heat calculated via ANN+deterministic Bateman and CESAR5.3 for PWR UOX fuel

The relative bias is low, and seems to tend towards zero when cooling time increases.

3.2.4.4.3 PWR UOX fuel, less than nominal burnup

This benchmark is for PWR UOX fuel irradiated below nominal burnup. The fuel composition is enriched uranium (mass enrichment = 4.5%). The fuel is irradiated up to 30GWd/tHM in 1304 days. Figure 3.33 represents the decay heat calculated via COSI-CESAR5.3 and COSI-Surrogate Models-Analytic Bateman.

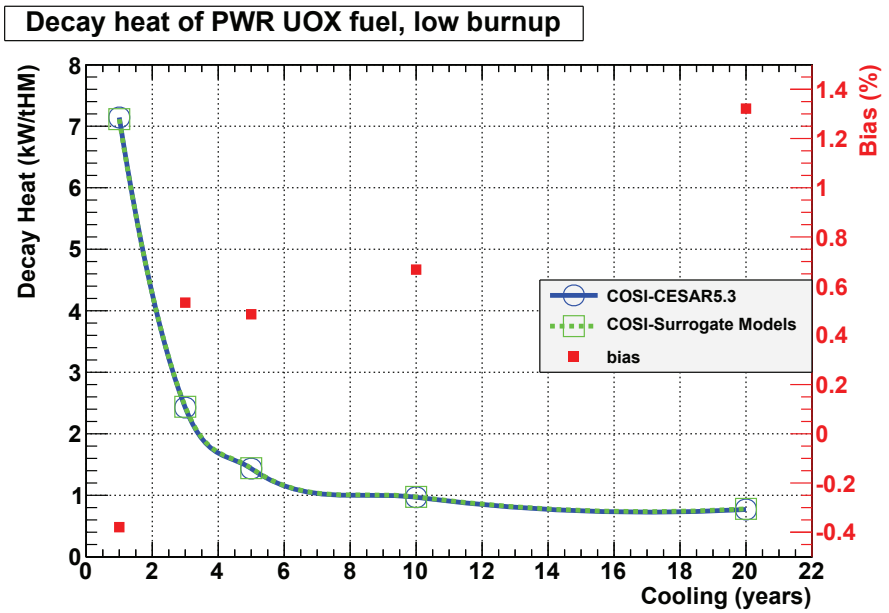

Figure 3.33: Comparison of decay heat calculated via ANN+deterministic Bateman and CESAR5.3 for PWR UOX fuel

Conclusions are similar: relative bias is low, and its absolute value decreases with time. The error at one year of cooling is higher. Analysis of output mass balance of the reactor showed that this error probably results from underestimation of ^{154}Eu with surrogate models. Other nuclides neglected may contribute as well given that decay heat analysis in table 3.38 concerns fuel irradiated at nominal burnup.

3.2.4.4.4 PWR repU fuel, nominal burnup

This benchmark is for PWR repU fuel irradiated around nominal burnup. The fresh fuel composition is given in table 3.64. The fuel is irradiated up to 45GWd/tHM in 1468 days. Figure 3.34 represents the decay heat calculated via COSI-CESAR5.3 and COSI-Surrogate Models-Analytic Bateman.

Nuclide	Mass fraction
^{234}U	0.11 %
^{235}U	4.05 %
^{236}U	1.38 %
^{238}U	94.46%

Table 3.64: Fresh fuel composition for PWR repU decay heat benchmark

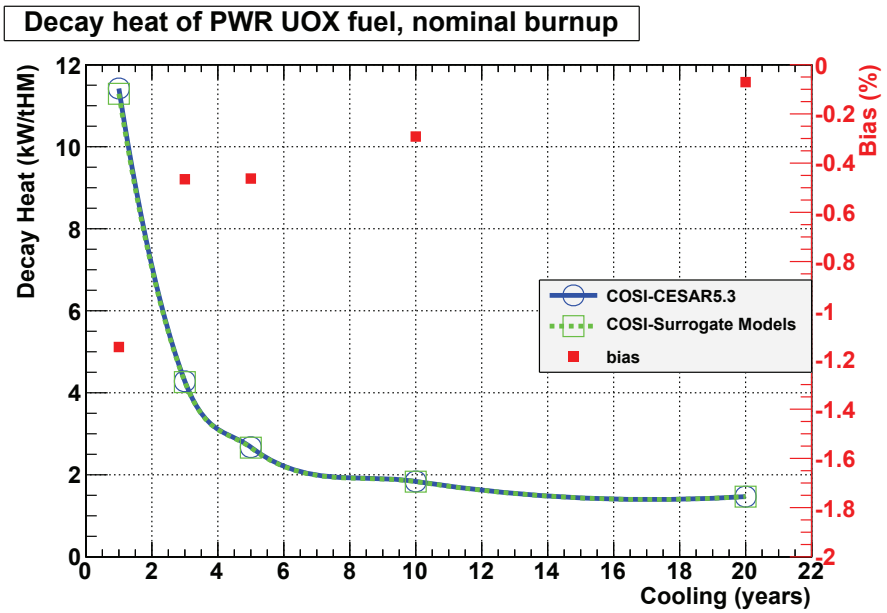

Figure 3.34: Comparison of decay heat calculated via ANN+deterministic Bateman and CESAR5.3 for PWR repU fuel

3.2.4.4.5 PWR MOX fuel, nominal burnup

The third benchmark is PWR MOX fuel irradiated around nominal burnup. Two plutonium vectors are considered, they are shown on table 3.65. Pu content is computed accordingly, using an equivalence model (mass content = 7.74% for isotopy A, 8.89% with isotopy B). The fuel is irradiated up to 46GWd/tHM in 1533 days. Figure 3.35 represents the decay heat calculated via COSI-CESAR5.3 and COSI-Surrogate Models-Analytic Bateman for fuel with isotopy A, and figure 3.36 in the case of isotopy B.

Nuclide	Isotopy A (mass content)	Isotopy B (mass content)
^{238}Pu	1.50%	2.50%
^{239}Pu	60.10 %	54.50%
^{240}Pu	25.30 %	25.20%
^{241}Pu	6.60%	8.60%
^{242}Pu	5.50%	7.90%
^{241}Am	1.00%	1.30%

Table 3.65: Plutonium vector for PWR MOX decay heat benchmark

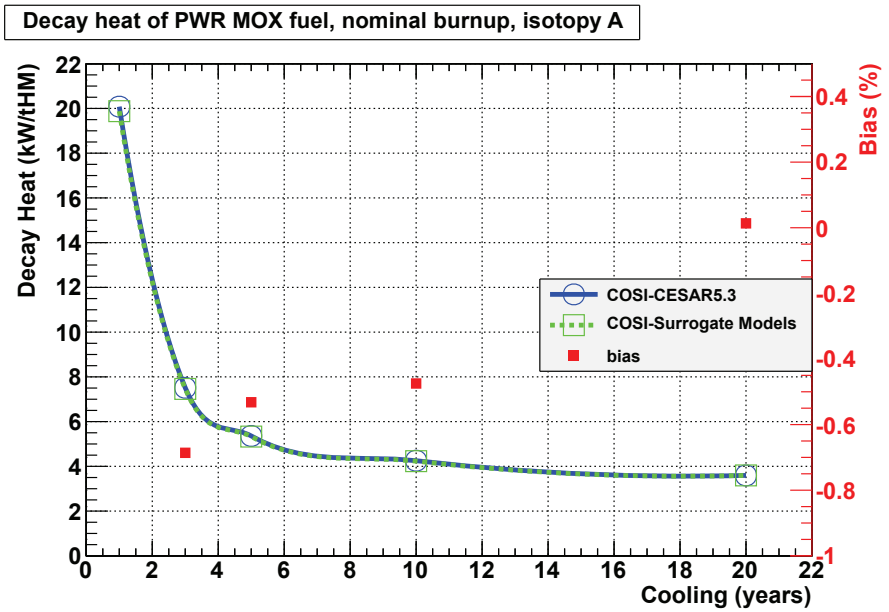

Figure 3.35: Comparison of decay heat calculated via ANN+deterministic Bateman and CESAR5.3 for PWR MOX fuel, nominal burnup, isotopy A

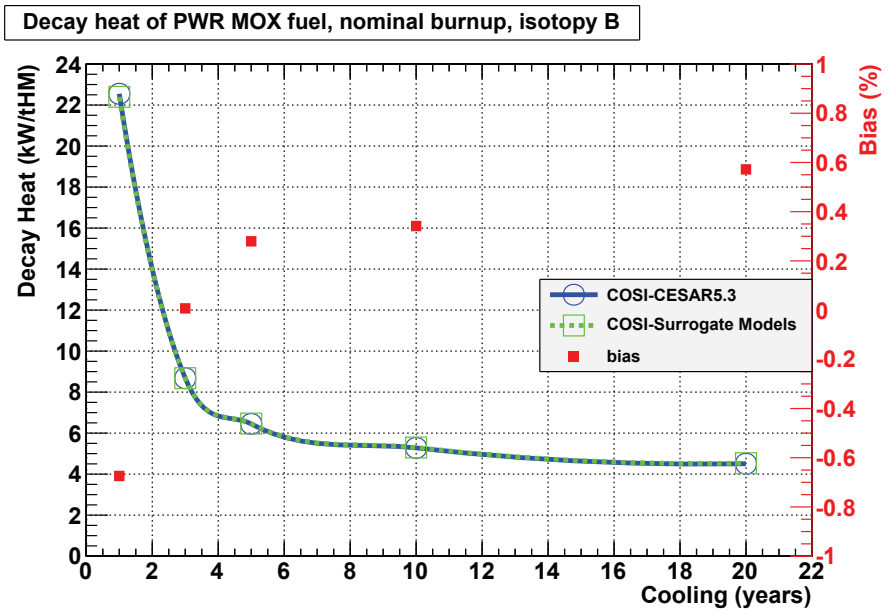

Figure 3.36: Comparison of decay heat calculated via ANN+deterministic Bateman and CESAR5.3 for PWR MOX fuel, nominal burnup, isotopy B

The surrogate models permit to estimate accurately decay heat in both cases. The bias for those two cases is different, but remains low.

3.2.4.4.6 PWR MOX fuel, less than nominal burnup

This benchmark is for PWR MOX fuel irradiated below nominal burnup. Plutonium composition is isotopy A, described in table 3.66. The fuel is irradiated up to 34.5GWd/tHM in 1150 days. Figure 3.37 represents the decay heat calculated via COSI-CESAR5.3 and COSI-Surrogate Models-Analytic Bateman.

Nuclide	Isotopy A (mass content)
^{238}Pu	1.50%
^{239}Pu	60.10 %
^{240}Pu	25.30 %
^{241}Pu	6.60%
^{242}Pu	5.50%
^{241}Am	1.00%

Table 3.66: Plutonium vector for PWR MOX low burnup, decay heat benchmark

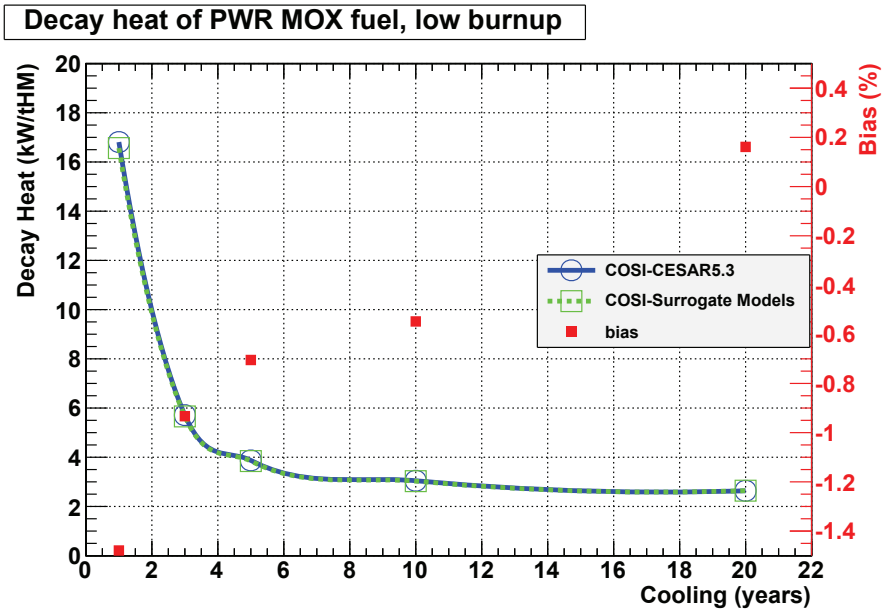

Figure 3.37: Comparison of decay heat calculated via ANN+deterministic Bateman and CESAR5.3 for PWR MOX fuel low burnup

Bias is low, and tends towards zero with cooling time. The contribution of ^{244}Cm is difficult to estimate very accurately in this burnup range, and its bias impacts the decay heat estimation.

3.2.4.4.7 SFR fuel, nominal burnup

The fourth benchmark is SFR MOX fuel irradiated at nominal burnup. The core model is CFV [3.13]. The Pu mass content of the fresh fuel is 21.32% and the plutonium vector composition is shown on table 3.67. The fuel is irradiated up to 116GWd/tHM in 2373 days. Figure 3.38 represents the decay heat calculated via COSI-CESAR5.3 and COSI-Surrogate Models-Analytic Bateman.

Nuclide	Mass fraction
^{238}Pu	2.66%
^{239}Pu	56.03 %
^{240}Pu	25.91 %
^{241}Pu	6.72%
^{242}Pu	7.30%
^{241}Am	1.38%

Table 3.67: Plutonium vector for SFR MOX decay heat benchmark

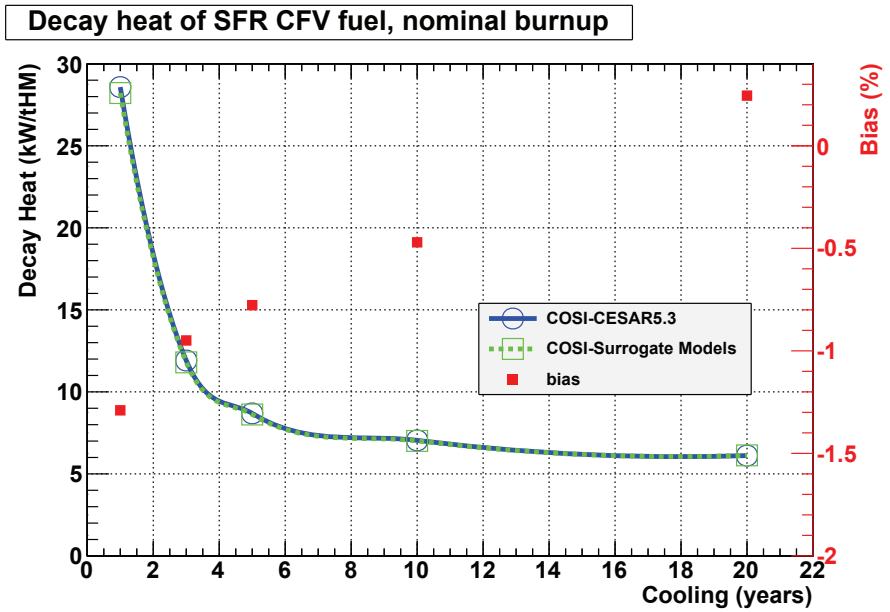

Figure 3.38: Comparison of decay heat calculated via ANN+deterministic Bateman and CESAR5.3 for SFR CFV fuel

The accuracy of decay heat estimator in the case of SFR fuel proves the lack of impact of the hypothesis of extension of the domain of validity of `list_FP` and `list_actinides`.

3.2.4.4.8 General validation

The following remarks can be made:

- the decay heat estimator is generally inferior to actual decay heat, however it can be superior after 20 years of cooling;
- overall the difference is below 2.0%;
- the relative difference tends to diminish with cooling time.

Given the shape of the error curve, we can assume that the difference mostly comes from the fact that several short-lived nuclides are not estimated by surrogate models or taken into account in the analytic solutions of the Bateman equation. However, most of the nuclides contributing to decay heat for t >1 year are calculated, therefore the error tends towards zero (+model bias) with time.

Figure 3.39 shows the different steps for the validation of the decay heat uncertainty propagation model. Black arrows represent the computation process and red arrows the different steps of the validation process.

A first sensitivity analysis, in function of nuclear data and other parameters, identifies the parameters impacting decay heat or concentration of isotopes involved in decay heat. Then surrogate models are validated, on two different levels: their accuracy is evaluated (relative error, mean error, etc.) as well as their variance propagation properties (q^2). A sensitivity study of the concentrations after cooling, obtained with Bateman equation, is performed, in order to guarantee decay heat is accurately calculated in function of the concentrations after irradiation. Finally, local tests of decay heat computation are performed for every surrogate model, in order to determine the local accuracy of the results. Analytic Bateman solutions are very accurate, therefore this step almost is transparent regards to uncertainty propagation (no further uncertainty is introduced, and the bias is very low), hence the uncertainty propagation properties of the decay heat model between 1 and 50 years are guaranteed by the variance properties of the irradiation surrogate models.

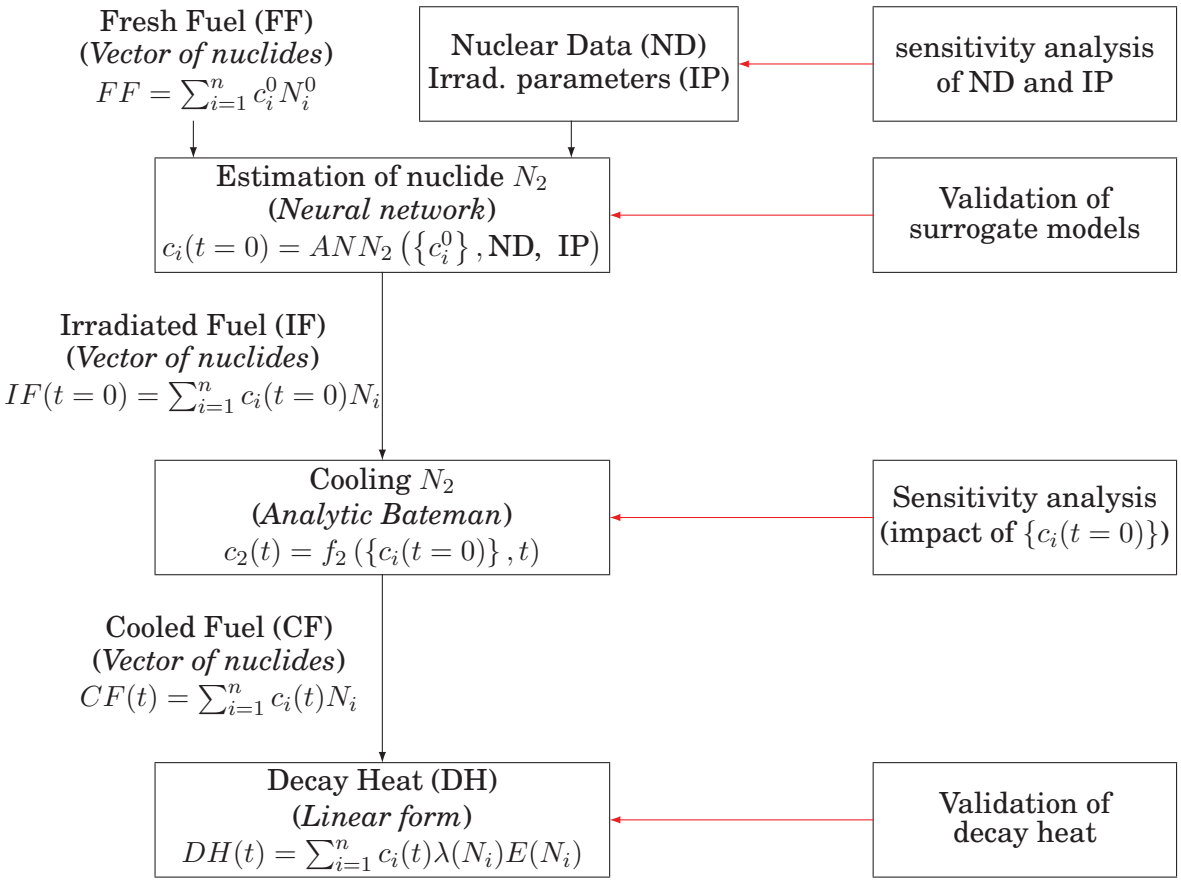

Figure 3.39: Different steps for validation of decay heat uncertainty propagation using MeSAR

The quality of these decay heat model is satisfying and it is therefore considered accurate enough to perform uncertainty propagation via decay heat. The uncertainty of decay heat will be transmitted to minimal cooling time uncertainty.

3.3 Blankets

3.3.1 Introduction

Several fuel types require a specific approach for the process of construction of irradiation models. In sections 3.1 and 3.2 , we only studied self-irradiated fuel, *ie* fuel producing its own irradiation spectrum. Several fuel types (ADS fuel, etc.) or blankets (fertile blankets, etc.) are irradiated by a spectrum produced by another material.

Although this phenomenon does not represent a conceptual difficulty, it makes the parameterization difficult. The next sections expose several examples that have been studied for this work.

3.3.2 Fertile blanket

3.3.2.1 Description

Fertile blankets are made of depleted uranium, they are irradiated by the flux produced in the core. Irradiation of fertile blankets produces initially plutonium through the reaction $^{238}\text{U} \xrightarrow{(n,\gamma),\beta-} {}^{239}\text{Pu}$. Given that the initial material is almost entirely composed of ^{238}U and the flux level is lower than in the core, production rate of heavier nuclides (^{240,242}Pu, Am, Cm) is sparse, therefore the quality (ratio of fissile isotopes of plutonium and total plutonium) of produced plutonium is relatively high and heavy nuclides are rare. Furthermore, the low fission rate in fertile blankets implicates low fission products concentration, consequently the low decay heat makes this material convenient in terms of handling, thus a reliable source of fresh plutonium.

In the case of fertile blankets, the concentration after irradiation of the blanket is a function of the parameters shown in table 3.68. The set of parameters is divided into two subsets, according to their material, or zone: the core and the blanket (potentially there can be different types of blankets). The burnup and the power are entirely determined by the core while mass fractions and cross-sections are material-dependent. However, in this work, me made the assumption that cross-sections perturbations are equal in the core and in the blankets.

		material	
		core	blanket
parameter	burnup	BU	
	power	$\mathcal{P}_{irrad}$	
	mass fractions	$m_i(core)$	$m_i(blanket)$
	Δ cross-sections	$\Delta\sigma_i(core)$	$\Delta\sigma_i(blanket)$

Table 3.68: Parameters of the (core + blanket) system

A relatively reliable method to model fertile blankets is to run one reference calculation, using ERANOS to model both the (reference) core and the blankets, and retrieve the output concentration vector. Given that SFR reactors are not subject to stretch-out, one output concentration vector is generally sufficient to describe every irradiated fertile blanket in a scenario calculation. This method does not take into account the core plutonium vector. However this approach is not satisfying in the case of uncertainty propagation in scenario studies, because the following parameters may vary:

- fertile blankets initial mass fractions;
- core initial mass fractions;
- cross-section perturbations;
- burnup.

3.3.2.2 Methods

3.3.2.2.1 Method 1

The first method consists in construction and implementation of surrogate models based on CESAR blankets libraries. Then, during the uncertainty propagation computation, the burnup of the core and the blankets is considered fully correlated.

The advantage of this method is that it is based on the same strategy as other depletion models. Consequently, it requires few developments.

The drawback is that the only link between a core and its blanket is full burnup correlation, consequently the following effects are neglected:

- actual correlation between core and blanker burnup;
- impact of core isotopy, plutonium content and cross-sections perturbations on the fertile blanket burnup and spectrum.

This method was used for construction of the following models:

- inferior fertile blanket in SFR CFV core;
- internal fertile blanket in SFR CFV core;
- americium bearing blanket in SFR CFV core.

3.3.2.2.2 Method 2

3.3.2.2.3 Overview

We propose another approach: building fertile blankets surrogate models based on ERANOS, parameterized with both core and blanket parameters. First these surrogate models can be used to calculate with a better precision that the fixed concentration, as it takes into account the core power and isotopy. Then it performs cross-section and potentially other nuclear data uncertainty propagation during irradiation of the blanket.

3.3.2.2.4 Sampling

The parameters of the core and the fertile blanket are sampled at the same time. Sampling is performed according to section 3.1.2 for the core zone: mass fractions, irradiation parameters and cross-section perturbations are taken into account.

The fertile blanket does not have peculiar irradiation parameters, as they fully depend on the core irradiation parameters. The neutron spectrum and flux are different, but they are functions of the core parameters, and are implicitly taken into account during the (transport + irradiation) calculation. However, the uranium composition of the fertile blanket can potentially slightly vary from a batch to another. Although not absolutely significant, the possibility of blanket

composition parameterization was taken into account, and the uranium vector of the blanket was sampled.

On a side note, the composition of the blanket is significant in the case of irradiation of minor actinides bearing blankets used for transmutation of minor actinides in SFR.

3.3.2.2.5 Regression

3.3.2.2.5.1 Qualitative analysis

Artificial neural networks were used as estimators for the blanket composition after irradiation in function of the different parameters. The construction process of ANN is the same as described in part 3.1.3.2. Fission products were not taken into account as fission is sparse in fertile blankets.

Fertile blankets are made of depleted uranium, and the flux is relatively low compared to other core regions. Therefore production rate of very heavy nuclides such as ^{242M,243}Am, $^{242,243,244...}$Cm is small, and substantially lower than production of common Np and Pu isotopes. Therefore it was chosen to only model the following list of nuclides:

$$\texttt{list_iso_Blanket} = \left\{^{235,236,238}\text{U},\ ^{237,239}\text{Np},\ ^{238,239,240,241,212}\text{Pu},\ ^{241}\text{Am}\right\}$$

Some of those nuclides (^{238,242}Pu, ^{241}Am) are modeled principally in order to assess precisely the quality of the output plutonium vector.

3.3.2.2.5.2 Application

ANN estimators were constructed for nuclides present in `list_iso_Blanket`. Table 3.69 summarizes the quality indexes of the estimators. Each estimator estimates the sum of the masses of a given nuclide in both the upper and lower blankets.

Estimators of plutonium isotopes are very accurate, and return the output concentration with a good precision. Estimators of U and ^{237}Np are not very accurate. The reason of this lack of fit is that the blanket uranium isotopy was not taken into account for this surrogate model. This isotopy could be taken into account, however the output concentrations in U and ^{237}Np are rather unimportant, therefore a model based on an average value will speed-up the computation without degrading too much the results in terms of physical meaning.

actinide	r^2	q^2	$max\|\hat{y}/y-1\|$	$mean\|\hat{y}/y-1\|$	$max\|(\hat{y}-y)/\bar{y}\|$	$mean\|(\hat{y}-y)/\bar{y}\|$
^{235}U	0.996548	0.98753	30.222 %	4.095 %	17.055 %	3.356 %
^{236}U	0.999467	0.998895	9.347 %	1.381 %	3.956 %	1.008 %
^{238}U	0.999288	0.997875	0.161 %	0.028 %	0.159 %	0.028 %
^{237}Np	0.998318	0.995949	2.186 %	0.65 %	2.569 %	0.643 %
^{239}Np	0.999737	0.997831	0.63 %	0.2 %	0.556 %	0.199 %
^{238}Pu	0.999414	0.998005	1.575 %	0.575 %	1.796 %	0.57 %
^{239}Pu	0.999867	0.999718	0.19 %	0.059 %	0.2 %	0.059 %
^{240}Pu	0.999867	0.999741	0.631 %	0.168 %	0.534 %	0.164 %
^{241}Pu	0.999884	0.999527	1.392 %	0.535 %	0.924 %	0.339 %
^{242}Pu	0.999901	0.999737	1.59 %	0.387 %	1.178 %	0.363 %
^{241}Am	0.999834	0.9996	1.669 %	0.339 %	1.252 %	0.321 %

Table 3.69: Quality indexes of fertile blankets in SFR reactor

Identity cards summarizing the information of the estimators were filled. Fertile blankets estimators are easier to build than irradiated fuel estimators because they are much less dependent on the composition. Furthermore this model was made for nominal burnup SFR core, which is not subject to stretch-out, therefore burnup is not the most important and non-linear parameter as it usually is.

Figure 3.40 shows an identity card of one of the output nuclides in a fertile blanket estimated by ANN surrogate models.

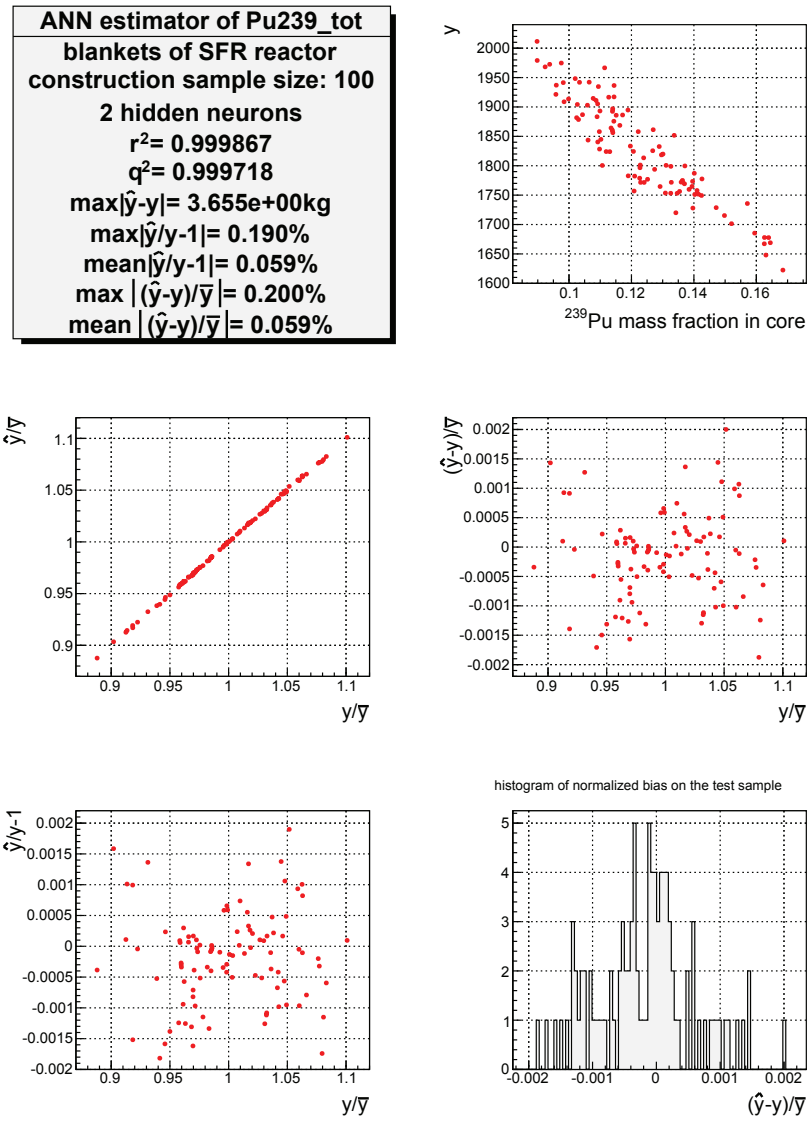

Figure 3.40: Identity card of the ^{239}Pu estimator in PWR UOX fuel, BU>38GWd/tHM

The ANN estimator of ^{239}Pu concentration after irradiation in fertile blanket was built on a restricted DOE (only 100 points in the construction sample and in the test sample) using only 2 hidden neurons, thus respecting the principle of parsimony.

3.3.2.2.6 Implementation

Two new types of fuel batches were implemented in COSI: a fissile batch, representing the core of the reactor, and a fertile batch, representing the blanket. These batches are special in the way they are linked together during a scenario computation[9]. They are composed of different fuel, but they are irradiated in the same reactor, at the same time. The link between those

[9]the list of tasks is overridden so that the core depletion is computed and stored first, and a specific method in the blanket object locates the core object and extracts parameters of interest, such as burnup and fresh fuel composition

batches allows the irradiation method to read data associated to both the blanket and the core during irradiation computation of the fertile blanket. The implementation also required the prioritization of the core batch irradiation, in order to calculate the initial mass fractions via equivalence model first, so as to use them later during the blanket irradiation computation.

Despite its implementation, method B was not used in this work. However, this method seems well adapted to description of coupled systems such as { SFR core - MABB }, and may be used in further studies.

3.4 Conclusions and perspectives

3.4.1 Conclusions

Depletion surrogate models were built. The method giving the best results is based on artificial neural networks. These models enable uncertainty propagation computation in scenario studies, because they estimate very fastly nuclides of interest, from the point of view of scenario studies, in spent fuel in function of the following parameters:

- fresh fuel composition;
- irradiation parameters;
- nuclear data perturbations.

3.4.2 Perspectives

The perspectives include the following tasks:

- addition of other cross-section perturbations in surrogate models, such as scattering and (n,2n);
- spent fuel concentrations sensitivity studies, so as to neglect several parameters in surrogate models:
  - cross-sections;
  - fission yields;
- comparison of results with a reference code, such as DARWIN;
- comparison of results with surrogate models made from other codes, such as DARWIN.

Bibliography

[3.1] M.B. Chadwick, M. Herman, P. Obložinský, et al. ENDF/B-VII.1 nuclear data for science and technology: Cross sections, covariances, fission product yields and decay data. *Nuclear Data Sheets,*, Volume 112, Issue 12:2887–2996, 2011.

[3.2] C. De Saint Jean, P. Archier, G. Noguere, O. Litaize, C. Vaglio-Gaudard, D. Bernard, and O. Leray. Estimation of multi-group cross section covariances for ^{235,238}U, ^{239}Pu, ^{241}Am, ^{56}Fe, ^{23}Na, and ^{27}Al. In *PHYSOR 2012 - Advances in Reactors Physics*, 2012.

[3.3] X.B. Ma, W.L. Zhong, L.Z. Wang, Y.X. Chen, and J. Cao. Improved calculation of the energy release in neutron-induced fission. *Physical review*, C88, 2013.

[3.4] K. Hornik. Approximation capabilities of multilayer feedforward networks. *Neural Networks*, 4(2):251–257, 1991.

[3.5] G. Cybenko. Approximations by superpositions of sigmoidal functions. *Mathematics of Control, Signal, and Systems*, 2(4):251–257, 1989.

[3.6] A.R. Barron. Universal approximation bounds for superpositions of a sigmoidal function. *IEFF Transactions on information theory*, 39(3):930–945, 1993.

[3.7] G. Dreyfus, J.-M. Martinez, M. Samuelides, M.B. Gordon, F. Badran, and L. Hérault S. Thiria. *Réseaux de neurones, Méthodologie et applications*. Editions Eyrolles, 2002.

[3.8] J. Shlens. A tutorial on principal component analysis. Technical report, Center for Neural Science, New York University, 2009.

[3.9] J.C. Benoît. *Développement d'un code de propagation des incertitudes des données nucléaires sur la puissance résiduelle dans les réacteurs à neutrons rapides*. PhD thesis, Université Paris-Sud, 2012.

[3.10] A.L. Nichols. Nuclear data requirements for decay heat calculation. International Atomic Energy Agency, Nuclear Data Section, Department of Nuclear Sciences and Applications, Vienna, Austria, 2002.

[3.11] A. Tzilanizara, C. Diop, B. Nimal, M. Detoc, L. Luneville, M. Chiron, T.D. Huynh, I. Bresard, I. Eid, J.C. Klein, et al. DARWIN: an evolution code system for a large range of applications. In *Procs of ICRS-9*, 1999.

[3.12] L. San-Felice, R. Eschbach, P. Bourdot, A. Tsilanizara, and T.D. Huynh. Experimental validation of the DARWIN2.3 package for fuel cycle applications. In *PHYSOR2012 - Advances in Reactor Physics*, 2012.

[3.13] B. Fontaine, N. Devictor, P. Le Coz, A. Zaetta, D. Verwaerde, and J-M. Hamy. The French R&D on SFR core design and ASTRID Project. In *Proceedings of GLOBAL2011, Paper No. 432757*, 2011.

Chapter 4

Equivalence models

Contents

4.1 Introduction 152
4.2 State of the art 152
4.2.1 Presentation 152
4.2.2 Perturbative SFR MOX model 152
4.2.3 Transport calculation for SFR MOX 155
4.2.4 Tabulated PWR MOX model 156
4.2.5 Conclusions 156
4.3 Data-driven equivalence models 157
4.3.1 Introduction 157
4.3.2 SFR MOX equivalence models 157
4.3.3 PWR MOX equivalence model 169
4.3.4 Implementation in COSI 174
4.4 Conclusions and perspectives 175

4.1 Introduction

In PWR UOX reactors, fuel composed of enriched uranium is irradiated. For a given core, uranium enrichment is invariant, and was once defined such as the core respects a criteria, formulated in terms of criticity, at the end of every irradiation cycle. This criteria ensures that, considering boron concentration and computation bias, the core is able to remain critical until irradiation cycle is over.

However, the problem is different for other fuel types (MOX, Th-^{233}U, repU, etc.) which are not directly made from natural elements.

MOX fuel is composed of a mix of depleted uranium and plutonium, which isotopic vector varies according to its origin; parameters include, *inter alia*, the nature of the fuel comes from (PWR UOX, PWR MOX, SFR MOX, fuel, etc.) and burnup.

Every plutonium isotope does not contribute equally to reactivity, and irradiation in general. For instance, ^{239}Pu is an efficient fissile material, it has relatively high fission cross-section in the thermal domain, fissioning more often than capturing, and has a high multiplicity factor, whereas ^{240}Pu captures more than it fissions. Therefore isotopic composition affects the so-called *quality* of plutonium. A simple measure of plutonium quality, in terms of reactivity, is the sum of fissile isotopes mass fractions:

$$q = \frac{m(^{239}\mathrm{Pu} + {}^{241}\mathrm{Pu})}{m(^{238}\mathrm{Pu} + {}^{239}\mathrm{Pu} + {}^{240}\mathrm{Pu} + {}^{241}\mathrm{Pu} + {}^{242}\mathrm{Pu} + {}^{241}\mathrm{Am})} \tag{4.1}$$

Intuitively, quality of a given plutonium vector is linked to the plutonium content necessary to maintain criticity over fuel irradiation: the higher the quality, the lower the plutonium content. However, this relation is qualitative, and gives no information on the numeric value of the content.

The concept of equivalence model generalizes the concept of isotopic quality to quantitative determination of fresh fuel mass content in function of the isotopic vector:

$$mass\ content = function(isotopic\ vector)$$

4.2 State of the art

4.2.1 Presentation

This section summarizes the state of the art of equivalence models used in nuclear scenario computations, and provides a brief analysis of these models, principally in terms of bias and uncertainty propagation.

4.2.2 Perturbative SFR MOX model

4.2.2.1 Equivalent plutonium content

Let H denote the Boltzmann operator, ρ the reactivity, ϕ and ϕ^+ the flux and adjoint flux of a system, ΔH the perturbation operator, P the production operator, and $\Delta\rho$ the reactivity variation

due to ΔH. Then, application of first order perturbation theory on the system (fuel) for reactivity gives ([4.1]):

$$\Delta\rho \approx \frac{\langle \phi^+, \Delta H \phi \rangle}{\langle \phi^+, P\phi \rangle} \tag{4.2}$$

Let us consider that two fuel compositions are equivalent if their initial reactivity is equal. It is then possible to give an equivalent fuel composed of ^{238}U and ^{239}Pu only. Let t be the plutonium mass content of the equivalent fuel:

$$t = \left. \frac{m(^{239}\mathbf{Pu})}{m(^{239}\mathbf{Pu}) + m(^{238}\mathbf{U})} \right|_{\text{equiv. fuel}} \tag{4.3}$$

And ξ'_i the contents of the different isotopes in the other fuel:

$$\xi'_i = \left. \frac{m(i)}{\sum\limits_i m(i)} \right|_{\text{other fuel}} \tag{4.4}$$

We denote:

$$\sigma^+ = \nu\sigma_f - \sigma_c \tag{4.5}$$

The numerator of equation 4.2 is null for two equivalent fuel compositions:

$$\int \left[\sum_{i \in \text{all isotopes}} \xi'_i \sigma_i^+(u) - (1-t)\sigma^+_{^{238}\mathbf{U}} - t\sigma^+_{^{239}\mathbf{Pu}}(u) \right] \phi^+(u)\phi(u)du = 0 \tag{4.6}$$

We denote:

$$\bar{\sigma^+} = \frac{\int \sigma^+(u)\phi(u)\phi^+(u)}{\int \phi(u)\phi^+(u)} \tag{4.7}$$

and:

$$\omega_i = \frac{\bar{\sigma_i^+} - \bar{\sigma^+_{^{238}\mathbf{U}}}}{\bar{\sigma^+_{^{239}\mathbf{Pu}}} - \bar{\sigma^+_{^{238}\mathbf{U}}}} \tag{4.8}$$

We obtain:

$$t = \sum_i \omega_i \xi'_i \tag{4.9}$$

Expression of the plutonium content in the other fuel is:

$$t' = \frac{t - \sum\limits_{i \in \mathbf{U}} \xi'_i \omega_i}{\sum\limits_{i \in \mathbf{Pu}} \xi'_i \omega_i - \sum\limits_{i \in \mathbf{U}} \xi'_i \omega_i} \tag{4.10}$$

The weights ω_i associated to reactions are computed using a transport code, such as ERANOS [4.2].

4.2.2.2 Uncertainty propagation

We make the hypothesis that changes in fuel composition are small enough to neglect both flux and cross-sections modifications throughout the cycle. This hypothesis is valid only because the spectrum is fast.

We derive the ω_i terms of equation 4.10 by cross-sections:

$$
\begin{aligned}
\forall i: \quad \frac{\partial \omega_{^{238}\mathrm{U}}}{\partial \sigma_i} &= 0 \\
\forall i: \quad \frac{\partial \omega_{^{239}\mathrm{Pu}}}{\partial \sigma_i} &= 0 \\
\forall i, \forall j \notin \{^{238}\mathrm{U}, {}^{239}\mathrm{Pu}, i\}: \quad \frac{\partial \omega_i}{\partial \sigma_j} &= 0 \\
\forall i \notin \{^{238}\mathrm{U}, {}^{239}\mathrm{Pu}\}: \quad \frac{\partial \omega_i}{\partial \sigma_{c,j}} &= \frac{-1}{\bar{\sigma}^+_{^{239}\mathrm{Pu}} - \bar{\sigma}^+_{^{238}\mathrm{U}}} \\
\frac{\partial \omega_i}{\partial \sigma_{f,i}} &= \frac{\nu}{\sigma^+_{^{239}\mathrm{Pu}} - \sigma^+_{^{238}\mathrm{U}}} \\
\frac{\partial \omega_i}{\partial \sigma_{c,^{238}\mathrm{U}}} &= \frac{\bar{\sigma}^+_{^{239}\mathrm{Pu}} - \bar{\sigma}^+_i}{\bar{\sigma}^+_{^{239}\mathrm{Pu}} - \bar{\sigma}^+_{^{238}\mathrm{U}}} \\
\frac{\partial \omega_i}{\partial \sigma_{f,^{238}\mathrm{U}}} &= \frac{(1-\nu)(\bar{\sigma}^+_{^{239}\mathrm{Pu}} - \bar{\sigma}^+_i)}{\bar{\sigma}^+_{^{239}\mathrm{Pu}} - \bar{\sigma}^+_{^{238}\mathrm{U}}} \\
\frac{\partial \omega_i}{\partial \sigma_{c,^{239}\mathrm{Pu}}} &= \frac{\bar{\sigma}^+_i - \bar{\sigma}^+_{^{238}\mathrm{U}}}{\bar{\sigma}^+_{^{239}\mathrm{Pu}} - \bar{\sigma}^+_{^{238}\mathrm{U}}} \\
\frac{\partial \omega_i}{\partial \sigma_{f,^{239}\mathrm{Pu}}} &= \frac{(1-\nu)(\bar{\sigma}^+_i - \bar{\sigma}^+_{^{238}\mathrm{U}})}{\bar{\sigma}^+_{^{239}\mathrm{Pu}} - \bar{\sigma}^+_{^{238}\mathrm{U}}}
\end{aligned}
\tag{4.11}
$$

Then we can sample the cross-sections according to their uncertainty distribution so as to calculate the perturbed ω_i using equation 4.11:

$$
\omega_i^{pert} = \omega_i + \sum_j \frac{\partial \omega_i}{\partial X_j} \Delta X_j \tag{4.12}
$$

This method enables to perform nuclear data uncertainty propagation in the equivalence model used in COSI for SFR fuel.

4.2.2.3 Advantages and drawbacks

This method is easy to implement and to use, and is compatible with existing equivalence model, to perform uncertainty propagation.

However, it has the following drawbacks:

- necessity to calculate new $\frac{\partial \omega_i}{\partial X}$ for any new fuel compositions;
- equivalence is calculated before irradiation, not at the end of a cycle;
- the method cannot be applied to PWR fuel because of the spectrum hypothesis.

4.2.3 Transport calculation for SFR MOX

4.2.3.1 Overview

For this case, we directly use the example of SFR CFV core [4.3]. The CFV core is divided into five fractions. At the end of a cycle, the core average burnup is:

$$\begin{aligned} \overline{\mathrm{BU}}_{end\ of\ cycle} &= L_{cycle} \times \left(\frac{1}{5} + \frac{2}{5} + \frac{3}{5} + \frac{4}{5} + \frac{5}{5} \right) \\ &= 3 \times L_{cycle} \end{aligned} \tag{4.13}$$

On a side note, generalization of this formula is shown on equation 4.14, n being the core fractionation:

$$\begin{aligned} \overline{\mathrm{BU}}_{end\ of\ cycle} &= \frac{n+1}{2} \times L_{cycle} \\ &= \frac{n+1}{2n} \times \mathrm{BU}_{end\ of\ irradiation} \end{aligned} \tag{4.14}$$

The equivalence condition is : *the core reactivity at the end of a cycle must be equal to zero*. Let $\{y_i\}$ be the plutonium isotopic vector. The problem is to find the mass content of plutonium t such as core reaches the target reactivity ρ^{core}_{target} at the end of a cycle:

$$\rho^{core}(t, \{y_i\}, \overline{\mathrm{BU}}_{end\ of\ cycle}) = \rho^{core}_{target} \tag{4.15}$$

A method implemented in ERANOS [4.2] resolves this equation iteratively using Newton's method, with a variable number of steps. Each step corresponds to a new irradiation calculation. The calculated plutonium content satisfies the following condition (ε is a convergence criterion):

$$\left| \rho^{core}(t, \{y_i\}, \overline{\mathrm{BU}}_{end\ of\ cycle}) - \rho^{core}_{target} \right| < \varepsilon \tag{4.16}$$

Numerical values for the computation usually are:

$$\begin{cases} \rho^{core}_{target} = 0 \\ \varepsilon = 100pcm \end{cases} \tag{4.17}$$

4.2.3.2 Advantages and drawbacks

The advantage is the accuracy of the result: as it is directly evaluated by a transport code, it is not subject to approximations due to use of first order perturbation theory or statistical estimators. We remark that performing perturbed transport computation allows to compute perturbed equivalence content.

However, the main drawback of this method is the computation time. Indeed as computation of one content takes around one hour (depending on the system), and implementation of the equivalence condition in COSI is such that several equivalence computations are often required to evaluate the plutonium content of one batch. Indeed plutonium is obtained from reprocessing of different fuel batches which composition may differ, and if the plutonium mass required to make fresh fuel is superior to the plutonium mass available in a batch, plutonium from reprocessing of another batch, which has a different composition, has to be added. This phenomenon changes fresh fuel isotopy. Therefore, another iteration of transport computations has to be performed.

This method is suited to reference computation and validation of other equivalence methods. However, computation of equivalence using this method for uncertainty propagation is not possible due to constraints on computation time.

4.2.4 Tabulated PWR MOX model

4.2.4.1 Presentation

Several tabulated equivalence models for PWR MOX are implemented in COSI. These models use regression techniques such as multiple linear and polynomial regressions, parameterized in isotopy, end-of-irradiation burnup and fractionation. Parameters are obtained through perturbative transport computations. Those models are validated on the MOX fuel loaded in CPY reactors of the French fleet.

4.2.4.2 Advantages and drawbacks

The main advantage is that these models give an accurate representation of the PWR MOX actual content. However, they cannot perform uncertainty propagation, as they are not parameterized with nuclear data. Furthermore, as they consist in regressions, it is not possible to obtain analytical expressions of the impact of perturbations as in section 4.2.2.

4.2.5 Conclusions

Models listed in the previous sections cannot be used to perform nuclear data uncertainty propagation studies.

Construction of an equivalence model based on the analytical expression of reactivity at the end of an irradiation cycle would be very interesting. However this expression is too complex to be evaluated without extremely strong hypotheses.

Performing nuclear data uncertainty propagation in equivalence models requires constructing a model with the following properties:

- equivalence condition at the end of a cycle;
- possibility of parameterization with nuclear data;
- short computation time.

Innovative models fullfilling these conditions are presented in section 4.3.

4.3 Data-driven equivalence models

4.3.1 Introduction

Statistical estimators based on perturbative transport computations are good candidates for uncertainty propagation in equivalence models. First of all, they can estimate the best fuel enrichment so as to reach a given equivalence condition at the end of a cycle. Then, if their construction process includes parameterization of the transport computation with nuclear data, they can perform nuclear data uncertainty propagation. Finally, as estimators, their computation time is most likely negligible compared to a scenario computation time.

4.3.2 SFR MOX equivalence models

4.3.2.1 Introduction

In sections 4.3.2.2 and 4.3.2.3, we will build enrichment estimators based on unperturbed computations, so as to build relatively simple equivalence models for scenario studies and compare them. Then, in section 4.3.2.4 we refine the method and add cross-section perturbations as parameters.

4.3.2.2 Method A: estimator based on iterative transport computations

4.3.2.2.1 Description of the method

The idea of method A is to produce an estimator of the results given by the method described in section 4.2.3.1. The method must produce, as a result, an estimator of the plutonium content in function of the plutonium isotopy of the core, such that the reactivity at the end of a cycle is null. The problem is to find $\hat{t}\left(\{y_i\}\right)$ such that:

$$\rho^{core}(\hat{t}\left(\{y_i\}\right), \{y_i\}, \overline{\mathrm{BU}}_{end\ of\ cycle}) = 0 \tag{4.18}$$

We propose the following method:

- sample the plutonium isotopic vector $\{y_i\}$;
- for each isotopic vector $\{y_i\}$, evaluate t such as $\rho^{core}(t, \{y_i\}, \overline{\mathrm{BU}}_{end\ of\ cycle}) = 0$ using ERANOS Newton's algorithm;
- build an estimator $\hat{t}\{y_i\}$ of the plutonium content evaluated by ERANOS.

4.3.2.2.2 Application

4.3.2.2.2.1 Sampling

This section shows the application of method A to create a CFV core equivalence model. Parameters are sampled uniformly, the intervals of variation are summarized in table 4.1. Intervals are determined so as to include the whole isotopic range in scenario studies. We denote $i(n)$ the isotopy of a nuclide $n \in \{\mathrm{Pu}, {}^{241}\mathrm{Am}\}$ such as:

$$i(n) = \frac{m(n)}{m(\mathrm{Pu} + {}^{241}\mathrm{Am})} \tag{4.19}$$

The plutonium vector isotopy is taken into account, as well as the ^{235}U content in depleted uranium. The isotopy $i(^{240}\text{Pu})$ is large enough to be used as a buffer for the other isotopies.

parameter	min (%)	max (%)
$i(^{238}\text{Pu})$	2.0	4.0
$i(^{239}\text{Pu})$	35.0	60.0
$i(^{240}\text{Pu})$	$100 - \sum_{n \in \text{Pu},^{241}\text{Am}} i(n)$	
$i(^{241}\text{Pu})$	7.0	12.0
$i(^{242}\text{Pu})$	6.0	15.0
$i(^{241}\text{Am})$	0.1	4.0
$m(^{235}\text{U})/m(\text{U})$	0.1	0.3
$m(^{238}\text{U})/m(\text{U})$	$100 - m(^{235}\text{U})/m(\text{U})$	

Table 4.1: Intervals of variation for CFV equivalence model, method A

ERANOS returns the volumetric enrichment in plutonium e. We use this result to calculate the mass enrichment t such as:

$$t = \frac{e \times \rho_{Pu}}{e \times \rho_{Pu} + (1 - e) \times \rho_U} \tag{4.20}$$

with:

$$\begin{cases} \rho_{Pu} &= \sum_{j \in Pu} i(j) \times \rho_j \\ \rho_U &= \sum_{j \in U} i(j) \times \rho_j \end{cases} \tag{4.21}$$

The DOE consists in 600 points sampled according to table 4.1, using LHS as the sampling algorithm. For each point of the DOE, we perform an ERANOS computation of the plutonium content such as $\rho^{core}(\hat{t}\left(\{y_i\}\right), \{y_i\}, \overline{\text{BU}}_{end\ of\ cycle}) = 0$.

Figure 4.1 illustrates the plutonium content computed by ERANOS in function of $i(^{239}\text{Pu})$. We can observe that the higher the ^{239}Pu isotopy is, the lower the Pu content necessary to achieve $\rho(\overline{\text{BU}}_{end\ of\ cycle}) = 0$ is.

4.3.2.2.2.2 Regression

We decide to build ANN estimators of the plutonium content. The ANN parameters are those described in table 4.1. The complexity of this model is relatively low. Consequently, there is no reason for the choice of ANN over polynomial regressions or any other estimator except the presence in COSI of a previous implementation of ANN for different studies[1]. First, we divide the DOE into two subsets of equal size (300 points): a construction sample, and a test sample.

We build ANN estimators based on the construction sample. Figure 4.2 represents the r^2 and q^2 estimators of the model in function of the number of neurons in the hidden layer. Table 4.2 summarizes a few quality criteria for each ANN, calculated on the test sample.

Even the simplest ANN estimator, composed of one neuron in the hidden layer, returns a satisfying plutonium content. On the contrary, increasing too much the number of neurons reduces the overall quality of the estimator because the construction sample is relatively small. According to

[1] irradiation models, see chapter 3 page 53

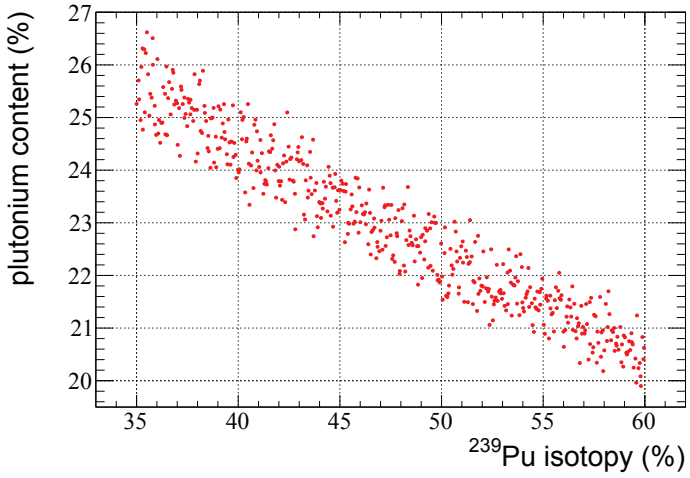

Figure 4.1: Plutonium content such that $\rho(\overline{\mathrm{BU}}_{end\ of\ cycle}) = 0$ in function of ^{239}Pu isotopy for SFR CFV equivalence model

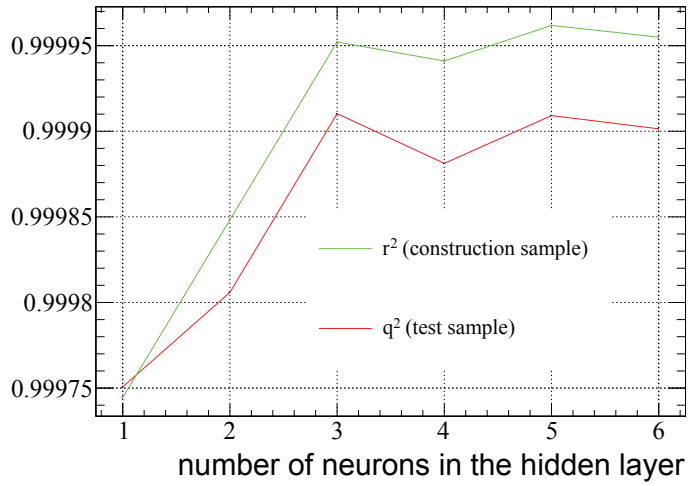

Figure 4.2: Global quality indicators of the plutonium content ANN estimators for SFR CFV equivalence model, method A

number of hidden neurons	$mean\|(\hat{t}-t)/t\|$	$max\|(\hat{t}-t)/t\|$	$mean\|(\hat{t}-t)/\bar{t}\|$	$max\|(\hat{t}-t)/\bar{t}\|$
1	0.08%	0.37%	0.08%	0.41%
2	0.07%	0.34%	0.04%	0.37%
3	0.03%	0.30%	0.04%	0.33%
4	0.04%	0.31%	0.04%	0.35%
5	0.03%	0.31%	0.03%	0.34%
6	0.04%	0.32%	0.04%	0.34%

Table 4.2: Bias of the Pu content estimators for SFR CFV equivalence model, method A

figure 4.2 and table 4.2, an ANN containing three neurons in the hidden layer seems adequate. For the rest of this study, only the ANN containing three neurons in the hidden layer will be considered.

Figure 4.3 represents the application of the plutonium content estimator on the test base in function of the plutonium content, and figure 4.4 the absolute error $(\hat{t}-t)$ in function of t. Globally the prediction quality is satisfying, the ANN with three neurons is a reliable estimator of the plutonium content, and the absolute error remains very low.

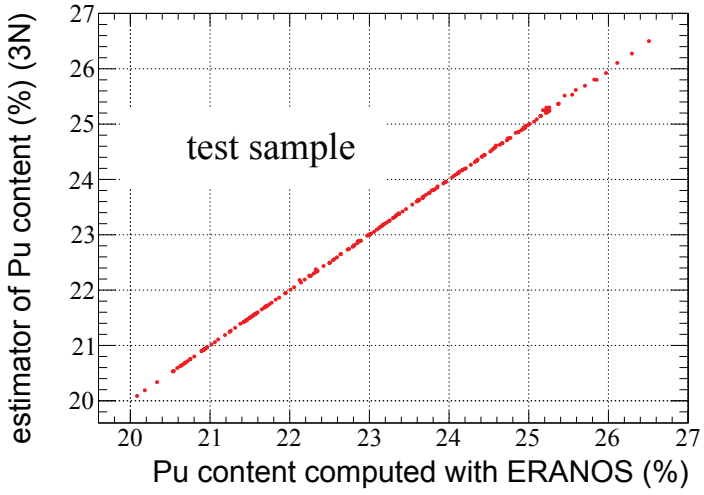

Figure 4.3: Comparison of the plutonium content (%) computed with ERANOS and its ANN estimator (3 neurons in hidden layer)

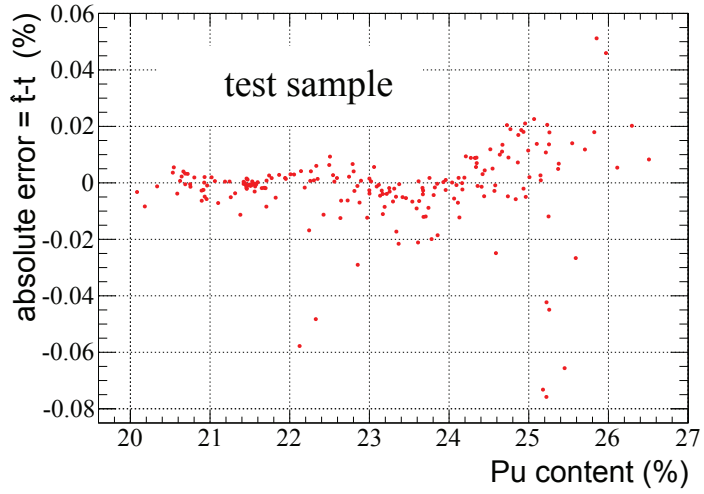

Figure 4.4: Absolute error of the Pu content (%) estimator in function of the Pu content (%)

On figure 4.4 we observe two zones where prediction worsens: for 22%<t<23% and t>25%. Section 4.3.2.2.2.3 is a short study of the reasons for this lack of fit.

4.3.2.2.2.3 Analysis of the lack of fit

Figure 4.5 represents the evolution of $\rho(\overline{\text{BU}}_{end\ of\ cycle})$ computed by ERANOS in function of the plutonium content. We can observe two non-physical jumps, around 23% and 25.5% contents. These jumps are due to a difference in the number of iterations in the use of Newton's algorithm, and their magnitude is the same order as ε. Therefore, they are present too in the data-driven function $t = f(\{y_i\})$.

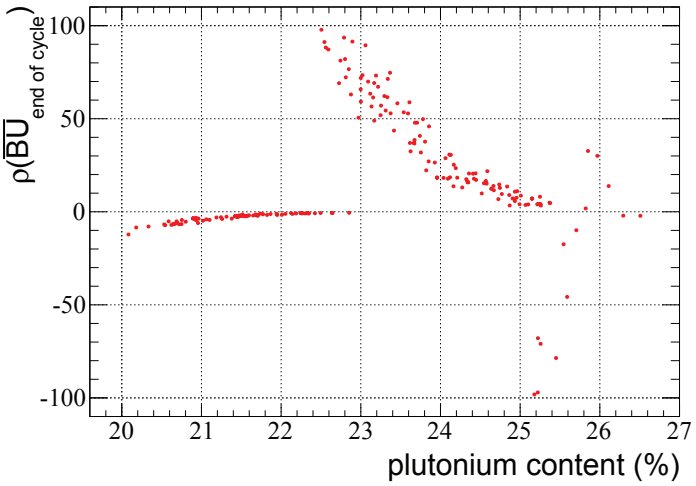

Figure 4.5: End of cycle reactivity in function of the plutonium content for SFR CFV core

Since these jumps affect the results, we can assess their impact on the quality of the ANN estimators, but reproducing the results through reproducing a series of ERANOS computation would be time-consuming. However, figure 4.1 (and a brief linearity analysis) showed that the plutonium content is close to be linear in function of the different parameters. A possibility is to represent the difference between a linear regression of the plutonium content, introducing very little non-linearity, and the ANN. Local non-linearity would be significant of a non-physical phenomenon.

Figure 4.6 shows the difference between the ANN estimators of the plutonium content, and the linear regression, for a given plutonium vector, in function of the plutonium content, for different numbers of hidden neurons. We observe the jump around a plutonium content of 22.5%, as in figure 4.5. We can conclude that the jump in reactivity (magnitude: $\varepsilon = 100$pcm) has indeed an impact on the plutonium content, and that the jump is *learnt* by the ANN estimators. However, the jump in plutonium content is relatively low: approximately 0.2% in relative terms, which means that a plutonium content of 22% will be estimated as 22% $\pm$ 0.044%, which is still adequate. Hence this phenomenon does not degrade drastically the prediction of plutonium content in function of the isotopy. A first solution for this problem would be to reduce ε, however computation time would increase accordingly. Another answer is explained in section 4.3.2.3.

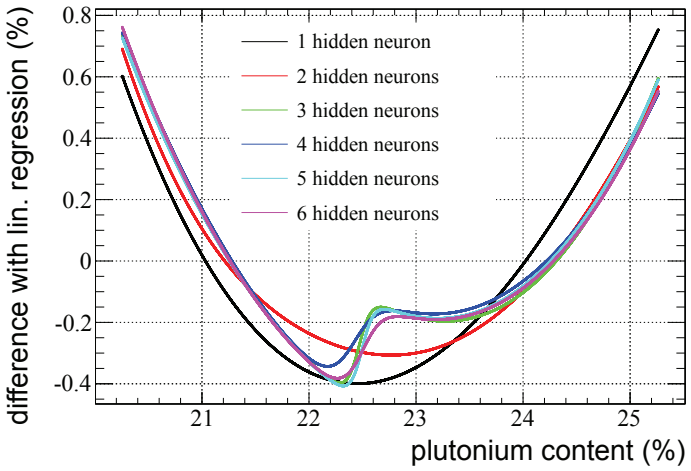

Figure 4.6: Relative difference with linear regression in function of the plutonium content for SFR CFV core

4.3.2.3 Method B: straightforward estimation

4.3.2.3.1 Description of the method

Method B is based on the observation that a significant part of the computation time in method A comes from the successive ERANOS calculations in the Newton's algorithm: for each point in the design of experiments, it usually takes 3 or more iterations to compute the plutonium content. Furthermore, although useful, the intermediate results (for instance core reactivity computed for a given composition and a plutonium content giving more or less than the target reactivity) are not used. These intermediate results return $\rho^{core}\left(t, \{y_i\}, \overline{\text{BU}}_{end\ of\ cycle}\right) \neq \rho^{core}_{target}$. Although they do not correspond to a core composition that will actually have to be calculated by an equivalence model, we can use those results as trends.

Computing a series of ρ^{core} using randomly generated $\{y_i\}$ and t will provide a set of data $\{\rho^{core}, \{y_i\}, t\}$. Using this data set, we can build the function $\hat{t}(\rho^{core}(\overline{\text{BU}}_{end\ of\ cycle}), \{y_i\})$ which estimates the plutonium content according to a composition and the core reactivity at the end of irradiation.

If we impose as an argument $\rho^{core}(\overline{\text{BU}}_{end\ of\ cycle}) = \rho^{core}_{target}$, the estimator will predict the plutonium content in function of the core composition such as the end of cycle reactivity is ρ^{core}_{target}, which constitues a solution to our problem.

4.3.2.3.2 Application

4.3.2.3.2.1 Sampling

This section shows the application of method B to create a CFV core equivalence model. Parameters are sampled uniformly, the intervals of variation are summarized in table 4.3. The core is divided into two zones of different volumetric enrichment, e_1 and e_2. The mean volumetric enrichment and the plutonium content are calculated in function of e_1 and e_2. It has to be noted that contrary to section 4.3.2.2, the enrichment is sampled.

parameter	min (%)	max (%)
$i(^{238}\text{Pu})$	2.0	4.0
$i(^{239}\text{Pu})$	35.0	60.0
$i(^{240}\text{Pu})$	$100 - \sum_{n \in \text{Pu},^{241}\text{Am}} i(n)$	
$i(^{241}\text{Pu})$	7.0	12.0
$i(^{242}\text{Pu})$	6.0	15.0
$i(^{241}\text{Am})$	0.1	4.0
$m(^{235}\text{U})/m(\text{U})$	0.1	0.3
$m(^{238}\text{U})/m(\text{U})$	$100 - m(^{235}\text{U})/m(\text{U})$	
e_1	18	26
e_2	$1.0502 \times e_1$	

Table 4.3: Intervals of variation for CFV equivalence model, method B

The DOE consists in 600 points sampled according to table 4.3, using LHS. For each point of the DOE, we perform an ERANOS computation of the end of cycle reactivity $\rho(\overline{\text{BU}}_{end\ of\ cycle})$.

In this method, the plutonium volumetric enrichment and isotopic vector are uncorrelated, however the end of cycle reactivity depends on both those sets of parameters. Figures 4.7 and 4.8 illustrate the end of cycle reactivity in function of the plutonium content and the ^{239}Pu isotopy. Both plutonium content and isotopy impact the reactivity at the end of cycle. The dispersion in figure 4.7 comes from the isotopic vector, and the dispersion in 4.8 comes from the isotopic vector (except ^{239}Pu) and the plutonium content.

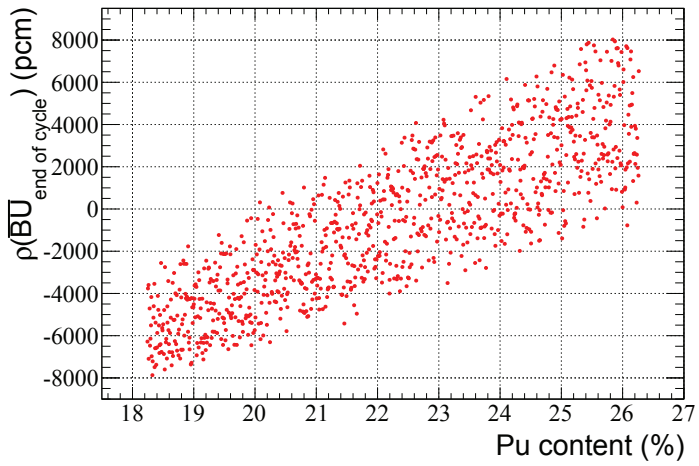

Figure 4.7: End of cycle reactivity in function of the plutonium content for SFR CFV core

4.3.2.3.2.2 Regression

Our aim is to build ANN estimators of the plutonium content such as $\rho(\overline{\text{BU}}_{end\ of\ cycle}) = 0$. The parameters of the ANN are Pu content, Pu isotopic vector and $\rho(\overline{\text{BU}}_{end\ of\ cycle})$.

We use the same method as in section 4.3.2.2.2.2: division of the DOE into two subsets, construction of the ANN on the first one and testing on the second one, selection of the most adequate

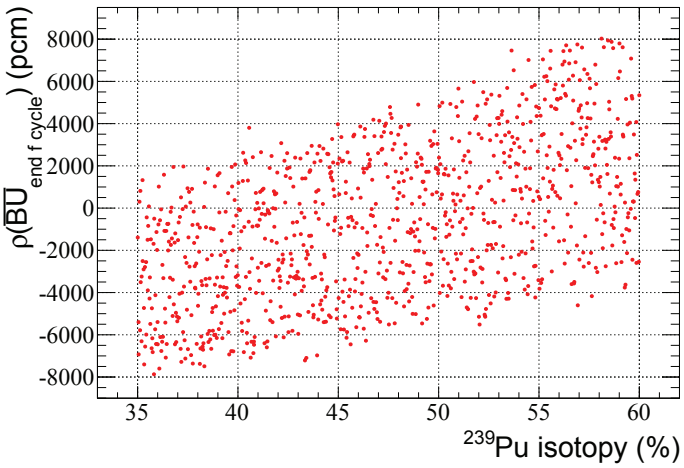

Figure 4.8: End of cycle reactivity in function of the ^{239}Pu isotopy for SFR CFV core

number of neurons in the hidden layer. Figure 4.9 and table 4.4 represent the r^2 and q^2 estimators of the model in function of the number of neurons in the hidden layer, and table 4.5 summarizes a few quality criteria for each ANN, calculated on the test sample.

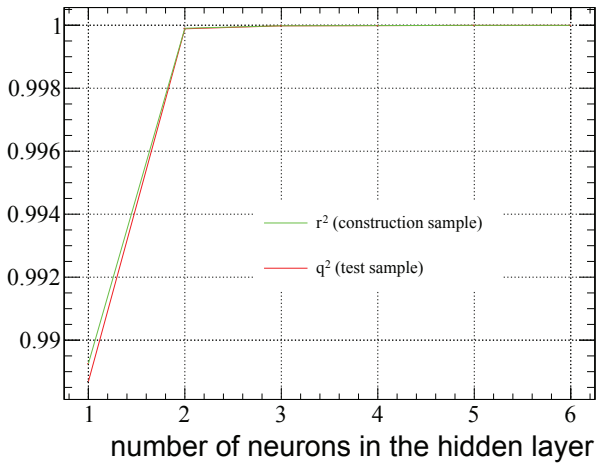

Figure 4.9: Global quality indicators of the plutonium content ANN estimators, method B

There are two main differences in the results of method A and B.

1. The ANN containing one hidden neuron has poor prediction properties in method B, whereas it is not so different from other estimators in method A. This phenomenon probably comes from the fact that in method B there is one more parameter, $\rho(\overline{\text{BU}}_{end\ of\ cycle})$, which interacts with other parameters in a non negligible manner, which is not taken into account with only one neuron;
2. ANN containing three or more hidden neurons are much better with method B than with method A. A plausible explanation is the absence of jump in plutonium content linked to Newton's method.

number of hidden neurons	r^2	q^2
1	0.98925	0.98868
2	0.99990	0.99989
3	0.99998	0.99998
4	0.99999	0.99999
5	1.00000	1.00000
6	1.00000	0.99999

Table 4.4: Global quality indicators of the plutonium content ANN estimators, method B

number of hidden neurons	$mean\|(\hat{t}-t)/t\|$	$max\|(\hat{t}-t)/t\|$	$mean\|(\hat{t}-t)/\bar{t}\|$	$max\|(\hat{t}-t)/\bar{t}\|$
1	0.86%	4.05%	0.84%	3.39%
2	0.08%	0.43%	0.08%	0.42%
3	0.03%	0.24%	0.03%	0.20%
4	0.03%	0.14%	0.03%	0.13%
5	0.02%	0.14%	0.01%	0.12%
6	0.02%	0.18%	0.02%	0.15%

Table 4.5: Bias of SFR CFV Pu content estimators, calculated on the test sample, method B

According to these results, we choose to use an ANN with 5 hidden neurons for the rest of the study.

Figure 4.10 represents the application of this estimator of the plutonium content on the DOE of method A (iterative computation of the Pu content with ERANOS). We observe that this ANN is a reliable estimator of the plutonium content computed iteratively by ERANOS. We also remark the same lack of fit as in method A, even more pronounced in this case, due to the absence of Pu content jumps during the production of this ANN. Overall we conclude that method B produces better estimators than method A. Furthermore, the sample construction of method B is faster because of the absence of transport iterations.

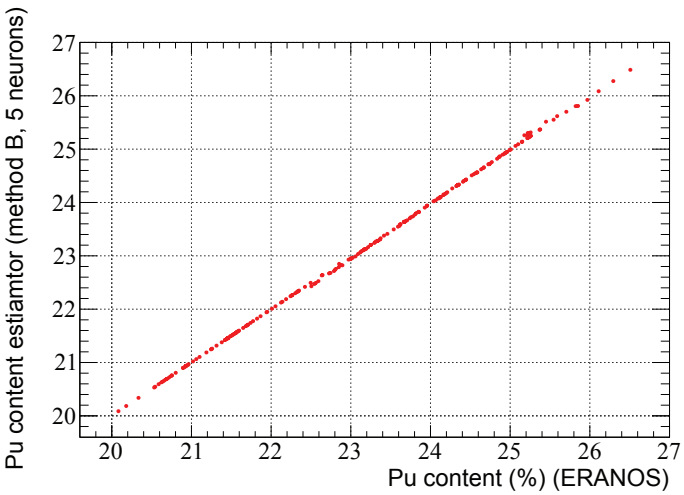

Figure 4.10: Comparison of the plutonium content computed iteratively with ERANOS and the ANN estimator made according to method B (5 neurons in hidden layer)

4.3.2.4 Equivalence models for uncertainty propagation studies

4.3.2.4.1 Introduction

The previous sections were aimed at producing accurate SFR equivalence models for scenario studies. These models have a low intrinsic bias, they fit the physical models in a very accurate way. However, they do not take nuclear data into account, although these data may have a significant impact on the equivalence criteria, and consequently on the fuel enrichment.

4.3.2.4.2 Parameters

The aim of this section is to build an equivalence model able to perform nuclear data uncertainty propagation in scenario studies. Analysis of the impact of several nuclear data on irradiation calculations was performed in section 3.1.2. Although in this case both irradiation and criticality are studied, most of the results of the sensitivity studies remain valid:

- fission and capture cross-section uncertainties have to be taken into account;
- scattering cross-section uncertainty is not taken into account[2];
- effective fission energy uncertainty is not taken into account;
- fission yields uncertainty is not taken into account;
- decay energy uncertainty is not taken into account;
- burnup and specific power are not subject to uncertainty for the equivalence calculation.

Table 4.6 summarizes the parameters taken into account or neglected. Neglected parameters are only taken into account as their mean value.

parameter	taken into account	neglected	number of parameters
burnup	×		(not a parameter)
irradiation length	×		(not a parameter)
specific power	×		(not a parameter)
non-uniform load factor		×	
fresh fuel mass fractions	×		9
actinides fission XS	×		19
actinides capture XS	×		19
FP capture XS		×	
actinides scattering XS		×	
FP scattering XS		×	
other nuclides scattering XS		×	
fission yields		×	
effective fission energy		×	
mass		×	
half-life		×	

Table 4.6: Summary of the parameters taken into account for SFR CFV equivalence models

[2] scattering cross-sections uncertainties should be taken into account in further studies

4.3.2.4.3 Sampling

The number of parameters for equivalence model able to perform cross-sections uncertainty propagation is much higher than in the case of regular equivalence models. Therefore the DOE size has to be increased. We chose to build our models on a DOE containing 2000 points, divided equally into a construction and a test subsets.

The sample construction for this equivalence model is based on the same principles as method B: the plutonium content is sampled, and there is no iteration. The content and isotopy parameters are the same as defined in table 4.3 page 163. Cross-section perturbations are defined according to their uncertainty distribution: they are sampled as uniform distributions, on intervals $[-3\sigma; +3\sigma]$, σ being the standard deviation. Correlations between cross-sections are not taken into account during this process[3].

4.3.2.4.4 Regression

We build ANN estimators of the plutonium content in function of the parameters previously described. The complexity of this model is much higher than in section 4.3.2.3 because of the increased number of input parameters, and their interaction.

Figure 4.11 represents the r^2 and q^2 estimators of the model in function of the number of neurons in the hidden layer, and table 4.7 summarizes some quality criteria for each ANN, calculated on the test sample.

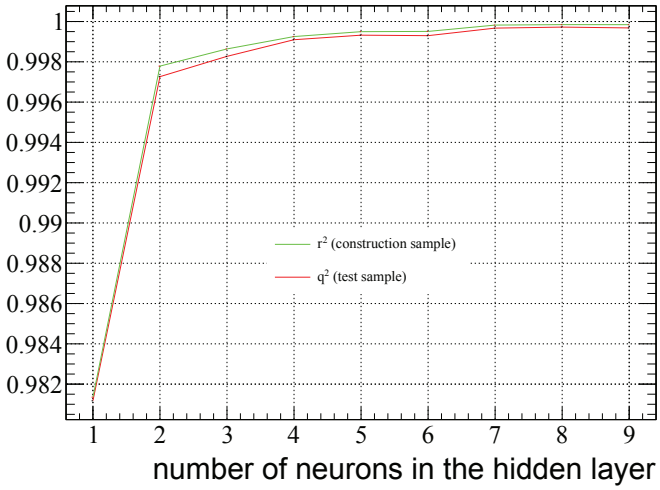

Figure 4.11: Global quality indicators of the plutonium content ANN estimators for SFR CFV equivalence model for cross-sections uncertainty propagation

We observe that the quality tends to increase with the number of neurons. The best results are obtained for 9 neurons in the hidden layer. Results with 10 neurons in the hidden layer are inferior. This may be due to different phenomena:

- the algorithm does not fully converge because of the high number of weights to assess;
- there may be some overfitting.

[3] since this is DOE construction, and not uncertainty propagation, this step does not generate bias

number of hidden neurons	$mean\|(\hat{t}-t)/t\|$	$max\|(\hat{t}-t)/t\|$	$mean\|(\hat{t}-t)/\bar{t}\|$	$max\|(\hat{t}-t)/\bar{t}\|$
1	1.15%	8.09%	1.14%	6.75%
2	0.44%	2.30%	0.43%	2.14%
3	0.35%	1.82%	0.34%	1.70%
4	0.25%	1.46%	0.25%	1.22%
5	0.22%	1.02%	0.21%	1.10%
6	0.22%	1.17%	0.22%	1.16%
7	0.15%	0.92%	0.15%	0.96%
8	0.14%	0.75%	0.14%	0.75%
9	0.14%	0.82%	0.14%	0.79%
10	0.15%	0.80%	0.15%	0.86%

Table 4.7: Bias of SFR CFV Pu content estimators for cross-sections uncertainty propagation, calculated on the test sample

The results obtained with 9 neurons in the hidden layer are satisfying, and consequently this model will be used in the next studies.

4.3.2.4.5 Uncertainty propagation

4.3.2.4.5.1 Equivalence model only

For a given plutonium vector, we calculate the content and the associated uncertainty, resulting from cross-sections uncertainty. Stochastic uncertainty propagation is performed. ANN equivalence model with 9 neurons in the hidden layer is used. Computation is done for the plutonium vector shown in table 4.8. Cross-sections were attributed the SFR uncertainty calculated in section 5.2.1, correlations are taken into account.

Nuclide	isotopy
^{238}Pu	2.59
^{239}Pu	55.2
^{240}Pu	25.85
^{241}Pu	7.27
^{242}Pu	7.87
^{241}Am	1.22

Table 4.8: Plutonium vector for SFR CFV equivalence model study

Let t be the mass plutonium content, $SD(t)$ its standard deviation and $RSD(t)$ its relative standard deviation. We obtain: $t = 0.223$, $SD(t) = 0.017$, $RSD(t) = 7.7\%$.

This plutonium content uncertainty is high. This value only considered cross-sections uncertainty, and the fresh fuel isotopy is fixed. In the case of scenario computations, both cross-sections and fresh fuel isotopy are subject to uncertainty.

We analyze the variance of the plutonium content. Since the model is very light in terms of memory and its execution is fast, it is possible to perform direct computation. For different parameters we compute the following quantity:

$$\text{part of variance of a parameter} = \frac{Var(t, \text{only a parameter is sampled})}{Var(t)} \tag{4.22}$$

2000 runs are performed for each run (numerator and denominator). Analysis of the variance shows the following results:

- correlation between cross-sections has almost no impact on the result (<1% of the uncertainty);
- $\sigma_c{}^{239}$Pu generates approximately 85% of the total variance;
- $\sigma_c{}^{241}$Pu generates approximately 12% of the total variance.

The uncertainty propagation in scenario calculation through SFR equivalence model is assessed in section 6.2.3 in the case of scenario C: French PWR fleet transition scenario, no minor actinides recycling.

4.3.2.4.5.2 Ranking

In order to determine which cross-sections uncertainty contribute most to the plutonium content uncertainty, we calculate the product sensitivity $\times$ uncertainty. Results are presented in table 4.9. The most important contributors are in **bold**.

The cross-sections generating most plutonium content uncertainty are $\sigma_c(^{239}\text{Pu})$ and $\sigma_c(^{241}\text{Pu})$. The quadratic combination of $\sigma_c(^{239}\text{Pu})$ and $\sigma_c(^{241}\text{Pu})$ cross-sections generate a 7.5% relative standard deviation on the plutonium content in the fresh fuel, while the total relative standard deviation, calculated in the previous paragraph, is 7.7%.

This result is interesting because a better knowledge of ^{239}Pu capture cross-section would significantly decrease the plutonium content uncertainty.

4.3.3 PWR MOX equivalence model

4.3.3.1 Description of the method

Equivalence models for PWR MOX fuel are constructed approximately as for SFR MOX equivalence models described in section 4.3.2.4: the isotopic vector as well as the plutonium content of the fresh fuel are sampled, the cross-section perturbations are taken into account, and the reactivity at the end of the cycle is computed using transport calculation.

However, there is a major difference between these models: burnup has to be taken into account for PWR MOX models. Indeed, several types of fuel corresponding to several different burnup values were irradiated in cores, and the plutonium content has to be calculated accordingly.

Equation 4.14 page 155 shows the expression of the end of cycle burnup in function of the length of cycle and the core fractioning, when k_∞ and the associated ρ_∞ have to be computed.

Our method consists in building an estimator of the plutonium content, such that $\rho_\infty = \rho_\infty^{target}$ at the variable end-of-cycle burnup.

cross-section	$\sigma/t \times \partial t/\partial\sigma$	$RSD(\%)$	$RSD \times \sigma/t \times \partial t/\partial\sigma$ (%)
$\sigma_c(^{235}\mathrm{U})$	0.047	20.7	0.97
$\sigma_f(^{235}\mathrm{U})$	0.029	0.6	0.02
$\sigma_c(^{238}\mathrm{U})$	0.284	1.4	0.40
$\sigma_f(^{238}\mathrm{U})$	-0.047	0.5	-0.03
$\sigma_c(^{238}\mathrm{Pu})$	0.036	7.8	0.28
$\sigma_f(^{238}\mathrm{Pu})$	-0.005	0.5	0.00
$\sigma_c(^{239}\mathrm{Pu})$	1.330	5.3	**7.05**
$\sigma_f(^{239}\mathrm{Pu})$	0.032	0.4	0.01
$\sigma_c(^{240}\mathrm{Pu})$	0.071	3.3	0.23
$\sigma_f(^{240}\mathrm{Pu})$	-0.007	1.1	-0.01
$\sigma_c(^{241}\mathrm{Pu})$	0.192	14.0	**2.69**
$\sigma_f(^{241}\mathrm{Pu})$	-0.039	0.7	-0.03
$\sigma_c(^{242}\mathrm{Pu})$	0.050	4.3	0.21
$\sigma_f(^{242}\mathrm{Pu})$	-0.013	1.9	-0.03
$\sigma_c(^{241}\mathrm{Am})$	0.009	27.8	0.25
$\sigma_f(^{241}\mathrm{Am})$	0.003	8.8	0.02
$\sigma_c(^{243}\mathrm{Am})$	0.000	4.9	0.00
$\sigma_f(^{243}\mathrm{Am})$	0.001	8.4	0.00
$\sigma_c(^{237}\mathrm{Np})$	0.002	87.9	0.17
$\sigma_f(^{237}\mathrm{Np})$	0.007	3.1	0.02
$\sigma_c(^{242}\mathrm{Cm})$	0.000	20.3	0.00
$\sigma_f(^{242}\mathrm{Cm})$	-0.003	5.3	-0.02
$\sigma_c(^{243}\mathrm{Cm})$	0.000	77.4	0.02
$\sigma_f(^{243}\mathrm{Cm})$	0.006	3.5	0.02
$\sigma_c(^{244}\mathrm{Cm})$	-0.001	22.5	-0.01
$\sigma_f(^{244}\mathrm{Cm})$	0.008	3.0	0.02
$\sigma_c(^{245}\mathrm{Cm})$	0.001	61.5	0.09
$\sigma_f(^{245}\mathrm{Cm})$	-0.013	3.3	-0.04

Table 4.9: Cross-sections uncertainty ranking for SFR CFV equivalence model

4.3.3.2 Application

4.3.3.2.1 Overview

The transport + evolution calculation is based on an APOLLO2 [4.4] data set of PWR MOX AFA3G fuel assembly in PWR UOX (3.7% enrichment) environment, the environment is irradiated at a fixed value of 23GWd/tHM. Transport equation is solved with collision probability method. APOLLO2 computes the value of k_∞ when the end of cycle burnup is reached. According to [4.5], the reference reactivity at the end of cycle is +3900pcm. This value is supposed to take into accound both physical uncertainties and computational bias. In practice, we can choose to use $k_\infty^{target} = 1.039$, or simply fit the uncertainty propagation equivalence model to a pre-existing equivalence model using k_∞^{target} as a parameter. This second method is employed in section 6.2.3.5.2.1 in the case of scenario C.

4.3.3.2.2 Sampling

Parameters taken into account are described in table 4.10. They are sampled without any correlation (except for the isotopy of ^{240}Pu which depends on the other nuclides). We denote $i(j)$ the isotopy of nuclide j in fresh fuel. The burnup range is chosen such as every PWR MOX end of cycle burnup (not end of irradiation burnup) in a typical scenario study of the French fleet is within the domain of validity of the equivalence model.

parameter	min	max
$i(^{238}\text{Pu})$	1.0%	4.0%
$i(^{239}\text{Pu})$	50.0%	64.0%
$i(^{240}\text{Pu})$	$100 - \sum_{n \in \text{Pu},^{241}\text{Am}} i(n)$	
$i(^{241}\text{Pu})$	0.5%	10.0%
$i(^{242}\text{Pu})$	3.0%	10.0%
$i(^{241}\text{Am})$	0.0%	7.0%
t	6.0%	10.0%
$\overline{\text{BU}}_{end\ of\ cycle}$	12.0GWd/tHM	35.0GWd/tHM

Table 4.10: Intervals of variation for PWR MOX equivalence model

4.3.3.2.3 Regression

We then build ANN estimators of the plutonium content in function of the parameters previously described.

Figure 4.12 represents the r^2 and q^2 of the estimators of the model in function of the number of neurons in the hidden layer, and table 4.11 summarizes a few quality criteria for each ANN, calculated on the test sample.

The bias tends to be higher than in the case of SFR MOX reactors. Indeed, the fuel behavior (evolution of the content in function of isotopy and burnup such that the equivalence criterion is satisfied) is much less linear in PWR MOX reactors. However the mean bias remains satisfying.

We observe that the quality tends to increase with the number of neurons. The best results are obtained for 10 neurons in the hidden layer. The results obtained with 10 neurons in the hidden

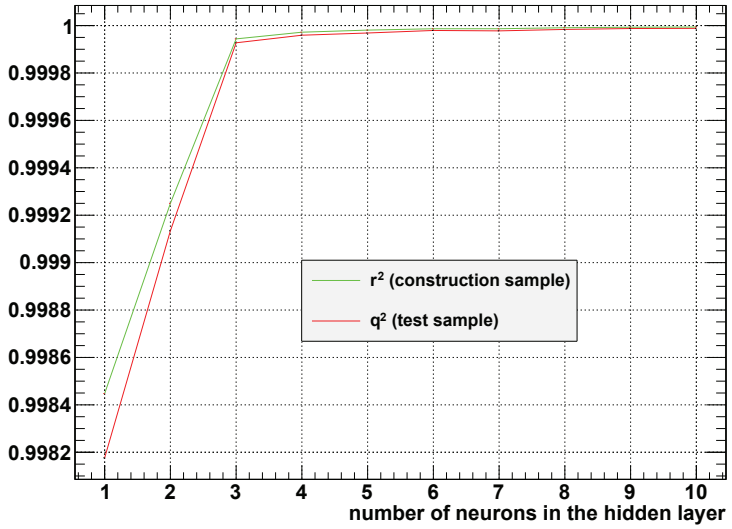

Figure 4.12: Global quality indicators of the plutonium content ANN estimators for PWR MOX equivalence model dedicated to cross-sections uncertainty propagation

number of hidden neurons	$mean\|(\hat{t}-t)/t\|$	$max\|(\hat{t}-t)/t\|$	$mean\|(\hat{t}-t)/\bar{t}\|$	$max\|(\hat{t}-t)/\bar{t}\|$
1	3.63%	24.89%	3.56%	30.89%
2	2.51%	22.99%	2.43%	28.53%
3	0.71%	7.86%	0.71%	9.76%
4	0.53%	6.90%	0.53%	7.57%
5	0.45%	6.54%	0.45%	7.18%
6	0.37%	4.28%	0.37%	4.70%
7	0.38%	5.06%	0.38%	6.28%
8	0.33%	3.33%	0.33%	3.88%
9	0.28%	2.81%	0.28%	3.41%
10	0.27%	4.07%	0.27%	4.74%

Table 4.11: Mean bias of the PWR MOX Pu content estimators for uncertainty propagation, calculated on the test sample

layer are satisfying, and consequently this model will be used in the next studies.

4.3.3.3 Analysis of the model

4.3.3.3.1 Introduction

The previous equivalence model will be used for uncertainty propagation in scenario studies. However, in order to understand its behavior during a scenario computation, it is possible to use the model separately and perform both uncertainty propagation and ranking studies to observe which uncertainty values have a large impact on the plutonium content.

4.3.3.3.2 Uncertainty propagation

4.3.3.3.2.1 Equivalence model only

For a given plutonium vector, we calculate the uncertainty associated to the content in function of cross-sections uncertainty. The computation is done for two different plutonium vectors, shown in table 4.12. The burnup at the end of irradiation is 46GWd/tHM and the core fractionation is 3 in both cases. PWR MOX cross-sections were attributed the uncertainty value calculated in section 5.2.1, the correlations are taken into account.

	vector 1	vector 2
^{238}Pu	0.027	0.015
^{239}Pu	0.545	0.601
^{240}Pu	0.264	0.253
^{241}Pu	0.076	0.066
^{242}Pu	0.078	0.055
^{241}Am	0.011	0.010

Table 4.12: Plutonium vectors for PWR MOX equivalence model study

Let t be the mass plutonium content $\left(= \frac{\text{plutonium mass in the fresh assembly}}{\text{heavy metal mass in the fresh assembly}}\right)$, $SD(t)$ its standard deviation and $RSD(t)$ its relative standard deviation. The results are as follows:

- vector 1: $t = 0.0856$, $SD(t) = 0.0198$, $RSD(t) = 23\%$;
- vector 2: $t = 0.0737$, $SD(t) = 0.0168$, $RSD(t) = 23\%$.

First, we observe that the plutonium vector 1 requires a higher plutonium content to reach ρ_∞^{target} at the end of irradiation. This result comes from the fact that overall quality of vector 1 is much lower than vector 2: the ratio of fissile isotopes (^{239,241}Pu) is lower.

Then, we remark that the uncertainty value is extremely high. It only considers capture and fission cross-sections uncertainties, the fresh fuel isotopy being fixed. However, in the case of scenario studies, not only cross-sections are subject to uncertainty, but the fresh fuel isotopy depends on cross-sections, because it is determined by previous equivalence and irradiation models, which are subject to cross-sections uncertainty. Therefore cross-sections have an impact through both (direct effect) equivalence computation and (indirect effect) fresh fuel composition. Therefore it is necessary to assess the plutonium content uncertainty in a scenario. We expect an even higher uncertainty in that case.

Analysis of the variance shows that ^{238}U fission cross-section uncertainty generates 86% of the variance[4]

$$\frac{Var(t, \sigma_f(^{238}\mathrm{U})\ only\ is\ sampled)}{Var(t)} \approx 0.86 \tag{4.23}$$

A comprehensive ranking study is shown in section 4.3.3.3.3.

4.3.3.3.2.2 Equivalence model in a scenario study

Uncertainty propagation in scenario calculation through PWR MOX equivalence models is assessed in section 6.2.3 in the case of scenario C: French PWR fleet transition scenario, without minor actinides recycling. The main results are:

- EPR MOX plutonium content uncertainty is extremely high (approximately 22%);
- irradiation impact is approximately 5% of the variance;
- equivalence impact is approximately 90% of the variance;
- therefore interaction terms are approximately 5% of the variance.

We observe that nuclear data in equivalence computation in scenario ($\sigma \approx 22\%$) computation and in direct equivalence computation ($\sigma \approx 23\%$) are similar. Therefore the indirect effect (fresh fuel composition) is weak. The slight difference may result from non full convergence of uncertainty propagation in the scenario study, or negative interaction between some terms.

4.3.3.3.3 Ranking

In order to determine which cross-sections uncertainty contribute most to the plutonium content uncertainty, we calculate the product sensitivity $\times$ uncertainty. Results are presented in table 4.13. The most important contributors are in **bold**.

First, we observe that the products sensitivity $\times$ uncertainty for each nuclide scarcely vary with the plutonium vector.

Then we remark that the uncertainty associated to several reactions have stronger influence on the content than other reactions. In both cases, the most influent cross-sections are (arbitrary criterion : $|RSD \times \sigma/t \times \partial t/\partial \sigma|$ > 1%): $\sigma_c(^{238}\mathrm{U})$, $\sigma_f(^{239}\mathrm{Pu})$, $\sigma_c(^{235}\mathrm{U})$, $\sigma_c(^{239}\mathrm{Pu})$, $\sigma_f(^{241}\mathrm{Pu})$, $\sigma_c(^{241}\mathrm{Pu})$ and $\sigma_f(^{235}\mathrm{U})$.

4.3.4 Implementation in COSI

Data-driven equivalence models for uncertainty propagation were implemented in COSI. When launched with graphical interface, the user must select `mox_propagation` (or `cfv_propagation`) in the case of PWR MOX fuel (resp. SFR CFV fuel), and then select `mod_propagation` (resp. `CFV_propagation`) as the equivalence model. In interface model COSI will not read nuclear data perturbation.

In command line mode, those equivalence models are used the same way, however nuclear data perturbations are taken into account.

[4] Recent developments in COMAC [4.6] produced a new 26 groups covariance matrix for ^{238}U. Condensation in PWR MOX spectrum according to the methodology explained in section 5.2.1 returns: $SD(\sigma_f(^{238}\mathrm{U})) \approx 5.9\%$. In that case, the plutonium content standard deviation is 12%, $\sigma_f(^{238}\mathrm{U})$ still generating 55% of the variance.

cross-section	$\sigma/t \times \partial t/\partial\sigma$		RSD (%)	$RSD \times \sigma/t \times \partial t/\partial\sigma$ (%)	
	vector 1	vector 2		vector 1	vector 2
$\sigma_c(^{235}\text{U})$	0.866	0.845	1.71	**1.5**	**1.4**
$\sigma_f(^{235}\text{U})$	-3.556	-3.528	0.31	**-1.1**	**-1.1**
$\sigma_c(^{238}\text{U})$	2.194	2.157	1.45	**3.2**	**3.1**
$\sigma_f(^{238}\text{U})$	-1.588	-1.557	0.52	-0.8	-0.8
$\sigma_c(^{238}\text{Pu})$	0.051	0.035	9.53	0.5	0.3
$\sigma_f(^{238}\text{Pu})$	-0.023	-0.011	0.31	-0.0	-0.0
$\sigma_c(^{239}\text{Pu})$	1.156	1.147	1.02	**1.2**	**1.2**
$\sigma_f(^{239}\text{Pu})$	-2.557	-2.519	0.74	**-1.9**	**-1.9**
$\sigma_c(^{240}\text{Pu})$	0.388	0.364	1.65	0.6	0.6
$\sigma_f(^{240}\text{Pu})$	-0.079	-0.066	1.18	-0.9	-0.8
$\sigma_c(^{241}\text{Pu})$	0.352	0.347	3.44	**1.2**	**1.2**
$\sigma_f(^{241}\text{Pu})$	-0.934	-0.915	1.42	**-1.3**	**-1.3**
$\sigma_c(^{242}\text{Pu})$	0.012	0.009	11.51	0.1	0.1
$\sigma_f(^{242}\text{Pu})$	-0.017	-0.014	1.86	-0.0	-0.0
$\sigma_c(^{241}\text{Am})$	0.008	0.006	4.88	0.0	0.0
$\sigma_f(^{241}\text{Am})$	-0.003	0.002	2.63	-0.0	0.0

Table 4.13: Cross-sections uncertainty ranking for PWR MOX equivalence model

4.4 Conclusions and perspectives

Equivalence model calculate the fresh fuel enrichment or content in function of the isotopic composition, and other parameters. The equivalence criterion generally is end of cycle reactivity.

A new type of equivalence model, able to perform uncertainty propagation studies, was created in this work, based on statistical estimators such as ANN. The estimators are constructed using {depletion + transport} computations, performed with reference codes. Those models enable propagation of cross-sections uncertainty in scenario computations. They were created in the case of SFR MOX fuel and PWR MOX fuel.

Preliminary uncertainty propagation and ranking studies were performed using these models. It appears that the fresh fuel content uncertainty is very high, and is mostly due to few cross-section, including:

- in thermal spectrum:
  - $\sigma_f(^{238}\text{U})$;
  - $\sigma_c(^{239}\text{Pu})$;
  - $\sigma_f(^{235}\text{U})$;
  - $\sigma_c(^{238}\text{U})$;
  - $\sigma_c(^{240}\text{Pu})$;
- in fast spectrum:
  - $\sigma_c(^{239}\text{Pu})$;
  - $\sigma_c(^{241}\text{Pu})$.

The perspectives include construction of a new PWR repU equivalence model using the same method, and refinement of the present models:

- equivalence models based on cores computations for PWR MOX;
- development of new equivalence criteria, such as dpa (displacements per atom) or linear power, in the case of SFR cores.

Bibliography

[4.1] Paul Reuss. *Précis de neutronique*. EDP Sciences, 2003.

[4.2] G. Rimpault, D. Plisson, J. Tommasi, R. Jacqmin, J-M. Rieunier, D. Verrier, and D. Biron. The ERANOS Code and Data System for Fast Reactors Neutronic Analyses. In *Proc. of PHYSOR 2002*, 2002.

[4.3] B. Fontaine, N. Devictor, P. Le Coz, A. Zaetta, D. Verwaerde, and J-M. Hamy. The French R&D on SFR core design and ASTRID Project. In *Proceedings of GLOBAL2011, Paper No. 432757*, 2011.

[4.4] A. Santamarina, D. Bernard, P. Blaise, L. Erradi, P. Leconte, R. Le Tellier, C. Vaglio, and J-F. Vidal. APOLLO2.8: a validated code package for PWR neutronics calculations. In *Advances in Nuclear Fuel Management IV (ANFM 2009), Hilton Island, South Carolina, USA*, 2009.

[4.5] Djamel Azzoug. *Etude phénoménologique du comportement des combustibles au plutonium dans les cycles de réacteurs à eau. Elaboration d'un modèle d'équivalence des plutoniums.* PhD thesis, Université de Paris-Sud, Centre d'Orsay, 1990.

[4.6] C. De Saint Jean, P. Archier, G. Noguere, O. Litaize, C. Vaglio-Gaudard, D. Bernard, and O. Leray. Estimation of multi-group cross section covariances for ^{235,238}U, ^{239}Pu, ^{241}Am, ^{56}Fe, ^{23}Na, and ^{27}Al. In *PHYSOR 2012 - Advances in Reactors Physics*, 2012.

Chapter 5

Uncertainty data

Contents

5.1 Introduction 180
5.2 Nuclear data 180
5.2.1 Condensation of covariance matrix 180
5.2.2 Fission yields 196
5.3 Scenario parameters and hypotheses 196
5.3.1 Introduction 196
5.3.2 Scenario hypotheses 196
5.3.3 Scenario parameters 197
5.3.4 Conclusions and perspectives 208

5.1 Introduction

5.2 Nuclear data

5.2.1 Condensation of covariance matrix

5.2.1.1 Introduction

The uncertainty data concerning cross-sections is stored in multi-group covariance matrices. In order to obtain 1-group uncertainty values, corresponding to the input data format used in scenario studies with COSI and CESAR, we have to condense the data using conservation laws. In the following part, we will underline energy-dependent vectors, underline twice energy×energy-dependent matrices and write in **bold** objects obtained through concatenation of objects depending on different reactions. We denote $Var(.)$ the variance, $cor(.,.)$ the correlation and $cov(.,.)$ the covariance.

5.2.1.2 Condensation of intra-reaction covariance matrices

The first step is the condensation of intra-reaction covariance matrices. In order to calculate the 1-group uncertainty of the cross-section of nuclear reaction a, we use the conservation of the reaction rate of $a \in \{(n,\gamma),(n,f),etc.\}$, τ_a.

$$Var(\tau_a)_{1g} = Var(\tau_a)_{Ng} \tag{5.1}$$

We calculate these variance values using the N-group covariance matrix through the sandwich rule.

$$\frac{Var(\tau_a)_{Ng}}{\tau_a^2} = {}^t\underline{S}_{Ng}\underline{\underline{D}}_{Ng}\underline{S}_{Ng} \tag{5.2}$$

With:

$$\underline{S}_{Ng} = \frac{\underline{\sigma}_a}{\tau_a}\frac{\partial \tau_a}{\partial \underline{\sigma}_a} \; ; \; \underline{\sigma}_a = \begin{bmatrix} \sigma_{a,1} \\ \vdots \\ \sigma_{a,N} \end{bmatrix} \text{ and } \underline{\underline{D}}_{Ng} = \begin{bmatrix} \frac{var(\sigma_{a,1})}{\sigma_{a,1}^2} & \cdots & \frac{cov(\sigma_{a,1},\sigma_{a,N})}{\sigma_{a,1}\sigma_{a,N}} \\ \vdots & \ddots & \vdots \\ \frac{cov(\sigma_{a,1},\sigma_{a,N})}{\sigma_{a,1}\sigma_{a,N}} & \cdots & \frac{var(\sigma_{a,N})}{\sigma_{a,N}^2} \end{bmatrix} \tag{5.3}$$

We expand the expression of $\underline{S}_{Ng}$:

$$\underline{S}_{Ng} = \begin{bmatrix} \frac{\sigma_{a,1}}{\tau_a} \\ \vdots \\ \frac{\sigma_{a,N}}{\tau_a} \end{bmatrix} \begin{bmatrix} \frac{\partial \tau_a}{\partial \sigma_{a,1}} \\ \vdots \\ \frac{\partial \tau_a}{\partial \sigma_{a,N}} \end{bmatrix} \tag{5.4}$$

The reaction rate is as follows:

$$\tau_a = {}^t\underline{\phi}\underline{\sigma}_a = \sum_{i=1}^{N} \phi_i \sigma_{a,i} \tag{5.5}$$

We make the following approximation :

$$\frac{\partial \phi_i \sigma_{a,i}}{\partial \phi_j} = 0 \text{ for } i \neq j \tag{5.6}$$

This approximation consists in neglecting the impact of a flux perturbation in one energy group on other energy groups.

Thus the sensitivity simplifies as:

$$\underline{S}_{Ng} = \begin{bmatrix} \frac{\tau_{a,1}}{\tau_a} \\ \vdots \\ \frac{\tau_{a,N}}{\tau_a} \end{bmatrix} = \frac{\underline{\tau}_a}{\tau_a} \tag{5.7}$$

The sandwich rule for 1 energy group is as follows:

$$\frac{Var(\tau_a)_{1g}}{\tau_a^2} = {}^t S_{1g} \underline{\underline{D}}_{1g} S_{1g} \tag{5.8}$$

The 1-group sensitivity expresses as follows:

$$S_{1g} = \frac{\sigma_a}{\tau_a}\frac{\partial \tau_a}{\partial \sigma_a} = \frac{\sigma_a}{\tau_a}\frac{\partial \phi \sigma_a}{\partial \sigma_a} = \frac{\sigma_a}{\tau_a}\phi = 1 \tag{5.9}$$

Therefore we can calculate the variance of τ_a using the relation:

$$\frac{Var(\tau_a)_{1g}}{\tau_a^2} = {}^t S_{1g} \frac{Var(\sigma_a)}{\sigma_a^2} S_{1g} = \frac{Var(\sigma_a)}{\sigma_a^2} \tag{5.10}$$

We inject relations 5.2, 5.7 and 5.10 in equation 5.1. We obtain the intra-reaction covariance data condensation formula:

$$\boxed{\frac{Var(\sigma_a)}{\sigma_a^2} = \frac{{}^t\underline{\tau}_a}{\tau_a} \underline{\underline{D}}_{Ng} \frac{\underline{\tau}_a}{\tau_a}} \tag{5.11}$$

All of the terms of the right member of equation 5.11 are known. Hence we can calculate the expression of $\frac{Var(\sigma_a)}{\sigma_a^2}$. This formula can be used for condensing intra-reaction covariance data when inter-reaction covariance is null.

5.2.1.3 Condensation of inter-reaction covariance matrices

The conservation of the uncertainty of a reaction rate allows to calculate the 1-group uncertainty of the associated cross-section. However, this does not allow the condensation of inter-reaction covariance data. Therefore it is necessary to impose another constraint. Let $cov(\tau_a, \tau_b)_{Ng}$ denote the scalar value of the covariance coefficient of the couple (τ_a, τ_b) calculated using N-groups covariance data (inter-reaction and intra-reaction covariance matrices) and $cov(\tau_a, \tau_b)_{1g}$ the scalar value of the equivalent covariance coefficient that corresponds to its value using the 1-group (scalar) values of variance of τ_a and τ_b. We **choose** to use the **conservation of the covariance of two reaction rates** as our last equivalence law to condense their corresponding inter-reaction covariance matrix. Therefore, while condensing covariance data associated to reactions a and b (for instance fission and radiative capture), we want to obtain $Var(\sigma_a)$, $Var(\sigma_b)$ and $cor(\sigma_a, \sigma_b)$ using the following laws:

$$\begin{cases} Var(\tau_a)_{1g} = Var(\tau_a)_{Ng} \\ Var(\tau_b)_{1g} = Var(\tau_b)_{Ng} \\ cor(\tau_a, \tau_b)_{1g} = cor(\tau_a, \tau_b)_{Ng} \end{cases} \tag{5.12}$$

We begin with the expression of the variance of the sum of two reaction rates, which is expressed as follows, for both N-groups and 1-group quantities:

$$Var(\tau_a + \tau_b) = Var(\tau_a) + Var(\tau_b) + 2cov(\tau_a, \tau_b) \tag{5.13}$$

The expressions $cor(\tau_a, \tau_b)_{1g} = cor(\tau_a, \tau_b)_{Ng}$ and $cov(\tau_a, \tau_b)_{1g} = cov(\tau_a, \tau_b)_{Ng}$ are equivalent because of the equality of variances calculated in 1 energy group and in N energy groups. Therefore we have:

$$cov(\tau_a, \tau_b) = \frac{1}{2}\left[Var(\tau_a + \tau_b) - Var(\tau_a) - Var(\tau_b)\right] \tag{5.14}$$

Then:

$$\frac{1}{2}\left[Var(\tau_a + \tau_b) - Var(\tau_a) - Var(\tau_b)\right]_{1g} = \frac{1}{2}\left[Var(\tau_a + \tau_b) - Var(\tau_a) - Var(\tau_b)\right]_{Ng} \tag{5.15}$$

The conservation laws of equation 5.12 simplify the previous equation as:

$$\boxed{Var(\tau_a + \tau_b)_{1g} = Var(\tau_a + \tau_b)_{Ng}} \tag{5.16}$$

First, we work with the 1 energy group side of equation 5.16. The 1-group intra- and inter-reaction correlation matrix expresses as:

$$\underline{\underline{\boldsymbol{D}}}_{\boldsymbol{1g}} = \begin{bmatrix} \dfrac{Var(\sigma_a)}{\sigma_a^2} & \dfrac{cov(\sigma_a, \sigma_b)}{\sigma_a \sigma_b} \\ \dfrac{cov(\sigma_a, \sigma_b)}{\sigma_a \sigma_b} & \dfrac{Var(\sigma_b)}{\sigma_b^2} \end{bmatrix} \tag{5.17}$$

The 1-group sandwich formula to propagate uncertainty from the covariance matrix to the sum of reaction rates is as follows:

$$\frac{Var(\tau_a+\tau_b)_{1g}}{(\tau_a+\tau_b)^2} = {}^t\boldsymbol{S_{1g}}\underline{\underline{\boldsymbol{D}}}_{\boldsymbol{1g}}\boldsymbol{S_{1g}} \tag{5.18}$$

With:

$$S_{1g} = \frac{\boldsymbol{\sigma_{1g}}}{\tau_a+\tau_b}\frac{\partial(\tau_a+\tau_b)}{\partial\boldsymbol{\sigma_{1g}}} \text{ and } \boldsymbol{\sigma_{1g}} = \begin{bmatrix}\sigma_a\\ \sigma_b\end{bmatrix} \tag{5.19}$$

Let ϕ be the 1-group flux (flux level). With $\tau_a = \phi\sigma_a$ and $\tau_b = \phi\sigma_b$, we can write:

$$\boldsymbol{S_{1g}} = \frac{\boldsymbol{\sigma_{1g}}}{\tau_a+\tau_b}\frac{\partial(\phi\sigma_a+\phi\sigma_b)}{\partial\boldsymbol{\sigma_{1g}}} = \begin{bmatrix}\frac{\sigma_a}{\tau_a+\tau_b}\\ \frac{\sigma_b}{\tau_a+\tau_b}\end{bmatrix}\cdot\begin{bmatrix}\frac{\partial(\phi\sigma_a+\phi\sigma_b)}{\partial\sigma_a}\\ \frac{\partial(\phi\sigma_a+\phi\sigma_b)}{\partial\sigma_b}\end{bmatrix} = \begin{bmatrix}\frac{\tau_a}{\tau_a+\tau_b}\\ \frac{\tau_b}{\tau_a+\tau_b}\end{bmatrix} \tag{5.20}$$

We inject relation 5.20 in 5.18. We obtain:

$$\frac{Var(\tau_a+\tau_b)_{1g}}{(\tau_a+\tau_b)^2} = \left[\frac{\tau_a}{\tau_a+\tau_b};\frac{\tau_b}{\tau_a+\tau_b}\right]\begin{bmatrix}\frac{Var(\sigma_a)}{\sigma_a^2} & \frac{cov(\sigma_a,\sigma_b)}{\sigma_a\sigma_b}\\ \frac{cov(\sigma_b,\sigma_a)}{\sigma_a\sigma_b} & \frac{Var(\sigma_b)}{\sigma_b^2}\end{bmatrix}\begin{bmatrix}\frac{\tau_a}{\tau_a+\tau_b}\\ \frac{\tau_b}{\tau_a+\tau_b}\end{bmatrix} \tag{5.21}$$

Therefore:

$$\frac{Var(\tau_a+\tau_b)_{1g}}{(\tau_a+\tau_b)^2} = \frac{\tau_a^2}{(\tau_a+\tau_b)^2}\frac{Var(\sigma_a)}{\sigma_a^2} + \frac{\tau_b^2}{(\tau_a+\tau_b)^2}\frac{Var(\sigma_b)}{\sigma_b^2} + \frac{2\tau_a\tau_b}{(\tau_a+\tau_b)^2}\frac{cov(\sigma_a,\sigma_b)}{\sigma_a\sigma_b} \tag{5.22}$$

Hence:

$$\frac{cov(\sigma_a,\sigma_b)}{\sigma_a\sigma_b} = \frac{1}{2}\left[\frac{Var(\tau_a+\tau_b)_{1g}}{(\tau_a+\tau_b)^2}\frac{(\tau_a+\tau_b)^2}{\tau_a\tau_b} - \frac{\tau_a}{\tau_b}\frac{Var(\sigma_a)}{\sigma_a^2} - \frac{\tau_b}{\tau_a}\frac{Var(\sigma_b)}{\sigma_b^2}\right] \tag{5.23}$$

Now, let's work with the N-group side of the equation 5.16. Let $\underline{\phi}$ be the N-group flux and $\underline{\tau_i}$ the N-group reaction rate of reaction i.

$$\underline{\phi} = \begin{bmatrix}\phi_1\\ \vdots\\ \phi_N\end{bmatrix} \;;\; \underline{\tau_a} = \begin{bmatrix}\tau_{a,1}\\ \vdots\\ \tau_{a,N}\end{bmatrix} \;;\; \underline{\tau_b} = \begin{bmatrix}\tau_{b,1}\\ \vdots\\ \tau_{b,N}\end{bmatrix} \tag{5.24}$$

The N-group covariance matrix of (σ_a,σ_b) is as follows:

$$\underline{\underline{\boldsymbol{D}}}_{\boldsymbol{Ng}} = \begin{bmatrix}\underline{\underline{D}}_{aa} & \underline{\underline{D}}_{ab}\\ {}^t\underline{\underline{D}}_{ab} & \underline{\underline{D}}_{bb}\end{bmatrix} \tag{5.25}$$

Where $\underline{\underline{D}}_{aa}$ is the N-groups intra-reaction covariance matrix of reaction a and $\underline{\underline{D}}_{ab}$ is the N-groups inter-reaction covariance matrix of reactions (a,b).

$$\underline{\underline{D}}_{aa} = \begin{bmatrix} \dfrac{Var(\sigma_{a,1})}{(\sigma_{a,1})^2} & \cdots & \dfrac{cov(\sigma_{a,1},\sigma_{a,N})}{\sigma_{a,1}\sigma_{a,N}} \\ \vdots & \ddots & \vdots \\ \dfrac{cov(\sigma_{a,N},\sigma_{a,1})}{\sigma_{a,n}\sigma_{a,1}} & \cdots & \dfrac{Var(\sigma_{a,N})}{(\sigma_{a,N})^2} \end{bmatrix} \tag{5.26}$$

$$\underline{\underline{D}}_{ab} = \begin{bmatrix} \dfrac{cov(\sigma_{a,1},\sigma_{b,1})}{\sigma_{a,1}\sigma_{b,1}} & \cdots & \dfrac{cov(\sigma_{a,1},\sigma_{b,N})}{\sigma_{a,1}\sigma_{b,N}} \\ \vdots & \ddots & \vdots \\ \dfrac{cov(\sigma_{a,N},\sigma_{b,1})}{\sigma_{a,N}\sigma_{b,1}} & \cdots & \dfrac{cov(\sigma_{a,N},\sigma_{b,N})}{\sigma_{a,N}\sigma_{b,N}} \end{bmatrix} \tag{5.27}$$

The expressions of $\underline{\sigma}_a$ and $\underline{\sigma}_b$ are as follows:

$$\underline{\sigma_a} = \begin{bmatrix} \sigma_{a,1} \\ \vdots \\ \sigma_{a,N} \end{bmatrix} \quad \text{and} \quad \underline{\sigma_b} = \begin{bmatrix} \sigma_{b,1} \\ \vdots \\ \sigma_{b,N} \end{bmatrix} \tag{5.28}$$

We also note:

$$\underline{\boldsymbol{\sigma}}_{Ng} = {}^t\left[\sigma_{a,1}\ldots\sigma_{a,N};\sigma_{b,1}\ldots\sigma_{b,N}\right] = \begin{bmatrix} \underline{\sigma_a} \\ \underline{\sigma_b} \end{bmatrix} \tag{5.29}$$

We proceed to condense the data contained in 5.25 through the sandwich formula.

$$\frac{Var(\tau_a+\tau_b)_{Ng}}{(\tau_a+\tau_b)^2} = {}^{\boldsymbol{t}}\underline{\boldsymbol{S}}_{\boldsymbol{Ng}}\underline{\underline{\boldsymbol{D}}}_{\boldsymbol{Ng}}\underline{\boldsymbol{S}}_{\boldsymbol{Ng}} \tag{5.30}$$

The sensitivity expression of the variance of a sum of reaction rate is as follows:

$$\underline{\boldsymbol{S}}_{\boldsymbol{Ng}} = \frac{\underline{\boldsymbol{\sigma}}_{Ng}}{\tau_a+\tau_b}\frac{\partial(\tau_a+\tau_b)}{\partial\underline{\boldsymbol{\sigma}}_{Ng}} = \begin{bmatrix} \dfrac{\underline{\sigma_a}}{\tau_a+\tau_b}\dfrac{\partial(\tau_a+\tau_b)}{\partial\underline{\sigma_a}} \\ \dfrac{\underline{\sigma_b}}{\tau_a+\tau_b}\dfrac{\partial(\tau_a+\tau_b)}{\partial\underline{\sigma_b}} \end{bmatrix} \tag{5.31}$$

It simply consists in a concatenation of sensitivity vectors for a and b reaction rates.

In order to compute the condensation of covariance we have to expand the expression of 5.31:

$${}^{\boldsymbol{t}}\underline{\boldsymbol{S}}_{\boldsymbol{Ng}} = \begin{bmatrix} \dfrac{\sigma_a\phi_1}{\tau_a+\tau_b} & \cdots & \dfrac{\sigma_a\phi_n}{\tau_a+\tau_b} & , & \dfrac{\sigma_b\phi_1}{\tau_a+\tau_b} & \cdots & \dfrac{\sigma_b\phi_n}{\tau_a+\tau_b} \end{bmatrix} \tag{5.32}$$

Putting 5.32 in the expression 5.30 leads to:

$$\frac{Var(\tau_a+\tau_b)_{Ng}}{(\tau_a+\tau_b)^2} = \begin{bmatrix} \frac{\sigma_a\phi_1}{\tau_a+\tau_b} \cdots \frac{\sigma_a\phi_n}{\tau_a+\tau_b} & \frac{\sigma_b\phi_1}{\tau_a+\tau_b} \cdots \frac{\sigma_b\phi_n}{\tau_a+\tau_b} \end{bmatrix} \begin{bmatrix} \underline{\underline{D}}_{aa} & \underline{\underline{D}}_{ab} \\ {}^t\underline{\underline{D}}_{ab} & \underline{\underline{D}}_{bb} \end{bmatrix} \begin{bmatrix} \frac{\sigma_a\phi_1}{\tau_a+\tau_b} \\ \vdots \\ \frac{\sigma_a\phi_n}{\tau_a+\tau_b} \\ \frac{\sigma_b\phi_1}{\tau_a+\tau_b} \\ \vdots \\ \frac{\sigma_b\phi_n}{\tau_a+\tau_b} \end{bmatrix} \tag{5.33}$$

Expanding this expression, we get:

$$\begin{aligned} \frac{Var(\tau_a+\tau_b)_{Ng}}{(\tau_a+\tau_b)^2} &= \begin{bmatrix} \frac{{}^t\underline{\tau}_a}{\tau_a+\tau_b} & , & \frac{{}^t\underline{\tau}_b}{\tau_a+\tau_b} \end{bmatrix} \begin{bmatrix} \underline{\underline{D}}_{aa} & \underline{\underline{D}}_{ab} \\ {}^t\underline{\underline{D}}_{ab} & \underline{\underline{D}}_{bb} \end{bmatrix} \begin{bmatrix} \frac{\underline{\tau}_a}{\tau_a+\tau_b} \\ , \\ \frac{\underline{\tau}_b}{\tau_a+\tau_b} \end{bmatrix} \\ &= \frac{{}^t\underline{\tau}_a}{\tau_a+\tau_b}\underline{\underline{D}}_{aa}\frac{\underline{\tau}_a}{\tau_a+\tau_b} + \frac{{}^t\underline{\tau}_a}{\tau_a+\tau_b}\underline{\underline{D}}_{ab}\frac{\underline{\tau}_b}{\tau_a+\tau_b} \\ &+ \frac{{}^t\underline{\tau}_b}{\tau_a+\tau_b}{}^t\underline{\underline{D}}_{ab}\frac{\underline{\tau}_a}{\tau_a+\tau_b} + \frac{{}^t\underline{\tau}_b}{\tau_a+\tau_b}\underline{\underline{D}}_{bb}\frac{\underline{\tau}_b}{\tau_a+\tau_b} \\ &= \frac{{}^t\underline{\tau}_a}{\tau_a+\tau_b}\underline{\underline{D}}_{aa}\frac{\underline{\tau}_a}{\tau_a+\tau_b} + 2\frac{{}^t\underline{\tau}_a}{\tau_a+\tau_b}\underline{\underline{D}}_{ab}\frac{\underline{\tau}_b}{\tau_a+\tau_b} + \frac{{}^t\underline{\tau}_b}{\tau_a+\tau_b}\underline{\underline{D}}_{bb}\frac{\underline{\tau}_b}{\tau_a+\tau_b} \end{aligned} \tag{5.34}$$

The relation $\frac{{}^t\underline{\tau}_a}{\tau_a+\tau_b}\underline{\underline{D}}_{ab}\frac{\underline{\tau}_b}{\tau_a+\tau_b} = \frac{{}^t\underline{\tau}_b}{\tau_a+\tau_b}{}^t\underline{\underline{D}}_{ab}\frac{\underline{\tau}_a}{\tau_a+\tau_b}$ comes from the equality of a scalar and its transpose.

The value of each term of the right-side member of expression 5.34 is known, therefore we can calculate $\frac{Var(\tau_a+\tau_b)_{Ng}}{(\tau_a+\tau_b)^2}$. Then we inject expression of $\frac{Var(\tau_a+\tau_b)_{Ng}}{(\tau_a+\tau_b)^2}$ in equation 5.23 using the equality 5.16:

$$\begin{aligned} \frac{cov(\sigma_a,\sigma_b)}{\sigma_a\sigma_b} &= \frac{1}{2}\left[\frac{Var(\tau_a+\tau_b)_{Ng}}{(\tau_a+\tau_b)^2}\frac{(\tau_a+\tau_b)^2}{\tau_a\tau_b} - \frac{\tau_a}{\tau_b}\frac{Var(\sigma_a)}{\sigma_a^2} - \frac{\tau_b}{\tau_a}\frac{Var(\sigma_b)}{\sigma_b^2}\right] \\ &= \frac{1}{2}\left[\left[\frac{{}^t\underline{\tau}_a}{\tau_a+\tau_b}\underline{\underline{D}}_{aa}\frac{\underline{\tau}_a}{\tau_a+\tau_b} + 2\frac{{}^t\underline{\tau}_a}{\tau_a+\tau_b}\underline{\underline{D}}_{ab}\frac{\underline{\tau}_b}{\tau_a+\tau_b} + \frac{{}^t\underline{\tau}_b}{\tau_a+\tau_b}\underline{\underline{D}}_{bb}\frac{\underline{\tau}_b}{\tau_a+\tau_b}\right]\frac{(\tau_a+\tau_b)^2}{\tau_a\tau_b}\right. \\ &- \left.\frac{\tau_a}{\tau_b}\frac{{}^t\underline{\tau}_a}{\tau_a}\underline{\underline{D}}_{aa}\frac{\underline{\tau}_a}{\tau_a} - \frac{\tau_b}{\tau_a}\frac{{}^t\underline{\tau}_b}{\tau_b}\underline{\underline{D}}_{bb}\frac{\underline{\tau}_b}{\tau_b}\right] \\ &= \frac{{}^t\underline{\tau}_a}{\tau_a}\underline{\underline{D}}_{ab}\frac{\underline{\tau}_b}{\tau_b} \end{aligned} \tag{5.35}$$

We know every term of the right-side member of expression 5.35, therefore we can calculate $cov(\sigma_a,\sigma_b)$.

Finally the correlation is calculated :

$$\boxed{cor(\sigma_a,\sigma_b)=\frac{cov(\sigma_a,\sigma_b)}{\sqrt{Var(\sigma_a)Var(\sigma_b)}}=\frac{\frac{{}^t\underline{\tau}_a}{\tau_a}\underline{\underline{D}}_{ab}\frac{\underline{\tau}_b}{\tau_b}}{\sqrt{Var(\sigma_a)Var(\sigma_b)}}} \tag{5.36}$$

5.2.1.4 Cross-sections correlation between different spectra

5.2.1.4.1 Intra-reaction correlations in different spectra

The energy-integrated cross-sections condensed in different spectra are correlated. This correlation is important in the frame of uncertainty propagation calculation in scenario studies, because those studies consider different types of reactors, associated with different spectra, in the same computation. This correlation is expected to be high (if we increase the value of 1-group cross-section in a spectrum, we can reasonably estimate that the value will increase in another more or less similar spectrum), but not total. Indeed a total correlation is not consistent with developments of section 5.2.1.3, because the global covariance matrix of two sections in two spectra would not be positive-definite, hence inconsistent.

Let σ be the microscopic cross-section of interest (not multiplied by the material concentration), τ^α its scalar reaction rate in spectrum α and τ^β in spectrum β. Let $\underline{\phi}^\alpha=\begin{bmatrix}\phi_1^\alpha\\ \vdots\\ \phi_N^\alpha\end{bmatrix}$ and $\underline{\phi}^\beta=\begin{bmatrix}\phi_1^\beta\\ \vdots\\ \phi_N^\beta\end{bmatrix}$ be the vector fluxes in spectra α and β, with $\phi^\alpha=\sum_{j=1}^N\phi_j^\alpha$ and $\phi^\beta=\sum_{j=1}^N\phi_j^\beta$. Let σ^α be the energy-integrated cross-section of the reaction of interest in spectrum α, and σ^β the cross-section of the same reaction in spectrum β. We have:

$$\sigma^\alpha=\frac{{}^t\underline{\phi}^\alpha\underline{\sigma}}{\phi^\alpha}\ ,\ \sigma^\beta=\frac{{}^t\underline{\phi}^\beta\underline{\sigma}}{\phi^\beta} \tag{5.37}$$

We choose to use the conservation of the correlation of the value of the energy-integrated cross-section in both spectra. Therefore, while condensing covariance data, we want to obtain $cor(\sigma^\alpha,\sigma^\beta)_{1g}$ using the following laws :

$$\begin{cases} Var(\sigma^\alpha)_{1g} &= Var(\sigma^\alpha)_{Ng}\\ cor(\sigma^\alpha,\sigma^\beta)_{1g} &= cor(\sigma^\alpha,\sigma^\beta)_{Ng}\end{cases} \tag{5.38}$$

We have:

$$cor(\sigma^\alpha,\sigma^\beta)_{Ng}=\frac{cov(\sigma^\alpha,\sigma^\beta)}{\sqrt{Var(\sigma^\alpha)Var(\sigma^\beta)}} \tag{5.39}$$

With:

$$cov(\sigma^\alpha,\sigma^\beta)=\frac{1}{2}\left[Var(\sigma^\alpha+\sigma^\beta)-Var(\sigma^\alpha)-Var(\sigma^\beta)\right] \tag{5.40}$$

We calculate the right term members of equation 5.40 using the covariance matrix.

$$\frac{Var(\sigma^{\alpha}+\sigma^{\beta})_{Ng}}{(\sigma^{\alpha}+\sigma^{\beta})^2} = {}^{t}\underline{S}_{Ng}\underline{\underline{D}}_{Ng}\underline{S}_{Ng} \tag{5.41}$$

With:

$$\begin{aligned}\underline{S}_{Ng} &= \frac{\underline{\sigma}}{\sigma^{\alpha}+\sigma^{\beta}}\frac{\partial(\sigma^{\alpha}+\sigma^{\beta})}{\partial\underline{\sigma}} \\ &= \frac{\underline{\tau}^{\alpha}/\phi^{\alpha}+\underline{\tau}^{\beta}/\phi^{\beta}}{\sigma^{\alpha}+\sigma^{\beta}}\end{aligned} \tag{5.42}$$

Hence we obtain:

$$cov(\sigma^{\alpha},\sigma^{\beta}) = \frac{1}{2}\left[(\sigma^{\alpha}+\sigma^{\beta})^2\cdot{}^{t}\underline{S}_{Ng}\underline{\underline{D}}_{Ng}\underline{S}_{Ng} - Var(\sigma^{\alpha}) - Var(\sigma^{\beta})\right] \tag{5.43}$$

Finally the correlation is calculated:

$$\boxed{cor(\sigma^{\alpha},\sigma^{\beta}) = \frac{cov(\sigma^{\alpha},\sigma^{\beta})}{\sqrt{Var(\sigma^{\alpha})Var(\sigma^{\beta})}}} \tag{5.44}$$

5.2.1.4.2 Inter-reaction correlations in different spectra

The last case concerns correlation between different cross-sections in different spectra. Let us denote σ_a^{α} cross-section a integrated in spectrum α and σ_b^{β} cross-section b integrated in spectrum β. Our conservation law is the conservation of inter-reaction, inter-spectra correlation of cross-section correlations:

$$\left\{\begin{array}{rcl} Var(\sigma_a^{\alpha})_{1g} &=& Var(\sigma_a^{\alpha})_{Ng} \\ Var(\sigma_b^{\beta})_{1g} &=& Var(\sigma_b^{\beta})_{Ng} \\ cor(\sigma_a^{\alpha},\sigma_b^{\beta})_{1g} &=& cor(\sigma_a^{\alpha},\sigma_b^{\beta})_{Ng}\end{array}\right. \tag{5.45}$$

Let us denote $\underline{\boldsymbol{\sigma}}_{\boldsymbol{Ng}} = {}^{t}\left[\sigma_{a,1}^{\alpha}\ldots\sigma_{a,N}^{\alpha},\sigma_{b,1}^{\beta}\ldots\sigma_{b,N}^{\beta}\right]$.

We have:

$$cov(\sigma_a^{\alpha},\sigma_b^{\beta})_{Ng} = \frac{1}{2}\left[Var(\sigma_a^{\alpha}+\sigma_b^{\beta}) - Var(\sigma_a^{\alpha}) - Var(\sigma_b^{\beta})\right] \tag{5.46}$$

We calculate the members of the right term of equation 5.46 using the covariance matrix defined in equation 5.25.

$$\frac{Var(\sigma_a^{\alpha}+\sigma_b^{\beta})}{\left(\sigma_a^{\alpha}+\sigma_b^{\beta}\right)^2} = {}^{t}\underline{\boldsymbol{S}}_{\boldsymbol{Ng}}\underline{\underline{\boldsymbol{D}}}_{\boldsymbol{Ng}}\underline{\boldsymbol{S}}_{\boldsymbol{Ng}} \tag{5.47}$$

With:

$$\begin{aligned}\underline{\boldsymbol{S}}_{\boldsymbol{Ng}} &= \frac{\underline{\boldsymbol{\sigma}}_{\boldsymbol{Ng}}}{\sigma_a^\alpha + \sigma_b^\beta}\frac{\partial(\sigma_a^\alpha + \sigma_b^\beta)}{\partial \underline{\boldsymbol{\sigma}}_{\boldsymbol{Ng}}} \\ &= {}^t\left[\frac{\tau_{a,1}^\alpha/\phi^\alpha}{\sigma_a^\alpha + \sigma_b^\beta} \quad \cdots \quad \frac{\tau_{a,N}^\alpha/\phi^\alpha}{\sigma_a^\alpha + \sigma_b^\beta} \quad , \quad \frac{\tau_{b,1}^\beta/\phi^\beta}{\sigma_a^\alpha + \sigma_b^\beta} \quad \cdots \quad \frac{\tau_{b,N}^\beta/\phi^\beta}{\sigma_a^\alpha + \sigma_b^\beta}\right]\end{aligned} \tag{5.48}$$

The method is similar to the previous paragraphs. We obtain:

$$cov(\sigma_a^\alpha, \sigma_b^\beta) = \frac{1}{2}\left[(\sigma_a^\alpha + \sigma_b^\beta)^2 \cdot {}^t\underline{\boldsymbol{S}}_{\boldsymbol{Ng}}\underline{\underline{\boldsymbol{D}}}_{\boldsymbol{Ng}}\underline{\boldsymbol{S}}_{\boldsymbol{Ng}} - Var(\sigma_a^\alpha) - Var(\sigma_b^\beta)\right] \tag{5.49}$$

Finally the correlation is calculated:

$$\boxed{cor(\sigma_a^\alpha, \sigma_b^\beta) = \frac{cov(\sigma_a^\alpha, \sigma_b^\beta)}{\sqrt{Var(\sigma_a^\alpha)Var(\sigma_b^\beta)}} = \frac{\frac{1}{2}\left[(\sigma_a^\alpha + \sigma_b^\beta)^2 \cdot {}^t\underline{\boldsymbol{S}}_{\boldsymbol{Ng}}\underline{\underline{\boldsymbol{D}}}_{\boldsymbol{Ng}}\underline{\boldsymbol{S}}_{\boldsymbol{Ng}} - Var(\sigma_a^\alpha) - Var(\sigma_b^\beta)\right]}{\sqrt{Var(\sigma_a^\alpha)Var(\sigma_b^\beta)}}} \tag{5.50}$$

5.2.1.5 Results

In section 3.1.2.1.4.3 we show that impact of irradiation on cross-sections uncertainty is small: cross-sections uncertainty is approximately the same in fresh and depleted fuel. Consequently, we only perform the covariance condensation process in the following spectra:

- PWR UOX fuel (intermediate irradiation);
- half-irradiated PWR MOX fuel (intermediate irradiation) ;
- half-irradiated SFR fuel (intermediate irradiation).

Finally, we check that covariance matrices are positive-definite. In the case of PWR UOX and PWR MOX spectra, a first transport run was performed using APOLLO2 [5.1] with SHEM mesh (281 groups) and AUTOP_SHEM self-shielding. In the case of SFR spectrum, a transport run was performed using ERANOS [5.2].

Flux and reaction rates are computed in the fuel, and are condensed into a 33-group mesh adapted to thermal spectra. Condensation energy mesh is described in table 5.1. This computation is based on JEFF-3.1.1/CEA2005v4.1.1 data.

The 33-groups covariance matrices were processed from ENDF B-VII files with CadTui [5.3], a NJOY [5.4] script generator developed at CEA Cadarache.

The systems are as follows:

- PWR UOX spectrum: PWR 17×17 AFA, uranium mass enrichment is 4.4% (fresh fuel);
- PWR MOX spectrum: PWR 17×17 MOX AFA3G, 3 zones, mean plutonium mass enrichment is 8.65%, environment = UOX fuel, ^{235}U mass enrichment = 3.7% irradiated up to 23GWd/tHM. Computation is performed in fresh fuel. Plutonium vector is shown in table 5.2.
- SFR spectrum: SFR CFV core. Plutonium vector is shown in table 5.3. Plutonium volume enrichment is 21.2%.

Group	E_{max} (MeV)
1	1.96×10^{1}
2	1.00×10^{1}
3	6.07×10^{0}
4	3.68×10^{0}
5	2.23×10^{0}
6	1.35×10^{0}
7	8.21×10^{-1}
8	4.98×10^{-1}
9	3.02×10^{-1}
10	1.83×10^{-1}
11	1.11×10^{-1}
12	6.74×10^{-2}
13	4.09×10^{-2}
14	2.48×10^{-2}
15	1.50×10^{-2}
16	9.12×10^{-3}
17	5.53×10^{-3}
18	3.35×10^{-3}
19	2.03×10^{-3}
20	1.23×10^{-3}
21	7.49×10^{-4}
22	4.54×10^{-4}
23	3.04×10^{-4}
24	1.49×10^{-4}
25	9.17×10^{-5}
26	6.79×10^{-5}
27	4.02×10^{-5}
28	2.26×10^{-5}
29	1.37×10^{-5}
30	8.32×10^{-6}
31	4.00×10^{-6}
32	5.40×10^{-7}
33	1.00×10^{-7}
	1.00×10^{-11}

Table 5.1: 33 groups condensation mesh

Nuclide	isotopy
^{238}Pu	2.50
^{239}Pu	54.50
^{240}Pu	25.20
^{241}Pu	8.60
^{242}Pu	7.90
^{241}Am	1.30

Table 5.2: Plutonium vector in PWR MOX core

Nuclide	isotopy
^{238}Pu	2.50
^{239}Pu	54.50
^{240}Pu	25.20
^{241}Pu	8.60
^{242}Pu	7.90
^{241}Am	1.30

Table 5.3: Plutonium vector in SFR CFV core

^{234}U, ENDF B-VII		UOX		MOX		SFR	
			σ_f	σ_c	σ_f	σ_c	σ_f	σ_c
		RSD(%)	19.93	3.00	20.01	3.58	25.12	9.21
UOX	σ_f	19.93	1.00	0.00	1.00	0.00	1.00	-0.00
	σ_c	3.00		1.00	-0.00	0.99	0.00	0.26
MOX	σ_f	20.01			1.00	0.00	1.00	-0.00
	σ_c	3.58				1.00	-0.00	0.27
SFR	σ_f	25.12					1.00	0.00
	σ_c	9.21						1.00

Table 5.4: ^{234}U PWR UOX - PWR MOX - SFR MOX 1-group covariance matrix

^{235}U, ENDF B-VII			UOX		MOX		SFR	
			σ_f	σ_c	σ_f	σ_c	σ_f	σ_c
		RSD(%)	0.33	1.36	0.31	1.71	0.57	20.69
UOX	σ_f	0.33	1.00	-0.34	0.97	-0.23	0.10	-0.00
	σ_c	1.36		1.00	-0.30	0.89	-0.04	0.62
MOX	σ_f	0.31			1.00	-0.21	0.21	-0.01
	σ_c	1.71				1.00	-0.03	0.88
SFR	σ_f	0.57					1.00	-0.00
	σ_c	20.69						1.00

Table 5.5: ^{235}U PWR UOX - PWR MOX - SFR MOX 1-group covariance matrix

^{236}U, ENDF B-VII			UOX		MOX		SFR	
			σ_f	σ_c	σ_f	σ_c	σ_f	σ_c
		RSD(%)	22.03	3.75	22.27	3.88	25.29	2.85
UOX	σ_f	22.03	1.00	0.00	1.00	0.00	0.83	0.00
	σ_c	3.75		1.00	0.00	1.00	0.00	0.62
MOX	σ_f	22.27			1.00	0.00	0.81	-0.00
	σ_c	3.88				1.00	0.00	0.62
SFR	σ_f	25.29					1.00	0.00
	σ_c	2.85						1.00

Table 5.6: ^{236}U PWR UOX - PWR MOX - SFR MOX 1-group covariance matrix

^{238}U, ENDF B-VII			UOX		MOX		SFR	
			σ_f	σ_c	σ_f	σ_c	σ_f	σ_c
		RSD(%)	0.52	1.43	0.52	1.45	0.53	1.42
UOX	σ_f	0.52	1.00	0.00	1.00	0.00	0.99	-0.00
	σ_c	1.43		1.00	0.00	0.99	0.00	0.67
MOX	σ_f	0.52			1.00	0.00	0.99	-0.00
	σ_c	1.45				1.00	0.00	0.71
SFR	σ_f	0.53					1.00	-0.00
	σ_c	1.42						1.00

Table 5.7: ^{238}U PWR UOX - PWR MOX - SFR MOX 1-group covariance matrix

^{237}Np, ENDF B-VII			UOX		MOX		SFR	
			σ_f	σ_c	σ_f	σ_c	σ_f	σ_c
		RSD(%)	2.83	4.55	2.83	4.09	3.13	8.79
UOX	σ_f	2.83	1.00	0.00	1.00	0.00	0.99	-0.00
	σ_c	4.55		1.00	-0.00	0.96	-0.00	0.13
MOX	σ_f	2.83			1.00	0.00	0.99	-0.00
	σ_c	4.09				1.00	0.00	0.23
SFR	σ_f	3.13					1.00	0.00
	σ_c	8.79						1.00

Table 5.8: ^{237}Np PWR UOX - PWR MOX - SFR MOX 1-group covariance matrix

^{239}Np, ENDF B-VII			UOX		MOX		SFR	
			σ_f	σ_c	σ_f	σ_c	σ_f	σ_c
		RSD(%)	147.36	32.86	146.87	36.40	210.70	30.95
UOX	σ_f	147.36	1.00	0.00	1.00	0.00	1.00	0.00
	σ_c	32.86		1.00	0.00	0.98	0.00	0.86
MOX	σ_f	146.87			1.00	0.00	1.00	0.00
	σ_c	36.40				1.00	-0.00	0.91
SFR	σ_f	210.70					1.00	0.00
	σ_c	30.95						1.00

Table 5.9: ^{239}Np PWR UOX - PWR MOX - SFR MOX 1-group covariance matrix

^{238}Pu, ENDF B-VII			UOX		MOX		SFR	
			σ_f	σ_c	σ_f	σ_c	σ_f	σ_c
		RSD(%)	0.24	9.81	0.31	9.54	0.53	7.80
UOX	σ_f	0.24	1.00	0.00	1.00	-0.00	0.86	-0.00
	σ_c	9.81		1.00	-0.00	1.00	0.00	0.12
MOX	σ_f	0.31			1.00	0.00	0.86	-0.00
	σ_c	9.54				1.00	0.00	0.15
SFR	σ_f	0.53					1.00	0.00
	σ_c	7.80						1.00

Table 5.10: ^{238}Pu PWR UOX - PWR MOX - SFR MOX 1-group covariance matrix

^{239}Pu, ENDF B-VII			UOX		MOX		SFR	
			σ_f	σ_c	σ_f	σ_c	σ_f	σ_c
		RSD(%)	0.77	1.13	0.74	1.03	0.41	5.26
UOX	σ_f	0.77	1.00	-0.52	0.99	-0.48	0.14	0.00
	σ_c	1.13		1.00	-0.45	0.99	0.03	0.06
MOX	σ_f	0.74			1.00	-0.41	0.18	0.00
	σ_c	1.03				1.00	0.03	0.14
SFR	σ_f	0.41					1.00	0.01
	σ_c	5.26						1.00

Table 5.11: ^{239}Pu PWR UOX - PWR MOX - SFR MOX 1-group covariance matrix

^{240}Pu, ENDF B-VII			UOX		MOX		SFR	
			σ_f	σ_c	σ_f	σ_c	σ_f	σ_c
		RSD(%)	2.18	1.64	1.18	1.65	1.06	3.35
UOX	σ_f	2.18	1.00	0.00	0.96	0.00	0.59	-0.00
	σ_c	1.64		1.00	-0.00	1.00	-0.00	0.18
MOX	σ_f	1.18			1.00	0.00	0.77	-0.00
	σ_c	1.65				1.00	0.00	0.21
SFR	σ_f	1.06					1.00	0.00
	σ_c	3.35						1.00

Table 5.12: ^{240}Pu PWR UOX - PWR MOX - SFR MOX 1-group covariance matrix

^{241}Pu, ENDF B-VII			UOX		MOX		SFR	
			σ_f	σ_c	σ_f	σ_c	σ_f	σ_c
		RSD(%)	1.47	2.19	1.42	3.44	0.70	14.24
UOX	σ_f	1.47	1.00	0.00	1.00	0.00	0.17	0.00
	σ_c	2.19		1.00	-0.00	0.88	-0.00	0.18
MOX	σ_f	1.42			1.00	0.00	0.19	0.00
	σ_c	3.44				1.00	-0.00	0.28
SFR	σ_f	0.70					1.00	0.00
	σ_c	14.24						1.00

Table 5.13: ^{241}Pu PWR UOX - PWR MOX - SFR MOX 1-group covariance matrix

^{242}Pu, ENDF B-VII			UOX		MOX		SFR	
			σ_f	σ_c	σ_f	σ_c	σ_f	σ_c
		RSD(%)	1.87	11.51	1.87	11.51	1.90	4.31
UOX	σ_f	1.87	1.00	0.00	1.00	0.00	0.99	0.00
	σ_c	11.51		1.00	0.00	1.00	-0.00	0.67
MOX	σ_f	1.87			1.00	0.00	0.99	0.00
	σ_c	11.51				1.00	-0.00	0.68
SFR	σ_f	1.90					1.00	0.00
	σ_c	4.31						1.00

Table 5.14: ^{242}Pu PWR UOX - PWR MOX - SFR MOX 1-group covariance matrix

^{241}Am, ENDF B-VII			UOX		MOX		SFR	
			σ_f	σ_c	σ_f	σ_c	σ_f	σ_c
		RSD(%)	4.51	5.09	2.63	4.88	1.29	1.91
UOX	σ_f	4.51	1.00	0.01	0.96	0.01	0.12	0.00
	σ_c	5.09		1.00	0.01	1.00	0.00	0.03
MOX	σ_f	2.63			1.00	0.01	0.30	0.00
	σ_c	4.88				1.00	0.00	0.04
SFR	σ_f	1.29					1.00	-0.00
	σ_c	1.91						1.00

Table 5.15: ^{241}Am PWR UOX - PWR MOX - SFR MOX 1-group covariance matrix

^{242M}Am ENDF B-VII			UOX		MOX		SFR	
			σ_f	σ_c	σ_f	σ_c	σ_f	σ_c
		RSD(%)	4.66	23.60	4.30	21.94	8.74	27.76
UOX	σ_f	4.66	1.00	0.00	0.99	-0.00	0.03	-0.00
	σ_c	23.60		1.00	0.00	1.00	-0.00	0.03
MOX	σ_f	4.30			1.00	0.00	0.07	-0.00
	σ_c	21.94				1.00	-0.00	0.07
SFR	σ_f	8.74					1.00	0.00
	σ_c	27.76						1.00

Table 5.16: ^{242M}Am PWR UOX - PWR MOX - SFR MOX 1-group covariance matrix

^{243}Am, ENDF B-VII			UOX		MOX		SFR	
			σ_f	σ_c	σ_f	σ_c	σ_f	σ_c
		RSD(%)	8.08	3.63	8.33	3.82	8.43	4.89
UOX	σ_f	8.08	1.00	0.00	1.00	0.00	0.97	-0.00
	σ_c	3.63		1.00	-0.00	1.00	-0.00	0.43
MOX	σ_f	8.33			1.00	0.00	0.97	0.00
	σ_c	3.82				1.00	0.00	0.44
SFR	σ_f	8.43					1.00	0.00
	σ_c	4.89						1.00

Table 5.17: ^{243}Am PWR UOX - PWR MOX - SFR MOX 1-group covariance matrix

^{242}Cm, ENDF B-VII			UOX		MOX		SFR	
			σ_f	σ_c	σ_f	σ_c	σ_f	σ_c
		RSD(%)	4.68	13.85	4.99	15.44	5.29	20.33
UOX	σ_f	4.68	1.00	0.46	0.97	0.46	0.64	0.00
	σ_c	13.85		1.00	0.44	0.99	-0.00	0.24
MOX	σ_f	4.99			1.00	0.45	0.71	0.00
	σ_c	15.44				1.00	-0.00	0.27
SFR	σ_f	5.29					1.00	0.00
	σ_c	20.33						1.00

Table 5.18: ^{242}Cm PWR UOX - PWR MOX - SFR MOX 1-group covariance matrix

^{243}Cm, ENDF B-VII			UOX		MOX		SFR	
			σ_f	σ_c	σ_f	σ_c	σ_f	σ_c
		RSD(%)	6.27	28.15	3.67	25.88	3.48	77.45
UOX	σ_f	6.27	1.00	0.11	0.98	0.06	0.03	0.00
	σ_c	28.15		1.00	0.09	0.98	0.00	0.15
MOX	σ_f	3.67			1.00	0.05	0.09	0.00
	σ_c	25.88				1.00	0.00	0.30
SFR	σ_f	3.48					1.00	0.00
	σ_c	77.45						1.00

Table 5.19: ^{243}Cm PWR UOX - PWR MOX - SFR MOX 1-group covariance matrix

^{244}Cm, ENDF B-VII		UOX		MOX		SFR	
		σ_f	σ_c	σ_f	σ_c	σ_f	σ_c
	RSD(%)	4.11	8.28	3.70	8.40	2.99	22.49
UOX	σ_f 4.11	1.00	-0.04	0.99	-0.04	0.51	-0.00
	σ_c 8.28		1.00	-0.02	1.00	-0.00	0.18
MOX	σ_f 3.70			1.00	-0.02	0.61	-0.00
	σ_c 8.40				1.00	0.00	0.21
SFR	σ_f 2.99					1.00	0.00
	σ_c 22.49						1.00

Table 5.20: ^{244}Cm PWR UOX - PWR MOX - SFR MOX 1-group covariance matrix

^{245}Cm, ENDF B-VII		UOX		MOX		SFR	
		σ_f	σ_c	σ_f	σ_c	σ_f	σ_c
	RSD(%)	8.37	18.60	6.99	17.62	3.29	61.45
UOX	σ_f 8.37	1.00	0.11	0.99	0.09	0.03	0.00
	σ_c 18.60		1.00	0.10	0.93	0.00	0.21
MOX	σ_f 6.99			1.00	0.09	0.05	0.00
	σ_c 17.62				1.00	0.00	0.54
SFR	σ_f 3.29					1.00	0.00
	σ_c 61.45						1.00

Table 5.21: ^{245}Cm PWR UOX - PWR MOX - SFR MOX 1-group covariance matrix

^{246}Cm, ENDF B-VII		UOX		MOX		SFR	
		σ_f	σ_c	σ_f	σ_c	σ_f	σ_c
	RSD(%)	4.9	15.6	4.7	14.3	4.0	24.0
UOX	σ_f 4.9	1.00	-0.00	1.00	-0.00	0.72	0.00
	σ_c 15.6		1.00	-0.00	0.95	0.00	0.43
MOX	σ_f 4.7			1.00	-0.00	0.76	0.00
	σ_c 14.3				1.00	0.00	0.67
SFR	σ_f 4.0					1.00	0.00
	σ_c 24.0						1.00

Table 5.22: ^{246}Cm PWR UOX - PWR MOX - SFR MOX 1-group covariance matrix

5.2.2 Fission yields

5.2.2.1 Introduction

5.2.2.2 Fission yields uncertainty

ENDF B-VII data concerning fission yields uncertainty (available at http://www.oecd-nea.org/janis/) was used in this work. We made the hypothesis that fission yield relative uncertainty was the same in fast and thermal spectra. Further work may consider different uncertainty values.

We assumed a Gaussian distribution of the uncertainty. Fission yields which uncertainty is unknown are attributed a uniform distribution on the interval [-100%, +100%]. Fission yields are considered uncorrelated in this work.

The fission yields taken into account are (A $\rightarrow$ B) where:

A $\in$ { ^{235}U, ^{238}U, ^{238}Pu, ^{239}Pu, ^{240}Pu, ^{241}Pu, ^{242}Pu }

and

B $\in$ { ^{84}Kr, ^{85}Kr, ^{90}Sr, ^{95}Zr, ^{106}Ru, ^{132}Te, ^{133}I, ^{137}Cs, ^{144}Ce, ^{146}Nd, ^{147}Nd, ^{151}Pm, ^{152}Sm, ^{153}Sm }.

As explained in section 3.1.1.1, isotopes B were chosen such that a high percentage of fission products decay heat is taken into account in fuel cycle time scale (between 1 and 50 years).

5.3 Scenario parameters and hypotheses

5.3.1 Introduction

In this work we choose to distinct two types of scenario-related quantities: scenario hypotheses, which are decisions defining the structure of scenarios, and scenario parameters, which are subject to industrial and physical uncertainty.

5.3.2 Scenario hypotheses

We denote *scenario hypotheses* the hypotheses of a scenario that are not associated with uncertainty. Those parameters generally result from industrial decisions.

For instance, the type of fuel or the fuel management are considered as scenario hypotheses in this work. Scenario hypotheses include:

- type of fuel used in the scenario (SFR, etc.);
- reprocessing strategy (which spent fuel mix is used to produce fresh fuel, at any date of the scenario);
- load factors;
- reactors starting and shutdown dates, etc.

As this work is focused on uncertainty propagation studies, the impact of changes in scenario hypotheses was not assessed. However, sensitivity studies should be performed in order to measure the impact of those parameters.

5.3.3 Scenario parameters

5.3.3.1 Introduction

We denote *scenario parameters* the parameters of scenario studies that are associated with an uncertainty value. Those parameters are generally physical and industrial parameters (as opposed to decision-making parameters, which are not associated with an uncertainty in this work).

It is generally difficult to provide data concerning scenario parameters and their uncertainty. In this work, we try to give a description as complete as we can of those factors.

5.3.3.2 Natural uranium isotopic composition

Natural uranium stocks have a small range of variation. Values obtained from report [5.5] are shown in table 5.23.

isotope	min mole fraction	max mole fraction	$\frac{max - min}{mean}$
^{234}U	0.000053	0.000057	7%
^{235}U	0.007199	0.007207	0.1%
^{238}U	0.992739	0.992748	0.0009%

Table 5.23: Natural uranium isotopy range of variation

Impact study of natural uranium isotopy uncertainty is presented on section 6.2.4.5 page 266 in the case of scenario D. It appears that the impact is very small. Consequently we neglected the impact of natural uranium isotopy in other studies.

5.3.3.3 Durations

5.3.3.3.1 Front-end durations

Fuel cycle front-end includes enrichment, fuel fabrication and transportation up to loading. In scenario studies, the whole fuel fabrication duration is usually 2 years, which is considered as consistent from an industrial point of view. Front-end duration sensitivity study is performed in section 6.2.4.6.4 page 270 in the case of scenario D.

5.3.3.3.2 Back-end durations

Figure 5.1 represents the fuel cycle back-end in the case of a scenario with fuel reprocessing.

Figure 5.1: Fuel cycle back-end

A global duration is associated to transportation and reprocessing.

The transportation step and its duration represent the fact that decay heat prevents from reprocessing fuel that has just been irradiated. Fuel at the output of a reactor is considered unavailable, whereas it is considered available once it has reached the transportation duration.

There are two ways to define the transportation duration:

- a numerical value for the minimum duration before reprocessing is chosen (for instance $\Delta t = 5 years$). This duration must be representative of decay heat for the type of fuel considered;
- a numerical value for the maximum decay heat for fuel transportation and reprocessing is chosen (for instance DH $< 3.5 kW/assembly$).

Decay heat is subject to uncertainty from nuclear data and irradiation parameters. A numerical value for the minimum duration before reprocessing prevents from evaluating the impact of decay heat uncertainty on the fuel back-end. Consequently, in the case of uncertainty propagation in scenario studies, we use the maximum decay heat for fuel transportation as a criterion. Impact of decay heat uncertainty on scenario feasibility is discusses in section 6.2.4.6.5.

5.3.3.4 Enrichment plant

Uranium enrichment is considered fixed and therefore not subject to uncertainty. However uranium losses are subject to uncertainty. Impact of this uncertainty will not be estimated in this work, but we note that its most important impact on the fuel cycle is through natural consumption.

5.3.3.5 Fabrication plant

Besides fuel fabrication duration, mass losses are a parameter of the fabrication plant. We expect losses to be within the interval $[0.0\% \ , \ 0.2\%]$ of the total mass at fabrication plant.

5.3.3.6 Reprocessing plant

Mass losses at the reprocessing plant are subject to uncertainty.

Table 5.24 shows the recovery rate (= 1 - loss rate) of different plants and experiments. The results are extracted from [5.6].

We calculate recovery rates standard deviation calculated from this data and obtain:

- plutonium: σ = 0.8%;
- neptunium: not enough data;
- americium: σ = 0.3%;
- curium: σ = 0.3%.

In section 6.2.4.6.3, a sensitivity study shows the impact of recovery rate on scenario feasibility.

Reprocessing plant capacity is not associated with an uncertainty, and is considered as a scenario hypothesis.

Information type	Reference	reactor type	Recovery rate (%) Am	Np	Cm	Pu
experiment	EXAM	SFR	98.14			99.31
experiment	EXAM	PWR	98.26			
experiment	REX	SFR				99.58
industrial feedback		PWR				99.65
experiment	GANEX	SFR	99.75	98.90	99.30	
experiment	SANEX	SFR	99.64		99.80	
experiment	SANEX	PWR	99.76		99.86	
analogy	PWR analogy	SFR				99.94

Table 5.24: Recovery rates at reprocessing plant

5.3.3.7 Reactor

Equation 5.51 is the expression of electrical power produced by a reactor as a function of fuel and reactor parameters, with:

- Δt : irradiation duration in EFPD (effective full power days);
- BU : fuel burnup (energy extracted from fuel during Δt) ;
- ρ : reactor yield (transformation of thermal energy into electrical energy);
- f : load factor $= \dfrac{\text{mean power}}{\text{nominal power}}$;
- m : fuel mass in core.

$$\mathcal{P}_e = \frac{\text{BU} \times \rho \times f \times m}{\Delta t} \tag{5.51}$$

Δt is subject to uncertainty, however COSI structure is such that it is more convenient to consider the associated burnup and power uncertainty. Uncertainty concerning those parameters is detailed in section 5.3.3.8.

The mass m is not subject to uncertainty.

The load factor is a scenario hypothesis. It is adjusted such that energy production fulfills the energy demand.

The reactor yield is subject to uncertainty. However, its impact will not be assessed in this study. Indeed, as global electrical power, burnup and masses are determined in the study, introducing a reactor yield uncertainty would introduce uncertainty double-counting.

We note that our uncertainty propagation study does not take stretch-out into account. Indeed stretch-out results from decisions, and is therefore an hypothesis, not a parameter. However, even if stretch-out does not result from uncertainty, it is possible to produce sensitivity studies using the methodology developed in this work.

We note that in scenario studies made with COSI, start-up batches are taken into account.

5.3.3.8 Burnup

5.3.3.8.1 Definitions

We define a few parameters:

- discharge burnup: the burnup of a fuel assembly when it is discharged from the core;
- irradiation cycle: in a core whose fractionation is N, every fuel assembly is irradiated during N irradiation cycles;
- $cycle$: in this section, we denominate $cycle$ the burnup of an irradiation cycle. The discharge burnup is equal to $\sum_{i=1}^{fractionation} cycle_i$.

5.3.3.8.2 Preliminary remark concerning burnup and fractionation

In this burnup study, we consider a core at equilibrium. However, in scenario computations, start-up cores are modeled as well.

In COSI, irradiation of batches is parameterized with discharge burnup, and not end of cycle burnup. Therefore it is necessary to assess the uncertainty associated to discharge burnup. However, it is not possible to use directly this uncertainty value in scenario computations: although irradiation cycles are not correlated one to another, batches are.

Indeed let us consider a core fractionation of three, and 6 consecutive batches irradiated in the same core, noted A, B, C, D, E and F; other batches are noted X. The irradiation scheme is shown on figure 5.2, each box represents the state of the core during a cycle. We denote 1, 2, 3, 4, etc. the consecutive irradiation cycles.

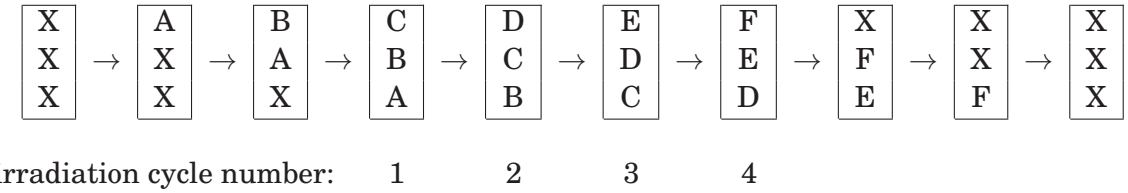

Figure 5.2: Batch sequence in a core

We observe that batches 1 and 2 have two irradiation cycles in common, and 1 and 3 have one irradiation cycle in common while 2 and 3 have two cycles in common.

For each batch, the discharge burnup is the sum of the burnup of the cycles it went through. Therefore, consecutive batches have a non-null correlation. More precisely, if we consider numerical ranking of batches, for a core fractionation N, batches between $(i-N+1)$ and $(i+N-1)$ are correlated with batch i.

We denote BU_A the discharge burnup of batch A, and $cycle_i$ the burnup of irradiation cycle i. We compute the correlation matrix associated to these batches with URANIE, the tasks sequence is as follows:

- sample $cycle_i$ for each i
- add $N = 3$ consecutive cycles:
  - $\mathrm{BU}_C = cycle_1 + cycle_2 + cycle_3$;

  - $\text{BU}_D = cycle_2 + cycle_3 + cycle_4$;
  - etc.
- compute the correlation matrix of (BU_A, BU_B, BU_C, etc.) from data.

We obtain the correlation matrix shown on table 5.25.

	BU_A	BU_B	BU_C	BU_D	BU_E	BU_F
BU_A	1	0.67	0.33	0	0	0
BU_B	0.67	1	0.67	0.33	0	0
BU_C	0.33	0.67	1	0.67	0.33	0
BU_D	0	0.33	0.67	1	0.67	0.33
BU_E	0	0	0.33	0.67	1	0.67
BU_F	0	0	0	0.33	0.67	1

Table 5.25: Burnup correlation matrix of consecutive batches in a core, fractionation $N = 3$

The pattern is clear: each batch is correlated to batches irradiated up to two cycles before or after it, and uncorrelated with others. B is correlated with A and C at the same level, with D, and not E: indeed B and E have no irradiation cycle in common.

The objective is to produce discharge burnup uncertainty using irradiation cycles uncertainty. There are several ways to tackle this problem:

- produce a correlated sample of discharge burnup taking into account fractionation;
- produce a non-correlated sample of cycles and calculate the discharge burnup from the irradiation cycles burnup;
- produce a non-correlated sample of discharge burnup which standard deviation is adjusted so as to be representative of correlations in the irradiation history.

In paragraph 5.3.3.8.3 we evaluate the irradiation cycle burnup uncertainty value, while in paragraph 5.3.3.8.4 our aim is to produce approximations of discharge burnup distributions.

5.3.3.8.3 Irradiation cycle uncertainty

5.3.3.8.3.1 Introduction

This section details the different uncertainty sources that have an impact on an irradiation cycle burnup, and describes its uncertainty evaluation. We take into account the following uncertainty sources:

- core reloading date uncertainty (section 5.3.3.8.3.2) and its impact on the cycle burnup $\sigma_{reloading}(cycle)$;
- irradiation power uncertainty (section 5.3.3.8.3.3) and its impact on the cycle burnup $\sigma_{power}(cycle)$.

We did not take into account the burnup measurement experimental uncertainty, because it is evaluated *a posteriori* and its value is not known at the time the scenario is computed: burnup uncertainty measure does not generate provisional electrical energy uncertainty (or other fuel cycle uncertainty).

5.3.3.8.3.2 Core reloading date

Core reloading is planned approximately two months before it is actually performed, in order to perform safety studies. However, the effective reloading date is subject to uncertainty. In this section, we estimate the impact of core reloading date on discharge burnup uncertainty for a given fuel batch.

We cannot assess this uncertainty directly because batches are correlated one to another. This work is based on PWR UOX data, however we will consider identical relative standard deviations in the case of different types of fuel.

Considering the PWR UOX effective power, this uncertainty represents approximately 200MWd/tHM on the core average burnup at reloading date [5.7] for fuel reaching 45GWd/tHM.

In our example, we will study a core divided in three batches. The core is represented on figure 5.3. Reloading is performed when the most irradiated fraction reaches discharge burnup.

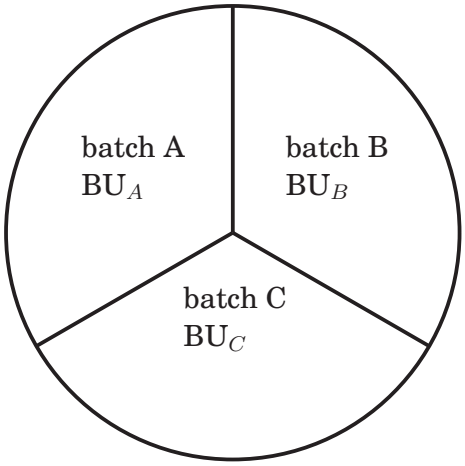

Figure 5.3: Representation of a core at the end of an irradiation cycle

Therefore the average core burnup at the end of a cycle is:

$$\overline{\mathrm{BU}}_{core} = \frac{1}{3} \times (\mathrm{BU}_A + \mathrm{BU}_B + \mathrm{BU}_C) \tag{5.52}$$

The uncertainty associated to $\overline{\mathrm{BU}}_{core}$ is 200MWd/tHM. We assume that each irradiation cycle follows a Gaussian distribution of mean $\mu = \mathrm{BU}/3 = 15$GWd/tHM and unknown standard deviation σ. We also assume that each irradiation cycle is uncorrelated with the previous ones[1]. We denote $cycle_i$ the burnup of each cycle.

At the end of the irradiation cycle the burnup of each batch is as follows:

$$\begin{cases} \mathrm{BU}_A &= cycle_1 + cycle_2 + cycle_3 \\ \mathrm{BU}_B &= cycle_1 + cycle_2 \\ \mathrm{BU}_C &= cycle_1 \end{cases} \tag{5.53}$$

[1] this assumption may be conservative given that compensations from one cycle to another would lead to negative correlations between cycles

With $corr(cycle_i, cycle_j) = 0 \; \forall i \neq j$.

The core mean burnup at the end of an irradiation cycle is calculated as the mean of the burnup of the batches:

$$\overline{\mathrm{BU}}_{core} = \frac{1}{3}\begin{pmatrix} & cycle_1 \\ + & cycle_1 + cycle_2 \\ + & cycle_1 + cycle_2 + cycle_3 \end{pmatrix} \tag{5.54}$$

We use URANIE to resolve numerically the problem and compute the standard deviation of $cycle_i$ leading to $\sigma_{reloading}(\overline{\mathrm{BU}}_{core})$ =200MWd/tHM and obtain: $\sigma_{reloading}(cycle_i) \approx$ 160.5MWd/tHM: the uncertainty associated to one irradiation cycle corresponding to an uncertainty of 200MWd/tHM on the core average burnup is 160.5MWd/tHM. Hence, given that cycles are uncorrelated, the uncertainty associated to the batch discharge burnup is:

$\sigma_{reloading}(\mathrm{BU}_3) = \sqrt{3 \times \sigma_{reloading}(cycle_i)^2} \approx$ 278MWd/tHM, i.e. $\dfrac{\sigma_{reloading}(\mathrm{BU}_{discharge})}{\mathrm{BU}_{discharge}} \approx 0.62\%$.

We performed the same computation in the case $N = 4$. Table 5.26 summarizes the results.

N	$\mathrm{BU}_{disch.}$ (GWd/tHM)	$\sigma_{cycle}(\overline{\mathrm{BU}}_{core})$ (MWd/tHM)	$\sigma_{reload.}(cycle)$ (MWd/tHM)	$\sigma_{reload.}(\mathrm{BU}_{disch.})$ (MWd/tHM)	$\dfrac{\sigma_{reload.}(\mathrm{BU}_{disch.})}{\mathrm{BU}_{disch.}}$	$\dfrac{\sigma_{reload.}(cycle)}{cycle}$
3	45	200	160.5	278	0.62%	1.07%
4	45	200	146	292	0.65%	1.30%

Table 5.26: Impact of reloading date on discharge burnup uncertainty

We observe that impact of fractionation on discharge burnup relative uncertainty is small, but impact on cycle relative uncertainty is slightly more important.

5.3.3.8.3.3 Irradiation power uncertainty

The burnup of an irradiated assembly is calculated from enthalpy measures according to the following process:

- instantaneous power measurement through enthalpy balance;
- integration of the power over time.

Therefore the burnup is subject to the uncertainty resulting from the combination of these steps. Overall it appears that the integration process reduces the uncertainty (smoothing of fluctuation).

Finally, uncertainty associated to discharge burnup is approximately $\dfrac{\sigma_{power}(\mathrm{BU}_{discharge})}{\mathrm{BU}_{discharge}} \approx 0.5\%$[2].

Discharge burnup uncertainty results from uncertainty of the consecutive irradiation cycles of the assembly. With the hypothesis of no correlation for consecutive cycles and for a core fractionation N, we have:

[2] private communication

$$\begin{cases} \mathrm{BU}_{discharge} &= N \times cycle \\ Var_{power}(\mathrm{BU}_{discharge}) &= N \times Var(cycle) \\ \dfrac{\sigma_{power}(\mathrm{BU}_{discharge})}{\mathrm{BU}_{discharge}} &= \dfrac{1}{\sqrt{N}} \dfrac{\sigma_{power}(cycle)}{cycle} \end{cases} \tag{5.55}$$

We use the last relation of equation 5.55 to calculate the standard deviation associated to a cycle: $\dfrac{\sigma_{power}(cycle)}{cycle} = \sqrt{N} \times \dfrac{\sigma_{power}(\mathrm{BU}_{discharge})}{\mathrm{BU}_{discharge}}$.

Table 5.27 shows numerical application in cases $N = 3$ and $N = 4$.

N	$\dfrac{\sigma_{power}(\mathrm{BU}_{discharge})}{\mathrm{BU}_{discharge}}$	$\dfrac{\sigma_{power}(cycle)}{cycle}$
3	0.5%	1.7%
4	0.5%	2.0%

Table 5.27: Impact of irradiation power on discharge burnup uncertainty

5.3.3.8.3.4 Combination of the uncertainties

We assume that uncertainty resulting from reloading date and irradiation power are uncorrelated. Therefore the total uncertainty of a cycle is given by:

$$\frac{\sigma_{total}(cycle)}{cycle} = \sqrt{\left(\frac{\sigma_{power}(cycle)}{cycle}\right)^2 + \left(\frac{\sigma_{reloading}(cycle)}{cycle}\right)^2} \tag{5.56}$$

Numerical application extracted from tables 5.26 and 5.27 gives the following cycle burnup uncertainty:

$$\boxed{\begin{cases} N = 3 : & \dfrac{\sigma_{total}(cycle)}{cycle} \approx 2.0\% \\ N = 4 : & \dfrac{\sigma_{total}(cycle)}{cycle} \approx 2.4\% \end{cases}} \tag{5.57}$$

5.3.3.8.4 Simplified correlation laws

5.3.3.8.4.1 Introduction

This section describes the evaluation of discharge burnup uncertainty and correlation using irradiation cycles burnup uncertainty.

Sampling fuel cycles according to their distribution, and summation of consecutive cycles to calculate discharge burnup of fuel batches give an accurate representation of actual burnup correlation between different batches. We call this sampling method α. Sampling according to this law is time-consuming. Indeed, as explained in section 6.2.2.4.1, more than 5000 variables were necessary to model those batches, and creation of a COSI data set suited for uncertainty propagation using this law requires deep changes in the data structure.

Although this method works, and was used to perform uncertainty propagation in section 6.2.2.4, we chose to define another method which allows performing uncertainty propagation with no modification of the data set, and requiring very few scripting for sample construction.

5.3.3.8.4.2 Definition of correlation methods

Method α

We denote α the method that consists in sampling the burnup separately for each different cycle, then combining these cycles into discharge burnup. Discharge burnup is not sampled directly, but its distribution is a consequence of cycle uncertainty.

Method β

We build method β such that local properties (with regards to irradiated batches for instance) are conserved. The core fractionation is N.

Given that cycles are not correlated one to another, the discharge burnup variance for a given batch is the sum of variance of its cycles. Let $Var(cycle)$ be the cycle burnup standard deviation and $Var\left(BU_i^{\beta}\right)$ the discharge burnup standard deviation according to method β. Then:

$$\boxed{\forall i \; Var\left(BU_i^{\beta}\right) = N \times Var(cycle)} \tag{5.58}$$

Method γ

We build method γ such that global properties (with regard to inventories for instance) are conserved. The inventory is directly linked to the succession of discharge burnups. Consequently we must build a method such that the variance of the mean of series of (correlated) discharge burnup is conserved.

In this study, we consider the sequence of batches in a reactor, from its start-up to the time of uncertainty assessment (or in the whole reactor lifetime is uncertainty assessment is performed after shutdown).

Let $(\mathrm{BU}_1, \ldots, \mathrm{BU}_i, \ldots, \mathrm{BU}_M)$ be a series of M consecutive discharge burnups for a given reactor. Those burnup have the same mean and variance, but they are correlated together, because of the succession of irradiation cycles. The core fractionation is N.

We make the hypothesis that $M \gg N \geq 1$ (there are far more consecutive cycles in a reactor lifetime than cycles in the reactor at a given time, or uncertainty assessment is performed at least a few years after start-up).

Let BU_{mean} be the mean discharge burnup. Then:

$$\mathrm{BU}_{mean} = \frac{1}{M} \sum_{i=1}^{M} \mathrm{BU}_i \tag{5.59}$$

Variance of BU_{mean} is expressed as:

$$Var\left(\mathrm{BU}_{mean}\right) = \frac{1}{M^2} Var\left(\sum_{i=1}^{M} \mathrm{BU}_i\right) \tag{5.60}$$

With:

$$\mathrm{BU}_i = \sum_{k=1}^{N} cycle_{i,k} \tag{5.61}$$

Let $cycle_{i,k}$ be the irradiation cycle number k with $1 \leq k \leq N$ for batch i, and l an integer such that $1 \leq k+l \leq N$. Batch i discharge burnup is $\sum_{k=1}^{M} cycle_{i,k}$.

This notation is not convenient because it does not highlight several relation between different cycles of different batches. For instance, the second irradiation cycle of the third batch is the same as the first irradiation cycle of the fourth batch. We generalize this result:

$$cycle_{i,k+l} = cycle_{i+l,k} \tag{5.62}$$

We use this result to define uniquely the cycles:

$$cycle_{i,k} = cycle_{i+k-1,1} \tag{5.63}$$

We inject expression 5.63 in expression 5.60:

$$\begin{aligned} Var\left(\mathrm{BU}_{mean}\right) &= \frac{1}{M^2} Var\left(\sum_{i=1}^{M}\sum_{k=1}^{N} cycle_{i,k}\right) \\ &= \frac{1}{M^2} Var\left(\sum_{i=1}^{M}\sum_{k=1}^{N} cycle_{i+k-1,1}\right) \end{aligned} \tag{5.64}$$

We separate this sum into:

- cycles that irradiate N batches;
- cycles that irradiate less than N batches (the $(N-1)$ first and $(N-1)$ last cycles).

$$\begin{aligned} Var\left(\mathrm{BU}_{mean}\right) &= \frac{1}{M^2} Var\Big(N \times \sum_{i=1}^{M-N+1} cycle_{i+N-1,1} \\ &\quad + \sum_{i=1}^{N-1} i \times cycle_{i,1} + \sum_{i=M+1}^{N+M-1} (N+M-i) \times cycle_{i,1}\Big) \\ &= \frac{1}{M^2} Var\Big(N \times \sum_{i=1}^{M-N+1} cycle_{i+N-1,1} \\ &\quad + \sum_{i=1}^{N-1} i \times cycle_{i,1} + \sum_{i=1}^{N-1} (N-i) \times cycle_{i+M,1}\Big) \end{aligned} \tag{5.65}$$

We expand the variance sum:

$$\begin{aligned} Var\left(\mathrm{BU}_{mean}\right) &= \frac{1}{M^2}\Big(Var\Big(N \times \sum_{i=1}^{M-N+1} cycle_{i+N-1,1}\Big) \\ &\quad + Var\Big(\sum_{i=1}^{N-1} i \times cycle_{i,1} + \sum_{i=1}^{N-1} (N-i) \times cycle_{i+M,1}\Big) \\ &\quad + 2cov(N \times \sum_{i=1}^{M-N+1} cycle_{i+N-1,1}, \sum_{i=1}^{N-1} i \times cycle_{i,1} + \sum_{i=1}^{N-1} (N-i) \times cycle_{i+M,1})\Big) \end{aligned} \tag{5.66}$$

In the next few steps we build an approximation of equation 5.66 based on the assumption that the mean discharge burnup is calculated on many irradiation cycles. The aim is to prove that edge effects (start-up and last batches) are negligible.

Given that all cycles have the same variance and are not correlated, we have a finite sum:

$$\lim_{M\to\infty} Var\left(\sum_{i=1}^{N-1} i \times cycle_{i,1} + \sum_{i=1}^{N-1}(N-i)\times cycle_{i+M,1}\right) = K < \infty \tag{5.67}$$

And, as an infinite sum of uncorrelated cycles:

$$\lim_{M\to\infty} Var\left(N \times \sum_{i=1}^{M-N+1} cycle_{i+N-1,1}\right) = \infty \tag{5.68}$$

Therefore:

$$\lim_{M\to\infty} \frac{Var\left(\sum_{i=1}^{N-1} i \times cycle_{i,1} + \sum_{i=1}^{N-1}(N-i)\times cycle_{i+M,1}\right)}{Var\left(N \times \sum_{i=1}^{M-N+1} cycle_{i+N-1,1}\right)} = 0 \tag{5.69}$$

Given that the covariance term of equation 5.66 are uncorrelated or positively correlated the covariance is positive. Furthermore:

$$\leq \frac{\left|cov(N \times \sum_{i=1}^{M-N+1} cycle_{i+N-1,1}, \sum_{i=1}^{N-1} i \times cycle_{i,1} + \sum_{i=1}^{N-1}(N-i)\times cycle_{i+M,1})\right|}{\sqrt{Var\left(N \times \sum_{i=1}^{M-N+1} cycle_{i+N-1,1}\right) Var\left(\sum_{i=1}^{N-1} i \times cycle_{i,1} + \sum_{i=1}^{N-1}(N-i)\times cycle_{i+M,1}\right)}} \tag{5.70}$$

Using expressions 5.67 and 5.68 in the previous inequality, we obtain:

$$\lim_{M\to\infty} \frac{cov(...)}{Var\left(N \times \sum_{i=1}^{M-N+1} cycle_{i+N-1,1}\right)} = 0 \tag{5.71}$$

We use inequality $M \gg N \geq 1$ and we inject equations 5.69 and 5.71 in 5.66:

$$Var\left(\text{BU}_{mean}\right) \approx \frac{1}{M^2} Var\left(N \times \sum_{i=1}^{M} cycle_{i+N-1,1}\right) \tag{5.72}$$

The cycles $(cycle_{i+N-1,1})$ are uncorrelated one to another. Consequently, we obtain:

$$Var\left(\text{BU}_{mean}\right) \approx \frac{N^2}{M^2} \sum_{i=1}^{M} Var\left(cycle_{i+N-1,1}\right) \tag{5.73}$$

Those cycles have the same variance. Hence:

$$Var\left(\text{BU}_{mean}\right) \approx \frac{N^2}{M} Var\left(cycle_{M,1}\right) \tag{5.74}$$

Now let us consider a series of M consecutive and uncorrelated batches which variance is the same, and which burnup is $\text{BU}^{\gamma}_{1\leq i\leq M}$ such that the variance of the mean of this series is the same of the variance of the mean of the actual batch series, $Var(\text{BU}_{mean})$. We have:

$$Var\left(mean_i\left(\text{BU}^{\gamma}_i\right)\right) = Var\left(\text{BU}_{mean}\right) \tag{5.75}$$

Consequently:

$$\begin{array}{rcl} Var\left(\frac{1}{M}\sum_{i=1}^{M}\mathrm{BU}_i^{\gamma}\right) & = & Var\left(\mathrm{BU}_{mean}\right) \\ & \approx & \frac{N^2}{M}Var\left(cycle_{M,1}\right) \\ \frac{1}{M^2}Var\left(\sum_{i=1}^{M}\mathrm{BU}_i^{\gamma}\right) & \approx & \frac{N^2}{M}Var\left(cycle_{M,1}\right) \\ \frac{1}{M^2}\sum_{i=1}^{M}Var\left(\mathrm{BU}_i^{\gamma}\right) & \approx & \frac{N^2}{M}Var\left(cycle_{M,1}\right) \end{array} \tag{5.76}$$

Given that the BU_i^{γ} have the same variance we obtain:

$$\forall i \ \frac{1}{M}Var\left(\mathrm{BU}_i^{\gamma}\right) \approx \frac{N^2}{M}Var\left(cycle_{M,1}\right) \tag{5.77}$$

Finally:

$$\boxed{\forall i \ Var(\mathrm{BU}_i^{\gamma}) \approx N^2 \times Var(cycle_{M,1})} \tag{5.78}$$

5.3.3.8.4.3 Impact of the correlation laws

Impact of these different correlation laws is analyzed in section 6.2.2.4.6 in the case of scenario B.

5.3.3.8.5 Remark concerning blankets

In the case of system composed of both core and blankets (fertile blankets, americium or minor actinides bearing blankets), the blanket burnup is strongly correlated to the core blanket. For instance, if the core burnup is higher than expected, then it will be the same for the blanket.

However, in COSI, core and blankets are separated systems, and burnup of one is independent from burnup of the other. Therefore, it was necessary to implement a method so as to establish links between the parts of such composed systems.

We chose a total correlation between parts of a composed system: if the core burnup is increased by 1%, then blanket burnup is increased by 1% too.

5.3.4 Conclusions and perspectives

The scenario-related quantities were classified into two categories: scenario hypotheses, which define the structure of the scenario, and scenario parameters, which are subject to uncertainty.

In this section, we provided a description of the uncertainty of the scenario parameters.

The perspectives include:

- refinement of scenario parameters uncertainty;
- addition of complementary uncertainties.

There is another long-term perspective to this work: feasibility studies in self-adjusted scenarios. Feasibility studies were performed in this work, and are presented in chapter 6. In the present feasibility studies, when nuclear data and scenario parameters are perturbed, the scenario hypotheses remain unchanged, and the scenario feasibility is calculated accordingly. However, minor changes in scenario hypotheses may change the feasibility of a given perturbed scenario.

Let us consider a perturbed scenario in the sample. Adjustment of scenario hypotheses such as the mix of spent fuel reprocessed at the reprocessing plant at any date of the scenario may make the scenario feasible, with minor, acceptable changes in its structure. These adjustments could be based on optimization techniques.

Such adjustment could be performed on any non-feasible scenario of the sample, so as to compute the adjusted feasibility of the scenario family.

Bibliography

[5.1] A. Santamarina, D. Bernard, P. Blaise, L. Erradi, P. Leconte, R. Le Tellier, C. Vaglio, and J-F. Vidal. APOLLO2.8: a validated code package for PWR neutronics calculations. In *Advances in Nuclear Fuel Management IV (ANFM 2009), Hilton Island, South Carolina, USA*, 2009.

[5.2] G. Rimpault, D. Plisson, J. Tommasi, R. Jacqmin, J-M. Rieunier, D. Verrier, and D. Biron. The ERANOS Code and Data System for Fast Reactors Neutronic Analyses. In *Proc. of PHYSOR 2002*, 2002.

[5.3] G. Noguere and J.C. Sublet. A nuclear data oriented interface code for processing applications. *Annals of Nuclear Energy*, 35:2259–2269, 2008.

[5.4] R.E. MacFarlane and A.C. Kahler. Methods for processing ENDF B-II with NJOY. *Nuclear Data Sheets*, 111:2739–2890, 2010.

[5.5] S. Buerger, S.F. Boulyga, J.A. Cunningham, A. Koepf, and J. Poths. The range of variation of uranium isotope ratios in natural uranium samples and potential application to nuclear safeguards. report iaea-cn-184/256. Technical report, IAEA, 2014.

[5.6] CEA communication, 2009.

[5.7] P. Paulin N. Kerkar. *Exploitation des cœurs REP*. EDP Sciences, 2008.

Chapter 6

Uncertainty propagation studies

Contents

6.1 Irradiation computation 212
6.1.1 Uncertainty propagation in irradiation computation 212
6.1.2 Irradiation surrogate models in scenario computations 219
6.2 Uncertainty propagation in scenario studies 223
6.2.1 Scenario A: Historical French PWR fleet 223
6.2.2 Scenario B: French PWR fleet transition scenario, industrial application 230
6.2.3 Scenario C: French PWR fleet transition scenario, no minor actinides recycling 243
6.2.4 Scenario D: French PWR fleet transition scenario, americium recycling 254

6.1 Irradiation computation

6.1.1 Uncertainty propagation in irradiation computation

6.1.1.1 Introduction

Irradiation is an elementary component of a scenario computation. In the frame of uncertainty propagation studies, depletion computation introduces both irradiation and nuclear data uncertainties in the fuel cycle. In this section, we assess the impact of cross-sections uncertainty on spent fuel concentrations. Although fresh fuel composition and irradiation parameters change during a scenario computation, we expect the general trends to stay the same. This section provides relative standard deviation of spent fuel concentrations generated by cross-section uncertainty, as well as a decomposition of variance. Results were obtained using a correlated sampling of cross-sections, with the surrogate models library developed according to section 3. The sample size is 1000 for the relative standard deviation computation, and 1000 for every part of variance computation.

Results can be interpreted with the help of the decay chains diagram in figure 6.1.

6.1.1.2 PWR UOX fuel

6.1.1.2.1 Description of the study

In this study we consider fresh PWR UOX fuel, whose ^{235}U mass enrichment is 4.5%. Fuel is irradiated up to 45GWd/tHM at nominal power. The 1-group cross-section covariance matrix processed in section 5.2.1.5 page 188 is taken into account. Intra-nuclide inter-reaction correlation is taken into account, inter-nuclide correlation is not taken into account. Spent fuel composition is analyzed at the end of irradiation (no cooling time).

6.1.1.2.2 Computation

Table 6.1 summarizes the results of the study. The table is divided into three parts:

- RSD: the nuclide's mass relative standard deviation in spent fuel. It is computed using stochastic uncertainty propagation. The sample size is 1000.
- correlation impact: the part of variance (positive or negative) due to inter-reaction correlations. It is computed using the same sample properties as for the RSD, but correlation between cross-sections is not taken into account. In the case where the impact of correlation is negligible (*i.e.* variance is the same with or without correlations), the impact is noted N;
- part of variance: the part of variance (positive) due to a given cross section's uncertainty.

The part of variance of mass m is computed the following way:

$$\text{part of variance}(m, \sigma_i) = 1 - \frac{Var(m, \text{every parameter except } \sigma_i \text{ is sampled})}{Var(m, \text{every parameter is sampled})} \tag{6.1}$$

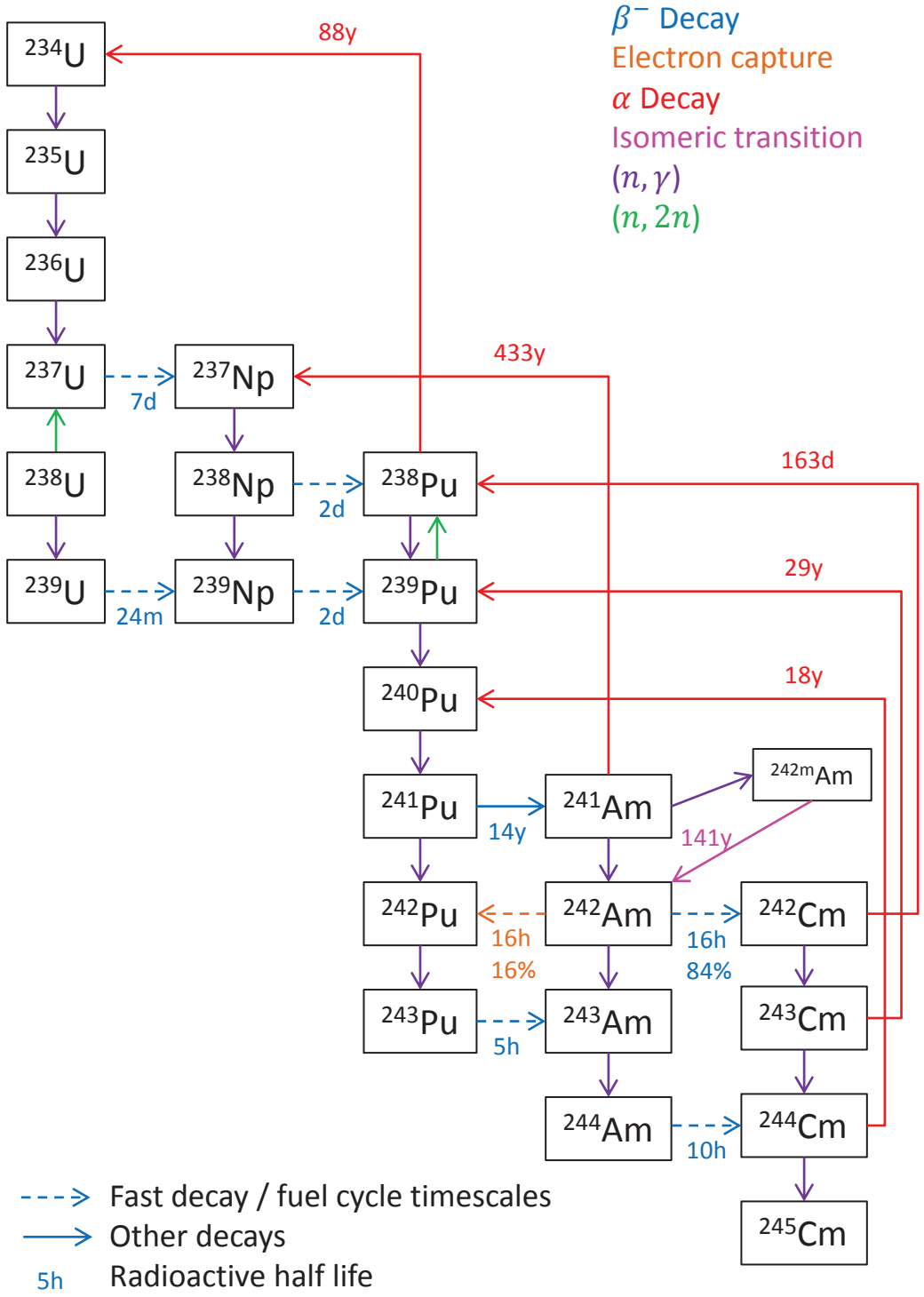

Figure 6.1: Actinides decay chains

This part of variance is an approximation, as it does not take into account the correlation between variables. Interactions between parameters may lead to a sum of the different parts of variance greater than 1.

If the part of variance is inferior to 1%, it is not shown on the table.

		^{238}Pu	^{239}Pu	^{240}Pu	^{241}Pu	^{242}Pu	^{241}Am
RSD (%)		4.8	1.5	1.9	1.7	3.6	4.0
correlation impact		N	N	N	N	N	N
part of variance (%)	$\sigma_c(^{235}\text{U})$	5					
	$\sigma_f(^{235}\text{U})$						
	$\sigma_c(^{236}\text{U})$	28					
	$\sigma_f(^{236}\text{U})$	2					
	$\sigma_c(^{238}\text{U})$	5	83	35	28	1	14
	$\sigma_f(^{238}\text{U})$			2			
	$\sigma_c(^{237}\text{Np})$	38					
	$\sigma_f(^{237}\text{Np})$	1					
	$\sigma_c(^{238}\text{Pu})$	23					
	$\sigma_f(^{238}\text{Pu})$	2					
	$\sigma_c(^{239}\text{Pu})$		6	17	24	6	4
	$\sigma_f(^{239}\text{Pu})$		10	7	2	1	
	$\sigma_c(^{240}\text{Pu})$			41	8	2	2
	$\sigma_f(^{240}\text{Pu})$						
	$\sigma_c(^{241}\text{Pu})$				6	26	1
	$\sigma_f(^{241}\text{Pu})$				26	4	3
	$\sigma_c(^{242}\text{Pu})$					57	
	$\sigma_f(^{242}\text{Pu})$						
	$\sigma_c(^{241}\text{Am})$						74
	$\sigma_f(^{241}\text{Am})$						
	$\sigma_c(^{242M}\text{Am})$						
	$\sigma_f(^{242M}\text{Am})$						
	$\sigma_c(^{243}\text{Am})$	1					
	$\sigma_f(^{243}\text{Am})$						
	$\sigma_c(^{242}\text{Cm})$	1					
	$\sigma_f(^{242}\text{Cm})$						
	$\sigma_c(^{243}\text{Cm})$						
	$\sigma_f(^{243}\text{Cm})$						
	$\sigma_c(^{244}\text{Cm})$						
	$\sigma_f(^{244}\text{Cm})$						
	sum	106	99	102	94	97	98

Table 6.1: Cross-sections uncertainty sources in PWR UOX irradiation calculation

We observe that the role of correlation is negligible in every case. Indeed we always have:

$$\frac{|Var(m,\ \text{correlations}) - Var(m,\ \text{no correlations})|}{Var(m,\ \text{correlations})} < 1\%$$

We observe that capture cross-sections uncertainty weight heavily on the uncertainty of the nuclides chains: every reaction leading to one nuclide contributes to the nuclide's concentration's uncertainty. The fission cross-section mostly contribute to the uncertainty of the fissioning nuclide, and barely impacts the concentration of other nuclides.

In the case of ^{238}Pu, the parts of variance show that in the case of UOX fuel irradiated in PWR, the uncertainty comes from ^{236}U and ^{237}Np cross-sections, while the impact of ^{241}Am and ^{242}Cm is almost negligible.

In the case of ^{239}Pu, 83% of the variance results from ^{238}U capture cross-section uncertainty.

6.1.1.3 PWR MOX fuel

6.1.1.3.1 Description

In this study we consider fresh PWR MOX fuel, whose plutonium mass content is 8.65%, Pu vector is shown in table 6.2. Fuel is irradiated up to 45GWd/tHM at nominal power. The 1-group cross-section covariance matrix processed in section 5.2.1.5 page 188 is taken into account. Intra-nuclide inter-reaction correlation is taken into account, inter-nuclide correlation is not taken into account. Spent fuel composition is analyzed at the end of irradiation (no cooling time).

isotope	mass fraction (%)
^{238}Pu	2.5
^{239}Pu	54.5
^{240}Pu	25.2
^{241}Pu	8.6
^{242}Pu	7.9
^{241}Am	1.3

Table 6.2: Pu vector for cross-section uncertainty propagation in PWR MOX fuel

6.1.1.3.2 Computation

Table 6.3 summarizes the results of the study. The method is the same as described in section 6.1.1.2.

We observe that the role of correlation is negligible in every case. Indeed we always have:

$$\frac{|Var(m,\ \text{correlations}) - Var(m,\ \text{no correlations})|}{Var(m,\ \text{correlations})} < 1\%$$

The uncertainty sources are different than in PWR UOX because of the two following factors:

- fuel composition is different;
- cross-section uncertainty is different.

We observe a higher impact of plutonium and heavier nuclides in general, in comparison with PWR UOX.

In the case of ^{238}Pu, we remark than contrary to PWR UOX fuel, ^{237}Np cross-sections uncertainty do not contribute to ^{238}Pu mass uncertainty: it only results from its own capture, and capture on ^{241}Am leading to ^{242}Cm then ^{238}Pu through α decay.

		^{238}Pu	^{239}Pu	^{240}Pu	^{241}Pu	^{242}Pu	^{241}Am	^{243}Am	^{242}Cm	^{244}Cm
RSD (%)		2.4	0.9	1.0	1.3	3.5	3.8	9.6	1.6	10.5
correlation impact		N	N	N	N	N	N	N	N	N
part of variance (%)	$\sigma_c(^{235}\mathrm{U})$									
	$\sigma_f(^{235}\mathrm{U})$									
	$\sigma_c(^{236}\mathrm{U})$									
	$\sigma_f(^{236}\mathrm{U})$									
	$\sigma_c(^{238}\mathrm{U})$		69	5					1	
	$\sigma_f(^{238}\mathrm{U})$									
	$\sigma_c(^{237}\mathrm{Np})$									
	$\sigma_f(^{237}\mathrm{Np})$									
	$\sigma_c(^{238}\mathrm{Pu})$	86	2							
	$\sigma_f(^{238}\mathrm{Pu})$									
	$\sigma_c(^{239}\mathrm{Pu})$		16	15	2					
	$\sigma_f(^{239}\mathrm{Pu})$		10							
	$\sigma_c(^{240}\mathrm{Pu})$		1	78	42	1	3		5	
	$\sigma_f(^{240}\mathrm{Pu})$									
	$\sigma_c(^{241}\mathrm{Pu})$				21	9			1	
	$\sigma_f(^{241}\mathrm{Pu})$		1		32				5	
	$\sigma_c(^{242}\mathrm{Pu})$					90		97		92
	$\sigma_f(^{242}\mathrm{Pu})$									
	$\sigma_c(^{241}\mathrm{Am})$	13					95		84	
	$\sigma_f(^{241}\mathrm{Am})$									
	$\sigma_c(^{242M}\mathrm{Am})$									
	$\sigma_f(^{242M}\mathrm{Am})$									
	$\sigma_c(^{243}\mathrm{Am})$							2		7
	$\sigma_f(^{243}\mathrm{Am})$									
	$\sigma_c(^{242}\mathrm{Cm})$								2	
	$\sigma_f(^{242}\mathrm{Cm})$									
	$\sigma_c(^{243}\mathrm{Cm})$									
	$\sigma_f(^{243}\mathrm{Cm})$									
	$\sigma_c(^{244}\mathrm{Cm})$									1
	$\sigma_f(^{244}\mathrm{Cm})$									
	sum	99	99	98	97	100	98	99	98	100

Table 6.3: Cross-sections uncertainty sources in PWR MOX irradiation calculation

We remark that in the case heavy nuclides, including ^{242}Cm and ^{244}Cm, the uncertainty does not depend on the nuclide's own cross-sections, but the on cross-sections of lighter nuclides leading to its formation.

It has to be noted that ^{244}Am cross-section was not taken into account for this study. However, we calculated the ^{244}Cm sensitivity to ^{244}Am capture cross-section in PWR MOX spectrum and obtained: $\left|\frac{\partial m(^{244}\text{Cm})}{\partial \sigma_c(^{244}\text{Am})}\frac{\sigma_c(^{244}\text{Am})}{m(^{244}\text{Cm})}\right| \approx 2 \times 10^{-7}$ and $\left|\frac{\partial m(^{244}\text{Cm})}{\partial \sigma_f(^{244}\text{Am})}\frac{\sigma_f(^{244}\text{Am})}{m(^{244}\text{Cm})}\right| \approx 4 \times 10^{-7}$ which is negligible.

6.1.1.4 SFR MOX fuel

6.1.1.4.1 Description

In this study we consider fresh SFR MOX fuel, whose plutonium mass content is 21.32%, Pu vector is shown in table 6.4. Fuel is irradiated up to 116GWd/tHM at nominal power. The 1-group cross-section covariance matrix processed in section 5.2.1.5 page 188 is taken into account. Intra-nuclide inter-reaction correlation is taken into account, inter-nuclide correlation is not taken into account. Spent fuel composition is analyzed at the end of irradiation (no cooling time).

Nuclide	Mass fraction
^{238}Pu	2.66%
^{239}Pu	56.03 %
^{240}Pu	25.91 %
^{241}Pu	6.72%
^{242}Pu	7.30%
^{241}Am	1.38%

Table 6.4: Pu vector for cross-section uncertainty propagation in PWR MOX fuel

6.1.1.4.2 Computation

Table 6.5 summarizes the results of the study. The method is the same as described in section 6.1.1.2.

We observe that the role of correlation is negligible in every case. Indeed we always have:

$$\frac{|Var(m,\ \text{correlations}) - Var(m,\ \text{no correlations})|}{Var(m,\ \text{correlations})} < 1\%$$

The part of variance in SFR MOX fuel is generally more or less similar to PWR MOX fuel. This comes from the fact that plutonium is the main fissile in both fuels.

However, several isotopes have different variance sources, including:

- ^{239}Pu uncertainty mostly comes from $\sigma_c(^{238}\text{U})$ in PWR MOX and from ($\sigma_c(^{238}\text{U})$, $\sigma_c(^{239}\text{Pu})$) in SFR;
- ^{240}Pu uncertainty mostly comes from $\sigma_c(^{240}\text{Pu})$ in PWR MOX and from $\sigma_c(^{239}\text{Pu})$ in SFR;
- ^{242}Pu uncertainty comes from $\sigma_c(^{242}\text{Pu})$ in PWR MOX and from $\sigma_c(^{241}\text{Pu})$ in SFR;
- ^{244}Cm uncertainty comes from $\sigma_c(^{242}\text{Pu})$ in PWR MOX and from ($\sigma_c(^{242}\text{Pu})$, $\sigma_c(^{243}\text{Am})$) in SFR.

		^{238}Pu	^{239}Pu	^{240}Pu	^{241}Pu	^{242}Pu	^{241}Am	^{243}Am	^{242}Cm	^{244}Cm
RSD (%)		1.5	1.1	1.7	2.7	1.9	1.4	4.3	1.4	6.1
correlation impact		N	N	N	N	N	N	N	N	N
part of variance (%)	$\sigma_c(^{235}\text{U})$									
	$\sigma_f(^{235}\text{U})$									
	$\sigma_c(^{236}\text{U})$									
	$\sigma_f(^{236}\text{U})$									
	$\sigma_c(^{238}\text{U})$		47				2		3	
	$\sigma_f(^{238}\text{U})$									
	$\sigma_c(^{237}\text{Np})$	2								
	$\sigma_f(^{237}\text{Np})$									
	$\sigma_c(^{238}\text{Pu})$	87	1							
	$\sigma_f(^{238}\text{Pu})$	2								
	$\sigma_c(^{239}\text{Pu})$		49	88	7				4	
	$\sigma_f(^{239}\text{Pu})$		3				1			
	$\sigma_c(^{240}\text{Pu})$	1		11	53	1	30		15	
	$\sigma_f(^{240}\text{Pu})$			1						
	$\sigma_c(^{241}\text{Pu})$	1			38	81	23	6	12	2
	$\sigma_f(^{241}\text{Pu})$				2				1	
	$\sigma_c(^{242}\text{Pu})$					17		82		42
	$\sigma_f(^{242}\text{Pu})$					1				
	$\sigma_c(^{241}\text{Am})$	6					42		53	
	$\sigma_f(^{241}\text{Am})$									
	$\sigma_c(^{242M}\text{Am})$									
	$\sigma_f(^{242M}\text{Am})$									
	$\sigma_c(^{243}\text{Am})$							11		40
	$\sigma_f(^{243}\text{Am})$							1		
	$\sigma_c(^{242}\text{Cm})$								8	
	$\sigma_f(^{242}\text{Cm})$								1	
	$\sigma_c(^{243}\text{Cm})$									
	$\sigma_f(^{243}\text{Cm})$									
	$\sigma_c(^{244}\text{Cm})$									15
	$\sigma_f(^{244}\text{Cm})$									
	sum	99	100	100	100	100	98	98	100	99

Table 6.5: Cross-sections uncertainty sources in SFR MOX irradiation calculation

6.1.2 Irradiation surrogate models in scenario computations

6.1.2.1 Implementation

6.1.2.1.1 Algorithm

Artificial neural networks were implemented in JAVA in COSI using the same formalism as URANIE. Each irradiation ANN model is associated to a given fuel type.

First, fresh fuel mass is normalized so as to work with intensive properties (mass fraction and concentrations).

Then, generic methods, common for every irradiation ANN, perform the following tasks:

- recognition of the parameters and attribution of the weights;
- construction of the ANN network and computation of the concentration after irradiation.

Once every concentration after irradiation is computed, the mass default (input - output) is filled with a fictive stable nuclide. Finally, concentration is transformed into mass and the problem is un-normalized.

6.1.2.1.2 Nuclear data management

6.1.2.1.2.1 Cross-section perturbations

Energy-integrated cross-sections and their uncertainty are spectrum-dependent. Therefore we implemented a set of methods which read ASCII cross-sections perturbation files corresponding to different irradiation model and associate cross-sections perturbation to the corresponding model. These methods are user-friendly. For instance, if we add in the scenario data set perturbation files corresponding to irradiation models names A, B and C while simulation utilizes models B, C, and D, then A will be read but not taken into account, B and C perturbation are read once (before simulation) and applied in every irradiation computations of B and C, while D computation are not perturbed.

An irradiation model A will apply perturbation from file `A.pert` only. The formalism of the perturbation file is as follows:

`A.pert`

```
DN:capture_U235 5.81e-01
DN:fission_Pu241 -4.1412
stop
```

`B.pert`

```
DN:capture_Pu240 1.18e01
stop
```

Perturbation keywords are `DN:capture_` and `DN:fission_`. Unknown nuclides are ignored (no error). Nuclides formalism is (element)(atomic number). Element is case-sensitive. Perturbation is signed, in percent. Scientific notation ($e+$) is accepted but not mandatory. Data written after string `stop` is not read and can be used for comments.

6.1.2.1.2.2 Fission yields perturbations

Although fission yields are spectrum-dependent, we only considered one perturbation for every spectrum (fission yields vary in different spectra, but the perturbation is the same). We implemented a set of methods which read ASCII fission yields perturbation file and associate perturbation to every irradiation model. The file name is always `yPF.pert`. The formalism of the perturbation file is as follows:

yPF.pert

```
y:U235_KR84 1.007e+00
y:Pu239_CE144 9.94e-01
stop
```

Keyword `y:` indicates fissile nuclide and underscore sign _ separates fissile nuclide from fission product. Fission product is in upper case. Perturbation is a multiplier of the fission product (and not a signed perturbation in percent). For instance the first line indicates that the fission yield $^{235}\mathrm{U} \rightarrow {}^{84}\mathrm{Kr}$ is multiplied by 1.007. Scientific notation ($e+$) is accepted but not mandatory. Data written after string `stop` is not read and can be used for comments.

6.1.2.2 Remarks concerning uncertainty propagation

6.1.2.2.1 Introduction

Irradiation surrogate models have two roles in scenario uncertainty propagation studies:

1. estimation of the spent fuel composition in function of fresh fuel composition and irradiation parameters;
2. uncertainty propagation.

Irradiation surrogate models local quality indicators such as mean bias or maximum bias provide information concerning the precision of the first task (estimation of the spent fuel composition). Another method for assessment of estimation quality in scenario computations is comparison of COSI-CESAR and COSI-MeSAR runs. For instance, COSI-CESAR and COSI-MeSAR runs are compared in section 6.2.1 for scenario A.

Concerning the second task, the approach is different, and must answer the following question: *given a fresh fuel composition and an irradiation history, what is the variance propagation ability of the surrogate model?*

In the following sections we discuss the propagation of burnup and nuclear data uncertainty in scenario studies.

6.1.2.2.2 Nuclear data uncertainty propagation in scenario studies

There are two different types of results in COSI:

- local results, such as decay heat, which are the output of an irradiation computation;
- global results, such as inventories, which are combination of many irradiation computations, equivalence models, etc.

Local results have the same uncertainty propagation properties as irradiation models. The construction process of surrogate models showed that the impact of cross-sections is more or less linear on irradiation calculations. Linear impacts are easily modeled using estimators such as artificial neural networks or multiple polynomial regressions.

For instance, in the case of PWR UOX irradiation (nominal burnup or higher) ANN model, we calculated q^2 and $mean|(\hat{y}-y)/\bar{y}|$ for two different problems:

- irradiation parameters, fuel composition and nuclear data are sampled;
- nuclear data only are sampled.

Results are shown in table 6.6 for ^{239}Pu and ^{244}Cm, which are typical *easy* and *difficult* cases in terms of estimation.

nuclide	$mean\|(\hat{y}-y)/\bar{y}\|$	$mean\|(\hat{y}-y)/\bar{y}\|$ (ND only)	q^2	q^2 (ND only)
^{239}Pu	0.31%	0.15%	0.9999	0.9999
^{244}Cm	0.94%	1.29%	0.9996	0.9980

Table 6.6: Comparison of the quality of estimators on the whole domain of validity and for a fixed set of irradiation parameters, PWR UOX high burnup fuel

First, we observe that the mean bias is different in the case where nuclear data only are sampled. This is because fuel composition and irradiation parameters are the main contributors to bias.

Then we remark that the q^2 remains very high for a fixed composition, even for the difficult case of ^{244}Cm: the nuclear data variance propagation properties remain satisfying for a fixed composition.

Surrogate models can perform nuclear data uncertainty propagation in scenario studies.

6.1.2.2.3 Burnup uncertainty propagation in scenario studies

We showed in section 3.1.3.1.2.3 that burnup has a nonlinear impact on concentrations in spent fuel. For instance, figure 3.19 page 87 represents the evolution of final curium concentration in function of the burnup in PWR UOX fuel, which are particularly nonlinear in function of the burnup.

In the case of PWR UOX irradiation (nominal burnup or higher) ANN model, we calculated q^2 and $mean|(\hat{y}-y)/\bar{y}|$ for two different problems:

- irradiation parameters, fuel composition and nuclear data are sampled;
- burnup only is sampled.

Results are shown in table 6.7 for ^{239}Pu and ^{244}Cm, which are typical *easy* and *difficult* cases in terms of estimation.

nuclide	$mean\|(\hat{y}-y)/\bar{y}\|$	$mean\|(\hat{y}-y)/\bar{y}\|$ (BU only)	q^2	q^2 (BU only)
^{239}Pu	0.31%	0.02%	0.9999	0.9533
^{244}Cm	0.94%	0.92%	0.9996	0.9987

Table 6.7: Comparison of the quality of estimators on the whole domain of validity and for a fixed composition and nuclear data set, PWR UOX high burnup fuel

We observe that for a given set of initial parameters, the burnup variance propagation properties remain good ($q^2 > 0.95$).

We can provide simple sensitivity comparison test between COSI-CESAR and COSI-MeSAR. This test do not give information concerning interaction between variables or a measure of the variance propagation properties on the whole domain. However, it enables comparison of first order effects.

Table 6.8 shows the sensitivity calculated using OAT method in both COSI-CESAR and COSI-MeSAR for a variation of +1% of the burnup on a given fuel batches type (nominal PWR UOX enriched at 3.7%, irradiated up to 45.3GWd/tHM), which is the same order of magnitude as burnup perturbations. Perturbation is applied on all nominal PWR UOX batches of the scenario[1]. Impact is assessed on the whole Pu, Am, Np and Cm inventory with the exception of fuel in the pile.

We denote:

- $\left(\frac{\Delta \text{inv.}}{\text{inv.}}\right)_{\text{C.-C.}}$ the sensitivity calculated with COSI-CESAR5.3 $\left(= \frac{\text{perturbed inv.} - \text{inv.}}{\text{inventory}}\right)$;
- $\left(\frac{\Delta \text{inv.}}{\text{inv.}}\right)_{\text{C.-MeSAR}}$ the sensitivity calculated with COSI-MeSAR;
- $\delta_{\text{CESAR-MeSAR}}$ the relative difference between the sensitivity calculated with COSI-CESAR and COSI-MeSAR.

inventory	C.-CESAR	C.-MeSAR	$\left(\frac{\Delta \text{inv.}}{\text{inv.}}\right)_{\text{C.-CESAR}}$	$\left(\frac{\Delta \text{inv.}}{\text{inv.}}\right)_{\text{C.-MeSAR}}$	$\delta_{\text{CESAR-MeSAR}}$
Pu	425.5t	424.2t	0.31%	0.29%	5%
Am	102.8t	103.4t	0.37%	0.37%	<1%
Np	45.1t	44.7t	0.58%	0.53%	8%
Cm	46.9t	45.6t	2.24%	2.26%	1%

Table 6.8: COSI-CESAR and COSI-MeSAR burnup sensitivity-uncertainty comparison

We observe that the sensitivity calculated with COSI-MeSAR is close to the sensitivity calculated with COSI-CESAR in the burnup uncertainty magnitude. This sensitivity is directly linked to burnup uncertainty propagation. From these two evaluations, we can conclude:

Surrogate models can perform burnup uncertainty propagation in scenario studies.

[1] this study is based on scenario C (see section 6.2.3)

6.2 Uncertainty propagation in scenario studies

6.2.1 Scenario A: Historical French PWR fleet

6.2.1.1 Introduction

Comparison with experimental data is an important step of the validation process of a calculation code. Sometimes experimental data is abundant, and the code qualification on a large domain is feasible. That is the case, for instance, for neutron transport codes, where data accumulated for decades, in ZPRs (Zero Power Reactors) or PIE (Post-Irradiated Experiments) provides a wide range of cases available for comparison.

However, there is no actual experimentation with fully available data in the case of nuclear fleet evolution scenarios. Some data is available, but the overwhelming volume of information necessary to describe accurately a scenario, as well as the difficulty to gather complete and accurate data from sources make this task particularly difficult.

In 2011, the LECy has started a data gathering work aimed at providing a consistent data set as complete as possible, related to the French nuclear fleet history. As industrial accounting is not publicly available, data was mainly extracted from internal resources. However some information remains incomplete and hypotheses were mandatory. The present work is entirely based on the results of [6.1–3].

Measurement-wise, data aggregation and analysis of the inventories of materials related to the nuclear fuel cycle in 2010 was performed by ANDRA in 2012 [6.3]. Although this document does not give detailed information concerning every mass balance, isotopy or inventory of the fuel cycle, it provides useful results in terms of global masses and flows.

Results of [6.1] and [6.3] were compared in the frame of the LECy activities. The outcome of this comparison will be exposed in conjunction with the results of the present study, whose aim is to determine whether nuclear data uncertainty makes both results compatible.

6.2.1.2 Objectives

The objectives of this study are as follows:

- comparison of COSI-CESAR5.3 and COSI-MeSAR results;
- comparison of bias between (COSI, ANDRA) and uncertainty due to nuclear data.

6.2.1.3 Description of the scenario

Scenario A represents the historical French PWR fleet. The simulation begins with the starting of the Fessenheim power plant in 1978, and the fleet is modeled until 2011. UNGG reactors such as EDF1, EDF2 and EDF3 in Chinon, EDF4 and EDF5 in Saint-Laurent, as well as Bugey1 are not taken into account.

Due to the high irregularity of Phenix and Superphenix irradiation cycles, those reactors were not directly modeled, but the associated input and output mass balances were taken into account.

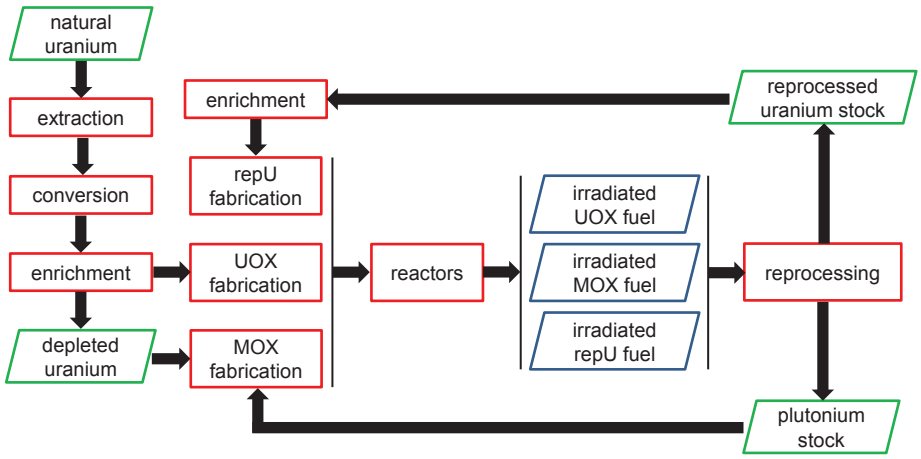

Figure 6.2: Scenario A: fuel cycle in 2010

The nuclear fuel cycle in 2010 is shown on figure 6.2. The black arrows represent mass flows, called *balances*, and the boxes represents plants and stocks. The content of a box is called *inventory*.

The scenario uses the following surrogate models:

- PWR UOX
  - low burnup;
  - high burnup;
- PWR MOX
  - low burnup;
  - high burnup;
- PWR repU.

The 58 PWR of the French fleet are separately modeled. The fleet is composed of:

- 6 CP0 (900MWe);
- 28 CPY (900MWe);
- 20 P4 and P′4 (1300MWe);
- 4 N4 (1450MWe).

PWR UOX fuel is loaded in CP0, CPY, P4, P′4 and N4 reactors. PWR MOX fuel is loaded in 20 CPY reactors (30% MOX) in 2010, and PWR repU fuel is loaded in two CPY.

The following parameters are taken into account:

- reactor characteristics
  - first grid connection date
  - year-integrated load factor
  - reactor yields
  - time-dependent irradiation cycle length
  - succession of loadings and changes in the operating fuel cycle
- fuel characteristics
  - batch-dependent fresh fuel composition (^{235}U enrichment or Pu content)
  - batch-dependent burnup
  - batch-dependent minimum cooling time

Result	COSI-CESAR (tons)	COSI-MeSAR (tons)	$\frac{\text{COSI-MeSAR}}{\text{COSI-CESAR}} - 1$	C.-MeSAR − C.-CESAR (tons)
U_{dep}	204071	204063	-0.004%	-8
Pu_{av}	35.86	36.00	0.39%	0.14
$SF_{PWR\ UOX}$	12037	12037	0%	0
$SF_{PWR\ repU}$	381	381	0%	0
$SF_{PWR\ MOX}$	1416	1416	0%	0

Table 6.9: Scenario A: comparison of COSI-CESAR and COSI-MeSAR on several results (31/12/2010)

- enrichment plant characteristics
  - enrichment technology
  - ^{235}U release rate
- fuel fabrication plant characteristics
  - fabrication time
  - heavy metal losses
- reprocessing plant characteristics
  - reprocessing time
  - batch order
  - time-dependent heavy metal capacity
  - heavy metal losses

6.2.1.4 Comparison of COSI-CESAR and COSI-MeSAR

In this section, we evaluate the impact of using surrogate models during scenario computation, on several results of interest, by comparison with the standard way of computation. We denote COSI-CESAR the standard computation route, and COSI-MeSAR the route using COSI, irradiation surrogate models and analytical cooling.

The scenario results of interest, calculated on 31 December 2010, are as follows:

- U_{dep} (tons), the depleted uranium inventory
- Pu_{av} (tons), the available plutonium inventory (sum of the plutonium stock at the reprocessing plant and the plutonium in PWR MOX fabrication plant)
- $SF_{PWR\ UOX}$ (tons), spent PWR UOX fuel inventory
- $SF_{PWR\ repU}$ (tons), spent PWR repU fuel inventory
- $SF_{PWR\ MOX}$ (tons), spent PWR MOX fuel inventory

Results are summarized in table 6.9.

The relative difference between COSI-CESAR and COSI-MeSAR on these results is low, MeSAR provides an accurate estimation of scenario results.

The result concerning the plutonium inventory is very satisfying. Indeed, this inventory is particularly sensitive to the value of the irradiation parameters computation. Furthermore, it consists in a small balance between two larger mass flows, the plutonium content in spent fuel, and the plutonium used to produce PWR MOX fuel.

Therefore, MeSAR will be used during the rest of the study.

We observe that for several results (spent fuel inventories), the difference is zero. That phenomenon comes from the absence of impact from the irradiation model on those results. For

Result	ANDRA (t)	COSI-MeSAR (t)	$\frac{\text{COSI-MeSAR}}{\text{ANDRA}} - 1$	$\frac{\sigma(\text{COSI-MeSAR})}{\text{COSI-MeSAR}}$ (%)
U_{dep}	271481	204063	-24.83%	0.04%
Pu_{av}	45.00	36.00	-20.00%	5.58%
$SF_{PWR\ UOX}$	12006	12037	0.26%	0.00%
$SF_{PWR\ repU}$	318	381	19.81%	0.00%
$SF_{PWR\ MOX}$	1287	1416	10.00%	0.00%

Table 6.10: Scenario A: comparison of ANDRA and COSI-MeSAR on several results (31/12/2010)

instance, the spent fuel composition heavily depends on the irradiation model, but its global mass does not, hence the absence of bias. Indeed, global mass is fixed by the assumption on successful loadings for each reactor.

6.2.1.5 Uncertainty propagation

6.2.1.5.1 Description of the study

As explained in section 6.2.1.1, this scenario was designed as the best-estimate computation for the historical French PWR fleet. The reactor yields, cycle length, starting and shutdown dates, load factor, etc. were estimated from available data.

We choose not to take into account scenario parameters uncertainty for this study. Indeed this study does not involve a provisional electro-nuclear scenario and its associated uncertainty, but only the knowledge of the historical fleet. Therefore, the present study can be considered as an accuracy test for our fleet history knowledge, or at least an indicator of divergence between our available data and data used by ANDRA in [6.3], supposed to be representative of reality.

Irradiation surrogate models are used for this study. Nuclear data are associated with their uncertainty and correlation values given in section 5.2.1.

In the next paragraphs we will use the notation $\mu \pm \sigma$ with μ the mean and σ the standard deviation.

6.2.1.5.2 Results

Comparison of ANDRA results and COSI-MeSAR results is summarized in table 6.10. This table also includes the standard deviation, which takes into account nuclear data uncertainty (cross-sections and fission yields).

We observe that the differences between ANDRA and COSI results are significant in several cases. We will try to explain those differences in the following paragraphs.

6.2.1.5.2.1 Depleted uranium

In the case of U_{dep} (depleted uranium combined balance), the standard deviation due to nuclear data is far from explaining the difference. The impact of nuclear data on U_{dep} is very small, as they only contribute to changes in the U_{dep} mass required to fabricate PWR MOX fuel through the associated equivalence model. For instance, if $\sigma_c(^{238}U)$ increases in PWR UOX fuel, then the following cascade of events happens:

1. more ^{239}Pu is created during irradiation;
2. ^{239}Pu concentration in spent fuel increases accordingly;
3. therefore, after reprocessing, the overall plutonium quality is higher;
4. since plutonium content is a decreasing function of the plutonium quality, the required plutonium content for PWR MOX fresh fuel is lower;
5. consequently on the other side the depleted uranium mass content increases;
6. hence the depleted uranium slight consumption increase.

Comparison of the depleted uranium balance uncertainty and bias shows that the uncertainty is not high enough to explain the bias.

However, the bias may result from other phenomena, including anticipation of reprocessing and fabrication, which is not taken into account in the simulation.

In [6.2], it was shown that the cumulative natural uranium consumption assessed by COSI is very close to industrial data (0.6% in 2000). Therefore we can make the hypothesis that the discrepancy results from the lack of knowledge such as the unknown fraction of foreign fuel in France.

6.2.1.5.2.2 Separated plutonium

In the case of Pu_{av} (available plutonium inventory = plutonium stock at the reprocessing plant + plutonium available at the fabrication plant) in 2010, the impact of nuclear data is complex, and results from different phenomena:

- changes in production and consumption of different plutonium isotopes in PWR UOX, PWR repU and PWR MOX;
- modification of the plutonium content in PWR MOX because of changes in the plutonium quality.

Analysis of the plutonium mass flows in the cycle shows that cumulative plutonium mass flows tend to be much more important than plutonium inventories.

For instance, figure 6.3 shows the balance and the inventory of the plutonium stock at the reprocessing plant in 2010. Although the inventory in 2010 is only 17±2.0 tons, the input balance is 10.8±0.2 tons (cumulative input balance: 153±2.0 tons) and the output balance is 8.5±0.2 tons (cumulative output balance: 136±2.0 tons). Given that any perturbation of the output is not fully correlated with perturbations of the input (irradiation model on one side, equivalence model on the other side), and the uncertainty associated to the input flow is larger than the uncertainty associated to the output flow, the absolute uncertainty of the stock tends to remain high; hence the large uncertainty of the plutonium stock inventory.

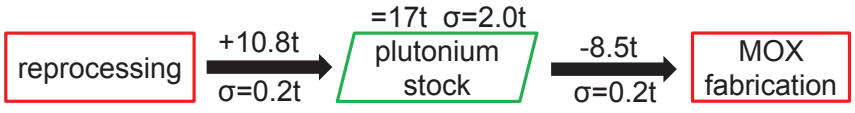

Figure 6.3: Scenario A: balance and inventory of the plutonium stock in 2010

However, nuclear data uncertainty is not high enough to explain the difference in plutonium inventory.

On a side note, even though uncertainty associated to the value of the mass flow of PWR MOX fuel fabrication is low, the uncertainty associated to the fuel fabrication date has a large impact on the plutonium stock: the difference whether the inventory be calculated before or after plutonium was brought to PWR MOX fabrication plant sums up to approximately eight tons (2010 input plutonium balance at PWR MOX fabrication plant in the COSI simulation).

We evaluate with COSI-MeSAR the plutonium stock inventory at several dates in 2010 and 2011, as well as the associated uncertainty. Results are shown in figure 6.11.

plutonium inventory	μ (t)	σ (t)	COSI-MeSAR − ANDRA (t)
COSI-MeSAR 30/06/2010	38.1	2.0	-6.9
COSI-MeSAR 31/12/2010	36.0	2.1	-9.0
COSI-MeSAR 30/06/2011	52.5	2.2	+7.5
ANDRA 31/12/2010	45.0		

Table 6.11: Scenario A: plutonium inventory in function of the accounting date and associated uncertainty

First, it appears that the plutonium inventory calculated by COSI is highly nonlinear time-dependent. This comes from the sequential management of the fuel batches, which reflects the actual fuel management. Indeed as explained in section 2.2.2.1, mass flows are not modeled as continuous flows but as a discrete number of batches. For instance, let m be the mass of PWR MOX fresh fuel to enter PWR MOX reactor at date t, c the plutonium mass content of this fuel (which is a function of the plutonium isotopy) and Δt the fuel fabrication and transportation time. Consequently at exact date $(t - \Delta t)$ a mass $(c \times m)$ of plutonium is withdrawn from the plutonium stock.

Then we observe that the plutonium inventory evaluated by ANDRA in December 2010 (45 tons) corresponds to the average of the inventories calculated by COSI mid-2010 and mid-2011. Hence, once again, a time shift in the accounting date of the inventory may explain the difference between COSI and ANDRA results.

A time shift in the accounting date is likely to occur because four different dates have an influence on the result:

- actual plutonium transportation date;
- ANDRA inventory accounting date (not accurately known);
- COSI plutonium transportation date (model);
- COSI inventory accounting date $\neq$ COSI plutonium transportation date.

Whether ANDRA estimates and COSI computes the inventory before or after transportation changes drastically the result, and if the (transportation, computation) chronology is reversed for COSI and ANDRA, the inventory is likely to be different.

6.2.1.5.2.3 Spent fuel

The mass of spent fuel is not subjected to uncertainty due to nuclear data. Indeed the input mass flow in a reactor is not subject to this uncertainty, and conservation of mass[2] ensures equality of the mass of spent fuel. The absence of uncertainty resulting from nuclear data in the input mass

[2] with minor exceptions such as neutrons leakage and mass-energy equivalence

flow comes from the fact that the input mass flows are parameters entirely defined by the user via the succession of loadings.

As a consequence nuclear data uncertainty does not explain the potential difference between COSI and ANDRA results.

In the case of PWR UOX spent fuel, the COSI result is satisfying.

In the case of PWR repU spent fuel, the difference is much larger. The COSI simulation overestimates by approximately 63 tons the irradiated PWR repU fuel inventory (ANDRA: 318 tons), which approximately corresponds to the mass of three or four repU batches in a core which fractionation is equal to 4. A lack of knowledge concerning the beginning of PWR repU campaigns may explain the bias, as well as a lack of knowledge in the ANDRA exact accounting date.

In the case of PWR MOX spent fuel, a previous analysis of this result [6.1] showed that this mass may have been overestimated in the ANDRA inventory.

6.2.1.5.2.4 Conclusions

The scenario A relative to the French nuclear fleet has been benchmarked by both COSI-CESAR and COSI-MeSAR. The model takes into account GEN II fleet only, together with the actual loads (UOX, MOX and repU). Results are compared in 2010.

This study shows an unexpected and interesting result: overall, nuclear data uncertainty does not explain the difference between COSI simulation and ANDRA results. The predominant factors that introduce bias in the results seem to be the lack of knowledge of the fuel cycle history and the accounting date, as well as the lack of appropriate data for validation of the results.

Although difficult to prevent, a shift in the accounting date can introduce a large bias in several quantities, especially when the balance is in the same order of magnitude or higher than the inventory. Therefore, it can be difficult to compare two separate evaluations, or scenarios, that may not be compatible in terms of accounting dates.

However, results of [6.1, 2] showed that the bias between COSI studies and ANDRA inventories do not increase over time: COSI simulations model trends accurately, and only specific bias due to punctual lack of knowledge introduces bias.

Finally, for a given scenario:

Evaluating the uncertainty at a precise date is still meaningful.

6.2.2 Scenario B: French PWR fleet transition scenario, industrial application

6.2.2.1 Introduction

Several scenario studies are made for academic purposes, for instance this is the case of scenarios A, C and D. Their outcome usually consists in trends, sensitivity studies, discovery of innovative concepts, or aggregation of knowledge and know-how. Other electro-nuclear scenarios, such as scenario B, are called *industrial scenarios*. They are aimed at proposing and discussing solutions with industrial partners, and must give account of the industrial feasibility of such scenarios.

In this work we will only perform burnup uncertainty propagation (no nuclear data or other scenario parameters), in EPR^{TM}only (no uncertainty propagation in GEN II or GEN IV reactors), in order to assess burnup impact and test method discussed in section 5.3.3.8.4 page 204. This work utilizes scenario B for such study. Reasons for this choice are explained in section 6.2.2.3.

6.2.2.2 Objectives

The objectives of this study are as follows:

- burnup uncertainty propagation on several results (no other uncertainty sources);
- analysis of the burnup sampling method.

6.2.2.3 Description of the scenario

Scenario B is an example of French industrial scenario.

Following 2006 French Act on radioactive materials, CEA and its industrial partners EDF and AREVA decided to work together on transition scenarios from the current fleet towards a natural uranium independent fleet. Scenario B is an intermediate step (available in January 2014) in the process of construction of a roadmap for a future SFR fleet deployment. This process is divided in five layers, each layer based on the previous layer and bringing new objectives in terms of scenario results. We summarize it roughly:

- step 0: modeling of the historical French fleet (PWR UOX + PWR MOX) until 2015;
- step A: steady replacement of PWR fleet by EPR^{TM}at constant electric power, stabilization of spent PWR UOX spent fuel and reprocessed uranium stocks;
- step B: steady replacement of PWR fleet by EPR^{TM}and SFR at constant electric power, stabilization of PWR UOX and MOX spent fuel and reprocessed uranium stocks;
- step C: long-term stabilization of plutonium inventory;
- step D: independence from natural uranium.

The present scenario is one of the candidates for the step B of this process, which are mostly aimed at choosing amongst several fuel reprocessing strategies. The historical fleet is replaced over time by 22 EPR^{TM}UOX, 10 EPR^{TM}30% MOX / 70% UOX and 3 SFR (1450MW$_e$) reactors. SFR reactors are deployed so as to consume (after reprocessing) the same amount of plutonium produced by PWR MOX reactors. Figure 6.4 represents the evolution of nuclear energy production over time in the fleet.

This scenario constitutes a very solid basis for a burnup uncertainty propagation study. Indeed, the degree of precision required for industrial scenario studies is such that reactors are modeled

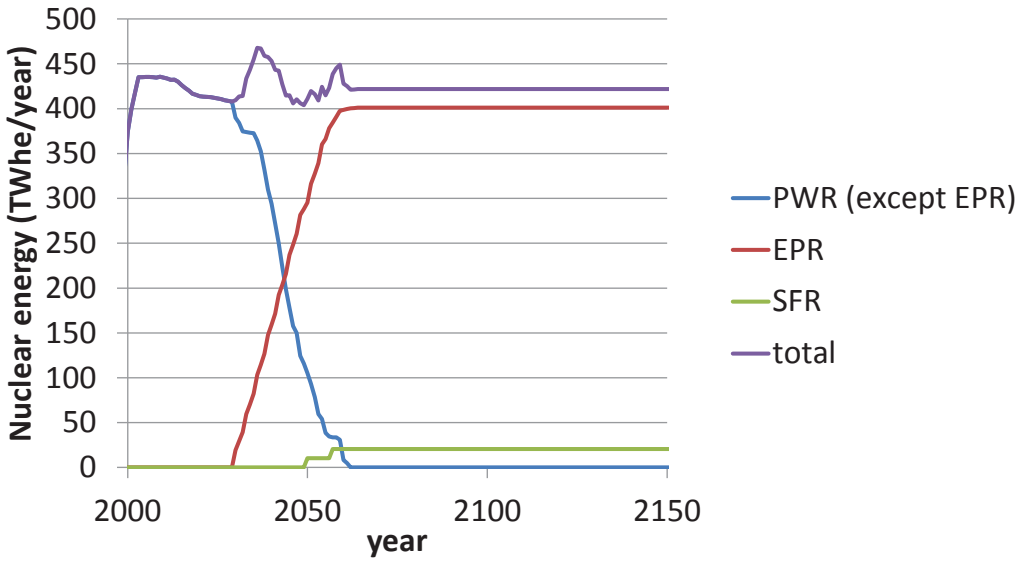

Figure 6.4: Scenario B: evolution of nuclear energy production

one by one. This constitutes a great opportunity because it makes it possible to model correlation (and absence of correlation) between the different fuel batches. Indeed this step cannot be performed in the case of studies using macro-reactors, because burnup of batches in different reactors at the same moment would be erroneously fully correlated.

The scenario uses the following surrogate models:

- PWR UOX
  - low burnup;
  - high burnup;
- PWR MOX
  - low burnup;
  - high burnup;
- PWR repU
- SFR CFV core
  - low burnup;
  - high burnup.

6.2.2.4 Burnup uncertainty propagation

6.2.2.4.1 Introduction

As explained in section 5.3.3.8, the different cycles are not correlated but the discharge burnup of consecutive batches are correlated, because they have up to $(n-1)$ cycles in common, n being the core fractionation.

Our present objective is to assess the impact of the burnup uncertainty (in EPR^{TM}reactors **only**) on several scenario results. In order to do so, we choose to sample the burnup according to its associated uncertainty.

The study is based on scenario B. We processed the scenario data so as to produce a completely

parameterized scenario so as to be able to modify and sample directly each fuel batch in every EPR™reactor. A script was written so as to produce, from a succession of loadings, a set of batches, each one associated to a different fuel type reaching a specific burnup. Therefore, we have access to the following parameters:

- 36 different reactors, each one associated with a different succession of loadings;
- for each succession of loadings, approximately 74 fuel loadings, each one associated with a different end of irradiation burnup.

The correlations between successive batches are taken into account:

- each cycle is taken into account, and has no correlation with other cycles;
- each end of irradiation burnup is calculated as the sum of three consecutive cycles.

When two types of fuel are present at the same time in a reactor, they are attributed the same irradiation cycles. In our case, both PWR MOX and UOX have a fractionation of three.

Therefore our problem contains approximately 5000 variables, half of them have to be sampled and the other half is obtained through simple operations on the first half.

However, construction of a correlated sampling according the correlation matrix of table 5.25 page 201 is difficult because of the difficulty to produce a sampling with URANIE with so many variables, especially when variables are correlated one another.

Therefore we decided to produce several smaller samples and to concatenate them. Scripts were written so as to perform the following tasks:

- read successions of loadings files and create batches and fuel type files for each batch of the succession of loadings;
- create modified succession of loadings files that handle those batches;
- for each succession of loadings, sample irradiation cycles according to their uncertainty and calculate the corresponding end of irradiation burnup;
- concatenate together those samples to create a complete DOE and run COSI on the DOE.

The uncertainty associated with an irradiation cycle burnup is 2.0%. This value was calculated for a core with fractionation of three in section 5.3.3.8.3.4 page 204.

As the construction of the global DOE shows it, there is no correlation test between parameters of different successions of loadings during the sampling process. *A posteriori* analysis of the DOE showed that absolute value of the correlation between cycles in different succession of loadings is below 5%, which is satisfying.

Important remark: The aim of this study is mostly to test correlation laws between end of irradiation burnup for different fuel batches. Burnup uncertainty is taken into account for EPR™only. Burnup associated with PWR historical fleet and SFR reactors is not subject to uncertainty in this study.

6.2.2.4.2 Inventories

First, we calculate the inventories in actinides and the associated uncertainty. Figure 6.5 represents the evolution of the inventories of four elements of interest over time: neptunium, plutonium americium and curium. Scale of Am, Np and Cm is adjusted to facilitate readability.

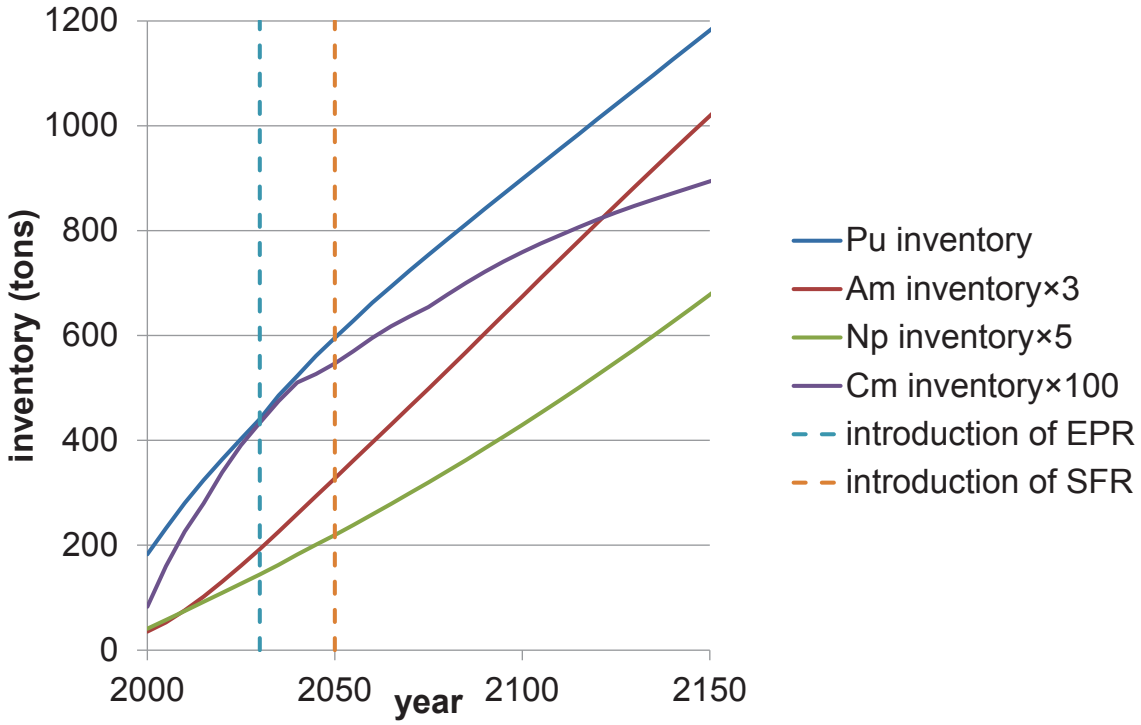

Figure 6.5: Scenario B: evolution of the inventories of different elements of interest

We observe that these inventories grow over time. Indeed in scenario B, there is no specific fuel management strategy to reduce or stabilize them.

Figure 6.6 shows the evolution of the relative standard deviation of these inventories. The relative standard deviation is null before 2030, and positive after EPR^{TM}introduction in 2030.

First of all, we observe that the uncertainty value remains very low: standard deviation is below 0.2% in any case, and below 0.03% in the case of Pu, Am and Np. This result is counter-intuitive. Indeed we observed in section 3.1 that burnup sensitivity of the reactor output concentrations, including Np, Pu, Am and Cm nuclides, is high. Therefore direct transposition of this observation into scenario studies tends to make us believe that the impact on inventories –as a sum of output concentrations moderately impacted by decay– would be tremendous. On the contrary, inventories uncertainty remains very low. The previous reasoning was erroneous because it considered full correlation between fuel batches end of irradiation burnup, which is false.

The standard deviation of inventories grows slowly over time, while the relative standard deviation seems to stabilize or even slightly decrease over time after a first period corresponding to introduction of uncertainty in the system with starting of EPR^{TM}reactors. The slope of the standard deviation changes in function of the following phenomena:

- type of reactors in the nuclear fleet;
- fuel management: origin of the reprocessed fuel.

Figure 6.7 represents the comparison between the empirical CDF of the inventories of interest in 2150 and fitted Gaussian distributions CDF. It appears that distributions of inventories are very close to Gaussian distributions.

Table 6.12 shows comparison of mean, median and nominal value of inventories. We call *nominal*

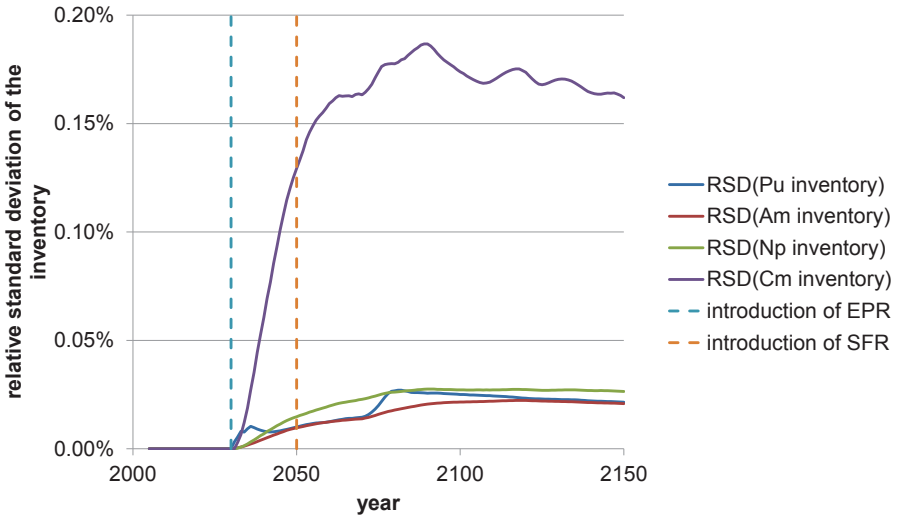

Figure 6.6: Scenario B: evolution of the inventories relative standard deviation for different elements of interest

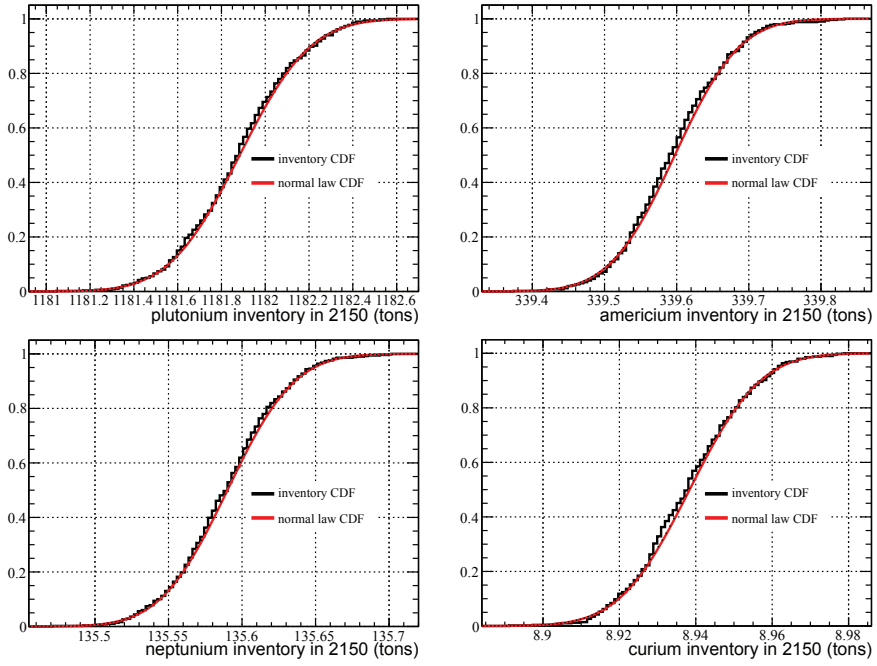

Figure 6.7: Scenario B: CDF of the inventories distributions in 2150

an inventory calculated with no perturbation on burnup.

inventory	mean (t)	median (t)	nominal (t)
plutonium	1181.9	1181.9	1181.8
americium	339.6	339.6	339.6
neptunium	135.6	135.6	135.6
curium	8.94	8.94	8.93

Table 6.12: Scenario B: mean, median and nominal value of the inventories in 2150

We observe that these three indicators are almost identical for the inventories of interest, therefore the nominal value is a good estimator for the mean.

On a side note, we could have expected a different distribution for curium inventory, because of the nonlinear impact of the burnup on the curium inventory after irradiation, but curium radioactive decay may reduce the distribution asymmetry, as decay rate is proportional to mass.

6.2.2.4.3 Fresh fuel isotopy and content

6.2.2.4.3.1 Fresh EPR™MOX fuel

The isotopy of a plutonium isotope (including ^{241}Am) is defined as the mass fraction of this isotope in (Pu + ^{241}Am). Figure 6.8 represents the EPR™MOX fresh fuel isotopy in scenario B. The date corresponds to the batch first irradiation day. The black arrows are discussed later.

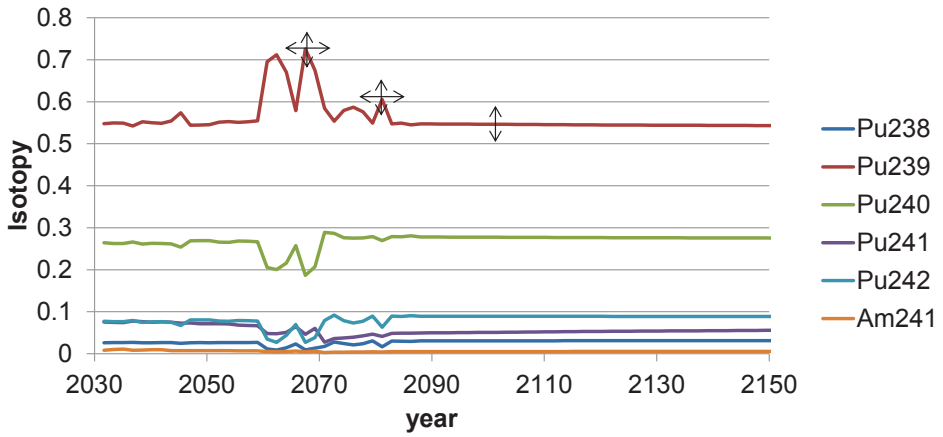

Figure 6.8: Scenario B: EPR™MOX fresh fuel isotopy

We observe three distinct zones:

- before 2060: fuel isotopy is relatively smooth. EPR™MOX fuel is made from historical nominal PWR UOX reprocessed batches;
- between 2060 and 2085: fuel isotopy is irregular. EPR™MOX fuel is made from historical nominal and shutdown PWR UOX batches, as well as starting EPR™UOX batches;
- after 2085: fuel isotopy is smooth again. EPR™MOX fuel is made from reprocessed EPR™UOX batches.

The oscillations in isotopy result from the reprocessing plant fuel management. In this simulation, batches are reprocessed chronologically[3] (first batch arrived at plant is reprocessed first) and we notice that changing the batch sequence at reprocessing plant could smoothen the results.

Figure 6.9 shows the relative standard deviation of EPR^{TM}MOX fresh fuel isotopy.

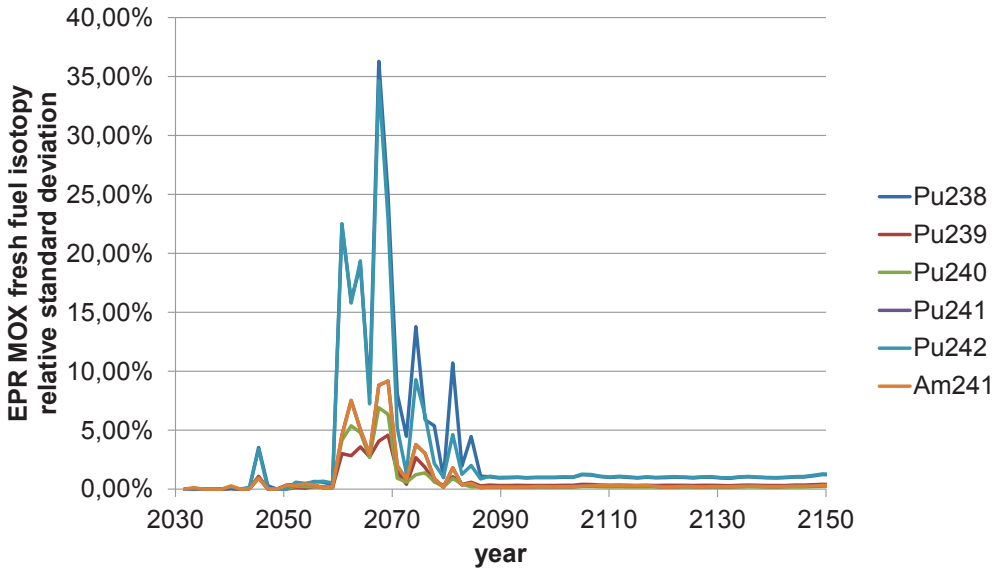

Figure 6.9: Scenario B: EPR^{TM}MOX fresh fuel isotopy relative standard deviation

We observe that the relative standard deviation is very irregular, and booms between 2060 and 2080. However, analysis of the fresh fuel batches shows that standard deviation does not correspond to isotopy uncertainty in this case, but both isotopy (vertical arrows on figure 6.8) and time uncertainty (horizontal arrows).

Indeed burnup uncertainty does not introduce enough uncertainty in plutonium isotopy to create such peaks. Changes in isotopy alter the reprocessed plutonium quality. Plutonium quality impacts the mass of plutonium required to make EPR^{TM}MOX fuel batches through equivalence model: a lower quality plutonium is required in larger amounts, and vice versa. Let us say that a fresh EPR^{TM}MOX batch is made from spent PWR then EPR^{TM}UOX fuel. The plutonium isotopy of this batch does depend on uncertainty, and subsequently does the plutonium mass required to make the MOX batch. This implies that the date of plutonium availability obtained from reprocessing of this batch is subject to uncertainty. Fuel reprocessing strategy in this scenario is chronological by assumption, which means the first batch arrived at the reprocessing plant is reprocessed first. Hence a few years after the transition period from PWR to EPR, EPR^{TM}batches are reprocessed alongside PWR batches. Those PWR batches are in part shutdown batches: their irradiation is lower, hence plutonium quality is higher. Therefore date when fresh fuel is made from spent PWR shutdown batches is subject to uncertainty. Finally, the standard deviation of fresh fuel isotopy can be as high as isotopy difference between nominal and shutdown spent batches (plus isotopy uncertainty).

Figure 6.10 represents the histograms of fresh fuel ^{239}Pu isotopy in 2069 and 2071 (year of two

[3]This simplifying assumption is not reflecting reality.

consecutive batches in a given EPR^{TM}MOX reactor). The number of cases per bin is directly representative of the PDF integrated on the bin. The sample is composed of 500 points. The histograms are highly non symmetrical: the mode is almost on the border of the distribution. In 2069, it appears that fresh fuel is most probably made from a spent shutdown batch with a high ^{239}Pu isotopy, with a chance of addition of nominal batch with a lower quality Pu. On the contrary, in 2071 the next batch is most probably made from a batch irradiated at nominal burnup, with a chance of addition of plutonium from a shutdown batch.

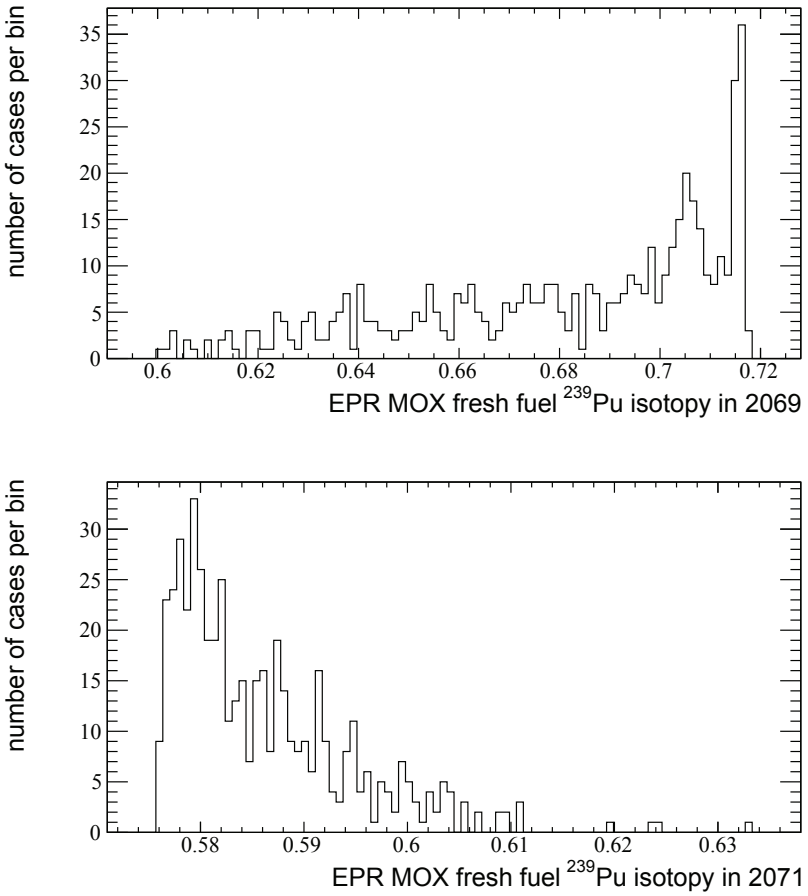

Figure 6.10: Scenario B: histogram of EPR^{TM}MOX fresh fuel ^{239}Pu isotopy in 2069 and 2071

Figure 6.11 represents a zoom on fresh fuel isotopy relative standard deviation after 2085. The burnup impact is much lower than in the previous period, and results from uncertainty in the plutonium stock composition.

The relative standard deviation is stable, and despite a few small peaks corresponding to fuel management changes, its value does not seem to increase over time. Stability is explained by the spent EPR^{TM}UOX fuel isotopic vector stability over time.

6.2.2.4.4 Spent fuel decay heat

In the case of this study, we did not consider SFR fuel burnup uncertainty, consequently we will only evaluate PWR fuel decay heat uncertainty.

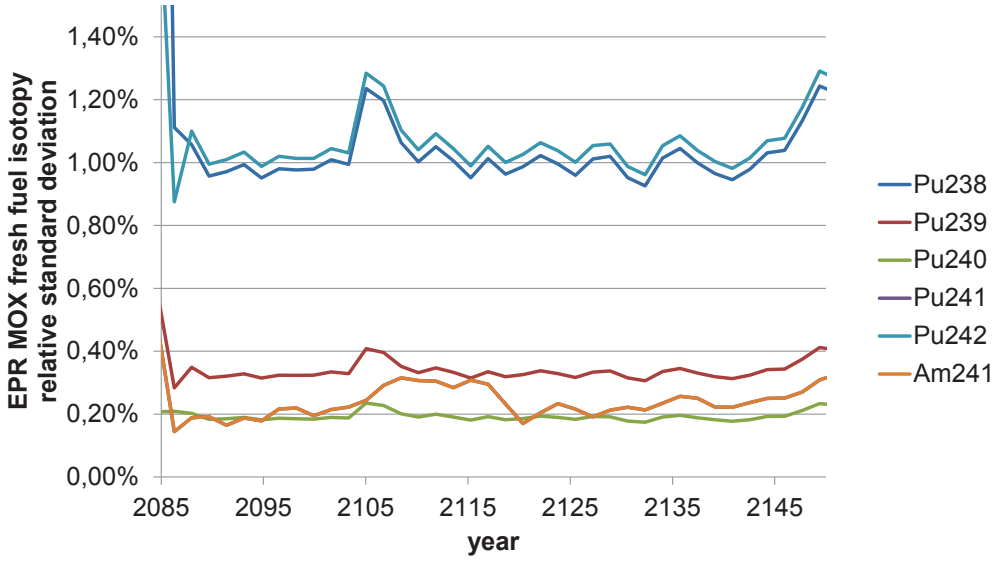

Figure 6.11: Scenario B: EPR^{TM}MOX fresh fuel isotopy relative standard deviation after 2090

Figure 6.12 represents the decay heat of EPR^{TM}MOX fuel after 3, 5, 10, 20 and 50 years of cooling. The date corresponds to the first irradiation day of the batch. The pattern is very similar to that of figure 6.8. This result was expected because fresh fuel plutonium isotopy[4] directly impacts spent fuel decay heat: the higher the quality, the lower the decay heat.

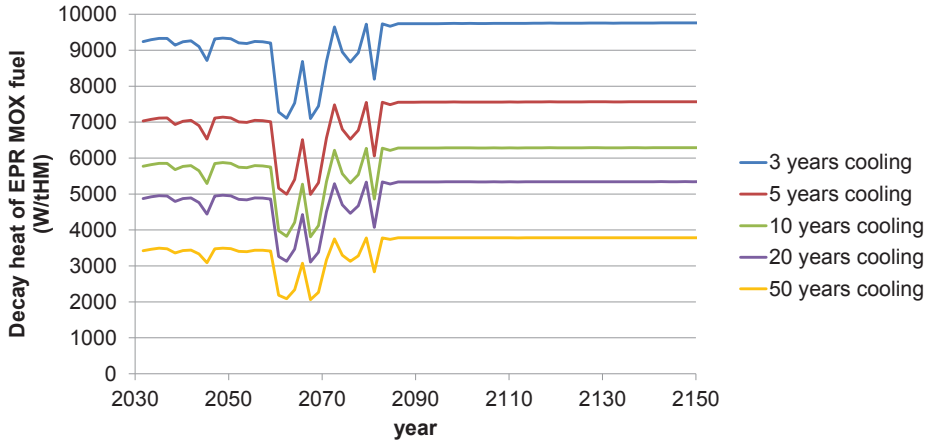

Figure 6.12: Scenario B: decay heat of EPR^{TM}MOX fuel

Figure 6.13 represents the decay heat relative standard deviation for EPR^{TM}MOX fuel after 3, 5, 10, 20 and 50 years of cooling. The pattern is more or less similar to that of figure 6.9, because variability in fuel quality creates horizontal uncertainty (uncertainty on the date) in decay heat. However decay heat also varies in function of the fuel burnup. Combination of standard deviation in fresh fuel plutonium quality and burnup creates a decay heat relative standard deviation between 1% and 2% once the date uncertainty vanishes (after 2090).

We notice that before 2060, standard deviation is almost as high. However, fresh fuel composition

[4] principally ^{238}Pu mass fraction

is almost subject to no uncertainty at that date, meaning that uncertainty before 2060 is mostly due to the burnup uncertainty.

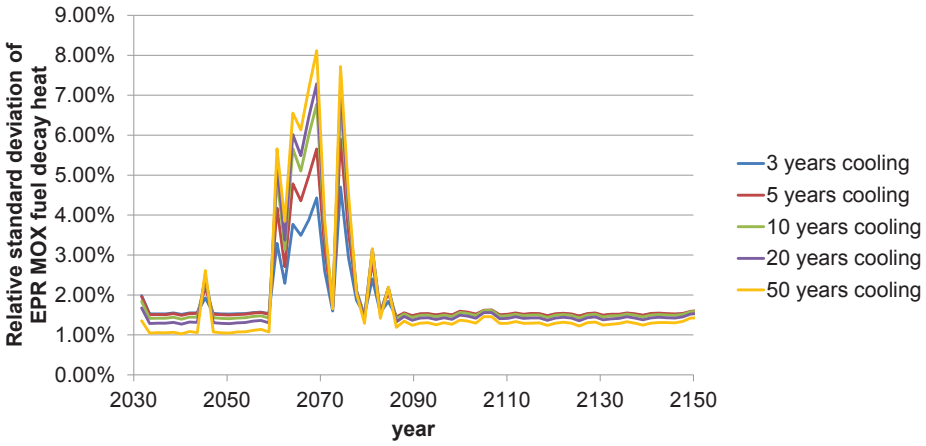

Figure 6.13: Scenario B: relative standard deviation of decay heat of EPR^{TM}MOX fuel

6.2.2.4.5 Conclusions

The aim of this study was to assess burnup impact on different scenario results. The data set structure of this scenario allowed accurate burnup sampling: irradiation cycles burnup were sampled separately and combined together into end-of-irradiation burnups. Consequently there is no simplification for the burnup impact.

Effects of burnup on global results are limited, in spite of a significant impact on local, intermediate results such as spent fuel composition. The plutonium, americium, neptunium and curium inventories are almost not impacted by burnup. This comes from the massive amount of more or less uncorrelated spent fuel batches.

Burnup has a moderate effect on local results. PWR MOX fuel decay heat uncertainty due to burnup is between 1% and 2%. We notice that this effect has the same magnitude as the burnup uncertainty.

Burnup generates standard deviation peaks in different local scenario results, such as decay heat, at several dates. These peaks are linked to fuel management, and are not directly uncertainty of the result, but uncertainty on the date an event occurs, such as changes in fuel management. Consequently, these peaks have the magnitude of the impact of the fuel management change on the scenario result. Fuel management models closer to actual fuel management at the reprocessing plant may reduce drastically these standard deviations. In particular, a model optimizing *on the fly* fuel management, rather than pre-defined settings, may return significantly better results.

6.2.2.4.6 Impact of the sampling method

6.2.2.4.6.1 Impact on local results

We denominate local the results which depend on a given batch. Decay heat of a single batch is an example of local result. Figure 6.14 shows the relative standard deviation of spent EPR^{TM}MOX

fuel after ten years of cooling, calculated according to methods α, β ang γ (see section 5.3.3.8.4) for burnup sampling. The date represents the first irradiation day of the batch. Methods α, β and γ are defined as follows:

- α: reference method, irradiation cycles are sampled and combined:

$$\text{end of irradiation burnup} = \sum_{cycles \in history} \text{irradiation cycle burnup}$$

- β: *local result* method, end of cycle irradiation burnup is sampled such that it conserves local results standard deviation:

$$Var(\text{end of irradiation burnup}) = \text{fractionation} \times Var(\text{irradiation cycle burnup})$$

- γ: *global result* method, end of cycle irradiation burnup is sampled such that it conserves global results standard deviation:

$$Var(\text{end of irradiation burnup}) = \text{fractionation}^2 \times Var(\text{irradiation cycle burnup})$$

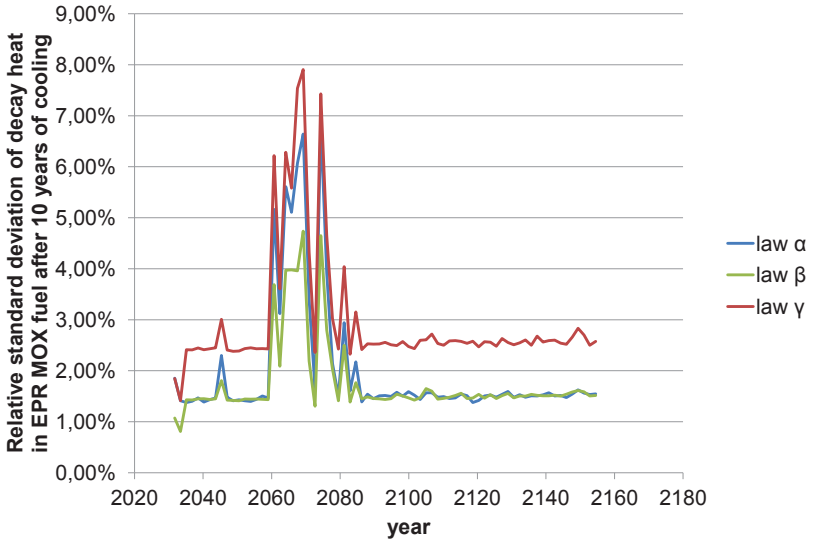

Figure 6.14: Scenario B: uncertainty of EPR^{TM}MOX decay heat (methods α, β and γ)

We observe that method β gives an accurate description of the decay heat standard deviation in this case, by comparison with the reference method α. Method β calculates correctly the burnup uncertainty for a given fuel batch, but introduces a bias in fresh fuel composition uncertainty in the case of fresh fuel made from reprocessed fuel, as it is the case for PWR MOX fuel.

However, method γ overestimates the uncertainty, and is not suited to calculate this uncertainty.

6.2.2.4.6.2 Impact on global results

We denominate global results the results that do not depend on the properties of a single fuel batch, but on the properties of a series of batches. Inventories are an example of global result. Figures 6.15 to 6.18 show the relative standard deviation of the inventories in Pu, Am, Np and Cm in function of time, calculated according to methods α, β and γ.

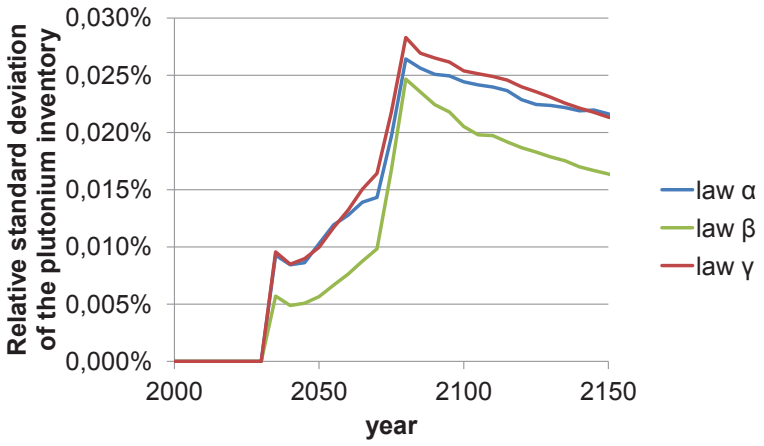

Figure 6.15: Scenario B: plutonium inventory relative standard deviation (methods α, β and γ)

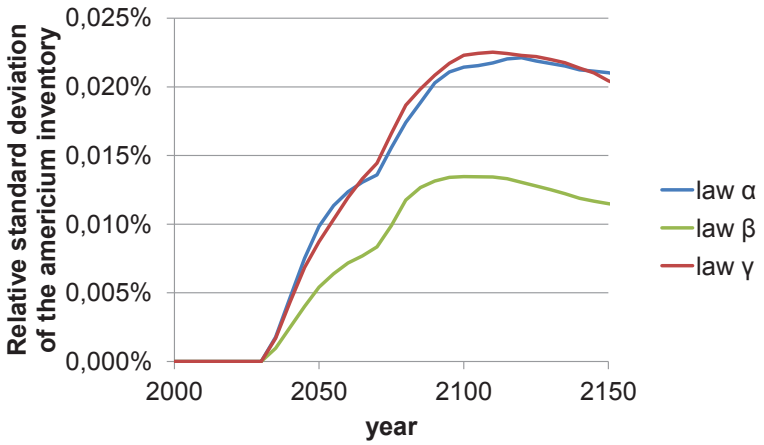

Figure 6.16: Scenario B: americium inventory relative standard deviation (methods α, β and γ)

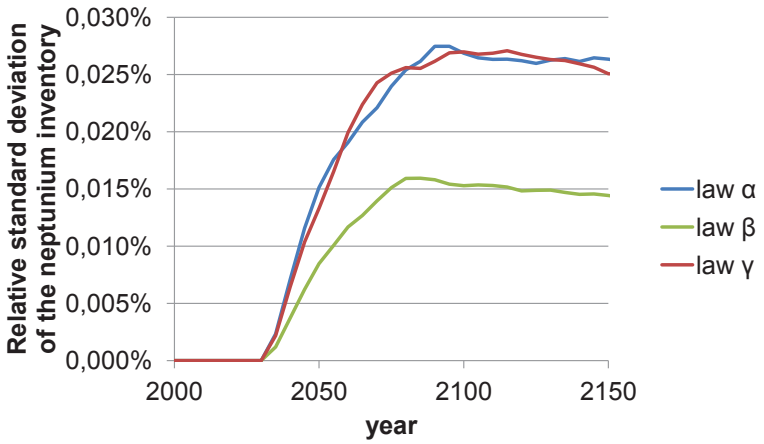

Figure 6.17: Scenario B: neptunium inventory relative standard deviation (methods α, β and γ)

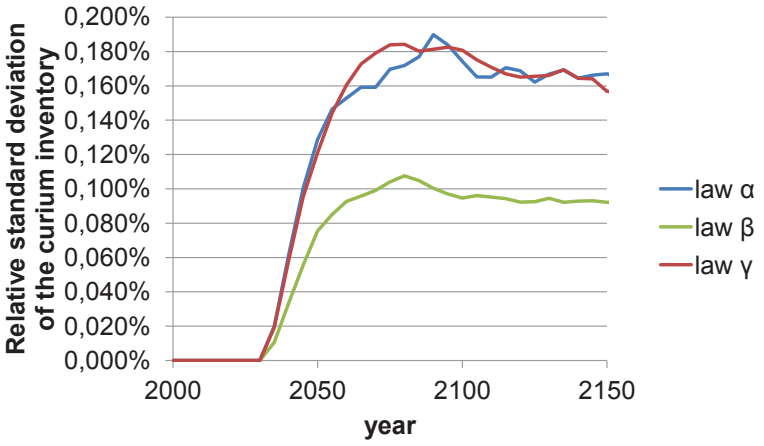

Figure 6.18: Scenario B: curium inventory relative standard deviation (methods α, β and γ)

We observe that method γ gives an accurate description of the relative standard deviation, while method β underestimates it. Therefore, use of method γ is advised in the case of burnup uncertainty propagation on global results.

6.2.2.4.7 Conclusions

Scenario B is an industrial scenario, and consists in steady replacement of PWR fleet by EPR, at constant electric power, with stabilization of spent PWR UOX fuel and reprocessed uranium stocks. Structure of scenario B (high level of detail) permitted to perform burnup uncertainty propagation with method α defined in section 5.3.3.8.4 as the reference method. In this study, only EPR^{TM}were associated with a burnup uncertainty.

Burnup generates little uncertainty on inventories: less than 0.2% for curium, and less than 0.05% for plutonium, neptunium and americium. This comes from the large number of reactors and fuel cycles in each reactor during a scenario computation: inventories behave as a large sum of uncorrelated terms.

The result is different for local results. In the case of fresh EPR^{TM}MOX fuel isotopy, we observe high uncertainty peaks on a constant uncertainty background. The uncertainty peaks are linked to fuel management, and do not correspond to actual isotopy variability for a given batch, but to batch uncertainty at a given date, and the magnitude is close to the gap between isotopies resulting from different fuel management strategies. The uncertainty background is lower, and correspond to the actual burnup impact on a given batch. Results are the same for spent fuel decay heat.

Scenario B also was an opportunity to compare the results of three sampling methods for burnup uncertainty. Method α is the reference method and returns standard deviation corresponding to the actual burnup uncertainty, but it requires a high refinement in the scenario structure and many scenario computations. Method β gives accurate results in the case of local results, such as decay heat, and will be used for local results in the next studies of this work. Method γ is satisfying for global results, and will be used for global results in this work.

6.2.3 Scenario C: French PWR fleet transition scenario, no minor actinides recycling

6.2.3.1 Introduction

In the frame of the French act for nuclear fuel management [6.4] and the ordinance-law [6.5] concerning sustainable material and radioactive waste, which emphasize the need to further study separation and transmutation of long-lived radioactive nuclides, a set of scenarios modeling the renewal of the French PWR fleet with SFR was created. These scenarios must assess the impact of minor actinides transmutation in SFR.

Scenario C can be perceived as the generic, common core of this set. It consists in an academic study of SFR deployment, with plutonium multi recycling, in the French nuclear fleet, which constitutes an energetic transition. Minor actinides are not recycled. This scenario is not industrial in the sense that it does not constitute a road-map to SFR deployment, but rather a basis, from which several options for fuel management and reprocessing in particular are studied. Consequently, hypotheses of scenario C are different than those of scenario B.

6.2.3.2 Objectives

The objectives of this study are as follows:

- burnup and nuclear data uncertainty propagation;
- equivalence model analysis.

6.2.3.3 Description of the scenario

Figure 6.19 represents the state of the fuel cycle before 2038: fuel is irradiated in PWR UOX, PWR repU and mixt (70% UOX, 30% MOX) PWR reactors. PWR UOX fuel is reprocessed and plutonium is recycled into PWR MOX fuel. EPR™deployment starts in 2020.

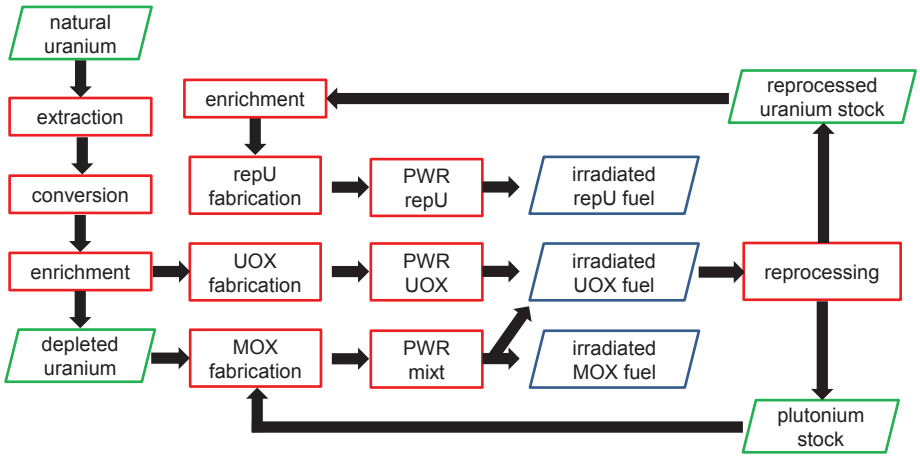

Figure 6.19: Scenario C: fuel cycle before 2038

The last PWR MOX batch is loaded in 2038, and the first SFR reactor with CFV design [6.6] starts in 2040. The energy production remains constant throughout the transition. Figure 6.20

represents transition from PWR fleet to a mixed PWR / SFR fleet. SFR MOX fuel is made from reprocessed PWR UOX and MOX fuel, and SFR fuel once available.

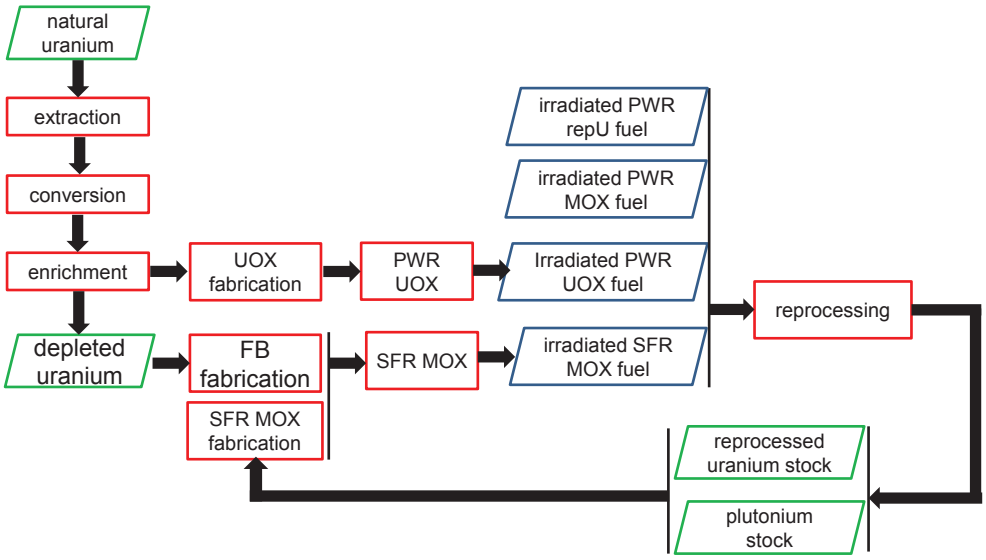

Figure 6.20: Scenario C: fuel cycle between 2038 and 2100

After 2100, all PWR are shut down and the fleet is completely replaced with SFR reactors. Figure 6.21 represents the fuel cycle after 2100. The specificity of this fuel cycle is that it does not require natural resources for an extended duration. The scenario is studied until 2150.

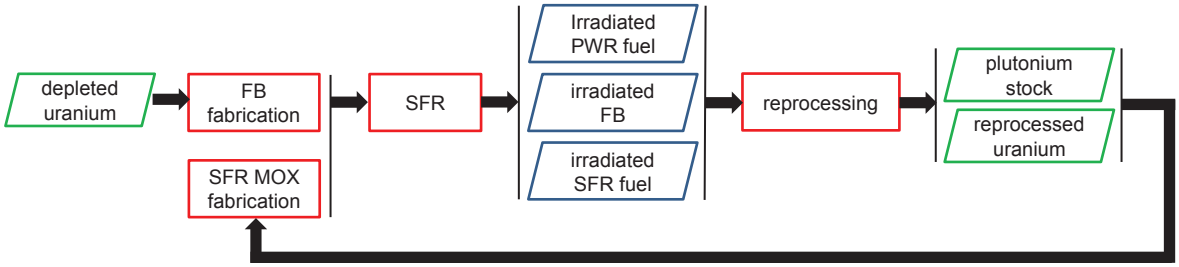

Figure 6.21: Scenario C: fuel cycle after 2100

This fuel cycle does not feature minor actinides reprocessing, plutonium inventory stabilization or any advanced objective. However, it provides a strong basis for such refinements.

The scenario uses the following surrogate models:

- PWR UOX
  - low burnup;
  - high burnup;
- PWR MOX
  - low burnup;
  - high burnup;
- PWR repU

- SFR CFV core
  - low burnup;
  - high burnup.

6.2.3.4 Uncertainty propagation

6.2.3.4.1 Parameters taken into account

In this study, the uncertainties associated to the following parameters are taken into account:

- burnup
  - method β for local results, all reactors
  - method γ for global results, all reactors
- nuclear data
  - actinides fission and capture cross-sections
    - 1-group uncertainty in PWR UOX, PWR MOX and SFR spectra;
    - intra-isotope inter-reaction inter-spectra correlations;
  - fission products capture cross-sections
    - 1-group uncertainty in PWR UOX, PWR MOX and SFR spectra;
    - no correlation;
  - fission yields
    - uncertainty;
    - no correlation / normalization.

6.2.3.4.2 Scenario results uncertainty

Figure 6.22 shows the evolution of plutonium, americium, neptunium and curium inventories in function of time for scenario C. We observe the following phenomena:

- plutonium inventory keeps increasing after 2100 however its production is slower because of this SFR fleet deployment[5];
- americium and neptunium inventories increase steadily as there is no transmutation strategy in this scenario (see section 6.2.4.3.3.1 page 256 for comparison of inventories uncertainties in a scenario with transmutation);
- curium inventory reduces after 2100 as a consequence of SFR fleet deployment and radioactive decay.

Figure 6.23 shows the relative standard deviation of those inventories.

Plutonium uncertainty remains low, and slightly decreases when fleet is SFR only.

Americium inventory uncertainty remains low, and steadily decreases during the SFR transition.

Neptunium relative uncertainty steadily decreases with time.

Curium relative uncertainty is higher, but decreases steadily with time. In particular, we note that the uncertainty drops when the last EPR is shut down. This comes from the lower curium uncertainty in SFR fuel.

[5]The SFR core breeding gain is slightly positive.

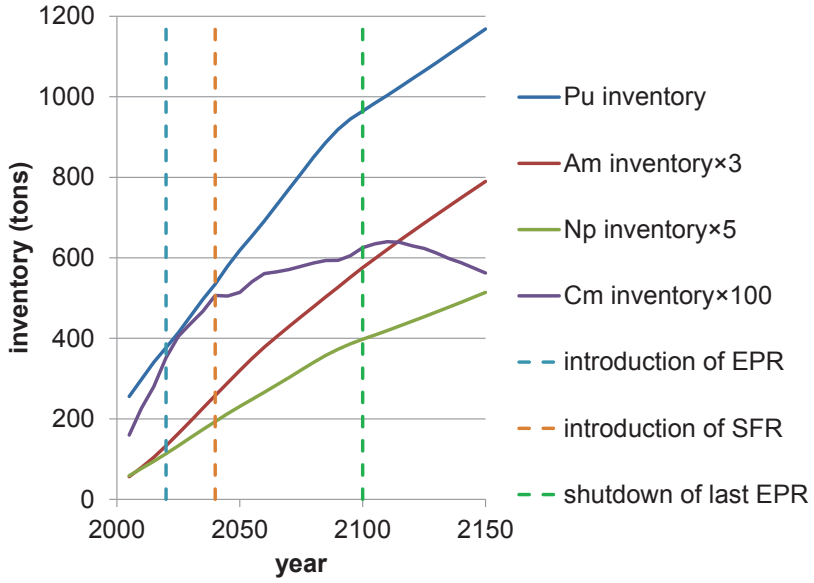

Figure 6.22: Scenario C: evolution of the inventories of different elements of interest

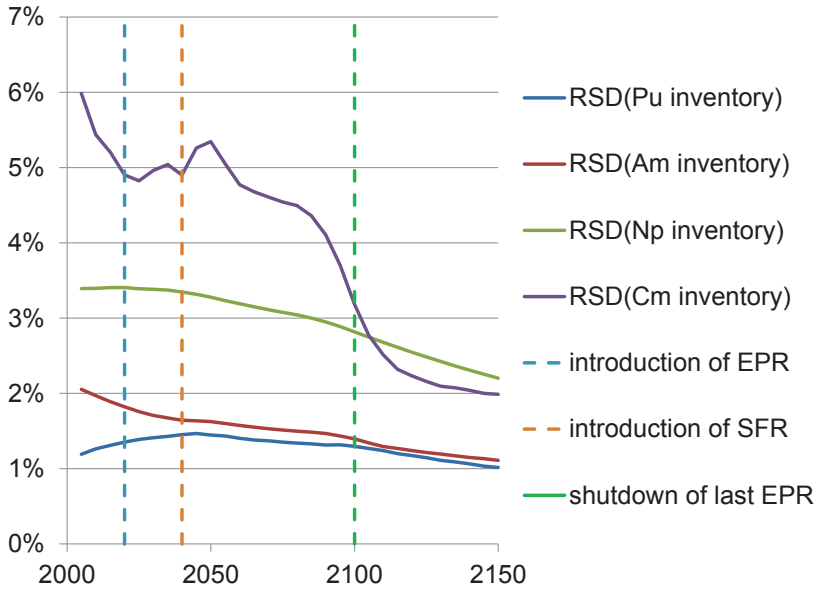

Figure 6.23: Scenario C: evolution of the inventories relative standard deviation for different elements of interest

6.2.3.5 Equivalence model analysis

6.2.3.5.1 Introduction

In this section, we assess the impact of using different equivalence models for scenario studies, and we use ANN equivalence models constructed in section 4 to perform a brief cross-sections uncertainty propagation study.

6.2.3.5.2 PWR MOX fuel

6.2.3.5.2.1 Comparison of different equivalence models

Figure 6.24 represents CPY MOX fresh fuel plutonium content calculated with different models (see section 4.3.3 page 169 for details on PWR MOX equivalence models). These batches are irradiated up to 46GWd/tHM in 3 cycles.

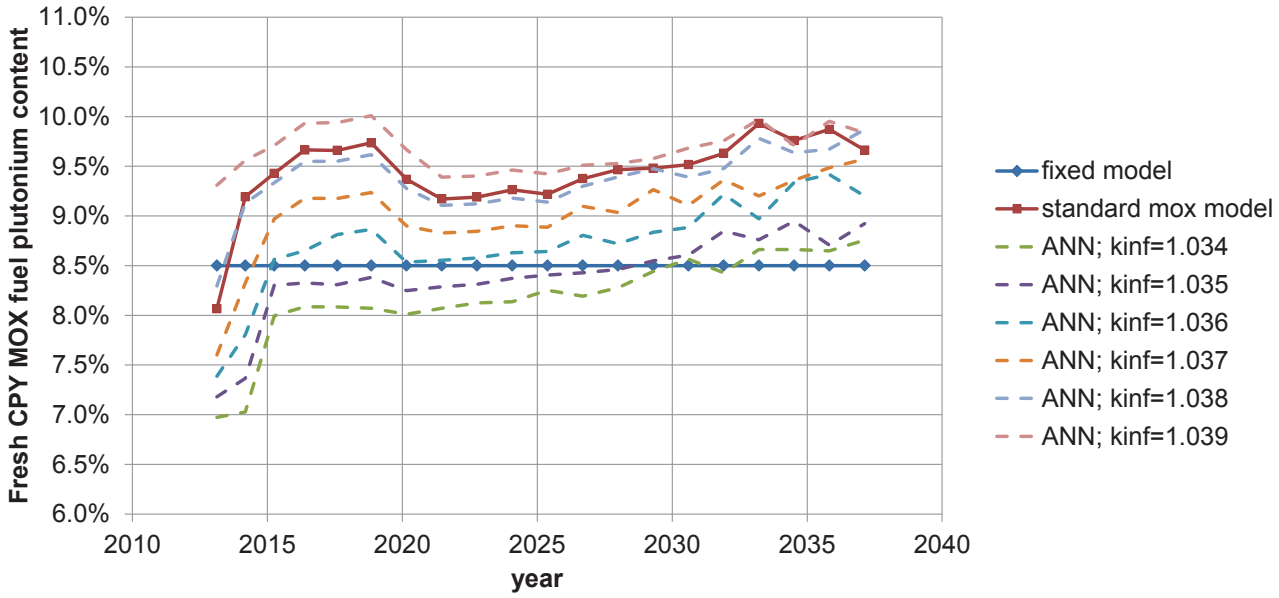

Figure 6.24: Scenario C: CPY MOX fresh fuel plutonium content, calculated with different equivalence models

First, we see that plutonium content is not constant over time. Indeed plutonium isotopy depends on the characteristics of previously irradiated PWR UOX batches, which are not identical. Then, we observe that the standard PWR MOX equivalence model in COSI gives results relatively similar to ANN equivalence models, with $k_{\infty}^{target} \approx 1.038$. As explained in section 4.3.3, the reference end of cycle reactivity for PWR MOX equivalence model is +3900pcm. This result is compatible with the ANN equivalence model.

We note that the fixed content equivalence model does not seem adapted to accurate description of plutonium content.

6.2.3.5.2.2 Cross-sections uncertainty propagation

For this study we used the artificial neural network adjusted to COSI PWR MOX model with $k_{\infty}^{target} = 1.038$. Figure 6.25 shows the fresh PWR MOX fuel plutonium content relative standard deviation in a reactor of the scenario in function of time (the date corresponds to the first irradiation day).

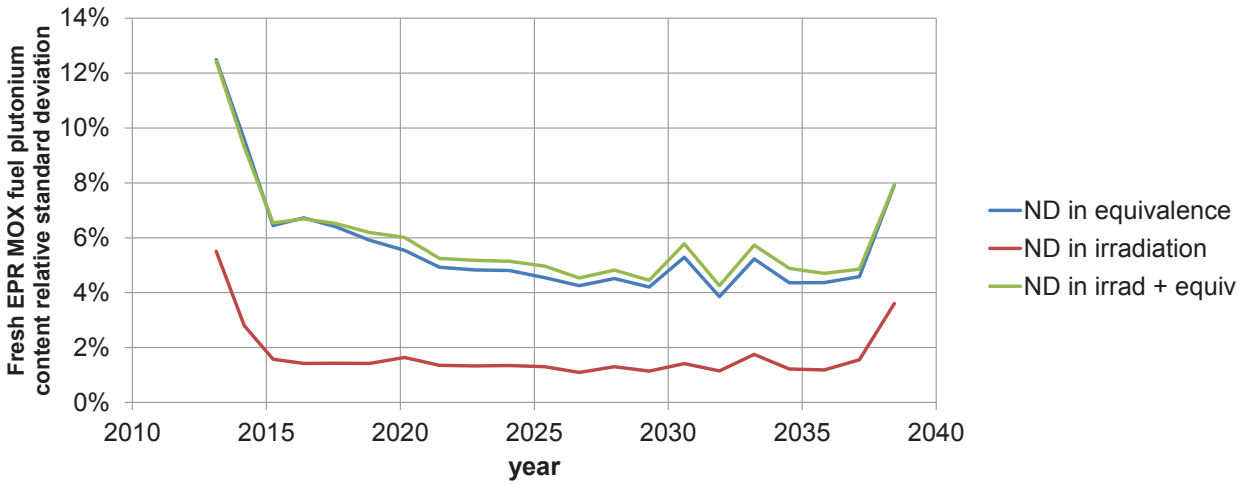

Figure 6.25: Scenario C: CPY MOX fresh fuel plutonium content relative standard deviation

We observe that even though nuclear data have a slight impact on fresh fuel plutonium content through irradiation model, the most significant part of the uncertainty (above 95% of the variance) comes from their impact through equivalence model. This result was more or less expected, as impact through equivalence is direct (ND are parameters of the models) while impact through irradiation is indirect (impact on spent fuel isotopy, which becomes fresh fuel again after reprocessing).

However it confirms the fact that nuclear data have a strong impact on equivalence calculation. Once fuel isotopy stabilization is achieved (after 2020), the plutonium content relative standard remains high (approximately 5%).

Plutonium quality (q) expression is given in equation 6.2, and expression of plutonium downgrade in equation 6.3. Figure 6.26 shows the quality of fresh and spent PWR MOX fuel in a reactor of the scenario, as well as the plutonium quality downgrade due to irradiation.

$$q = \frac{m(^{239}\mathrm{Pu} + {}^{241}\mathrm{Pu})}{m(^{238}\mathrm{Pu} + {}^{239}\mathrm{Pu} + {}^{240}\mathrm{Pu} + {}^{241}\mathrm{Pu} + {}^{242}\mathrm{Pu} + {}^{241}\mathrm{Am})} \tag{6.2}$$

$$\text{downgrade} = q_{\text{fresh fuel}} - q_{\text{spent fuel}} \tag{6.3}$$

We observe that with the exception of the very first batches, the plutonium fresh fuel quality is relatively constant. As a consequence, spent fuel quality is stable as well.

Figure 6.27 shows the fresh fuel quality relative standard deviation in function of time, calculated with the following uncertainty sources:

- nuclear data uncertainty in equivalence models only;

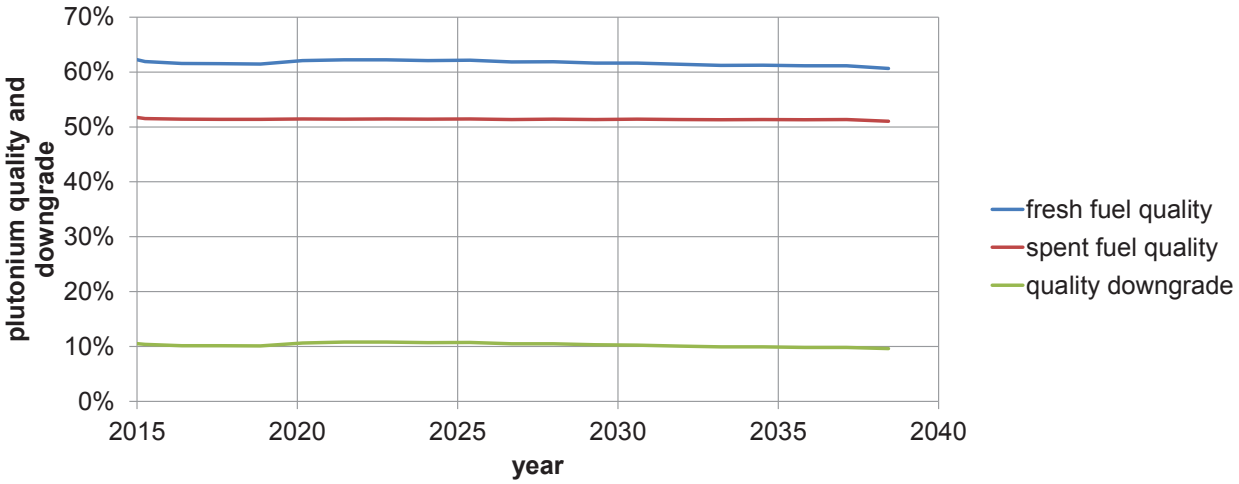

Figure 6.26: Scenario C: CPY MOX fresh/spent fuel plutonium quality and downgrade

- nuclear data uncertainty in irradiation models only;
- nuclear data uncertainty in both irradiation and equivalence models.

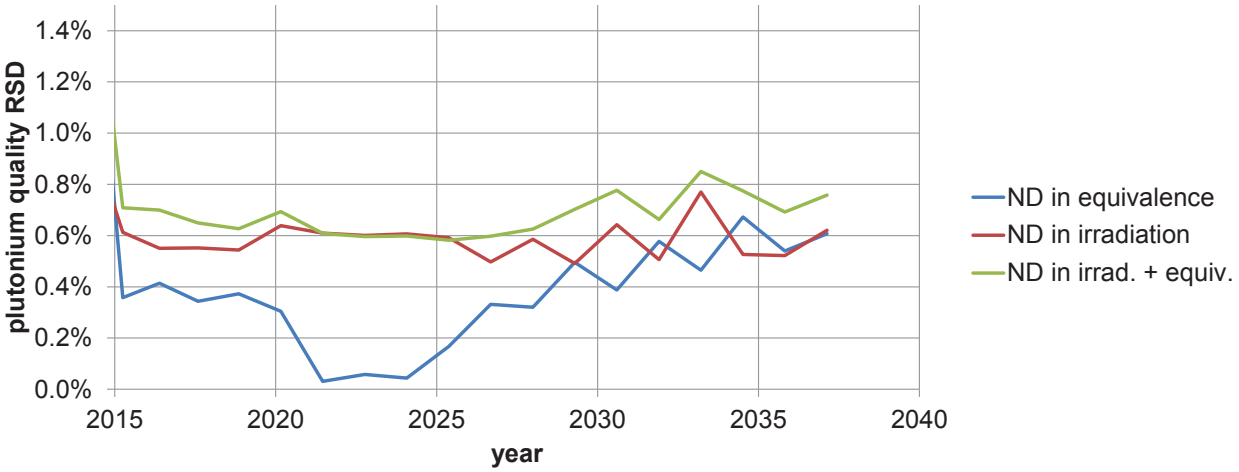

Figure 6.27: Scenario C: CPY MOX fresh fuel plutonium quality relative standard deviation

Plutonium quality relative standard deviation is low: slightly less than 1%. We observe that nuclear data have an impact on fresh plutonium quality through both irradiation and equivalence model. The magnitude of both effects is more or less similar. Both terms are indirect, and result from changes in the reprocessed spent fuel:

- equivalence model: mix of different batches due to different plutonium mass required for fresh fuel;
- irradiation model: changes in reprocessed PWR UOX spent fuel composition.

Figure 6.28 shows plutonium quality downgrade relative standard deviation.

Once again, after stabilization, both terms have the same magnitude. Combination of both terms is almost quadratic (little interaction). The relative standard deviation is high: approximately 15% after stabilization. Plutonium downgrade relative standard deviation in PWR MOX

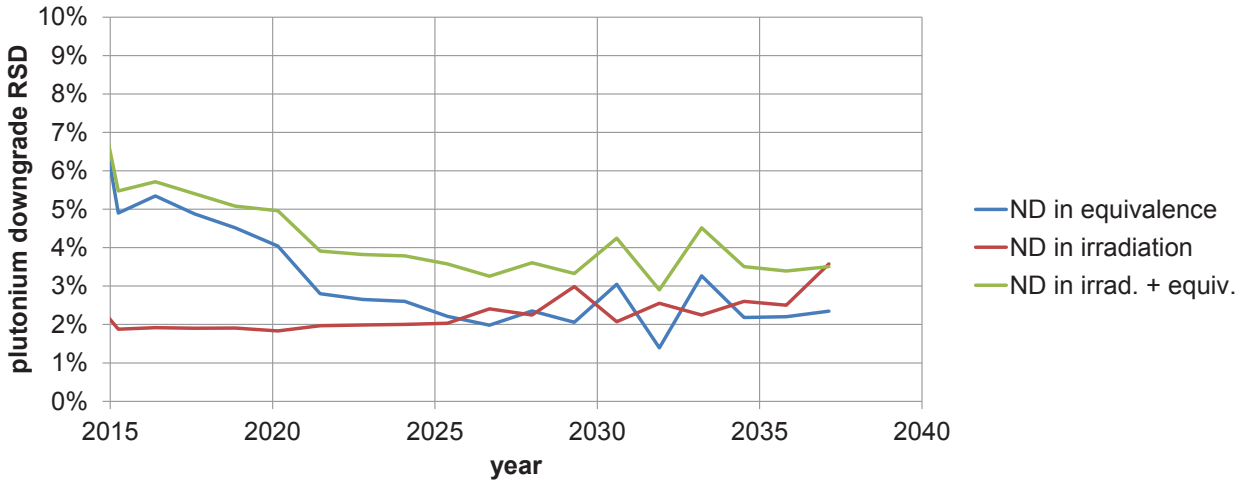

Figure 6.28: Scenario C: CPY MOX plutonium downgrade relative standard deviation

is mostly important in the case of studies concerning plutonium multi-recycling in PWR MOX reactors, because consecutive irradiation may stack uncertainty.

6.2.3.5.3 SFR fuel

6.2.3.5.3.1 Comparison of different equivalence models

Figure 6.29 shows fresh SFR fuel plutonium content calculated with different models. Batches are irradiated up to 116.3GWd/tHM in 5 cycles. The equivalence models used are as follows:

- Baker & Ross equivalence perturbative model (simplified model) with coefficients adjusted to CFV [6.6] core design with typical isotopy;
- ANN models made from ERANOS computations using method C (see section 4.3.2.3); the model has 9 neurons in the hidden layer and is adjusted to different end-of-cycle reactivity values ($\rho \in \{700; 2000; 2500\}$ pcm).

Plutonium content is not constant over time, because of several plutonium characteristics:

- plutonium origin: PWR UOX / PWR MOX / SFR spent fuel / fertile blankets (plutonium vector in spent fuel changes with fuel type);
- nominal / non nominal fuel batch (plutonium vectors depends on the burnup);
- old / recent (fissile ^{241}Pu decays into ^{241}Am, etc.).

We observe that Baker and Ross model gives the same trend as ANN estimators. However, while we initially expected $\rho^{target} \approx 0$pcm, the models seem to fit better $2000 < \rho^{target} < 2500$pcm.

6.2.3.5.3.2 Cross-sections uncertainty propagation

For the rest of the study, we considered $\rho^{target} = 2250$pcm. Figure 6.30 shows the fresh SFR CFV fuel plutonium content relative standard deviation in a reactor of the scenario (the first SFR CFV, first grid connection in 2040) in function of time, the date corresponds to the first irradiation day. Three different cases are evaluated:

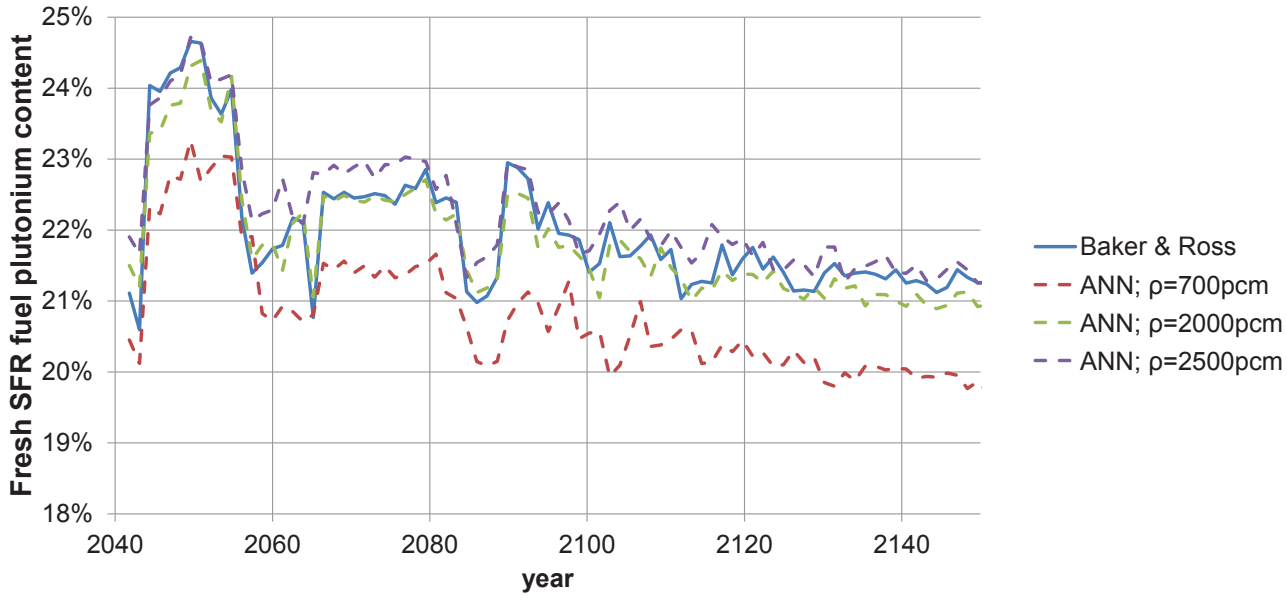

Figure 6.29: Scenario C: SFR MOX fresh fuel plutonium content, calculated with different equivalence models

- nuclear data are perturbed in equivalence models (SFR model only);
- nuclear data are perturbed in irradiation models only (all irradiation model);
- nuclear data are perturbed in both models (SFR equivalence model; all irradiation models).

We observe that nuclear data impact is high. The fresh fuel plutonium content relative standard deviation due to nuclear data is approximately 8%. Nuclear data most important impact on fresh fuel plutonium content is through equivalence model. This result is the same as for PWR MOX fuel: impact through equivalence is direct (ND are parameters of the models) while impact through irradiation is indirect (impact on spent fuel isotopy, which becomes fresh fuel again after reprocessing).

We observe that plutonium content relative standard deviation slowly increases with time, mostly because of the impact of equivalence model, while the irradiation model generates a constant relative standard deviation.

Two factors impact fresh fuel plutonium content:

- the equivalence computation (impact of equivalence model only);
- the fresh fuel plutonium isotopy (impact of both equivalence and irradiation models).

Figure 6.31 illustrates the fresh SFR fuel plutonium quality relative standard deviation, which is a function of plutonium isotopy.

We observe that nuclear data uncertainties in the equivalence model have a slightly higher impact on the fresh fuel quality than in the irradiation model. Equivalence model impact on fresh fuel quality has two mechanisms:

- 1. impact of ND in equivalence model on fresh fuel content;
  2. $\rightarrow$ impact on spent fuel isotopy;
  3. $\rightarrow$ impact on fresh fuel isotopy a few years later.
- 1. impact of ND in equivalence model on fresh fuel content;

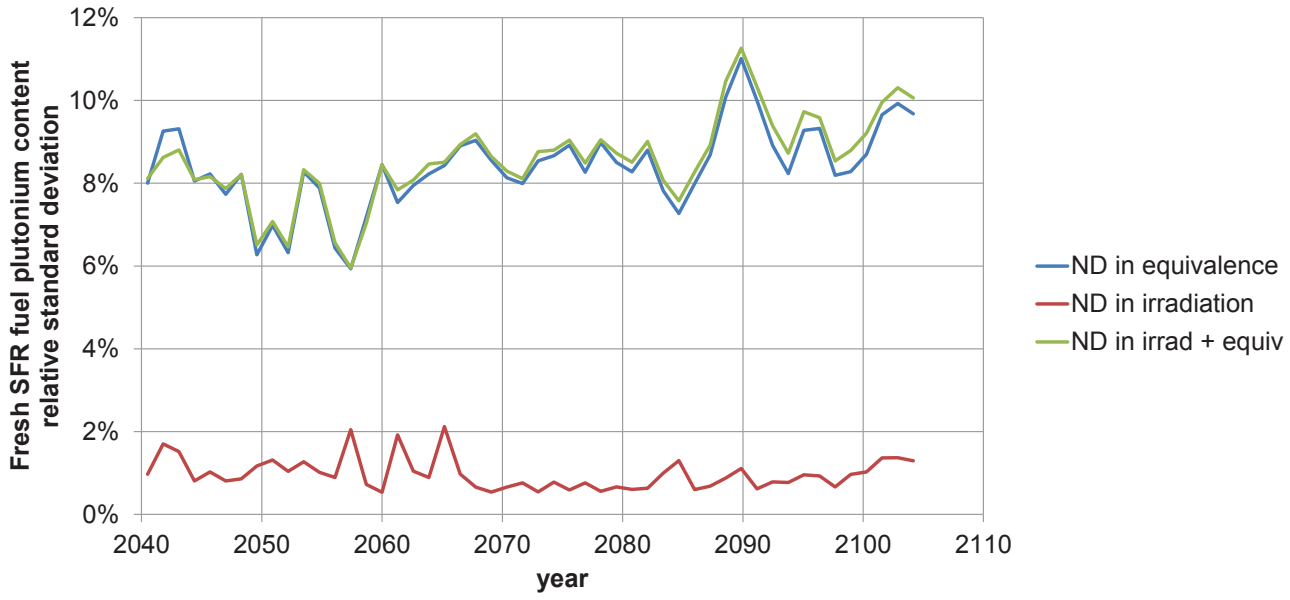

Figure 6.30: Scenario C: SFR MOX fresh fuel plutonium content relative standard deviation

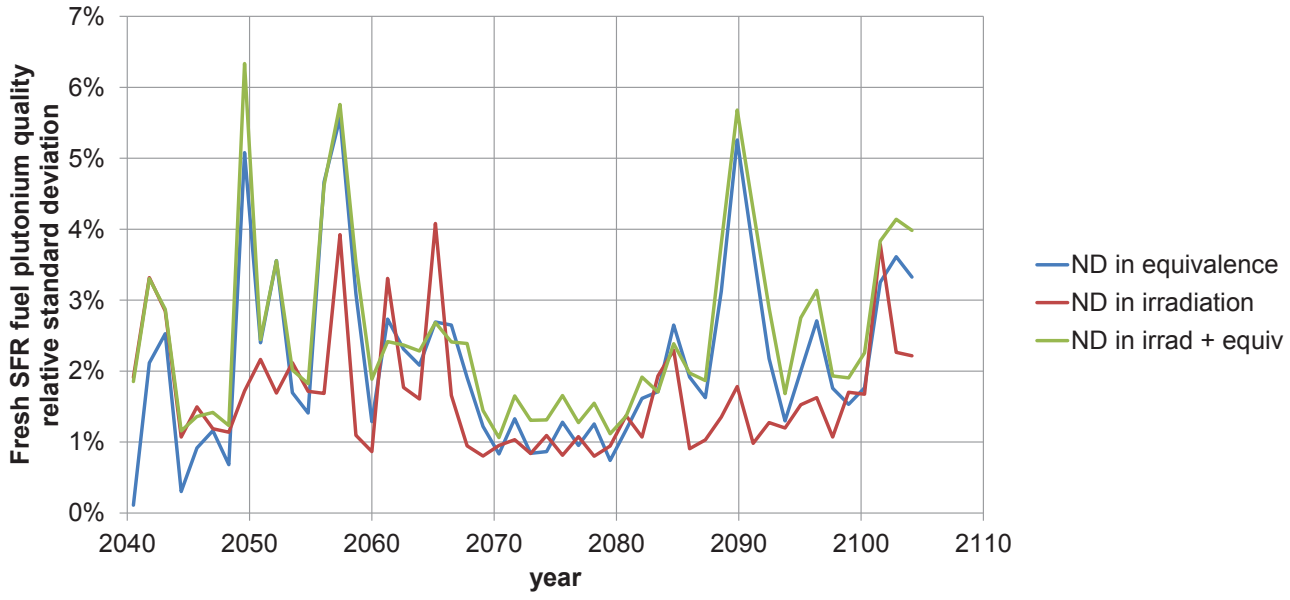

Figure 6.31: Scenario C: SFR MOX fresh fuel plutonium quality relative standard deviation

2. $\rightarrow$ impact on plutonium mass required;
3. $\rightarrow$ impact on spent fuel batch;
4. $\rightarrow$ impact on spent fuel batch isotopy;
5. $\rightarrow$ impact on fresh fuel isotopy.

6.2.3.5.4 Conclusions

The use of equivalence models in scenario computations is a complex problem that remains open.

Equivalence models have a strong impact on the whole scenario computation. Nuclear data uncertainty generates uncertainty in scenario results through both irradiation and equivalence models, although impact of equivalence model is dominant. Furthermore, uncertainty generated by nuclear data in equivalence model is rather hard to predict or approximate, as it is highly nonlinear and depends on the whole scenario history and fuel management.

In the case of PWR MOX equivalence models, uncertainty may be overestimated. Indeed, the equivalence model is built such that the end of cycle reactivity equals a given criterion. However, in practice, fuel may be produced with different end of cycle reactivity. Consequently, the uncertainty would propagate up to reactivity, not fresh fuel content.

However, we can approach the problem from a different perspective: in scenario computations, we may not calculate the actual fuel content, but assess the result of a future fuel content computation, which will be performed at time fuel is produced. In that case, nuclear data uncertainty may be representative of the content bias imposed by future industrial feedback, in the nuclear data generate uncertainty on the provisional value of the industrial measure.

This second approach is probably meaningless in the frame of PWR MOX reactors. Indeed industrial feedback has brought additional information to determine fresh fuel plutonium content: re-estimation of nuclear data might not even impact determination of fresh fuel content, provided sufficient information concerning end of cycle reactivity is available. However, for SFR reactors, as there is neither definitive reference industrial core nor sufficient industrial feedback, nuclear data will impact fresh fuel content.

In the case of PWR MOX reactors, it could be interesting to build equivalence models based on core computation (instead of assemblies computations), and to analyze differences with the present models, mainly in terms of variability (*is the impact of nuclear data on fresh fuel composition as strong as the present calculations suggest it is?*).

In the case of SFR MOX reactors, the very definition of present equivalence models is debatable. Indeed end of cycle reactivity is used as the equivalence criterion, which has the following drawbacks:

- reactivity is not always a decreasing function of burnup in SFR, it can be increasing or non-monotonous. Consequently, a criterion formulated in terms of reactivity condition on the whole cycle (for instance $\forall$ BU, $\alpha < \rho(\text{BU}) < \beta$) would be more representative;
- in SFR reactors, as plutonium isotopy range is wide, reactivity should not be the unique parameter for computation of the content. For instance, other physical criteria such as the number of displacements per atom or linear power might provide better information.

6.2.4 Scenario D: French PWR fleet transition scenario, americium recycling

6.2.4.1 Introduction

CEA studies transmutation of minor actinides, including americium. It consists in performing a succession of nuclear reactions on a nuclide such that it is transformed into another nuclide with a high fission cross-section. Fission of a minor actinide (before or after transmutation) is the last step of the process, and is called incineration. The idea behind this operation is that unstable fission products are short-lived, and therefore have a smaller contribution to long-term radio-toxicity.

Transmutation can be performed on both thermal and fast spectra. The following criteria in favor of transmutation in fast spectrum were observed:

- neutron consumption[6] [6.7] is positive in thermal spectrum and therefore requires higher fuel enrichment, whereas it is negative (production of neutrons) in fast spectrum;
- the ratio σ_c/σ_f is smaller in fast spectrum, thus a smaller production of very heavy nuclides for the same amount of incineration;

Consequently transmutation in SFR appears to be a better option.

However minor actinides tend to have a strong impact (via neutron sources, decay heat, etc.) on both fresh and spent fuel, and the core performances (alteration of void coefficient, etc.). Therefore partitioning and transmuting several minor actinides at a time (Np, Am, Cm) is a technological challenge.

Other than transmutation of minor actinides in the core (*homogeneous mode*), addition of minor actinides bearing blankets next to the core is studied. This mode is called *heterogeneous*.

Furthermore, restriction of minor actinides partitioning and transmutation to americium only is a way to reduce constraints and pressure imposed on the whole nuclear fuel cycle. Americium is the main contributor to waste toxicity after 500 years of cooling. It is produced both in PWR and SFR. Equation 6.4 represents the main reaction path leading to ^{241}Am. The half-life of ^{241}Pu is 14.4 years.

$$^{239}\mathrm{Pu} \xrightarrow{(n,\gamma)} {}^{240}\mathrm{Pu} \xrightarrow{(n,\gamma)} {}^{241}\mathrm{Pu} \xrightarrow{\beta-} {}^{241}\mathrm{Am} \tag{6.4}$$

The goal of scenario D is to evaluate the interest of americium heterogeneous transmutation in SFR cores with americium bearing blankets. The result expected from this scenario study is the stabilization of americium inventory.

6.2.4.2 Objectives

The objectives of this study are as follows:

- burnup and nuclear data uncertainty propagation;
- uncertainty propagation and analysis of other parameters;
- feasibility study.

[6] average number of neutrons required to incinerate a given nuclide

6.2.4.3 Description of the scenario

Scenario D is based on scenario C, with addition of americium management:

- americium bearing blankets (AmBB) with a fixed americium content (10% mass) in SFR core (CFV design);
- americium partitioning in spent fuel at the reprocessing plant.

Fuel management at the reprocessing plant is adapted to suit americium management. Every fuel type is reprocessed, and the reprocessing plant capacity is fixed.

Figure 6.32 represents the fuel cycle in scenario D after 2100 (FB = fertile blanket). The scenario is studied until 2150.

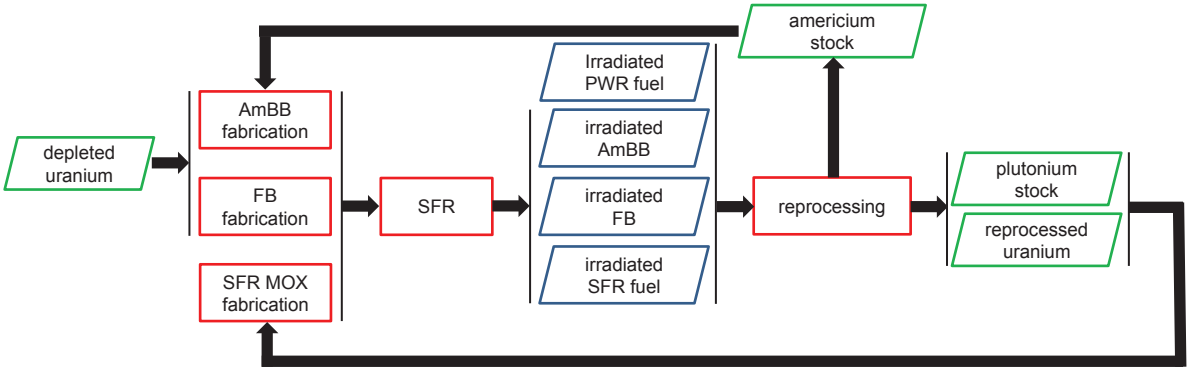

Figure 6.32: Scenario D: fuel cycle after 2100

The scenario uses the following surrogate models:

- PWR UOX
  - low burnup;
  - high burnup;
- PWR MOX
  - low burnup;
  - high burnup;
- PWR repU
- SFR CFV core
  - low burnup;
  - high burnup;
- intern fertile blanket;
- lower fertile blanket;
- americium bearing blanket.

6.2.4.3.1 Parameters taken into account

In this study, the uncertainties associated with the following parameters are taken into account:

- burnup
  - method β for local results, all reactors

isotope	mass fraction (%)
^{238}Pu	2.7
^{239}Pu	56.0
^{240}Pu	25.9
^{241}Pu	7.4
^{242}Pu	7.3
^{241}Am	0.7

Table 6.13: Infinite plutonium isotopy

  - method γ for global results, all reactors
- nuclear data
  - actinides fission and capture cross-sections
    - 1-group uncertainty in PWR UOX, PWR MOX and SFR spectra;
    - intra-isotope inter-reaction inter-spectra correlations;
  - fission products capture cross-sections
    - 1-group uncertainty in PWR UOX, PWR MOX and SFR spectra;
    - no correlation;
  - fission yields
    - uncertainty;
    - no correlation / normalization.

6.2.4.3.2 Description of the study

This uncertainty propagation study is straightforward: sampling of parameters associated with uncertainty according to the uncertainty distribution, impact analysis on the scenario results of interest. We define the plutonium margin as the sum of plutonium stock and plutonium in spent fuel already cooled and ready for reprocessing.

In the case where the scenario is not feasible because the plutonium margin becomes negative, separated *infinite plutonium* is injected in the fuel cycle. This introduces a bias in the plutonium inventory but it is necessary for uncertainty propagation. The artificial uncertainty reduction of plutonium inventory in section 6.2.4.3.3.1 is a consequence of this bias.

Table 6.13 shows *infinite plutonium* isotopy.

6.2.4.3.3 Results

6.2.4.3.3.1 Actinides inventories

Figure 6.33 shows plutonium, americium, neptunium and curium global inventories in function of the time. Global inventories are calculated on the whole fuel cycle (reactors + stocks + spent fuel + plants + waste).

- plutonium inventory increase is slightly more important in scenario D than in scenario C after 2100, because of plutonium production in blankets;
- americium inventory grows until 2100, and then stabilizes. This result proves the efficiency of AmBB for americium transmutation;

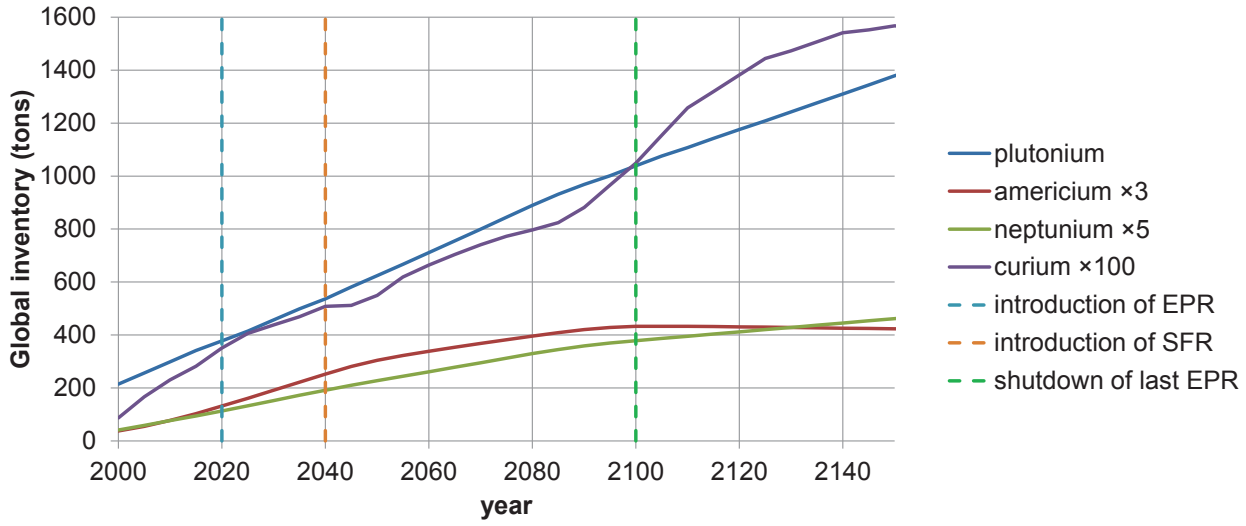

Figure 6.33: Scenario D: evolution of the inventories of different elements of interest

- neptunium inventory is more or less identical to scenario C;
- curium inventory is much higher than in scenario C: while in scenario C it decreases from 2100 onwards (shutdown of EPR), its slope increases in scenario D. This comes from the fact that not all of americium transmutation leads to incineration. A certain amount of americium is transformed into curium, and stays in the fuel cycle as such.

Figure 6.34 shows plutonium, americium, neptunium and curium inventories relative standard deviation in function of time.

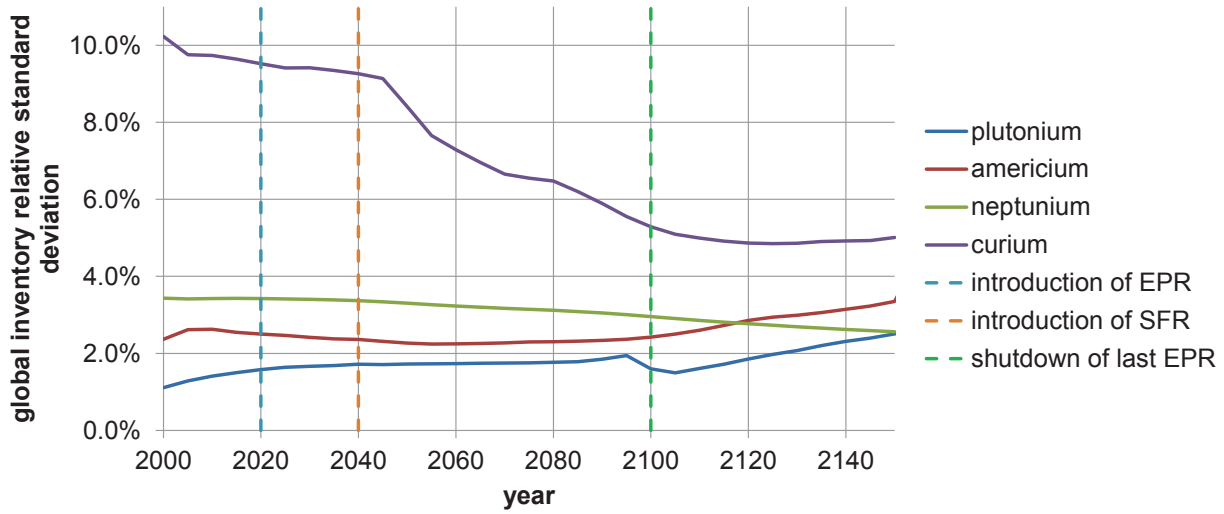

Figure 6.34: Scenario D: evolution of the inventories relative standard deviation for different elements of interest

Plutonium relative standard deviation is not heavily impacted by differences between scenarios C and D; however we observe that while in scenario C the plutonium uncertainty steadily decreases after 2100, it increases in the case of scenario D. We remark uncertainty drops around

2100. This drop is not representative of the actual value of the uncertainty, but is an artifact due to introduction of infinite plutonium in the scenario. Indeed, a high percentage (46%) of the scenarios are not feasible past 2100 due to lack of plutonium. So as to continue the study, the required amount of plutonium (*infinite plutonium*) is artificially injected in the fuel cycle. Isotopy of this plutonium is shown in table 6.13. On the uncertainty point of view, since if plutonium lacks then it is injected, therefore mass uncertainty is reduced. A study considering injection of plutonium from the start (as opposed to injection only when required) would partially avoid this artifact[7], but, the present study still gives a good insight of uncertainty behavior.

On the other hand, americium relative standard deviation becomes twice more important at the end of scenario D than in scenario C, and keep increasing. This comes from two phenomena:

- in scenario C, Am inventory does not stabilize, which contributes to lowering the relative standard deviation;
- americium transmutation causes inventory uncertainty to increase: both creation and incineration of americium generate uncertainties.

Neptunium uncertainty is similar in scenarios C and D.

Curium inventory relative standard deviation stabilizes more or less. However, the standard deviation is twice higher in scenario D. Given that curium has detrimental effects on the fuel cycle because of its radio-toxicity, this result is unfavorable for the scenario.

6.2.4.3.3.2 Natural uranium consumption

The parameters taken into account for this study have no impact on natural uranium consumption (RSD=0%). However, natural uranium isotopy has a small impact, which is discussed in section 6.2.4.5.

6.2.4.3.3.3 Fuel fabrication

a) PWR UOX, PWR MOX, SFR fuel fabrication

The parameters taken into account for this study have no impact on the fresh fuel fabrication need[8]. However mass losses at the fabrication plant have a simple, direct impact on the input balance of fabrication plants.

We remark that if we consider that the electric production is constant but the fuel burnup is not, then power production can be adjusted with cycles duration. The power production of one reactor is given in equation 5.51 page 199. Consequently, a perturbation δBU of the burnup has the impact $\delta(\Delta t)$ if the reactor energy production $\mathcal{P}$ is constant[9]:

$$\delta(\Delta t) = \frac{\delta\text{BU} \times \rho \times f \times m}{\mathcal{P}} \tag{6.5}$$

[7] However it would introduce bias on the plutonium inventory uncertainty on the whole scenario duration.
[8] It is fixed by the succession of loadings of each reactor, which is an hypothesis, not a parameter.
[9] Another solution would be to adjust electric power production of the whole fleet at the same time.

Different cycles durations have an impact on the fuel fabrication plant. The impact of burnup uncertainty on power production is small, because it is a sum of uncorrelated Gaussian distributions. Consequently the counter-impact on the fabrication plant would be small too.

b) AmBB fabrication

AmBB fabrication follows a different process, because those blankets are fabricated only when an americium stock has to be transmuted, and americium stock is subject to uncertainty. Figure 6.35 is the AmBB fabrication cumulative needs histogram in 2150. The peak on the right side of the histogram corresponds to the cases where the americium transmutation needs are superior than the reactors capacity (saturation effect).

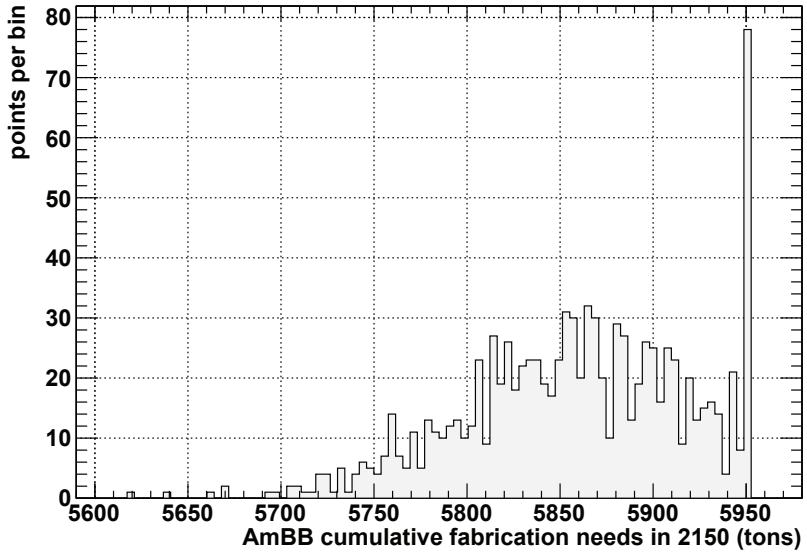

Figure 6.35: Scenario D: histogram of AmBB cumulative fabrication needs in 2150

We want to estimate the relative standard deviation without the peak. We make the assumption that spent AmBB fabrication is Gaussian. First, we estimate the mean as the median of our distribution: $\mu \approx 5862$ tons[10]. Then, we make the hypothesis the left side of the histogram is a half Gaussian, which variance is equal to:

$$Var(half\ Gaussian) = \sigma^2 \times (1 - \frac{2}{\pi}) \tag{6.6}$$

with σ the standard deviation of spent fuel if it were Gaussian. We measure on our histogram: $\sqrt{Var(half\ Gaussian)} \approx 40$ tons and calculate the standard deviation of the Gaussian fit: $\sigma \approx 65$ tons, which would be the standard deviation of the spent fuel inventory with adaptable AmBB capacity. We check the validity of the Gaussian hypothesis with figure 6.36: our distribution was indeed Gaussian, and the associated relative standard deviation is $\sigma/\mu \approx 1.1\%$.

We remark that σ is relatively close to the yearly production of this fabrication plant ($\approx$ 70 tons). Consequently the relative standard deviation of the cumulative production over the scenario corresponds to the yearly production.

[10]The mean is very close to the reference value, 5858 tons.

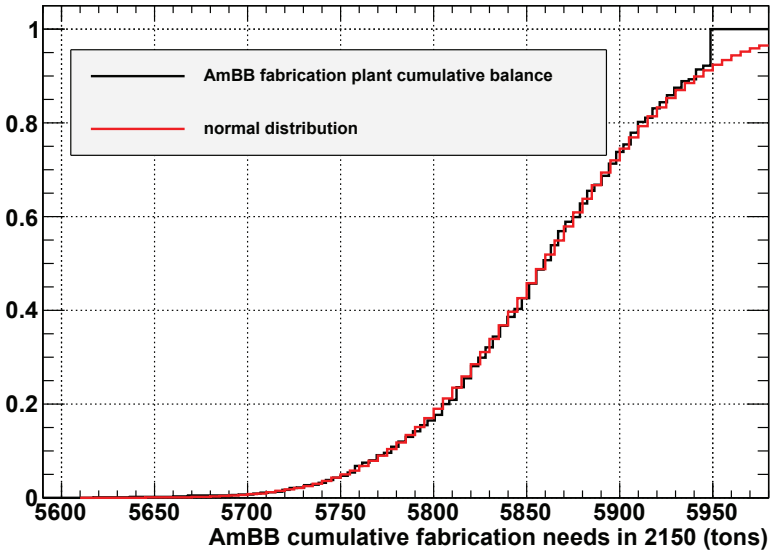

Figure 6.36: Scenario D: CDF of AmBB fabrication needs in 2150 and Gaussian fit

6.2.4.3.3.4 Spent fuel inventory

Figure 6.37 illustrates the spent fuel inventory dispersion, evaluated in 2150 (28% of the spent fuel inventory is already cooled and therefore available for reprocessing). The peak on the right side was identified: it corresponds to AmBB spent fuel distribution, which is similar to AmBB fabrication need, discussed in section 6.2.4.3.3.3.

The spent fuel inventory relative standard deviation would be 1.4% if the reprocessing capacity of the reactors could be adjusted to americium transmutation needs. We calculate that correlation between americium inventory in 2150 and spent fuel inventory is approximately 0.97, which indicates a very strong link between these terms: spent fuel inventory uncertainty results from AmBB fabrication uncertainty. Indeed as there is no fabrication uncertainty for other type of fuel, they do not contribute significantly to spent fuel inventory uncertainty[11].

Using the same method as in paragraph 6.2.4.3.3.3 for AmBB fabrication needs, we obtain: $\mu \approx 4247$ tons[12] and $\sigma/\mu \approx 1.4\%$ for a Gaussian fit. Figure 6.38 represents comparison of the effective spent fuel inventory dispersion and a Gaussian fit.

6.2.4.4 Comparison of burnup and ND uncertainty

6.2.4.4.1 Impact on relative standard deviation

6.2.4.4.1.1 Global results

Three different uncertainty propagation runs were performed in order to weigh the uncertainty sources impact on scenario results:

[11]There is a slight effect on mass through equivalence models, because plutonium isotopy in spent fuel uncertainty generates plutonium content uncertainty in fresh fuel and consequently output balance uncertainty at the spent fuel stock.

[12]The mean is very close to the reference value, 4243 tons.

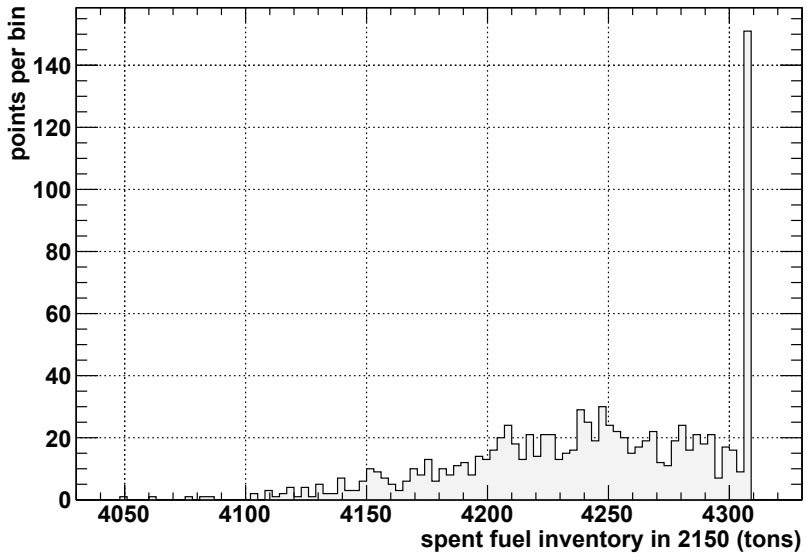

Figure 6.37: Scenario D: histogram of spent fuel inventory in 2150

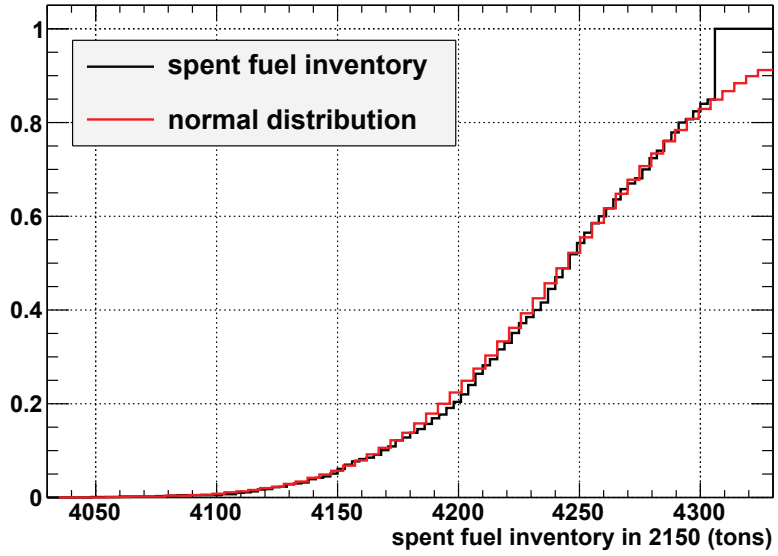

Figure 6.38: Scenario D: CDF of spent fuel inventory in 2150 and Gaussian fit

1. burnup only (global approach);
2. nuclear data only (cross-sections and fission yields);
3. nuclear data (cross-sections and fission yields) and burnup (global approach).

First, impact on global inventories (which are global results) is assessed. Figures 6.39 to 6.41 show plutonium, americium an curium inventories standard deviation in function of time calculated according to these sources of uncertainty. We generally have: $RSD(\text{burnup, nuclear data}) \approx RSD(\text{nuclear data})$, as the nuclear data generate far more uncertainty than burnup in global results.

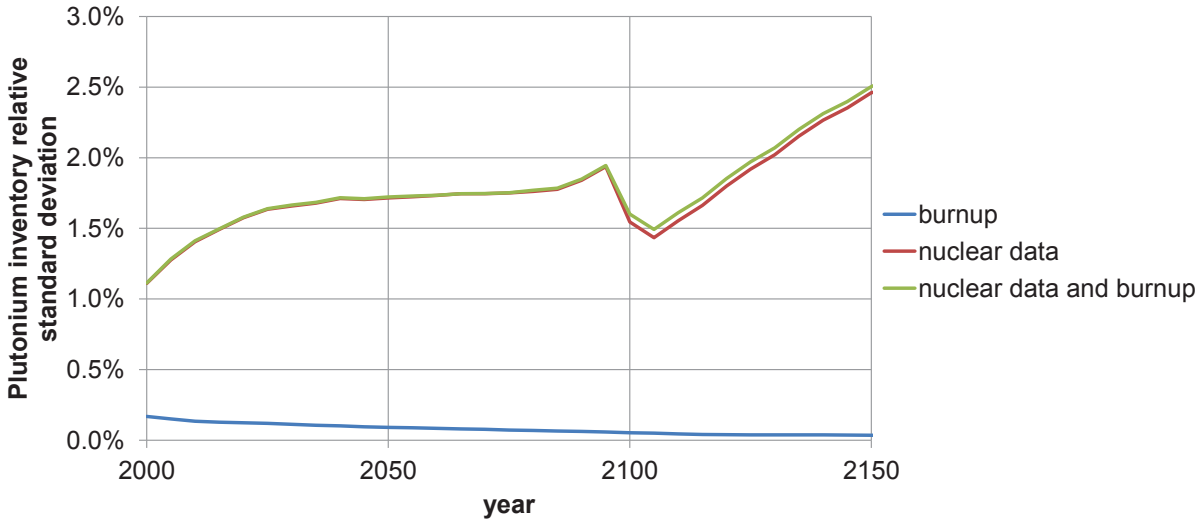

Figure 6.39: Scenario D: comparison of uncertainty sources for plutonium inventory

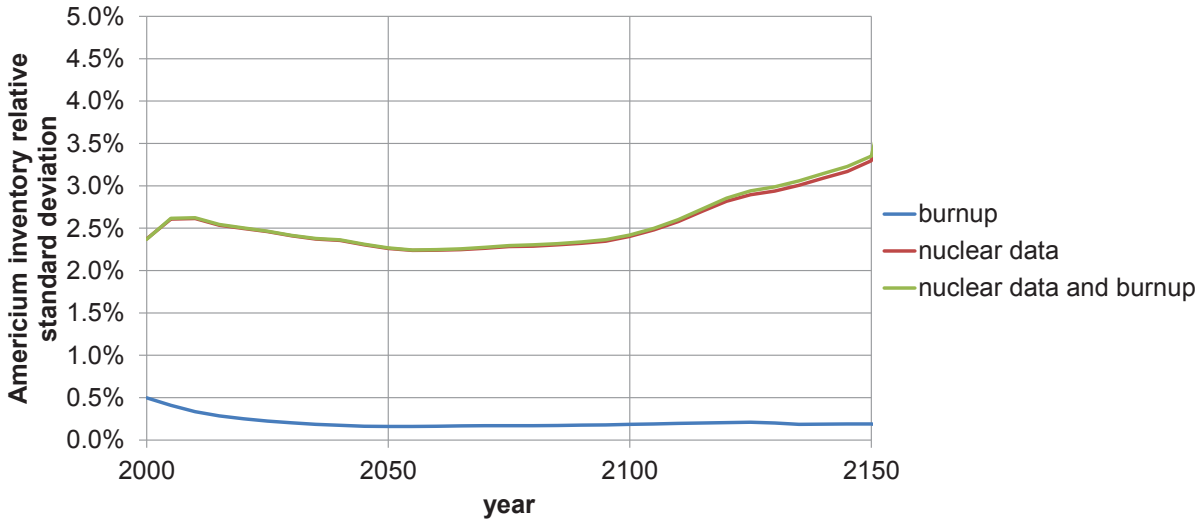

Figure 6.40: Scenario D: comparison of uncertainty sources for americium inventory

We observe that nuclear data uncertainty is by far the most important contributor to Pu, Am and Cm inventories uncertainties. Burnup contribution is very low in the cases of plutonium and americium. We remark that burnup contribution in the case of curium is slightly more im-

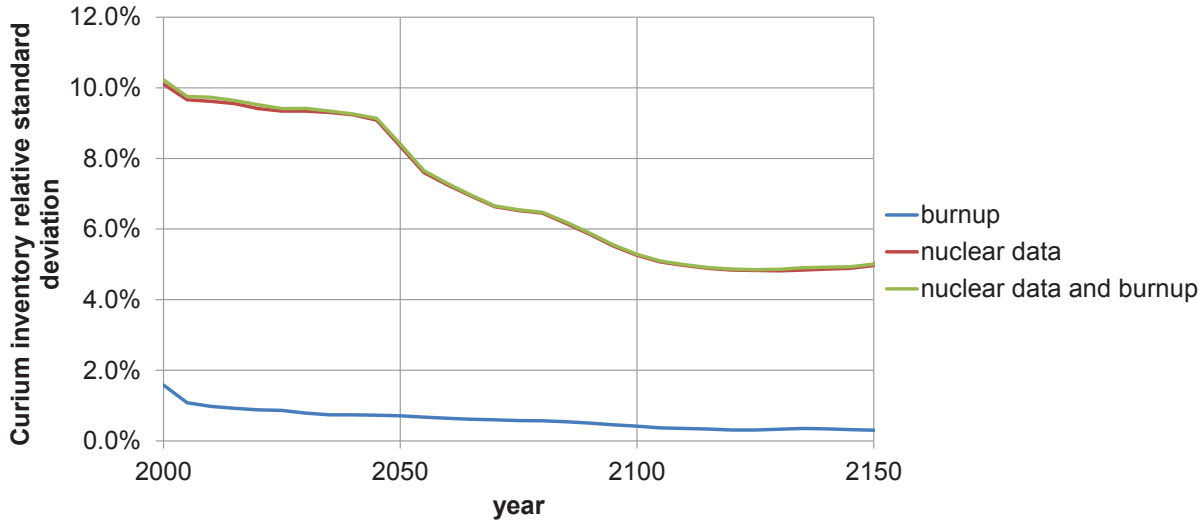

Figure 6.41: Scenario D: comparison of uncertainty sources for curium inventory

portant. This result comes from the fact that curium is more sensitive to burnup than plutonium and americium, because curium isotopes are heavier and require many neutron captures to be formed.

6.2.4.4.1.2 Local results

In this section we assess impact of ND and burnup uncertainty on a decay heat, which is a local result.

Figure 6.42 shows AmBB decay heat in function of cooling time (americium mass content = 10%).

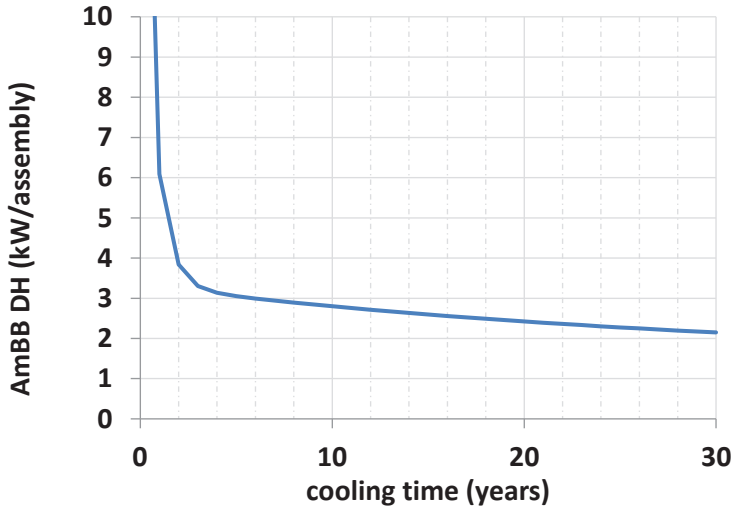

Figure 6.42: Scenario D: AmBB DH in function of cooling time

Figure 6.43 shows americium bearing blanket decay heat (after 5 years of cooling) relative standard deviation in function of time. Three cases are evaluated again:

- burnup uncertainty only;

- nuclear data uncertainty only;
- burnup and nuclear data uncertainty.

The date is the batch first day of irradiation. Decay heat is not an average, but the decay heat of the consecutive batches of one reactor in particular (in that case, the first SFR of the fleet).

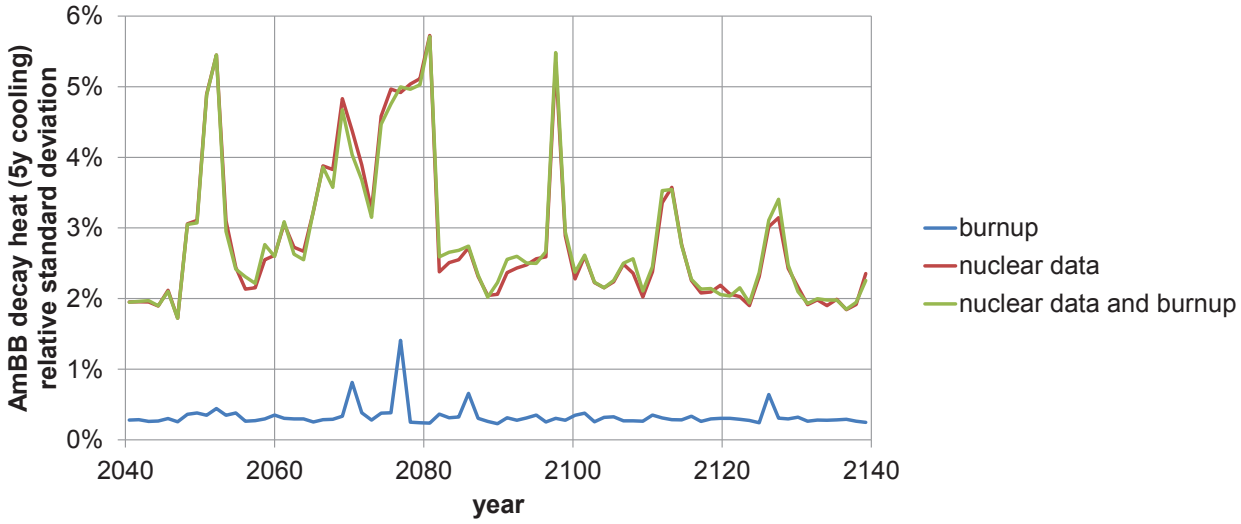

Figure 6.43: Scenario D: comparison of uncertainty sources for AmBB DH after 5 years of cooling

We observe that nuclear data are once again the most important contributor to decay heat uncertainty. The peaks come from changes in the americium source (PWR UOX, PWR MOX, SFR).

Figure 6.44 shows spent EPR^{TM}MOX fuel decay heat after five years of cooling. In the case of EPR^{TM}MOX spent fuel, nuclear data are still the factor generating the most uncertainty, however the contribution of burnup uncertainty is higher than in the case of AmBB decay heat. This result may be due to the fact that cross-sections of trans-plutonium nuclides are generally known with less precision than uranium and plutonium cross-sections, consequently they have a stronger impact in the total uncertainty in the case of AmBB. Another hypothesis is that AmBB are made from few, but heavily concentrated, different nuclides. Consequently, the uncertainty is not a sum of many uncorrelated Gaussian laws, but the sum of a few Gaussian laws. Consequently, the uncertainty might be higher.

We observe that figures 6.43 and 6.44 have very different patterns, while AmBB decay heat uncertainty has several peaks, the uncertainty is rather flat in the case of EPR^{TM}MOX. The explanation is that the fuel management is more regular in the case of EPR^{TM}MOX fuel, which is only made from reprocessed spent PWR UOX fuel, while AmBB is made from different types of fuel.

6.2.4.4.2 Remark concerning correlation

Correlation between parameters plays an important role on those uncertainty propagation studies. In section 6.2.4.4.1 we observed that nuclear data have an impact on results uncertainty more important than the burnup, despite burnup having a non-negligible uncertainty. This result was unexpected due to the high burnup sensitivity in irradiation calculations.

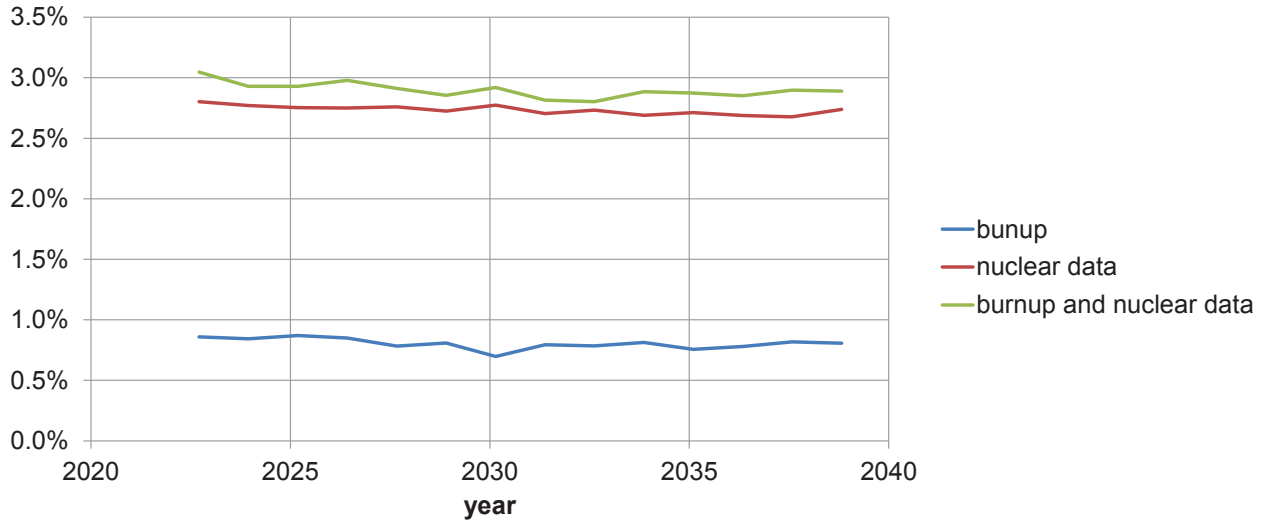

Figure 6.44: Scenario D: comparison of uncertainty sources for EPR^{TM}MOX DH after 5 years of cooling

On the other side, concerning nuclear data, we remarked that the uncertainty in irradiation calculation is on the same magnitude as in scenario calculations. These phenomena are linked to correlation and absence of correlation between parameters. Those correlations are described in table 6.14.

environment	burnup correlation	ND correlation
same reactor, different batches	0[13]	1
different reactors, same spectrum	0	1
different reactors, different spectra	0	usually > 0[14]

Table 6.14: Burnup and nuclear data correlation between different systems in a scenario calculation

These correlation values explain the following phenomena:

- nuclear data have a strong impact on scenario results, they are a systematic bias for every irradiation computation throughout the scenario;
- burnup has a strong impact on batch-wise properties, but impact of burnup on global results, which integrate a large amount of local results, tends to remain low.

6.2.4.4.3 Conclusions

This study showed that nuclear data have a stronger impact on scenario results than the burnup. Two factors contribute to this fact:

- the cross-sections uncertainty remains high;
- the cross-sections are correlated together in most of the cases while burnup is not.

[13] with the exception of consecutive batches, see section 5.3.3.8.2

[14] For instance, the correlation between ^{239}Pu capture cross-section in PWR UOX and PWR MOX is 0.93.

6.2.4.5 Impact of natural uranium isotopy

Natural uranium isotopy uncertainty is presented in section 5.3.3.2.

We assess the impact of natural uranium isotopy with normal distributions centered on the mean value, and standard deviation $\frac{max - min}{mean}$. So as to conserve $\sum_i (\text{mole fraction}) = 1$ we do not sample ^{238}U isotopy and calculate it from the other mole fractions.

Natural uranium isotopy uncertainty impact was assessed, using this distribution, in scenario D (section 6.2.4, transition scenario with SFR deployment, heterogeneous transmutation of americium). It appears that it is negligible: the relative standard deviation of every scenario result due to natural uranium isotopy is less than 0.05%. We summarize impact on a few scenario results in table 6.15.

scenario result	relative standard deviation
natural uranium consumption	0.14%
plutonium inventory	0.01%
americium inventory	0.07%
neptunium inventory	0.05%
curium inventory	0.10%
spent fuel stock	0.02%

Table 6.15: Scenario D: impact of natural uranium isotopic composition

Impact of natural uranium isotopy is very small on every scenario result of interest, including natural uranium consumption.

6.2.4.6 Feasibility study

6.2.4.6.1 Definition

In this context, scenario feasibility is defined by the absence of need for external plutonium: fuel cycle produces the plutonium (as main fissile material) it requires. More precisely, we consider the following algorithm:

- at any moment of the scenario, external plutonium is needed: feasibility = false;
- else: feasibility = true.

Figure 6.45 shows the plutonium margin for scenario D. It is calculated each year (on June 30th) as the sum of the following masses:

- plutonium stocks;
- plutonium in already cooled spent fuel, ready for reprocessing.

We observe that the plutonium margin drops in [2040; 2050] and [2080; 2100]. These two time intervals correspond to the deployment of two SFR fleet. Indeed deployment of a new SFR fleet requires high amounts of plutonium. In our scenario, the plutonium deficit occurs around 2100, corresponding to the last SFR cores deployment: it may not be possible to deploy the last SFR core on time.

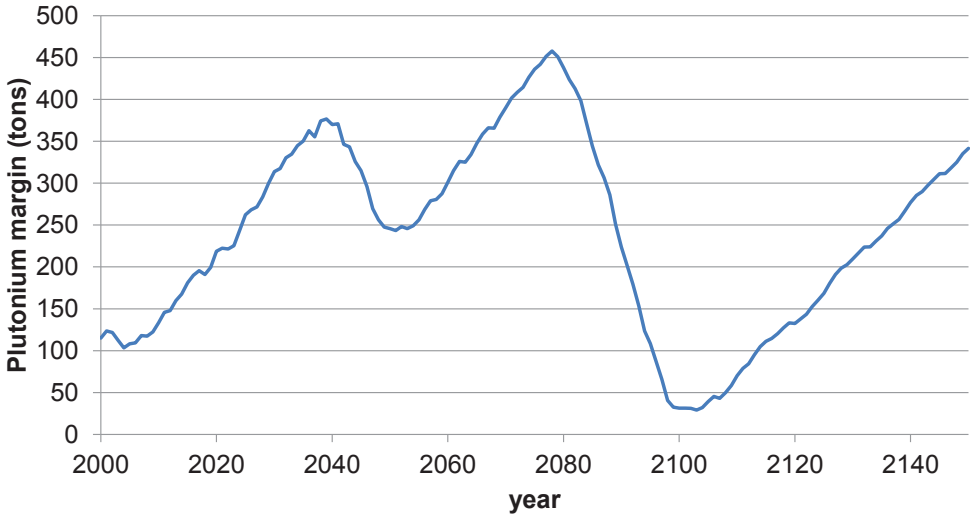

Figure 6.45: Scenario D: plutonium margin

6.2.4.6.2 Probabilistic analysis

In the case of scenario D, feasibility is only 54%. We note that the reprocessing plant recovery rate uncertainty is not taken into account for this value, only nuclear data and burnup uncertainty are taken into account. Other parameters are discussed in the next paragraphs). It means that the chance that given this set of scenario hypotheses, the probability distributions associated to the parameters makes achievement of the scenario highly uncertain, in terms of fissile material availability. In this computation, the reprocessing plant works with a fixed capacity. We note that the results may change with a different fuel management strategy.

Figure 6.46 shows the plutonium deficit complementary cumulative distribution function, which is equal to (1−CDF). For instance, it shows that the fleet has 10% chance to lack 30 tons of plutonium or more, between 2000 and 2150.

Let *year of first deficit* denote the first year plutonium lacks in a given scenario (not enough plutonium to build PWR MOX or SFR fuel). For instance, if in a scenario plutonium lacks for the first time in 2047, then the value is 2047. Figure 6.47 is a parallel plot between the plutonium deficit and the first year of plutonium deficit. The red bars are histograms of plutonium deficit and year of first deficit, and the green line link the associated values together (obtained from the same simulation).

We remark that most of the time, the deficit occurs approximately in 2100 (between 2098 and 2101), which corresponds to the starting of the last SFR reactors. Plutonium global inventory is approximately 1000 tons in 2100, but the available plutonium inventory (i.e. in separated stocks, or in already cooled spent fuel stocks) is much lower. It appears that if the deficit is less than 36 tons, then it occurs approximately in 2100. If it is more, then plutonium may lack too near the at the end of the first step of SFR deployment (2047) or in during the second step (2072 $\rightarrow$ 2076) of SFR deployment.

Recent scenario results are the fruit of precise optimization studies, in particular fuel management at reprocessing plant. However, we observed that the more refined a fuel cycle optimization study is, the more likely it tends to be barely half feasible. We conclude that fuel cycle

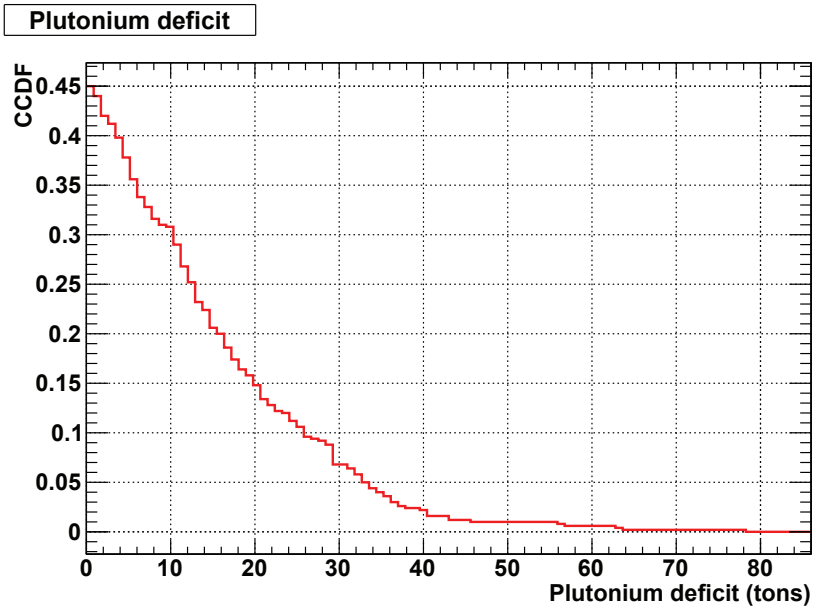

Figure 6.46: Scenario D: plutonium deficit complementary cumulative distribution function

Figure 6.47: Scenario D: parallel plot of plutonium deficit and first year deficit

over-optimization may be risky, and uncertainty should be taken into account. As a result, a tool performing optimization studies under uncertainty may prove itself useful, and could solve advanced problems such as: *how to optimize fuel management at the reprocessing plant such that decay heat technological constraint is as low as possible, while keeping a reasonable plutonium margin so as to maintain a high feasibility probability?*

6.2.4.6.3 Reprocessing plant recovery rate sensitivity study

Scenario feasibility is defined by the absence of need for external plutonium: fuel cycle produces the plutonium it requires. In this paragraph, we only study impact of the reprocessing plant on feasibility. In section 5.3.3.6 we provide experimental data concerning reprocessing plant recovery rates. Scenario D nominal reprocessing plant recovery rate is 99.88% for plutonium and 99.88% for americium, which is higher than industrial feedback or experimental data. For the present study, we make the following set of hypotheses.

- the recovery rate is on the interval $[99\%; 100\%]$;
- the recovery rates of different reprocessing plants, or in the same reprocessing plant at different time are fully correlated.

We define plutonium deficit as the plutonium mass necessary to make the scenario feasible. Isotopy of this plutonium is shown on table 6.13 page 256. Figure 6.48 illustrates the plutonium deficit in function of the feasibility. The red marker corresponds to the nominal recovery rate (used in scenario D study), and the red dotted line the separation between feasible scenarios (on the right side) and non-feasible scenarios (on the left side).

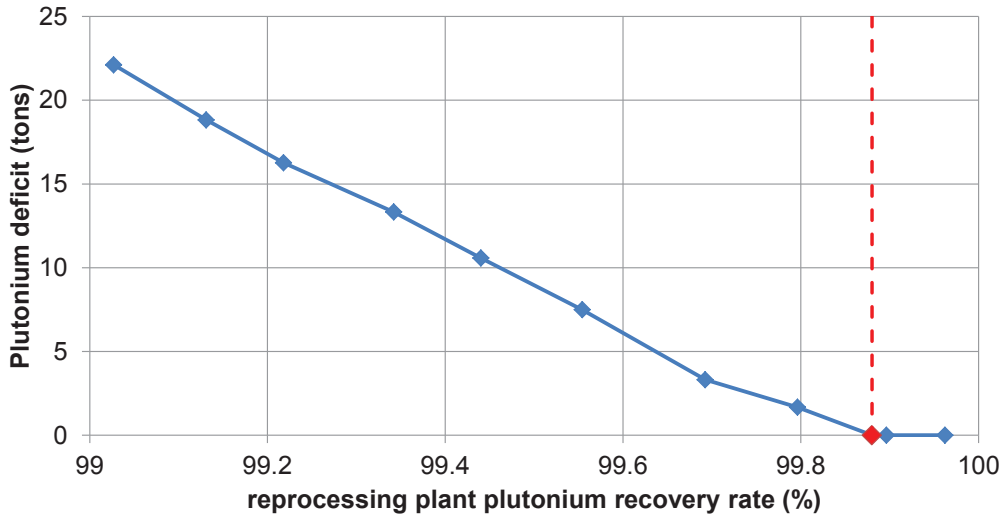

Figure 6.48: Scenario D: impact of reprocessing plant plutonium recovery rate on feasibility

We observe the red marker and the line match: scenario D recovery rate is the minimal recovery rate such that scenario is feasible. In scenario D, SFR cores have the following characteristics:

- fractionation $= 5$;
- heavy metal mass of a fissile batch $= 14$ tons;

- plutonium heavy metal mass content in fissile batch $\approx 20\%$[15].

Consequently, in scenario D, there is approximately 14 tons of plutonium in each SFR core. Therefore the plutonium deficit magnitude due to the reprocessing plant recovery rate is the same as the plutonium mass in a SFR core.

On figure 6.45 page 267 we observe that plutonium margin steadily increases after 2100, and becomes largely superior to 14 tons. Consequently, it may not be possible to deploy that core on time, but deployment a few months (or years) later is possible.

6.2.4.6.4 Front-end duration sensitivity analysis

6.2.4.6.4.1 PWR UOX

In this paragraph we assess PWR UOX fuel front-end duration impact on scenario feasibility. In the case of PWR UOX fuel, front-end duration represents the fuel enrichment and fabrication time. The nominal duration is two years. Sensitivity study was performed for PWR UOX front-end duration in the interval [1 year, 4 years]: there is no impact on scenario feasibility. On a side note, this duration has no impact on most of major scenario results (inventories, spent fuel stocks, decay heat, etc.), and only impacts fabrication date and natural uranium consumption[16].

6.2.4.6.4.2 PWR MOX

In the case of PWR MOX fuel, front-end duration represents the fuel fabrication time. The nominal duration is two years. Sensitivity study was performed for PWR MOX front-end duration in the interval [1 year, 4 years]: there is no impact on scenario feasibility, because plutonium mass in PWR MOX fleet is much lower than in the next SFR fleets.

6.2.4.6.4.3 SFR

In the case of SFR fuel, front-end duration is the fuel fabrication time. The nominal duration is two years. Sensitivity study was performed for SFR front-end duration in the interval [1 year, 4 years]. Figure 6.49 shows the impact of SFR fuel fabrication time on the scenario feasibility.

We observe that if the SFR fabrication time is any longer than the nominal value ($\Delta t_{\text{front-end}} > 2.06$ years), then the scenario is not feasible (blue curve: plutonium deficit >0) and there is a plutonium deficit. The deficit can be important, as its magnitude can be much superior to the plutonium mass in a SFR core, and means that one or two SFR reactors start-up have to be postponed by a few years.

The red curve represents the first year plutonium lacks. If the plutonium fabrication time is slightly superior to two years, then plutonium lacks during starting of the last SFR of the second SFR fleet, deployed up to 2100. However, if fabrication time is superior to 2.5 years, then the first SFR fleet, deployed between 2040 and 2050, is impacted. In that case, the whole scenario is impacted after 2040.

[15] SFR plutonium mass content $\in$ [18%,22%] in scenario D, depending on plutonium vector

[16] The cumulative natural uranium consumption at the end of the scenario is not impacted.

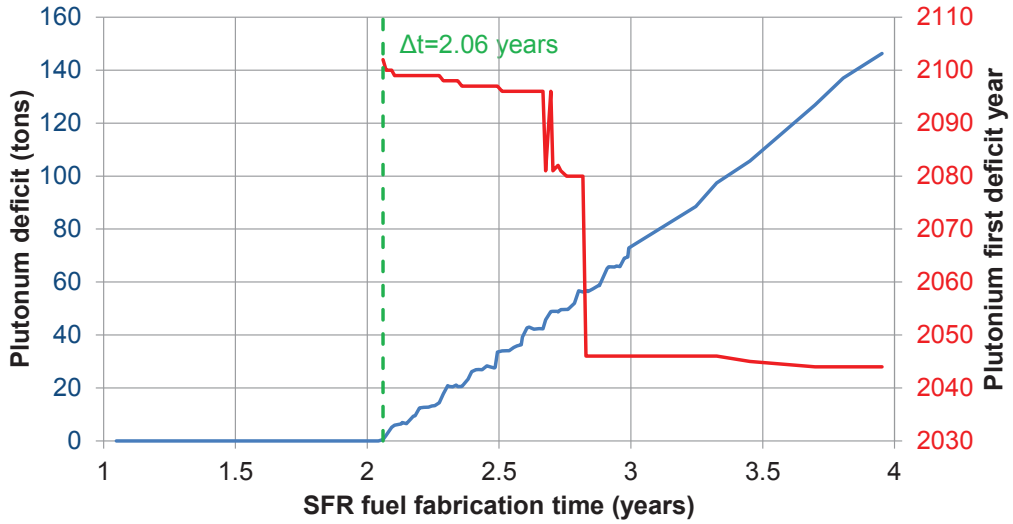

Figure 6.49: Scenario D: impact of SFR fuel fabrication time on scenario feasibility

6.2.4.6.5 Analysis of decay heat uncertainty impact

Thermal power of irradiated minor actinides bearing blankets (MABB) is one of the major problems of minor actinides recycling. However, it is still necessary, partly because plutonium is produced in AMBB. Previous studies [6.8] determined that reducing MA content in MABB and reducing the irradiation time of the blankets diminishes decay heat.

In the previous studies, a minimum cooling time for AmBB was taken into account. For instance, regardless of its actual decay heat, an AmBB (10% americium mass content, 5 irradiation cycles) could be reprocessed after five years of cooling. New developments in COSI made it possible to take decay heat into account: when spent fuel batches have to be reprocessed, their DH at the moment of reprocessing is checked. If DH is superior to a given threshold, then the batch cannot be reprocessed until next year, and other batches are checked instead.

A recent study showed that, in the case of scenario D, the threshold directly impacts scenario feasibility because of potential reduction of plutonium mass flow from AmBB reprocessing.

Decay heat in irradiated AmBB mostly results from the curium content. However, in the previous sections, we observed that curium concentration after irradiation is subject to high uncertainty, because of the following facts:

- curium production is highly non-linear in function of burnup;
- cross-section uncertainty of curium and lighter nuclides contributed to curium production uncertainty.

In our case, we calculated that the minimum decay heat threshold without impact on scenario feasibility is 3.5kW/assembly: if the threshold is inferior, then it is not possible to reprocess the AmBB fast enough to produce a sufficient amount of fissile material, i.e. plutonium lacks at a certain point of the scenario.

In order to determine the uncertainty associated to this threshold, we evaluated the feasibility quantiles of the scenario in function of the threshold. The sources of uncertainty taken into account for this study are:

- local burnup uncertainty;
- cross-sections uncertainty;
- fission yields uncertainty.

Local burnup uncertainty is considered given that the limiting factor for the study is AmBB DH, which is a local result.

Figure 6.42 page 263 represents the value of the decay heat of a typical AmBB blanket (americium content = 10%) in function of cooling time.

We notice the flat zone after 3 years: decay heat hardly decreases with time. In order to analyze it, we draw on figure 6.50 the main decay heat contributors in irradiated AmBB in function of cooling time. Four nuclides (^{238}Pu, ^{241}Am, ^{242}Cm and ^{244}Cm) are sufficient to describe more than 98% of its decay heat between 1 year and 30 years.

We observe that the following nuclides generate more than 64% of decay heat after 3 years of cooling:

- ^{238}Pu: $T_{1/2}$ =87.7 years;
- ^{241}Am: $T_{1/2}$ =432.9 years.

Consequently decay heat tends to slowly reduce on this timescale.

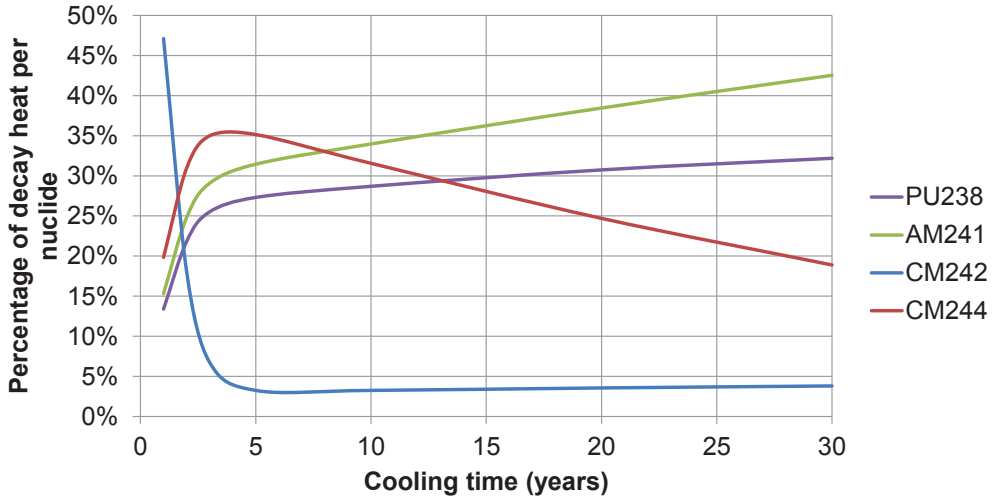

Figure 6.50: Scenario D: AmBB DH contributors in function of cooling time

However, as a local result, AmBB DH uncertainty is rather important (a few percents, see figure 6.43 page 264), due to impact of both burnup and nuclear data. Due to the flatness of DH in function of time, this transforms into a large time uncertainty to reach a given DH threshold. Figure 6.51 shows decay heat of a typical AmBB blanket and the median value plus and minus the standard deviation, in function of cooling time.

The vertical interval length between the curves represents approximately the 68% confidence interval because DH distribution is close to a Gaussian law. The vertical interval is relatively small: DH mean uncertainty is approximately 3% after a few years of cooling. However, transposition of the DH uncertainty at a given time into time uncertainty for a given DH produce very large time intervals: the standard deviation is superior to one year.

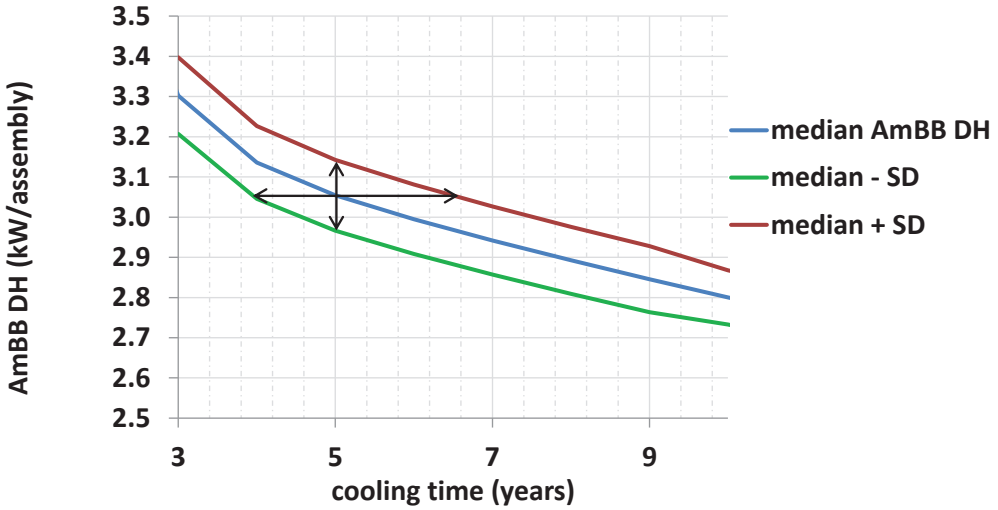

Figure 6.51: Scenario D: AmBB DH uncertainty in function of cooling time

On the contrary, in the case of short cooling times, decay heat is extremely time-dependent. For instance, DH reduces from 8 to 4kW/assembly between one and two years of cooling: DH uncertainty has little impact on minimum cooling time before reprocessing at short times.

We calculated the feasibility probability of the scenario in function of the AmBB maximum DH before reprocessing. Figure 6.52 summarizes the results. We denote max_{DH} the maximum AmBB decay heat before reprocessing. The blue curve represents the feasibility probability in function of the maximum DH before reprocessing. The red line represents the feasibility probability if DH is not checked before fuel reprocessing, and a minimum cooling time before reprocessing ($\Delta t = 5$ years) is applied.

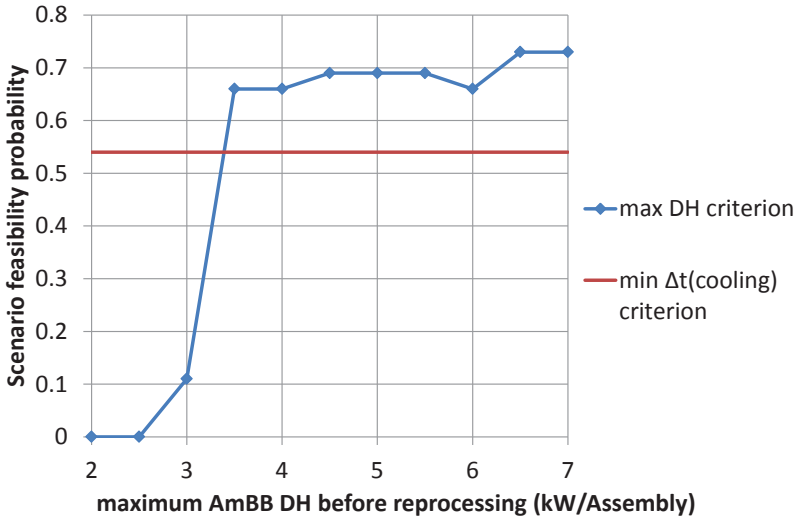

Figure 6.52: Scenario D: feasibility in function of max_{DH}

First, we observe that scenario is not feasible for $max_{DH} \leq 2.5$kW/assembly: plutonium always lacks at a certain moment (usually after 2100).

Then, scenario has a non-null feasibility probability for $max_{DH} = 3$kW/assembly, but this proba-

bility remains low: 11%. It means that for a 3kW/assembly DH constraint, the scenario is likely not feasible.

For $max_{DH} > 3$kW/assembly, feasibility probability reaches a plateau (approximately 70%), and increases very slowly. This plateau is above 50%, meaning that it is likely the scenario is feasible. However, a scenario with 70% feasibility probability cannot be considered reliable. The plateau is due to the shape of the left side of DH curve in function of time on figure 6.42: increasing maximum DH criterion before reprocessing provides diminishing returns after 3.5kW/tHM.

We remark that the value of 3kW/assembly corresponds to the beginning of the DH plateau on figure 6.42. Improving scenario feasibility using AmBB maximum DH before reprocessing is difficult, because gains in term of cooling time are very small (and not reliable) after 5 years.

6.2.4.7 Conclusions

Scenario D is an academic scenario created in the frame of minor actinides transmutation studies for the French fleet transition scenarios with SFR deployment.

Global inventories uncertainty remains moderate: approximately 2% for plutonium, 2.5% for neptunium, between 3% and 5% for americium and between 5% and 6% for curium. Nuclear data uncertainty generate most of the inventories uncertainty (approximately 99% of the variance) as opposed to burnup uncertainty, which impact on global results remains very low.

Nuclear data also generate most of the uncertainty of spent fuel decay heat, even though the burnup impact is slightly more significant.

Feasibility study shows that there is a high chance (46%) that the fuel cycle runs out of available plutonium (i.e. separated or in already cooled spent fuel and ready for reprocessing) in the general case, where only nuclear data and burnup uncertainty are taken into account. It also appears that reprocessing plant recovery rate uncertainty may reduce the scenario feasibility. Indeed, in scenario D, recovery rate is the lowest possible such that scenario remains feasible, but this value is still higher than any industrial feedback data. There are two critical dates in scenario D from the point of view of plutonium margin, corresponding to the end of the first SFR fleet deployment (2050) and the end of the second SFR fleet deployment (2100). A sensitivity study showed that if the recovery rate varies in bounds corresponding to industrial feedback, then a plutonium mass approximately equal to the plutonium mass in a SFR CFV core will lack. Production of a plutonium stock equal to this mass only takes a few years. Consequently, postponing deployment of the last SFR of each fleet for a few years may solve the problem.

Sensitivity analysis of PWR UOX and MOX fuel front-end durations have no impact on the fuel cycle most significant results. However, in the case of SFR front-end duration, any duration longer than the nominal duration will prevent the scenario feasibility. The SFR fabrication time impact on fuel cycle is more important than recovery rate, and more difficult to estimate. Therefore this result is very important, because there is no industrial feedback on SFR fabrication time, consequently a thorough analysis has to be performed, and scenarios might be adjusted so as to take this result into account.

Physical analysis of decay heat impact on the scenario feasibility also showed that this parameter must be taken into account more precisely than simply in terms of fixed nominal minimal cooling duration. Indeed decay heat carries more information for a precise calculation of the actual minimal cooling duration, and can take into account perturbations.

Bibliography

[6.1] C. Cany and C. Coquelet-Pascal. Validation du code de scénarios COSI, estimation des biais du scénario F4. Master's thesis, PHELMA, 2012.

[6.2] R. Eschbach, M. Meyer, C. Coquelet-Pascal, M. Tiphine, G. Krivtchik, and C. Cany. New developments and prospects on COSI, the simulation software for fuel cycle analysis. In *Global 2013*, 2013.

[6.3] ANDRA. Rapport de synthèse, inventaire national des matières et déchets radioactifs. Technical report, ANDRA, 2012.

[6.4] Loi numéro 2006-739 du 28 juin 2006 de programme relative à la gestion durable des matières et déchets radioactifs.

[6.5] Ordonnance numéro 2012-6 du 5 janvier 2012 modifiant les livres Ier et V du code de l'environnement.

[6.6] B. Fontaine, N. Devictor, P. Le Coz, A. Zaetta, D. Verwaerde, and J-M. Hamy. The French R&D on SFR core design and ASTRID Project. In *Proceedings of GLOBAL2011, Paper No. 432757*, 2011.

[6.7] Paul Reuss. *Précis de neutronique*. EDP Sciences, 2003.

[6.8] C. Coquelet-Pascal, M. Meyer, R. Eschbach, C. Chabert, C. Garzenne, P. Barbrault, L. Van Den Durpel, T. Duquesnoy, M. Caron-Charles, B. Carlier, and J.-C. Lefevre. Comparison of different scenarios for the deployment of fast reactors in france - results obtained with COSI. In *Proceedings of GLOBAL 2011*, 2011.

Chapter 7

Conclusions

7.1 Introduction

In this work, we developed an uncertainty propagation method in the frame of dynamic transition scenario studies. Scenario simulations are complex objects, and the results are far from being linear in function of the input data. Consequently, a stochastic methodology was adopted so as to perform uncertainty propagation: sampling parameters according to their distribution and analysis of the results.

However, the computation time of recent scenario simulations is too high to allow direct application of this methodology. Analysis of the computation time showed that two physical models represent more than 95% of the total process: cooling and depletion models.

7.2 Physical models for uncertainty propagation

7.2.1 Introduction

The strategy adpoted consists in reducing the amount of data calculated during a scenario computation, and replacing depletion and cooling physical models with faster models, which remain accurate and allow uncertainty propagation studies.

Reduction of the amount of data was achieved with definition of a shortened list of nuclides of interest for scenario studies. Nuclides of interest are defined in function of their contribution to different scenario results, including:

- nuclide representing a non-negligible part of a given mass balance or inventory;
- nuclides contributing to decay heat.

7.2.2 Nuclides of interest

The list of actinides taken into account is as follows:

$$\left\{{}^{234,235,236,238}\mathrm{U};\ {}^{237,239}\mathrm{Np};\ {}^{238,239,240,241,242}\mathrm{Pu};\ {}^{241,242M,243}\mathrm{Am};\ {}^{242,243,244,245,246}\mathrm{Cm}\right\}$$

and the list of fission products taken into account is:

$$\left\{^{85}\text{Kr};\ ^{90}\text{Sr};\ ^{90}\text{Y};\ ^{95}\text{Zr};\ ^{95}\text{Nb};\ ^{106}\text{Rh};\ ^{106}\text{Ru};\ ^{134}\text{Cs};\ ^{137}\text{Cs};\ ^{137M}\text{Ba};\ ^{144}\text{Ce};\ ^{144}\text{Pr};\ ^{147}\text{Pm};\ ^{154}\text{Eu}\right\}$$

We note that those nuclides are sufficient to calculate the scenario results of interest in the fuel cycle, but are not sufficient to perform depletion calculation[1]. We also note that several nuclides contributing to scenario results are indirectly modeled through simplified chains, such as ^{239}U or ^{147}Nd.

Only those nuclides are modeled, and other are replaced with a neutral nuclide representing them all. The reduction of the number of nuclides significantly diminishes the RAM necessary for a scenario computation.

7.2.3 Cooling model

In the case of the cooling model, we replaced the CESAR computation with Bateman equations analytical solutions, for nuclides of interest only. This model was already implemented in COSI, so we updated it, added several actinides decay chains, and implemented decay chains for fission products of interest.

7.2.4 Depletion models

In the case of the depletion model, we built surrogate models (simple analytical model, usually based on regression techniques) of CESAR and implemented them in COSI. Surrogate models of CESAR compute the concentration vector of nuclides of interest in spent fuel, for a given type of fuel, in function of the following parameters:

- fresh fuel composition;
- irradiation parameters (burnup, specific power, etc.).

Given that these surrogate models must be able to perform uncertainty propagation studies, the following parameters were added:

- actinides and fission products cross-sections perturbations;
- fission yields perturbations.

Surrogate models were built according to the usual sampling / regression / testing process. First, the parameters listed above were sampled altogether. The design of experiment range is calculated so as to be compatible with perturbative irradiation computation in typical scenario studies. A CESAR computation is run for each point of the design of experiment, and the results are saved in an input/output data table.

Then, a regression is performed for each nuclide of interest. Two different types of estimators were used:

- multiple polynomial regression;
- artificial neural networks (ANN).

[1] As explained later, depletion models are based on reference depletion computation, considering more nuclides.

Finally, results are tested on a test sample, different from the construction sample. Different quality criteria are taken into account, including local criteria (mean bias, etc.) and global criteria (part of variance calculated by the surrogate model).

The parameters of multiple polynomial regressions have the advantage to be representative of a physical effect (linear/non-linear contribution of a parameter, slope, interaction between terms, etc.), however their lack of fit in the case of transplutonium nuclides, which behavior is nonlinear[2] in function of the burnup, degrade their prediction capacity.

ANN estimators are well adapted to moderately nonlinear dependencies and relatively high number of parameters, and give better results than polynomial regressions. Consequently, the rest of the study was performed with ANN estimators.

The total number of parameters exceed 200, which complicates the ANN construction process, and makes them less reliable. Consequently, sensitivity studies were made so as to determine which parameter are negligible for estimation of a given nuclide. The results are nuclide-dependent, and are linked to formation of the nuclide. In the general case, ANN estimators were built on samples containing 5000 points, and have 7 to 10 neurons in the hidden layer.

One or two depletion surrogate model were constructed per CESAR BBL (parameterized energy-integrated cross-sections library). The following models were created:

- PWR UOX
  - approximately nominal burnup or more;
  - lower than nominal burnup;
- PWR MOX
  - approximately nominal burnup or more;
  - lower than nominal burnup;
- SFR MOX (CFV core)
  - approximately nominal burnup or more;
  - lower than nominal burnup;
- fertile blankets
  - internal blanket;
  - inferior blanket;
- americium-bearing blanket.

This library of surrogate models, which allows performing uncertainty propagation computation in a wide range of transition scenario studies, has been implemented in COSI.

7.2.5 Equivalence models

Another physical models generates uncertainty in scenario studies: the equivalence model, which computes fresh fuel enrichment / content in function of the fuel isotopic composition, such that an equivalence criterion is satisfied. The equivalence criterion is generally formulated in terms of target reactivity at the end of an irradiation cycle. A study of the state of the art showed that the equivalence models implemented in COSI cannot perform uncertainty propagation computations. Consequently, we developed a new type of equivalence models based on perturbed (depletion + transport) computations.

[2] and not low-degree polynomial

This type of model is based on the same regression techniques as depletion surrogate models. The process giving the best results is as follows:

1. sample the parameters:
   - fresh fuel isotopy;
   - fresh fuel content;
   - cross-sections perturbations;
   - irradiation parameters;
2. perform a (depletion + transport) computation to compute the reactivity at the end of an irradiation cycle
   - thermal spectrum: APOLLO2;
   - fast spectrum: ERANOS;
3. build an estimator of the fresh fuel content in function of the other parameters and the reactivity.

Consequently, we obtained estimators of the fresh fuel content, parameterized with the fuel isotopy, the irradiation parameters, the cross-sections perturbations and the reactivity.

Those models were implemented in COSI, and results compared with the pre-existing models. The plutonium contents computed with ANN estimators and the pre-existing models are relatively close in the case of PWR MOX and SFR MOX fuel.

7.2.6 Conclusions for physical models

A new computation scheme, COSI-MeSAR, performing depletion computation with surrogate models and cooling computation with analytic solutions of Bateman equation was implemented. Any available equivalence can be chosen, including equivalence model suited to uncertainty propagation built in this work. Several other functions were implemented in COSI, including a set of methods which read and use cross-sections and fission yields perturbations. In particular, the method adapted to cross-sections stores a set of perturbations per type of reactor in the scenario, consequently in a scenario different cross-sections perturbations can be used at the same time. This options is convenient because perturbations of energy-integrated cross-sections are spectrum-dependent.

This scheme is compatible with distributed computations during the uncertainty propagation process. The time gain is superior to 1000 in the general case, which is sufficient to perform uncertainty propagation studies.

The results accuracy was validated in different cases, including calculations of decay heat and inventories.

7.3 Data

7.3.1 Introduction

The parameters generating uncertainty in scenario computations were listed, and the associated uncertainty was assessed. There are two main types of parameters: physical parameters, such as cross-sections, and scenario parameters, such as burnup.

7.3.2 Physical parameters

In the case of physical parameters, cross-sections and fission yields uncertainty values were obtained. First, the uncertainty associated with energy-integrated cross-sections was evaluated.

The process is as follows:

1. creation of a covariance matrix from available evaluations (ENDF B-VII was used in this work) using CADTOOL, a NJOY script generator;
2. condensation of the covariance matrix in the spectra of interest.

The condensation method adapted to energy-integrated cross-sections was developed and implemented in this work. It computes spectrum-dependent standard deviations as well as intra-nuclide inter-reactions inter-spectra correlations, based on the following principles:

- conservation of reactions rate standard deviation;
- conservation of normalized reaction rates correlations.

In the case of actinides, energy-integrated fission and capture cross-sections relative standard deviation in PWR UOX, PWR MOX, SFR spectra and the associated energy-integrated correlations were obtained for the following nuclides:

$$\left\{ {}^{234,235,236,238}\mathrm{U};\ {}^{237,239}\mathrm{Np};\ {}^{238,239,240,241,242}\mathrm{Pu};\ {}^{241,242M,243}\mathrm{Am};\ {}^{242,243,244,245,246}\mathrm{Cm} \right\}$$

In the case of fission products, a list of fission products capture cross-section was established, according to their contribution (product sensitivity $\times$ uncertainty) to concentration of fission products generating decay heat. Energy-integrated capture cross-sections relative standard deviation in PWR UOX, PWR MOX spectra were obtained for the following fission products:

$$\left\{ {}^{133}\mathrm{Cs};\ {}^{134}\mathrm{Cs};\ {}^{147}\mathrm{Pm};\ {}^{152}\mathrm{Sm};\ {}^{153}\mathrm{Eu};\ {}^{154}\mathrm{Eu} \right\}$$

Data concerning fission yields uncertainty was already available in nuclear data evaluations.

7.3.3 Scenario parameters

In the case of scenario parameters, uncertainties and intervals were obtained with industrial feedback. The parameters studied are:

- natural uranium isotopic composition;
- front-end durations;
- back-end durations;
- mass losses at different plants;
- reprocessing plant recovery rate;
- irradiation parameters, including the burnup.

A specific study was done in the case of the burnup so as to determine simplified distributions, which allows simplification of the uncertainty propagation computation in scenario studies.

Other parameters, called scenario hypotheses, result from industrial decisions. They are not subject to physical or industrial uncertainty, so impact of changes in scenario hypotheses was not assessed in this work. However, their sensitivity can be assessed using COSI-CESAR5.3 or the new COSI-MeSAR scheme, for faster computations and scenario exploration.

7.4 Application

Four different scenarios were studied.

The scenario A relative to the French nuclear fleet has been benchmarked by both COSI-CESAR and COSI-MeSAR. The model takes into account GEN II fleet only, together with the actual loads (UOX, MOX and repU). Results are compared in 2010 with results coming from ANDRA inventories of the French fuel cycle. Overall, nuclear data uncertainty does not explain the difference between COSI simulation and ANDRA data, which seems to result from a lack of knowledge, as well as the lack of appropriate data for validation of the results. The accounting dates shift also introduce a large bias, consequently it can be difficult to compare two separate evaluations, or scenarios, that may not be compatible in terms of accounting dates.

Scenario B is an industrial scenario, and consists in steady replacement of PWR fleet by EPR, at constant electric power, with stabilization of spent PWR UOX fuel and reprocessed uranium stocks. Structure of scenario B (high level of detail) permitted to perform burnup uncertainty propagation with method α defined in section 5.3.3.8.4 as the reference method. In this study, only EPR were associated with a burnup uncertainty. Burnup generates little uncertainty on inventories: less than 0.2% for curium, and less than 0.05% for plutonium, neptunium and americium. This comes from the large number of reactors and fuel cycles in each reactor during a scenario computation: inventories behave as a large sum of uncorrelated terms. In the case of local results, such as isotopy, we observe peaks, that correspond to different fuel management operations. Scenario B was also used to validate two simple sampling methods for burnup uncertainty.

Scenario C is an academic study of SFR deployment, with plutonium multi recycling, in the french nuclear fleet, which constitutes an energetic transition. Minor actinides are not recycled. In scenario C we studied the impact of burnup and nuclear data uncertainty in equivalence models. Equivalence models have a strong impact on the whole scenario computation. Nuclear data uncertainty generates uncertainty in scenario results through both irradiation and equivalence models, although impact of equivalence model is dominant. Furthermore, uncertainty generated by nuclear data in equivalence model is rather hard to predict or approximate, as it is highly nonlinear and depends on the whole scenario history and fuel management.

Scenario D is an academic scenario created in the frame of minor actinides transmutation studies for the French fleet transition scenarios. It is based on scenario C. Global inventories uncertainty remains moderate: approximately 2% for plutonium, 2.5% for neptunium, between 3% and 5% for americium and between 5% and 6% for curium. Consequently, the uncertainty of the long-term impact of this fuel cycle in terms of toxicity is moderate too. Nuclear data uncertainty generate most of the inventories uncertainty (approximately 99% of the variance) as opposed to burnup uncertainty, which impact on global results remains very low. Nuclear data also generate most of the uncertainty of spent fuel decay heat, even though the burnup impact is slightly more significant. Feasibility studies, evaluating the fissile material margin in function of changes in different parameters (recovery rates, etc.), show that there is a high chance that the fuel cycle runs out of available plutonium in the general case, where only nuclear data and burnup uncertainty are taken into account. However, in most of the cases, postponing deployment of the last SFR of each fleet for a few years may solve the problem.

Appendix A

Design of experiments for irradiation surrogate models

Contents

A.1 DOE for polynomial regressions 284
A.1.1 PWR UOX fuel, low burnup 284
A.1.2 PWR UOX fuel, nominal burnup 285
A.1.3 PWR repU fuel 286
A.1.4 PWR MOX fuel, low burnup 287
A.1.5 PWR MOX fuel, nominal burnup 288
A.1.6 SFR MOX fuel, low burnup 289
A.1.7 SFR MOX fuel, nominal burnup 290
A.2 DOE for ANN 292
A.2.1 PWR UOX fuel, low burnup 292
A.2.2 PWR UOX fuel, nominal burnup 293
A.2.3 PWR MOX fuel, low burnup 294
A.2.4 PWR MOX fuel, nominal burnup 295
A.2.5 PWR repU fuel 296
A.2.6 SFR MOX fuel, low burnup 297
A.2.7 SFR MOX fuel, nominal burnup 298
A.2.8 SFR internal blanket 299
A.2.9 SFR inferior blanket 300
A.2.10 SFR americium bearing blanket 301

A.1 DOE for polynomial regressions

A.1.1 PWR UOX fuel, low burnup

parameter	distribution	support	unit
^{234}U mass fraction	uniform	$[3.27 \cdot 10^{-4}, 4.61 \cdot 10^{-4}]$	1
^{235}U mass fraction	uniform	$[3.25 \cdot 10^{-2}, 4.60 \cdot 10^{-2}]$	1
BU	uniform	$[13, 41]$	GWd/tHM
$\mathcal{P}_{irrad}$	uniform	$[29, 40]$	W/gHM
$\Delta\sigma_c(^{235}\text{U})/\sigma_c(^{235}\text{U})$	uniform	$[-6.25, 6.25]$	%
$\Delta\sigma_f(^{235}\text{U})/\sigma_f(^{235}\text{U})$	uniform	$[-0,65, 0,65]$	%
$\Delta\sigma_c(^{238}\text{U})/\sigma_c(^{238}\text{U})$	uniform	$[-1.65, 1.65]$	%
$\Delta\sigma_f(^{238}\text{U})/\sigma_f(^{238}\text{U})$	uniform	$[-5.11, 5.11]$	%
$\Delta\sigma_c(^{238}\text{Pu})/\sigma_c(^{238}\text{Pu})$	uniform	$[-36.00, 36.00]$	%
$\Delta\sigma_f(^{238}\text{Pu})/\sigma_f(^{238}\text{Pu})$	uniform	$[-5.76, 5.76]$	%
$\Delta\sigma_c(^{239}\text{Pu})/\sigma_c(^{239}\text{Pu})$	uniform	$[-4.79, 4.79]$	%
$\Delta\sigma_f(^{239}\text{Pu})/\sigma_f(^{239}\text{Pu})$	uniform	$[-3.08, 3.08]$	%
$\Delta\sigma_c(^{240}\text{Pu})/\sigma_c(^{240}\text{Pu})$	uniform	$[-2.72, 2.72]$	%
$\Delta\sigma_f(^{240}\text{Pu})/\sigma_f(^{240}\text{Pu})$	uniform	$[-6.96, 6.96]$	%
$\Delta\sigma_c(^{241}\text{Pu})/\sigma_c(^{241}\text{Pu})$	uniform	$[-9.75, 9.75]$	%
$\Delta\sigma_f(^{241}\text{Pu})/\sigma_f(^{241}\text{Pu})$	uniform	$[-1.31, 1.31]$	%
$\Delta\sigma_c(^{242}\text{Pu})/\sigma_c(^{242}\text{Pu})$	uniform	$[-12.18, 12.18]$	%
$\Delta\sigma_f(^{242}\text{Pu})/\sigma_f(^{242}\text{Pu})$	uniform	$[-7.05, 7.05]$	%
$\Delta\sigma_c(^{241}\text{Am})/\sigma_c(^{241}\text{Am})$	uniform	$[-5.90, 5.90]$	%
$\Delta\sigma_f(^{241}\text{Am})/\sigma_f(^{241}\text{Am})$	uniform	$[-2.26, 2.26]$	%
$\Delta\sigma_c(^{243}\text{Am})/\sigma_c(^{243}\text{Am})$	uniform	$[-8.22, 8.22]$	%
$\Delta\sigma_f(^{243}\text{Am})/\sigma_f(^{243}\text{Am})$	uniform	$[-5.10, 5.10]$	%
$\Delta\sigma_c(^{237}\text{Np})/\sigma_c(^{237}\text{Np})$	uniform	$[-2.28, 2.28]$	%
$\Delta\sigma_f(^{237}\text{Np})/\sigma_f(^{237}\text{Np})$	uniform	$[-8.26, 8.26]$	%
$\Delta\sigma_c(^{242}\text{Cm})/\sigma_c(^{242}\text{Cm})$	uniform	$[-15.48, 15.48]$	%
$\Delta\sigma_f(^{242}\text{Cm})/\sigma_f(^{242}\text{Cm})$	uniform	$[-7.74, 7.74]$	%
$\Delta\sigma_c(^{243}\text{Cm})/\sigma_c(^{243}\text{Cm})$	uniform	$[-46.85, 46.85]$	%
$\Delta\sigma_f(^{243}\text{Cm})/\sigma_f(^{243}\text{Cm})$	uniform	$[-5.70, 5.70]$	%
$\Delta\sigma_c(^{244}\text{Cm})/\sigma_c(^{244}\text{Cm})$	uniform	$[-11.97, 11.97]$	%
$\Delta\sigma_f(^{244}\text{Cm})/\sigma_f(^{244}\text{Cm})$	uniform	$[-5.03, 5.03]$	%
$\Delta\sigma_c(^{245}\text{Cm})/\sigma_c(^{245}\text{Cm})$	uniform	$[-31.25, 31.25]$	%
$\Delta\sigma_f(^{245}\text{Cm})/\sigma_f(^{245}\text{Cm})$	uniform	$[-4.57, 4.57]$	%
^{238}U mass fraction	1- ^{234}U - ^{235}U	$\varnothing$	1
irradiation length	TCT/P_{irrad}	$\varnothing$	d

Table A.1: PWR UOX, low burnup sampling distributions for polynomial estimator

A.1.2 PWR UOX fuel, nominal burnup

parameter	distribution	support	unit
^{234}U mass fraction	uniform	$[3.27 \cdot 10^{-4}, 4.61 \cdot 10^{-4}]$	1
^{235}U mass fraction	uniform	$[3.25 \cdot 10^{-2}, 4.60 \cdot 10^{-2}]$	1
BU	uniform	$[41, 56]$	GWd/tHM
$\mathcal{P}_{irrad}$	uniform	$[29, 40]$	W/gHM
$\Delta\sigma_c(^{235}\text{U})/\sigma_c(^{235}\text{U})$	uniform	$[-6.25, 6.25]$	%
$\Delta\sigma_f(^{235}\text{U})/\sigma_f(^{235}\text{U})$	uniform	$[-0,65, 0,65]$	%
$\Delta\sigma_c(^{238}\text{U})/\sigma_c(^{238}\text{U})$	uniform	$[-1.65, 1.65]$	%
$\Delta\sigma_f(^{238}\text{U})/\sigma_f(^{238}\text{U})$	uniform	$[-5.11, 5.11]$	%
$\Delta\sigma_c(^{238}\text{Pu})/\sigma_c(^{238}\text{Pu})$	uniform	$[-36.00, 36.00]$	%
$\Delta\sigma_f(^{238}\text{Pu})/\sigma_f(^{238}\text{Pu})$	uniform	$[-5.76, 5.76]$	%
$\Delta\sigma_c(^{239}\text{Pu})/\sigma_c(^{239}\text{Pu})$	uniform	$[-4.79, 4.79]$	%
$\Delta\sigma_f(^{239}\text{Pu})/\sigma_f(^{239}\text{Pu})$	uniform	$[-3.08, 3.08]$	%
$\Delta\sigma_c(^{240}\text{Pu})/\sigma_c(^{240}\text{Pu})$	uniform	$[-2.72, 2.72]$	%
$\Delta\sigma_f(^{240}\text{Pu})/\sigma_f(^{240}\text{Pu})$	uniform	$[-6.96, 6.96]$	%
$\Delta\sigma_c(^{241}\text{Pu})/\sigma_c(^{241}\text{Pu})$	uniform	$[-9.75, 9.75]$	%
$\Delta\sigma_f(^{241}\text{Pu})/\sigma_f(^{241}\text{Pu})$	uniform	$[-1.31, 1.31]$	%
$\Delta\sigma_c(^{242}\text{Pu})/\sigma_c(^{242}\text{Pu})$	uniform	$[-12.18, 12.18]$	%
$\Delta\sigma_f(^{242}\text{Pu})/\sigma_f(^{242}\text{Pu})$	uniform	$[-7.05, 7.05]$	%
$\Delta\sigma_c(^{241}\text{Am})/\sigma_c(^{241}\text{Am})$	uniform	$[-5.90, 5.90]$	%
$\Delta\sigma_f(^{241}\text{Am})/\sigma_f(^{241}\text{Am})$	uniform	$[-2.26, 2.26]$	%
$\Delta\sigma_c(^{243}\text{Am})/\sigma_c(^{243}\text{Am})$	uniform	$[-8.22, 8.22]$	%
$\Delta\sigma_f(^{243}\text{Am})/\sigma_f(^{243}\text{Am})$	uniform	$[-5.10, 5.10]$	%
$\Delta\sigma_c(^{237}\text{Np})/\sigma_c(^{237}\text{Np})$	uniform	$[-2.28, 2.28]$	%
$\Delta\sigma_f(^{237}\text{Np})/\sigma_f(^{237}\text{Np})$	uniform	$[-8.26, 8.26]$	%
$\Delta\sigma_c(^{242}\text{Cm})/\sigma_c(^{242}\text{Cm})$	uniform	$[-15.48, 15.48]$	%
$\Delta\sigma_f(^{242}\text{Cm})/\sigma_f(^{242}\text{Cm})$	uniform	$[-7.74, 7.74]$	%
$\Delta\sigma_c(^{243}\text{Cm})/\sigma_c(^{243}\text{Cm})$	uniform	$[-46.85, 46.85]$	%
$\Delta\sigma_f(^{243}\text{Cm})/\sigma_f(^{243}\text{Cm})$	uniform	$[-5.70, 5.70]$	%
$\Delta\sigma_c(^{244}\text{Cm})/\sigma_c(^{244}\text{Cm})$	uniform	$[-11.97, 11.97]$	%
$\Delta\sigma_f(^{244}\text{Cm})/\sigma_f(^{244}\text{Cm})$	uniform	$[-5.03, 5.03]$	%
$\Delta\sigma_c(^{245}\text{Cm})/\sigma_c(^{245}\text{Cm})$	uniform	$[-31.25, 31.25]$	%
$\Delta\sigma_f(^{245}\text{Cm})/\sigma_f(^{245}\text{Cm})$	uniform	$[-4.57, 4.57]$	%
^{238}U mass fraction	1- ^{234}U - ^{235}U	$\varnothing$	1
irradiation length	TCT/P_{irrad}	$\varnothing$	d

Table A.2: PWR UOX, nominal burnup sampling distributions for polynomial estimator

A.1.3 PWR repU fuel

parameter	distribution	support	unit
^{234}U mass fraction	uniform	$[1.12 \cdot 10^{-3}, 1.20 \cdot 10^{-3}]$	1
^{235}U mass fraction	uniform	$[4.05 \cdot 10^{-2} - \varepsilon, 4.05 \cdot 10^{-2} + \varepsilon]$	1
^{236}U mass fraction	uniform	$[1.37 \cdot 10^{-2} - \varepsilon, 1.37 \cdot 10^{-2} + \varepsilon]$	1
BU	uniform	$[11, 46]$	GWd/tHM
$\mathcal{P}_{irrad}$	uniform	$[29.00, 30.00]$	W/gHM
$\Delta\sigma_c(^{235}\text{U})/\sigma_c(^{235}\text{U})$	uniform	$[-6.25, 6.25]$	%
$\Delta\sigma_f(^{235}\text{U})/\sigma_f(^{235}\text{U})$	uniform	$[-0,65, 0,65]$	%
$\Delta\sigma_c(^{238}\text{U})/\sigma_c(^{238}\text{U})$	uniform	$[-1.65, 1.65]$	%
$\Delta\sigma_f(^{238}\text{U})/\sigma_f(^{238}\text{U})$	uniform	$[-5.11, 5.11]$	%
$\Delta\sigma_c(^{238}\text{Pu})/\sigma_c(^{238}\text{Pu})$	uniform	$[-36.00, 36.00]$	%
$\Delta\sigma_f(^{238}\text{Pu})/\sigma_f(^{238}\text{Pu})$	uniform	$[-5.76, 5.76]$	%
$\Delta\sigma_c(^{239}\text{Pu})/\sigma_c(^{239}\text{Pu})$	uniform	$[-4.79, 4.79]$	%
$\Delta\sigma_f(^{239}\text{Pu})/\sigma_f(^{239}\text{Pu})$	uniform	$[-3.08, 3.08]$	%
$\Delta\sigma_c(^{240}\text{Pu})/\sigma_c(^{240}\text{Pu})$	uniform	$[-2.72, 2.72]$	%
$\Delta\sigma_f(^{240}\text{Pu})/\sigma_f(^{240}\text{Pu})$	uniform	$[-6.96, 6.96]$	%
$\Delta\sigma_c(^{241}\text{Pu})/\sigma_c(^{241}\text{Pu})$	uniform	$[-9.75, 9.75]$	%
$\Delta\sigma_f(^{241}\text{Pu})/\sigma_f(^{241}\text{Pu})$	uniform	$[-1.31, 1.31]$	%
$\Delta\sigma_c(^{242}\text{Pu})/\sigma_c(^{242}\text{Pu})$	uniform	$[-12.18, 12.18]$	%
$\Delta\sigma_f(^{242}\text{Pu})/\sigma_f(^{242}\text{Pu})$	uniform	$[-7.05, 7.05]$	%
$\Delta\sigma_c(^{241}\text{Am})/\sigma_c(^{241}\text{Am})$	uniform	$[-5.90, 5.90]$	%
$\Delta\sigma_f(^{241}\text{Am})/\sigma_f(^{241}\text{Am})$	uniform	$[-2.26, 2.26]$	%
$\Delta\sigma_c(^{243}\text{Am})/\sigma_c(^{243}\text{Am})$	uniform	$[-8.22, 8.22]$	%
$\Delta\sigma_f(^{243}\text{Am})/\sigma_f(^{243}\text{Am})$	uniform	$[-5.10, 5.10]$	%
$\Delta\sigma_c(^{237}\text{Np})/\sigma_c(^{237}\text{Np})$	uniform	$[-2.28, 2.28]$	%
$\Delta\sigma_f(^{237}\text{Np})/\sigma_f(^{237}\text{Np})$	uniform	$[-8.26, 8.26]$	%
$\Delta\sigma_c(^{242}\text{Cm})/\sigma_c(^{242}\text{Cm})$	uniform	$[-15.48, 15.48]$	%
$\Delta\sigma_f(^{242}\text{Cm})/\sigma_f(^{242}\text{Cm})$	uniform	$[-7.74, 7.74]$	%
$\Delta\sigma_c(^{243}\text{Cm})/\sigma_c(^{243}\text{Cm})$	uniform	$[-46.85, 46.85]$	%
$\Delta\sigma_f(^{243}\text{Cm})/\sigma_f(^{243}\text{Cm})$	uniform	$[-5.70, 5.70]$	%
$\Delta\sigma_c(^{244}\text{Cm})/\sigma_c(^{244}\text{Cm})$	uniform	$[-11.97, 11.97]$	%
$\Delta\sigma_f(^{244}\text{Cm})/\sigma_f(^{244}\text{Cm})$	uniform	$[-5.03, 5.03]$	%
$\Delta\sigma_c(^{245}\text{Cm})/\sigma_c(^{245}\text{Cm})$	uniform	$[-31.25, 31.25]$	%
$\Delta\sigma_f(^{245}\text{Cm})/\sigma_f(^{245}\text{Cm})$	uniform	$[-4.57, 4.57]$	%
^{238}U mass fraction	$1 - \sum_i y_i$	$\varnothing$	1
irradiation length	TCT/P_{irrad}	$\varnothing$	d

Table A.3: PWR repU sampling distributions for polynomial estimator

A.1.4 PWR MOX fuel, low burnup

parameter	distribution	support	unit
^{234}U mass fraction	uniform	$[5.43 \cdot 10^{-5}, 1.46 \cdot 10^{-4}]$	1
^{235}U mass fraction	uniform	$[2.29 \cdot 10^{-3}, 2.33 \cdot 10^{-2}]$	1
^{236}U mass fraction	uniform	$[9.22 \cdot 10^{-6}, 1.90 \cdot 10^{-5}]$	1
^{238}Pu mass fraction	uniform	$[1.03 \cdot 10^{-3}, 2.25 \cdot 10^{-3}]$	1
^{239}Pu mass fraction	uniform	$[3.96 \cdot 10^{-2}, 5.25 \cdot 10^{-2}]$	1
^{240}Pu mass fraction	uniform	$[1.75 \cdot 10^{-2}, 2.26 \cdot 10^{-2}]$	1
^{241}Pu mass fraction	uniform	$[3.92 \cdot 10^{-3}, 6.21 \cdot 10^{-3}]$	1
^{242}Pu mass fraction	uniform	$[3.96 \cdot 10^{-3}, 6.21 \cdot 10^{-3}]$	1
^{241}Am mass fraction	uniform	$[1.24 \cdot 10^{-3}, 2.29 \cdot 10^{-3}]$	1
^{237}Np mass fraction	uniform	$[4.05 \cdot 10^{-6}, 1.57 \cdot 10^{-5}]$	1
BU	uniform	$[15, 45]$	GWd/tHM
$\mathcal{P}_{irrad}$	uniform	$[29, 40]$	W/gHM
$\Delta\sigma_c(^{235}\text{U})/\sigma_c(^{235}\text{U})$	uniform	$[-6.25, 6.25]$	%
$\Delta\sigma_f(^{235}\text{U})/\sigma_f(^{235}\text{U})$	uniform	$[-0,65, 0,65]$	%
$\Delta\sigma_c(^{238}\text{U})/\sigma_c(^{238}\text{U})$	uniform	$[-1.65, 1.65]$	%
$\Delta\sigma_f(^{238}\text{U})/\sigma_f(^{238}\text{U})$	uniform	$[-5.11, 5.11]$	%
$\Delta\sigma_c(^{238}\text{Pu})/\sigma_c(^{238}\text{Pu})$	uniform	$[-36.00, 36.00]$	%
$\Delta\sigma_f(^{238}\text{Pu})/\sigma_f(^{238}\text{Pu})$	uniform	$[-5.76, 5.76]$	%
$\Delta\sigma_c(^{239}\text{Pu})/\sigma_c(^{239}\text{Pu})$	uniform	$[-4.79, 4.79]$	%
$\Delta\sigma_f(^{239}\text{Pu})/\sigma_f(^{239}\text{Pu})$	uniform	$[-3.08, 3.08]$	%
$\Delta\sigma_c(^{240}\text{Pu})/\sigma_c(^{240}\text{Pu})$	uniform	$[-2.72, 2.72]$	%
$\Delta\sigma_f(^{240}\text{Pu})/\sigma_f(^{240}\text{Pu})$	uniform	$[-6.96, 6.96]$	%
$\Delta\sigma_c(^{241}\text{Pu})/\sigma_c(^{241}\text{Pu})$	uniform	$[-9.75, 9.75]$	%
$\Delta\sigma_f(^{241}\text{Pu})/\sigma_f(^{241}\text{Pu})$	uniform	$[-1.31, 1.31]$	%
$\Delta\sigma_c(^{242}\text{Pu})/\sigma_c(^{242}\text{Pu})$	uniform	$[-12.18, 12.18]$	%
$\Delta\sigma_f(^{242}\text{Pu})/\sigma_f(^{242}\text{Pu})$	uniform	$[-7.05, 7.05]$	%
$\Delta\sigma_c(^{241}\text{Am})/\sigma_c(^{241}\text{Am})$	uniform	$[-5.90, 5.90]$	%
$\Delta\sigma_f(^{241}\text{Am})/\sigma_f(^{241}\text{Am})$	uniform	$[-2.26, 2.26]$	%
$\Delta\sigma_c(^{243}\text{Am})/\sigma_c(^{243}\text{Am})$	uniform	$[-8.22, 8.22]$	%
$\Delta\sigma_f(^{243}\text{Am})/\sigma_f(^{243}\text{Am})$	uniform	$[-5.10, 5.10]$	%
$\Delta\sigma_c(^{237}\text{Np})/\sigma_c(^{237}\text{Np})$	uniform	$[-2.28, 2.28]$	%
$\Delta\sigma_f(^{237}\text{Np})/\sigma_f(^{237}\text{Np})$	uniform	$[-8.26, 8.26]$	%
$\Delta\sigma_c(^{242}\text{Cm})/\sigma_c(^{242}\text{Cm})$	uniform	$[-15.48, 15.48]$	%
$\Delta\sigma_f(^{242}\text{Cm})/\sigma_f(^{242}\text{Cm})$	uniform	$[-7.74, 7.74]$	%
$\Delta\sigma_c(^{243}\text{Cm})/\sigma_c(^{243}\text{Cm})$	uniform	$[-46.85, 46.85]$	%
$\Delta\sigma_f(^{243}\text{Cm})/\sigma_f(^{243}\text{Cm})$	uniform	$[-5.70, 5.70]$	%
$\Delta\sigma_c(^{244}\text{Cm})/\sigma_c(^{244}\text{Cm})$	uniform	$[-11.97, 11.97]$	%
$\Delta\sigma_f(^{244}\text{Cm})/\sigma_f(^{244}\text{Cm})$	uniform	$[-5.03, 5.03]$	%
$\Delta\sigma_c(^{245}\text{Cm})/\sigma_c(^{245}\text{Cm})$	uniform	$[-31.25, 31.25]$	%
$\Delta\sigma_f(^{245}\text{Cm})/\sigma_f(^{245}\text{Cm})$	uniform	$[-4.57, 4.57]$	%
^{238}U mass fraction	1-$\sum_i y_i$	$\varnothing$	1
irradiation length	TCT/P_{irrad}	$\varnothing$	d

Table A.4: PWR MOX, low burnup sampling distributions for polynomial estimator

A.1.5 PWR MOX fuel, nominal burnup

parameter	distribution	support	unit
^{234}U mass fraction	uniform	$[5.43 \cdot 10^{-5}, 1.46 \cdot 10^{-4}]$	1
^{235}U mass fraction	uniform	$[2.29 \cdot 10^{-3}, 2.33 \cdot 10^{-2}]$	1
^{236}U mass fraction	uniform	$[9.22 \cdot 10^{-6}, 1.90 \cdot 10^{-5}]$	1
^{238}Pu mass fraction	uniform	$[1.03 \cdot 10^{-3}, 2.25 \cdot 10^{-3}]$	1
^{239}Pu mass fraction	uniform	$[3.96 \cdot 10^{-2}, 5.25 \cdot 10^{-2}]$	1
^{240}Pu mass fraction	uniform	$[1.75 \cdot 10^{-2}, 2.26 \cdot 10^{-2}]$	1
^{241}Pu mass fraction	uniform	$[3.92 \cdot 10^{-3}, 6.21 \cdot 10^{-3}]$	1
^{242}Pu mass fraction	uniform	$[3.96 \cdot 10^{-3}, 6.21 \cdot 10^{-3}]$	1
^{241}Am mass fraction	uniform	$[1.24 \cdot 10^{-3}, 2.29 \cdot 10^{-3}]$	1
^{237}Np mass fraction	uniform	$[4.05 \cdot 10^{-6}, 1.57 \cdot 10^{-5}]$	1
BU	uniform	$[45, 49]$	GWd/tHM
$\mathcal{P}_{irrad}$	uniform	$[29, 40]$	W/gHM
$\Delta\sigma_c(^{235}\text{U})/\sigma_c(^{235}\text{U})$	uniform	$[-6.25, 6.25]$	%
$\Delta\sigma_f(^{235}\text{U})/\sigma_f(^{235}\text{U})$	uniform	$[-0,65, 0,65]$	%
$\Delta\sigma_c(^{238}\text{U})/\sigma_c(^{238}\text{U})$	uniform	$[-1.65, 1.65]$	%
$\Delta\sigma_f(^{238}\text{U})/\sigma_f(^{238}\text{U})$	uniform	$[-5.11, 5.11]$	%
$\Delta\sigma_c(^{238}\text{Pu})/\sigma_c(^{238}\text{Pu})$	uniform	$[-36.00, 36.00]$	%
$\Delta\sigma_f(^{238}\text{Pu})/\sigma_f(^{238}\text{Pu})$	uniform	$[-5.76, 5.76]$	%
$\Delta\sigma_c(^{239}\text{Pu})/\sigma_c(^{239}\text{Pu})$	uniform	$[-4.79, 4.79]$	%
$\Delta\sigma_f(^{239}\text{Pu})/\sigma_f(^{239}\text{Pu})$	uniform	$[-3.08, 3.08]$	%
$\Delta\sigma_c(^{240}\text{Pu})/\sigma_c(^{240}\text{Pu})$	uniform	$[-2.72, 2.72]$	%
$\Delta\sigma_f(^{240}\text{Pu})/\sigma_f(^{240}\text{Pu})$	uniform	$[-6.96, 6.96]$	%
$\Delta\sigma_c(^{241}\text{Pu})/\sigma_c(^{241}\text{Pu})$	uniform	$[-9.75, 9.75]$	%
$\Delta\sigma_f(^{241}\text{Pu})/\sigma_f(^{241}\text{Pu})$	uniform	$[-1.31, 1.31]$	%
$\Delta\sigma_c(^{242}\text{Pu})/\sigma_c(^{242}\text{Pu})$	uniform	$[-12.18, 12.18]$	%
$\Delta\sigma_f(^{242}\text{Pu})/\sigma_f(^{242}\text{Pu})$	uniform	$[-7.05, 7.05]$	%
$\Delta\sigma_c(^{241}\text{Am})/\sigma_c(^{241}\text{Am})$	uniform	$[-5.90, 5.90]$	%
$\Delta\sigma_f(^{241}\text{Am})/\sigma_f(^{241}\text{Am})$	uniform	$[-2.26, 2.26]$	%
$\Delta\sigma_c(^{243}\text{Am})/\sigma_c(^{243}\text{Am})$	uniform	$[-8.22, 8.22]$	%
$\Delta\sigma_f(^{243}\text{Am})/\sigma_f(^{243}\text{Am})$	uniform	$[-5.10, 5.10]$	%
$\Delta\sigma_c(^{237}\text{Np})/\sigma_c(^{237}\text{Np})$	uniform	$[-2.28, 2.28]$	%
$\Delta\sigma_f(^{237}\text{Np})/\sigma_f(^{237}\text{Np})$	uniform	$[-8.26, 8.26]$	%
$\Delta\sigma_c(^{242}\text{Cm})/\sigma_c(^{242}\text{Cm})$	uniform	$[-15.48, 15.48]$	%
$\Delta\sigma_f(^{242}\text{Cm})/\sigma_f(^{242}\text{Cm})$	uniform	$[-7.74, 7.74]$	%
$\Delta\sigma_c(^{243}\text{Cm})/\sigma_c(^{243}\text{Cm})$	uniform	$[-46.85, 46.85]$	%
$\Delta\sigma_f(^{243}\text{Cm})/\sigma_f(^{243}\text{Cm})$	uniform	$[-5.70, 5.70]$	%
$\Delta\sigma_c(^{244}\text{Cm})/\sigma_c(^{244}\text{Cm})$	uniform	$[-11.97, 11.97]$	%
$\Delta\sigma_f(^{244}\text{Cm})/\sigma_f(^{244}\text{Cm})$	uniform	$[-5.03, 5.03]$	%
$\Delta\sigma_c(^{245}\text{Cm})/\sigma_c(^{245}\text{Cm})$	uniform	$[-31.25, 31.25]$	%
$\Delta\sigma_f(^{245}\text{Cm})/\sigma_f(^{245}\text{Cm})$	uniform	$[-4.57, 4.57]$	%
^{238}U mass fraction	1-$\sum_i y_i$	$\varnothing$	1
irradiation length	TCT/P_{irrad}	$\varnothing$	d

Table A.5: PWR MOX, nominal burnup sampling distributions for polynomial estimator

A.1.6 SFR MOX fuel, low burnup

parameter	distribution	support	unit
^{234}U mass fraction	uniform	$[1.92 \cdot 10^{-4}, 3.71 \cdot 10^{-4}]$	1
^{235}U mass fraction	uniform	$[5.43 \cdot 10^{-3}, 7.16 \cdot 10^{-3}]$	1
^{236}U mass fraction	uniform	$[3.17 \cdot 10^{-3}, 4.50 \cdot 10^{-3}]$	1
^{238}Pu mass fraction	uniform	$[1.12 \cdot 10^{-3}, 2.25 \cdot 10^{-3}]$	1
^{239}Pu mass fraction	uniform	$[1.07 \cdot 10^{-1}, 1.35 \cdot 10^{-1}]$	1
^{240}Pu mass fraction	uniform	$[5.54 \cdot 10^{-2}, 8.17 \cdot 10^{-2}]$	1
^{241}Pu mass fraction	uniform	$[4.92 \cdot 10^{-3}, 1.70 \cdot 10^{-2}]$	1
^{242}Pu mass fraction	uniform	$[6.37 \cdot 10^{-3}, 2.88 \cdot 10^{-2}]$	1
^{241}Am mass fraction	uniform	$[4.99 \cdot 10^{-4}, 2.41 \cdot 10^{-3}]$	1
BU	uniform	$[25, 96]$	GWd/tHM
$\mathcal{P}_{irrad}$	uniform	$[50.0, 54.1]$	W/gHM
$\Delta\sigma_c(^{235}\text{U})/\sigma_c(^{235}\text{U})$	uniform	$[-6.25, 6.25]$	%
$\Delta\sigma_f(^{235}\text{U})/\sigma_f(^{235}\text{U})$	uniform	$[-0,65, 0,65]$	%
$\Delta\sigma_c(^{238}\text{U})/\sigma_c(^{238}\text{U})$	uniform	$[-1.65, 1.65]$	%
$\Delta\sigma_f(^{238}\text{U})/\sigma_f(^{238}\text{U})$	uniform	$[-5.11, 5.11]$	%
$\Delta\sigma_c(^{238}\text{Pu})/\sigma_c(^{238}\text{Pu})$	uniform	$[-36.00, 36.00]$	%
$\Delta\sigma_f(^{238}\text{Pu})/\sigma_f(^{238}\text{Pu})$	uniform	$[-5.76, 5.76]$	%
$\Delta\sigma_c(^{239}\text{Pu})/\sigma_c(^{239}\text{Pu})$	uniform	$[-4.79, 4.79]$	%
$\Delta\sigma_f(^{239}\text{Pu})/\sigma_f(^{239}\text{Pu})$	uniform	$[-3.08, 3.08]$	%
$\Delta\sigma_c(^{240}\text{Pu})/\sigma_c(^{240}\text{Pu})$	uniform	$[-2.72, 2.72]$	%
$\Delta\sigma_f(^{240}\text{Pu})/\sigma_f(^{240}\text{Pu})$	uniform	$[-6.96, 6.96]$	%
$\Delta\sigma_c(^{241}\text{Pu})/\sigma_c(^{241}\text{Pu})$	uniform	$[-9.75, 9.75]$	%
$\Delta\sigma_f(^{241}\text{Pu})/\sigma_f(^{241}\text{Pu})$	uniform	$[-1.31, 1.31]$	%
$\Delta\sigma_c(^{242}\text{Pu})/\sigma_c(^{242}\text{Pu})$	uniform	$[-12.18, 12.18]$	%
$\Delta\sigma_f(^{242}\text{Pu})/\sigma_f(^{242}\text{Pu})$	uniform	$[-7.05, 7.05]$	%
$\Delta\sigma_c(^{241}\text{Am})/\sigma_c(^{241}\text{Am})$	uniform	$[-5.90, 5.90]$	%
$\Delta\sigma_f(^{241}\text{Am})/\sigma_f(^{241}\text{Am})$	uniform	$[-2.26, 2.26]$	%
$\Delta\sigma_c(^{243}\text{Am})/\sigma_c(^{243}\text{Am})$	uniform	$[-8.22, 8.22]$	%
$\Delta\sigma_f(^{243}\text{Am})/\sigma_f(^{243}\text{Am})$	uniform	$[-5.10, 5.10]$	%
$\Delta\sigma_c(^{237}\text{Np})/\sigma_c(^{237}\text{Np})$	uniform	$[-2.28, 2.28]$	%
$\Delta\sigma_f(^{237}\text{Np})/\sigma_f(^{237}\text{Np})$	uniform	$[-8.26, 8.26]$	%
$\Delta\sigma_c(^{242}\text{Cm})/\sigma_c(^{242}\text{Cm})$	uniform	$[-15.48, 15.48]$	%
$\Delta\sigma_f(^{242}\text{Cm})/\sigma_f(^{242}\text{Cm})$	uniform	$[-7.74, 7.74]$	%
$\Delta\sigma_c(^{243}\text{Cm})/\sigma_c(^{243}\text{Cm})$	uniform	$[-46.85, 46.85]$	%
$\Delta\sigma_f(^{243}\text{Cm})/\sigma_f(^{243}\text{Cm})$	uniform	$[-5.70, 5.70]$	%
$\Delta\sigma_c(^{244}\text{Cm})/\sigma_c(^{244}\text{Cm})$	uniform	$[-11.97, 11.97]$	%
$\Delta\sigma_f(^{244}\text{Cm})/\sigma_f(^{244}\text{Cm})$	uniform	$[-5.03, 5.03]$	%
$\Delta\sigma_c(^{245}\text{Cm})/\sigma_c(^{245}\text{Cm})$	uniform	$[-31.25, 31.25]$	%
$\Delta\sigma_f(^{245}\text{Cm})/\sigma_f(^{245}\text{Cm})$	uniform	$[-4.57, 4.57]$	%
^{238}U mass fraction	1-$\sum_i y_i$	$\varnothing$	1
irradiation length	TCT/P_{irrad}	$\varnothing$	d

Table A.6: SFR MOX, BU<96GWd/tHM sampling distributions

A.1.7 SFR MOX fuel, nominal burnup

parameter	distribution	support	unit
^{234}U mass fraction	uniform	$[1.92 \cdot 10^{-4}, 3.71 \cdot 10^{-4}]$	1
^{235}U mass fraction	uniform	$[5.43 \cdot 10^{-3}, 7.16 \cdot 10^{-3}]$	1
^{236}U mass fraction	uniform	$[3.17 \cdot 10^{-3}, 4.50 \cdot 10^{-3}]$	1
^{238}Pu mass fraction	uniform	$[1.12 \cdot 10^{-3}, 2.25 \cdot 10^{-3}]$	1
^{239}Pu mass fraction	uniform	$[1.07 \cdot 10^{-1}, 1.35 \cdot 10^{-1}]$	1
^{240}Pu mass fraction	uniform	$[5.54 \cdot 10^{-2}, 8.17 \cdot 10^{-2}]$	1
^{241}Pu mass fraction	uniform	$[4.92 \cdot 10^{-3}, 1.70 \cdot 10^{-2}]$	1
^{242}Pu mass fraction	uniform	$[6.37 \cdot 10^{-3}, 2.88 \cdot 10^{-2}]$	1
^{241}Am mass fraction	uniform	$[4.99 \cdot 10^{-4}, 2.41 \cdot 10^{-3}]$	1
BU	not a distribution	116.3	GWd/tHM
$\mathcal{P}_{irrad}$	uniform	$[50.0, 54.1]$	W/gHM
$\Delta\sigma_c(^{235}\text{U})/\sigma_c(^{235}\text{U})$	uniform	$[-6.25, 6.25]$	%
$\Delta\sigma_f(^{235}\text{U})/\sigma_f(^{235}\text{U})$	uniform	$[-0,65, 0,65]$	%
$\Delta\sigma_c(^{238}\text{U})/\sigma_c(^{238}\text{U})$	uniform	$[-1.65, 1.65]$	%
$\Delta\sigma_f(^{238}\text{U})/\sigma_f(^{238}\text{U})$	uniform	$[-5.11, 5.11]$	%
$\Delta\sigma_c(^{238}\text{Pu})/\sigma_c(^{238}\text{Pu})$	uniform	$[-36.00, 36.00]$	%
$\Delta\sigma_f(^{238}\text{Pu})/\sigma_f(^{238}\text{Pu})$	uniform	$[-5.76, 5.76]$	%
$\Delta\sigma_c(^{239}\text{Pu})/\sigma_c(^{239}\text{Pu})$	uniform	$[-4.79, 4.79]$	%
$\Delta\sigma_f(^{239}\text{Pu})/\sigma_f(^{239}\text{Pu})$	uniform	$[-3.08, 3.08]$	%
$\Delta\sigma_c(^{240}\text{Pu})/\sigma_c(^{240}\text{Pu})$	uniform	$[-2.72, 2.72]$	%
$\Delta\sigma_f(^{240}\text{Pu})/\sigma_f(^{240}\text{Pu})$	uniform	$[-6.96, 6.96]$	%
$\Delta\sigma_c(^{241}\text{Pu})/\sigma_c(^{241}\text{Pu})$	uniform	$[-9.75, 9.75]$	%
$\Delta\sigma_f(^{241}\text{Pu})/\sigma_f(^{241}\text{Pu})$	uniform	$[-1.31, 1.31]$	%
$\Delta\sigma_c(^{242}\text{Pu})/\sigma_c(^{242}\text{Pu})$	uniform	$[-12.18, 12.18]$	%
$\Delta\sigma_f(^{242}\text{Pu})/\sigma_f(^{242}\text{Pu})$	uniform	$[-7.05, 7.05]$	%
$\Delta\sigma_c(^{241}\text{Am})/\sigma_c(^{241}\text{Am})$	uniform	$[-5.90, 5.90]$	%
$\Delta\sigma_f(^{241}\text{Am})/\sigma_f(^{241}\text{Am})$	uniform	$[-2.26, 2.26]$	%
$\Delta\sigma_c(^{243}\text{Am})/\sigma_c(^{243}\text{Am})$	uniform	$[-8.22, 8.22]$	%
$\Delta\sigma_f(^{243}\text{Am})/\sigma_f(^{243}\text{Am})$	uniform	$[-5.10, 5.10]$	%
$\Delta\sigma_c(^{237}\text{Np})/\sigma_c(^{237}\text{Np})$	uniform	$[-2.28, 2.28]$	%
$\Delta\sigma_f(^{237}\text{Np})/\sigma_f(^{237}\text{Np})$	uniform	$[-8.26, 8.26]$	%
$\Delta\sigma_c(^{242}\text{Cm})/\sigma_c(^{242}\text{Cm})$	uniform	$[-15.48, 15.48]$	%
$\Delta\sigma_f(^{242}\text{Cm})/\sigma_f(^{242}\text{Cm})$	uniform	$[-7.74, 7.74]$	%
$\Delta\sigma_c(^{243}\text{Cm})/\sigma_c(^{243}\text{Cm})$	uniform	$[-46.85, 46.85]$	%
$\Delta\sigma_f(^{243}\text{Cm})/\sigma_f(^{243}\text{Cm})$	uniform	$[-5.70, 5.70]$	%
$\Delta\sigma_c(^{244}\text{Cm})/\sigma_c(^{244}\text{Cm})$	uniform	$[-11.97, 11.97]$	%
$\Delta\sigma_f(^{244}\text{Cm})/\sigma_f(^{244}\text{Cm})$	uniform	$[-5.03, 5.03]$	%
$\Delta\sigma_c(^{245}\text{Cm})/\sigma_c(^{245}\text{Cm})$	uniform	$[-31.25, 31.25]$	%
$\Delta\sigma_f(^{245}\text{Cm})/\sigma_f(^{245}\text{Cm})$	uniform	$[-4.57, 4.57]$	%
^{238}U mass fraction	1-$\sum_i y_i$	$\varnothing$	1
irradiation length	TCT/P_{irrad}	$\varnothing$	d

Table A.7: SFR MOX, BU<96GWd/tHM sampling distributions

A.2 DOE for ANN

A.2.1 PWR UOX fuel, low burnup

parameter	distribution	support	unit
^{234}U mass fraction	uniform	$[1.01 \cdot 10^{-4}, 4.61 \cdot 10^{-4}]$	1
^{235}U mass fraction	uniform	$[2.00 \cdot 10^{-2}, 4.80 \cdot 10^{-2}]$	1
BU	exponential	$[10, 43]$	GWd/tHM
$\mathcal{P}_{irrad}$	uniform	$[29, 40]$	W/gHM
$\Delta\sigma_c(^{234}\text{U})/\sigma_c(^{234}\text{U})$	uniform	$[-9, 9]$	%
$\Delta\sigma_f(^{234}\text{U})/\sigma_f(^{234}\text{U})$	uniform	$[-60, 60]$	%
$\Delta\sigma_c(^{235}\text{U})/\sigma_c(^{235}\text{U})$	uniform	$[-5, 5]$	%
$\Delta\sigma_f(^{235}\text{U})/\sigma_f(^{235}\text{U})$	uniform	$[-1, 1]$	%
$\Delta\sigma_c(^{236}\text{U})/\sigma_c(^{236}\text{U})$	uniform	$[-12, 12]$	%
$\Delta\sigma_f(^{236}\text{U})/\sigma_f(^{236}\text{U})$	uniform	$[-70, 70]$	%
$\Delta\sigma_c(^{238}\text{U})/\sigma_c(^{238}\text{U})$	uniform	$[-2, 2]$	%
$\Delta\sigma_f(^{238}\text{U})/\sigma_f(^{238}\text{U})$	uniform	$[-5, 5]$	%
$\Delta\sigma_c(^{238}\text{Pu})/\sigma_c(^{238}\text{Pu})$	uniform	$[-15, 15]$	%
$\Delta\sigma_f(^{238}\text{Pu})/\sigma_f(^{238}\text{Pu})$	uniform	$[-9, 9]$	%
$\Delta\sigma_c(^{239}\text{Pu})/\sigma_c(^{239}\text{Pu})$	uniform	$[-30, 30]$	%
$\Delta\sigma_f(^{239}\text{Pu})/\sigma_f(^{239}\text{Pu})$	uniform	$[-1, 1]$	%
$\Delta\sigma_c(^{240}\text{Pu})/\sigma_c(^{240}\text{Pu})$	uniform	$[-5, 5]$	%
$\Delta\sigma_f(^{240}\text{Pu})/\sigma_f(^{240}\text{Pu})$	uniform	$[-3, 3]$	%
$\Delta\sigma_c(^{241}\text{Pu})/\sigma_c(^{241}\text{Pu})$	uniform	$[-5, 5]$	%
$\Delta\sigma_f(^{241}\text{Pu})/\sigma_f(^{241}\text{Pu})$	uniform	$[-7, 7]$	%
$\Delta\sigma_c(^{242}\text{Pu})/\sigma_c(^{242}\text{Pu})$	uniform	$[-35, 35]$	%
$\Delta\sigma_f(^{242}\text{Pu})/\sigma_f(^{242}\text{Pu})$	uniform	$[-6, 6]$	%
$\Delta\sigma_c(^{241}\text{Am})/\sigma_c(^{241}\text{Am})$	uniform	$[-15, 15]$	%
$\Delta\sigma_f(^{241}\text{Am})/\sigma_f(^{241}\text{Am})$	uniform	$[-15, 15]$	%
$\Delta\sigma_c(^{242M}\text{Am})/\sigma_c(^{242M}\text{Am})$	uniform	$[-70, 70]$	%
$\Delta\sigma_f(^{242M}\text{Am})/\sigma_f(^{242M}\text{Am})$	uniform	$[-15, 15]$	%
$\Delta\sigma_c(^{243}\text{Am})/\sigma_c(^{243}\text{Am})$	uniform	$[-40, 40]$	%
$\Delta\sigma_f(^{243}\text{Am})/\sigma_f(^{243}\text{Am})$	uniform	$[-30, 30]$	%
$\Delta\sigma_c(^{237}\text{Np})/\sigma_c(^{237}\text{Np})$	uniform	$[-15, 15]$	%
$\Delta\sigma_f(^{237}\text{Np})/\sigma_f(^{237}\text{Np})$	uniform	$[-9, 9]$	%
$\Delta\sigma_c(^{242}\text{Cm})/\sigma_c(^{242}\text{Cm})$	uniform	$[-45, 45]$	%
$\Delta\sigma_f(^{242}\text{Cm})/\sigma_f(^{242}\text{Cm})$	uniform	$[-15, 15]$	%
$\Delta\sigma_c(^{243}\text{Cm})/\sigma_c(^{243}\text{Cm})$	uniform	$[-90, 90]$	%
$\Delta\sigma_f(^{243}\text{Cm})/\sigma_f(^{243}\text{Cm})$	uniform	$[-20, 20]$	%
$\Delta\sigma_c(^{244}\text{Cm})/\sigma_c(^{244}\text{Cm})$	uniform	$[-25, 25]$	%
$\Delta\sigma_f(^{244}\text{Cm})/\sigma_f(^{244}\text{Cm})$	uniform	$[-15, 15]$	%
$\Delta\sigma_c(^{245}\text{Cm})/\sigma_c(^{245}\text{Cm})$	uniform	$[-60, 60]$	%
$\Delta\sigma_f(^{245}\text{Cm})/\sigma_f(^{245}\text{Cm})$	uniform	$[-25, 25]$	%
$\Delta\sigma_c(^{133}\text{Cs})/\sigma_c(^{133}\text{Cs})$	uniform	$[-15, 15]$	%
$\Delta\sigma_c(^{134}\text{Cs})/\sigma_c(^{134}\text{Cs})$	uniform	$[-100, 100]$	%
$\Delta\sigma_c(^{147}\text{Pm})/\sigma_c(^{147}\text{Pm})$	uniform	$[-60, 60]$	%
$\Delta\sigma_c(^{152}\text{Sm})/\sigma_c(^{152}\text{Sm})$	uniform	$[-10, 10]$	%
$\Delta\sigma_c(^{153}\text{Eu})/\sigma_c(^{153}\text{Eu})$	uniform	$[-15, 15]$	%
$\Delta\sigma_c(^{154}\text{Eu})/\sigma_c(^{154}\text{Eu})$	uniform	$[-100, 100]$	%
$\tilde{f}(X \to Y)$ $X \in \{^{235,238}\text{U}, ^{238,239,240,241,242}\text{Pu}\}$ $Y \in \{^{84,85}\text{Kr}, ^{90}\text{Sr}, ^{95}\text{Zr}, ^{106}\text{Ru}, ^{132}\text{Te}, ^{133}\text{I}, ^{137}\text{Cs}, ^{144}\text{Ce}, ^{146,147}\text{Nd}, ^{151}\text{Pm}, ^{152,153}\text{Sm}\}$	uniform (98 parameters)	$[0.5, 1.5]$	1
^{238}U mass fraction	1- ^{234}U - ^{235}U	$\varnothing$	1
irradiation length	TCT/P_{irrad}	$\varnothing$	d

Table A.8: PWR UOX, low burnup sampling distributions for ANN estimator

A.2.2 PWR UOX fuel, nominal burnup

parameter	distribution	support	unit
^{234}U mass fraction	uniform	$[1.01 \cdot 10^{-4}, 4.61 \cdot 10^{-4}]$	1
^{235}U mass fraction	uniform	$[2.00 \cdot 10^{-2}, 4.80 \cdot 10^{-2}]$	1
BU	uniform	$[38, 56]$	GWd/tHM
$\mathcal{P}_{irrad}$	uniform	$[29, 40]$	W/gHM
$\Delta\sigma_c(^{234}\text{U})/\sigma_c(^{234}\text{U})$	uniform	$[-9, 9]$	%
$\Delta\sigma_f(^{234}\text{U})/\sigma_f(^{234}\text{U})$	uniform	$[-60, 60]$	%
$\Delta\sigma_c(^{235}\text{U})/\sigma_c(^{235}\text{U})$	uniform	$[-5, 5]$	%
$\Delta\sigma_f(^{235}\text{U})/\sigma_f(^{235}\text{U})$	uniform	$[-1, 1]$	%
$\Delta\sigma_c(^{236}\text{U})/\sigma_c(^{236}\text{U})$	uniform	$[-12, 12]$	%
$\Delta\sigma_f(^{236}\text{U})/\sigma_f(^{236}\text{U})$	uniform	$[-70, 70]$	%
$\Delta\sigma_c(^{238}\text{U})/\sigma_c(^{238}\text{U})$	uniform	$[-2, 2]$	%
$\Delta\sigma_f(^{238}\text{U})/\sigma_f(^{238}\text{U})$	uniform	$[-5, 5]$	%
$\Delta\sigma_c(^{238}\text{Pu})/\sigma_c(^{238}\text{Pu})$	uniform	$[-15, 15]$	%
$\Delta\sigma_f(^{238}\text{Pu})/\sigma_f(^{238}\text{Pu})$	uniform	$[-9, 9]$	%
$\Delta\sigma_c(^{239}\text{Pu})/\sigma_c(^{239}\text{Pu})$	uniform	$[-30, 30]$	%
$\Delta\sigma_f(^{239}\text{Pu})/\sigma_f(^{239}\text{Pu})$	uniform	$[-1, 1]$	%
$\Delta\sigma_c(^{240}\text{Pu})/\sigma_c(^{240}\text{Pu})$	uniform	$[-5, 5]$	%
$\Delta\sigma_f(^{240}\text{Pu})/\sigma_f(^{240}\text{Pu})$	uniform	$[-3, 3]$	%
$\Delta\sigma_c(^{241}\text{Pu})/\sigma_c(^{241}\text{Pu})$	uniform	$[-5, 5]$	%
$\Delta\sigma_f(^{241}\text{Pu})/\sigma_f(^{241}\text{Pu})$	uniform	$[-7, 7]$	%
$\Delta\sigma_c(^{242}\text{Pu})/\sigma_c(^{242}\text{Pu})$	uniform	$[-35, 35]$	%
$\Delta\sigma_f(^{242}\text{Pu})/\sigma_f(^{242}\text{Pu})$	uniform	$[-6, 6]$	%
$\Delta\sigma_c(^{241}\text{Am})/\sigma_c(^{241}\text{Am})$	uniform	$[-15, 15]$	%
$\Delta\sigma_f(^{241}\text{Am})/\sigma_f(^{241}\text{Am})$	uniform	$[-15, 15]$	%
$\Delta\sigma_c(^{242M}\text{Am})/\sigma_c(^{242M}\text{Am})$	uniform	$[-70, 70]$	%
$\Delta\sigma_f(^{242M}\text{Am})/\sigma_f(^{242M}\text{Am})$	uniform	$[-15, 15]$	%
$\Delta\sigma_c(^{243}\text{Am})/\sigma_c(^{243}\text{Am})$	uniform	$[-40, 40]$	%
$\Delta\sigma_f(^{243}\text{Am})/\sigma_f(^{243}\text{Am})$	uniform	$[-30, 30]$	%
$\Delta\sigma_c(^{237}\text{Np})/\sigma_c(^{237}\text{Np})$	uniform	$[-15, 15]$	%
$\Delta\sigma_f(^{237}\text{Np})/\sigma_f(^{237}\text{Np})$	uniform	$[-9, 9]$	%
$\Delta\sigma_c(^{242}\text{Cm})/\sigma_c(^{242}\text{Cm})$	uniform	$[-45, 45]$	%
$\Delta\sigma_f(^{242}\text{Cm})/\sigma_f(^{242}\text{Cm})$	uniform	$[-15, 15]$	%
$\Delta\sigma_c(^{243}\text{Cm})/\sigma_c(^{243}\text{Cm})$	uniform	$[-90, 90]$	%
$\Delta\sigma_f(^{243}\text{Cm})/\sigma_f(^{243}\text{Cm})$	uniform	$[-20, 20]$	%
$\Delta\sigma_c(^{244}\text{Cm})/\sigma_c(^{244}\text{Cm})$	uniform	$[-25, 25]$	%
$\Delta\sigma_f(^{244}\text{Cm})/\sigma_f(^{244}\text{Cm})$	uniform	$[-15, 15]$	%
$\Delta\sigma_c(^{245}\text{Cm})/\sigma_c(^{245}\text{Cm})$	uniform	$[-60, 60]$	%
$\Delta\sigma_f(^{245}\text{Cm})/\sigma_f(^{245}\text{Cm})$	uniform	$[-25, 25]$	%
$\Delta\sigma_c(^{133}\text{Cs})/\sigma_c(^{133}\text{Cs})$	uniform	$[-15, 15]$	%
$\Delta\sigma_c(^{134}\text{Cs})/\sigma_c(^{134}\text{Cs})$	uniform	$[-100, 100]$	%
$\Delta\sigma_c(^{147}\text{Pm})/\sigma_c(^{147}\text{Pm})$	uniform	$[-60, 60]$	%
$\Delta\sigma_c(^{152}\text{Sm})/\sigma_c(^{152}\text{Sm})$	uniform	$[-10, 10]$	%
$\Delta\sigma_c(^{153}\text{Eu})/\sigma_c(^{153}\text{Eu})$	uniform	$[-15, 15]$	%
$\Delta\sigma_c(^{154}\text{Eu})/\sigma_c(^{154}\text{Eu})$	uniform	$[-100, 100]$	%
$\tilde{f}(X \to Y)$ $X \in \{^{235,238}\text{U}, ^{238,239,240,241,242}\text{Pu}\}$ $Y \in \{^{84,85}\text{Kr}, ^{90}\text{Sr}, ^{95}\text{Zr}, ^{106}\text{Ru}, ^{132}\text{Te}, ^{133}\text{I}, ^{137}\text{Cs}, ^{144}\text{Ce}, ^{146,147}\text{Nd}, ^{151}\text{Pm}, ^{152,153}\text{Sm}\}$	uniform (98 parameters)	$[0.5, 1.5]$	1
^{238}U mass fraction	1-$\sum_i y_i$	∅	1
irradiation length	TCT/P_{irrad}	∅	d

Table A.9: PWR UOX, nominal burnup sampling distributions for ANN estimator

A.2.3 PWR MOX fuel, low burnup

parameter	distribution	support	unit
^{234}U mass fraction	uniform	$[5.43 \cdot 10^{-5}, 1.46 \cdot 10^{-4}]$	1
^{235}U mass fraction	uniform	$[2.29 \cdot 10^{-3}, 2.33 \cdot 10^{-2}]$	1
^{236}U mass fraction	uniform	$[9.22 \cdot 10^{-6}, 1.90 \cdot 10^{-5}]$	1
^{238}Pu mass fraction	uniform	$[1.03 \cdot 10^{-3}, 2.25 \cdot 10^{-3}]$	1
^{239}Pu mass fraction	uniform	$[3.96 \cdot 10^{-2}, 5.25 \cdot 10^{-2}]$	1
^{240}Pu mass fraction	uniform	$[1.75 \cdot 10^{-2}, 2.26 \cdot 10^{-2}]$	1
^{241}Pu mass fraction	uniform	$[3.92 \cdot 10^{-3}, 6.21 \cdot 10^{-3}]$	1
^{242}Pu mass fraction	uniform	$[3.96 \cdot 10^{-3}, 6.21 \cdot 10^{-3}]$	1
^{241}Am mass fraction	uniform	$[1.24 \cdot 10^{-3}, 2.29 \cdot 10^{-3}]$	1
^{237}Np mass fraction	uniform	$[4.05 \cdot 10^{-6}, 1.57 \cdot 10^{-5}]$	1
BU	exponential	$[10, 45]$	GWd/tHM
$\mathcal{P}_{irrad}$	uniform	$[29, 40]$	W/gHM
$\Delta\sigma_c(^{234}\text{U})/\sigma_c(^{234}\text{U})$	uniform	$[-12, 12]$	%
$\Delta\sigma_f(^{234}\text{U})/\sigma_f(^{234}\text{U})$	uniform	$[-60, 60]$	%
$\Delta\sigma_c(^{235}\text{U})/\sigma_c(^{235}\text{U})$	uniform	$[-6, 6]$	%
$\Delta\sigma_f(^{235}\text{U})/\sigma_f(^{235}\text{U})$	uniform	$[-1, 1]$	%
$\Delta\sigma_c(^{238}\text{U})/\sigma_c(^{238}\text{U})$	uniform	$[-2, 2]$	%
$\Delta\sigma_f(^{238}\text{U})/\sigma_f(^{238}\text{U})$	uniform	$[-5, 5]$	%
$\Delta\sigma_c(^{238}\text{Pu})/\sigma_c(^{238}\text{Pu})$	uniform	$[-30, 30]$	%
$\Delta\sigma_f(^{238}\text{Pu})/\sigma_f(^{238}\text{Pu})$	uniform	$[-1, 1]$	%
$\Delta\sigma_c(^{239}\text{Pu})/\sigma_c(^{239}\text{Pu})$	uniform	$[-5, 5]$	%
$\Delta\sigma_f(^{239}\text{Pu})/\sigma_f(^{239}\text{Pu})$	uniform	$[-3, 2]$	%
$\Delta\sigma_c(^{240}\text{Pu})/\sigma_c(^{240}\text{Pu})$	uniform	$[-5, 5]$	%
$\Delta\sigma_f(^{240}\text{Pu})/\sigma_f(^{240}\text{Pu})$	uniform	$[-5, 5]$	%
$\Delta\sigma_c(^{241}\text{Pu})/\sigma_c(^{241}\text{Pu})$	uniform	$[-12, 12]$	%
$\Delta\sigma_f(^{241}\text{Pu})/\sigma_f(^{241}\text{Pu})$	uniform	$[-5, 5]$	%
$\Delta\sigma_c(^{242}\text{Pu})/\sigma_c(^{242}\text{Pu})$	uniform	$[-35, 35]$	%
$\Delta\sigma_f(^{242}\text{Pu})/\sigma_f(^{242}\text{Pu})$	uniform	$[-6, 6]$	%
$\Delta\sigma_c(^{241}\text{Am})/\sigma_c(^{241}\text{Am})$	uniform	$[-15, 15]$	%
$\Delta\sigma_f(^{241}\text{Am})/\sigma_f(^{241}\text{Am})$	uniform	$[-10, 10]$	%
$\Delta\sigma_c(^{242M}\text{Am})/\sigma_c(^{242M}\text{Am})$	uniform	$[-70, 70]$	%
$\Delta\sigma_f(^{242M}\text{Am})/\sigma_f(^{242M}\text{Am})$	uniform	$[-15, 15]$	%
$\Delta\sigma_c(^{243}\text{Am})/\sigma_c(^{243}\text{Am})$	uniform	$[-30, 30]$	%
$\Delta\sigma_f(^{243}\text{Am})/\sigma_f(^{243}\text{Am})$	uniform	$[-12, 12]$	%
$\Delta\sigma_c(^{237}\text{Np})/\sigma_c(^{237}\text{Np})$	uniform	$[-12, 12]$	%
$\Delta\sigma_f(^{237}\text{Np})/\sigma_f(^{237}\text{Np})$	uniform	$[-9, 9]$	%
$\Delta\sigma_c(^{242}\text{Cm})/\sigma_c(^{242}\text{Cm})$	uniform	$[-50, 50]$	%
$\Delta\sigma_f(^{242}\text{Cm})/\sigma_f(^{242}\text{Cm})$	uniform	$[-15, 15]$	%
$\Delta\sigma_c(^{243}\text{Cm})/\sigma_c(^{243}\text{Cm})$	uniform	$[-80, 80]$	%
$\Delta\sigma_f(^{243}\text{Cm})/\sigma_f(^{243}\text{Cm})$	uniform	$[-12, 12]$	%
$\Delta\sigma_c(^{244}\text{Cm})/\sigma_c(^{244}\text{Cm})$	uniform	$[-25, 25]$	%
$\Delta\sigma_f(^{244}\text{Cm})/\sigma_f(^{244}\text{Cm})$	uniform	$[-15, 15]$	%
$\Delta\sigma_c(^{245}\text{Cm})/\sigma_c(^{245}\text{Cm})$	uniform	$[-60, 60]$	%
$\Delta\sigma_f(^{245}\text{Cm})/\sigma_f(^{245}\text{Cm})$	uniform	$[-25, 25]$	%
$\Delta\sigma_c(^{133}\text{Cs})/\sigma_c(^{133}\text{Cs})$	uniform	$[-20, 20]$	%
$\Delta\sigma_c(^{134}\text{Cs})/\sigma_c(^{134}\text{Cs})$	uniform	$[-100, 100]$	%
$\Delta\sigma_c(^{147}\text{Pm})/\sigma_c(^{147}\text{Pm})$	uniform	$[-65, 65]$	%
$\Delta\sigma_c(^{152}\text{Sm})/\sigma_c(^{152}\text{Sm})$	uniform	$[-10, 10]$	%
$\Delta\sigma_c(^{153}\text{Eu})/\sigma_c(^{153}\text{Eu})$	uniform	$[-20, 20]$	%
$\Delta\sigma_c(^{154}\text{Eu})/\sigma_c(^{154}\text{Eu})$	uniform	$[-100, 100]$	%
$\tilde{f}(X \to Y)$ $X \in \{^{235,238}\text{U}, ^{238,239,240,241,242}\text{Pu}\}$ $Y \in \{^{84,85}\text{Kr}, ^{90}\text{Sr}, ^{95}\text{Zr}, ^{106}\text{Ru}, ^{132}\text{Te}, ^{133}\text{I}, ^{137}\text{Cs}, ^{144}\text{Ce}, ^{146,147}\text{Nd}, ^{151}\text{Pm}, ^{152,153}\text{Sm}\}$	uniform (98 parameters)	$[0.5, 1.5]$	1
^{238}U mass fraction	1- ^{234}U - ^{235}U	$\varnothing$	1
irradiation length	TCT/P_{irrad}	$\varnothing$	d

Table A.10: PWR MOX, low burnup sampling distributions for ANN estimator

A.2.4 PWR MOX fuel, nominal burnup

parameter	distribution	support	unit
^{234}U mass fraction	uniform	$[5.43 \cdot 10^{-5}, 1.46 \cdot 10^{-4}]$	1
^{235}U mass fraction	uniform	$[2.29 \cdot 10^{-3}, 2.33 \cdot 10^{-2}]$	1
^{236}U mass fraction	uniform	$[9.22 \cdot 10^{-6}, 1.90 \cdot 10^{-5}]$	1
^{238}Pu mass fraction	uniform	$[1.03 \cdot 10^{-3}, 2.25 \cdot 10^{-3}]$	1
^{239}Pu mass fraction	uniform	$[3.96 \cdot 10^{-2}, 5.25 \cdot 10^{-2}]$	1
^{240}Pu mass fraction	uniform	$[1.75 \cdot 10^{-2}, 2.26 \cdot 10^{-2}]$	1
^{241}Pu mass fraction	uniform	$[3.92 \cdot 10^{-3}, 6.21 \cdot 10^{-3}]$	1
^{242}Pu mass fraction	uniform	$[3.96 \cdot 10^{-3}, 6.21 \cdot 10^{-3}]$	1
^{241}Am mass fraction	uniform	$[1.24 \cdot 10^{-3}, 2.29 \cdot 10^{-3}]$	1
^{237}Np mass fraction	uniform	$[4.05 \cdot 10^{-6}, 1.57 \cdot 10^{-5}]$	1
BU	uniform	$[45, 49]$	GWd/tHM
$\mathcal{P}_{irrad}$	uniform	$[29, 40]$	W/gHM
$\Delta\sigma_c(^{234}\text{U})/\sigma_c(^{234}\text{U})$	uniform	$[-12, 12]$	%
$\Delta\sigma_f(^{234}\text{U})/\sigma_f(^{234}\text{U})$	uniform	$[-60, 60]$	%
$\Delta\sigma_c(^{235}\text{U})/\sigma_c(^{235}\text{U})$	uniform	$[-6, 6]$	%
$\Delta\sigma_f(^{235}\text{U})/\sigma_f(^{235}\text{U})$	uniform	$[-1, 1]$	%
$\Delta\sigma_c(^{238}\text{U})/\sigma_c(^{238}\text{U})$	uniform	$[-2, 2]$	%
$\Delta\sigma_f(^{238}\text{U})/\sigma_f(^{238}\text{U})$	uniform	$[-5, 5]$	%
$\Delta\sigma_c(^{238}\text{Pu})/\sigma_c(^{238}\text{Pu})$	uniform	$[-30, 30]$	%
$\Delta\sigma_f(^{238}\text{Pu})/\sigma_f(^{238}\text{Pu})$	uniform	$[-1, 1]$	%
$\Delta\sigma_c(^{239}\text{Pu})/\sigma_c(^{239}\text{Pu})$	uniform	$[-5, 5]$	%
$\Delta\sigma_f(^{239}\text{Pu})/\sigma_f(^{239}\text{Pu})$	uniform	$[-3, 2]$	%
$\Delta\sigma_c(^{240}\text{Pu})/\sigma_c(^{240}\text{Pu})$	uniform	$[-5, 5]$	%
$\Delta\sigma_f(^{240}\text{Pu})/\sigma_f(^{240}\text{Pu})$	uniform	$[-5, 5]$	%
$\Delta\sigma_c(^{241}\text{Pu})/\sigma_c(^{241}\text{Pu})$	uniform	$[-12, 12]$	%
$\Delta\sigma_f(^{241}\text{Pu})/\sigma_f(^{241}\text{Pu})$	uniform	$[-5, 5]$	%
$\Delta\sigma_c(^{242}\text{Pu})/\sigma_c(^{242}\text{Pu})$	uniform	$[-35, 35]$	%
$\Delta\sigma_f(^{242}\text{Pu})/\sigma_f(^{242}\text{Pu})$	uniform	$[-6, 6]$	%
$\Delta\sigma_c(^{241}\text{Am})/\sigma_c(^{241}\text{Am})$	uniform	$[-15, 15]$	%
$\Delta\sigma_f(^{241}\text{Am})/\sigma_f(^{241}\text{Am})$	uniform	$[-10, 10]$	%
$\Delta\sigma_c(^{242M}\text{Am})/\sigma_c(^{242M}\text{Am})$	uniform	$[-70, 70]$	%
$\Delta\sigma_f(^{242M}\text{Am})/\sigma_f(^{242M}\text{Am})$	uniform	$[-15, 15]$	%
$\Delta\sigma_c(^{243}\text{Am})/\sigma_c(^{243}\text{Am})$	uniform	$[-30, 30]$	%
$\Delta\sigma_f(^{243}\text{Am})/\sigma_f(^{243}\text{Am})$	uniform	$[-12, 12]$	%
$\Delta\sigma_c(^{237}\text{Np})/\sigma_c(^{237}\text{Np})$	uniform	$[-12, 12]$	%
$\Delta\sigma_f(^{237}\text{Np})/\sigma_f(^{237}\text{Np})$	uniform	$[-9, 9]$	%
$\Delta\sigma_c(^{242}\text{Cm})/\sigma_c(^{242}\text{Cm})$	uniform	$[-50, 50]$	%
$\Delta\sigma_f(^{242}\text{Cm})/\sigma_f(^{242}\text{Cm})$	uniform	$[-15, 15]$	%
$\Delta\sigma_c(^{243}\text{Cm})/\sigma_c(^{243}\text{Cm})$	uniform	$[-80, 80]$	%
$\Delta\sigma_f(^{243}\text{Cm})/\sigma_f(^{243}\text{Cm})$	uniform	$[-12, 12]$	%
$\Delta\sigma_c(^{244}\text{Cm})/\sigma_c(^{244}\text{Cm})$	uniform	$[-25, 25]$	%
$\Delta\sigma_f(^{244}\text{Cm})/\sigma_f(^{244}\text{Cm})$	uniform	$[-15, 15]$	%
$\Delta\sigma_c(^{245}\text{Cm})/\sigma_c(^{245}\text{Cm})$	uniform	$[-60, 60]$	%
$\Delta\sigma_f(^{245}\text{Cm})/\sigma_f(^{245}\text{Cm})$	uniform	$[-25, 25]$	%
$\Delta\sigma_c(^{133}\text{Cs})/\sigma_c(^{133}\text{Cs})$	uniform	$[-20, 20]$	%
$\Delta\sigma_c(^{134}\text{Cs})/\sigma_c(^{134}\text{Cs})$	uniform	$[-100, 100]$	%
$\Delta\sigma_c(^{147}\text{Pm})/\sigma_c(^{147}\text{Pm})$	uniform	$[-65, 65]$	%
$\Delta\sigma_c(^{152}\text{Sm})/\sigma_c(^{152}\text{Sm})$	uniform	$[-10, 10]$	%
$\Delta\sigma_c(^{153}\text{Eu})/\sigma_c(^{153}\text{Eu})$	uniform	$[-20, 20]$	%
$\Delta\sigma_c(^{154}\text{Eu})/\sigma_c(^{154}\text{Eu})$	uniform	$[-100, 100]$	%
$\tilde{f}(X \to Y)$ $X \in \{^{235,238}\text{U}, ^{238,239,240,241,242}\text{Pu}\}$ $Y \in \{^{84,85}\text{Kr}, ^{90}\text{Sr}, ^{95}\text{Zr}, ^{106}\text{Ru}, ^{132}\text{Te}, ^{133}\text{I}, ^{137}\text{Cs}, ^{144}\text{Ce}, ^{146,147}\text{Nd}, ^{151}\text{Pm}, ^{152,153}\text{Sm}\}$	uniform (98 parameters)	$[0.5, 1.5]$	1
^{238}U mass fraction	1-$\sum_i y_i$	$\varnothing$	1
irradiation length	TCT/P_{irrad}	$\varnothing$	d

Table A.11: PWR MOX, nominal burnup sampling distributions for ANN estimator

A.2.5 PWR repU fuel

parameter	distribution	support	unit
^{234}U mass fraction	uniform	$[0.00 \cdot 10^{-3}, 2.00 \cdot 10^{-3}]$	1
^{235}U mass fraction	uniform	$[4.00 \cdot 10^{-2}, 4.10 \cdot 10^{-2}]$	1
^{236}U mass fraction	uniform	$[1.00 \cdot 10^{-2}, 1.60 \cdot 10^{-2}]$	1
BU	exponential	$[10, 50]$	GWd/tHM
$\mathcal{P}_{irrad}$	uniform	$[29, 40]$	W/gHM
$\Delta\sigma_c(^{234}\text{U})/\sigma_c(^{234}\text{U})$	uniform	$[-9, 9]$	%
$\Delta\sigma_f(^{234}\text{U})/\sigma_f(^{234}\text{U})$	uniform	$[-60, 60]$	%
$\Delta\sigma_c(^{235}\text{U})/\sigma_c(^{235}\text{U})$	uniform	$[-5, 5]$	%
$\Delta\sigma_f(^{235}\text{U})/\sigma_f(^{235}\text{U})$	uniform	$[-1, 1]$	%
$\Delta\sigma_c(^{236}\text{U})/\sigma_c(^{236}\text{U})$	uniform	$[-12, 12]$	%
$\Delta\sigma_f(^{236}\text{U})/\sigma_f(^{236}\text{U})$	uniform	$[-70, 70]$	%
$\Delta\sigma_c(^{238}\text{U})/\sigma_c(^{238}\text{U})$	uniform	$[-2, 2]$	%
$\Delta\sigma_f(^{238}\text{U})/\sigma_f(^{238}\text{U})$	uniform	$[-5, 5]$	%
$\Delta\sigma_c(^{238}\text{Pu})/\sigma_c(^{238}\text{Pu})$	uniform	$[-15, 15]$	%
$\Delta\sigma_f(^{238}\text{Pu})/\sigma_f(^{238}\text{Pu})$	uniform	$[-9, 9]$	%
$\Delta\sigma_c(^{239}\text{Pu})/\sigma_c(^{239}\text{Pu})$	uniform	$[-30, 30]$	%
$\Delta\sigma_f(^{239}\text{Pu})/\sigma_f(^{239}\text{Pu})$	uniform	$[-1, 1]$	%
$\Delta\sigma_c(^{240}\text{Pu})/\sigma_c(^{240}\text{Pu})$	uniform	$[-5, 5]$	%
$\Delta\sigma_f(^{240}\text{Pu})/\sigma_f(^{240}\text{Pu})$	uniform	$[-3, 3]$	%
$\Delta\sigma_c(^{241}\text{Pu})/\sigma_c(^{241}\text{Pu})$	uniform	$[-5, 5]$	%
$\Delta\sigma_f(^{241}\text{Pu})/\sigma_f(^{241}\text{Pu})$	uniform	$[-7, 7]$	%
$\Delta\sigma_c(^{242}\text{Pu})/\sigma_c(^{242}\text{Pu})$	uniform	$[-35, 35]$	%
$\Delta\sigma_f(^{242}\text{Pu})/\sigma_f(^{242}\text{Pu})$	uniform	$[-6, 6]$	%
$\Delta\sigma_c(^{241}\text{Am})/\sigma_c(^{241}\text{Am})$	uniform	$[-15, 15]$	%
$\Delta\sigma_f(^{241}\text{Am})/\sigma_f(^{241}\text{Am})$	uniform	$[-15, 15]$	%
$\Delta\sigma_c(^{242M}\text{Am})/\sigma_c(^{242M}\text{Am})$	uniform	$[-70, 70]$	%
$\Delta\sigma_f(^{242M}\text{Am})/\sigma_f(^{242M}\text{Am})$	uniform	$[-15, 15]$	%
$\Delta\sigma_c(^{243}\text{Am})/\sigma_c(^{243}\text{Am})$	uniform	$[-40, 40]$	%
$\Delta\sigma_f(^{243}\text{Am})/\sigma_f(^{243}\text{Am})$	uniform	$[-30, 30]$	%
$\Delta\sigma_c(^{237}\text{Np})/\sigma_c(^{237}\text{Np})$	uniform	$[-15, 15]$	%
$\Delta\sigma_f(^{237}\text{Np})/\sigma_f(^{237}\text{Np})$	uniform	$[-9, 9]$	%
$\Delta\sigma_c(^{242}\text{Cm})/\sigma_c(^{242}\text{Cm})$	uniform	$[-45, 45]$	%
$\Delta\sigma_f(^{242}\text{Cm})/\sigma_f(^{242}\text{Cm})$	uniform	$[-15, 15]$	%
$\Delta\sigma_c(^{243}\text{Cm})/\sigma_c(^{243}\text{Cm})$	uniform	$[-90, 90]$	%
$\Delta\sigma_f(^{243}\text{Cm})/\sigma_f(^{243}\text{Cm})$	uniform	$[-20, 20]$	%
$\Delta\sigma_c(^{244}\text{Cm})/\sigma_c(^{244}\text{Cm})$	uniform	$[-25, 25]$	%
$\Delta\sigma_f(^{244}\text{Cm})/\sigma_f(^{244}\text{Cm})$	uniform	$[-15, 15]$	%
$\Delta\sigma_c(^{245}\text{Cm})/\sigma_c(^{245}\text{Cm})$	uniform	$[-60, 60]$	%
$\Delta\sigma_f(^{245}\text{Cm})/\sigma_f(^{245}\text{Cm})$	uniform	$[-25, 25]$	%
$\Delta\sigma_c(^{133}\text{Cs})/\sigma_c(^{133}\text{Cs})$	uniform	$[-15, 15]$	%
$\Delta\sigma_c(^{134}\text{Cs})/\sigma_c(^{134}\text{Cs})$	uniform	$[-100, 100]$	%
$\Delta\sigma_c(^{147}\text{Pm})/\sigma_c(^{147}\text{Pm})$	uniform	$[-60, 60]$	%
$\Delta\sigma_c(^{152}\text{Sm})/\sigma_c(^{152}\text{Sm})$	uniform	$[-10, 10]$	%
$\Delta\sigma_c(^{153}\text{Eu})/\sigma_c(^{153}\text{Eu})$	uniform	$[-15, 15]$	%
$\Delta\sigma_c(^{154}\text{Eu})/\sigma_c(^{154}\text{Eu})$	uniform	$[-100, 100]$	%
$\tilde{f}(X \to Y)$ $X \in \{^{235,238}\text{U}, ^{238,239,240,241,242}\text{Pu}\}$ $Y \in \{^{84,85}\text{Kr}, ^{90}\text{Sr}, ^{95}\text{Zr}, ^{106}\text{Ru}, ^{132}\text{Te}, ^{133}\text{I}, ^{137}\text{Cs}, ^{144}\text{Ce}, ^{146,147}\text{Nd}, ^{151}\text{Pm}, ^{152,153}\text{Sm}\}$	uniform (98 parameters)	$[0.5, 1.5]$	1
^{238}U mass fraction	1-$\sum_i y_i$	$\varnothing$	1
irradiation length	TCT/P_{irrad}	$\varnothing$	d

Table A.12: PWR repU sampling distributions for ANN estimator

A.2.6 SFR MOX fuel, low burnup

parameter	distribution	support	unit
^{234}U mass fraction	uniform	$[1.00 \cdot 10^{-4}, 4.60 \cdot 10^{-4}]$	1
^{235}U mass fraction	uniform	$[2.00 \cdot 10^{-3}, 8.00 \cdot 10^{-3}]$	1
^{238}Pu mass fraction	uniform	$[1.30 \cdot 10^{-3}, 1.00 \cdot 10^{-2}]$	1
^{239}Pu mass fraction	uniform	$[1.00 \cdot 10^{-1}, 1.40 \cdot 10^{-1}]$	1
^{240}Pu mass fraction	uniform	$[5.00 \cdot 10^{-2}, 8.50 \cdot 10^{-2}]$	1
^{241}Pu mass fraction	uniform	$[4.00 \cdot 10^{-3}, 2.00 \cdot 10^{-2}]$	1
^{242}Pu mass fraction	uniform	$[4.00 \cdot 10^{-3}, 3.00 \cdot 10^{-2}]$	1
^{241}Am mass fraction	uniform	$[1.00 \cdot 10^{-4}, 4.00 \cdot 10^{-3}]$	1
BU	exponential	$[10, 96]$	GWd/tHM
$\mathcal{P}_{irrad}$	uniform	$[45, 55]$	W/gHM
$\Delta\sigma_c(^{234}\text{U})/\sigma_c(^{234}\text{U})$	uniform	$[-30, 30]$	%
$\Delta\sigma_f(^{234}\text{U})/\sigma_f(^{234}\text{U})$	uniform	$[-180, 80]$	%
$\Delta\sigma_c(^{235}\text{U})/\sigma_c(^{235}\text{U})$	uniform	$[-60, 60]$	%
$\Delta\sigma_f(^{235}\text{U})/\sigma_f(^{235}\text{U})$	uniform	$[-2, 2]$	%
$\Delta\sigma_c(^{236}\text{U})/\sigma_c(^{236}\text{U})$	uniform	$[-12, 12]$	%
$\Delta\sigma_f(^{236}\text{U})/\sigma_f(^{236}\text{U})$	uniform	$[-70, 70]$	%
$\Delta\sigma_c(^{238}\text{U})/\sigma_c(^{238}\text{U})$	uniform	$[-5, 5]$	%
$\Delta\sigma_f(^{238}\text{U})/\sigma_f(^{238}\text{U})$	uniform	$[-1.5, 1.5]$	%
$\Delta\sigma_c(^{238}\text{Pu})/\sigma_c(^{238}\text{Pu})$	uniform	$[-25, 25]$	%
$\Delta\sigma_f(^{238}\text{Pu})/\sigma_f(^{238}\text{Pu})$	uniform	$[-1.5, 1.5]$	%
$\Delta\sigma_c(^{239}\text{Pu})/\sigma_c(^{239}\text{Pu})$	uniform	$[-16, 16]$	%
$\Delta\sigma_f(^{239}\text{Pu})/\sigma_f(^{239}\text{Pu})$	uniform	$[-1, 1]$	%
$\Delta\sigma_c(^{240}\text{Pu})/\sigma_c(^{240}\text{Pu})$	uniform	$[-10, 10]$	%
$\Delta\sigma_f(^{240}\text{Pu})/\sigma_f(^{240}\text{Pu})$	uniform	$[-4, 4]$	%
$\Delta\sigma_c(^{241}\text{Pu})/\sigma_c(^{241}\text{Pu})$	uniform	$[-35, 35]$	%
$\Delta\sigma_f(^{241}\text{Pu})/\sigma_f(^{241}\text{Pu})$	uniform	$[-3, 3]$	%
$\Delta\sigma_c(^{242}\text{Pu})/\sigma_c(^{242}\text{Pu})$	uniform	$[-15, 15]$	%
$\Delta\sigma_f(^{242}\text{Pu})/\sigma_f(^{242}\text{Pu})$	uniform	$[-6, 6]$	%
$\Delta\sigma_c(^{241}\text{Am})/\sigma_c(^{241}\text{Am})$	uniform	$[-6, 6]$	%
$\Delta\sigma_f(^{241}\text{Am})/\sigma_f(^{241}\text{Am})$	uniform	$[-5, 5]$	%
$\Delta\sigma_c(^{242M}\text{Am})/\sigma_c(^{242M}\text{Am})$	uniform	$[-70, 70]$	%
$\Delta\sigma_f(^{242M}\text{Am})/\sigma_f(^{242M}\text{Am})$	uniform	$[-30, 30]$	%
$\Delta\sigma_c(^{243}\text{Am})/\sigma_c(^{243}\text{Am})$	uniform	$[-30, 30]$	%
$\Delta\sigma_f(^{243}\text{Am})/\sigma_f(^{243}\text{Am})$	uniform	$[-15, 15]$	%
$\Delta\sigma_c(^{237}\text{Np})/\sigma_c(^{237}\text{Np})$	uniform	$[-30, 30]$	%
$\Delta\sigma_f(^{237}\text{Np})/\sigma_f(^{237}\text{Np})$	uniform	$[-10, 10]$	%
$\Delta\sigma_c(^{242}\text{Cm})/\sigma_c(^{242}\text{Cm})$	uniform	$[-65, 65]$	%
$\Delta\sigma_f(^{242}\text{Cm})/\sigma_f(^{242}\text{Cm})$	uniform	$[-20, 20]$	%
$\Delta\sigma_c(^{243}\text{Cm})/\sigma_c(^{243}\text{Cm})$	uniform	$[-90, 90]$	%
$\Delta\sigma_f(^{243}\text{Cm})/\sigma_f(^{243}\text{Cm})$	uniform	$[-12, 12]$	%
$\Delta\sigma_c(^{244}\text{Cm})/\sigma_c(^{244}\text{Cm})$	uniform	$[-70, 70]$	%
$\Delta\sigma_f(^{244}\text{Cm})/\sigma_f(^{244}\text{Cm})$	uniform	$[-10, 10]$	%
$\Delta\sigma_c(^{245}\text{Cm})/\sigma_c(^{245}\text{Cm})$	uniform	$[-90, 90]$	%
$\Delta\sigma_f(^{245}\text{Cm})/\sigma_f(^{245}\text{Cm})$	uniform	$[-10, 10]$	%
$\Delta\sigma_c(^{133}\text{Cs})/\sigma_c(^{133}\text{Cs})$	uniform	$[-50, 50]$	%
$\Delta\sigma_c(^{134}\text{Cs})/\sigma_c(^{134}\text{Cs})$	uniform	$[-100, 100]$	%
$\Delta\sigma_c(^{147}\text{Pm})/\sigma_c(^{147}\text{Pm})$	uniform	$[-60, 60]$	%
$\Delta\sigma_c(^{152}\text{Sm})/\sigma_c(^{152}\text{Sm})$	uniform	$[-50, 50]$	%
$\Delta\sigma_c(^{153}\text{Eu})/\sigma_c(^{153}\text{Eu})$	uniform	$[-50, 50]$	%
$\Delta\sigma_c(^{154}\text{Eu})/\sigma_c(^{154}\text{Eu})$	uniform	$[-100, 100]$	%
$\tilde{f}(X \to Y)$ $X \in \{^{235,238}\text{U}, ^{238,239,240,241,242}\text{Pu}\}$ $Y \in \{^{84,85}\text{Kr}, ^{90}\text{Sr}, ^{95}\text{Zr}, ^{106}\text{Ru}, ^{132}\text{Te}, ^{133}\text{I}, ^{137}\text{Cs}, ^{144}\text{Ce}, ^{146,147}\text{Nd}, ^{151}\text{Pm}, ^{152,153}\text{Sm}\}$	uniform (98 parameters)	$[0.5, 1.5]$	1
^{238}U mass fraction	1-$\sum_i y_i$	$\varnothing$	1
irradiation length	TCT/P_{irrad}	$\varnothing$	d

Table A.13: SFR MOX, low burnup sampling distributions for ANN estimator

A.2.7 SFR MOX fuel, nominal burnup

parameter	distribution	support	unit
^{234}U mass fraction	uniform	$[1.00 \cdot 10^{-4}, 4.60 \cdot 10^{-4}]$	1
^{235}U mass fraction	uniform	$[2.00 \cdot 10^{-3}, 8.00 \cdot 10^{-3}]$	1
^{238}Pu mass fraction	uniform	$[1.30 \cdot 10^{-3}, 1.00 \cdot 10^{-2}]$	1
^{239}Pu mass fraction	uniform	$[1.00 \cdot 10^{-1}, 1.40 \cdot 10^{-1}]$	1
^{240}Pu mass fraction	uniform	$[5.00 \cdot 10^{-2}, 8.50 \cdot 10^{-2}]$	1
^{241}Pu mass fraction	uniform	$[4.00 \cdot 10^{-3}, 2.00 \cdot 10^{-2}]$	1
^{242}Pu mass fraction	uniform	$[4.00 \cdot 10^{-3}, 3.00 \cdot 10^{-2}]$	1
^{241}Am mass fraction	uniform	$[1.00 \cdot 10^{-4}, 4.00 \cdot 10^{-3}]$	1
BU	uniform	$[107, 126]$	GWd/tHM
$\mathcal{P}_{irrad}$	uniform	$[45, 55]$	W/gHM
$\Delta\sigma_c(^{234}\text{U})/\sigma_c(^{234}\text{U})$	uniform	$[-30, 30]$	%
$\Delta\sigma_f(^{234}\text{U})/\sigma_f(^{234}\text{U})$	uniform	$[-180, 80]$	%
$\Delta\sigma_c(^{235}\text{U})/\sigma_c(^{235}\text{U})$	uniform	$[-60, 60]$	%
$\Delta\sigma_f(^{235}\text{U})/\sigma_f(^{235}\text{U})$	uniform	$[-2, 2]$	%
$\Delta\sigma_c(^{236}\text{U})/\sigma_c(^{236}\text{U})$	uniform	$[-12, 12]$	%
$\Delta\sigma_f(^{236}\text{U})/\sigma_f(^{236}\text{U})$	uniform	$[-70, 70]$	%
$\Delta\sigma_c(^{238}\text{U})/\sigma_c(^{238}\text{U})$	uniform	$[-5, 5]$	%
$\Delta\sigma_f(^{238}\text{U})/\sigma_f(^{238}\text{U})$	uniform	$[-1.5, 1.5]$	%
$\Delta\sigma_c(^{238}\text{Pu})/\sigma_c(^{238}\text{Pu})$	uniform	$[-25, 25]$	%
$\Delta\sigma_f(^{238}\text{Pu})/\sigma_f(^{238}\text{Pu})$	uniform	$[-1.5, 1.5]$	%
$\Delta\sigma_c(^{239}\text{Pu})/\sigma_c(^{239}\text{Pu})$	uniform	$[-16, 16]$	%
$\Delta\sigma_f(^{239}\text{Pu})/\sigma_f(^{239}\text{Pu})$	uniform	$[-1, 1]$	%
$\Delta\sigma_c(^{240}\text{Pu})/\sigma_c(^{240}\text{Pu})$	uniform	$[-10, 10]$	%
$\Delta\sigma_f(^{240}\text{Pu})/\sigma_f(^{240}\text{Pu})$	uniform	$[-4, 4]$	%
$\Delta\sigma_c(^{241}\text{Pu})/\sigma_c(^{241}\text{Pu})$	uniform	$[-35, 35]$	%
$\Delta\sigma_f(^{241}\text{Pu})/\sigma_f(^{241}\text{Pu})$	uniform	$[-3, 3]$	%
$\Delta\sigma_c(^{242}\text{Pu})/\sigma_c(^{242}\text{Pu})$	uniform	$[-15, 15]$	%
$\Delta\sigma_f(^{242}\text{Pu})/\sigma_f(^{242}\text{Pu})$	uniform	$[-6, 6]$	%
$\Delta\sigma_c(^{241}\text{Am})/\sigma_c(^{241}\text{Am})$	uniform	$[-6, 6]$	%
$\Delta\sigma_f(^{241}\text{Am})/\sigma_f(^{241}\text{Am})$	uniform	$[-5, 5]$	%
$\Delta\sigma_c(^{242M}\text{Am})/\sigma_c(^{242M}\text{Am})$	uniform	$[-70, 70]$	%
$\Delta\sigma_f(^{242M}\text{Am})/\sigma_f(^{242M}\text{Am})$	uniform	$[-30, 30]$	%
$\Delta\sigma_c(^{243}\text{Am})/\sigma_c(^{243}\text{Am})$	uniform	$[-30, 30]$	%
$\Delta\sigma_f(^{243}\text{Am})/\sigma_f(^{243}\text{Am})$	uniform	$[-15, 15]$	%
$\Delta\sigma_c(^{237}\text{Np})/\sigma_c(^{237}\text{Np})$	uniform	$[-30, 30]$	%
$\Delta\sigma_f(^{237}\text{Np})/\sigma_f(^{237}\text{Np})$	uniform	$[-10, 10]$	%
$\Delta\sigma_c(^{242}\text{Cm})/\sigma_c(^{242}\text{Cm})$	uniform	$[-65, 65]$	%
$\Delta\sigma_f(^{242}\text{Cm})/\sigma_f(^{242}\text{Cm})$	uniform	$[-20, 20]$	%
$\Delta\sigma_c(^{243}\text{Cm})/\sigma_c(^{243}\text{Cm})$	uniform	$[-90, 90]$	%
$\Delta\sigma_f(^{243}\text{Cm})/\sigma_f(^{243}\text{Cm})$	uniform	$[-12, 12]$	%
$\Delta\sigma_c(^{244}\text{Cm})/\sigma_c(^{244}\text{Cm})$	uniform	$[-70, 70]$	%
$\Delta\sigma_f(^{244}\text{Cm})/\sigma_f(^{244}\text{Cm})$	uniform	$[-10, 10]$	%
$\Delta\sigma_c(^{245}\text{Cm})/\sigma_c(^{245}\text{Cm})$	uniform	$[-90, 90]$	%
$\Delta\sigma_f(^{245}\text{Cm})/\sigma_f(^{245}\text{Cm})$	uniform	$[-10, 10]$	%
$\Delta\sigma_c(^{133}\text{Cs})/\sigma_c(^{133}\text{Cs})$	uniform	$[-50, 50]$	%
$\Delta\sigma_c(^{134}\text{Cs})/\sigma_c(^{134}\text{Cs})$	uniform	$[-100, 100]$	%
$\Delta\sigma_c(^{147}\text{Pm})/\sigma_c(^{147}\text{Pm})$	uniform	$[-60, 60]$	%
$\Delta\sigma_c(^{152}\text{Sm})/\sigma_c(^{152}\text{Sm})$	uniform	$[-50, 50]$	%
$\Delta\sigma_c(^{153}\text{Eu})/\sigma_c(^{153}\text{Eu})$	uniform	$[-50, 50]$	%
$\Delta\sigma_c(^{154}\text{Eu})/\sigma_c(^{154}\text{Eu})$	uniform	$[-100, 100]$	%
$\tilde{f}(X \to Y)$ $X \in \{^{235,238}\text{U}, ^{238,239,240,241,242}\text{Pu}\}$ $Y \in \{^{84,85}\text{Kr}, ^{90}\text{Sr}, ^{95}\text{Zr}, ^{106}\text{Ru}, ^{132}\text{Te}, ^{133}\text{I}, ^{137}\text{Cs}, ^{144}\text{Ce}, ^{146,147}\text{Nd}, ^{151}\text{Pm}, ^{152,153}\text{Sm}\}$	uniform (98 parameters)	$[0.5, 1.5]$	1
^{238}U mass fraction	1-$\sum_i y_i$	$\varnothing$	1
irradiation length	TCT/P_{irrad}	$\varnothing$	d

Table A.14: SFR MOX, nominal burnup sampling distributions for ANN estimator

A.2.8 SFR internal blanket

parameter	distribution	support	unit
BU	uniform	$[10, 60]$	GWd/tHM
$\mathcal{P}_{irrad}$	uniform	$[21, 24]$	W/gHM
$\Delta\sigma_c(^{234}\mathrm{U})/\sigma_c(^{234}\mathrm{U})$	uniform	$[-30, 30]$	%
$\Delta\sigma_f(^{234}\mathrm{U})/\sigma_f(^{234}\mathrm{U})$	uniform	$[-180, 80]$	%
$\Delta\sigma_c(^{235}\mathrm{U})/\sigma_c(^{235}\mathrm{U})$	uniform	$[-60, 60]$	%
$\Delta\sigma_f(^{235}\mathrm{U})/\sigma_f(^{235}\mathrm{U})$	uniform	$[-2, 2]$	%
$\Delta\sigma_c(^{236}\mathrm{U})/\sigma_c(^{236}\mathrm{U})$	uniform	$[-12, 12]$	%
$\Delta\sigma_f(^{236}\mathrm{U})/\sigma_f(^{236}\mathrm{U})$	uniform	$[-70, 70]$	%
$\Delta\sigma_c(^{238}\mathrm{U})/\sigma_c(^{238}\mathrm{U})$	uniform	$[-5, 5]$	%
$\Delta\sigma_f(^{238}\mathrm{U})/\sigma_f(^{238}\mathrm{U})$	uniform	$[-1.5, 1.5]$	%
$\Delta\sigma_c(^{238}\mathrm{Pu})/\sigma_c(^{238}\mathrm{Pu})$	uniform	$[-25, 25]$	%
$\Delta\sigma_f(^{238}\mathrm{Pu})/\sigma_f(^{238}\mathrm{Pu})$	uniform	$[-1.5, 1.5]$	%
$\Delta\sigma_c(^{239}\mathrm{Pu})/\sigma_c(^{239}\mathrm{Pu})$	uniform	$[-16, 16]$	%
$\Delta\sigma_f(^{239}\mathrm{Pu})/\sigma_f(^{239}\mathrm{Pu})$	uniform	$[-1, 1]$	%
$\Delta\sigma_c(^{240}\mathrm{Pu})/\sigma_c(^{240}\mathrm{Pu})$	uniform	$[-10, 10]$	%
$\Delta\sigma_f(^{240}\mathrm{Pu})/\sigma_f(^{240}\mathrm{Pu})$	uniform	$[-4, 4]$	%
$\Delta\sigma_c(^{241}\mathrm{Pu})/\sigma_c(^{241}\mathrm{Pu})$	uniform	$[-35, 35]$	%
$\Delta\sigma_f(^{241}\mathrm{Pu})/\sigma_f(^{241}\mathrm{Pu})$	uniform	$[-3, 3]$	%
$\Delta\sigma_c(^{242}\mathrm{Pu})/\sigma_c(^{242}\mathrm{Pu})$	uniform	$[-15, 15]$	%
$\Delta\sigma_f(^{242}\mathrm{Pu})/\sigma_f(^{242}\mathrm{Pu})$	uniform	$[-6, 6]$	%
$\Delta\sigma_c(^{241}\mathrm{Am})/\sigma_c(^{241}\mathrm{Am})$	uniform	$[-6, 6]$	%
$\Delta\sigma_f(^{241}\mathrm{Am})/\sigma_f(^{241}\mathrm{Am})$	uniform	$[-5, 5]$	%
$\Delta\sigma_c(^{242M}\mathrm{Am})/\sigma_c(^{242M}\mathrm{Am})$	uniform	$[-70, 70]$	%
$\Delta\sigma_f(^{242M}\mathrm{Am})/\sigma_f(^{242M}\mathrm{Am})$	uniform	$[-30, 30]$	%
$\Delta\sigma_c(^{243}\mathrm{Am})/\sigma_c(^{243}\mathrm{Am})$	uniform	$[-30, 30]$	%
$\Delta\sigma_f(^{243}\mathrm{Am})/\sigma_f(^{243}\mathrm{Am})$	uniform	$[-15, 15]$	%
$\Delta\sigma_c(^{237}\mathrm{Np})/\sigma_c(^{237}\mathrm{Np})$	uniform	$[-30, 30]$	%
$\Delta\sigma_f(^{237}\mathrm{Np})/\sigma_f(^{237}\mathrm{Np})$	uniform	$[-10, 10]$	%
$\Delta\sigma_c(^{242}\mathrm{Cm})/\sigma_c(^{242}\mathrm{Cm})$	uniform	$[-65, 65]$	%
$\Delta\sigma_f(^{242}\mathrm{Cm})/\sigma_f(^{242}\mathrm{Cm})$	uniform	$[-20, 20]$	%
$\Delta\sigma_c(^{243}\mathrm{Cm})/\sigma_c(^{243}\mathrm{Cm})$	uniform	$[-90, 90]$	%
$\Delta\sigma_f(^{243}\mathrm{Cm})/\sigma_f(^{243}\mathrm{Cm})$	uniform	$[-12, 12]$	%
$\Delta\sigma_c(^{244}\mathrm{Cm})/\sigma_c(^{244}\mathrm{Cm})$	uniform	$[-70, 70]$	%
$\Delta\sigma_f(^{244}\mathrm{Cm})/\sigma_f(^{244}\mathrm{Cm})$	uniform	$[-10, 10]$	%
$\Delta\sigma_c(^{245}\mathrm{Cm})/\sigma_c(^{245}\mathrm{Cm})$	uniform	$[-90, 90]$	%
$\Delta\sigma_f(^{245}\mathrm{Cm})/\sigma_f(^{245}\mathrm{Cm})$	uniform	$[-10, 10]$	%
$\Delta\sigma_c(^{133}\mathrm{Cs})/\sigma_c(^{133}\mathrm{Cs})$	uniform	$[-50, 50]$	%
$\Delta\sigma_c(^{134}\mathrm{Cs})/\sigma_c(^{134}\mathrm{Cs})$	uniform	$[-100, 100]$	%
$\Delta\sigma_c(^{147}\mathrm{Pm})/\sigma_c(^{147}\mathrm{Pm})$	uniform	$[-60, 60]$	%
$\Delta\sigma_c(^{152}\mathrm{Sm})/\sigma_c(^{152}\mathrm{Sm})$	uniform	$[-50, 50]$	%
$\Delta\sigma_c(^{153}\mathrm{Eu})/\sigma_c(^{153}\mathrm{Eu})$	uniform	$[-50, 50]$	%
$\Delta\sigma_c(^{154}\mathrm{Eu})/\sigma_c(^{154}\mathrm{Eu})$	uniform	$[-100, 100]$	%
$\tilde{f}(X \to Y)$ $X \in \{^{235,238}\mathrm{U}, ^{238,239,240,241,242}\mathrm{Pu}\}$ $Y \in \{^{84,85}\mathrm{Kr}, ^{90}\mathrm{Sr}, ^{95}\mathrm{Zr}, ^{106}\mathrm{Ru}, ^{132}\mathrm{Te}, ^{133}\mathrm{I}, ^{137}\mathrm{Cs}, ^{144}\mathrm{Ce}, ^{146,147}\mathrm{Nd}, ^{151}\mathrm{Pm}, ^{152,153}\mathrm{Sm}\}$	uniform (98 parameters)	$[0.5, 1.5]$	1
irradiation length	TCT/P_{irrad}	$\varnothing$	d

Table A.15: SFR internal blanket sampling distributions for ANN estimator

A.2.9 SFR inferior blanket

parameter	distribution	support	unit
BU	uniform	$[0, 13.9]$	GWd/tHM
$\mathcal{P}_{irrad}$	uniform	$[5.0, 5.9]$	W/gHM
$\Delta\sigma_c(^{234}\mathrm{U})/\sigma_c(^{234}\mathrm{U})$	uniform	$[-30, 30]$	%
$\Delta\sigma_f(^{234}\mathrm{U})/\sigma_f(^{234}\mathrm{U})$	uniform	$[-180, 80]$	%
$\Delta\sigma_c(^{235}\mathrm{U})/\sigma_c(^{235}\mathrm{U})$	uniform	$[-60, 60]$	%
$\Delta\sigma_f(^{235}\mathrm{U})/\sigma_f(^{235}\mathrm{U})$	uniform	$[-2, 2]$	%
$\Delta\sigma_c(^{236}\mathrm{U})/\sigma_c(^{236}\mathrm{U})$	uniform	$[-12, 12]$	%
$\Delta\sigma_f(^{236}\mathrm{U})/\sigma_f(^{236}\mathrm{U})$	uniform	$[-70, 70]$	%
$\Delta\sigma_c(^{238}\mathrm{U})/\sigma_c(^{238}\mathrm{U})$	uniform	$[-5, 5]$	%
$\Delta\sigma_f(^{238}\mathrm{U})/\sigma_f(^{238}\mathrm{U})$	uniform	$[-1.5, 1.5]$	%
$\Delta\sigma_c(^{238}\mathrm{Pu})/\sigma_c(^{238}\mathrm{Pu})$	uniform	$[-25, 25]$	%
$\Delta\sigma_f(^{238}\mathrm{Pu})/\sigma_f(^{238}\mathrm{Pu})$	uniform	$[-1.5, 1.5]$	%
$\Delta\sigma_c(^{239}\mathrm{Pu})/\sigma_c(^{239}\mathrm{Pu})$	uniform	$[-16, 16]$	%
$\Delta\sigma_f(^{239}\mathrm{Pu})/\sigma_f(^{239}\mathrm{Pu})$	uniform	$[-1, 1]$	%
$\Delta\sigma_c(^{240}\mathrm{Pu})/\sigma_c(^{240}\mathrm{Pu})$	uniform	$[-10, 10]$	%
$\Delta\sigma_f(^{240}\mathrm{Pu})/\sigma_f(^{240}\mathrm{Pu})$	uniform	$[-4, 4]$	%
$\Delta\sigma_c(^{241}\mathrm{Pu})/\sigma_c(^{241}\mathrm{Pu})$	uniform	$[-35, 35]$	%
$\Delta\sigma_f(^{241}\mathrm{Pu})/\sigma_f(^{241}\mathrm{Pu})$	uniform	$[-3, 3]$	%
$\Delta\sigma_c(^{242}\mathrm{Pu})/\sigma_c(^{242}\mathrm{Pu})$	uniform	$[-15, 15]$	%
$\Delta\sigma_f(^{242}\mathrm{Pu})/\sigma_f(^{242}\mathrm{Pu})$	uniform	$[-6, 6]$	%
$\Delta\sigma_c(^{241}\mathrm{Am})/\sigma_c(^{241}\mathrm{Am})$	uniform	$[-6, 6]$	%
$\Delta\sigma_f(^{241}\mathrm{Am})/\sigma_f(^{241}\mathrm{Am})$	uniform	$[-5, 5]$	%
$\Delta\sigma_c(^{242M}\mathrm{Am})/\sigma_c(^{242M}\mathrm{Am})$	uniform	$[-70, 70]$	%
$\Delta\sigma_f(^{242M}\mathrm{Am})/\sigma_f(^{242M}\mathrm{Am})$	uniform	$[-30, 30]$	%
$\Delta\sigma_c(^{243}\mathrm{Am})/\sigma_c(^{243}\mathrm{Am})$	uniform	$[-30, 30]$	%
$\Delta\sigma_f(^{243}\mathrm{Am})/\sigma_f(^{243}\mathrm{Am})$	uniform	$[-15, 15]$	%
$\Delta\sigma_c(^{237}\mathrm{Np})/\sigma_c(^{237}\mathrm{Np})$	uniform	$[-30, 30]$	%
$\Delta\sigma_f(^{237}\mathrm{Np})/\sigma_f(^{237}\mathrm{Np})$	uniform	$[-10, 10]$	%
$\Delta\sigma_c(^{242}\mathrm{Cm})/\sigma_c(^{242}\mathrm{Cm})$	uniform	$[-65, 65]$	%
$\Delta\sigma_f(^{242}\mathrm{Cm})/\sigma_f(^{242}\mathrm{Cm})$	uniform	$[-20, 20]$	%
$\Delta\sigma_c(^{243}\mathrm{Cm})/\sigma_c(^{243}\mathrm{Cm})$	uniform	$[-90, 90]$	%
$\Delta\sigma_f(^{243}\mathrm{Cm})/\sigma_f(^{243}\mathrm{Cm})$	uniform	$[-12, 12]$	%
$\Delta\sigma_c(^{244}\mathrm{Cm})/\sigma_c(^{244}\mathrm{Cm})$	uniform	$[-70, 70]$	%
$\Delta\sigma_f(^{244}\mathrm{Cm})/\sigma_f(^{244}\mathrm{Cm})$	uniform	$[-10, 10]$	%
$\Delta\sigma_c(^{245}\mathrm{Cm})/\sigma_c(^{245}\mathrm{Cm})$	uniform	$[-90, 90]$	%
$\Delta\sigma_f(^{245}\mathrm{Cm})/\sigma_f(^{245}\mathrm{Cm})$	uniform	$[-10, 10]$	%
$\Delta\sigma_c(^{133}\mathrm{Cs})/\sigma_c(^{133}\mathrm{Cs})$	uniform	$[-50, 50]$	%
$\Delta\sigma_c(^{134}\mathrm{Cs})/\sigma_c(^{134}\mathrm{Cs})$	uniform	$[-100, 100]$	%
$\Delta\sigma_c(^{147}\mathrm{Pm})/\sigma_c(^{147}\mathrm{Pm})$	uniform	$[-60, 60]$	%
$\Delta\sigma_c(^{152}\mathrm{Sm})/\sigma_c(^{152}\mathrm{Sm})$	uniform	$[-50, 50]$	%
$\Delta\sigma_c(^{153}\mathrm{Eu})/\sigma_c(^{153}\mathrm{Eu})$	uniform	$[-50, 50]$	%
$\Delta\sigma_c(^{154}\mathrm{Eu})/\sigma_c(^{154}\mathrm{Eu})$	uniform	$[-100, 100]$	%
$\tilde{f}(X \to Y)$ $X \in \{^{235,238}\mathrm{U}, ^{238,239,240,241,242}\mathrm{Pu}\}$ $Y \in \{^{84,85}\mathrm{Kr}, ^{90}\mathrm{Sr}, ^{95}\mathrm{Zr}, ^{106}\mathrm{Ru}, ^{132}\mathrm{Te}, ^{133}\mathrm{I}, ^{137}\mathrm{Cs}, ^{144}\mathrm{Ce}, ^{146,147}\mathrm{Nd}, ^{151}\mathrm{Pm}, ^{152,153}\mathrm{Sm}\}$	uniform (98 parameters)	$[0.5, 1.5]$	1
irradiation length	TCT/P_{irrad}	$\varnothing$	d

Table A.16: SFR inferior blanket sampling distributions for ANN estimator

A.2.10 SFR americium bearing blanket

parameter	distribution	support	unit
^{237}Np mass fraction	uniform	$[3.00 \cdot 10^{-4}, 8.00 \cdot 10^{-4}]$	1
^{238}Pu mass fraction	uniform	$[1.00 \cdot 10^{-6}, 1.00 \cdot 10^{-4}]$	1
^{239}Pu mass fraction	uniform	$[1.00 \cdot 10^{-6}, 1.50 \cdot 10^{-5}]$	1
^{242}Pu mass fraction	uniform	$[1.00 \cdot 10^{-7}, 1.50 \cdot 10^{-5}]$	1
^{241}Am mass fraction	uniform	$[6.00 \cdot 10^{-2}, 8.50 \cdot 10^{-2}]$	1
^{242M}Am mass fraction	uniform	$[1.00 \cdot 10^{-4}, 4.00 \cdot 10^{-4}]$	1
^{243}Am mass fraction	uniform	$[1.50 \cdot 10^{-2}, 3.00 \cdot 10^{-2}]$	1
^{242}Cm mass fraction	uniform	$[1.00 \cdot 10^{-7}, 1.00 \cdot 10^{-5}]$	1
BU	uniform	$[9.0, 10.5]$	GWd/tHM
$\mathcal{P}_{irrad}$	uniform	$[3.8, 4.4]$	W/gHM
$\Delta\sigma_c(^{234}\text{U})/\sigma_c(^{234}\text{U})$	uniform	$[-30, 30]$	%
$\Delta\sigma_f(^{234}\text{U})/\sigma_f(^{234}\text{U})$	uniform	$[-180, 80]$	%
$\Delta\sigma_c(^{235}\text{U})/\sigma_c(^{235}\text{U})$	uniform	$[-60, 60]$	%
$\Delta\sigma_f(^{235}\text{U})/\sigma_f(^{235}\text{U})$	uniform	$[-2, 2]$	%
$\Delta\sigma_c(^{236}\text{U})/\sigma_c(^{236}\text{U})$	uniform	$[-12, 12]$	%
$\Delta\sigma_f(^{236}\text{U})/\sigma_f(^{236}\text{U})$	uniform	$[-70, 70]$	%
$\Delta\sigma_c(^{238}\text{U})/\sigma_c(^{238}\text{U})$	uniform	$[-5, 5]$	%
$\Delta\sigma_f(^{238}\text{U})/\sigma_f(^{238}\text{U})$	uniform	$[-1.5, 1.5]$	%
$\Delta\sigma_c(^{238}\text{Pu})/\sigma_c(^{238}\text{Pu})$	uniform	$[-25, 25]$	%
$\Delta\sigma_f(^{238}\text{Pu})/\sigma_f(^{238}\text{Pu})$	uniform	$[-1.5, 1.5]$	%
$\Delta\sigma_c(^{239}\text{Pu})/\sigma_c(^{239}\text{Pu})$	uniform	$[-16, 16]$	%
$\Delta\sigma_f(^{239}\text{Pu})/\sigma_f(^{239}\text{Pu})$	uniform	$[-1, 1]$	%
$\Delta\sigma_c(^{240}\text{Pu})/\sigma_c(^{240}\text{Pu})$	uniform	$[-10, 10]$	%
$\Delta\sigma_f(^{240}\text{Pu})/\sigma_f(^{240}\text{Pu})$	uniform	$[-4, 4]$	%
$\Delta\sigma_c(^{241}\text{Pu})/\sigma_c(^{241}\text{Pu})$	uniform	$[-35, 35]$	%
$\Delta\sigma_f(^{241}\text{Pu})/\sigma_f(^{241}\text{Pu})$	uniform	$[-3, 3]$	%
$\Delta\sigma_c(^{242}\text{Pu})/\sigma_c(^{242}\text{Pu})$	uniform	$[-15, 15]$	%
$\Delta\sigma_f(^{242}\text{Pu})/\sigma_f(^{242}\text{Pu})$	uniform	$[-6, 6]$	%
$\Delta\sigma_c(^{241}\text{Am})/\sigma_c(^{241}\text{Am})$	uniform	$[-6, 6]$	%
$\Delta\sigma_f(^{241}\text{Am})/\sigma_f(^{241}\text{Am})$	uniform	$[-5, 5]$	%
$\Delta\sigma_c(^{242M}\text{Am})/\sigma_c(^{242M}\text{Am})$	uniform	$[-70, 70]$	%
$\Delta\sigma_f(^{242M}\text{Am})/\sigma_f(^{242M}\text{Am})$	uniform	$[-30, 30]$	%
$\Delta\sigma_c(^{243}\text{Am})/\sigma_c(^{243}\text{Am})$	uniform	$[-30, 30]$	%
$\Delta\sigma_f(^{243}\text{Am})/\sigma_f(^{243}\text{Am})$	uniform	$[-15, 15]$	%
$\Delta\sigma_c(^{237}\text{Np})/\sigma_c(^{237}\text{Np})$	uniform	$[-30, 30]$	%
$\Delta\sigma_f(^{237}\text{Np})/\sigma_f(^{237}\text{Np})$	uniform	$[-10, 10]$	%
$\Delta\sigma_c(^{242}\text{Cm})/\sigma_c(^{242}\text{Cm})$	uniform	$[-65, 65]$	%
$\Delta\sigma_f(^{242}\text{Cm})/\sigma_f(^{242}\text{Cm})$	uniform	$[-20, 20]$	%
$\Delta\sigma_c(^{243}\text{Cm})/\sigma_c(^{243}\text{Cm})$	uniform	$[-90, 90]$	%
$\Delta\sigma_f(^{243}\text{Cm})/\sigma_f(^{243}\text{Cm})$	uniform	$[-12, 12]$	%
$\Delta\sigma_c(^{244}\text{Cm})/\sigma_c(^{244}\text{Cm})$	uniform	$[-70, 70]$	%
$\Delta\sigma_f(^{244}\text{Cm})/\sigma_f(^{244}\text{Cm})$	uniform	$[-10, 10]$	%
$\Delta\sigma_c(^{245}\text{Cm})/\sigma_c(^{245}\text{Cm})$	uniform	$[-90, 90]$	%
$\Delta\sigma_f(^{245}\text{Cm})/\sigma_f(^{245}\text{Cm})$	uniform	$[-10, 10]$	%
$\Delta\sigma_c(^{133}\text{Cs})/\sigma_c(^{133}\text{Cs})$	uniform	$[-50, 50]$	%
$\Delta\sigma_c(^{134}\text{Cs})/\sigma_c(^{134}\text{Cs})$	uniform	$[-100, 100]$	%
$\Delta\sigma_c(^{147}\text{Pm})/\sigma_c(^{147}\text{Pm})$	uniform	$[-60, 60]$	%
$\Delta\sigma_c(^{152}\text{Sm})/\sigma_c(^{152}\text{Sm})$	uniform	$[-50, 50]$	%
$\Delta\sigma_c(^{153}\text{Eu})/\sigma_c(^{153}\text{Eu})$	uniform	$[-50, 50]$	%
$\Delta\sigma_c(^{154}\text{Eu})/\sigma_c(^{154}\text{Eu})$	uniform	$[-100, 100]$	%
$\tilde{f}(X \to Y)$ $X \in \{^{235,238}\text{U}, ^{238,239,240,241,242}\text{Pu}\}$ $Y \in \{^{84,85}\text{Kr}, ^{90}\text{Sr}, ^{95}\text{Zr}, ^{106}\text{Ru}, ^{132}\text{Te}, ^{133}\text{I}, ^{137}\text{Cs}, ^{144}\text{Ce}, ^{146,147}\text{Nd}, ^{151}\text{Pm}, ^{152,153}\text{Sm}\}$	uniform (98 parameters)	$[0.5, 1.5]$	1
^{238}U mass fraction	1-$\sum_i y_i$	$\varnothing$	1
irradiation length	TCT/P_{irrad}	$\varnothing$	d

Table A.17: SFR americium bearing blanket sampling distributions for ANN estimator

Appendix B

Surrogate models: quality indices

Contents

B.1 Polynomial regressions quality indices 304
B.1.1 PWR UOX fuel, low burnup, ^{240}Pu estimator 304
B.1.2 PWR UOX fuel, nominal burnup, ^{239}Pu estimator 305
B.1.3 PWR repU fuel, ^{239}Pu estimator 306
B.1.4 PWR MOX fuel, low burnup, ^{241}Am estimator 307
B.1.5 PWR MOX fuel, nominal burnup, ^{241}Am estimator 308
B.1.6 SFR MOX fuel, low burnup, ^{239}Pu estimator 309
B.2 ANN quality indices 310
B.2.1 PWR UOX fuel, low burnup, ^{244}Cm estimator 310
B.2.2 PWR MOX fuel, nominal burnup, ^{241}Am estimator 311

B.1 Polynomial regressions quality indices

B.1.1 PWR UOX fuel, low burnup, ^{240}Pu estimator

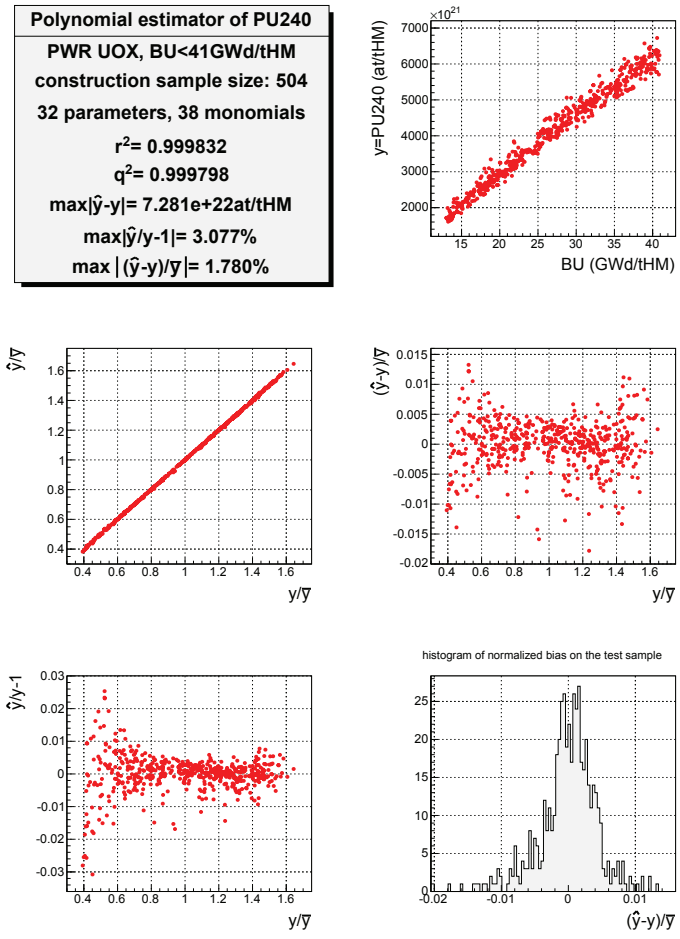

Figure B.1: Identity card of the ^{240}Pu polynomial estimator in PWR UOX fuel, BU<41GWd/tHM

The quality of this ^{240}Pu estimator (figure B.1) is relatively satistying. The maximum of the relative error is high (3.08%), however the bottom-left box shows that this maximum occurs for low ^{240}Pu concentrations. The absolute bias is more or less constant in function of the burnup, with the exception of extremal values, and is usually below 0.5%. This estimator is suited to uncertainty propagation.

B.1.2 PWR UOX fuel, nominal burnup, ^{239}Pu estimator

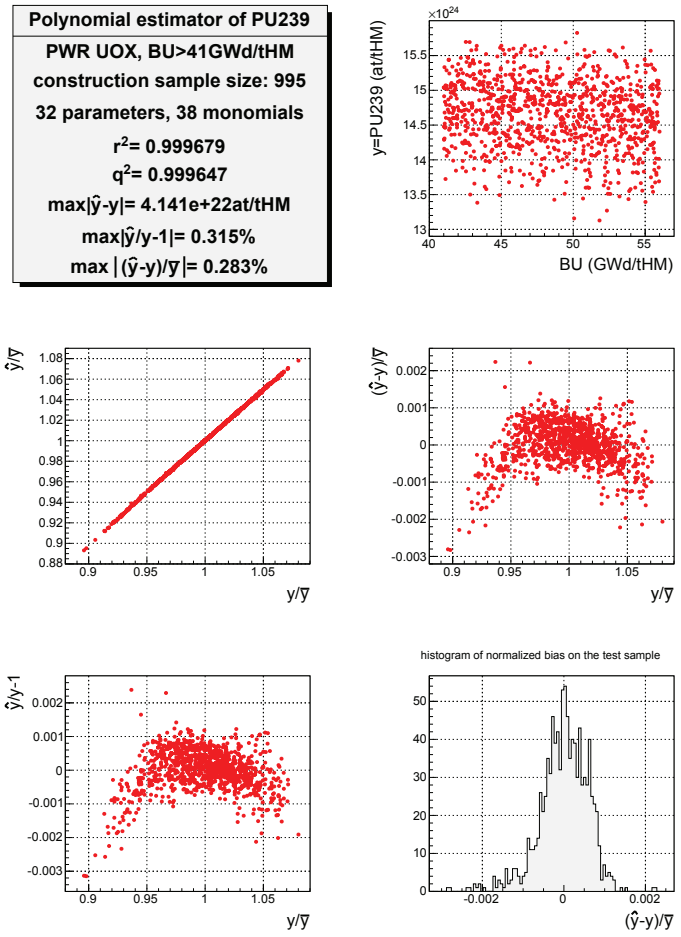

Figure B.2: Identity card of the ^{239}Pu polynomial estimator in PWR UOX fuel, BU$\geq$41GWd/tHM

The quality of this ^{239}Pu estimator (figure B.2) is satisfying. The maximum of relative error is low (0.315%), and the bias usually is inferior to 0.1% of the mean value. This estimator is well suited to uncertainty propagation.

B.1.3 PWR repU fuel, ^{239}Pu estimator

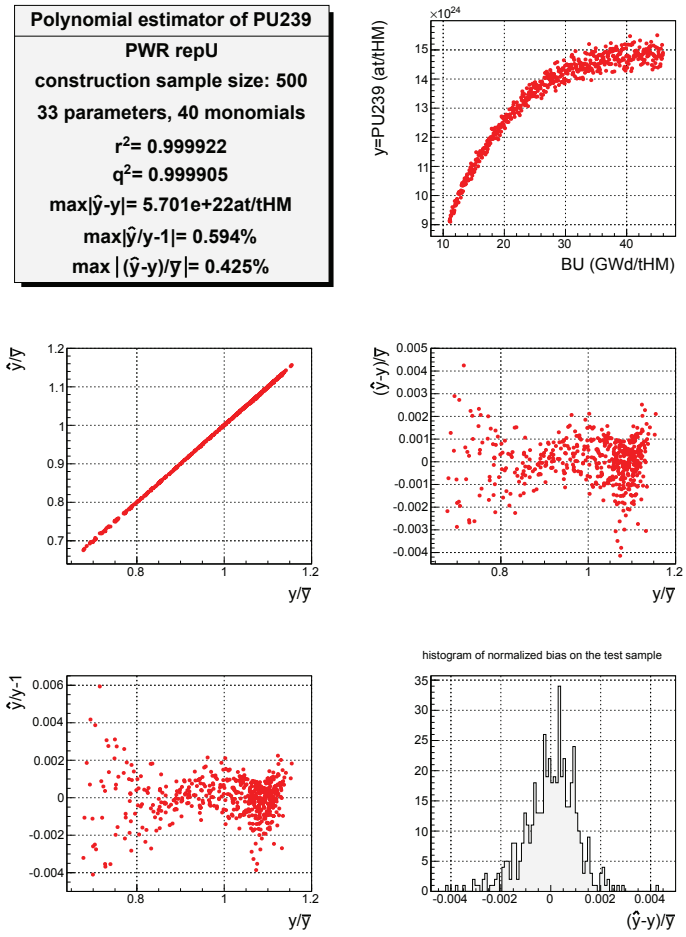

Figure B.3: Identity card of the ^{239}Pu polynomial estimator in PWR repU fuel

The quality of this estimator is satisfying. The relative error is below 0.6% and the maximum absolute error is only 0.4% of the mean value of the concentration after irradiation. This estimator is well-suited for uncertainty propagation.

B.1.4 PWR MOX fuel, low burnup, ^{241}Am estimator

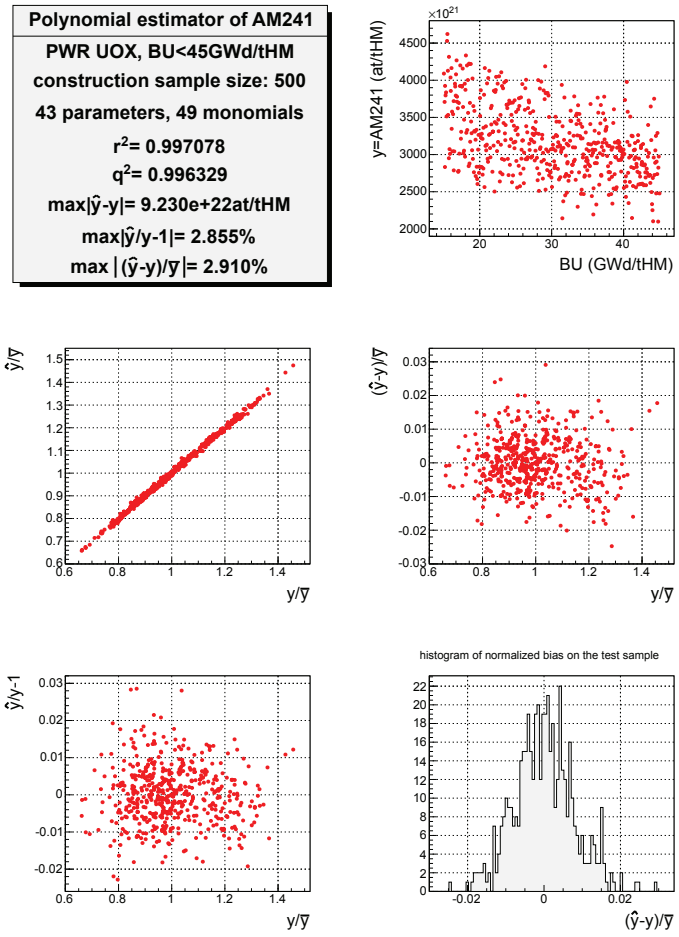

Figure B.4: Identity card of the ^{241}Am polynomial estimator in PWR MOX fuel, BU<45GWd/tHM

The quality of this ^{241}Am estimator (figure B.4) is not satisfying. The ratio of the mean absolute error and the mean is high (2.91%), which is a lot above 0.5% despite ^{241}Am being an important nuclide for the fuel cycle. This case is symptomatic of the limitations of polynomial regressions: when too many parameters (mass fractions, burnup and cross-sections) have a more or less similar effect in terms of intensity, and interactions at the same time, polynomials of reasonable size and degree fail to predict the result accurately. This estimator is not well adapted for ^{241}Am estimation or uncertainty propagation, and construction of a more precise model is considered, as shown in section 3.1.3.2.

B.1.5 PWR MOX fuel, nominal burnup, ^{241}Am estimator

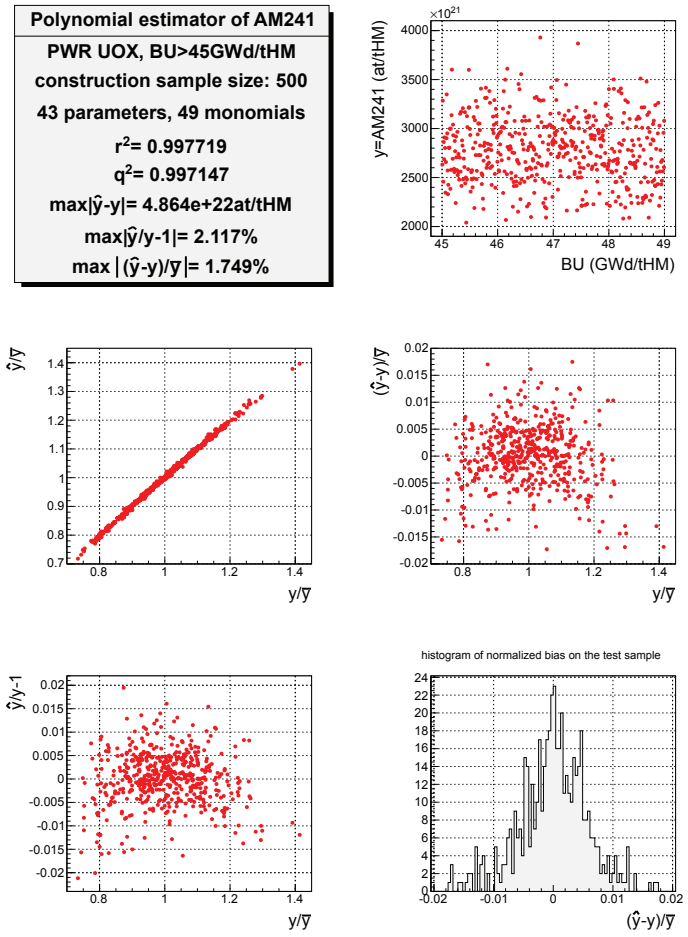

Figure B.5: Identity card of the ^{241}Am polynomial estimator in PWR MOX fuel, BU$\geq$45GWd/tHM

The quality of this estimator is not fully satisfying, the absolute error can be up to 1.75% of the mean value. However, it is slightly better than the previous estimator (at less than nominal burnup), because of the smaller impact of the burnup in that range. This estimator can be compared with the ANN version (built on a DOE with a wider range) presented in section B.2.2.

B.1.6 SFR MOX fuel, low burnup, ^{239}Pu estimator

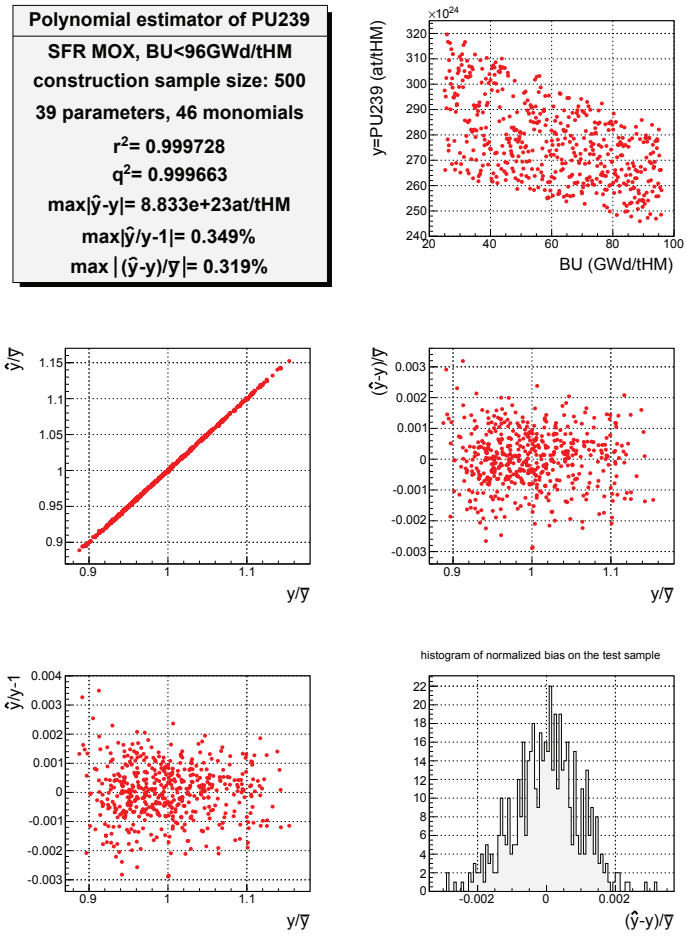

Figure B.6: Identity card of the ^{239}Pu estimator in SFR MOX fuel, BU<96GWd/tHM

The quality of this estimator is satisfying. The relative error is very low (<0.35%) on the whole domain of validity.

B.2 ANN quality indices

B.2.1 PWR UOX fuel, low burnup, ^{244}Cm estimator

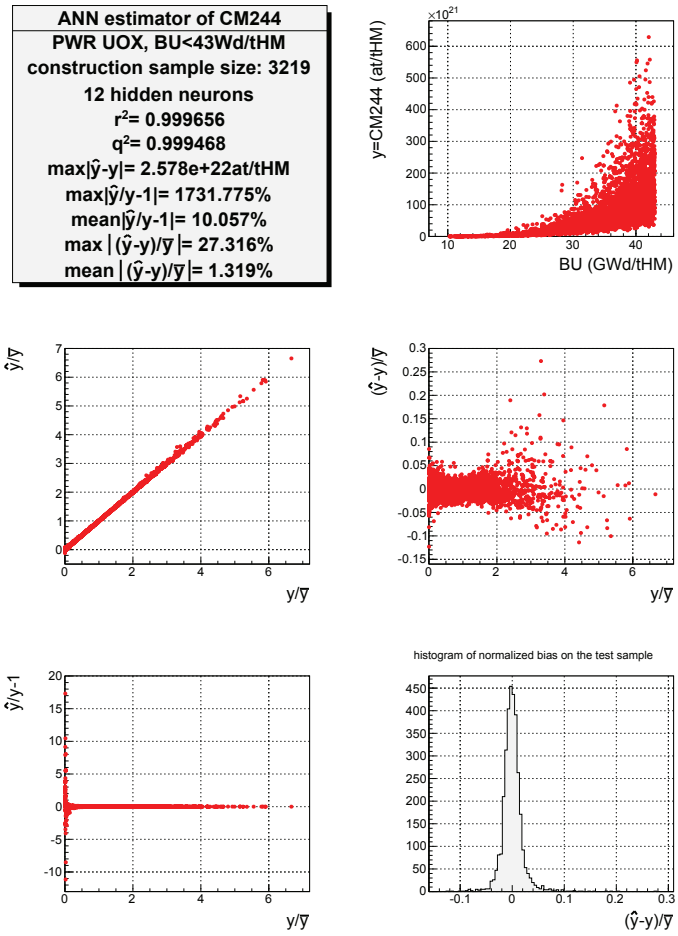

Figure B.7: Identity card of the ^{244}Cm ANN estimator in PWR UOX fuel, BU<43GWd/tHM

Figure B.7 represents the identity card of ^{244}Cm in the case of PWR UOX fuel at less than nominal burnup. The overall quality of this estimator is satisfying, the absolute error remains low. q^2 value is very high, this is due to the extreme variability of the concentration in ^{244}Cm after irradiation. Discussion with experts highlighted that the estimated uncertainty of ^{244}Cm concentration in an irradiated fuel rod is much higher than the surrogate model mean bias. Estimation of ^{244}Cm (and ^{246}Cm, which appears in much smaller concentrations) in PWR UOX fuel with less than nominal irradiation constitutes the most difficult case of every estimator in every fuel type, given that the strong non-linearity of ^{244}Cm formation in function of the burnup. Figure 3.22 page 94 is the polynomial regression corresponding to ^{244}Cm in the same fuel. Even though the domain of validity of the ANN estimator is much wider[1], its quality is still better. For instance, the indicator $mean\left(\frac{\hat{y}-y}{\bar{y}}\right)$ is approximately four times smaller with ANN.

[1]burnup and cross-section ranges were extended for ANN, consequently the top-right curve is thicker

B.2.2 PWR MOX fuel, nominal burnup, ^{241}Am estimator

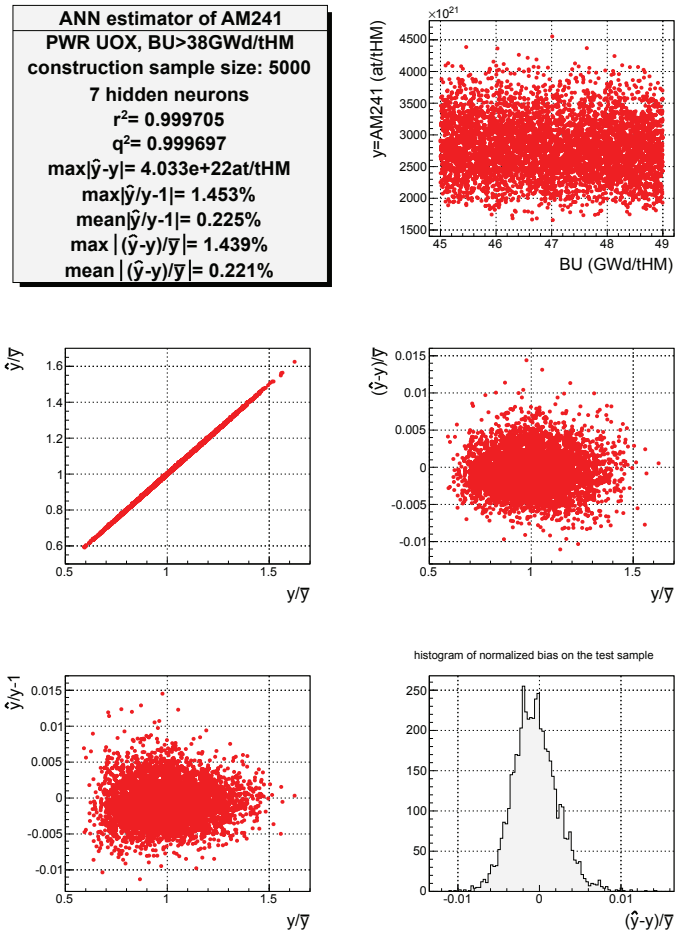

Figure B.8: Identity card of the ^{241}Am ANN estimator in PWR MOX fuel, BU>38GWd/tHM

Figure B.8 represents the identity card of ^{241}Am in the case of PWR MOX fuel irradiated at nominal burnup or more. The overall quality of this estimator is satisfying, the relative error remains very low. PWR MOX fuel is subject to a relatively high number of parameters because of the impact of plutonium vector, all of them varying in wide ranges and producing interactions with burnup and cross-sections. It is a good example of a case well-adapted to ANN estimators. In comparison, production of ^{241}Am polynomial estimator on a restricted DOE (figure B.5 page 308) returns a mean error of 1.749% (opposed to 0.221% in this case).

Appendix C

Résumé en Français

Contents

C.1 Contexte 314
C.2 Codes de calcul 315
C.2.1 CESAR 315
C.2.2 COSI 316
C.3 Analyse du problème 316
C.4 Modèles physiques adaptés à la propagation des incertitudes 319
C.4.1 Noyaux d'intérêt 319
C.4.2 Calcul de refroidissement 319
C.4.3 Calcul d'irradiation 320
C.4.4 Modèles d'équivalence 325
C.5 Paramètres associés à une incertitude 328
C.5.1 Classification 328
C.5.2 Données nucléaires 328
C.5.3 Paramètres et hypothèses des scénarios 330
C.6 Études de propagation d'incertitude 331
C.6.1 Méthode 331
C.6.2 Applications 331
C.7 Conclusions 348

C.1 Contexte

Les scénarios électronucléaires simulent l'ensemble du cycle du combustible (réacteurs et usines) sur une période donnée, depuis l'extraction des ressources naturelles (ex: uranium) jusqu'au stockage géologique. Les études des scénarios de transitions permettent de comparer différentes options d'évolutions d'un parc de récteurs électonucléaires, telles que l'introduction des RNR, ainsi que différentes options de gestion du combustible, comme le recyclage du plutonium ou bien la séparation et la transmutation des actinides mineurs. Les conséquences de ces choix sont observées sur le cycle du combustible du futur. Ainsi, ces études constituent une aide à la prise de décision. Par conséquent, les études de propagation d'incertitudes, sont nécessaires pour évaluer la robustesses des études de scénarios.

Dans le cadre de la loi du 28 juin 2006 sur la gestion des matières et déchets radioactifs, ces études évaluent la faisabilité du déploiement des RNR en termes de disponibilité du plutonium, ainsi que l'impact de la transmutation des actinides mineurs sur le cycle futur.

COSI est un code de scénario contenant des modèles physiques avancés, validés par rapport aux codes de référence, pour les calculs suivant:

- refroidissement (Bateman hors irradiation) ;
- irradiation (Batement sous irradiation) ;
- équivalence (calcul de la teneur initiale du combustible).

COSI modélise les flux de matière (actinides, produits de fission, etc.) ainsi que leur composition isotopique dans les différentes installations du cycle du combustible, tout au long de la période d'étude :

- usine d'enrichissement ;
- usines de fabrication du combustible ;
- usine de traitement du combustible irradié ;
- réacteurs ;
- sites d'entreposage ou de stockage du combustible, etc.

Cependant, certains paramètres génèrent de l'incertitude dans les études de scénario:

- les données nucléaires, telles que les sections efficaces et les rendements de fission ;
- les paramètres de scénario, associés aux réacteurs ainsi qu'aux installations du cycle du combustible, telles que le taux de combustion ou bien les taux de récupération des actinides à l'usine de retraitement.

Le besoin d'évaluer l'impact de la propagation des incertitudes sur les résultats des scénarios est d'autant plus important que les noyaux transplutoniums ont un effet important sur les installations du cycle, et que leurs sections efficaces sont associées à de fortes valeurs d'incertitudes. De plus, les études de scénario les plus récentes sont l'aboutissement d'études sophistiquées d'optimisation, par conséquent leur faisabilité peut être d'autant plus impactée par ces sources d'incertitude.

L'objectif de ce travail est de développer une méthodologie de propagation d'incertitude adaptée aux systèmes dynamiques que sont les scénarios électronucléaires, puis d'appliquer cette méthodologie aux scénarios de référence.

Ce travail est limité au cycle uranium-plutonium.

C.2 Codes de calcul

C.2.1 CESAR

CESAR est un code de calcul d'évolution. Il permet de calculer rapidement l'évolution en réacteur et hors réacteur des grandeurs physiques d'intérêt, tels que les bilans matière, la puissance résiduelle, la radiotoxicité, etc. pour des chaînes d'évolution décrivant des noyaux lourds, des produits de fission et des produits d'activation des impuretés de l'oxyde et des structures. CESAR permet également de traiter l'évolution hors flux d'une source radioactive aux échelles de temps géologiques.

CESAR utilise des bibliothèques de sections efficaces intégrées en énergie dans les spectres d'intérêts. Ces bibliothèques sont basées sur des calculs neutroniques effectuées en amont, par des codes de transport tels qu'APOLLO2 dans le cadre de spectres thermiques et ERANOS pour des spectres rapides.

La figure C.1 montre le processus de génération des bibliothèques de données nucléaires pour CESAR ainsi que celui du calcul d'évolution. On note la présence des grandeurs suivantes:

- $\sigma(E)$: sections efficaces non intégrées en énergie ;
- $\sigma(BU)$: sections efficaces intégrées en énergie pour différentes valeurs de burnup, pour un assemblage donné ;
- y_0 : composition du combustible neuf ;
- BU : burnup ;
- N : composition isotopique de l'assemblage irradié ;
- ND : données nucléaires.

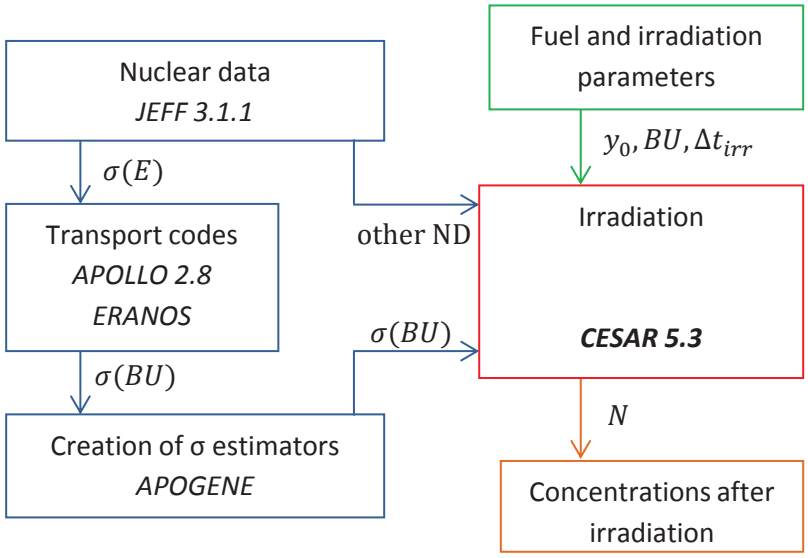

Figure C.1: Génération de bibliothèques de sections efficaces pour CESAR5.3

C.2.2 COSI

COSI est un logiciel qui simule le fonctionnement d'un parc de réacteurs électronucléaires et des installations du cycle du combustible qui lui sont associées. Il a été conçu pour effectuer des études de scénarios, qui permettent de connaître et d'analyser les conséquences des choix opérés sur la taille et la nature du parc de réacteurs, ainsi que sur les caractéristiques des différentes installations du cycle, c'est-à-dire les usines, entreposages et stockages. Il permet l'étude de scénarios de transition et considère les isotopies des éléments. Le code COSI traite l'ensemble des flux de matières mis en jeu dans le cycle du combustible.

Le diagramme de la figure C.2 illustre les demandes et flux de matières modélisés par le code COSI.

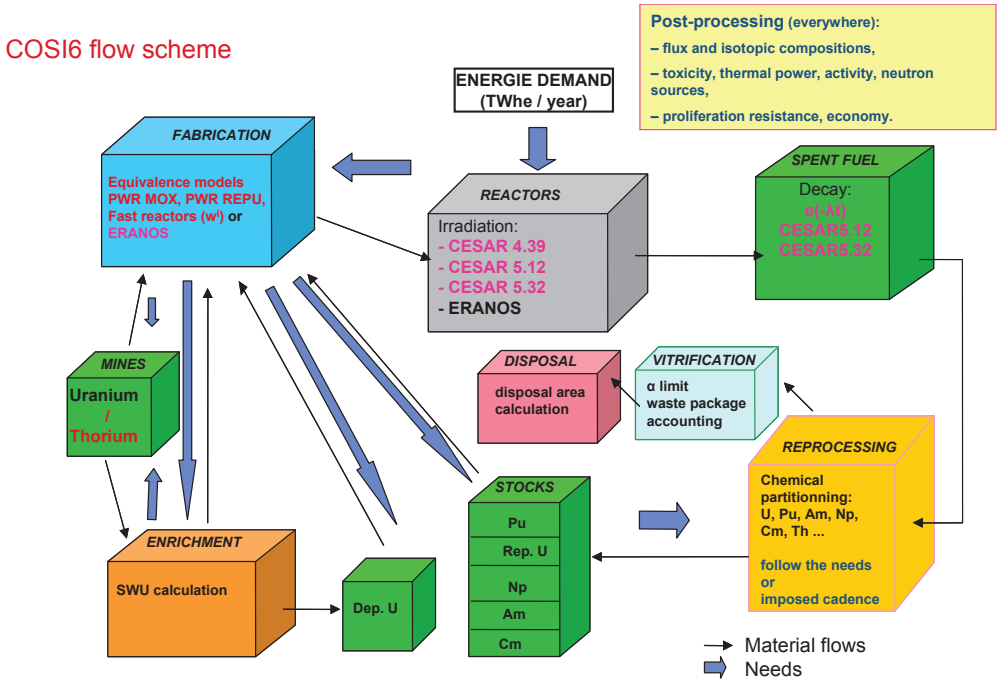

Figure C.2: Flux de masse dans le cycle du combustible simulés par COSI

Le code de scénario COSI fait appel au code d'irradiation CESAR pour effectuer les calculs d'irradiation et de refroidissement.

C.3 Analyse du problème

Les scénarios électronucléaires sont des objets complexes. Les simulations récentes modélisent le comportement et l'interaction de dizaines de réacteurs nucléaires (typiquement le parc Français actuel et futur), les installations du cycle du combustible, les flux de masses, des phénomènes continus et discontinus, avec la présence de nombreux effets de seuil :

- continus : modèles d'irradiation et de refroidissement, etc.
- discontinus : gestion du combustible et stratégie de retraitement (les lots de combustible ne sont pas homogénéisés).

Une première proposition de méthode de calcul de propagation d'incertitude est l'application de la théorie des perturbation aux équations du cycle du combustible. Des études récentes [C.1] ont montré que l'obtention de formules analytiques pour le cycle nécessitent des hypothèses simplificatrices concernant les données suivantes :

- flux ;
- spectres ;
- géométrie des cœurs ;
- modèles d'équivalence ;
- sections efficaces, etc.

Ces hypothèses ont très certainement un impact considérable non seulement sur les résultats d'intérêt des études de scénarios, mais également sur leur incertitude, par conséquent une autre méthode est préférable.

Les méthodes stochastiques de calcul de propagation d'incertitude semblent tout à fait adaptées à des problèmes aussi complexes que les études de scénarios. Elles sont basées sur la construction d'un plan d'expérience réalisé avec l'échantillonnage des pramètres en fonction de leur distribution, correspondant à leur incertitude, et des corrélations associées. Puis, l'analyse des résultats des calculs (variance, corrélations, etc.) donne des informations concernant la propagation de l'incertitude dans le système. Cette méthode ne requiert ni hypothèse ni simplification de la physique des modèles en place, et est tout à fait adaptée à l'étude des interactions entre les différentes variables.

Un des inconvénients principaux de cette méthode est le temps de calcul, ainsi que le nombre d'évalutations requies afin de calculer la variance et les autres résultats d'intérêt, avec une précision satisfaisante. Il est difficile d'estimer ce nombre a priori, mais il croît avec le nombre de paramètres et la complexité du système.

Dans les scénarios électronucléaires, de nombreux paramètres sont associées à une incertitude. Parmi ces paramètres, on note :

- les données nucléaires, utilisées lors des calculs d'irradiation ainsi que dans les modèles d'équivalence :
  - sections efficaces : l'incertitude est contenue dans les matrices de covariance, et de très nombreux noyaux génèrent de l'incertitude dans les calculs de scénarios, en particulier les actinides et les produits de fission ;
  - rendements de fission : l'incertitude des rendements de fission intégrés en énergie associée à de nombreux couples (actinide, produit de fission) doit être prise en compte ;
- paramètres de scénarios, associés au combustible et aux installations du cycle du combustible :
  - les taux et rendements de différentes installations ;
  - le burnup du combustible ainsi que la puissance, le rendement, le facteur de charge des réacteurs, etc. ;
  - la stratégie de retraitement du combustible irradié ;
  - la composition isotopique de l'uranium naturel, etc.

Le nombre total de paramètres associés à une valeur d'incertitude s'élève généralement à approximativement 200 pour une étude de scénario (même si certaines études de propagation de

l'incertitude du burnup ont nécessité environ 5000 paramètres), ce qui implique que le nombre de calculs de scénario nécessaires pour calculer l'incertitude est supérieur à 200.

Dans le cas des études de scénario récentes, le temps d'exécution de COSI va de quelques heures (pour le calcul des bilans matière) à plus de 24 heures (pour le calcul des inventaires). Le temps de calcul dépend fortement de la compléxité du scénario et du niveau de détail de celui-ci, du type de réacteurs utilisé et de la durée temporelle de l'étude (généralement, plus de 150 ans). En prenant en compte le fait qu'une simulation COSI requiert une quantité élevée de RAM, et que ce calcul n'est pas distribuable dans le cas général (chevauchement de calculs simultanés), on arrive à des délais tout à fait déraisonnables en termes de temps de calcul. Par conséquent, il convient de trouver une méthode d'accélaration du temps de calcul.

Une solution à ce problème serait le calcul de propagation d'incertitudes sur des scénarios simplifiés, puis la généralisation des résultats à des scénarios complexes, possiblement par le biais d'un facteur tenant compte de l'étape de transposition des résultats. Un tel facteur de transposition peut par exemple être bâti selon une valeur de représentativité, obtenu par produit scalaire entre les vecteurs de sensibilité des deux scénarios, pondéré par la matrice de covariance. Cependant, les calculs de scénarios sont très non-linéaires, et de très nombreux effets de seuil surviennent (ou disparaissent) lors de l'étape de *complexification* du scénario. Par conséquent de telles mesures de sensitivité ne sont pas suffisantes pour établir ce facteur. Les incertitudes obtenues avec des scénarios simplifiés ne sont pas nécessairement représentatives de la valeur réelle de l'incertitude.

Le processus de simplification ne peut être appliqué au scénario lui-même. Cependant, les modèles physiques peuvent éventuellement être simplifié, étant donné que toute l'information présente dans le système ne contribue pas nécessairement à l'incertitude des résultats d'intérêt, et que beaucoup de paramètres ont un effet potentiellement négligeable.

La décomposition du temps de calcul d'un scénario typique est approximativement :

- modèles d'irradiation et de refroidissment $\approx 99\%$ du temps de calcul ;
- autres modèles physiques (équivalence, puissance résiduelle, gestion du combustible, etc.) $\ll 1\%$;
- diverses opérations $\approx 1\%$.

On remarque que les modèles d'irradiation et de refroidissement représentent la quasi-totalité du temps de calcul, alors que l'impact des autres modèles et opérations est négligeable. On observe également qu'au plus un scénario est complexe et détaillé, au plus le temps de calcul des autres modèles est réduit. Par conséquent, le problème de temps de calcul peut être résolu par la simplification de ces modèles physiques, pourvu que les modèles simplifiés puissent calculer les résultats d'intérêt avec une précision satisfaisante et que le gain de temps de calcul soit important.

C.4 Modèles physiques adaptés à la propagation des incertitudes

C.4.1 Noyaux d'intérêt

La plupart des résultats des études de scénarios sont en lien direct avec la composition isotopiques de stocks ou bien de lots d'assemblages combustibles. Par conséquent, il est impossible de réduire le système à une masse scalaire unique.

De plus, de précédentes études au Laboratoire d'Études du Cycle ont montré que la simplification du calcul en un système composé uniquement de quelques éléments, tels que l'uranium et le plutonium, donne des résultats non satisfaisants dès lors que des combustibles REP MOX ou SFR MOX sont introduits (problèmes d'isotopie et de décroissance notamment).

Cependant, tous les noyaux ne contribuent pas de manière égale aux résultats d'intérêt des scénarios. Par exemple, les produits de fission stables n'ont pas d'impact sur la puissance résiduelle ou bien sur la masse d'actinides en cycle. Par conséquent, il n'est pas nécessaire de les calculer dans le cadre de notre travail. De plus, la réduction de la liste de noyaux à calculer réduit d'autant la quantité de mémoire RAM nécessaire au calcul de scénario, et accélère le déroulement des calculs de flux de masse.

Les noyaux lourds suivants ont été modélisés dans le cadre de notre travail:

$$\left\{^{234,235,236,238}\mathrm{U};\ ^{237,239}\mathrm{Np};\ ^{238,239,240,241,242}\mathrm{Pu};\ ^{241,242M,243}\mathrm{Am};\ ^{242,243,244,245,246}\mathrm{Cm}\right\}$$

Ces noyaux représentent la quasi-totalité de la masse en actinides et de la puissance résiduelle issue des actinides.

La liste de produits de fission pris en compte est la suivante :

$$\left\{^{85}\mathrm{Kr};\ ^{90}\mathrm{Sr};\ ^{90}\mathrm{Y};\ ^{95}\mathrm{Zr};\ ^{95}\mathrm{Nb};\ ^{106}\mathrm{Rh};\ ^{106}\mathrm{Ru};\ ^{134}\mathrm{Cs};\ ^{137}\mathrm{Cs};\ ^{137M}\mathrm{Ba};\ ^{144}\mathrm{Ce};\ ^{144}\mathrm{Pr};\ ^{147}\mathrm{Pm};\ ^{154}\mathrm{Eu}\right\}$$

Ces noyaux représentent la quasi-totalité de la puissance résiduelle issue des produits de fission.

On note qu'il s'agit des noyaux pris en compte pour le cycle du combustible hors calculs d'irradiation. Les calculs d'irradiation sont effectués en considérant un très grand nombre de noyaux, comme expliqué en section C.4.3.

C.4.2 Calcul de refroidissement

Tout d'abord, dans le cas du refroidissement, COSI exécute le code CESAR pour les calculs de refroidissement de chaque stock et lot de combustible. Dans COSI, chaque fois que le code accède à une information concernant un lot ou un stock, un calcul de refroidissement est effectué pour connaître la composition à la date voulue. Le code accède très fréquemment à l'isotopie de ces objects car la majorité des opérations et résultats intermédiaires requièrent cette information. Par conséquent, plusieurs milliers de calculs de refroidissement sont opérés par CESAR lors d'un calcul de scénario.

Dans ce travail, nous avons remplacé les calculs de refroidissement CESAR par des formules analytiques. L'implémentation de chaînes d'actinides et produits de fission d'intérêt du point de vue du cycle du combustible a été effectuée.

C.4.3 Calcul d'irradiation

C.4.3.1 Métamodèles

Les métamodèles sont des modèles analytiques simples d'un code de calcul. Ils sont généralement construits lorsque des opérations nécessitant un grand nombre d'exécution d'un code sont effectuées, telles que des calculs d'optimisation ou de propagation d'incertitude.

Un exemple simple de métamodèle est la régression multilinéaire. Il s'agit d'un bon estimateur des sorties d'un système en fonction de l'entrée pour peu que le système soit localement linéaire.

Il existe de nombreux types de métamodèles :

- les régressions multilinéaires ;
- les régression polynomiales ;
- les splines ;
- les réseaux de neurones artificiels ;
- le krigeage, etc.

Le type de métamodèle est généralement choisi en fonction de la nature du problème : nombre de paramètres, non-linéarité, présence d'interactions, taille de la base d'apprentissage, etc.

Dans le cadre de ce travail, nous construisons des métamodèles de CESAR appliqués au calcul de propagation de l'incertitude dans les études de scénarios.

C.4.3.2 Paramètres pris en compte

Deux types de résultats doivent être pris en compte dans les métamodèles. Tout d'abord, les métamodèles doivent estimer de manière correcte les résultats du code de calcul, par conséquent les paramètres avec une sensibilité non nulle doivent être inclus. La liste des paramètres pris en compte est la suivante :

- description de l'assemblage neuf
  - la géométrie de l'assemblage (indirectement prise en compte via la bibliothèque de sections efficaces intégrées en énergie de CESAR) ;
  - la composition du combustible neuf (ensemble des fractions massiques) ;
- les paramètres d'irradiation (burnup et puissance d'irradiation).

De plus, les métamodèles doivent également être capable d'être utilisés pour des études de propagation d'incertitude, ces paramètres doivent donc être inclus. Cependant, certains paramètres associés à une incertitude, tels que les sections efficaces, ne sont pas directement inclus dans les jeux de données CESAR, par conséquent il faut réaliser des calculs perturbatifs d'irradiation de sorte à prendre ces paramètres en compte. Dans le cas des sections efficaces, les perturbations des sections efficaces de capture et fission d'une vingtaine d'actinides, ainsi que l'impact des sections efficaces de capture de quelques produits de fission est pris en compte. Nous montrons également que l'impact de la perturbation des sections efficaces de diffusion, dans des intervalles correspondant à leur incertitude, est généralement faible sur le bilan matière, et peut donc être négligée.

Les rendements de fission sont également pris en compte. La sélection des rendements de fission influents est déterminée par une étude de sensibilité.

Des études de sensibilité concernant différents paramètres physiques, tels que les énergies effectives de fission, montrent qu'il est possible de négliger l'impact de leur perturbation lors du calcul de propagation d'incertitude.

Le tableau C.1 résume la liste des paramètres pris en compte pour la construction de métamodèles des concentrations d'actinides et de produits de fission dans le combustible irradié.

grandeur	pris en compte	négligé	nombre de paramètres
géométrie de l'assemblage	×		(1 métamodèle par
spectre	×		type d'assemblage)
burnup	×		1
durée d'irradiation	×		(calculée)
puissance d'irradiation intégrée	×		1
facteur de charge non uniforme		×	
fractions massique du combustible neuf	×		$2 \rightarrow 9$
σ_f des actinides	×		19
σ_c des actinides	×		19
σ_c des produits de fission	×		6
σ_s des actinides		×	
σ_s des produits de fission		×	
σ des autres noyaux		×	
rendements de fission	×		94
énergie effective de fission		×	
masse des noyaux		×	
demi-vies radioactives		×	

Table C.1: Résumé des paramètres pris en compte pour la construction de métamodèles des concentrations du combustible irradié

C.4.3.3 Construction de métamodèles

Dans le cadre de notre travail, nous avons construit des métamodèles du code d'irradiation CESAR, ce qui signifie que nous avons contruit des estimateurs des sorties de ce code en fonction des entrées.

Cependant, il est nécessaire de modéliser la concentration de tous les noyaux d'intérêt pour chaque calcul d'irradiation. Par conséquent, nos métamodèles ne sont pas directement des estimateurs des sorties, mais des ensembles d'estimateurs : au moins un par noyau d'intérêt.

De plus, le domaine de définition de CESAR est très vaste. Il couvre la majorité des types de combustible existant, et l'irradiation associée: REP UOX, REP MOX, REP URE, RNR MOX, couvertures fissiles, couvertures chargées en actinides mineurs, etc. Par conséquent, nous avons divisé le domaine de validité de CESAR en différents sous-domaines, et construit un ensemble d'estimateurs sur chaque sous-domaine.

Tout d'abord, nous avons construit des régressions polynomiales pour les actinides. Ce type d'estimateur a été choisi de par le sens physique de ses paramètres internes: les termes linéraires sont des pentes, les interations entre paramètres sont modélisées sous forme de multiplications, etc.

Ces estimateurs ont été construits selon le processus habituel:

- création du plan d'expérience et échantillonnage des paramètres ;
- exécution du code de calcul sur le plan d'expérience ;
- régression (construction des estimateurs) ;
- test des estimateurs.

Le processus de construction des estimateurs est illustré sur la figure C.3.

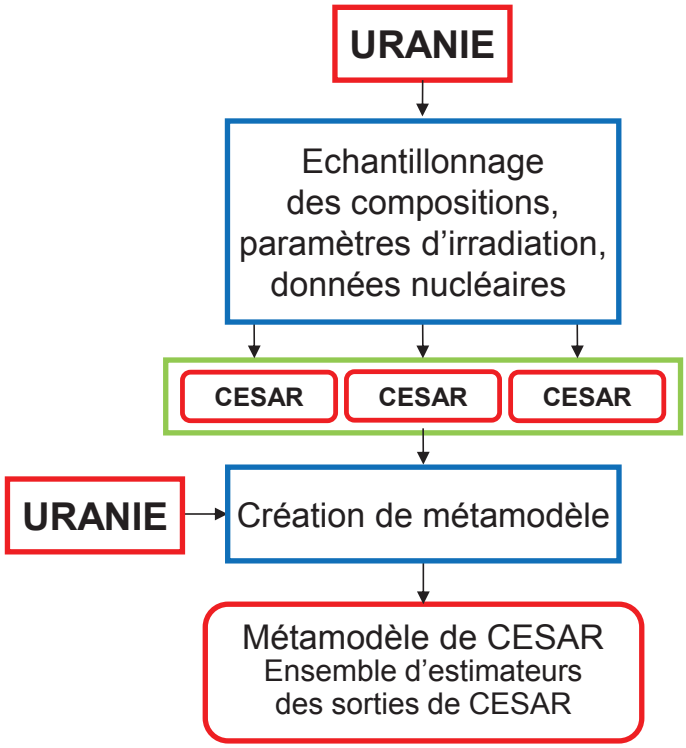

Figure C.3: Processus de fabrication de métamodèles d'irradiation

Dans le cas général, les estimateurs polynomiaux donnent des résultats satisfaisants pour les actinides : les résultats de l'estimation sont proches des résultats du code de calcul. Cependant, la prédiction de la concentration après irradiation en certains noyaux reste difficile à effectuer. C'est le cas par exemple de la majorité des isotopes du curium. Plutôt que d'augmenter la complexité des estimateurs polynomiaux (nombre de monômes, degré maximum), ce qui offre des rendements décroissants, nous avons décidé d'utiliser un autre type d'estimateur. Les réseaux de neurones artificiels (artificial neural networks, ANN) semblent convenir aux caractéristiques des calculs d'irradiation. En effet, ils sont adaptés aux résultats *modérément* non linéaires de fonctions d'un nombre *modérément* élevé de paramètres. Leur construction suit le même principe que les estimateurs polynomiaux. La figure C.4 illustre le fonctionnement d'un estimateur type *réseau de neurone à une couche cachée*, qui a été utilisé pour ces travaux. Du fait de leurs propriétés, ces estimateurs ont été utilisés pour l'estimation d'actinides mineurs et de produits de fission dans le combustible irradié.

L'expression de la sortie en fonction des entrées est donnée par l'équation C.1, avec N le nombre

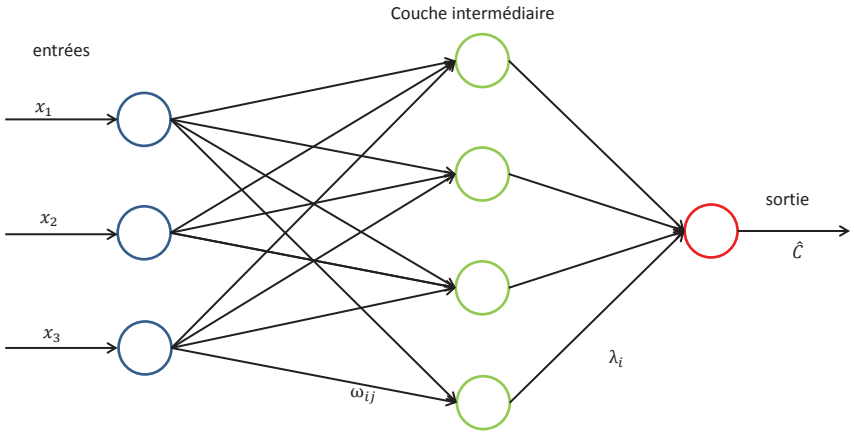

Figure C.4: Fonctionnement d'un réseau de neurones

de neurones dans la couche cachée et H le nombre de paramètres :

$$\begin{cases} \hat{C} = S\left[\sum_{h=1}^{H} \lambda_h \times S\left(\sum_{n=1}^{N} \omega_{hn} \times x_n\right)\right] \\ S(x) = \dfrac{1}{1+e^{-x}} \end{cases} \tag{C.1}$$

Plusieurs études de sensibilité ont été faites afin de réduire le nombre de paramètres en éliminant les paramètres négligeables, ce qui permet d'améliorer la qualité générale des réseaux de neurones. En particulier, l'étude de la formation de différents produits de fission, présentant un intérêt de par leur contribution à la puissance résiduelle, a été menée. Le nombre de neurones cachés, ainsi que la taille des échantillons de fabrication des estimateurs, ont été déterminés par des études paramétriques. De manière générale, des échantillons de taille entre 1000 et 5000 points ont été utilisés, et le nombre de neurones dans la couche cachée varie entre 7 et 10 selon la complexité des voies de formation du noyau.

Une étape essentielle de la construction des réseaux de neurones est leur validation, à la fois en termes de précision des résultats et en capacité à propager les incertitudes. Chaque estimateur a été testé sur un échantillon dédié, différent de l'échantillon de fabrication. Différents indicateurs de qualité on été utilisés :

- des indicateurs locaux, testant le biais de l'estimateur en chaque point ;
- des indicateurs globaux, testant la capacité du modèle à propager la variance.

C.4.3.4 Implementation

Les régressions polynomiales et réseaux de neurones on été implémentés dans COSI. Une nouvelle voie de calcul rapide, COSI-MeSAR, a ainsi été élaborée. Le gain de temps peut être supérieur à 1000 pour des scénarios complexes, avec des temps de calcul entre quelques secondes et quelques minutes. L'implémentation a été faite de telle sorte qu'il est très facile d'importer un jeu de données de la voie de calcul standard vers la nouvelle voie de calcul adaptée à la propagation d'incertitudes. La nouvelle voie de calcul donne des résultats de calcul très proches de la voie de calcul standard. En particulier, la puissance résiduelle, dont le calcul par la nouvelle voie est explicité en schéma C.5, entre 1 et 20 ans de refroidissement est très bien modélisée.

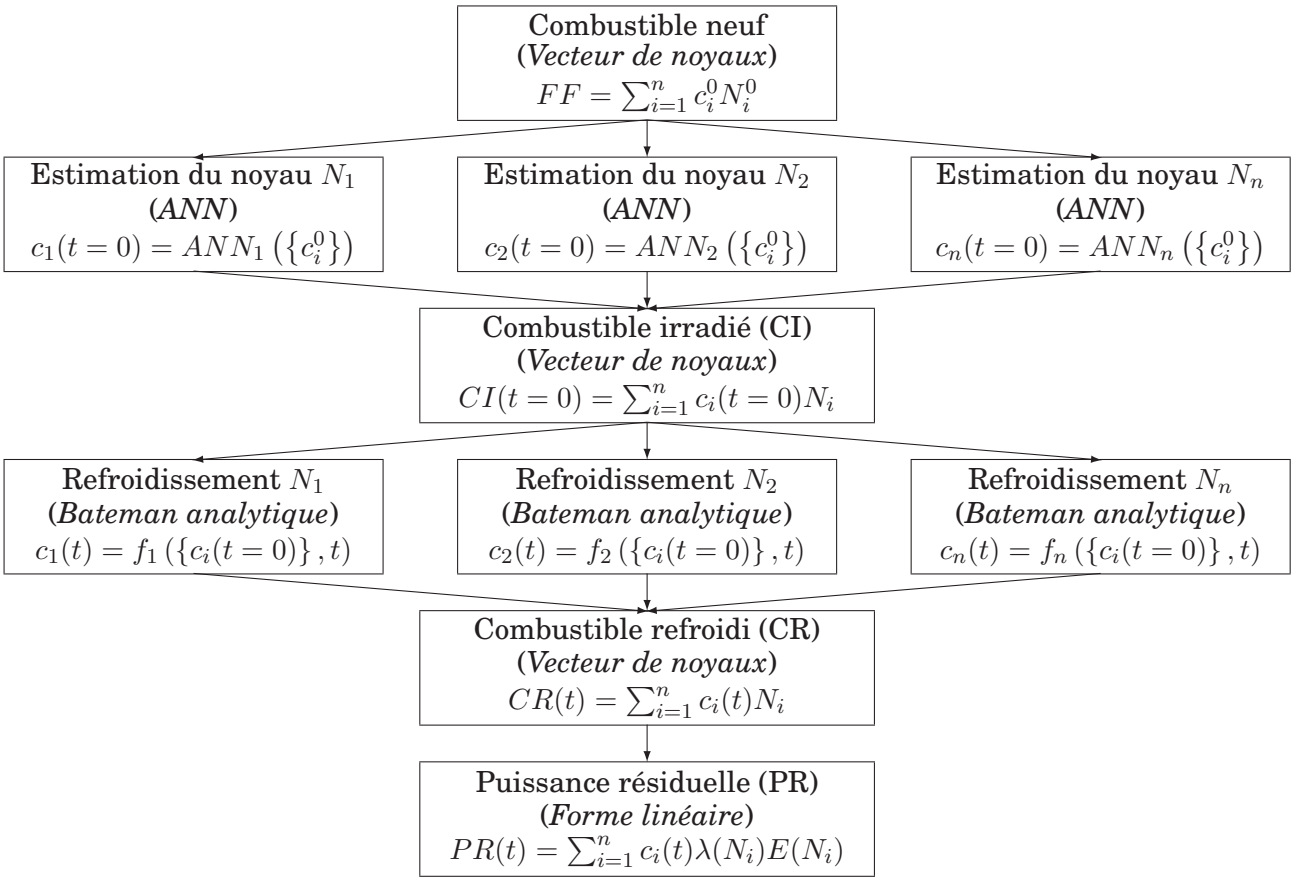

Figure C.5: Calcul de la puissance résiduelle via réseaux de neurones et solutions analytiques de l'équation de Bateman

La figure C.6 montre un exemple de comparaison des voies de calcul COSI-CESAR5.3 et COSI-MeSAR pour le calcul de la puissance résiduelle de combustible REP MOX irradié à un 46GWj/tML puis refroidi entre 1 et 20 ans.

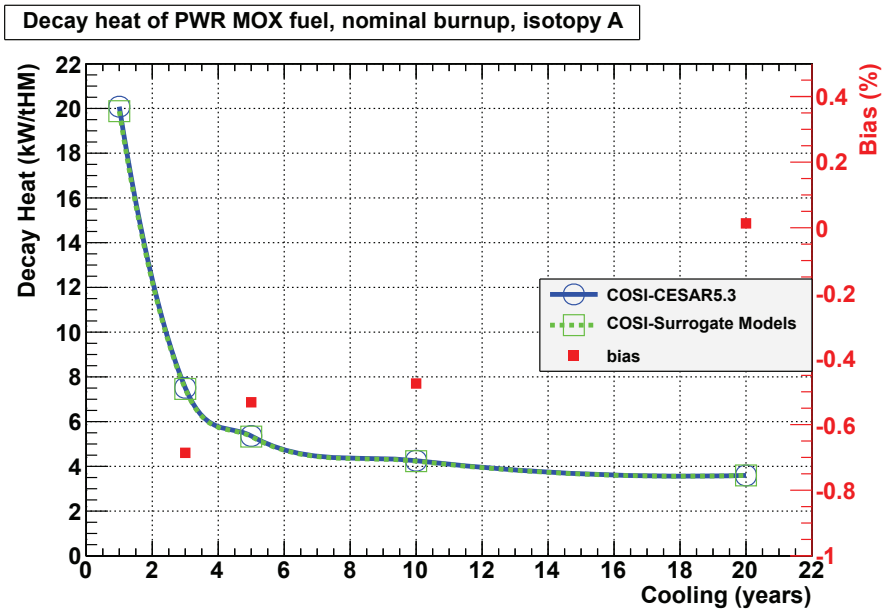

Figure C.6: Comparaison de la puissance résiduelle calculée via (ANN et solutions analytique de Bateman) et CESAR5.3 pour du combustible REP MOX irradié à 46GWj/tML

C.4.4 Modèles d'équivalence

Un autre type de modèle physique génère de l'incertitude dans les calculs de scénarios : les modèles d'équivalence. Les modèles d'équivalence calculent l'enrichissement du combustible neuf (par exemple la teneur massique en plutonium dans le combustible REP MOX), de sorte à être représentatif, équivalent d'un assemblage nominal. L'équivalence est généralement formulée en termes de réactivité moyenne du cœur en fin de cycle d'irradiation. Ce calcul de réactivité, ainsi que le calcul d'irradiation qui précède, sont soumis aux incertitudes des données nucléaires. Nous exposons tout d'abord l'état de l'art des modèles d'équivalence présents dans COSI:

- modèles *boîte noire* pour les REP MOX, établis sous forme de régressions multi-paramétriques en fonction de la composition du combustible neuf. Ces modèles ne permettent pas de considérer des perturbations sur les données nucléaires ;
- modèles analytiques pour les RNR, basés sur la théorie des perturbations appliquée au combustible neuf (l'équivalence est calculée avant irradiation). Ces modèles sont basés sur de lourdes hypothèses physiques, et ne permettent pas de calculer l'impact des perturbation des sections efficaces en irradiation ;
- modèles faisant appel à des calculs de transport et irradiation pour les RNR. Ces calculs sont trop chronophages pour permettre un calcul stochastique de propagation d'incertitude.

Par conséquent, un nouveau type de modèle d'équivalence a été développé. Ces modèles sont basés sur des réseaux de neurones artificiels. Ils sont construits à partir de données calculées avec des codes de transport et irradiation, selon la démarche suivante:

1. échantillonnage des paramètres :
   - paramètres d'irradiation (burnup, durée d'irradiation, fractionnement du cœur) ;
   - isotopie du combustible neuf ;
   - teneur massique du combustible neuf ;
   - perturbation des sections efficaces ;
2. réalisation d'un calcul d'irradiation et de transport en fin d'irradiation pour déterminer la réactivité du combustible en fin de cycle d'irradiation :
   - spectre thermique : APOLLO2 ;
   - spectre rapide : ERANOS.
3. construction de l'estimateur de la teneur du combustible neuf en fonction des autres paramètres :
   - isotopie ;
   - perturbation des sections efficaces ;
   - paramètres d'irradiation ;
   - réactivité en fin de cycle ;
4. validation de l'estimateur.

L'étape de construction d'estimateurs est de nouveau réalisée en utilisant des réseaux de neurones artificiels.

La figure C.7 représente la comparaison de teneurs calculées avec ERANOS (en abscisse) et avec le modèle statistique (en ordonnée) sur l'échantillonnage de test de l'estimateur, pour le modèle d'équivalence de RNR.

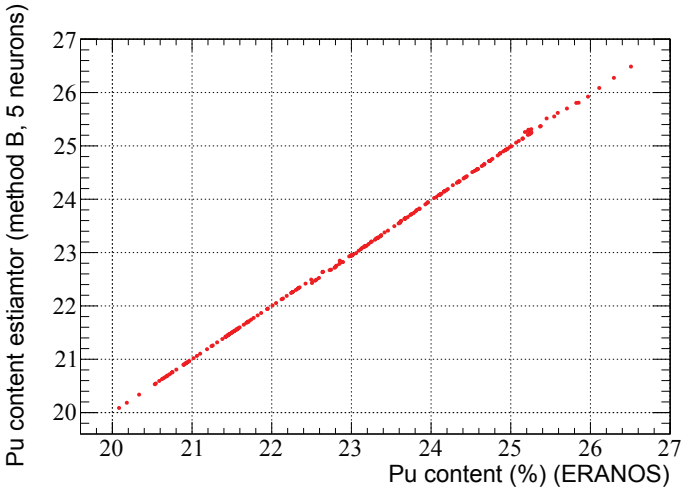

Figure C.7: Comparaison des teneurs calculées avec le modèle d'équivalence statistique et ERANOS

On observe que le modèle d'équivalence statistique pour RNR adapté à la propagation d'incertitude calcule la teneur avec précision. Les résultats sont similaires pour le modèle statistique adapté aux REP MOX.

Une étude préliminaire de propagation d'incertitude est opérée pour les modèles d'équivalence. Par exemple, dans le cadre du modèle d'équivalence pour RNR, les résultats sont donnés dans le tableau C.3. Les résultats sont obtenus pour le vecteur plutonium indiqué sur le tableau C.2. On note RSD l'écart-type relatif. La dernière colonne indique le produit sensibilité $\times$ incertitude.

Nuclide	isotopy
^{238}Pu	2.59
^{239}Pu	55.2
^{240}Pu	25.85
^{241}Pu	7.27
^{242}Pu	7.87
^{241}Am	1.22

Table C.2: Vecteur plutonium pour l'étude du modèle d'équivalence RNR

section efficace	sensibilité $\sigma/t \times \partial t/\partial\sigma$	incertitude $RSD(\%)$	produit sensibilité-incertitude $RSD \times \sigma/t \times \partial t/\partial\sigma$
$\sigma_c(^{235}\text{U})$	0.047	20.7	0.0098
$\sigma_f(^{235}\text{U})$	0.029	0.6	0.0002
$\sigma_c(^{238}\text{U})$	0.284	1.4	0.0040
$\sigma_f(^{238}\text{U})$	-0.047	0.5	-0.0003
$\sigma_c(^{238}\text{Pu})$	0.036	7.8	0.0028
$\sigma_f(^{238}\text{Pu})$	-0.005	0.5	0.0000
$\sigma_c(^{239}\text{Pu})$	1.330	5.3	**0.0705**
$\sigma_f(^{239}\text{Pu})$	0.032	0.4	0.0001
$\sigma_c(^{240}\text{Pu})$	0.071	3.3	0.0023
$\sigma_f(^{240}\text{Pu})$	-0.007	1.1	-0.0001
$\sigma_c(^{241}\text{Pu})$	0.192	14.0	**0.0269**
$\sigma_f(^{241}\text{Pu})$	-0.039	0.7	-0.0003
$\sigma_c(^{242}\text{Pu})$	0.050	4.3	0.0021
$\sigma_f(^{242}\text{Pu})$	-0.013	1.9	-0.0003
$\sigma_c(^{241}\text{Am})$	0.009	27.8	0.0025
$\sigma_f(^{241}\text{Am})$	0.003	8.8	0.0002
$\sigma_c(^{243}\text{Am})$	0.000	4.9	0.0000
$\sigma_f(^{243}\text{Am})$	0.001	8.4	0.0000
$\sigma_c(^{237}\text{Np})$	0.002	87.9	0.0017
$\sigma_f(^{237}\text{Np})$	0.007	3.1	0.0002
$\sigma_c(^{242}\text{Cm})$	0.000	20.3	0.0000
$\sigma_f(^{242}\text{Cm})$	-0.003	5.3	-0.0002
$\sigma_c(^{243}\text{Cm})$	0.000	77.4	0.0002
$\sigma_f(^{243}\text{Cm})$	0.006	3.5	0.0002
$\sigma_c(^{244}\text{Cm})$	-0.001	22.5	-0.0001
$\sigma_f(^{244}\text{Cm})$	0.008	3.0	0.0002
$\sigma_c(^{245}\text{Cm})$	0.001	61.5	0.0009
$\sigma_f(^{245}\text{Cm})$	-0.013	3.3	-0.0004

Table C.3: Analyse préliminaire de propagation d'incertitude pour le modèle d'équivalence RNR statistique

On remarque que deux sections efficaces contribuent fortement à l'incertitude de la teneur du combustible neuf :

- la capture du ^{239}Pu ;
- la capture du ^{241}Pu.

C.5 Paramètres associés à une incertitude

C.5.1 Classification

Nous avons réalisé la classification des paramètres introduisant de l'incertitude dans les calculs de scénario :

- les données nucléaires, telles que les sections efficaces ;
- les données des scénarios, qui sont liées au fonctionnement de l'industrie nucléaire.

C.5.2 Données nucléaires

Plusieurs paramètres physiques introduisent de l'incertitude dans les études de scénario, via les modèles d'évolution et d'équivalence. Tout d'abord, nous avons étudié les sections efficaces. Les matrices de covariance contiennent les valeurs d'incertitude en fonction de l'énergie ainsi que les corrélations associées, pour un maillage énergétique donné. Cependant, les modèles physiques présents dans COSI ne permettent pas de manipuler des données multi-groupes. Par conséquent, il a été nécessaire de produire des valeurs d'incertitude intégrées en énergie, adaptées à chaque spectre d'intérêt, à partir des matrices de covariance. De plus, étant donné que les scénarios de transition modélisent différents types de réacteurs lors d'une seule simulation (présence d'irradiations en REP UOX, REP MOX, RNR, etc. en un seul calcul de scénario), la connaissance des corrélations des sections efficaces entre différents spectres est requise.

Par conséquent, nous avons développé une méthode qui calcule une telle incertitude, ainsi que les corrélations entre différentes réactions dans différents spectres. Le processus global est le suivant :

1. création de matrices de covariances depuis les évaluations disponibles (ENDF B-VII a été utilisé pour ce travail) en utilisant CADTOOL, un générateur de scripts pour NJOY ;
2. condensation des matrices de covariance dans les spectres d'intérêt.

La méthode de condensation est basée sur les principes suivants :

- conservation des écarts-types des taux de réaction ;
- conservation des corrélations des taux de réaction.

L'équation C.2 indique la formule de condensation utilisée. On note (a, b) les réactions considérées (par exemple capture et fission du plutonium 239), (α, β) les spectres considéres (par exemple des spectres REP UOX et REP MOX), $\underline{\underline{D}}_{Ng}$ la matrice de covariance du couple (a, b) à N groupes énergétiques et $\underline{S}$ un vecteur de sensibilité dont l'expression est donnée dans l'équation C.3, avec $\tau^{\alpha}_{a,i}$ le taux de la réaction a dans le spectre α dans le groupe i et ϕ^{α} le flux dans le spectre α.

$$cov(\sigma_a^\alpha, \sigma_b^\beta) = \frac{1}{2}\left[(\sigma_a^\alpha + \sigma_b^\beta)^2 \cdot {}^t\underline{\boldsymbol{S}}_{\boldsymbol{Ng}}\underline{\underline{\boldsymbol{D}}}_{\boldsymbol{Ng}}\underline{\boldsymbol{S}}_{\boldsymbol{Ng}} - Var(\sigma_a^\alpha) - Var(\sigma_b^\beta)\right] \tag{C.2}$$

$$\begin{aligned} \underline{\boldsymbol{S}}_{\boldsymbol{Ng}} &= \frac{\underline{\boldsymbol{\sigma}}_{\boldsymbol{Ng}}}{\sigma_a^\alpha + \sigma_b^\beta}\frac{\partial(\sigma_a^\alpha + \sigma_b^\beta)}{\partial \underline{\boldsymbol{\sigma}}_{\boldsymbol{Ng}}} \\ &= {}^t\left[\frac{\tau_{a,1}^\alpha/\phi^\alpha}{\sigma_a^\alpha + \sigma_b^\beta} \quad \cdots \quad \frac{\tau_{a,N}^\alpha/\phi^\alpha}{\sigma_a^\alpha + \sigma_b^\beta} \quad , \quad \frac{\tau_{b,1}^\beta/\phi^\beta}{\sigma_a^\alpha + \sigma_b^\beta} \quad \cdots \quad \frac{\tau_{b,N}^\beta/\phi^\beta}{\sigma_a^\alpha + \sigma_b^\beta}\right] \end{aligned} \tag{C.3}$$

Dans le cas des actinides, les écart-types et corrélations des sections efficaces intégrées en énergie de capture et de fission ont été calculées dans les spectres REP UOX, REP MOX et RNR pour les noyaux suivants :

$$\left\{{}^{234,235,236,238}\text{U};\ {}^{237,239}\text{Np};\ {}^{238,239,240,241,242}\text{Pu};\ {}^{241,242M,243}\text{Am};\ {}^{242,243,244,245,246}\text{Cm}\right\}$$

Le tableau C.4 illustre les résultats de l'application de la méthode aux réactions de fission et capture du ^{239}Pu dans les spectre REP UOX, REP MOX et RNR Na.

^{239}Pu, ENDF B-VII			UOX		MOX		RNR Na	
			σ_f	σ_c	σ_f	σ_c	σ_f	σ_c
		RSD(%)	0.77	1.13	0.74	1.03	0.41	5.26
UOX	σ_f	0.77	1.00	-0.52	0.99	-0.48	0.14	0.00
	σ_c	1.13		1.00	-0.45	0.99	0.03	0.06
MOX	σ_f	0.74			1.00	-0.41	0.18	0.00
	σ_c	1.03				1.00	0.03	0.14
RNR Na	σ_f	0.41					1.00	0.01
	σ_c	5.26						1.00

Table C.4: Matrice de covariance du ^{239}Pu dans les spectres REP UOX - REP MOX - RNR Na

La ligne et la colonne RSD indiquent l'écart-type relatif des sections intégrées en énergie dans les spectres considérés. Les valeurs du tableau indiquent les corrélations entre les différentes sections. On observe les résultats suivants:

- la fission et la capture sont anticorrélées en spectre REP UOX (-0.52) et en spectre MOX (-0.48) ;
- la fission en spectre REP UOX est très corrélée à la fission en spectre REP MOX (0.99) ;
- la capture en spectre REP UOX est très corrélée à la capture en spectre REP MOX (0.99) ;
- la capture en spectre REP UOX est anticorrélée à la fission dans en spectre REP MOX (-0.45) ;
- la capture et la fission sont décorrélées en spectre RNR Na ;
- la fission en RNR Na est faiblement corrélée à la fission en REP UOX (0.14) et en REP MOX (0.18) ;
- la capture en RNR Na est faiblement corrélée à la capture en REP UOX (0.06) et en REP MOX (0.14).

Dans le cas des produits de fission, une liste de noyaux a été établie, dont la contribution (produit sensibilité $\times$ incertitude) est importante du point de vue de la concentration en fin d'irradiation

de noyaux contributeurs à la puissance résiduelle. Les valeurs d'écart-type relatifs intégrés à un groupe d'énergie ont été obtenus pour les produits de fission suivants :

$$\left\{ {}^{133}\mathrm{Cs};\ {}^{134}\mathrm{Cs};\ {}^{147}\mathrm{Pm};\ {}^{152}\mathrm{Sm};\ {}^{153}\mathrm{Eu};\ {}^{154}\mathrm{Eu} \right\}$$

Les rendements de fission génèrent également de l'incertitude dans les calculs de scénarios. Cependant, leur incertitude est disponible dans un format pratique, du point de vue de leur utilisation dans COSI, dans les évaluations disponibles. Nous avons choisi d'utiliser l'évaluation ENDF B-VII afin d'être cohérent avec les données d'incertitude des sections efficaces.

Nous notons également que les résultats de ces calculs d'incertitudes des données nucléaires ont étéf utilisés lors de la réalisation de plans d'expérience pour la construction de métamodèles d'irradiation, ainsi que pour la construction de modèles d'équivalence du combustible.

C.5.3 Paramètres et hypothèses des scénarios

Plusieurs paramètres et hypothèses des scénarios, issus des grandeurs de l'industrie nucléaire, sont associés avec de l'incertitude, de la variabilité ou bien de l'indécision. Tout d'abord, nous séparons ces paramètres en deux sous-ensembles :

- les paramètres des scénarios, qui génèrent de l'incertitude dans les études ;
- les hypothèses des scénarios, qui constituent la charpente du scénario, et dépendent d'hypothèses décisionnelles et non pas de la mesure ou de la prédiction d'incertitudes.

La liste des paramètres des scénarios a été établie, et regroupe notamment les éléments suivants :

- isotopie de l'uranium naturel ;
- durée de l'amont du cycle ;
- durée de l'aval du cycle ;
- pertes de matière aux usines de fabrication du combustible ;
- taux de récupération des actinides à l'usine de retraitement du combustible ;
- puissance d'irradiation, burnup des réacteurs.

Les écarts-types ou intervalles de variation de ces paramètres ont été évalués en analysant le retour d'expérience industriel, ou bien en utilisant des valeurs conservatives.

Certaines grandeurs ont fait l'objet d'études et de développements particuliers. Dans le cas de la durée d'aval du cycle, un modèle basé sur l'analyse la puissance résiduelle a été couplé à la voie de calcul par métamodèles, ce qui permet de remplacer une incertitude formulée en termes de durée par une incertitude en termes de sections efficaces et paramètres d'irradiation, et évite donc le *double-counting* de cette incertitude.

L'incertitude associée au burnup a fait l'objet d'une étude approfondie. Tout d'abord, l'incertitude associée au burnup de l'ensemble d'une campagne d'irradiation a été estimée, à partir d'incertitudes issues du REX industriel sur la puissance d'irradiation sur la date de rechargement. Cependant, ce format d'incertitude est mal adapté à la structure des jeux de données du code COSI, car la paramétrisation de l'ensemble des campagnes d'un parc de réacteurs introduit des milliers de paramètres, et que la corrélation entre des burnup au déchargement de lots irradiés consécutivements dans un même coeur rend la tâche malaisée.

Pour cela, nous avons mis en place une stratégie de condensation de l'incertitude associée au burnup. Deux formules ont été calculées, permettant de conserver l'effet des corrélations entre les lots consécutifs, pour les résultats d'intérêt, selon qu'ils soient locaux (ex: puissance résiduelle d'un assemblage irradié, etc.) ou globaux (inventaire total en americium, etc.)

Ces deux méthodes simplifiées de calcul de propagation d'incertitude du burnup ont ensuite été validées par rapport à la méthode de référence sur un scénario d'intérêt (voir section C.6.2.3).

Les hypothèses de scénario ne sont pas associées à une valeur d'incertitude lors de notre étude : nous considérons que changer ces hypothèses produit un scénario différent. Ces paramètrent incluent :

- le type de combustible ;
- le stretch-out ;
- les dates de démarrage et d'arrêt des réacteurs ;
- la capacité de l'usine de retraitement, etc.

Bien que notre travail ne considère pas d'incertitude associée, il est tout à fait possible de mener des études de sensibilité afin d'évaluer l'impact du changement de ces hypothèses sur le cycle du combustible.

C.6 Études de propagation d'incertitude

C.6.1 Méthode

La méthodologie de calcul de propagation d'incertitudes est tout à fait directe : nous échantillonons les paramètres associés à une incertitude en fonction de leur distribution, et analysons la distribution des résultats. Les corrélations entre les différents paramètres sont prises en compte lorsque disponibles. Les paramètres sont échantillonnés en même temps.

Nous avons aussi réalisé d'autres études, par exemple de partage de la variance, qui consistent à estimer et comparer l'impact de différents paramètres sur un même résultat d'intérêt. Des études de faisabilité ont également été menées, afin de déterminer la probabilité qu'un scénario échoue à un moment donné, par exemple du fait d'un manque de matière fissile disponible.

C.6.2 Applications

C.6.2.1 Propagation d'incertitudes dans les calculs d'irradiation

Tout d'abord, nous calculons l'incertitude des concentrations dans le combustible irradié, à l'issue d'un calcul d'irradiation sujet à l'incertitude des données nucléaires uniquement.

Le tableau C.5 illustre les résultats de ce calcul dans le cas d'un combustible REP UOX enrichi à 4.5% irradié à 45GWj/tML. L'impact des corrélations est noté N lorsqu'il est négligeable (<1% de la valeur de l'incertitude). La part de la variance due à une incertitude de section efficace est calculée selon l'équation C.4.

$$\text{part de la variance}(m, \sigma_i) = \frac{Var(m, \sigma_i \text{ seulement échantillonné})}{Var(m)} \tag{C.4}$$

		^{238}Pu	^{239}Pu	^{240}Pu	^{241}Pu	^{242}Pu	^{241}Am
RSD (%)		4.8	1.5	1.9	1.7	3.6	4.0
impact corrélation		N	N	N	N	N	N
part de la variance (%)	$\sigma_c(^{235}\text{U})$	5					
	$\sigma_f(^{235}\text{U})$						
	$\sigma_c(^{236}\text{U})$	28					
	$\sigma_f(^{236}\text{U})$	2					
	$\sigma_c(^{238}\text{U})$	5	83	35	28	1	14
	$\sigma_f(^{238}\text{U})$			2			
	$\sigma_c(^{237}\text{Np})$	38					
	$\sigma_f(^{237}\text{Np})$	1					
	$\sigma_c(^{238}\text{Pu})$	23					
	$\sigma_f(^{238}\text{Pu})$	2					
	$\sigma_c(^{239}\text{Pu})$		6	17	24	6	4
	$\sigma_f(^{239}\text{Pu})$		10	7	2	1	
	$\sigma_c(^{240}\text{Pu})$			41	8	2	2
	$\sigma_f(^{240}\text{Pu})$						
	$\sigma_c(^{241}\text{Pu})$				6	26	1
	$\sigma_f(^{241}\text{Pu})$				26	4	3
	$\sigma_c(^{242}\text{Pu})$					57	
	$\sigma_f(^{242}\text{Pu})$						
	$\sigma_c(^{241}\text{Am})$						74
	$\sigma_f(^{241}\text{Am})$						
	$\sigma_c(^{242M}\text{Am})$						
	$\sigma_f(^{242M}\text{Am})$						
	$\sigma_c(^{243}\text{Am})$	1					
	$\sigma_f(^{243}\text{Am})$						
	$\sigma_c(^{242}\text{Cm})$	1					
	$\sigma_f(^{242}\text{Cm})$						
	$\sigma_c(^{243}\text{Cm})$						
	$\sigma_f(^{243}\text{Cm})$						
	$\sigma_c(^{244}\text{Cm})$						
	$\sigma_f(^{244}\text{Cm})$						
	sum	106	99	102	94	97	98

Table C.5: Impact des incertitudes des sections efficaces sur l'irradiation d'un combustible REP UOX

Tout d'abord, on note l'absence d'impact des sections efficaces des noyaux sur des noyaux plus légers qu'eux-même. Cela provient du fait que les noyaux plus lourd ne font généralement pas partie des voies de formation. Il existe des exceptions, notamment lié aux désintégrations alpha, mais la faible concentration en noyaux très lourds (en particulier curium) du combustible REP UOX fait que ces voies n'apparaissent pas lors du calcul de la variance. On remarque par exemple le faible impact de la disparition du ^{242}Cm sur la formation du ^{238}Pu dans ce combustible.

Ensuite, on note l'impact fort de certaines sections efficaces sur la majorité des noyaux d'intérêt, telles que la capture de l'^{238}U ou bien celle du ^{239}Pu. On remarque que la plupart des sections efficaces ayant un impact fort sont des sections de capture, dont la perturbation change le mode de formation des noyaux plus lourds, la perturbation des sections efficaces de fission tenant davantage de l'effet du second ordre.

Les résultats dans le cadre des REP MOX sont présentés dans le tableau C.7, pour le vecteur plutonium donné en table C.6 avec une teneur massique de 8.65%. Le combustible est irradié à 45GWj/tML.

isotope	mass fraction (%)
^{238}Pu	2.5
^{239}Pu	54.5
^{240}Pu	25.2
^{241}Pu	8.6
^{242}Pu	7.9
^{241}Am	1.3

Table C.6: Vecteur plutonium pour la propagation de l'incertitude des sections efficaces dans du combustible REP MOX

On note que la répartition de l'incertitude est parfois différente. On prend l'exemple de la concentration en ^{238}Pu après irradiation. Alors que dans les REP UOX elle est principalement sensible à sa formation depuis le ^{237}Np (formé par captures successives sur l'^{235}U, l'^{236}U), elle dépend avant tout de la section efficace de capture, donc de sa disparition, dans le combustible MOX. Ceci est lié au fait que la concentration initiale en ^{238}Pu a une grande importance dans la concentration finale. De plus, on note l'influence de la capture sur l'^{241}Am, qui forme du ^{242}Cm puis le ^{238}Pu après désintégration alpha.

De manière générale, la tendance à être sensible aux sections efficace de capture des isotopes plus légers est conservée. On notera le fait que les curiums sont peu sensibles à leur propre section efficace, et dépendent presque exclusivement de leurs voies de formation. Ce résultat est intéressant, étant donné que les sections efficaces de voies de formation sont généralement mieux connues que celles des istopes du curium.

C.6.2.2 Scénario A : Parc REP historique français

La comparaison avec les données expérimentales est une partie importante du processus de validation d'un code de calcul. Parfois les données sont importantes, et la qualification du code sur un large domaine est possible. Cependant, il n'y a pas d'expérience avec des données entièrement disponibles pour les études de scénarios. Une certaine quantité de données est disponible, mais l'immense volume d'informations nécessaires à la description précise d'un scénario, couplé

		^{238}Pu	^{239}Pu	^{240}Pu	^{241}Pu	^{242}Pu	^{241}Am	^{243}Am	^{242}Cm	^{244}Cm
RSD (%)		2.4	0.9	1.0	1.3	3.5	3.8	9.6	1.6	10.5
correlation impact		N	N	N	N	N	N	N	N	N
part of variance (%)	$\sigma_c(^{235}\text{U})$									
	$\sigma_f(^{235}\text{U})$									
	$\sigma_c(^{236}\text{U})$									
	$\sigma_f(^{236}\text{U})$									
	$\sigma_c(^{238}\text{U})$		69	5					1	
	$\sigma_f(^{238}\text{U})$									
	$\sigma_c(^{237}\text{Np})$									
	$\sigma_f(^{237}\text{Np})$									
	$\sigma_c(^{238}\text{Pu})$	86	2							
	$\sigma_f(^{238}\text{Pu})$									
	$\sigma_c(^{239}\text{Pu})$		16	15	2					
	$\sigma_f(^{239}\text{Pu})$		10							
	$\sigma_c(^{240}\text{Pu})$		1	78	42	1	3		5	
	$\sigma_f(^{240}\text{Pu})$									
	$\sigma_c(^{241}\text{Pu})$				21	9			1	
	$\sigma_f(^{241}\text{Pu})$		1		32				5	
	$\sigma_c(^{242}\text{Pu})$					90		97		92
	$\sigma_f(^{242}\text{Pu})$									
	$\sigma_c(^{241}\text{Am})$	13					95		84	
	$\sigma_f(^{241}\text{Am})$									
	$\sigma_c(^{242M}\text{Am})$									
	$\sigma_f(^{242M}\text{Am})$									
	$\sigma_c(^{243}\text{Am})$							2		7
	$\sigma_f(^{243}\text{Am})$									
	$\sigma_c(^{242}\text{Cm})$								2	
	$\sigma_f(^{242}\text{Cm})$									
	$\sigma_c(^{243}\text{Cm})$									
	$\sigma_f(^{243}\text{Cm})$									
	$\sigma_c(^{244}\text{Cm})$									1
	$\sigma_f(^{244}\text{Cm})$									
	sum	99	99	98	97	100	98	99	98	100

Table C.7: Impact des incertitudes des sections efficaces sur l'irradiation d'un combustible REP MOX

à la difficulté de rassembler des données précises et complètes, rend cette tâche particulièrement délicate.

En 2011, le Laboratoire d'Études du Cycle a commencé un travail [C.2, 3] destiné à fournir un recueil de données aussi cohérent et complet que possible, en rapport avec l'historique du parc REP français actuel. Etant donné que la comptabilité tenue par les industriels n'est pas disponible au public, les données ont principalement été extraites de ressources internes. Cependant, l'information reste incomplète et l'introduction d'hypothèses est obligatoire.

Du point de vue de la mesure, l'ANDRA a accumulé et analysé les données des inventaires des différentes matières reliées au cycle du combustible électronucléaire. L'inventaire de l'année 2010 est paru en 2012 [C.4]. Bien que ce document ne donne pas d'information concernant chaque bilan matière ou isotopie dans le cycle du combustible, il fournit des résultats utiles en termes d'inventaires et flux de matières globaux.

La présente étude a trois objectifs :

- comparaison des résultats de COSI-CESAR5.3 à ceux de COSI-MeSAR ;
- comparaison des résultats COSI aux résultats ANDRA ;
- comparaison du biais (COSI, ANDRA) à l'incertitude issue des données nucléaires.

Le cycle du combustible est illustré sur le schéma C.8.

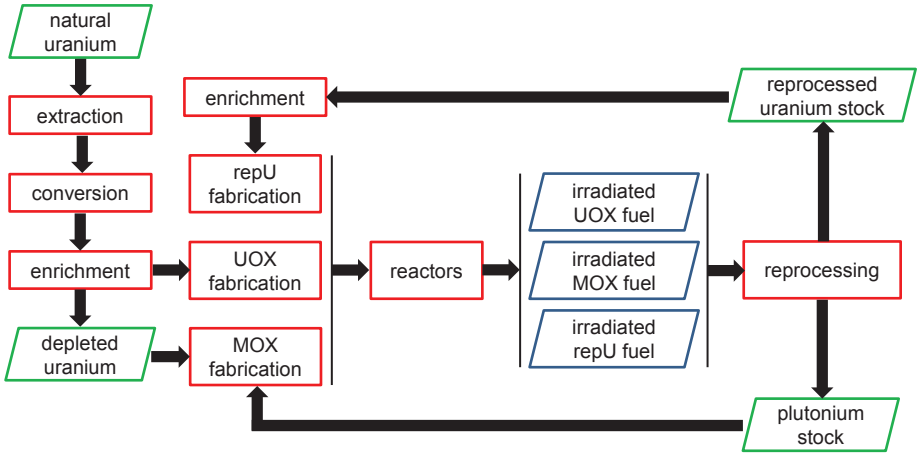

Figure C.8: Scenario A : cycle du combustible 2010

Le tableau C.8 permet de comparer les résultats de COSI-CESAR5.3 et COSI-MeSAR à la date du 31 décembre 2010. On utilise les notations suivantes :

- U_{app} : stock d'uranium appauvri ;
- Pu_{dispo} : inventaire de plutonium disponible (somme du plutonium séparé et du plutonium dans les combustibles irradiés suffisamment refroidis pour être retraités) ;
- CI : masse de combustible irradié.

On observe que l'accord entre COSI-CESAR5.3 et la nouvelle voie de calcul COSI-MeSAR est très bon pour ces résultats. Par conséquent, COSI-MeSAR est utilisé pour la suite de l'étude.

Le tableau C.9 montre l'écart entre les relevés de l'ANDRA et les résultats COSI à la date du 31/12/2010, ainsi que l'incertitude des résultats COSI-MeSAR liés aux incertitudes des données nucléaires.

Résultat	COSI-CESAR (tonnes)	COSI-MeSAR (tonnes)	$\frac{\text{COSI-MeSAR}}{\text{COSI-CESAR}} - 1$	C.-M. − C.-C. (tonnes)
U_{app}	204071	204066	-0.002%	-5
Pu_{dispo}	35.86	36.00	0.39%	0.14
$CI_{REP\ UOX}$	12037	12037	0%	0
$CI_{REP\ URE}$	381	381	0%	0
$CI_{REP\ MOX}$	1416	1416	0%	0

Table C.8: Scénario A : comparaison de COSI-CESAR et COSI-MeSAR pour différents résultats d'intérêt, au 31/12/2010

Résultat	ANDRA (t)	COSI-MeSAR (t)	$\frac{\text{COSI-MeSAR}}{\text{ANDRA}} - 1$	$\frac{\sigma(\text{COSI-MeSAR})}{\text{COSI-MeSAR}}$ (%)
U_{dep}	271481	204063	-24.83%	0.04%
Pu_{av}	45.00	36.00	-20.00%	5.58%
$SF_{PWR\ UOX}$	12006	12037	0.26%	0.00%
$SF_{PWR\ repU}$	318	381	19.81%	0.00%
$SF_{PWR\ MOX}$	1287	1416	10.00%	0.00%

Table C.9: Scénario A : comparaison ANDRA, COSI-MeSAR et incertitude, au 31/12/2010

On observe un fort biais sur la masse d'uranium appauvri. Celui-ci ne peut pas être expliqué par les incertitudes des données nucléaires, et provient donc d'un défaut de modélisation ou d'un manque de connaissance. Etant donné que la consommation d'uranium naturel est correctement calculée par COSI (écart $\approx 0.6\%$), il est probable que l'écart provienne de la présence de matière étrangere sur le sol français, mais néanmoins comptabilisée par l'ANDRA.

La masse de plutonium séparé présente un écart également supérieur à l'amplitude de l'incertitude liée aux données nucléaires. Cependant, on peut supposer que l'écart provienne d'un décalage dans la date de comptage : selon le jour de l'année où le plutonium a été compté, la masse de plutonium peut varier dans de très larges intervalles étant donné que les flux de masses de plutonium (issus du retraitement et en direction de l'usine de fabrication du MOX) sont de la même magnitude que l'inventaire de plutonium disponible lui-même. On remarque également, comme l'indique le tableau C.10, que le relevé de l'inventaire plutonium de l'ANDRA du 31/12/2010 est encadré par les calculs COSI aux dates du 30/06/2010 et 30/06/2011.

inventaire en plutonium séparé	μ (t)	σ (t)	COSI-MeSAR − ANDRA (t)
COSI-MeSAR 30/06/2010	38.1	2.0	-6.9
COSI-MeSAR 31/12/2010	36.0	2.1	-9.0
COSI-MeSAR 30/06/2011	52.5	2.2	+7.5
ANDRA 31/12/2010	45.0		

Table C.10: Scénario A :inventaire en plutonium disponible calculé à différentes dates en fonction de la date de comptage, et incertitude associée

Les masses de combustible irradié ne sont pas soumises à l'incertitude des données nucléaires, mais sont fixées par hypothèse sur les successions de campagnes. Par conséquent celles-ci ne peuvent expliquer l'écart entre les résultats COSI et les relevés ANDRA. Dans le cas des combustibles irradiés UOX, COSI donne un résultat très proche de l'ANDRA. Dans le cas des combustible REP URE, la différence est plus importante, et peut être expliquée par un manque de connaissances concernant le démarrage des campagnes REP URE. Il peut également y avoir un

biais dans la date de comptage. Dans le cas des combustibles irradiés REP MOX, une analyse précédente du résultat suggère une surestimation de l'inventaire par l'ANDRA.

De manière générale, nous avons pu constater que les écarts entre la simulation COSI et les relevés de l'ANDRA sont davantage reliés à un manque de connaissance de l'historique exact du parc, ainsi qu'à des incertitudes quant à la date de comptage des inventaires par l'ANDRA.

C.6.2.3 Scénario B : scénario industriel de transition

Dans la continuité de la loi 2006 concernant les matières et déchets radioactifs, le CEA et ses partenaires industriels EDF et AREVA ont décidé de travailler ensemble à l'élaboration de scénarios de transition de la flotte REP actuelle vers l'indépendence vis à vis de l'uranium naturel. Le présent scénario est une étape intermédiaire dans le processus de la définition d'un plan de route pour le futur déploiement des RNR. Ce processus est divisé en cinq strates, ou paliers, chaque palier reposant sur le précédent et apportant de nouveaux objectifs en termes de résultats de scénario. Nous résumons brièvement ces étapes :

- palier 0 : modélisation de la flotte historique française (REP UOX et REP MOX) jusqu'en 2015 ;
- palier A : remplacement progressif des REP actuels par des EPR en conservant la production électrique constante, stabilisation des inventaires en combustible REP UOX irradié et uranium de retraitement ;
- palier B : remplacement progressif des REP actuels par des EPR en conservant la production électrique constante, stabilisation des inventaires en combustible REP UOX MOX irradié (via l'introduction de quelques RNR) et uranium de retraitement ;
- palier C : stabilisation à long terme de l'inventaire en plutonium ;
- palier D : indépendance vis à vis de l'uranium naturel.

Ce scénario est un des candidats au palier B, qui sont principalement destinés à choisir parmi différentes stratégies de retraitement du combustible. Le parc historique est remplacé petit à petit par 22 EPR UOX, 10 EPR 30% MOX / 70% UOX et 3 RNR. Du fait de sa structure, ce scénario constitue une base solide pour une étude de la propagation des incertitudes liées au burnup. On étudie ici uniquement la propagation de l'incertitude issue du burnup des réacteurs EPR.

La figure C.9 illustre l'évolution des inventaires en éléments d'intérêt en fonction du temps. La figure C.10 représente l'évolution des écarts-types associés, liés à l'incertitude du burnup.

On observe que les incertitudes relatives restent très basses : l'écart-type relatif est inférieur à 0.2% dans tous les cas, et inférieur à 0.03% pour le plutonium, l'américium et le neptunium. Ce résultat est contre-intuitif car on a observé dans les études précédentes que la sensibilité au burnup de la composition isotopique du combustible irradié est très forte. La différence provient du fait que dans un scénario, les burnup de différents réacteurs ne sont pas corrélés entre eux, et les burnup de lots irradiés de manière non consécutive dans un même réacteur ne sont pas non plus corrélés. Étant donné que les inventaires se comportent, de manière générale, comme des sommes de bilan matière en sortie des réacteurs (ce résultat est une approximation, la décroissance et le retraitement du combustible entrent également en compte), ils forment donc une somme d'un grand nombre de termes gaussiens décorrélés pour la plupart. Par conséquent, l'écart-type relatif décroît avec l'augmentation du nombre de lots irradiés, d'où le résultat.

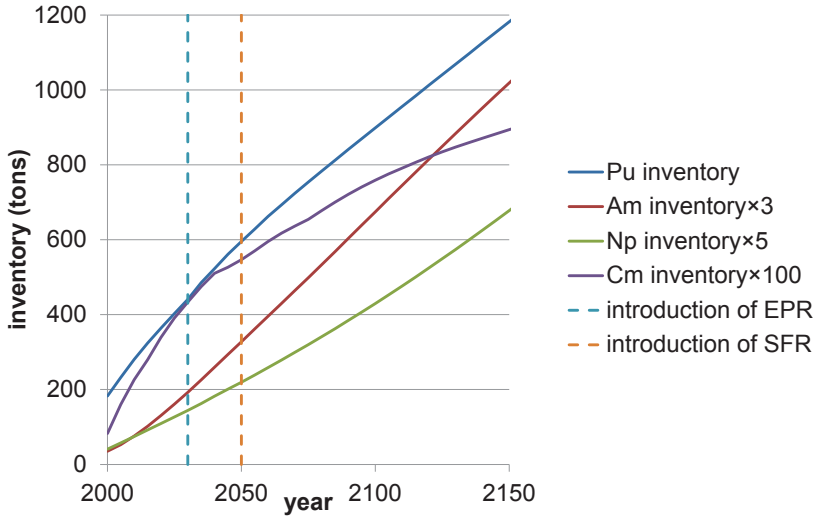

Figure C.9: Scénario B : évolution des inventaires de différents éléments d'intérêt

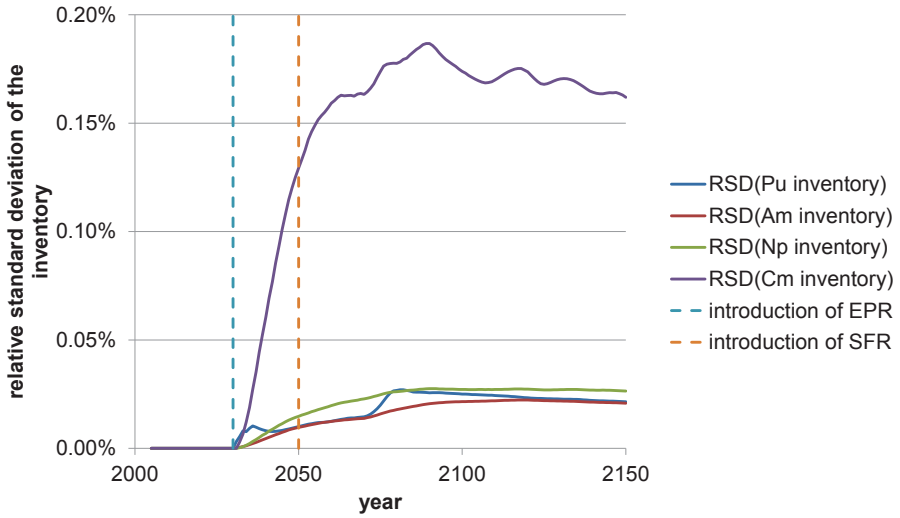

Figure C.10: Scenario B : évolution des écart-types relatifs des inventaires de différents éléments d'intérêt

De manière générale, nous constatons que l'impact du burnup sur les grandeurs du cycle est relativement faible. Ce résultat a été évalué pour les grandeurs suivantes :

- inventaires ;
- isotopie du combustible EPR MOX neuf (présence de pics d'incertitudes lié à des changement de gestion du combustible) ;
- puissance résiduelle (incertitude de l'ordre de quelques pourcents, quelques pics liés à des changements de gestion du combustible).

Ce scénario a également servi de base de test aux méthodes simplifiées d'échantillonnage du burnup définies en C.5.3. Trois méthodes sont comparées :

- méthode α : méthode de référence, les burnup de chaque cycle d'irradiation sont échantillonnés indépendamment et combinés entre eux pour produire des burnup au déchargement ;
- méthode β : méthode servant à conserver l'incertitude des résultats locaux (liés à un lot de combustible) ;
- méthode γ : méthode servant à conserver l'incertitude des résultats globaux (intégrés sur le cycle).

La figure C.11 représente l'application des méthodes au calcul de l'incertitude de la puissance résiduelle du combustible mixte REP MOX irradié, puis refroidi dix ans (ce qui constitue un résultat local). La figure C.12 représente l'application de ces mêmes méthodes au calcul de l'incertitude de l'inventaire en américium au cours du scénario (ce qui constitue un résultat global).

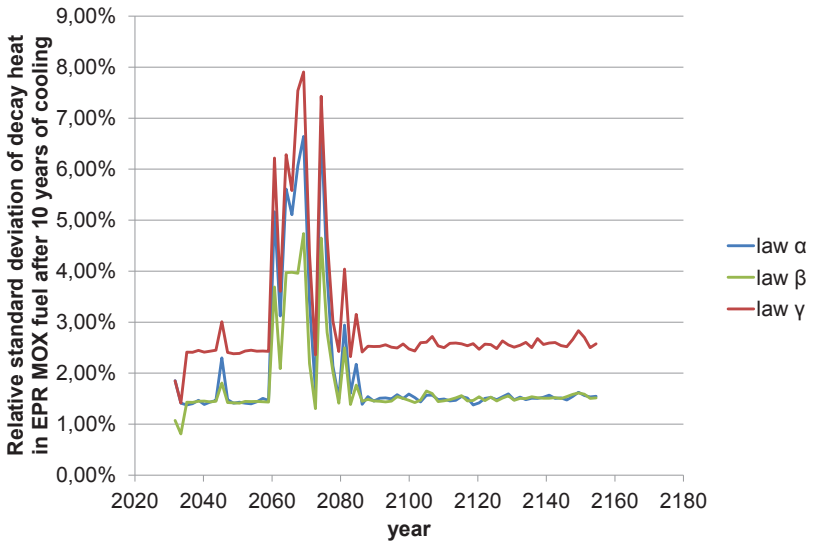

Figure C.11: Scenario B : incertitude de la puissance résiduelle du combustible EPR MOX refroidi 10 ans (méthodes α, β et γ)

On constate que les méthodes fournissent le résultat demandé, c'est à dire la reconstitution de l'incertitude des résultats d'intérêt tout en simplifiant considérablement le processus d'échantillonnage. Les méthodes β et γ ont été implémentées dans COSI et sont utilisables avec la nouvelle voie de calcul COSI-MeSAR.

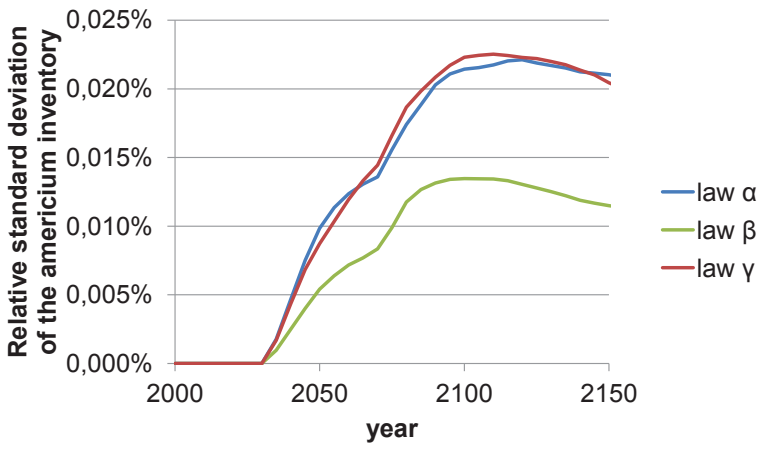

Figure C.12: Scenario B : incertitude de l'inventaire en américium (méthodes α, β et γ)

C.6.2.4 Scénario C : Scénario académique de transition sans recyclage des actinides mineurs

Dans le cadre de la loi de 2006 sur les matériaux et déchets radioactifs, qui souligne le besoin d'étudier de manière approfondie la séparation et la transmutation des noyaux à vie longue, un ensemble de scénarios a été mis au point. Ces scénarios ont pour objectif l'estimation de l'impact de la transmutation des actinides mineurs en RNR sur le cycle du combustible.

Le scénario C peut être vu comme le tronc commun de ces scénarios. Il est un scénario académique de transition vers les RNR, avec multirecyclage du plutonium, sans recyclage des actinides mineurs. Il ne s'agit pas d'un scénario industriel, mais plutôt d'un support aux études de sensibilité, et est basé sur un jeu d'hypothèses différent du scénario B.

La figure C.13 représente le cycle du combustible avant 2038 : le combustible est irradié en REP UOX, REP URE et REP MOX (70% UOX, 30% MOX). Le combustible UOX est retraité, le plutonium est recyclé en REP MOX. Le déploiement des EPR commence en 2020.

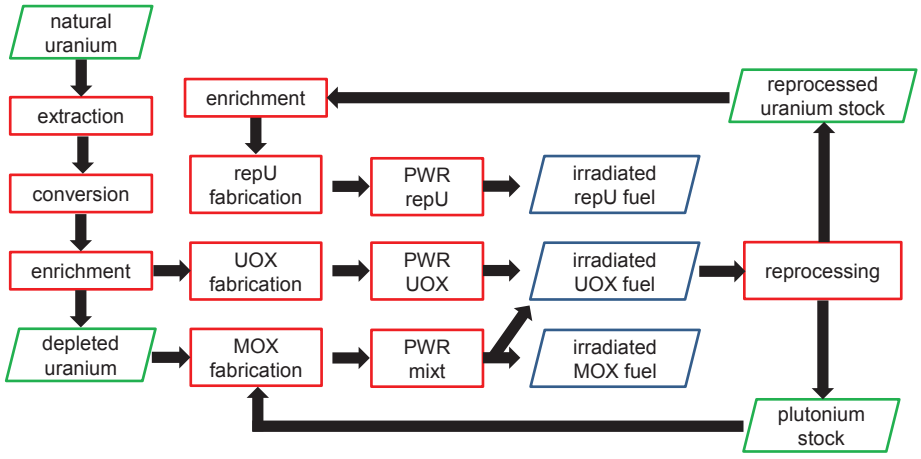

Figure C.13: Scenario C : cycle du combustible avant 2038

Le dernier lot REP MOX est irradié en 2038, et le premier RNR (avec un design CFV [C.5]) démarre en 2040. La figure C.14 représente la transition de la flotte REP vers une flotte mixte

REP / RNR. Le combustible RNR est fabriqué à partir des matières issues du traitement des combustibles REP UOX et REP MOX, puis à partir de combustible RNR retraité.

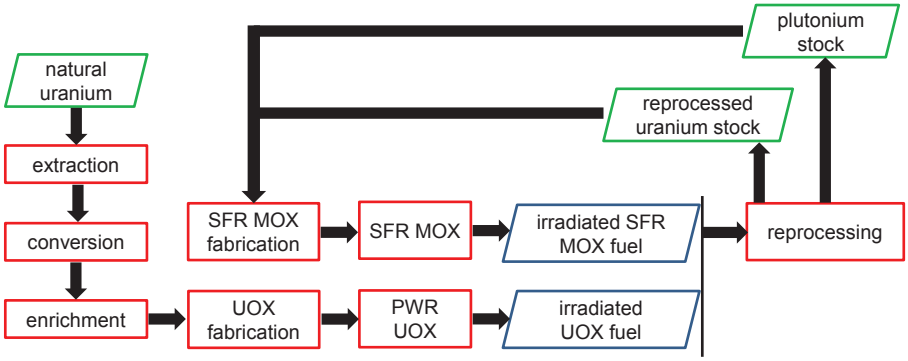

Figure C.14: Scenario C : cycle du combustible entre 2038 et 2100

Après 2100, tous les REP sont éteints et le parc est entièrement remplacé par des RNR (en deux strates). La figure C.15 représente le cycle du combustible après 2100. La spécificité de ce cycle est qu'il ne requiert pas d'apport de ressources naturelles pour une longue durée.

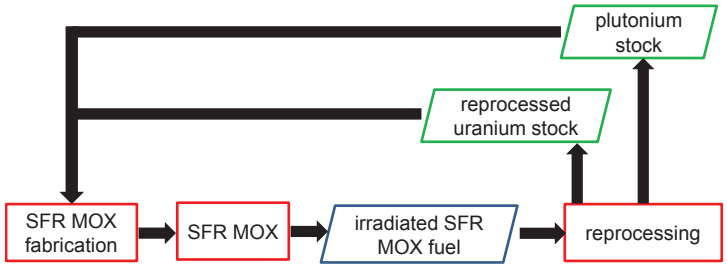

Figure C.15: Scenario C : cycle du combustible après 2100

Les incertitudes prises en compte pour cette étude sont les suivantes :

- burnup ;
- données nucléaires :
  - sections efficaces des actinides et produits de fission, corrélations associées ;
  - rendements de fission (sans condition de renormalisation).

On commence par l'étude des inventaires globaux. La figure C.16 illustre l'évolution des inventaires en éléments d'intérêt, et la figure C.17 montre les écarts-types relatifs associés.

On constate tout d'abord que les incertitudes sont nettement plus importantes que dans l'étude précédente : les données nucléaires introduisent une incertitude très supérieure au burnup pour les inventaires globaux.

On observe ensuite que l'incertitude sur les inventaires du plutonium, de l'américium et du neptunium sont relativement stables, alors que l'incertitude du curium augmente fortement avec le temps. Ceci est lié au fait que l'inventaire en curium diminue lorsque l'ensemble du parc est remplacé par des RNR, mais qu'il continue tout de même à être formé.

Le scénario C est un bon support à l'étude des modèles d'équivalence. Tout d'abord, on peut comparer les résultats obtenus, en termes de teneur du combustible neuf, pour différents modèles d'équivalence. La figure 6.24 illustre la teneur du combustible neuf en réacteur REP MOX (type

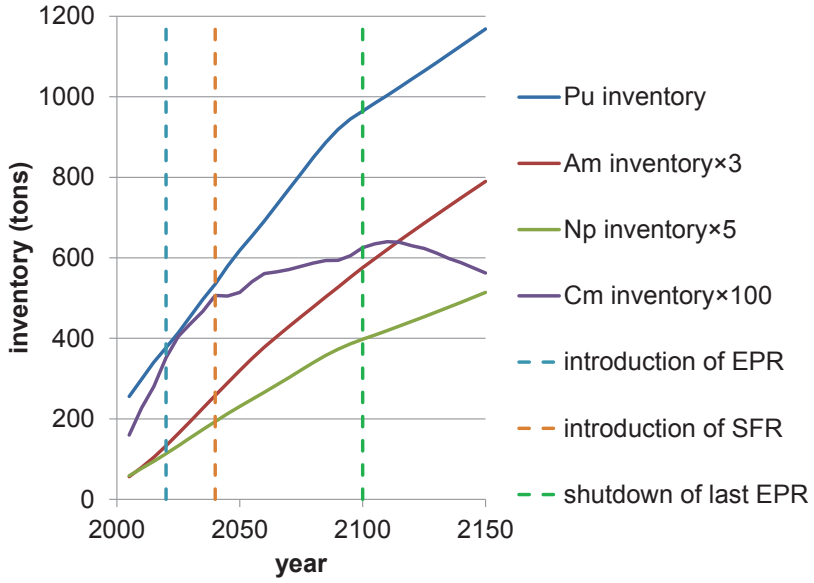

Figure C.16: Scenario C : évolution des inventaires en différents éléments d'intérêt

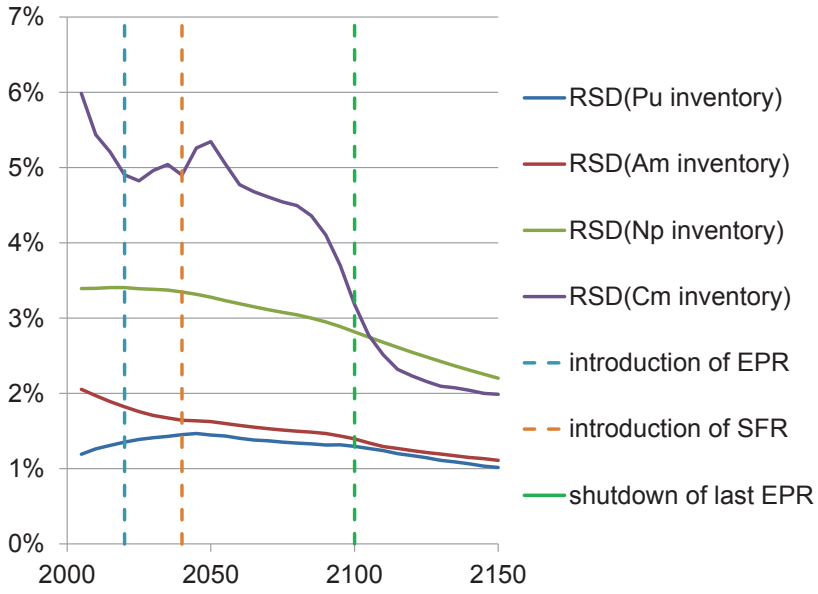

Figure C.17: Scenario C : évolution des écarts-types relatifs des inventaires en différents éléments d'intérêt

CPY) en fonction de l'année (la date correspond au premier jour d'irradiation du lot). Plusieurs modèles sont comparés :

- un modèle imposant la teneur initiale (fixed model) ;
- le modèle standard REP MOX (standard MOX model), présent dans COSI ;
- le modèle statistique, développé dans cette étude, testé pour différentes valeurs de réactivité du cœur cible en fin de cycle.

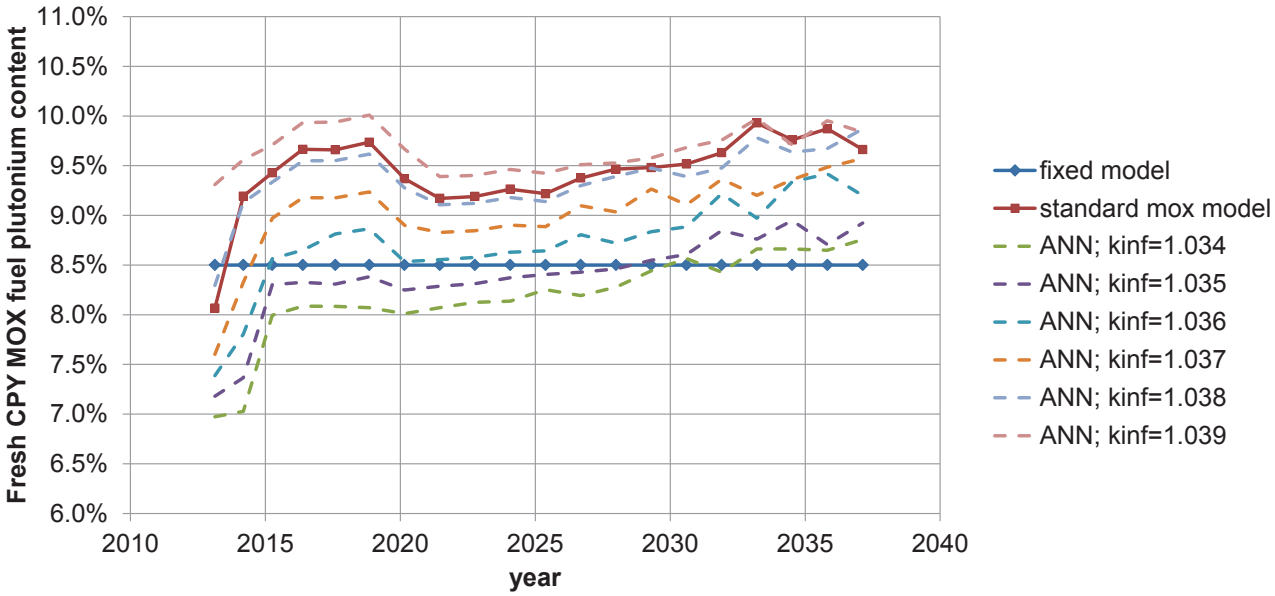

Figure C.18: Scenario C : teneur plutonium en CPY MOX, calculée avec différents modèles d'équivalence

On constate tout d'abord que la teneur du combustible varie fortement en fonction de l'isotopie du combustible neuf, excepté dans le cas du modèle fixe. On peut donc s'interroger sur la pertinence de l'utilisation de ce modèle.

Ensuite, on constate que l'on retrouve approximativement les résultats du modèle standard MOX avec le modèle statistique pour une réactivité cible de +3800pcm en fin d'irradiation. Ce résultat est à rapprocher de la réactivité fin de cycle de +3900pcm préconisée dans [C.6].

On réalise ensuite le calcul de propagation des incertitudes dans le scénario, et on évalue l'impact des incertitudes des sections efficaces sur la teneur initiale du combustible MOX. La figure C.19 illustre l'écart-type relatif de la teneur du combustible neuf (courbe *ND in irrad + equiv*), ainsi que la part de la variance due d'une part à la propagation de l'incertitude dans les modèles d'équivalence uniquement (courbe *ND in equivalence*), et d'autre part à la propagation de l'incertitude dans les modèles d'irradiation uniquement (courbe *ND in irradiation*).

Tout d'abord, on remarque que l'incertitude de la teneur initiale est importante : approximativement 8%. Ensuite, on constate que l'effet des données nucléaires dans les modèles d'équivalence domine celui dans les modèles d'irradiation. Ce résultat provient du fait que l'effet des données nucléaires dans les modèles d'irradiation est un second ordre concernant la teneur du combustible, car il modifie la composition isotopique du combustible irradié puis retraité, mais n'influe pas directement sur le calcul de la teneur.

Une analyse semblable est menée pour les modèles d'équivalence RNR, avec des conclusions glob-

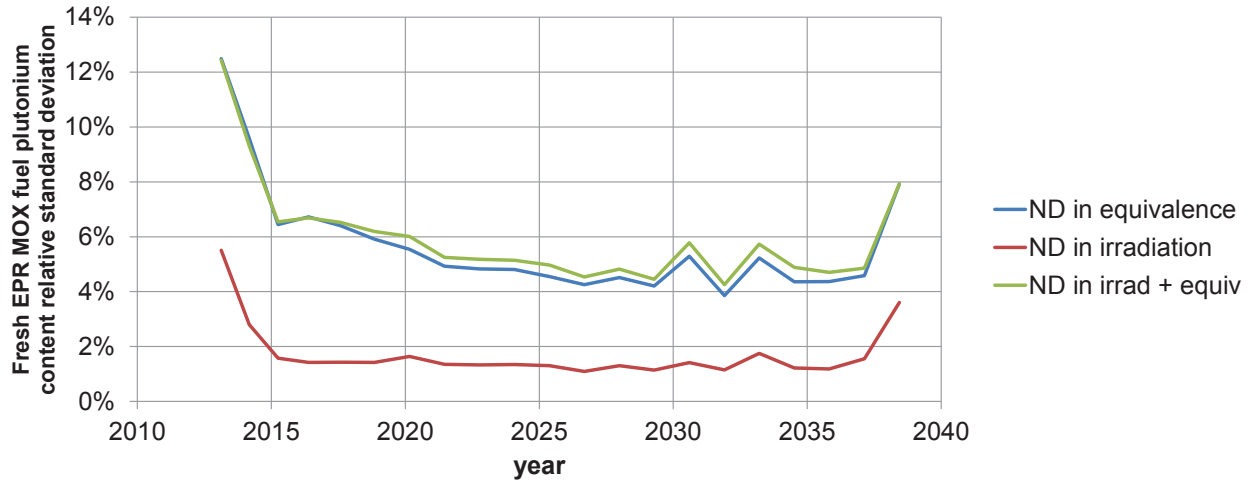

Figure C.19: Scénario C : écart-type relatif de la teneur plutonium en CPY MOX

alement similaires. La figure C.20 illustre les contributions des données nucléaires à travers les modèles d'équivalence et d'irradiation à l'incertitude totale de la teneur. On notera que l'incertitude de la teneur est plus faible pour les RNR que pour les REP MOX.

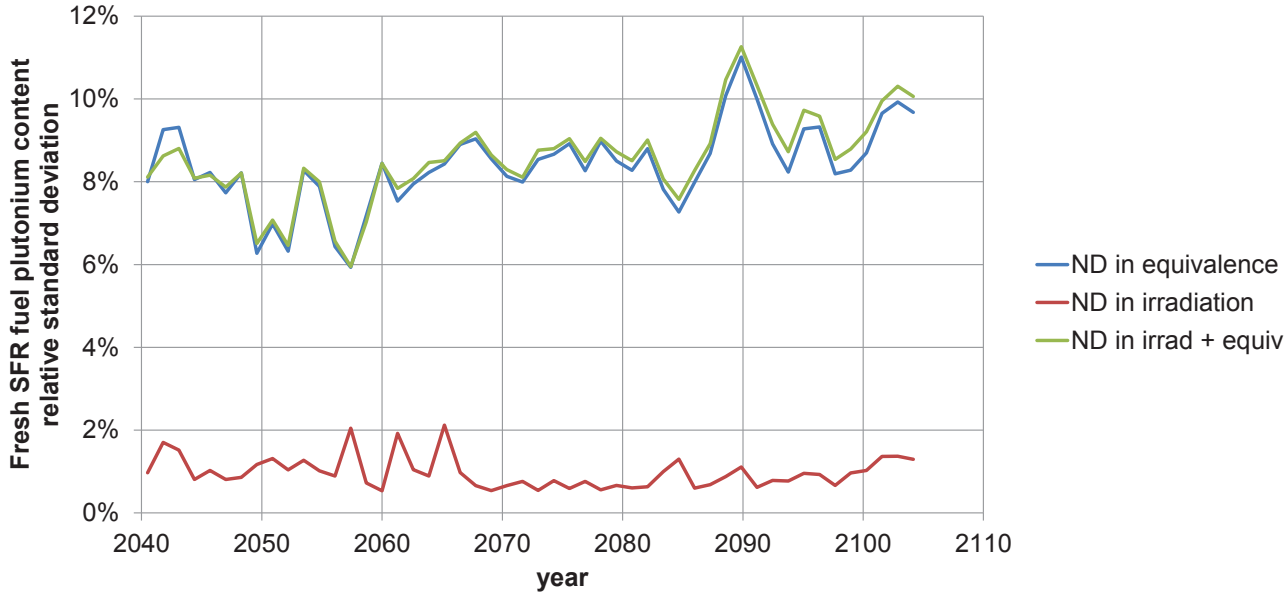

Figure C.20: Scenario C : écart-type relatif de la teneur plutonium en RNR

C.6.2.5 Scénario D : Scénario académique de transition avec recyclage des actinides mineurs

Le CEA étudie la transmutation des actinides mineurs, tels que l'américium. Cela consiste à faire subir une série de réactions à un noyau de sorte à ce qu'il soit transformé en un noyau ayant une forte section efficace de fission. La fission d'un actinide mineur (avant ou après transmutation) est la dernière étape du processus, et est appelée incinération. L'objectif de l'opération

est de produire des noyaux radioactifs à vie courte, qui ont par conséquent une contribution plus faible à la radiotoxicité aux temps longs.

L'objectif du scénario D est d'évaluer l'intérêt de la transmutation hétérogène (en couvertures) de l'américium en RNR. Le résultat attendu de l'étude est la stabilisation de l'inventaire en américium. Le scénario D est basé sur le scénario C décrit plus haut, mais ajoute la gestion de l'américium :

- présence de couverture chargées en américium (CCAm) avec une teneur fixe en américium (10% massique) en RNR ;
- séparation de l'américium à l'usine de retraitement.

Les incertitudes prises en compte pour cette étude sont les suivantes :

- burnup ;
- données nucléaires :
  - sections efficaces des actinides et produits de fission, corrélations associées ;
  - rendements de fission (sans condition de renormalisation).

Le cycle du combustible après 2100 est représenté sur la figure C.21.

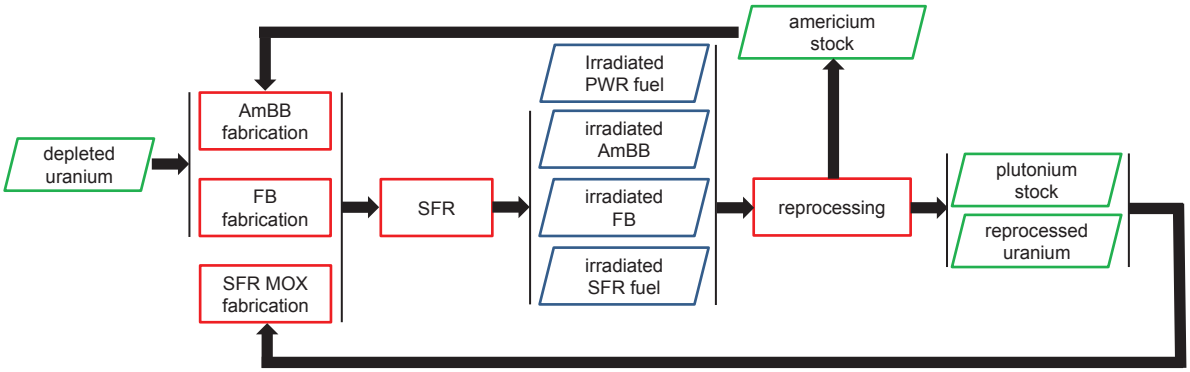

Figure C.21: Scenario D : cycle du combustible après 2100

La figure C.22 illustre l'évolution de l'inventaires en différents éléments d'intérêt. On note la stabilisation de l'inventaire en américium après 2100.

La figure C.23 illustre l'incertitude des inventaires en éléments d'intérêt.

On observe que l'incertitude de l'américium croît en fin de scénario. Ceci est lié à la stabilisation de l'inventaire en américium, dont la formation ainsi que la transmutation sont sources d'incertitude.

Les impacts des incertitudes du burnup et des sections efficaces sont comparés pour plusieurs résultats d'intérêt. Par exemple, la figure C.24 illustre l'incertitude de l'inventaire en américium, ainsi que ses composantes en burnup et en données nucléaires, de même la figure C.25 illustre la contribution de ces données à la puissance résiduelle des CCAm. Il apparaît que les données nucléaires introduisent, de manière générale, une incertitude très supérieure à celle du burnup.

Une étude de faisabilité du scénario D est ensuite menée, en évaluant la probabilité de manquer de matière fissile (plutonium en particulier) à un moment donné du scénario. En considérant uniquement les incertitudes sur le burnup et les données nucléaires, la faisabilité du scénario

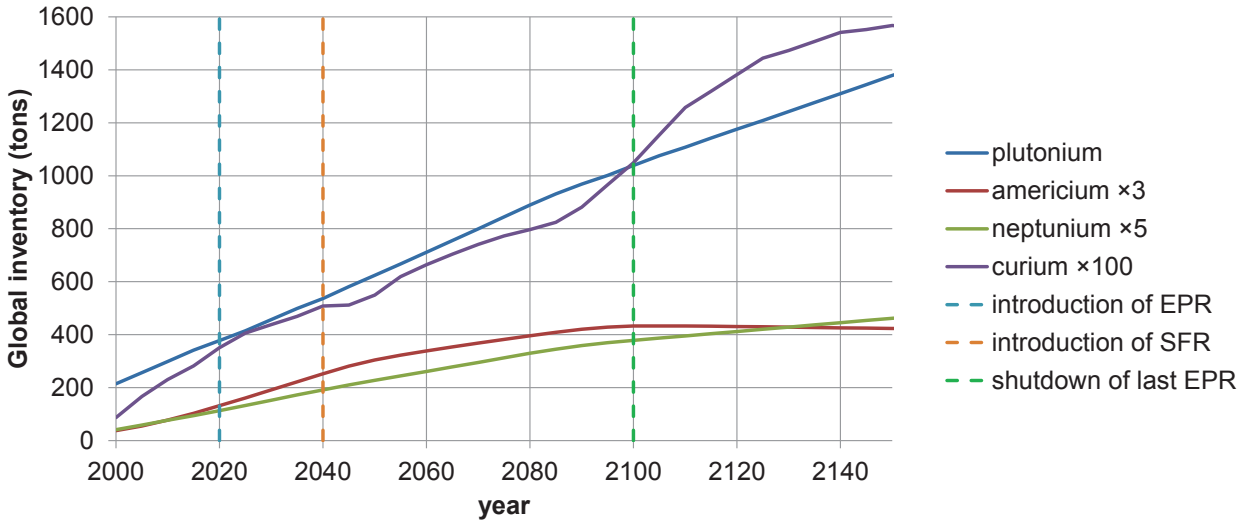

Figure C.22: Scenario D : inventaires de différents éléments d'intérêt

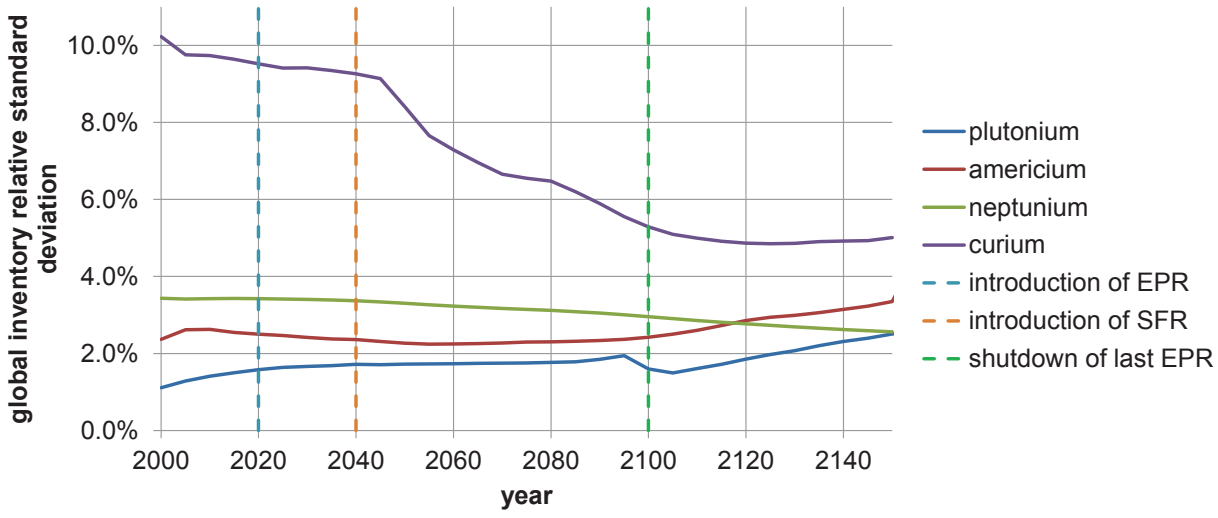

Figure C.23: Scenario D: evolution of the inventories relative standard deviation for different elements of interest

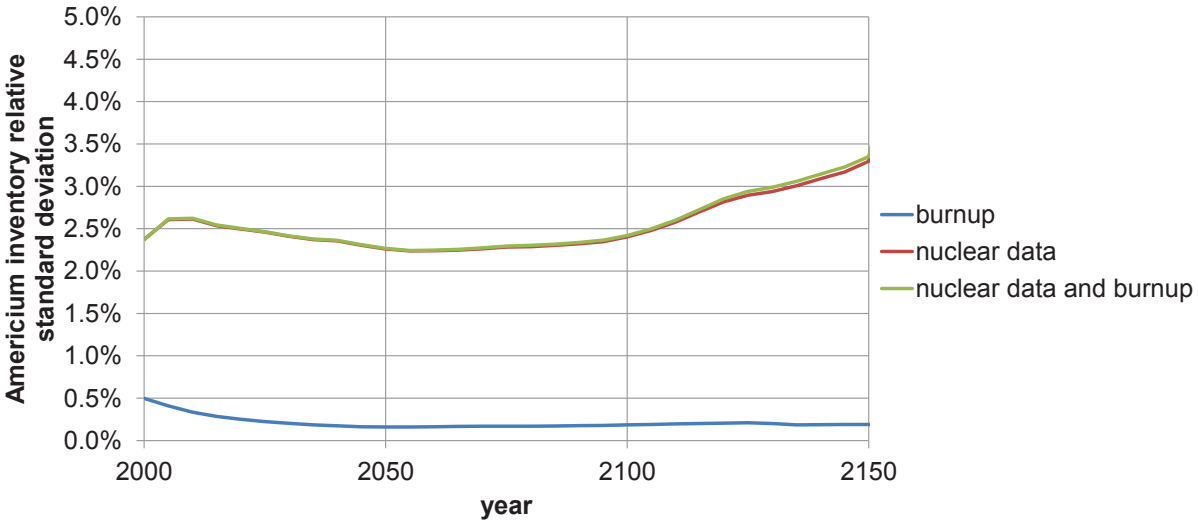

Figure C.24: Scenario D : comparaison des sources d'incertidue pour l'inventaire en américium

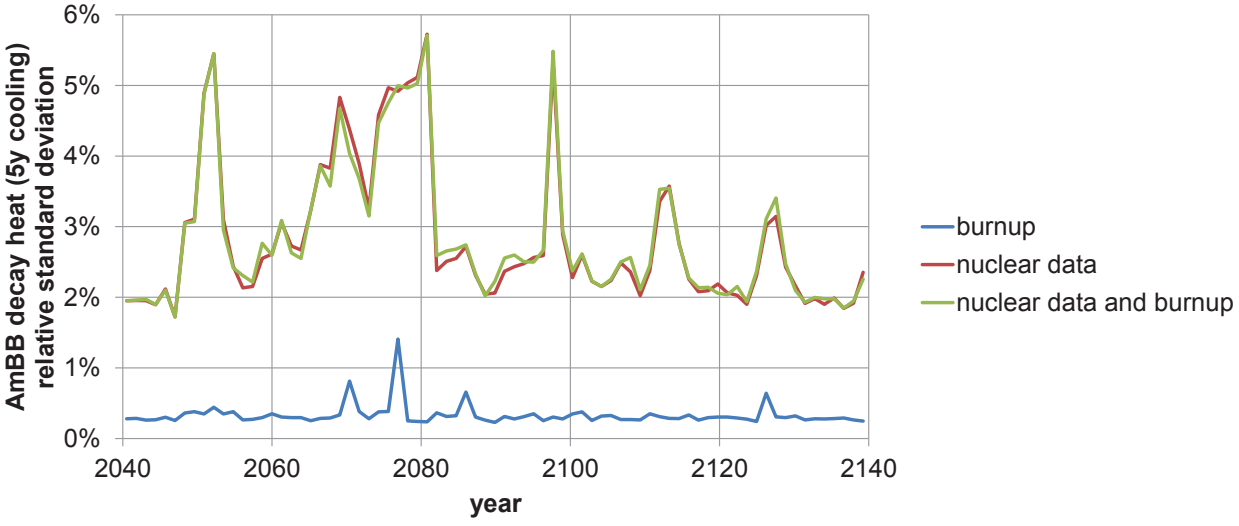

Figure C.25: Scenario D : comparaison des sources d'incertitude pour la puissance résiduelle des CCAm après 5 ans de refroidissement

est de 54%, ce qui est faible. Le plutonium tend à manquer lors du déploiement des derniers RNR de chaque strate, soit 2050 et 2100.

Une analyse des contributions à la non-faisabilité souligne l'impact de l'incertitude associée aux paramètres suivants :

- taux de récupération du plutonium à l'usine de retraitement ;
- durée de fabrication du combustible RNR ;
- puissance résiduelle (incertitude issue notamment des données nucléaires).

De manière générale, un scénario déclaré *non faisable* peut devenir faisable en décalant de quelques années le démarrage du dernier RNR de chaque strate.

C.7 Conclusions

Nous avons développé dans ce travail une méthode permettant d'effectuer des calculs stochastiques de propagation d'incertitude dant tout scénario électronucléaire, y compris de transition.

Plusieurs modèles physiques ont été développés :

- métamodèles d'irradiation du code CESAR, permettant le calcul rapide d'irradiation et la prise en compte des perturbations des données nucléaires ;
- modèles d'équivalence statistiques, permettant de prendre en compte les données nucléaires lors du calcul de la teneur du combustible neuf.

Ces modèles ont été ensuite implémentés dans le code de scénario COSI.

Les incertitudes des données suivantes ont été calculées, recueillies ou obtenues par retour d'expérience :

- données nucléaires :
  - incertitudes et corrélations des sections efficaces intégrées en énergie dans les spectres d'intérêt ;
  - rendements de fission ;
- paramètres de scénario :
  - paramètres du combustible (en particulier burnup) ;
  - paramètres des différentes usines du cycle.

La méthode de calcul de propagation d'incertitudes a ensuite été appliquée à différents scénarios d'intérêt :

- le scénario historique du parc français ;
- un scénario industriel de déploiement des RNR ;
- un scénario académique de déploiement des RNR sans transmutation ;
- un scénario académique de déploiement des RNR avec transmutation de l'américium en hétérogène.

Les incertitudes des inventaires en plutonium, américium, neptunium et curium sont généralement de l'ordre de quelques pourcents.

De manière générale, les données nucléaires ont un impact nettement supérieur au burnup sur les résultats des études de scénarios. Ce résulta provient principalement du fait que les données

nucléaires sont corrélées entre différents lots de combustible et différents réacteurs du parc, tandis que le burnup ne l'est pas (l'incertitude du burnup se *dilue* dans le parc).

La faisabilité des scénarios de transition vers les RNR est impactée par les incertitudes des données nucléaires, du burnup, et des autres paramètres des scénarios. Ce pendant, une analyse de l'ordre de grandeur du déficit en matière fissile indique qu'il est généralement possible de poursuivre le scénario en décalant de quelques années le démarrage de certains RNR.

Bibliography

[C.1] R. Craplet and J. Ahn. Mathematical modeling and its applications for mass flow in a nuclear fuel cycle. *Nuclear technology*, 177:pages 314–335, 2012.

[C.2] C. Cany and C. Coquelet-Pascal. Validation du code de scénarios COSI, estimation des biais du scénario F4. Master's thesis, PHELMA, 2012.

[C.3] R. Eschbach, M. Meyer, C. Coquelet-Pascal, M. Tiphine, G. Krivtchik, and C. Cany. New developments and prospects on COSI, the simulation software for fuel cycle analysis. In *Global 2013*, 2013.

[C.4] ANDRA. Rapport de synthèse, inventaire national des matières et déchets radioactifs. Technical report, ANDRA, 2012.

[C.5] B. Fontaine, N. Devictor, P. Le Coz, A. Zaetta, D. Verwaerde, and J-M. Hamy. The French R&D on SFR core design and ASTRID Project. In *Proceedings of GLOBAL2011, Paper No. 432757*, 2011.

[C.6] Djamel Azzoug. *Etude phénoménologique du comportement des combustibles au plutonium dans les cycles de réacteurs à eau. Elaboration d'un modèle d'équivalence des plutoniums.* PhD thesis, Université de Paris-Sud, Centre d'Orsay, 1990.

Résumé : Les études des scénarios électronucléaires modélisent le fonctionnement d'un parc nucléaire sur une période de temps donnée. Elles permettent la comparaison de différentes options d'évolution du parc nucléaire et de gestion des matières du cycle, depuis l'extraction du minerai jusqu'au stockage ultime des déchets, en se basant sur des critères tels que les puissances installées par filière, les inventaires et les flux, en cycle et aux déchets. Les incertitudes sur les données nucléaires et les hypothèses de scénarios (caractéristiques des combustibles, des réacteurs et des usines) se propagent le long des chaînes isotopiques lors des calculs d'évolution et au cours de l'historique du scénario, limitant la précision des résultats obtenus. L'objet du présent travail est de développer, implémenter et utiliser une méthodologie stochastique de propagation d'incertitudes dans les études de scénario. La méthode retenue repose sur le développement de métamodèles de calculs d'irradiation, permettant de diminuer le temps de calcul des études de scénarios et de prendre en compte des perturbations des paramètres du calcul, et la fabrication de modèles d'équivalence permettant de tenir compte des perturbations des sections efficaces lors du calcul de teneur du combustible neuf. La méthodologie de calcul de propagation d'incertitudes est ensuite appliquée à différents scénarios électronucléaires d'intérêt, considérant différentes options d'évolution du parc REP français avec le déploiement de RNR.

Mots clés : cycle du combustible, modèle d'équivalence, irradiation, refroidissement, métamodèle, propagation d'incertitudes, données nucléaires

Abstract: Nuclear scenario studies model nuclear fleet over a given period. They enable the comparison of different options for the reactor fleet evolution, and the management of the future fuel cycle materials, from mining to disposal, based on criteria such as installed capacity per reactor technology, mass inventories and flows, in the fuel cycle and in the waste. Uncertainties associated with nuclear data and scenario parameters (fuel, reactors and facilities characteristics) propagate along the isotopic chains in depletion calculations, and throughout the scenario history, which reduces the precision of the results. The aim of this work is to develop, implement and use a stochastic uncertainty propagation methodology adapted to scenario studies. The method chosen is based on development of depletion computation surrogate models, which reduce the scenario studies computation time, and whose parameters include perturbations of the depletion model; and fabrication of equivalence model which take into account cross-sections perturbations for computation of fresh fuel enrichment. Then the uncertainty propagation methodology is applied to different scenarios of interest, considering different options of evolution for the French PWR fleet with SFR deployment.

Keywords: nuclear fuel cycle, equivalence model, depletion, cooling, surrogate model, uncertainty propagation, nuclear data